

UNCLASSIFIED

AD NUMBER

AD857475

NEW LIMITATION CHANGE

TO

**Approved for public release, distribution
unlimited**

FROM

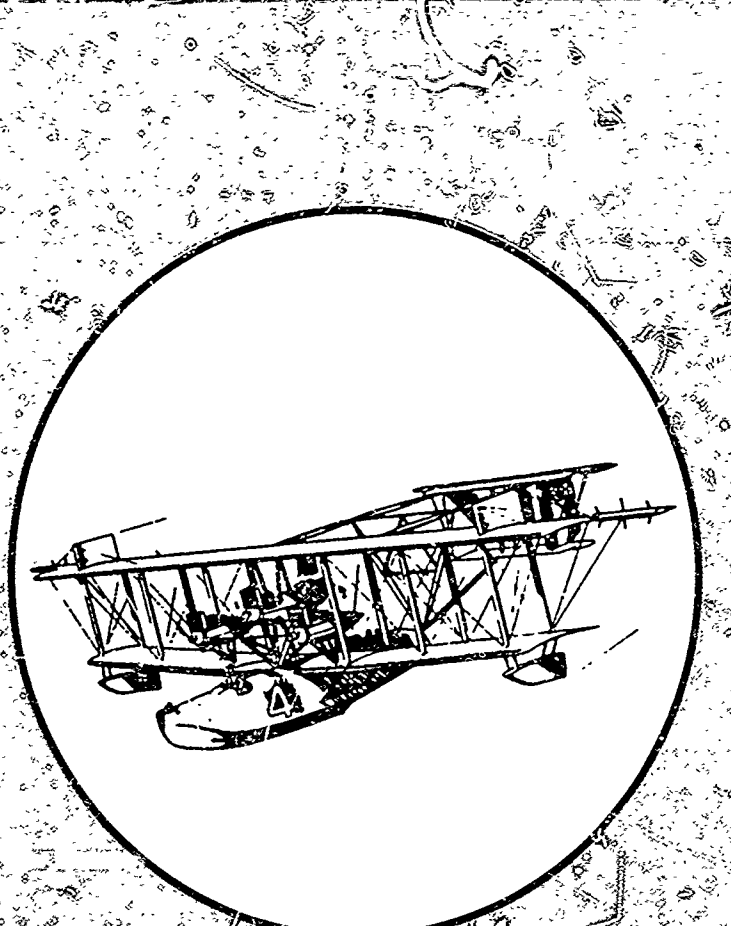
**Distribution authorized to U.S. Gov't.
agencies and their contractors; Critical
Technology; JUN 1969. Other requests shall
be referred to Naval Weapons Center, China
Lake, CA.**

AUTHORITY

USNWC ltr dtd 30 Aug 1974

THIS PAGE IS UNCLASSIFIED

AD 852425



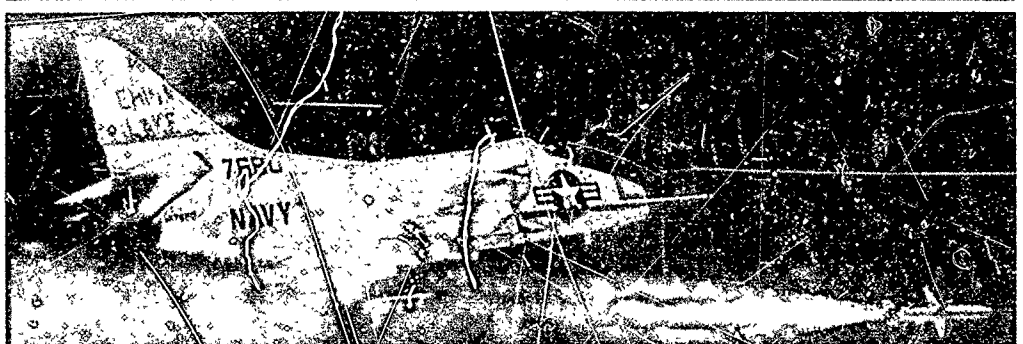
PROCEEDINGS OF THE
8TH NAVY SYMPOSIUM
ON AEROBALLISTICS

SEP 2 1969

VOLUME 3

6, 7, 8 MAY 1969

NAVAL WEAPONS CENTER • Corona Laboratories • Corona, California



SPONSORED BY THE NAVAL AEROBALLISTICS ADVISORY COMMITTEE
FOR THE
NAVAL AIR SYSTEMS COMMAND • NAVAL ORDNANCE SYSTEMS COMMAND

DISTRIBUTION STATEMENT

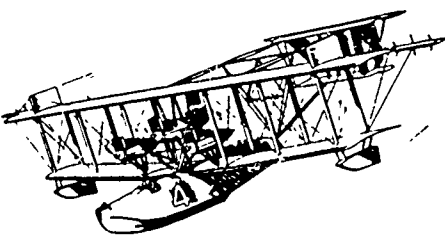
THIS DOCUMENT IS SUBJECT TO SPECIAL EXPORT CONTROLS AND EACH TRANSMITTAL
TO FOREIGN GOVERNMENTS OR FOREIGN NATIONALS MAY BE MADE ONLY WITH
PRIOR APPROVAL OF THE NAVAL WEAPONS CENTER.

PROCEEDINGS OF THE
8TH NAVY SYMPOSIUM
ON AEROBALLISTICS

VOLUME 3

6, 7, 8 MAY 1969

NAVAL WEAPONS CENTER • Corona Laboratories • Corona, California



SPONSORED BY THE NAVAL AEROBALLISTICS ADVISORY COMMITTEE
FOR THE
NAVAL AIR SYSTEMS COMMAND•NAVAL ORDNANCE SYSTEMS COMMAND

DISTRIBUTION STATEMENT

THIS DOCUMENT IS SUBJECT TO SPECIAL EXPORT CONTROLS
AND EACH TRANSMITTAL TO FOREIGN GOVERNMENTS OR
FOREIGN NATIONALS MAY BE MADE ONLY WITH PRIOR
APPROVAL OF THE NAVAL WEAPONS CENTER.

NAVAL WEAPONS CENTER • CHINA LAKE, CALIFORNIA
JUNE 1969

FOREWORD

These *Proceedings*, published in five volumes, comprise the 49 papers presented at the Eighth Navy Symposium on Aeroballistics held at the Naval Weapons Center Corona Laboratories, Corona, Calif., 6, 7, and 8 May 1969.

This symposium was the eighth in a series begun in 1950 under the sponsorship of the then Bureau of Ordnance Committee on Aeroballistics, and currently conducted by the Naval Aeroballistics Advisory Committee as sponsoring committee for the Naval Air Systems Command and the Naval Ordnance Systems Command. The continuing purpose of the symposiums has been to disseminate the results of aeroballistics research and to bring the research findings of industry, the universities, and government laboratories to bear upon the Navy's aeroballistics research and development programs.

Over 200 research scientists representing more than 72 organizations attended this eighth symposium. Sessions 1 and 2 covered the subjects of heat transfer and aerophysics, nozzles and jet effects; Sessions 3 and 4 were concerned with aerodynamics and missile stability; and Session 5 dealt with structures and aeroelasticity, and external carriage and store separation.

The papers in these *Proceedings* have been reproduced in facsimile. They appear in the order of presentation except that all classified papers have been taken out of sequence and grouped together as Volume 5, a confidential volume. Volumes 1 through 4 are unclassified. This is Volume 3.

Requests for or comments on individual papers should be addressed to the respective authors.

RAY W. VAN AKEN
General Chairman
Symposium Committee

Published by the Publishing Division of the Technical Information Department, NWC; first printing, June 1969, 250 copies.

8th Navy Symposium on Aeroballistics

Vol. 3

CONTENTS

Volume 1

Paper		Page
Authors		viii
Greetings		ix
Welcome		x
Introductory Remarks, Rear Admiral R. J. Schneider, USN		xi
U.S. Navy Symposiums on Aeroballistics		xiii
Naval Aeroballistics Advisory Committee		xiv
Paper Selection Committee		xv
Attendees		xvi
1 Base and Lee Side Flow Studies of Slender Bodies at High Angles of Attack by George S. Pick		1
2 An Experimental Investigation of the Hypersonic Aerodynamic Characteristics of Slender Bodies of Revolution at High Angles of Attack by Robert Feldhuhn, Allen Winkelmann and Lionel Pasiuk		29
3 Analytical Investigation on Laminar Flow Field and Heat Transfer on Leeward Side of a Sharp Nosed Hypersonic Cone at Large Angle of Attack by Paul K. Chang, Mario J. Casarella, and Russell A. Smith		95
4 Pressure Distribution on Bodies at Large Angle of Attack by Howard R. Kelly		129
5 Compact Gas-Transpiration Cooling System Analysis by R. W. Allen and R. W. Newman		153
6 Experimental Investigation of Transpiration Cooling Near the Stagnation Point of a Cylinder by Richard L. Humphrey		181
7 Ballistics Range Experiments on the Effect of Unit Reynolds Number on Boundary-Layer Transition by Norman W. Sheetz, Jr.		201
8 Calculation of Blunt Body Flows Using Padé Fractions and the Method of Characteristics by Andrew H. Van Tuyl		215

Volume 2

9 Applications of the Time-Dependent Technique for the Computation of Compressible Flows by John D. Anderson, Jr., Lorenzo M. Albacete and Allen E. Winkelmann ..	239
10 Nonequilibrium Flow Over Blunt Bodies Using Method of Integral Relations by T. C. Tai	267
11 Supersonic Laminar and Turbulent Ablation Studies With Teflon by E. M. Winkler, R. L. Humphrey, J. A. Koenig, and M. T. Madden ..	311
12 Recent Progress in the Calculation of Turbulent Boundary Layers by Tuncer Cebeci, A.M.O. Smith, and G. Mosinskis	351
13 An Experimental Investigation of the Compressible Turbulent Boundary Layer With a Favorable Pressure Gradient by William J. Yanta, David L. Brott, Robert L. Voisin, and Roland E. Lee ..	389
14 An Experimental Reynolds Analogy for the Highly Cooled Turbulent Boundary Layer by Donald M. Wilson	411
15 The Effect of Flow Field Irregularities on Swept Leading Edge Heat Transfer by Albert F. Gollnick	441
16 An Experimental Study of Mass Addition Effects in the Near Wake by Norman G. Paul, H. J. Unger, F. K. Hill, and J. M. Cameron	473

8th Navy Symposium on Aeroballistics

Vol. 3

Paper	Page
17 Isothermal Leading Edges by Bertram K. Ellis	507
18 Spikes as a Means of Reducing Drag and Rain Erosion of Blunt Bodies at Supersonic Speeds by Isidor C. Patapis	531

Volume 3

21 Research on an Asymmetric Glide Reentry Vehicle by Herbert R. Little, Robert H. Burt, and Jerry Coble	545
24 An Analysis of a Slewed-Launch Technique for Air-Launched Missiles by Eugene E. Kluth	587
26 Stabilization of a Liquid-Filled Shell by Inserting a Cylindrical Partition in the Liquid Cavity by John T. Frasier and William P. D'Amico	629
27 Effects of Roll on the Free-Flight Motion of Bodies by C. J. Welsh and R. M. Watt	651
28 Dynamic Stability of the 5-Inch/54 Rocket Assisted Projectile (The Influence of a Non-Linear Magnus Moment) for Eighth United States Navy Symposium on Aeroballistics by W. R. Chadwick	671
29 The University of Virginia Cold Magnetic Wind Tunnel Balance by Hermon M. Parker and Ricardo N. Zapata	695
30 Wind Tunnel Measurements of the Aerodynamic Characteristics of the 2.75 Wraparound Fin Rocket Using a Magnetic Suspension System by Milivoj Vlajinac	717
31 Nonlinear Aerodynamic Stability Characteristics of the 2.75 Wrap-Around Fin Configuration by John D. Nicolaides, Charles W. Ingram, James M. Martin, and Alfred M. Morrison	751
32 A Study to Eliminate Flight Instabilities on a High-Drag Air Delivered Mine by Jack C. Hopps	833
34 Two-Dimensional Jet-Interaction Experiments Results of Flow-Field and Scale Effect Studies by Michael J. Werle, Richard T. Driftmyer, and David G. Shaffer	865
35 Interaction Between High Speed Flows and Transverse Jets: A Method for Predicting the Resultant Surface Pressure Distribution by Louis G. Kaufman II	885
36 Aerodynamic and Heat Transfer Effects of Saturn V Plume-Induced Flow Separation by Calvin L. Wilkinson	921

Volume 4

38 Structural Qualification of the Low Speed FAE Weapon Dispenser by Jack D. Brannan and Wallace W. Parmenter	941
40 Stiffness Matrix for Missile Structures Using Thin Shell Theory by Pao C. Huang	981
41 An Experimental Investigation of Aircraft/Missile Interference Effects by C. Franklyn Markarian	1005
42 Store Separation From the McDonnell Douglas F-4 Aircraft by David L. Schoch	1025
43 Aircraft/Munitions Compatibility-U.S. Air Force Project "Seek Eagle" by Charles S. Epstein	1077
44 Prediction of Store Launch Characteristics Through Statistical Methods by Michael A. Sekellick	1103
45 External Store Airloads Prediction by R. D. Gallagher and P. E. Browne	1131

8th Navy Symposium on Aeroballistics

Vol. 3

Paper	Page
46 Estimation of Aircraft Store Separation Behavior on the Basis of Captive Load Data by D. A. Jones	1159
47 Prediction of Store Separation Trajectories at the Naval Weapons Center by J. V. Netzer	1185
49 An Analytical, Numerical Program for Calculating the Aerodynamic Forces External to Aircraft by Hyman Serbin	1205

Volume 5 (Classified Papers)

19 The Simulation of Ramjet Configurations With Pod Inlets for Stability and Control Wind Tunnel Testing by James C. Hagan	1213
20 Pitch Control Effectiveness of Flap Controls Mounted on a Body of Revolution by E. F. Lucero	1229
22 Wing-Tail Interference in Hypersonic Missile Configurations by H. H. Hart	1243
23 An Investigation of the Aerodynamic Behavior of Submissiles During Ejection from a High-Speed Rocket by Chris A. Kalivretenos and David N. Bixler	1257
25 Feasibility of Increasing Sidewinder Maneuverability by Means of Enlarged Canards by R. E. Meeker	1277
33 A Summary of the Sonic Lateral Jet Studies With 9-Degree Cones at Mach Numbers 6 to 20 by W. T. Strike	1297
37 Aerodynamic Design of Reaction Jet Controlled Tactical Missiles by L. A. Cassel, D. P. Engh and L. Y. Lam	1337
39 Evaluation of Radomes for Hypersonic Flight by L. B. Weckesser and R. K. Frazer	1371
48 Weapon-Aircraft Separation: A Review of a Particular Weapon Problem by R. E. Smith	1401

8th Navy Symposium on Aeroballistics

Vol. 3

AUTHORS

Albacete, Lorenzo M., Paper No. 9	239	Lucero, E. F., Paper No. 20	1229
Allen, R. W., Paper No. 5	153	Madden, M. T., Paper No. 11	311
Anderson, John D., Jr., Paper No. 9	239	Markarian, C. Franklyn, Paper No. 41	1005
Bixler, David N., Paper No. 23	1257	Martin, James M., Paper No. 31	751
Brannan, Jack D., Paper No. 38	941	Meeker, R. E., Paper No. 25	1277
Brott, David L., Paper No. 13	389	Morrison, Alfred M., Paper No. 31	751
Browne, P. E., Paper No. 45	1131	Mosinskis, Gediminas J., Paper No. 12	351
Burt, Robert H., Paper No. 21	545	Netzer, J. V., Paper No. 47	1185
Cameron, J. M., Paper No. 16	473	Newman, R. W., Paper No. 5	153
Casarella, Mario J., Paper No. 3	95	Nicolaides, John D., Paper No. 31	751
Cassel, L. A., Paper No. 37	1337	Parker, Hermon M., Paper No. 29	695
Cebeci, Tuncer, Paper No. 12	351	Parmenter, Wallace W., Paper No. 38	941
Chadwick, William R., Paper No. 28	671	Pasiuk, Lionel, Paper No. 2	29
Chang, Paul K., Paper No. 3	95	Patapis, Isidor, Paper No. 18	531
Coble, Jerry G., Paper No. 21	545	Paul, N. G., Paper No. 16	473
D'Amico, W. P., Paper No. 26	629	Pick, George S., Paper No. 1	1
Driftmyer, Richard T., Paper No. 34	865	Schoch, David L., Paper No. 42	1025
Ellis, Bertram K., Paper No. 17	507	Sekellick, Michael A., Paper No. 44	1103
Engh, D. P., Paper No. 37	1337	Serbin, Hyman, Paper No. 49	1205
Epstein, Charles S., Paper No. 43	1077	Shaffer, David G., Paper No. 34	865
Feldhuhn, Robert, Paper No. 2	29	Sheetz, Norman W., Jr., Paper No. 7	201
Frasier, J. T., Paper No. 26	629	Smith, A. M. O., Paper No. 12	351
Frazer, R. K., Paper No. 39	1371	Smith, R. E., Paper No. 48	1401
Gallagher, R. D., Paper No. 45	1131	Smith, Russell A., Paper No. 3	95
Gollnick, Albert F., Jr., Paper No. 15	441	Strike, William T., Jr., Paper No. 33	1297
Hagan, J. C., Paper No. 19	1213	Tai, T. C., Paper No. 10	267
Hart, H. H., Paper No. 22	1243	Unger, H. J., Paper No. 16	473
Hill, F. K., Paper No. 16	473	Van Tuyl, Andrew H., Paper No. 8	215
Hopps, J. C., Paper No. 32	833	Vlajinac, Milan, Paper No. 30	717
Huang, Pao C., Paper No. 40	981	Voisinet, Robert L. P., Paper No. 13	389
Humphrey, Richard L., Paper No. 6, 11, 181, 311		Watt, R. M., Paper No. 27	651
Ingram, Charles W., Paper No. 31	751	Weckesser, L. B., Paper No. 39	1371
Jones, D. A., Paper No. 46	1159	Welsh, C. J., Paper No. 27	651
Kalivretenos, Chris A., Paper No. 23	1257	Werle, Michael J., Paper No. 34	865
Kaufman, Louis G., II, Paper No. 35	885	Wilkinson, Calvin L., Paper No. 36	921
Kelly, Howard R., Paper No. 4	129	Wilson, Donald M., Paper No. 14	411
Kluth, Eugene E., Paper No. 24	587	Winkelmann, Allen E., Paper No. 2, 9	29, 239
Koenig, J. A., Paper No. 11	311	Winkler, Eva M., Paper No. 11	311
Lam, L. Y., Paper No. 37	1337	Yanta, William J., Paper No. 13	389
Lee, Roland E., Paper No. 13	389	Zapata, Ricardo N., Paper No. 29	695
Little, Herbert R., Paper No. 21	545		

Paper No. 21

RESEARCH ON AN ASYMMETRIC GLIDE REENTRY VEHICLE*

(U)

(Paper UNCLASSIFIED)

by

Herbert R. Little, Robert H. Burt, and Jerry Coble
ARO, INC.
Arnold Air Force Station, Tenn. 37389

ABSTRACT. (U) The results of an experimental study of 9-deg cones having canted bases are presented. Force and static stability data, obtained at Mach numbers from 6 to 21, provide the basis for predicting the behavior of the asymmetric vehicle under continuum hypersonic laminar conditions. Newtonian impact theory, used as the inviscid, high Mach number limit, is demonstrated to be quite accurate in describing behavioral characteristics when variations in nose bluntness and base cant angle occur.

(U) Detailed evidence for the full cone (no base cant) is presented to show that Mach number influence is negligible at Mach numbers above 10; similar behavior is shown in summary form for the asymmetric body. At Mach number 10, the effects of nose transpiration cooling on forces and moments are shown; there is evidence that a substantial change in trim angle could occur on the asymmetric body with blowing. Base pressures for sting-mounted models are shown to be constant when the base cant varies; however, there are changes in aerodynamic forces and moments as a result of the canted base.

*The work reported herein was supported by the Arnold Engineering Development Center, Air Force Systems Command, under Contract F40600-69-C-0001 with ARO, Inc. Further reproduction is authorized to satisfy needs of the U. S. Government.

8th Navy Symposium on Aeroballistics

Vol. 3

NOMENCLATURE

A_b	Axial projection of the model base area, in. ²
c.g.	Center of gravity
C_{A_b}	Base axial-force coefficient, $-(p_b - p_\infty) A_b / q_\infty S$
C_{A_f}	Total axial-force coefficient, total axial force/ $q_\infty S$
C_i	Normalized mass injection rate, $\dot{m} / p_\infty U_\infty S$
C_l	Rolling-moment coefficient about body x-axis, rolling moment/ $q_\infty S D_b$
C_m^t	Pitching-moment coefficient referenced as shown in Fig. 1a, pitching moment/ $q_\infty S D_b$
C_n^t	Yawing-moment coefficient about moment reference (see Fig. 1a), yawing moment/ $q_\infty S D_b$
C_N^t	Normal-force coefficient, normal force/ $q_\infty S$
C_Y^t	Side-force coefficient, side force/ $q_\infty S$
C_∞	Constant of proportionality in linear viscosity law, $(T_\infty / T_w)(\mu_w / \mu_\infty)$
D_b	Moment coefficient reference length, $2R_b$, in.
H	Stagnation enthalpy, Btu/lb
K	Proportionality constant used in the Newtonian theory
ℓ	Blunted cone length, in.
L	Sharp cone length, in.
L/D	Lift-to-drag ratio based on C_{A_f}
\dot{m}	Mass injection rate, lb/sec
M	Mach number
p_b	Model base pressure, lb/in. ²

8th Navy Symposium on Aeroballistics

Vol. 3

p	Pressure, lb/in ²
p'_0	Total pressure behind a normal shock at free-stream conditions, lb/in ²
q	Dynamic pressure, lb/in ²
R_b	Cone base radius, in. (see Fig. 1)
Re_∞	Free-stream Reynolds number per foot, ft ⁻¹
$Re_{\infty,l}$	Free-stream Reynolds number based on model length
R_n	Model nose radius, in.
S	Coefficient reference area, πR_b^2 , in ²
T	Temperature, °K
U	Velocity, ft/sec
\bar{v}_∞	Hypersonic viscous parameter, $M_\infty (C_\infty / Re_{\infty,l})^{1/2}$
X, Y, Z ; X', Y', Z' ; X_T, Y_T, Z_T	Orthogonal body, aeroballistic, and wind axes respectively
x	Distance from model apex to forward extremity of the model base, in. (see Fig. 1a)
x_{cp}	Center-of-pressure location
x_2	Limit of integration used in the Newtonian theory as defined in Eqs. 1a and 1b
α'	Total angle of attack, degrees
$\Delta\phi$	Integration stepsize used in the Newtonian theory, degrees
θ_c	Cone half angle, degrees
ρ	Mass density, lb/ft ³ , or the coordinate which defines the distance from the model apex to a position on the body surface as used in the Newtonian theory, in.
μ	Viscosity, lb/ft-sec

8th Navy Symposium on Aeroballistics

Vol. 3

σ Asymmetric base cant angle, degrees

ϕ' Aerodynamic roll angle and angular coordinate which defines circumferential position in a cross-sectional plane as used in Newtonian theory, degrees

ϕ'_a, ϕ'_b Limits of integration, used in Newtonian theory as defined in Eqs. 5a and 5b

ϕ'_2 Angle defining circumferential position where the model surface becomes shielded from the flow, used in the Newtonian theory (see Eqn. 5), degrees

ψ Nose bluntness ratio, R_n/R_b

SUBSCRIPTS

o Free-stream stagnation conditions

w Wall conditions

∞ Free-stream conditions

SUPERSCRIPT

$'$ Refers force and moment coefficients to aeroballistic axis system. All unprimed values are in standard body axis system.

INTRODUCTION

(U) The use of slender cones for reentry vehicles is widespread since these configurations are generally characterized by low drag and relatively high volumetric efficiency. Usually the cones are symmetric for non-maneuvering reentry whereas flaps or fins are employed to obtain the moments necessary for maneuvering. These control devices can accomplish the desired moments either by using large control surfaces and small deflections or small control surfaces and large deflections. The first method is generally plagued with structural problems where the second method presents aerodynamic heating problems generated by the large deflections. In an attempt to minimize these problems the present study is concerned with the high Mach number behavior of a cone rendered asymmetric by canting the base, and the selected results are taken from a recent study at AEDC. The complete results of this study will be published as an AEDC Technical Report.

(U) The symmetric cone can be trimmed at angles of attack by shifting the center of gravity (c.g.) laterally, however with slender cones the lateral dimensions are small and the lateral c.g. shift is very limited. Canting the base is one method considered for producing the moments necessary to trim the vehicle at an angle of attack, preferably near the angle of attack corresponding to its peak lift-to-drag ratio. It was discovered after this study had been initiated that a similar vehicle had been studied experimentally by Varwig and Mason (Ref. 1) and Ellinwood and Varwig (Ref. 2) for a 7-deg half-angle cone and one base cant angle ($\sigma = 30$ deg).

(U) The basic model in the present study is a 9-deg half-angle cone on which the effects of nose bluntness ($\psi = 0.05, 0.10$, and 0.15) and base cant ($\sigma = 22.5$ and 45 deg) are investigated. Data were also obtained on the basic cone ($\sigma = 0$) for comparison with the canted base data. The data presented are primarily experimental and were obtained at Mach numbers from 6 to 21 and several Reynolds numbers in order to determine both Mach number and viscous effects. In general, data were obtained on each configuration at angles of attack from 0 to 25 deg and model roll angles from 0 to 180 deg (22.5 deg increments). The test matrix, however, is more complete at the lower Mach numbers (6, 8, and 10) where the majority of the data were obtained. An analysis using Newtonian impact theory is performed in order to better assess the data trends obtained at high Reynolds number.

8th Navy Symposium on Aeroballistics

Vol. 3

(U) Base pressure distributions are presented from a detailed investigation of base pressure measurements on the extreme base cant ($\sigma = 45$ deg) at Mach number 10. Limited data were obtained on the full cone to determine the effects of nose transpiration on the force and stability characteristics (using nitrogen as the injected gas).

(U) For convenience the test body will be referred to by the acronym AGRV (Asymmetric Glide Reentry Vehicle).

TEST APPARATUS

(U) The experimental data were obtained in three of the VKF hypersonic wind tunnels. The Gas Dynamic Wind Tunnels, Hypersonic (B and C), are closed circuit, continuous operation facilities having axisymmetric contoured nozzles expanding to 50-in diameter test sections. Each tunnel has two interchangeable throat sections to produce Mach 6 or 8 (Tunnel B) and Mach 10 or 12 (Tunnel C) flows. Varying supply pressures yield a range of Reynolds numbers. A special feature of each tunnel is a model injection system whereby the model may be injected into or removed from the test section without interrupting the tunnel flow. Further descriptions of the continuous flow tunnels are included in Ref. 3 and extensive details of their design and calibrations are presented in Ref. 4.

(U) Tunnel F is an electric arc-heated impulse hypersonic wind tunnel of the Hotshot type developed at AEDC. The test gas, nitrogen or air, is initially confined in an arc chamber by a diaphragm located near the throat of a convergent-divergent nozzle. The gas is heated and compressed by an electric arc discharge resulting in rupture of the diaphragm and subsequent expansion through a 4-deg half-angle conical nozzle to a maximum 108-in diameter test section. Testing is possible at either the maximum diameter for Mach numbers from 13 to 21 or at the 54-in diameter station for Mach numbers 10 to 15. Useful run times between 50 and 200 msec are obtained. A recent innovation in Tunnel F testing is the addition of a free-jet test section immediately downstream of the arc chamber for studies of ablation and cross-hatching. Models having diameters of about 4 in can be tested at Mach numbers from 5 to 10 under laminar or turbulent conditions. Reference 3 includes a description of Tunnel F, and Refs. 5 and 6 include detailed descriptions of the testing techniques and tunnel calibrations.

(U) Differing test techniques required separate models for the continuous-flow tunnels and the impulse tunnel. The model nomenclature and basic dimensions of all models are shown in Fig. 1a. The Tunnel B and C basic model was a 9-deg half-angle cone with an 8-in base diameter machined from 303 stainless steel. This model had inter-

changeable noses to provide bluntness ratios of 0.05, 0.10, and 0.15, and interchangeable bases to provide base cant angles of 22.5 and 45 deg as well as the basic cone (Fig. 1b). The 45-deg base was later instrumented with 14 pressure orifices (0.063-in diam) for the base pressure distribution test.

(U) In Tunnel F, the model weight had to be minimized to reduce dynamic effects; thus the basic construction was of balsa with an epoxy sheath to protect the model surface. The base diameter of the basic cone was 3.5 in and three separate models were fabricated to provide the full cone and canted bases (Fig. 1c) each having a bluntness ratio of 0.05.

INSTRUMENTATION

(U) Six-component, internal, strain gage balances (acceleration compensated in Tunnel F) were used to measure the forces and moments. Only the balance used for the standard force test in Tunnel C had sufficient sensitivity to measure the rolling moments with an acceptable degree of accuracy. For this reason only Mach number 10 rolling moment data are presented.

(U) Base pressures were monitored by single balance cavity pressure measurements. Full base pressure distributions were obtained at Mach 10 for the extreme base cant ($\sigma = 45$ deg) to substantiate these measurements.

(U) A special balance was used for the mass injection tests in Tunnel C which allowed the injectant gas to pass through the center of the balance and into the model through stainless steel bellows designed and arranged so as to isolate the balance from the injectant pressure. The large size of the water jacket (3.25 in diam) required for the mass injection balance prevented its use on the models with canted bases. Injection mass flow rates (\dot{m}) were monitored using sonic orifice plates which are a standard feature of the Tunnel C mass injection system. The accuracy of the mass flow rate measurements is estimated to be within ± 1 percent for this system.

TEST CONDITIONS

(U) The moderate pressures and temperatures necessary for the Mach number 6 and 8 flows in Tunnel B allow the use of perfect-gas relationships to determine free-stream and post-shock conditions. Measured quantities are reservoir pressure and temperature (in conjunction with calibrations).

8th Navy Symposium on Aeroballistics

Vol. 3

(U) In Tunnel C, reservoir pressures and temperatures are sufficiently high to require the use of real gas properties to calculate test section conditions. The Beattie-Bridgeman equation of state is used in the form presented in Ref. 7. In addition to reservoir pressure and temperature, a test section pitot pressure measurement is made periodically to monitor the flow conditions.

(U) In Tunnel F, very high temperatures and pressures demand specialized techniques to define the free-stream flows. Timewise measurements of reservoir pressure, test section pitot pressure and hemisphere-cylinder stagnation point heat-transfer rate are used in conjunction with Fay-Riddell heat-transfer theory (Ref. 8) to determine reservoir enthalpy and free-stream conditions as described in Ref. 9. Validation of the method of calculation is given in Ref. 10.

(U) A complete listing of all test conditions is summarized in Table I.

PRECISION

(U) Considering the vast amount of instrumentation used on these tests and the large number of test entries, each requiring different instrumentation, it would be extremely difficult to present the estimated precision for all data. The following table is presented to show the maximum expected deviations in the measurements considering all the data. On some entries the precision was much better than indicated in the table.

Coefficient	C_N^t	C_m^t	C_{A_t}	C_Y^t	C_n^t	C_d	$X_{c.p.}$	p_b/p_∞
Uncertainty								
Tunnel B,C	$\pm .006$	$\pm .003$	$\pm .003$	$\pm .006$	$\pm .003$	$\pm .0002$	$\pm .015\%$	$\pm 10\%$
Tunnel F	$\pm .02$	$\pm .008$	$\pm .01$	$\pm .02$	$\pm .008$	---	$\pm 1.0\%$	$\pm 20\%$

NEWTONIAN IMPACT THEORY

(U) For axisymmetric reentry shapes it has been shown extensively that the Newtonian impact theory can readily provide good estimates of normal force, pitching moment, and center-of-pressure location but it underpredicts axial force and consequently gives optimistic estimates of the lift-drag ratio; (see for example, Refs. 11 and 12).

(U) A study was conducted to apply the Newtonian theory to the present asymmetric body. The general equations as set forth by Clark and Trimmer, Ref. 13, were modified to handle the base cant. A reference sketch showing the nomenclature is shown in Fig. 2. The modification consisted of changing the upper limit, X_2 on the ρ integration.

For $0 \leq \alpha' \leq \theta_c$ the limit becomes:

$$X_2 = (R_b/\tan \theta_c - R_b \tan \sigma) \left\{ -\cos(\pi - \theta_c) - [\tan \sigma \sin(\pi - \theta_c)] \right. \\ \left. \left[\cos \left(-\frac{\pi}{2} + \frac{\pi}{\Delta \phi'} \right) \right] + \tan \sigma \sin(\pi - \theta_c) \cos \phi' \sin \left(-\frac{\pi}{2} + \frac{\pi}{\Delta \phi'} \right) \right\}^{-1} \quad (1a)$$

and for $\theta_c < \alpha' \leq \frac{\pi}{2} - \theta_c$

$$X_2 = (R_b/\tan \theta_c - R_b \tan \sigma) \left\{ -\cos(\pi - \theta_c) - [\tan \sigma \sin(\pi - \theta_c)] \right. \\ \left. \left[\cos \left(-\sin^{-1} \left[\frac{\tan \theta_c}{\tan \alpha'} \right] + \frac{\pi + 2 \sin^{-1} \left[\frac{\tan \theta_c}{\tan \alpha'} \right]}{2\Delta \phi'} \right) \right] + [\tan \sigma \sin(\pi - \theta_c)] \right. \\ \left. \left[\cos \phi' \sin \left(-\sin^{-1} \left[\frac{\tan \theta_c}{\tan \alpha'} \right] + \frac{\pi + 2 \sin^{-1} \left[\frac{\tan \theta_c}{\tan \alpha'} \right]}{2\Delta \phi'} \right) \right] \right\}^{-1} \quad (1b)$$

The equations, which may be integrated numerically, are:

Normal-Force Coefficient

$$0 \leq \alpha' \leq \theta_c$$

$$C'_N = \frac{K}{S} \left[\int_{-\pi/2}^{\frac{3\pi}{2}} \int_{\frac{R_n}{\tan \theta_c}}^{X_2} \left(\cos^2 \alpha' \sin^3 \theta_c \cos \theta_c \sin \phi' + (2 \sin \alpha' \cos \alpha' \sin^2 \theta_c) \right. \right. \\ \left. \left. (\cos^2 \theta_c \sin^2 \phi') + \sin^2 \alpha' \sin \theta_c \cos^3 \theta_c \sin^3 \phi' \right) \rho d\rho d\phi' + \frac{\pi R_n^2}{2} \right. \\ \left. \cos \alpha' \sin \alpha' \cos^4 \theta_c \right] \quad (2a)$$

8th Navy Symposium on Aeroballistics

Vol. 3

$$\underline{\theta_C < \alpha' \leq (\pi/2 - \theta_C)}$$

$$C_N' = \frac{K}{S} \left[\int_{\phi'_2}^{\pi - \phi'_2} \int_{\frac{R_n}{\tan \theta_C}}^{X_2} \left(\cos^2 \alpha' \sin^3 \theta_C \cos \theta_C \sin \phi' + (2 \sin \alpha' \cos \alpha' \sin^2 \theta_C) \right. \right. \\ \left. \left. (\cos^2 \theta_C \sin^2 \phi') + \sin^2 \alpha' \sin \theta_C \cos^3 \theta_C \sin^3 \phi' \right) \rho d\rho d\phi' + \frac{R_n^2 \sin \alpha'}{2} \right. \\ \left. \left\{ \cos^{-1} \left(\frac{\sin \theta_C}{\sin \alpha'} \right) + \cos \alpha' \cos^4 \theta_C \left[\pi/2 + \sin^{-1} \left(\frac{\tan \theta_C}{\tan \alpha'} \right) \right] + \frac{\sin \theta_C}{3} \right. \right. \\ \left. \left. \left[\sin^2 \theta_C \left(3 - \frac{1}{\sin^2 \alpha'} - 5 \right) \right] \sqrt{\sin^2 \alpha' - \sin^2 \theta_C} \right\} \right] \quad (2b)$$

Axial-Force Coefficient

$$\underline{0 \leq \alpha' \leq \theta_C}$$

$$C_{Af} = \frac{K}{S} \left[\int_{-\pi/2}^{\frac{3\pi}{2}} \int_{\frac{R_n}{\tan \theta_C}}^{X_2} \left(\cos^2 \alpha' \sin^4 \theta_C + (2 \sin \alpha' \cos \alpha' \sin^3 \theta_C) \right. \right. \\ \left. \left. (\cos \theta_C \sin \phi') + \sin^2 \alpha' \sin^2 \theta_C \cos^2 \theta_C \sin^2 \phi' \right) \rho d\rho d\phi' \right. \\ \left. + \left(\frac{\pi R_n}{2} \right) \left(\frac{\sin \alpha' \cos^4 \theta_C}{2} - \cos^2 \alpha' \sin^4 \theta_C + \cos^2 \alpha' \right) \right] \quad (3a)$$

$$\theta_C < \alpha' \leq (\pi/2 - \theta_C)$$

$$\begin{aligned}
 C_{A+} = & \frac{K}{S} \left[\int_{\phi'/2}^{\pi-\phi'/2} \int_{R_n}^{X_2} \frac{(\cos^2 \alpha' \sin^4 \theta_C + 2 \sin \alpha' \cos \alpha' \sin^3 \theta_C \cos \theta_C \sin \phi' \right. \\
 & \left. + \sin^2 \alpha' \sin^2 \theta_C \cos^2 \theta_C \sin^2 \phi') \rho d\rho d\phi' + \frac{R_n^2}{2} \left\{ \cos \alpha' \cos^{-1} \left(\frac{\sin \theta_C}{\sin \alpha'} \right) \right. \right. \\
 & \left. + \left(\frac{\sin^2 \alpha' \cos^4 \theta_C}{2} - \cos^2 \alpha' \sin^4 \theta_C + \cos^2 \alpha' \right) \left[\frac{\pi}{2} + \sin^{-1} \left(\frac{1}{\tan \alpha' \cot \theta_C} \right) \right] \right. \\
 & \left. + \frac{\cos \alpha' \sin \theta_C}{2} (1 - 3 \sin^2 \theta_C) \sqrt{\sin^2 \alpha' - \sin^2 \theta_C} \right] \quad (3b)
 \end{aligned}$$

Pitching-Moment Coefficient

$$\begin{aligned}
 0 \leq \alpha' \leq \theta_C
 \end{aligned}$$

$$\begin{aligned}
 C_m^1 = & \frac{2X}{3D_b} C_N^1 - \frac{KR_n^3}{SD_b} \frac{\pi}{2} \sin \alpha' \cos \alpha' \frac{\cos^4 \theta_C}{\sin \theta_C} - \frac{K}{SD_b} \left\{ \int_{-\pi/2}^{\frac{3\pi}{2}} \int_{R_n}^{X_2} (\sin \phi' \cos^2 \theta_C \right. \\
 & \left. + \sin^2 \theta_C) (\cos^2 \alpha' \sin^3 \theta_C + 2 \sin \alpha' \cos \alpha' \sin^2 \theta_C \cos \theta_C \sin \phi' \right. \\
 & \left. + \sin^2 \alpha' \sin \theta_C \cos^2 \theta_C \sin \phi') \rho^2 d\rho d\phi' \right\} \quad (4a)
 \end{aligned}$$

$$\theta_c < \alpha' \leq (\pi/2 - \theta_c)$$

$$C_m' = \frac{2X}{3D_b} C_N' - \frac{kR_n^3}{2SD_b} \frac{\sin \alpha'}{\sin \theta_c} \left\{ \cos^{-1} \left(\frac{\sin \theta_c}{\sin \alpha'} \right) + \cos \alpha' \cos^4 \theta_c \left[\frac{\pi}{2} + \sin^{-1} \left(\frac{\tan \theta_c}{\tan \alpha'} \right) \right] + \frac{\sin \theta_c}{3} \left[\sin^3 \theta_c \left(3 - \frac{1}{\sin \alpha'} \right) - 5 \right] \sqrt{\sin^2 \alpha' - \sin^2 \theta_c} \right\} - \frac{K}{SD_b}$$

$$\left\{ \int_{\phi'_2}^{\pi - \phi'_2} \int_{R_n / \tan \theta_c}^{x_2} (\sin \phi' \cos^2 \theta_c + \sin^2 \theta_c) (\cos^2 \alpha' \sin^3 \theta_c + 2 \sin \alpha' \cos \alpha' \sin^2 \theta_c \cos \theta_c \sin \phi') \rho^2 d\rho d\phi' \right\} \quad (4b)$$

$$+ 2 \sin \alpha' \cos \alpha' \sin^2 \theta_c \cos \theta_c \sin \phi' + \sin^2 \alpha' \sin \theta_c \cos \theta_c \sin \phi') \rho^2 d\rho d\phi' \}$$

where the beginning of the shadowed region is defined as

$$\phi'_2 = - \sin^{-1} (\tan \theta_c / \tan \alpha'). \quad (5)$$

This theory was used to provide estimates and a basis for data comparison for all the configurations tested. Results of these computations for selected configurations are presented in Fig. 3. It should be noted here that $K = 2.0$ for these computations.

EXPERIMENTAL RESULTS

A great deal of experimental data were obtained in the course of the AGRV study and only summaries of these data are presented. The aeroballistic axis system was used for referencing the force and moment coefficients and model attitude. This system is described in detail in Ref. 14 and is simply an orthogonal system which pitches with the model but remains fixed when the model rolls about its own axial centerline. The coefficients in this system are denoted by prime quantities except rolling moment and axial force which are normal body axis coefficients

and with no roll ($\phi' = 0$) all coefficients correspond to the body-axis system.

(U) The experimental data are compared with the Newtonian predictions in Fig. 4. In Fig. 4a, Newtonian theory is shown to predict the normal force coefficient quite well, however, this theory under-predicts the axial force coefficient as shown in Fig. 4c. It should be noted that Newtonian theory assumes that the free-stream static pressure is present on any surface shielded from the flow. Therefore, the experimental axial force coefficient should be corrected for base pressure in order to make direct comparisons with Newtonian theory. Typical results of a rather detailed investigation on base pressure distributions are presented in Fig. 4d for $\psi = 0.05$, $\sigma = 45$ deg and $M_\infty = 10$. These data show that the base pressure corrections are small at these conditions and do not affect the comparison with theory significantly. The base pressure level expected with the turbulent boundary layers from Ref. 15 is also indicated. Also notice in Fig. 4c that the comparison becomes worse at the higher Mach numbers (also higher \bar{v}_∞); the disparity is caused by viscous effects and will be discussed later.

(U) Lift-to-drag ratios, computed using normal force and total axial force, are presented in Fig. 5a for the basic cone and both canted bases in two attitudes. This figure shows that the maximum L/D actually occurs with the base cant leeward and at a lower angle of attack than with the cant windward. The rolling moments presented in Fig. 5b, however, show that the vehicle is not stable in roll with the cant leeward (vehicle center of gravity assumed to be on axial centerline), but is stable in roll with the cant windward. Note here that the rolling moments were obtained at $M_\infty = 10$, while the L/D and trim characteristics (Fig. 5a) presented were obtained at $M_\infty = 8$. This was necessary since the test matrix was more complete at $M_\infty = 8$, but precise rolling moment measurements were only obtained at $M_\infty = 10$, as previously mentioned. Peak L/D values occurred at $\alpha \approx 12$ deg for both base cant angles with the cant windward. Figure 5c shows that the vehicle with $\sigma = 45$ deg can be trimmed ($C_m^t = 0$) at an angle of attack near the peak L/D ($\alpha \approx 10$ deg), with the c.g. axially located to favor the shortened cone produced by the base cant (see sketch on Fig. 5c). The vehicle with $\sigma = 22.5$ deg is shown to trim at $\alpha \approx 7.5$ deg which is further from its peak L/D, but the magnitude of L/D at trim is about the same as for $\sigma = 45$ deg. This occurs because the peak L/D values are different for the two vehicles. An adverse effect on trim angle caused by nose blunting is indicated in Fig. 5d.

(U) The vehicle with $\sigma = 45$ deg was selected to show the effect of roll angle on the aerodynamic characteristics at an angle of attack near its trim angle, 10-deg. These results are shown in Fig. 6a (C_N^t , C_m^t and L/D) and Fig. 6b (C_Y^t , C_n^t and C_{A+}). Newtonian predictions

8th Navy Symposium on Aeroballistics

Vol. 3

are also shown for comparison.

Viscous interaction effect on axial force coefficients is presented in Fig. 7 for base cants of 0, 22.5 and 45 deg at several attitudes. The increase in $C_{A\ddot{t}}$ with \bar{v}_∞ is shown to be similar for each configuration, however, the levels are displaced. The viscous effect is more pronounced at the higher angle of attack with the base cant windward ($\phi' = 180$ deg.) as would be expected since the windward surface area varies significantly at this attitude. The solid symbols shown on each plot near $\bar{v}_\infty = 0$ are variations caused by Mach number and wall temperature effects. Wh tfield and Griffith have demonstrated these effects quite thoroughly in Ref. 16. The Newtonian values are also shown on each plot for each configuration to show inviscid levels of the axial force coefficient. Viscous and Mach number effects on C'_N and C'_m were also examined but these effects were small compared to those on $C_{A\ddot{t}}$ and therefore are not presented.

The viscous effects obtained during the present study have been extended on the basic cone by using data obtained from Ref. 17. These results are shown in Fig. 8 where the Mach number and Reynolds number effects have been separated to show the effect of each on center of pressure location. Sufficiently high Reynolds number ($\bar{v}_\infty < 0.015$) was maintained to show the Mach number effects. The Newtonian value and the value obtained from Whifford and Wolny in Ref. 18 are shown for comparison. The point of interest here is the rearward shift of the center of pressure with decreasing Reynolds number (based on total model length, ℓ). These data show approximately an 8 percent shift in center of pressure with three orders of magnitude decrease in Reynolds number.

The effects of mass injection to simulate a transpiration cooled nose on the basic cone were also investigated at $M_\infty = 10$. Nose transpiration simulation was accomplished by injecting nitrogen through a porous nose, shown in Fig. 9. This nose which corresponded to the bluntest nose tested ($\psi = 0.15$) was made of 60 percent dense nickel Foametal[®] vacuum brazed to the conical afterbody. Several mass flow rates were obtained by varying the nitrogen supply pressure.

The results of these tests are presented in Fig. 10. C'_N was unaffected by the mass injection as shown in Fig. 10a. Variations in C'_m were caused by the mass injection as shown in Fig. 10b. These variations are more apparent at angles of attack near 10-deg. At this angle of attack C'_m decreased with increasing mass flow rate until $\dot{m} = 0.003$ lb/sec, $Re_{\infty, \ell} = 2.83$ million. No change in C'_m was observed for $\dot{m} > 0.003$ lb/sec. A further decrease in C'_m was observed when the Reynolds number was reduced. Note the vehicle with $\sigma = 45$ deg trimmed at this angle of attack, and these decreases in C'_m indicate that the trim angle would be further reduced. Variations in $C_{A\ddot{t}}$, Fig. 10c,

with mass injection were detected, however these variations are slight. Slight effects were also observed on base pressure, Fig. 10d, but these two are not considered significantly different from those obtained without mass injection.

(U) It was unfortunate that some data were not obtained with turbulent boundary layers both with and without mass injection. A test entry was being proposed to obtain these data by using boundary layer trips when the present study was terminated.

CONCLUDING REMARKS

(U) Analysis of the experimental data obtained at Mach numbers from 6 to 21 and theoretical predictions on configurations of an asymmetric reentry glide vehicle, which was rendered asymmetric by canting the base, leads to the following conclusions:

- 1) Canting the base produces significant changes in the aerodynamic force and moment coefficients.
- 2) Effect of base pressure on the force and moment coefficients of the canted bases was insignificant at these high Mach numbers.
- 3) Higher values of L/D were obtained with the base cant leeward but with the c.g. on the axial centerline the vehicle was stable in roll only with the base cant windward. Off axis c.g. locations should be investigated.
- 4) Viscous effects not only caused significant effects in axial force but also in center-of-pressure location.
- 5) Mass injection through a porous nose cap produced changes in the moment characteristics of the full cone.
- 6) It is recommended that data be obtained on these configurations with turbulent boundary layers using trip devices in order to better simulate the conditions encountered by vehicles of this type.

REFERENCES

1. Varwig, Robert L. and Mason, Stephen B. "Experimental Measurement of the Performance of a 1/10 Scale Model MARV Configuration." Aerospace Corporation Report No. TOR-1001 (2240-10)-1, June 1967.

8th Navy Symposium on Aeroballistics

Vol. 3

2. Ellinwood, John W. and Varwig, Robert L. "Effect of Base Cant on Conical MARV Configuration." Aerospace Corporation Report No. TOR-0158 (3240-10)-1, December 1967.
3. Test Facilities Handbook (Seventh Edition), "von Karman Gas Dynamics Facility, Vol. 4." Arnold Engineering Development Center, July 1968.
4. Sivells, J. C. "Aerodynamic Design and Calibration of the VKF 50-inch Hypersonic Wind Tunnels." AEDC-TDR-62-230 (AD 299774), March 1963.
5. Griffith, B. J. and Weddington, E. D. "Recent Refinements and Advancements of Hypersonic Testing Techniques in the 100-inch Tunnel F of the VKF." Proceedings of the Fourth Hypervelocity Techniques Symposium (Meeting held at AEDC, November 15-16, 1965).
6. Weddington, E. D. and Griffith, B. J. "Calibration and Status of the AEDC-VKF 100-inch Hotshot Tunnel (F)." AEDC-TR-66-191 (AD 800778), October 1966.
7. Matthews, R. K. and Trimmer, L. L. "Operating Conditions and Flow Parameters for the VKF Hypersonic Wind Tunnels." AEDC-TM-64-19, June 1964.
8. Fay, J. A. and Riddell, F. R. "Theory of Stagnation Point Heat Transfer in Dissociated Air." Journal of the Aeronautical Sciences, Vol. 25, No. 2, February 1958, pp. 73-85, 121.
9. Grabau, Martin, Smithson, H. K., and Little, W. J. "A Data Reduction Program for Hotshot Tunnels Based on the Fay-Riddell Heat-Transfer Rate Using Nitrogen at Stagnation Temperatures from 1500 to 5000°K." AEDC-TR-64-50 (AD 601070), June 1964.
10. Griffith, B. J. and Lewis, C. H. "Laminar Heat Transfer to Spherically Blunted Cones at Hypersonic Conditions." AIAA Journal, Vol. 2, No. 3, March 1964, pp. 438-444.
11. Penland, Jim A. "Aerodynamic Force Characteristics of a Series of Lifting Cone and Cone-Cylinder Configurations at a Mach Number of 6.83 and Angles of Attack up to 130°." NASA TN D-840, June 1961.
12. Penland, Jim A. and Bernot, Peter T. "Aerodynamic Characteristics of Three Axisymmetric Low-Fineness-Ratio-Reentry Shapes at Mach 6.9." NASA TN D-4122, August 1967.

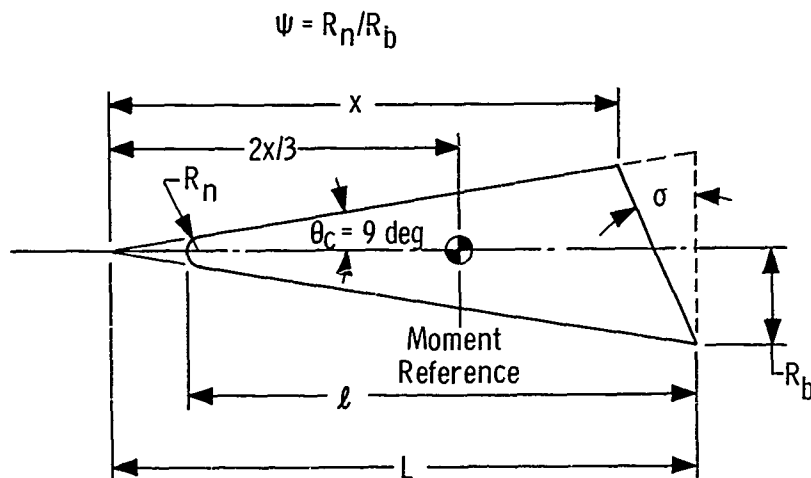
8th Navy Symposium on Aeroballistics

Vol. 3

13. Clark, E. L. and Trimmer, L. L. "Equations and Charts for the Evaluation of the Hypersonic Aerodynamic Characteristics of Lifting Configurations by the Newtonian Theory." AEDC-TDR-64-25, March 1964.
14. Wright, John. "A Compilation of Aerodynamic Nomenclature and Axes Systems." NOLR-1241, August 1962.
15. Cassanto, J. M., Rasmussen, N. S., and Coars, J. D. "Correlation of Measured Free Flight Base Pressure Data for $M = 4$ to $M = 19$ in Laminar and Turbulent Flow." Paper presented at AIAA Fluid and Plasma Dynamics Conference held at Los Angeles, California, June 24-26, 1968.
16. Whitfield, Jack D. and Griffith, B. J. "Hypersonic Viscous Drag Effects on Blunt Slender Cones." AIAA Journal, Vol. 2, No. 10, October 1964, pp. 1714-1722.
17. Boylan, D. E. and Potter, J. L. "Aerodynamics of Typical Lifting Bodies Under Conditions Simulating Very High Altitudes." AIAA Journal, Vol. 5, No. 2, February 1967, pp. 226-232.
18. Whitfield, Jack D. and Wolny, W. "Hypersonic Static Stability of Blunt Slender Cones." AEDC-TDR-62-166, August 1966.

Table I Test Conditions

Tunnel	Type Test	Test Gas	M_∞	$Re_\infty \times 10^{-6}$	P_0 , psia	T_0 , °K	H_0 , Btu/lb	P'_0 , psia	q_∞ , psia	$P_\infty \times 10^3$, psia	$P_\infty \times 10^4$, lb/ft ³	T_∞ , °K	U_∞ , ft/sec
B	Force	Air	6.02	1.78	96	472	204	2.80	1.50	60.0	15.2	57.2	3,000
B			6.06	5.15	280	472	204	8.00	4.34	170.0	43.4	56.7	3,000
B			7.97	2.00	430	830	315	3.65	2.00	45.0	13.2	52.2	3,780
B			8.01	3.50	800	880	328	6.75	3.65	81.0	22.8	53.9	3,860
C	Force		10.14	0.600	500	1056	478	1.45	0.74	10.0	3.40	47.8	4,570
C	Force		10.25	2.00	1,730	1056	478	4.80	2.46	34.0	10.4	51.1	4,780
C	Mass Addition		10.14	1.54	1,200	1022	461	3.32	1.80	25.4	7.50	50.0	4,720
C	Base Press.		10.08	0.640	500	1022	461	1.45	0.76	11.0	3.40	47.8	4,570
C	Force		10.16	1.54	1,200	1022	461	3.32	1.79	25.0	7.50	50.0	4,720
C			10.07	0.64	500	1017	458	1.45	0.76	11.0	3.40	47.8	4,570
F	Force		15.08	1.23	11,000	2100	1082	4.37	2.35	14.8	4.08	52.5	7,300
F			21.4	0.057	6,360	3980	2126	0.288	0.147	0.429	0.131	51.5	10,329
F			18.3	0.390	8,370	2320	1198	1.02	0.547	2.20	0.862	37.5	7,684
F			19.8	0.864	14,870	2000	1051	1.67	0.904	3.32	1.63	29.7	7,175



Tunnel B and C Models

R_n , in.	R_b , in.	Ψ	l , in.
0	4.00	0	25.26
0.20		0.05	24.18
0.40		0.10	23.10
0.60		0.15	22.02

L , in.	σ , deg	x , in.	S , in. ²	A_b , in. ²
25.26	0	25.26	50.26	50.26
	22.5	22.24	50.26	46.43
↓	45.0	18.35	50.26	35.54

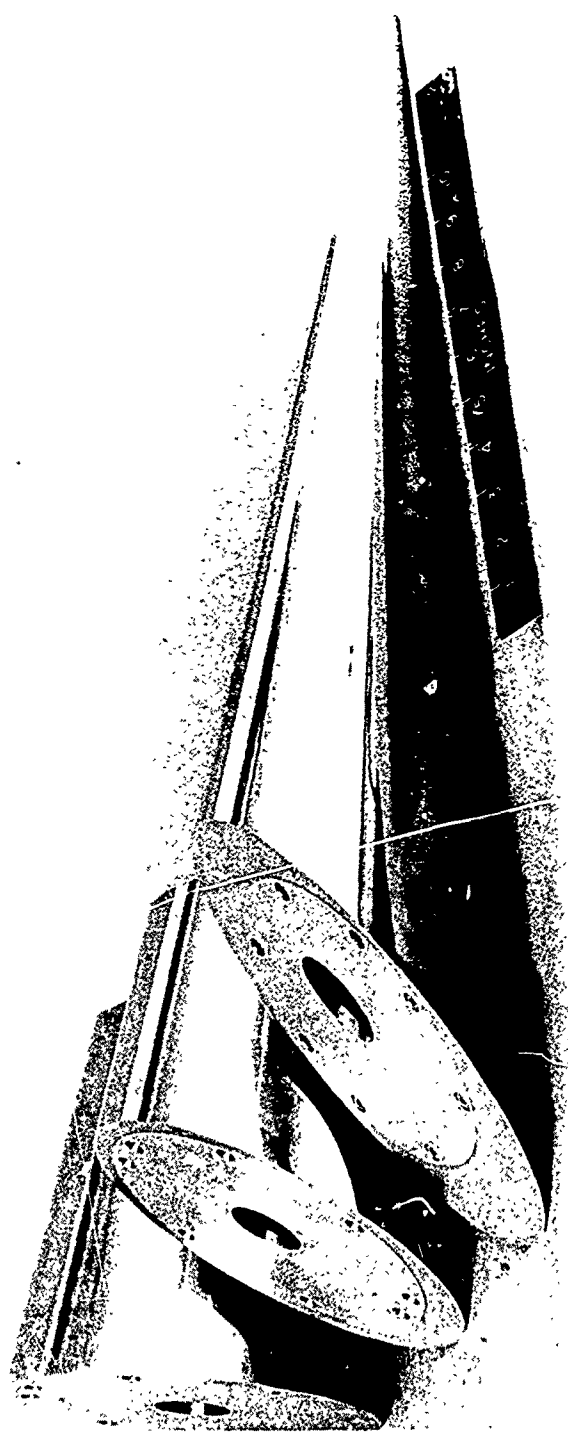
Tunnel F Models

R_n , in.	R_b , in.	Ψ	l , in.
0.088	1.75	0.05	10.58

L , in.	σ , deg	x , in.	S , in. ²	A_b , in. ²
11.05	0	11.05	9.62	9.62
	22.5	9.69	9.62	8.89
↓	45.0	8.03	9.62	6.80

a. Model Dimensions

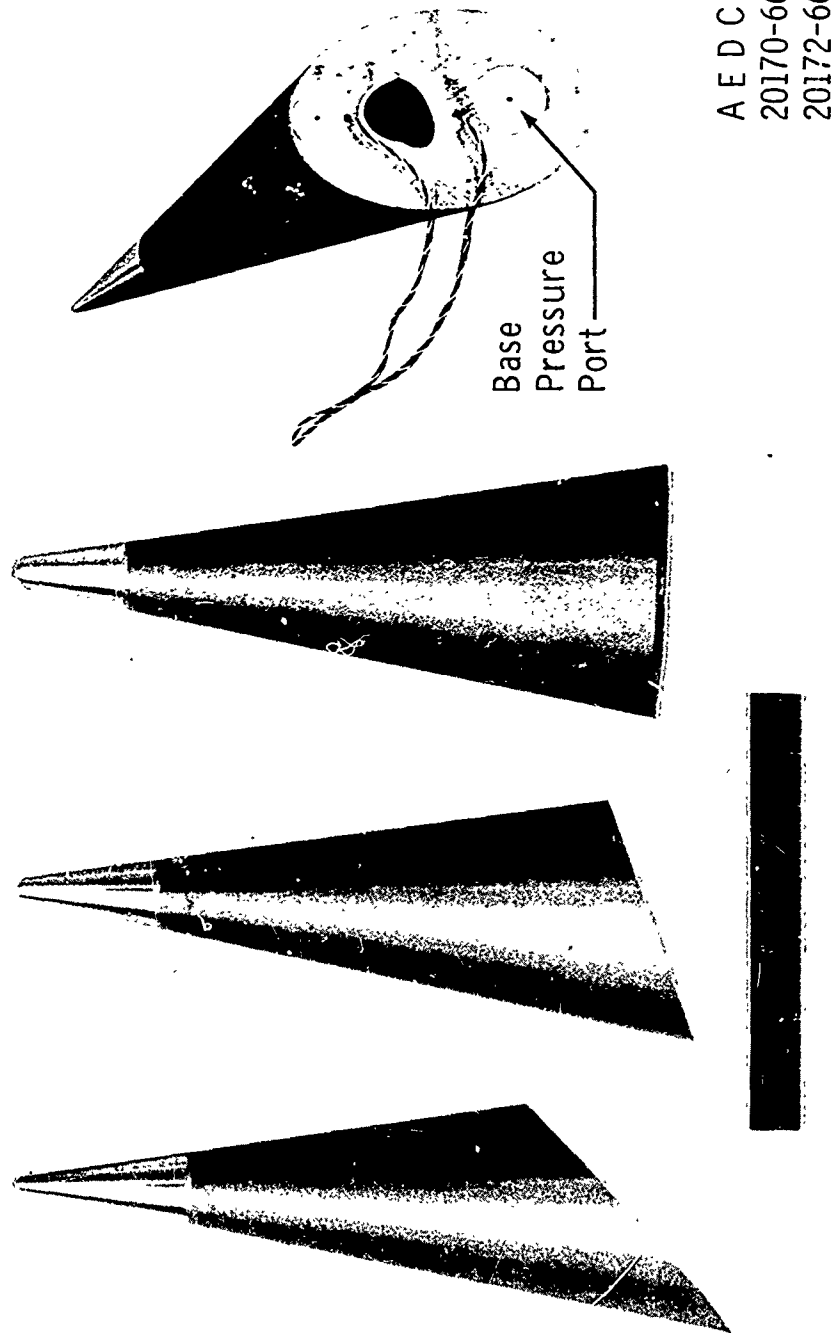
Fig. 1 AGRV Models



A E D C
21728-66

b. Tunnel B and C Models

Fig. 1 Continued



c. Tunnel F Models

Fig. 1 Concluded

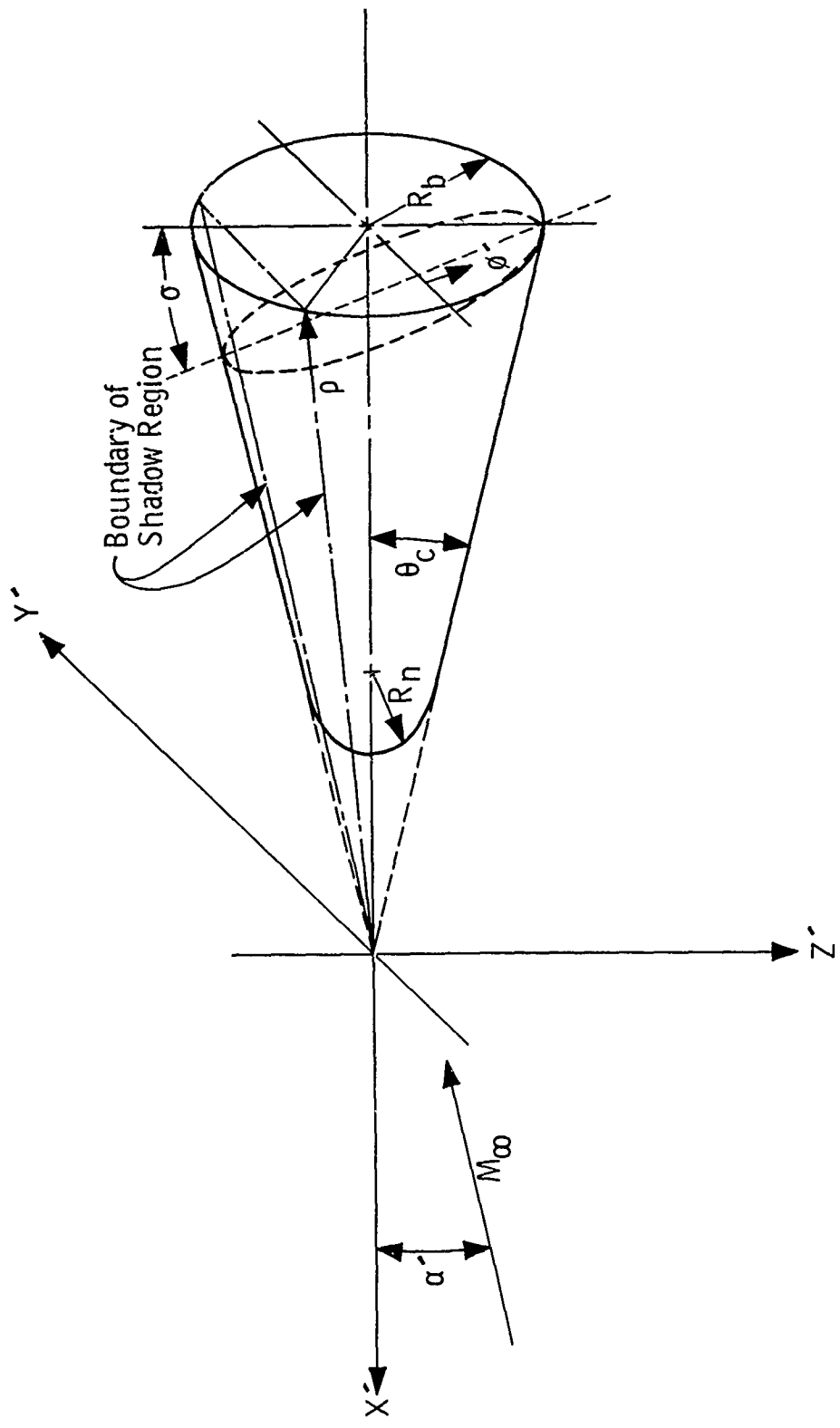
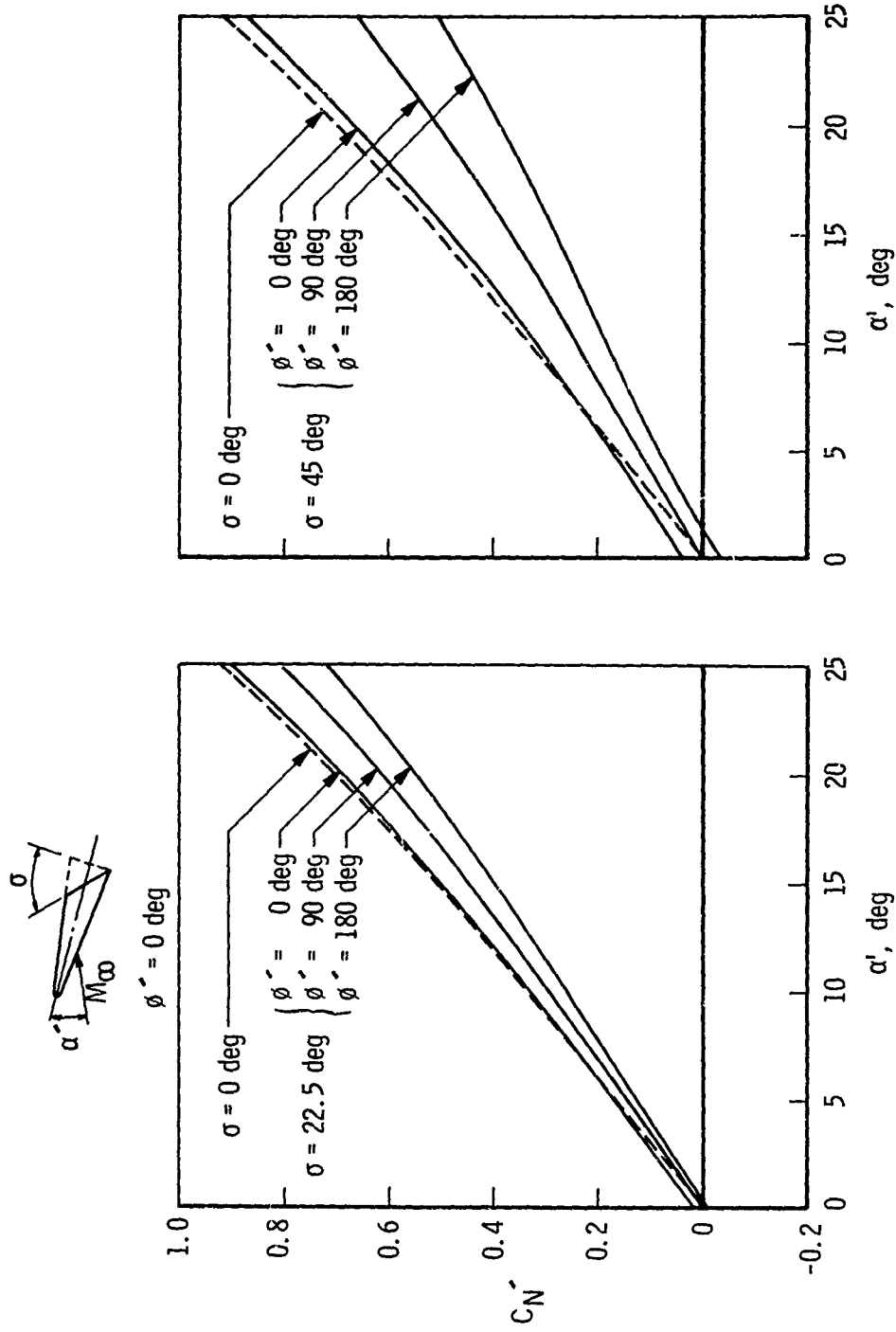
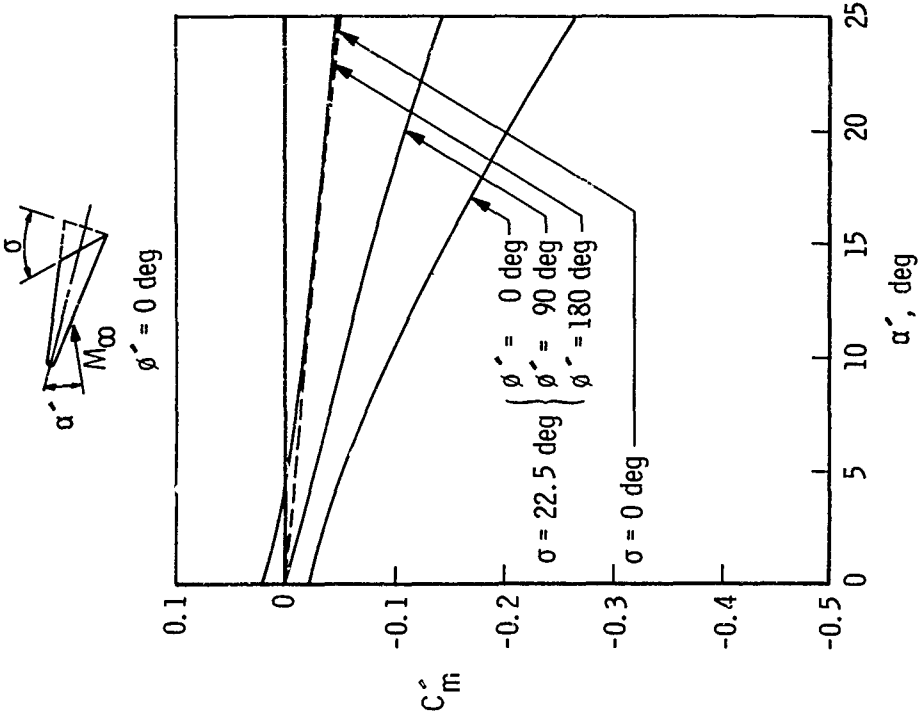
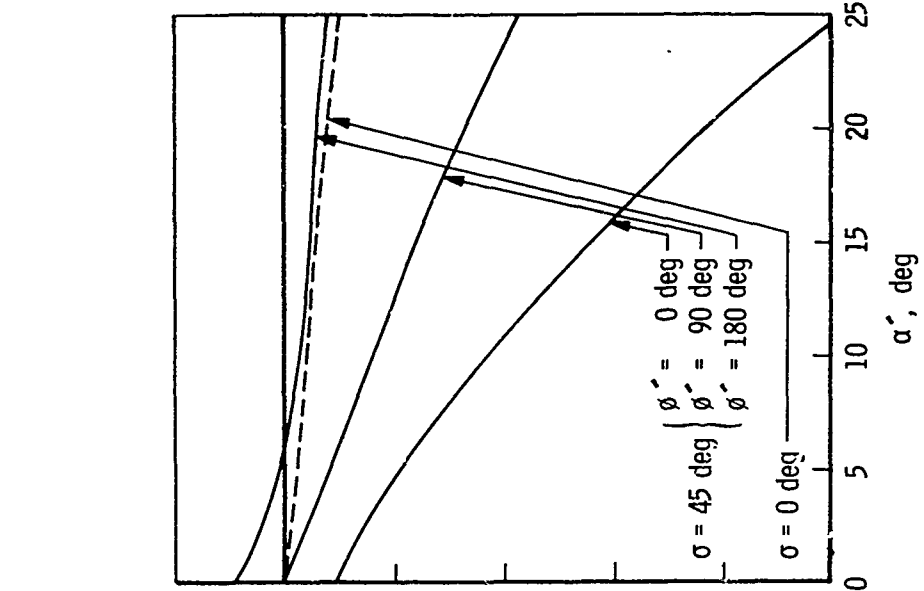


Fig. 2 Geometry and Nomenclature of Spherically Blunted Cone with Canted Base
for Newtonian Analysis

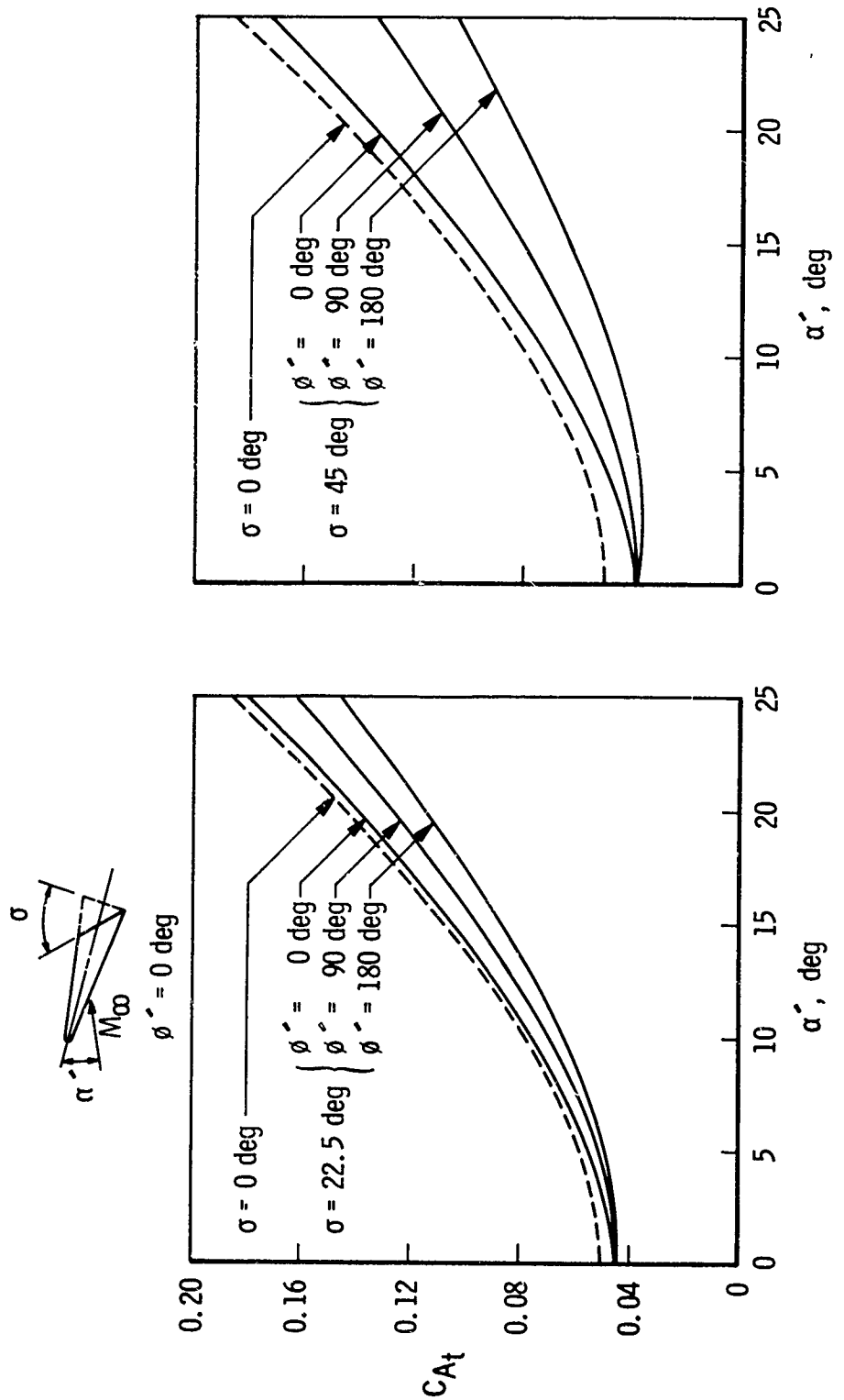


a. Normal-Force Coefficient

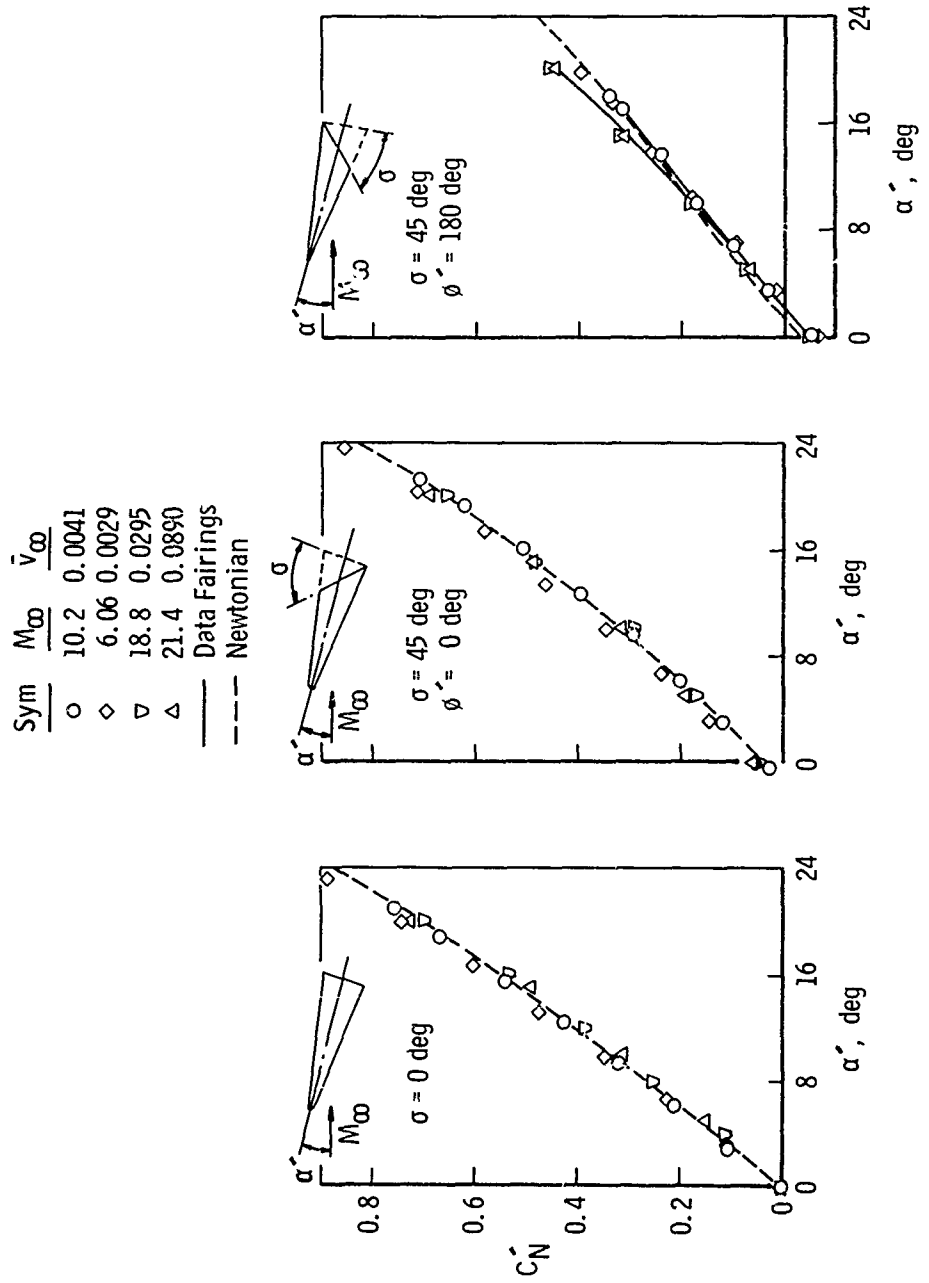
Fig. 3 Newtonian Predictions for the AGRV, $\psi = 0.05$



b. Pitching-Moment Coefficient
Fig. 3 Continued

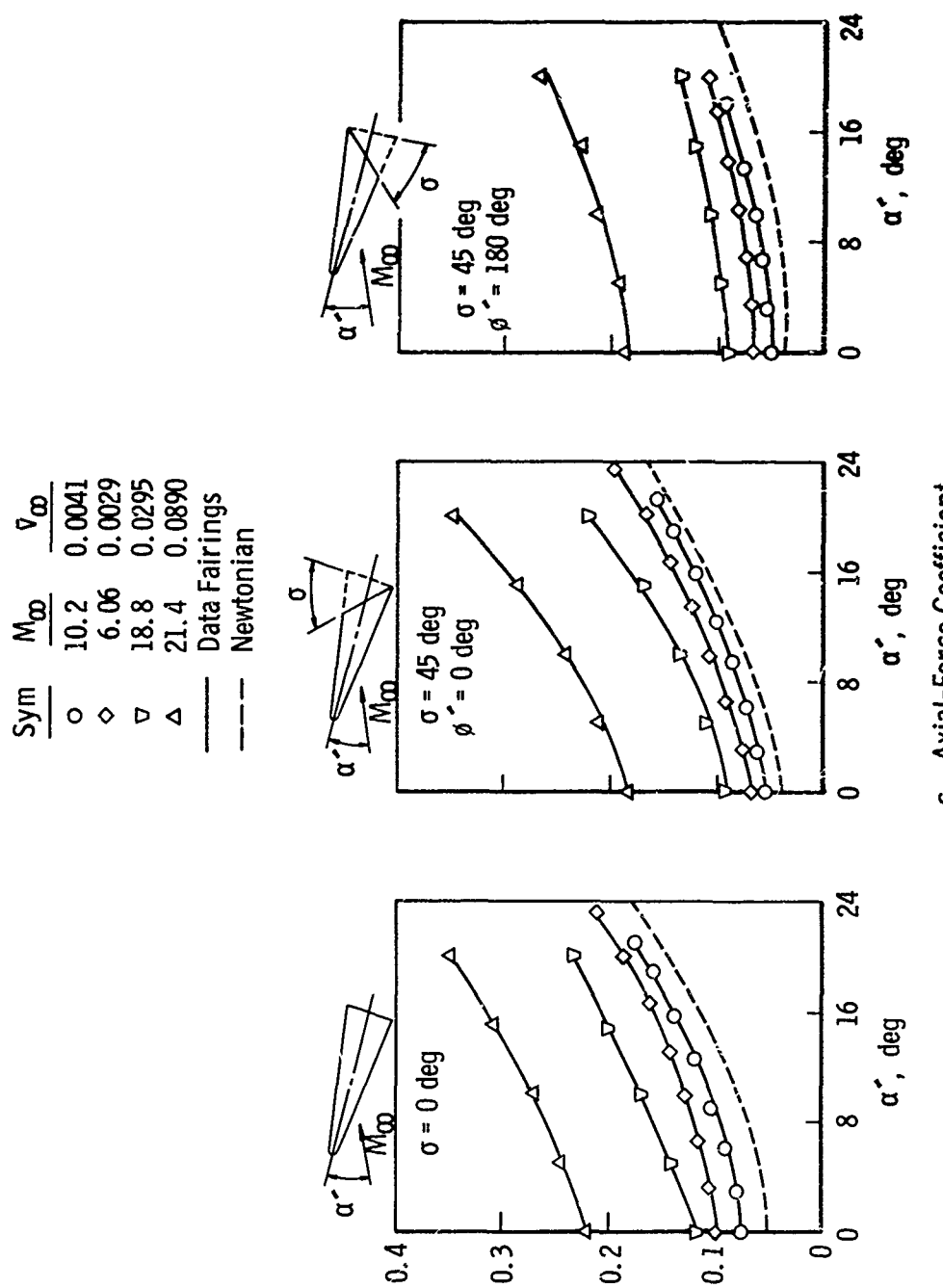


c. Axial-Force Coefficient
Fig. 3 Concluded



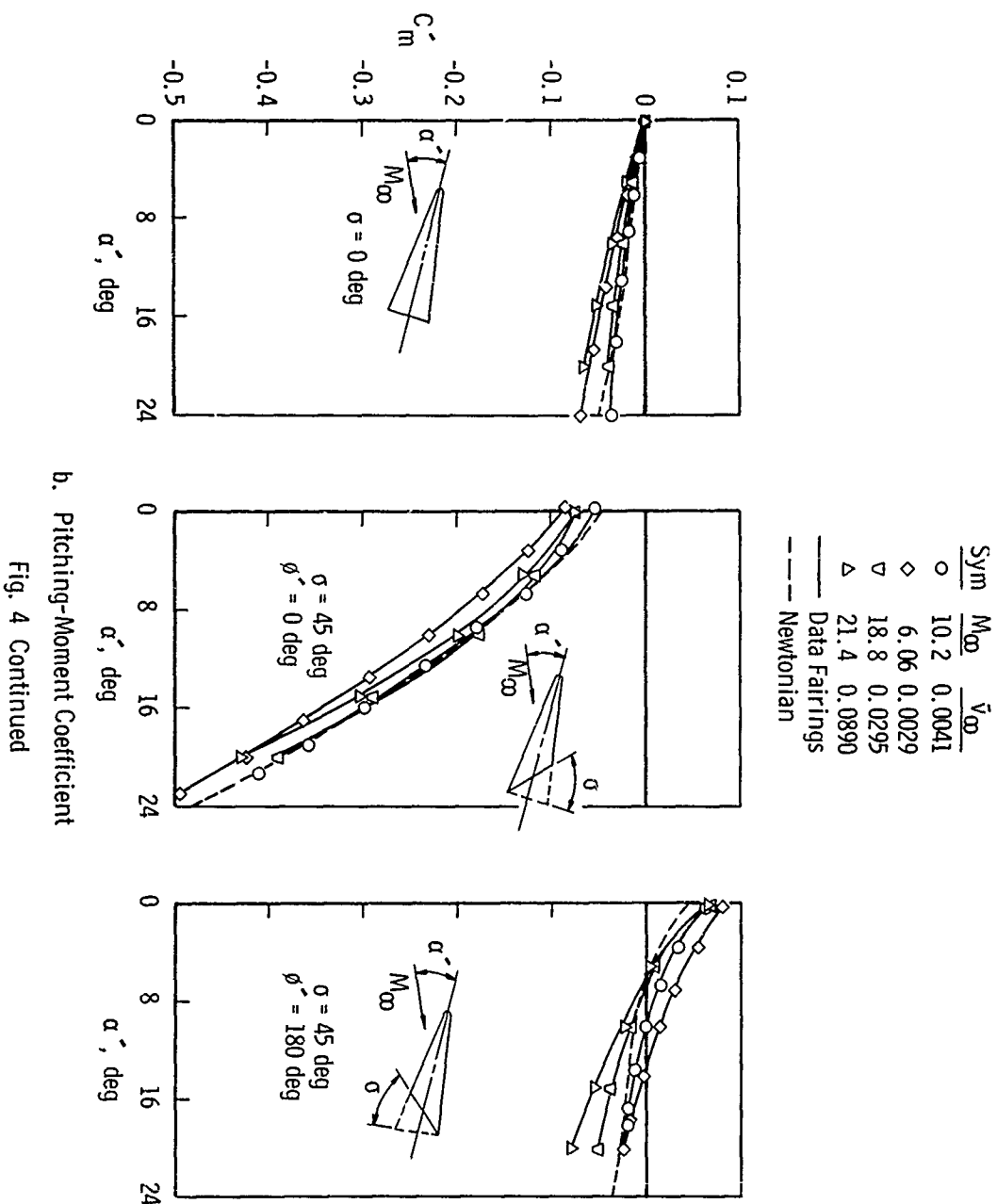
a. Normal-Force Coefficient

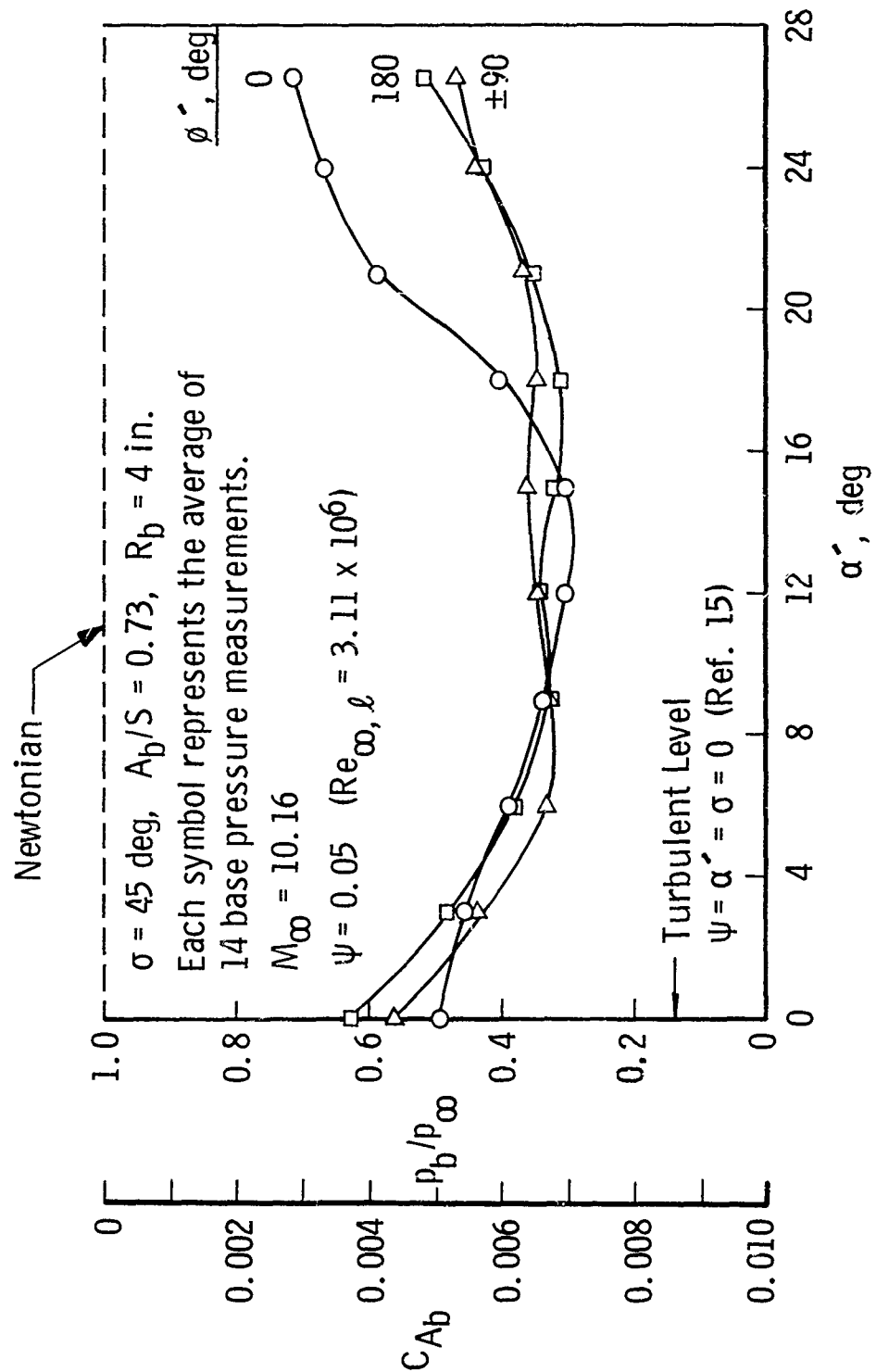
Fig. 4 Comparison of Experimental Data with
Newtonian Predictions, $\psi = 0.05$



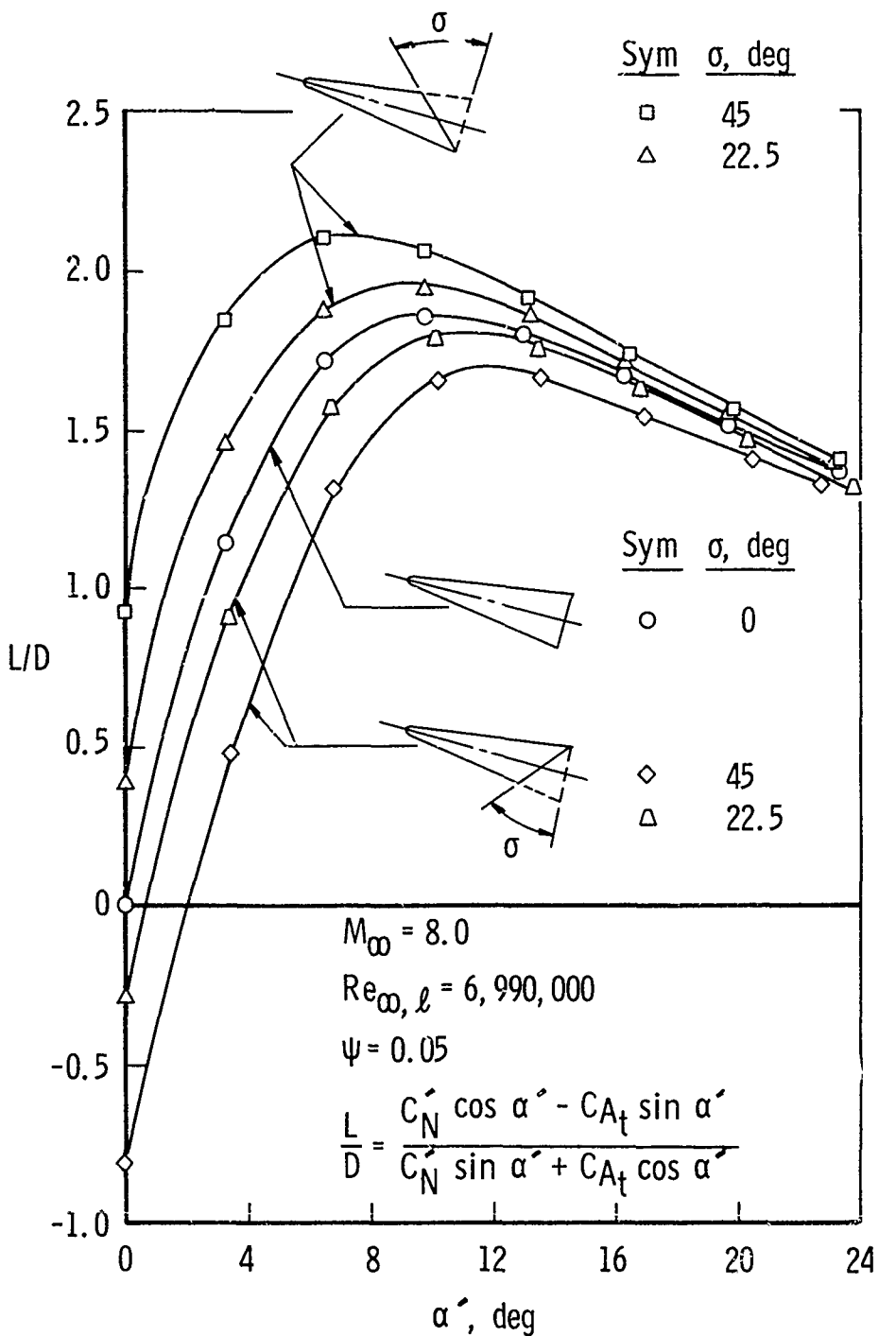
c. Axial-Force Coefficient

Fig. 4 Continued





d. Base Pressure
Fig. 4 Concluded



a. Lift-to-Drag Ratio, $\Psi = 0.05$, $M_\infty = 8$

Fig. 5 Lift-to-Drag and Trim Characteristics of the AGRV

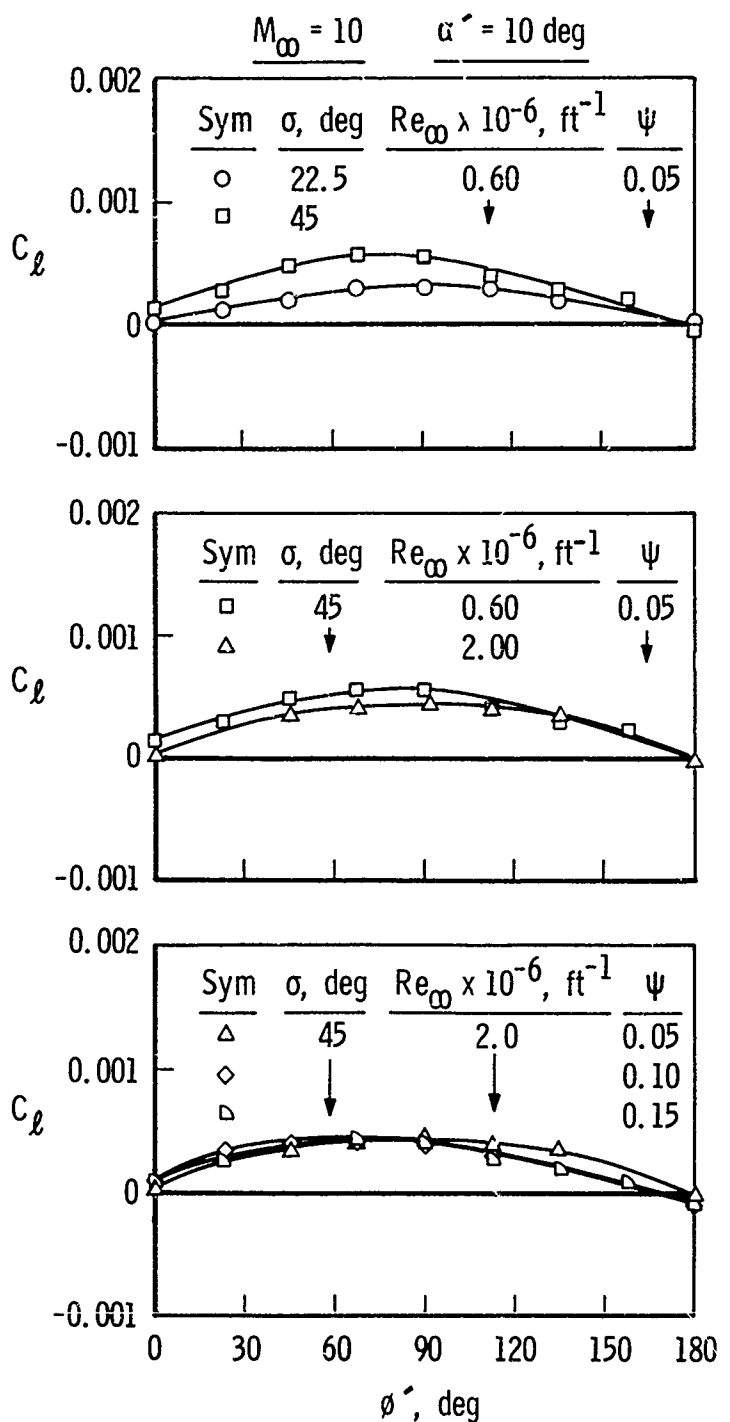
b. Rolling-Moment Coefficient, $M_{\infty} = 10$, $\alpha' = 10 \text{ deg}$

Fig. 5 Continued

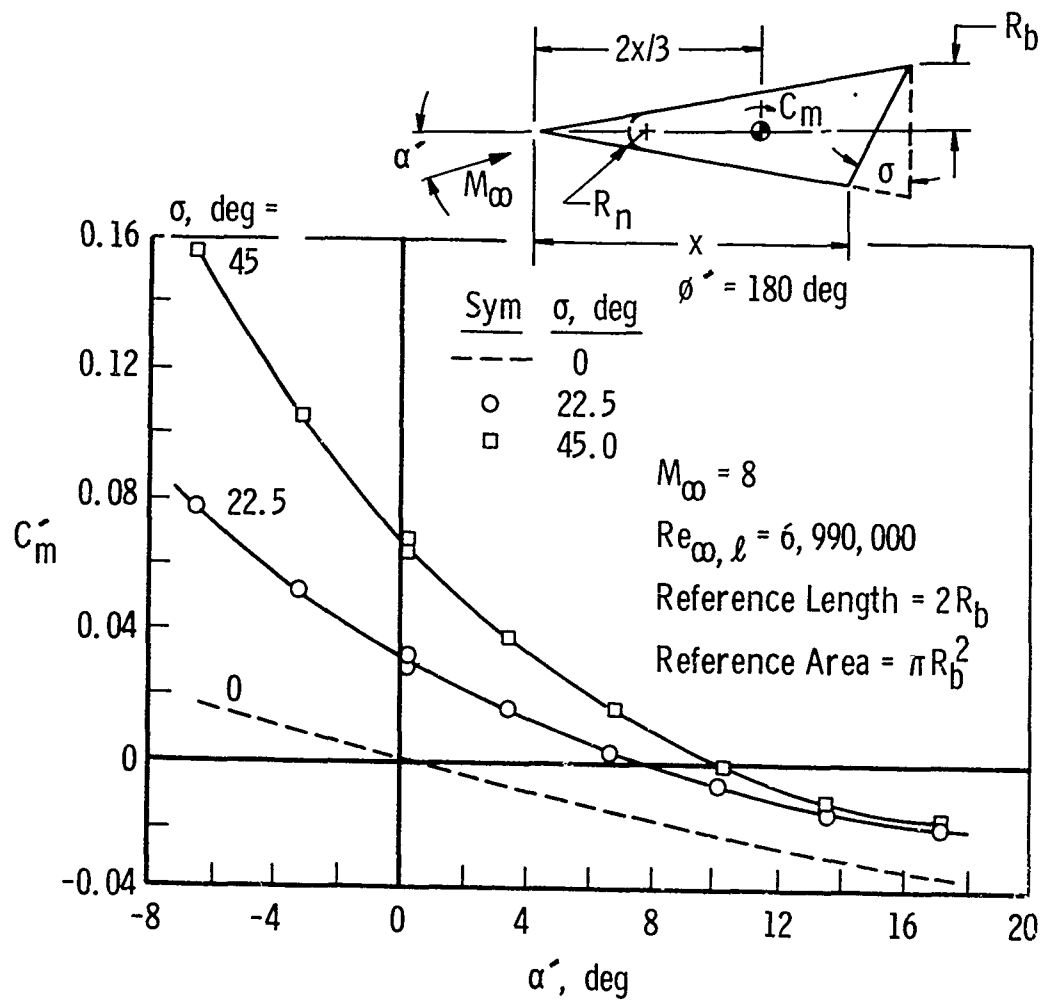
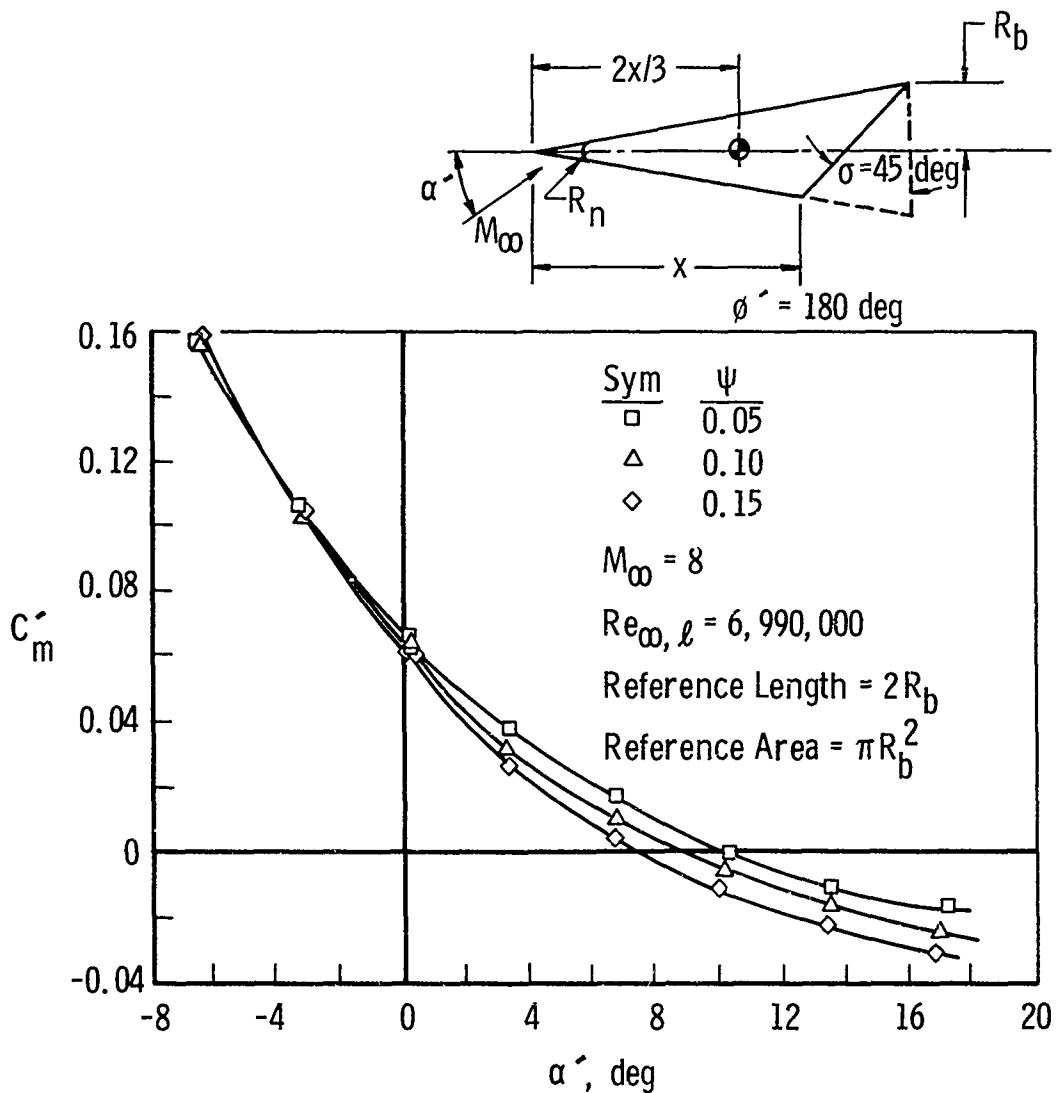
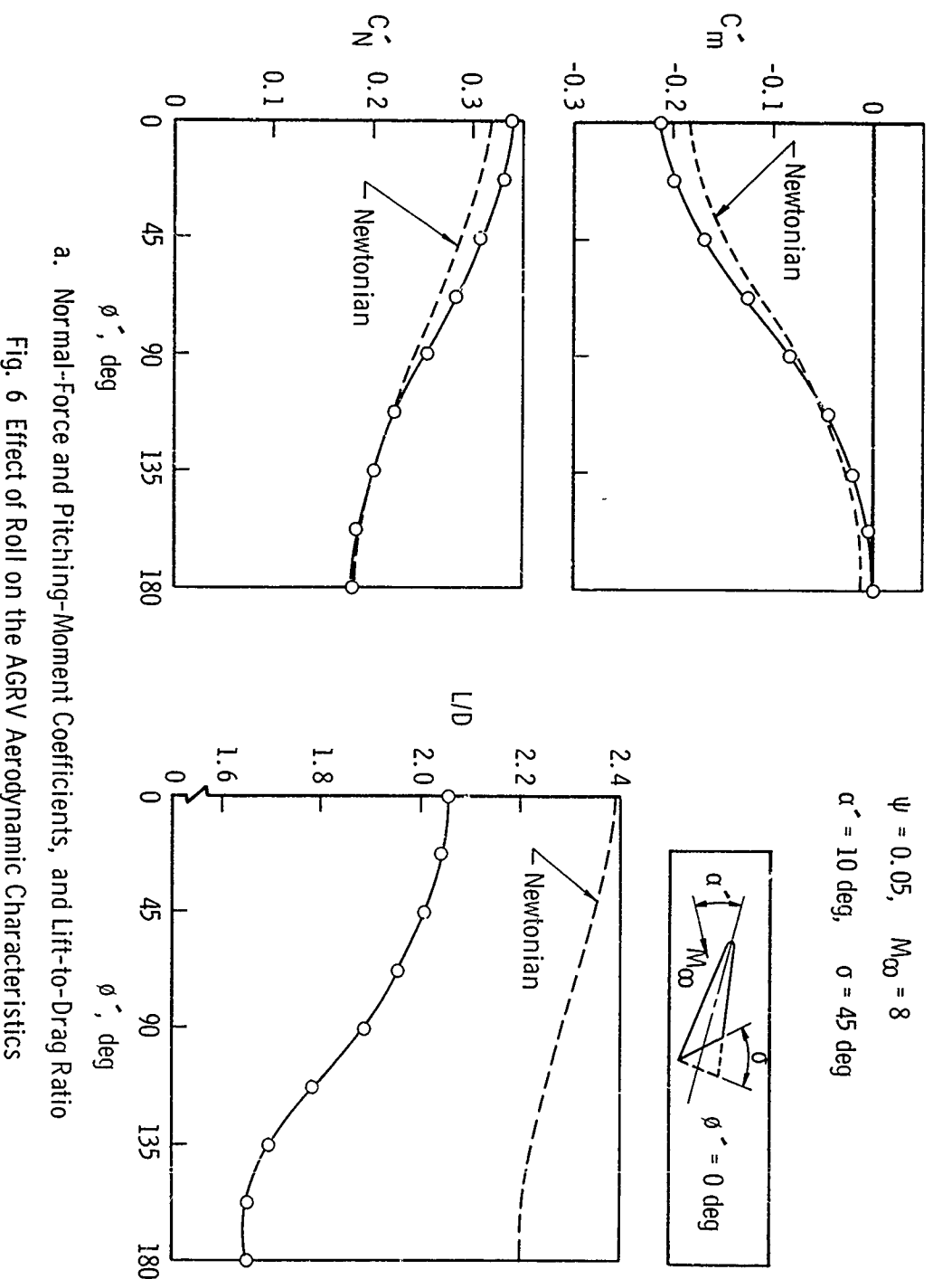
c. Effect of Base Cant on Trim Angle, $\psi = 0.05$, $M_\infty = 8$

Fig. 5 Continued



d. Effect of Nose Blunting on Trim Angle,
 $\sigma = 45$ deg, $M_\infty = 8$

Fig. 5 Concluded



a. Normal-Force and Pitching-Moment Coefficients, and Lift-to-Drag Ratio

Fig. 6 Effect of Roll on the AGRV Aerodynamic Characteristics

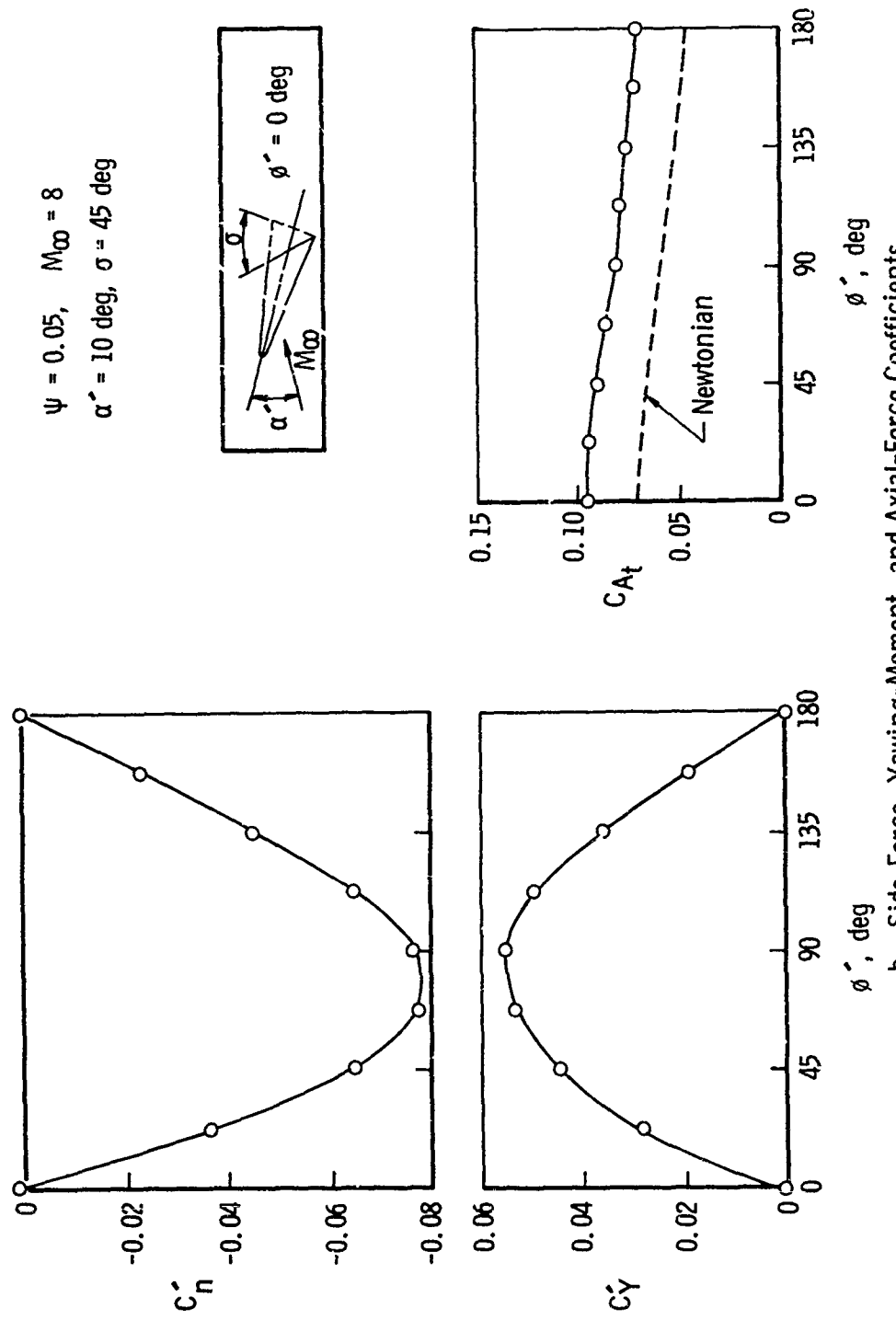


Fig. 6 Concluded

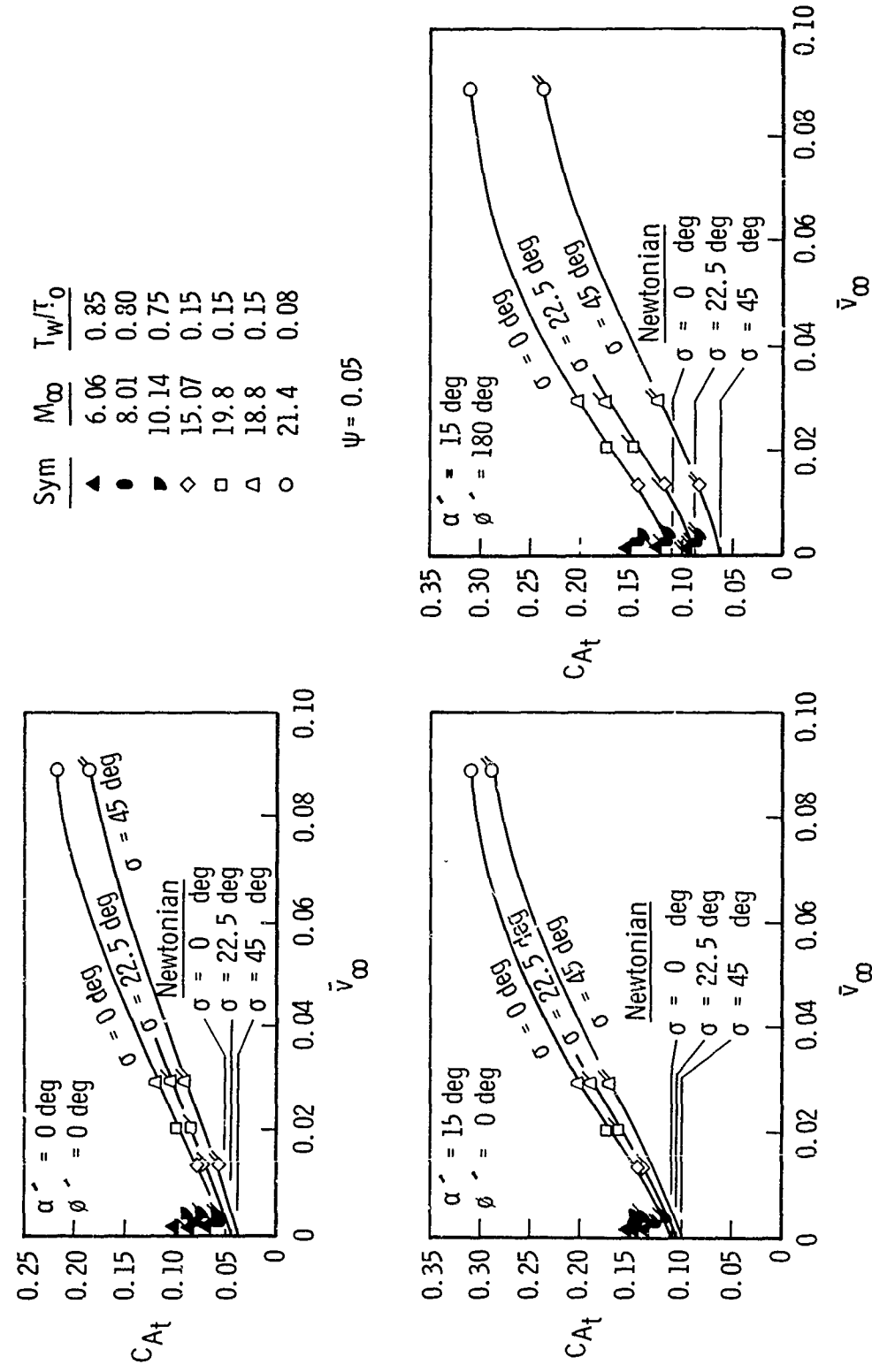


Fig. 7 Effect of Viscous Interaction on the AGRV Axial-Force Coefficient

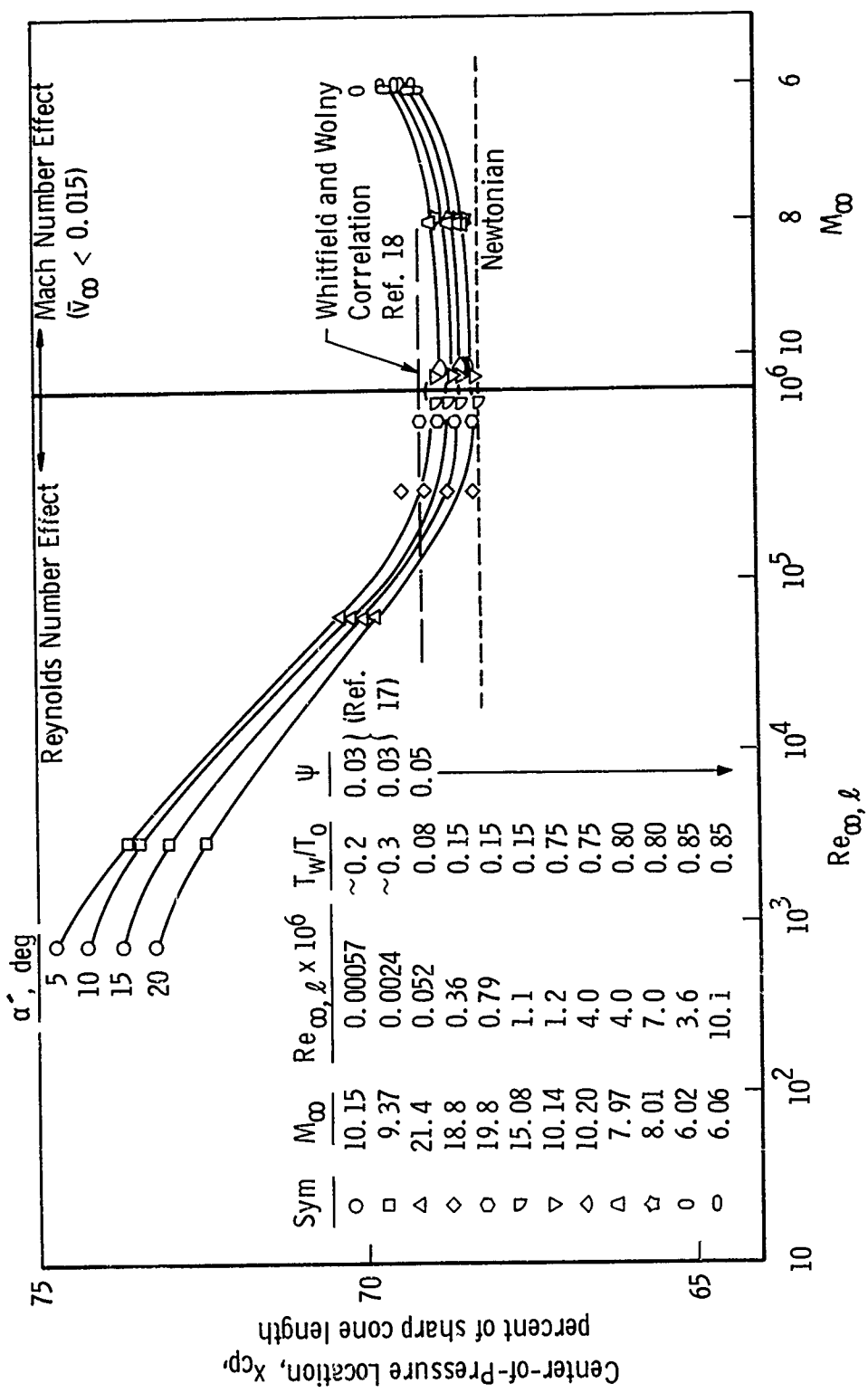


Fig. 8 Effect of Mach Number and Reynolds Number on
Basic Cone Center-of-Pressure Location

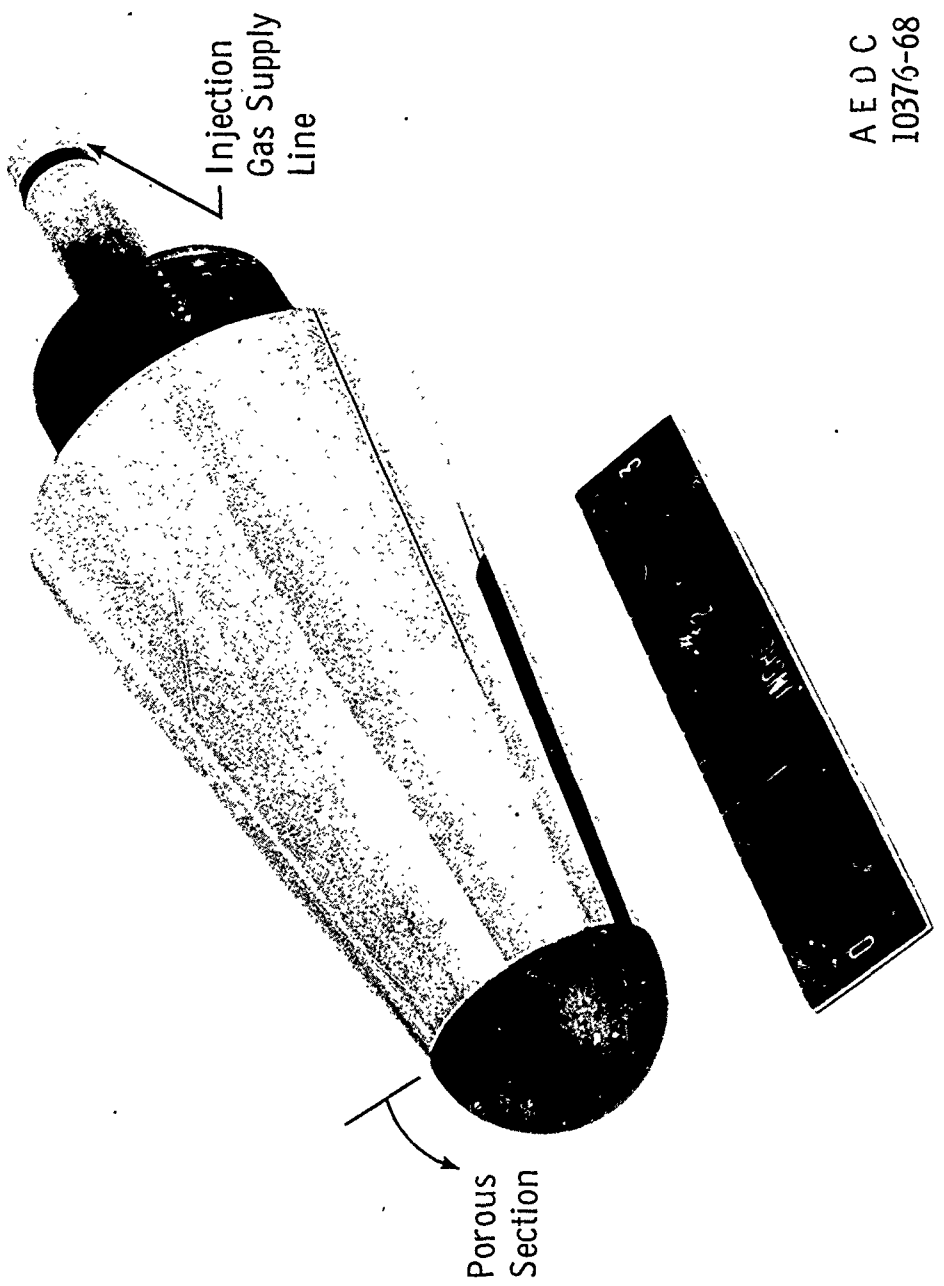
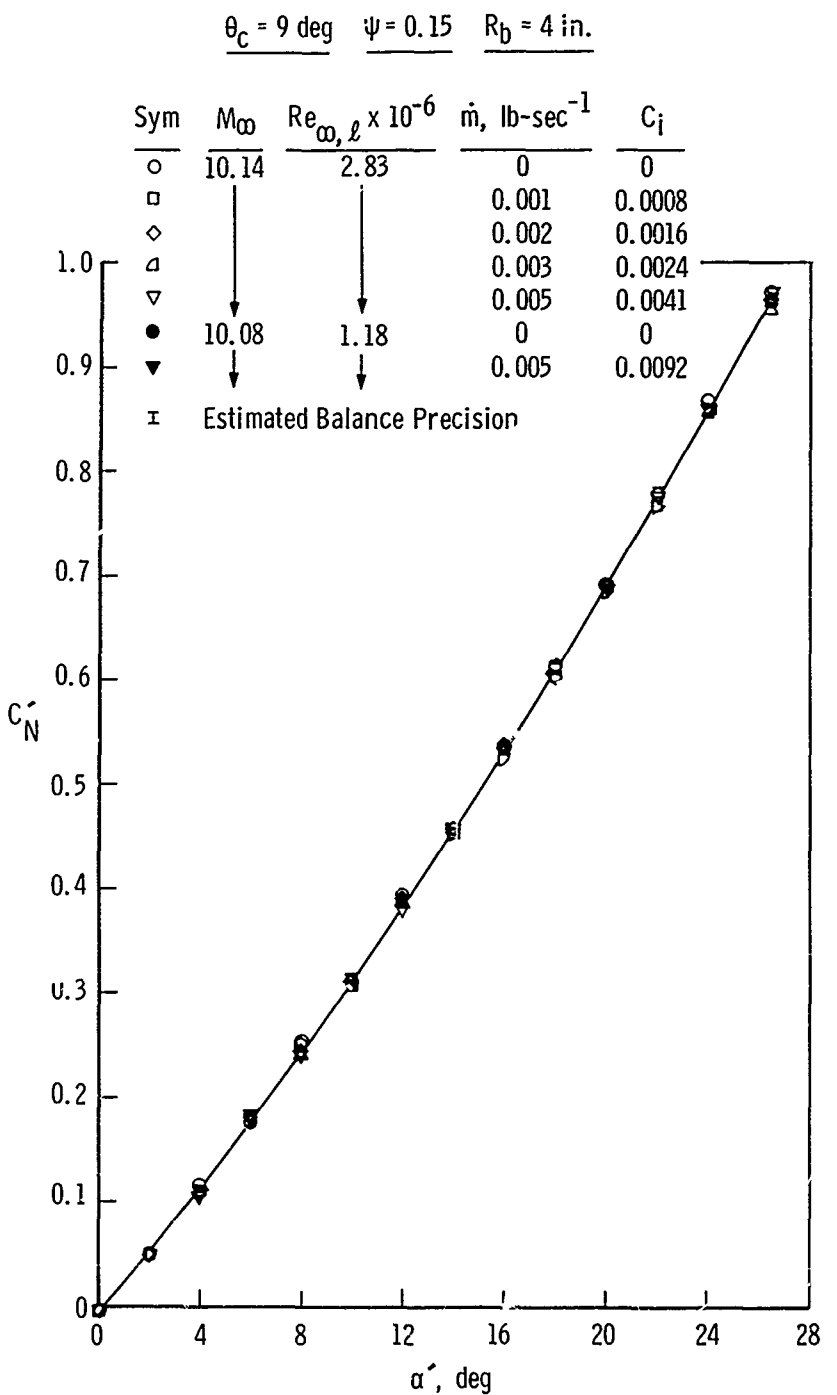
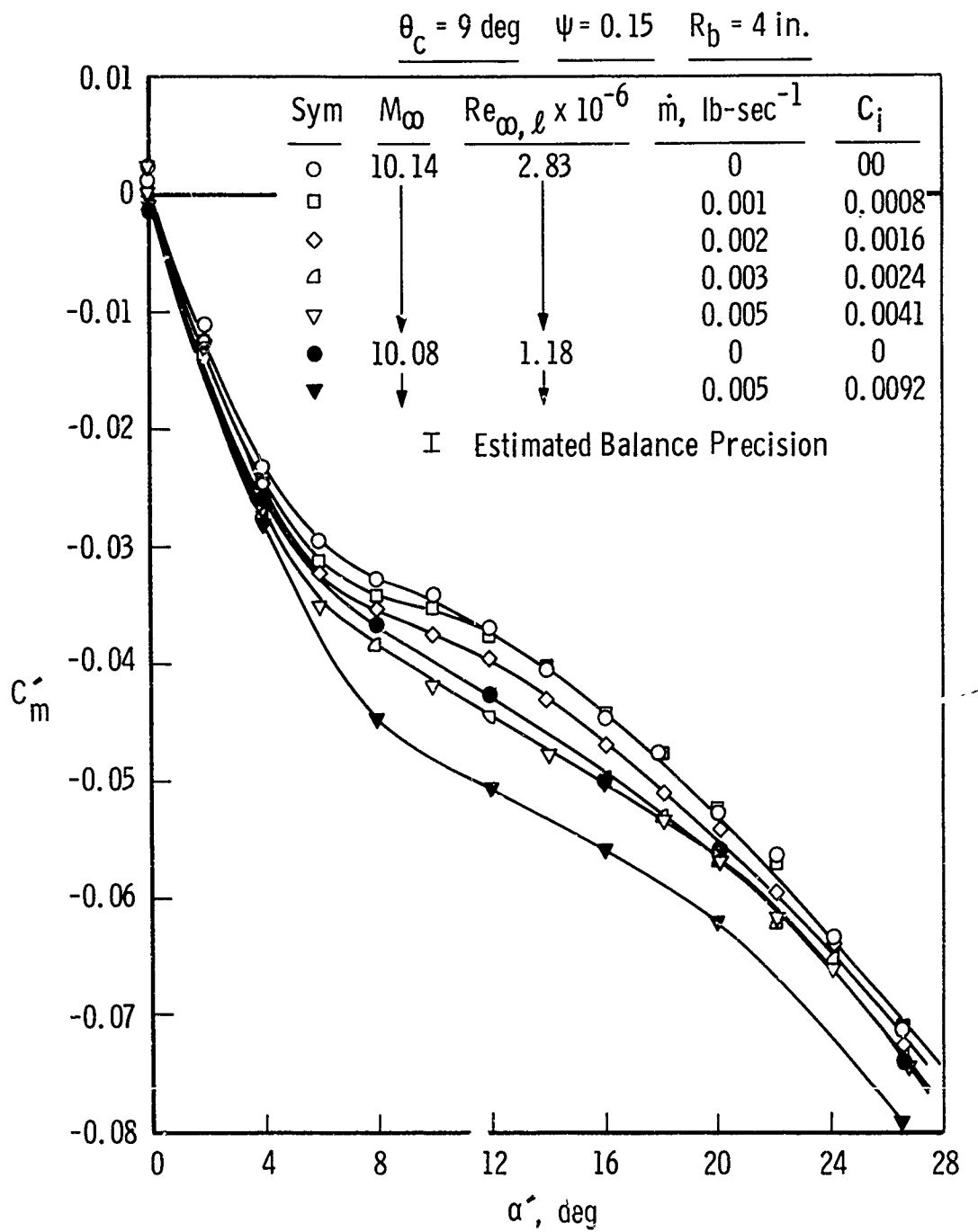


Fig. 9 Porous Nose Used in Mass Injection Test



a. Normal-Force Coefficient

Fig. 10 Effect of Mass Injection on Basic Cone Aerodynamics, $M_\infty = 10$



b. Pitching-Moment Coefficient

Fig. 10 Continued

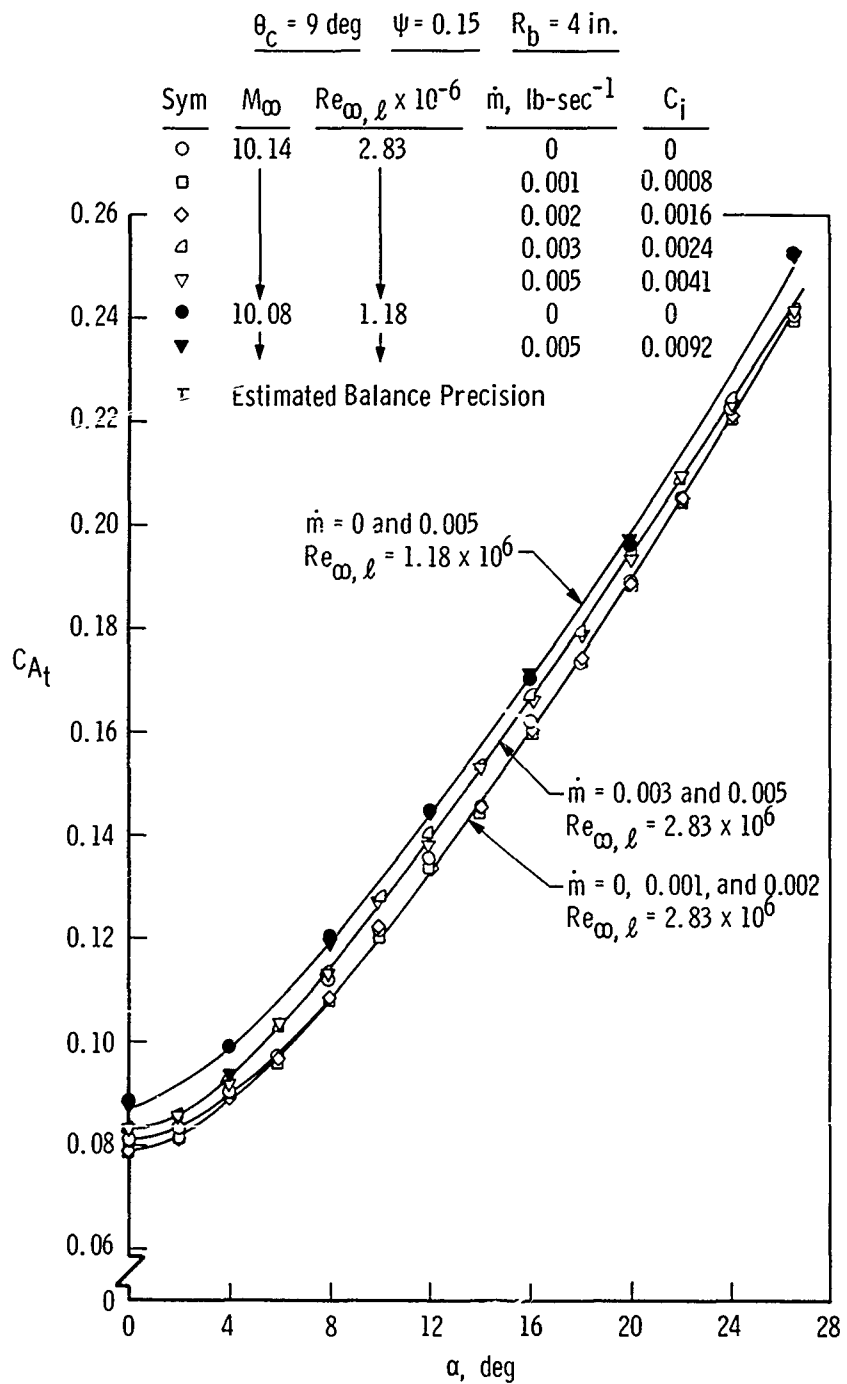
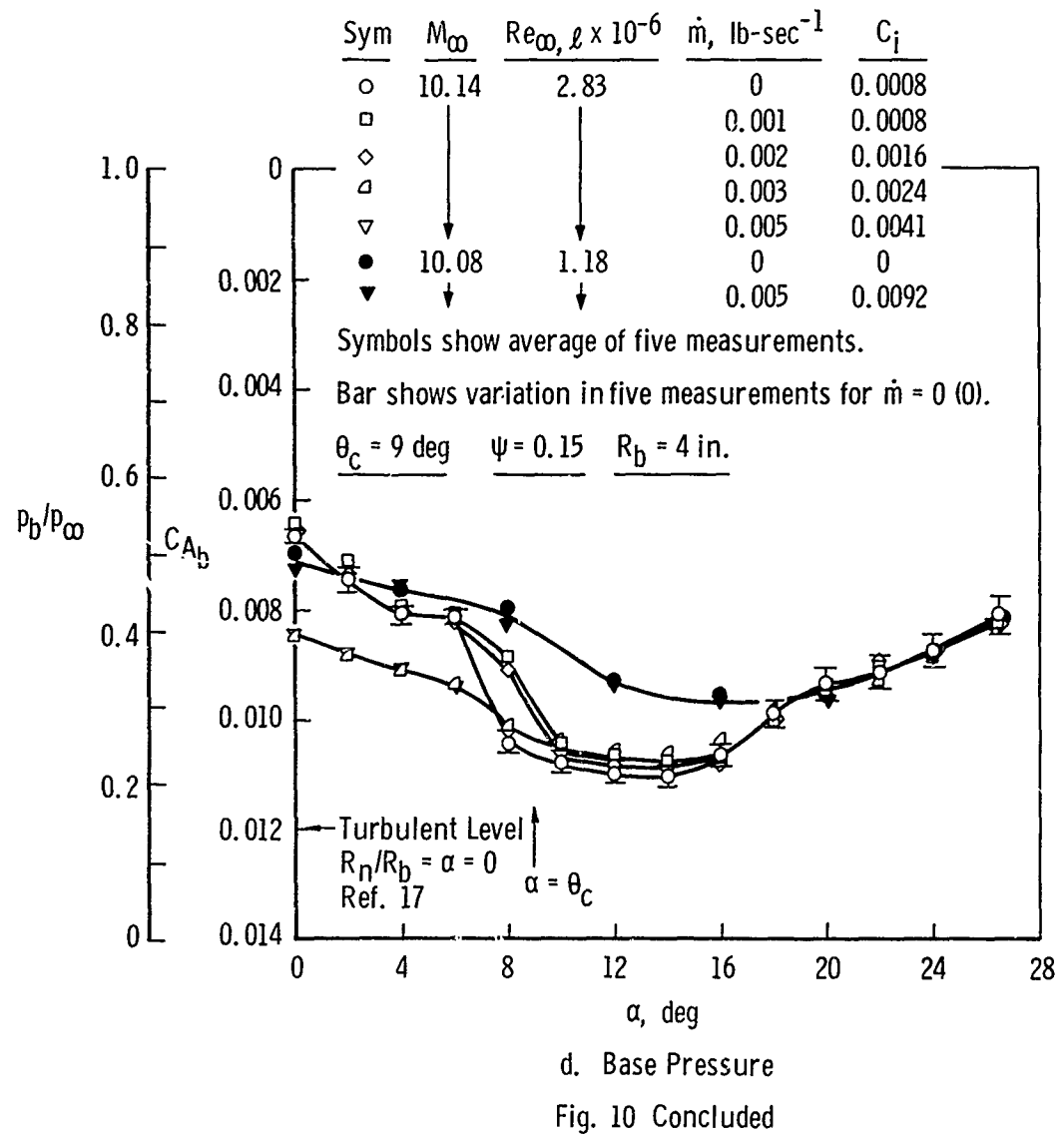


Fig. 10 Continued



Paper No. 24

AN ANALYSIS OF A SLEwed-LAUNCH
TECHNIQUE FOR AIR-LAUNCHED MISSILES

(U)

(Paper UNCLASSIFIED)

by

Eugene E. Kluth
U.S. Naval Ordnance Laboratory
White Oak, Silver Spring, Md. 20910

ABSTRACT. Slewed launch, a new missile-launch technique, is being studied. The aerodynamic problems associated with slewing a missile about its center of gravity during the initial portion of its flight from the aircraft, prior to ignition of the propulsion system, are being determined.

Simplified computer trajectories of the slewing phase have been made utilizing experimental aerodynamic data obtained over an angle-of-attack range of 0 degrees to 180 degrees and a Mach number range of 0.5 to 4.1 for a missile configuration. The slewing performance was evaluated by varying the following parameters: (1) static margin of stability, (2) missile moment of inertia, (3) magnitude of reaction-jet control, (4) launch Mach number and (5) launch altitude.

Expanded computer trajectories, to determine the vehicle flight performance after slewing and ignition as well as the slewing phase, revealed no adverse developments in flight performance as the vehicle decelerated to minimum velocity and then accelerated towards the target.

8th Navy Symposium on Aeroballistics

Vol. 3

SYMBOLS

A	reference area
a	acceleration
$C_A \sim f(a, M)$	axial force coefficient
$C_N \sim f(a, M)$	normal force coefficient
$C_X \sim f(a, \theta, M)$	force coefficient in the X direction
$C_Y \sim f(a, \theta, M)$	force coefficient in the Y direction
$C_m \sim f(a, M)$	moment coefficient
$C_{m\dot{\theta}} \sim f(M)$	damping coefficient
d	reference diameter
F	force
F_A	force component along body axis
F_N	force component normal to body axis
F_X, F_Y	force component in X, Y directions
I	transverse moment of inertia
M	Mach number
M_{ext}	moment
$m \sim f(t)$	missile instantaneous mass
q	dynamic pressure
$T_j \sim f(\theta, \dot{\theta})$	reaction-jet control thrust
T_J	reaction-jet control thrust magnitude

8th Navy Symposium on Aeroballistics

Vol. 3

$T_m \sim f(t)$	missile motor thrust
t	time
t_i	time of motor ignition
v	velocity
x	position along body axis
x_{cg}	center-of-gravity location with respect to the nose of the missile
x_j	location of reaction jet with respect to the nose of the missile
X, Y, Z	position of missile with respect to earths' axes system where Z is the altitude
α	angle of attack
θ	angle of rotation in X-Y plane
θ_f	desired final angle of rotation
ρ	density
($\vec{}$)	indicates vector quantity
(\cdot)	d/dt
($\cdot\cdot$)	d^2/dt^2

SUBSCRIPTS

(a)	pertains to aerodynamic force
(j)	pertains to reaction-jet force
(m)	pertains to missile motor force
(o)	initial condition
(t)	terminating condition

INTRODUCTION

The anticipated development of full-area radar coverage for high-performance aircraft makes an air-to-air missile, which is capable of attacking targets approaching from the side or rear, a desirable system and would provide a major improvement in the offensive and/or defensive capability of current and future aircraft. The Naval Ordnance Laboratory (NOL) is currently investigating the aerodynamic feasibility of slewing a missile immediately after ejection from a high-performance aircraft by the use of a reaction-jet control system. As such, it is intended that the missile be ejected from the launch aircraft in a forward-facing manner, slewed unpowered from 0 degrees up to 180 degrees (as required by the target location) and then boosted to intercept the target. Such a system would allow offensive or defensive actions in any quadrant without the time-consuming maneuvers of vectoring the aircraft towards the target prior to missile launch or the missile pulling a high-g turn to vector on the target. A qualitative pictorial sequence of the slewing technique is illustrated in Fig. 1.

IBM 7090 FORTRAN IV programs, for the calculation of the trajectory of a Slew-Launched Interceptor Missile (SLIM), have been written to determine the aerodynamic problems associated with: (1) slewing a missile about its center of gravity during the initial portion of its flight prior to ignition of the propulsion system; and (2) the portion of flight where the motor is ignited and the missile accelerates towards the target.

MATHEMATIC FORMULATION OF SLEWING TECHNIQUE

ASSUMPTIONS

In order to formulate the problem of the slewed-launch technique, a straightforward approach was made with the following assumptions used in the development of the equations of motion.

1. The center of gravity and the moment of inertia of the missile remained constant, although the mass of the fuel expended was taken into account.

2. The missile would be attitude-stabilized in pitch and roll.

3. The altitude of the missile remained constant, i.e., all motion would be confined to the X-Y plane. Thus, during the unpowered slewing phase, the missile would rotate about a transverse axis, through the missile center of gravity, perpendicular to the X-Y plane.

AERODYNAMIC DATA

For a missile to perform the slewed-launch maneuver, it is desirable, from an aerodynamic standpoint, that the missile have a good center-of-pressure location and have very little center-of-pressure movement with angle of attack over a wide range of Mach numbers.

With this in mind, a shrouded-tail configuration (Fig. 2) investigated in earlier work at NOL showed promise in that there was little shift in center-of-pressure location through moderately high angle of attack and a Mach number range of 0.5 to 4.1. Since data over an angle-of-attack range of 0 degrees to 180 degrees was necessary for the trajectory calculations, additional wind-tunnel measurements were made to complete the angle-of-attack range needed for Mach numbers 0.5 to 4.1 (Ref. 1). Fig. 3 illustrates the center-of-pressure location for different angles of attack and Mach numbers. The center-of-gravity locations investigated for the trajectory studies were within the shaded band. For angles of attack less than 130 degrees, the center of pressure does not vary appreciably with Mach number and the missile is never drastically stable or unstable. For angles of attack greater than 130 degrees, the center of pressure moves quite rapidly to the tail of the missile, which is a very unstable condition since the missile is flying backwards.

All static aerodynamic data used as an input into the trajectory programs were obtained experimentally and reduced in the body axis system with the nose tip used as a reference for all moments and forces. Since no dynamic data have been obtained experimentally, slender-body theory was applied to obtain the damping moment coefficients.

8th Navy Symposium on Aeroballistics

Vol. 3

RIGID BODY EQUATIONS OF MOTION

The force and moment equations for a rigid body can be written in the form

$$\sum \bar{F} = \bar{m}\bar{a}$$

$$\sum \bar{M}_{ext} = I\bar{\theta}$$

The external forces acting on the missile are the static aerodynamic forces, the reaction-jet control thrust, and the motor thrust (Fig. 4). Since the static aerodynamic coefficient data introduced into the program are in the body axis system, it is necessary to resolve the resultant aerodynamic forces into the X-Y axes system. Taking all forces into account, and resolving them into the X-Y axes system, the resulting force equations are:

$$\ddot{X} = \frac{1}{m} \left[qAC_X - T_j \sin\theta + T_m \cos\theta \right] \quad (1)$$

$$\ddot{Y} = \frac{1}{m} \left[qAC_Y + T_j \cos\theta + T_m \sin\theta \right] \quad (2)$$

The moments acting on the missile are the static aerodynamic moment, the dynamic damping moment, and the moment due to the reaction-jet control thrust. The moment equation can then be written as:

$$\ddot{\theta} = \frac{1}{I} \left[qAd \left(C_m + C_{m\dot{\theta}} \left(\frac{\dot{\theta}d}{2V} \right) \right) + T_j (x_{cg} - x_j) \right] \quad (3)$$

The trajectory programs utilize an integration subroutine, FNOL3, a FORTRAN IV version of FNOL2 described in Ref. 2, to integrate the above differential equations. FNOL3 accomplishes the integration of the equations of motion by utilizing the Runge-Kutta and Adams-Moulton fourth-order techniques for the integration of a system of first-order ordinary differential equations. This subroutine will numerically integrate up to 30 simultaneous, first-order differential equations. The interval of integration can be automatically adjusted to hold the absolute or relative truncation error within specified bounds.

Eqs. (1), (2) and (3) are integrated over a time interval to obtain \dot{X} , \dot{Y} and $\dot{\theta}$, respectively. These are then integrated over the time interval to obtain X , Y and θ .

PHYSICAL CHARACTERISTICS OF MISSILE

A cursory look at several mission profiles indicated a missile size on the order of 350 pounds. Estimates of the vehicle components indicated this was a reasonable size and the moment of inertia was estimated to be approximately 30 slug-ft². These two physical estimates were then used for all the trajectories, except where the moment of inertia was the parameter being investigated.

No attempts were made to optimize the missile size or performance, since the object of the study was to evaluate the slewed-launch concept, and not a missile system.

REACTION-JET CONTROL SYSTEM

A reaction-jet control system was selected to perform the unpowered slew maneuver because of the large rotation angles desired - up to 180 degrees. For convenience of calculations, the reaction jets were placed at the nose of the missile. Jet-interaction effects were not taken into account for these preliminary trajectories, i.e., the reaction jets were assumed to have a magnification of one for all conditions.

A survey of current and predicted valving techniques revealed that it would be possible to pulse the reaction-jet control system at 10-millisecond intervals, that is, the minimum time the jets could be "on" or "off" would be 10 milliseconds.

For these studies, it was decided to attempt to slew the missile 180 degrees in approximately one second. It was felt this could be easily accomplished by slewing the missile at a constant slew rate of approximately 200 degrees/second until the missile approached the desired slew angle, θ_f , where the reaction jets would then decrease the slew rate and stop the rotation with the missile pointed in the desired direction.

The computer-simulated command spectrum utilized in the trajectory calculations is illustrated in Fig. 5. This spectrum dictates when the jets should be (1) on to produce a positive moment, or (2) on to produce a negative moment, or (3) off. The unshaded portion indicates the acceptable range of desired slew rates as a function of the rotation angle. As can be seen, the desired slew rate decreases linearly from the constant value when the rotation angle reaches three-quarters of the desired slew angle.

8th Navy Symposium on Aeroballistics

Vol. 3

The reaction jets control the slew rate by commands from the guidance, which senses the actual value of the slew rate and compares it with the desired slew rate. If the actual rate is less than desired, the jets act "positively" to increase the slew rate; likewise, the jets act "negatively" to decrease the slew rate if the actual slew rate is greater than desired. If the actual rate is within the acceptable limits, the reaction jets remain off.

MOTOR CHARACTERISTICS

The motor selected for these studies was a dual-thrust solid-propellant motor with a total impulse of 34,500 pounds-seconds. The performance of the motor is illustrated in Fig. 6. The boost phase of 5000 pounds' thrust for three seconds accelerates the missile towards the target and the eight seconds' sustain burn of 2000 pounds' thrust maintains a desirable velocity, with a one-second period of transition from boost to sustain phases where the thrust is assumed to decay linearly from 5000 to 2000 pounds. The corresponding rates of propellant consumption are also illustrated. The instantaneous mass used in the equations of motions was the initial mass of the missile minus the amount of propellant burnt.

TRAJECTORY ANALYSIS

A large number of unpowered and powered SLIM trajectories have been calculated to determine the feasibility of the slewed-launch concept. For the unpowered SLIM trajectories, the missile was constrained to two degrees of motion: motion in the X direction and rotational motion about the missile center of gravity. The missile was slewed 180 degrees, held in that position, and allowed to decelerate due to the aerodynamic forces only, i.e., without motor thrust applied, for a total flight time of four seconds.

For the powered SLIM trajectories, the above restraint was removed and motions in the X and Y directions, as well as rotational motion, were resolved. The missile was slewed to desired headings of 45, 90, 135 and 180 degrees, the motor ignited at some time, t_i , when the missile rotated to within five degrees of the desired heading, and the missile then accelerated towards the target. For desired headings of 45, 90 and 135 degrees, the trajectories were calculated for flight times of eight seconds and for the 180-degree trajectory headings, 15 seconds.

UNPOWERED SLIM TRAJECTORIES

The performance of the missile while slewing about its center of gravity during the initial portion of its flight was evaluated by varying:

1. the center-of-gravity location from 47.5 percent to 60 percent from the nose,
2. the missile moment of inertia from 10 to 50 slug-ft²,
3. the magnitude of the reaction-jet control thrust from 300 to 1000 pounds,
4. the launch number from 0.75 to 2.03, and
5. the launch altitude from 500 to 30,000 feet.

Center-of-Gravity Location

The margin of static stability, directly dependent on the center-of-gravity location, had a significant effect on the slewing performance of the missile. Fig. 7 clearly illustrates this point. For center-of-gravity locations forward, represented by the curves for c.g.'s 4.4966 and 4.7333 feet from the nose, the missile is quite stable. The reaction jets did not produce enough torque to overcome the restoring moment and would not turn the missile to the desired heading. Once the velocity had dropped enough to reduce the restoring moment to a value less than that of the reaction-jet torque, the missile proceeded to slew to the desired heading. This resulted in slew times greater than two seconds.

With the center of gravity located rearward, the missile was unstable, so much so that the reaction jets operating negatively could not overcome the destabilizing moment. The missile slew rate became excessive and could not be adequately controlled.

For angles of attack between 0 and 135 degrees, the center of pressure varies from 43 percent to 60 percent of the length from the nose, for the configuration investigated. It was found from many trajectory calculations similar to those above, if the center-of-gravity band investigated was narrowed down to 50 to 52.5 percent of the length, the missile could be slewed with little difficulty over the range of launch Mach numbers and altitudes investigated.

Vol. 3

This center-of-gravity band lies in the middle of the center-of-pressure band and, thus, the missile is never drastically stable or unstable.

Moment of Inertia

The variations in the slewing performance were quite small and were considered insignificant for variations in the transverse moment of inertia of 10 to 50 slug-ft² (Fig. 8). For moments of inertia of 10 slug-ft², it was found the missile responded quite rapidly to changes in the aerodynamic moment as the missile slewed, making it somewhat more difficult to control the slew rate. However, the variations in the time to slew to the desired heading were quite small.

Reaction-Jet Control Thrust

The magnitude and location of the reaction-jet control thrust can be resolved by determining the maximum stabilizing or destabilizing moment the missile may encounter over its complete flight regime. Figs. 9, 10, 11 and 12 illustrate the effect of the magnitude of the reaction-jet thrust on the ability to slew the missile.

An insufficient magnitude of jet thrust results in an inability to slew the missile at the desired slew rate for high-speed, low-altitude launches. The torque developed either cannot overcome the restoring moment, as seen in Figs. 10 and 11, or cannot adequately control the destabilizing moment, as illustrated in Fig. 12.

Reaction-jet thrust levels of 750 to 1000 pounds control the slew rate quite adequately, except for low-altitude, high-speed launches; however, the time to slew to 180 degrees is accomplished in only two seconds for these adverse conditions.

Launch Conditions

The launch conditions, per se, have little effect on the slewing performance of the configuration investigated; however, configurations with large center-of-pressure shifts may experience some difficulty in slewing under certain launch conditions and may be restricted in use. The only noticeable effects on the slew performance in the current trajectories were for low-altitude, high-speed launches where the dynamic pressure was quite high; nevertheless, the missile was slewed 180 degrees in less than two seconds.

Damping Characteristics

Since slender-body theory was used in the absence of experimental data to obtain the damping moment coefficients for the trajectory analysis, a limited number of trajectories were computed with various values of the damping coefficients. Trajectories utilizing damping moment coefficient values one-half and twice the calculated slender-body values were run with insignificant differences in the results.

POWERED SLIM TRAJECTORIES

The analysis of the unpowered SLIM trajectory results defined the critical parameters, established various limitations of the system, and revealed that the vehicle could be slewed through 180 degrees in 1.0 to 1.5 seconds. Powered SLIM trajectories were then computed to determine the ability of the reaction-jet control system to: (1) control the missile as it passed through minimum velocity for 180-degree slew launches; or (2) maintain the desired heading, at slew angles other than 180 degrees where the restoring or destabilizing moments may be quite large, as the missile accelerated towards the target.

No problems were encountered as the missile slewed 180 degrees, decelerated to minimum velocity, and accelerated towards the target. Unlike an aerodynamic control system which is dependent upon some dynamic pressure to be effective, the reaction-jet control system is a positive control system and not dependent upon any aerodynamic forces for control. Figs. 13 through 16 illustrate the velocity and angular histories for SLIM for high- and low-speed launches at low and high altitudes. As can be seen, there were no fluctuations in the angular orientation of the missile as it decelerated to minimum velocity. It should be noted the missile never decelerated to zero velocity because a Y component of velocity was generated by the acceleration in the Y direction due to the aerodynamic and reaction-jet forces during the slewing phase.

Powered SLIM trajectories were calculated where it was desired to slew the missile 45, 90, 135 and 180 degrees. Figs. 17 through 20 show there was no difficulty maintaining the missile at the desired orientation as the missile accelerated towardsthe target, except in a few cases. The missile is unstable from Mach 0.75 to 1.1 and tends to drift off from the desired heading as it accelerates through this range. Once through this range, as illustrated in Figs. 18, 20 and 21, the reaction jets quickly restored the missile to

Vol. 3

the desired heading. Fig. 21 reveals the effect of the center-of-gravity location on the amount of angular drift-off. The most rearward center-of-gravity location produces the largest drift-off angle and the longest period of drift-off.

Figs. 22 through 27 illustrate the position of the missile with respect to a fixed point in space as it is ejected from the launch aircraft at time equal to zero, slews to the desired heading and accelerates towards the target. The effect of launch Mach number and launch altitude are clearly shown. The effect of the angular drift-off on the position of the missile is revealed in Fig. 26 for the Mach 1.25 launch at a desired heading of 135 degrees.

The configuration studied, utilizing the slewed-launch techniques, was compared to the same configuration commanded to pull a maximum turn of 20 or 30 g's under power utilizing either reaction jets or Thrust Vector Control (TVC) and also to a typical winged configuration commanded to pull a maximum turn under power utilizing aerodynamic controls. Fig. 28 summarizes the results of this comparison.

The missile utilizing the slewed-launch technique has essentially the same performance as the missile with TVC or the typical winged missile for targets in the forward hemisphere, i.e., ± 90 degrees with respect to the longitudinal axis of the launch aircraft, except for targets close to the launch aircraft, where it has a distinct advantage. For targets in the rear hemisphere, the slewed-launch missile has an unmistakable advantage over the other two missiles, since the time to target is considerably reduced.

CONCLUSIONS

The ability to slew a missile, after ejection from the launch aircraft, to any desired heading prior to ignition of the motor and to control the missile as it accelerates to the target through the use of a reaction-jet control system appears feasible, offers distinct advantages to current launch techniques and missile systems, and provides a major improvement in the offensive and/or defensive capability of current and future aircraft. The time consuming maneuvers of vectoring the aircraft towards the target prior to missile launch or the missile performing a high-g turn to vector on the target would be eliminated and the time to target in the rearward hemisphere of the launch aircraft would be substantially reduced.

Trajectory studies to date have revealed that the most critical parameter affecting the slewed-launch performance is the static margin of stability. A missile too stable is difficult to slew and a missile too unstable is difficult to control, particularly for low-altitude, high-speed launches. A configuration utilizing the slewed-launch technique should be aerodynamically designed such that the center-of-pressure shift with Mach number and angle of attack would be kept to a minimum; otherwise, the missile could be restricted in its use. The size and location of the reaction jets can be resolved by determining the maximum static moment to be encountered in the missile launch envelope.

The missile moment of inertia and the dynamic damping have little effect on the slew performance.

In the near future, target intercept studies will commence with a missile utilizing the slewed-launch technique to determine the effectiveness of the reaction-jet control system on the missile maneuverability. In addition, the SLIM studies will be expanded to six degrees of freedom to determine the ability of the reaction-jet control system to stabilize the missile in pitch and roll as the missile slews.

REFERENCES

1. U. S. Naval Ordnance Laboratory. A Wind Tunnel Investigation of the Hypersonic Air-to-Ground Rocket (HAGR) over an Angle-of-Attack Range of 0° to 180° at Subsonic, Transonic and Supersonic Speeds, by R. T. Hall. White Oak, Silver Spring, Md., NOL, April 1969. (NOLTR 69-70, in publication, publication UNCLASSIFIED.)
2. U. S. Naval Ordnance Laboratory. FNOL2, A FORTRAN (IBM 7090) Subroutine for the Solution of Ordinary Differential Equations with Automatic Adjustment of the Interval of Integration, by J. S. Linnekin and L. J. Belliveau. White Oak, Silver Spring, Md., NOL, July 1960. 28 pp. (NOLTR 63-171, publication UNCLASSIFIED.)

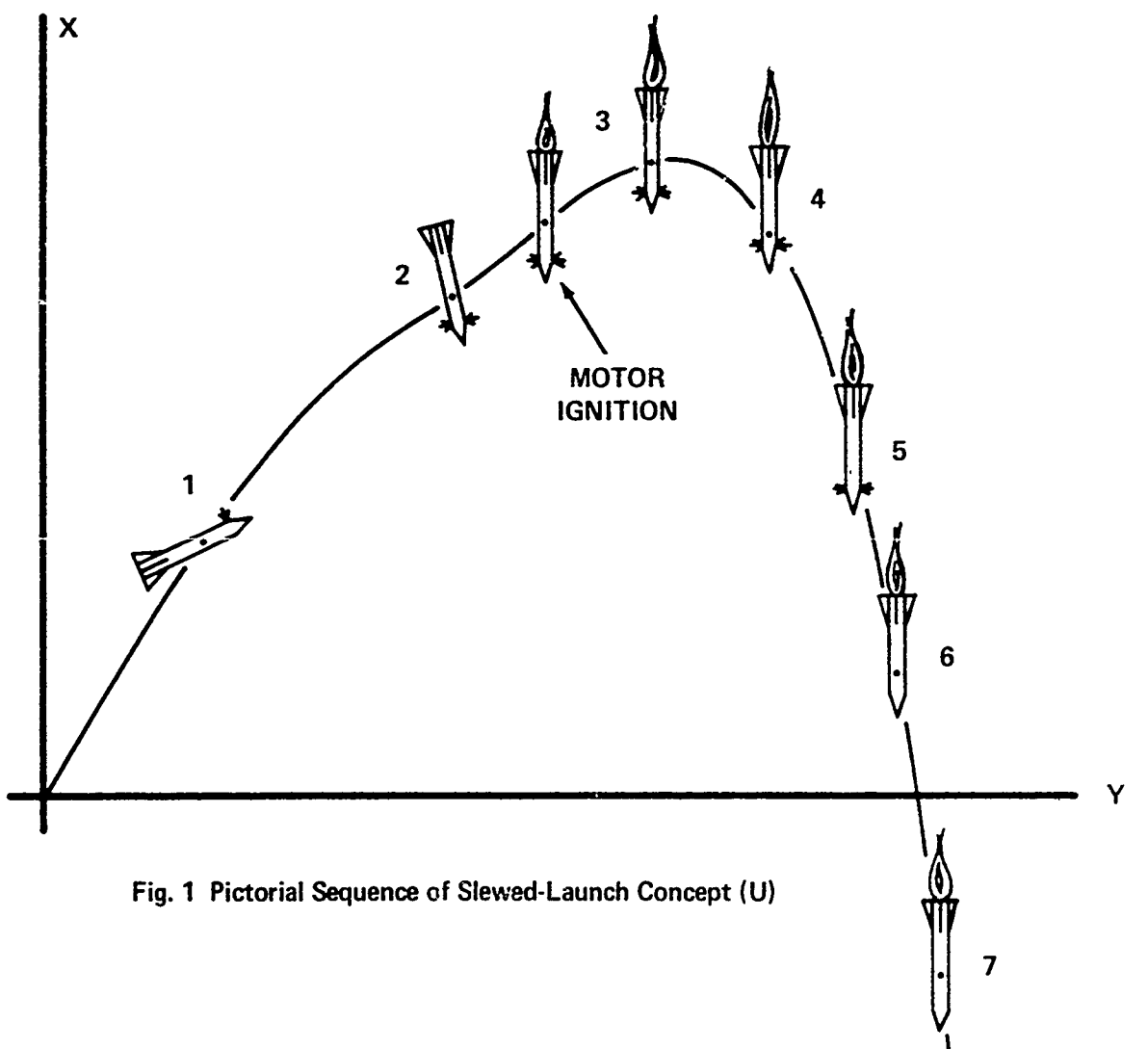


Fig. 1 Pictorial Sequence of Slewed-Launch Concept (U)

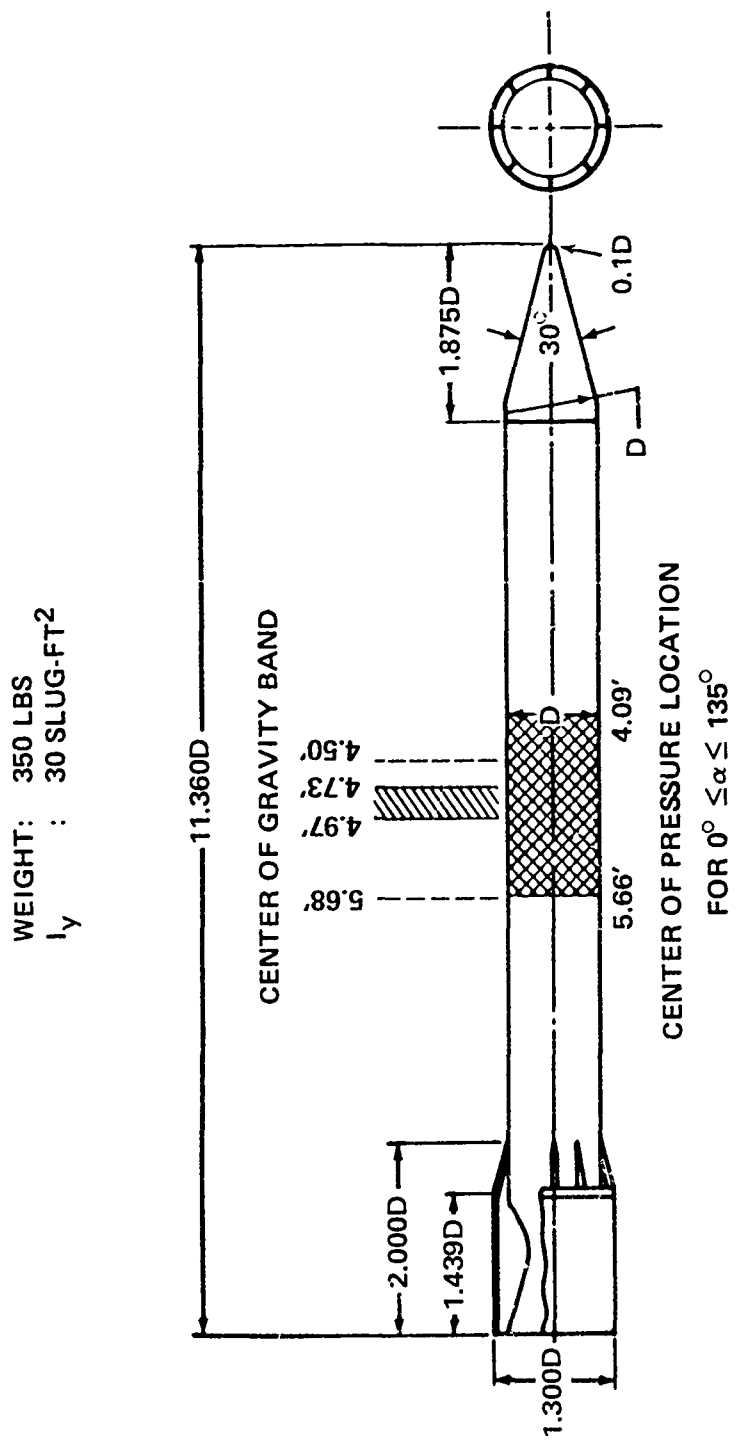


Fig. 2 Configuration Used For Slim Studies (U)

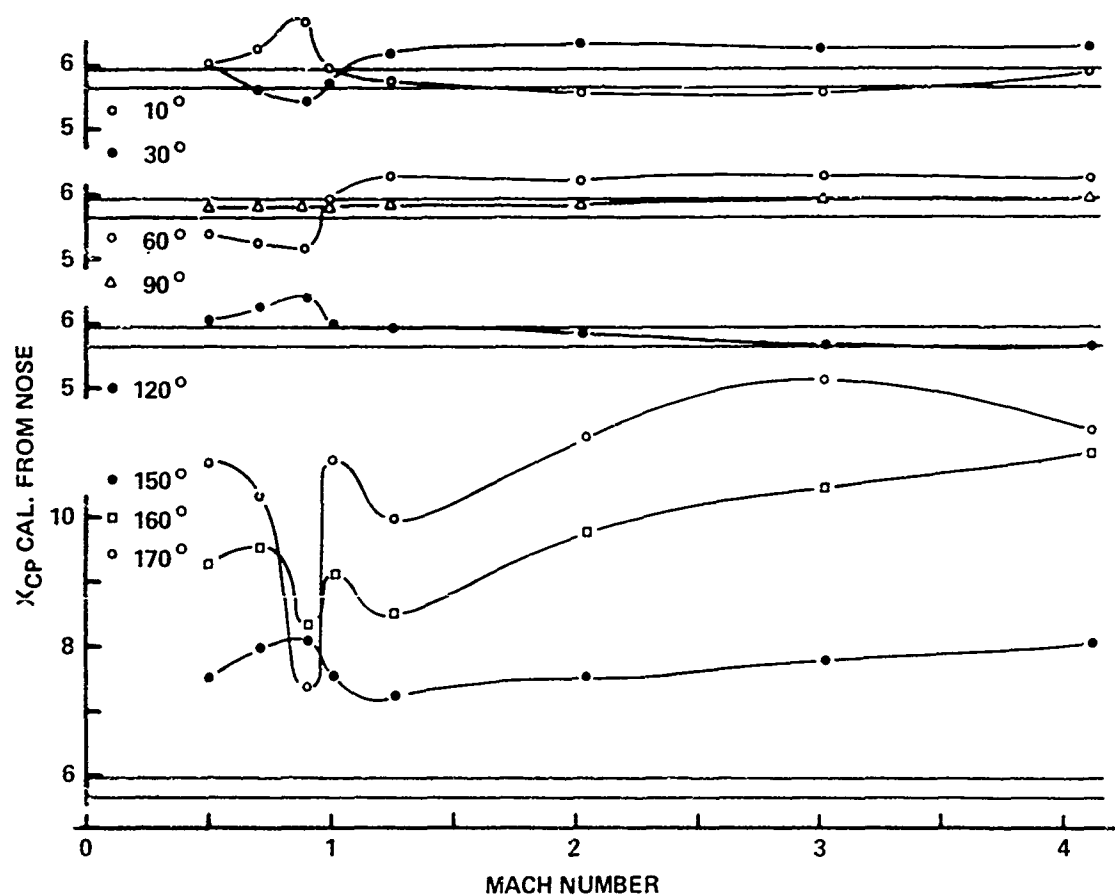


Fig. 3 Center of Pressure Versus Mach Number (U)

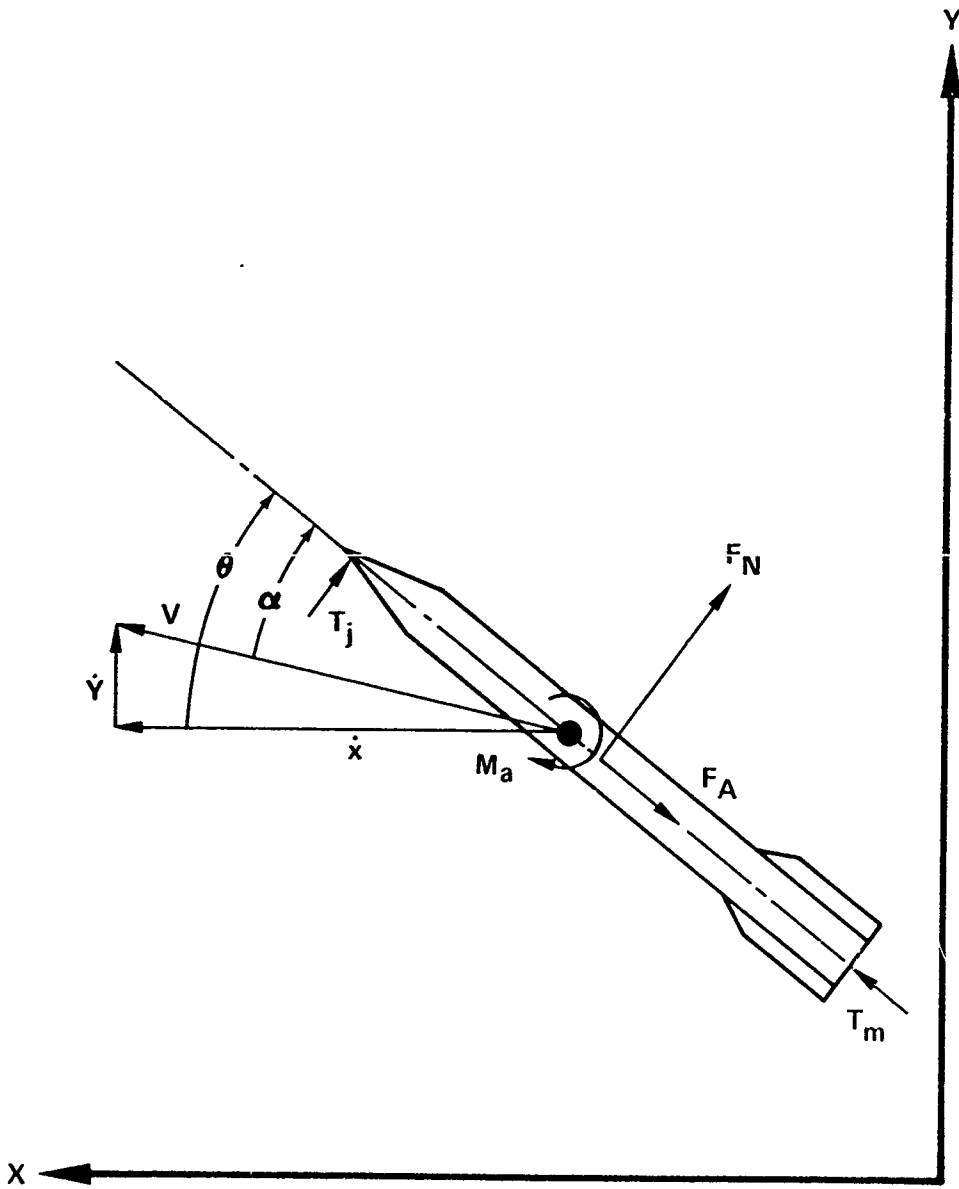


Fig. 4 Slew-Launched Interceptor Missile Orientation (U)

8th Navy Symposium on Aeroballistics

Vol. 3

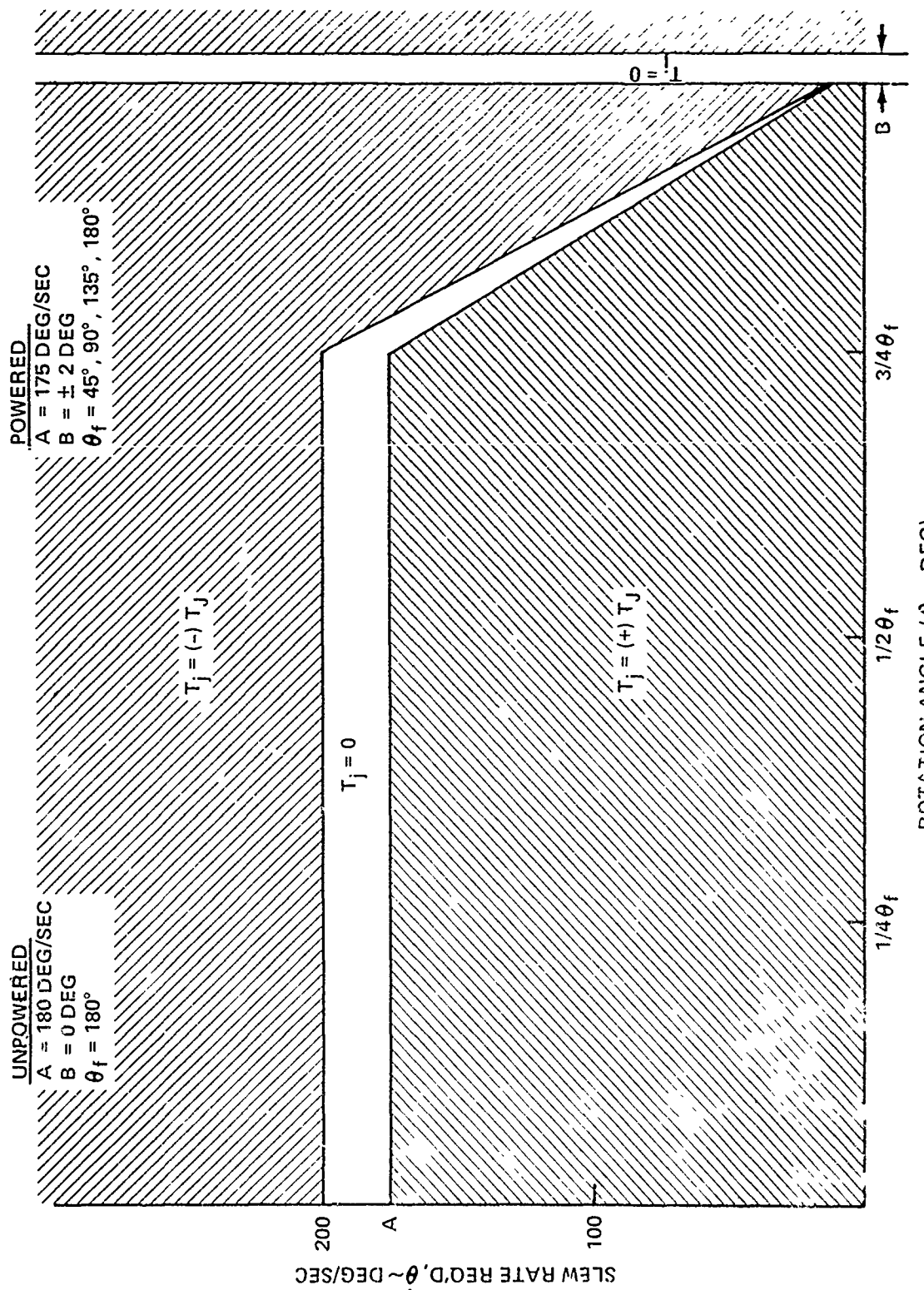


Fig. 5 Slew Rate Required Versus Rotation Angle (U)

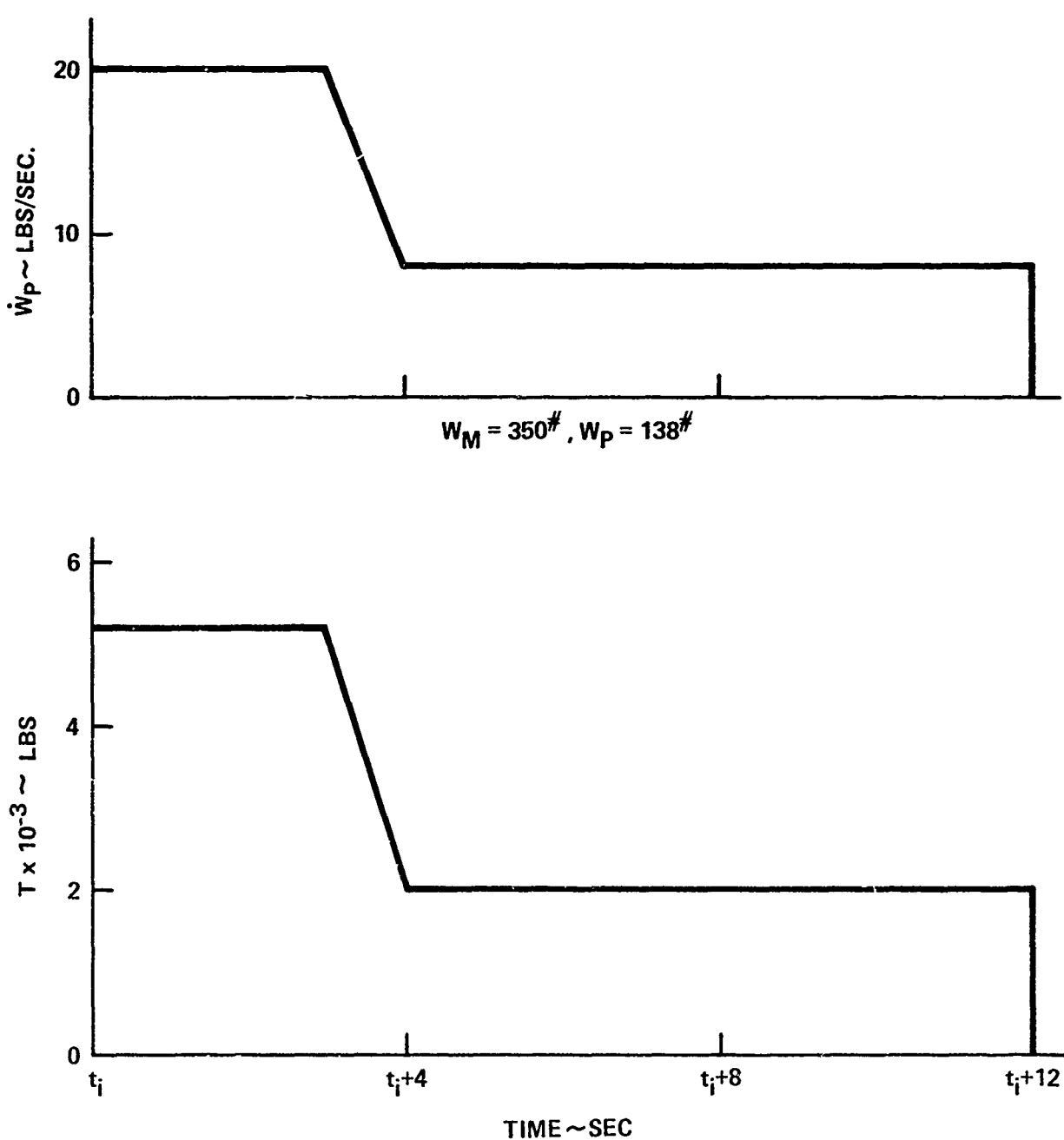


Fig. 6 Motor Performance (U)

Vol. 3

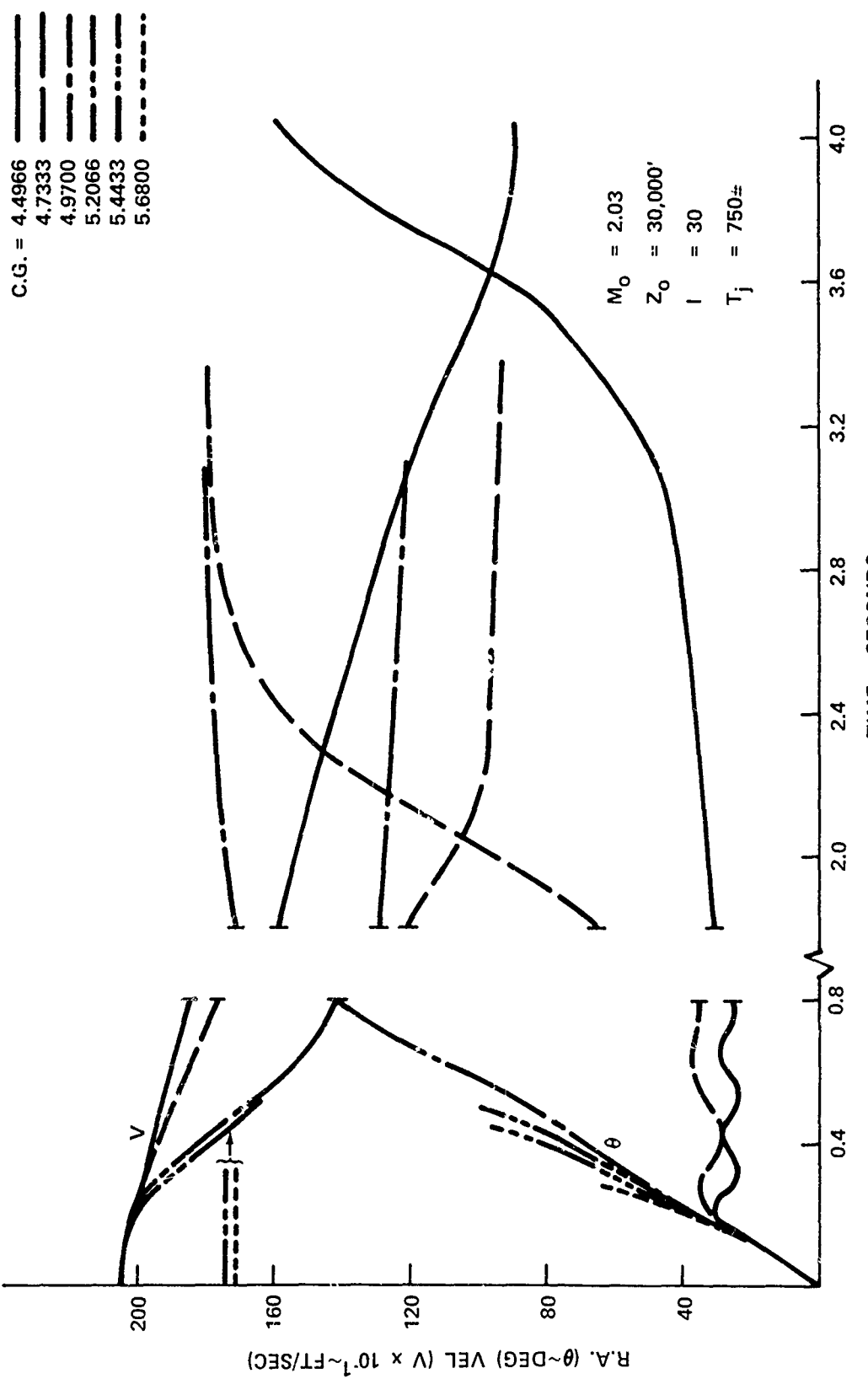


Fig. 7 Rotation Angle & Velocity Versus Time

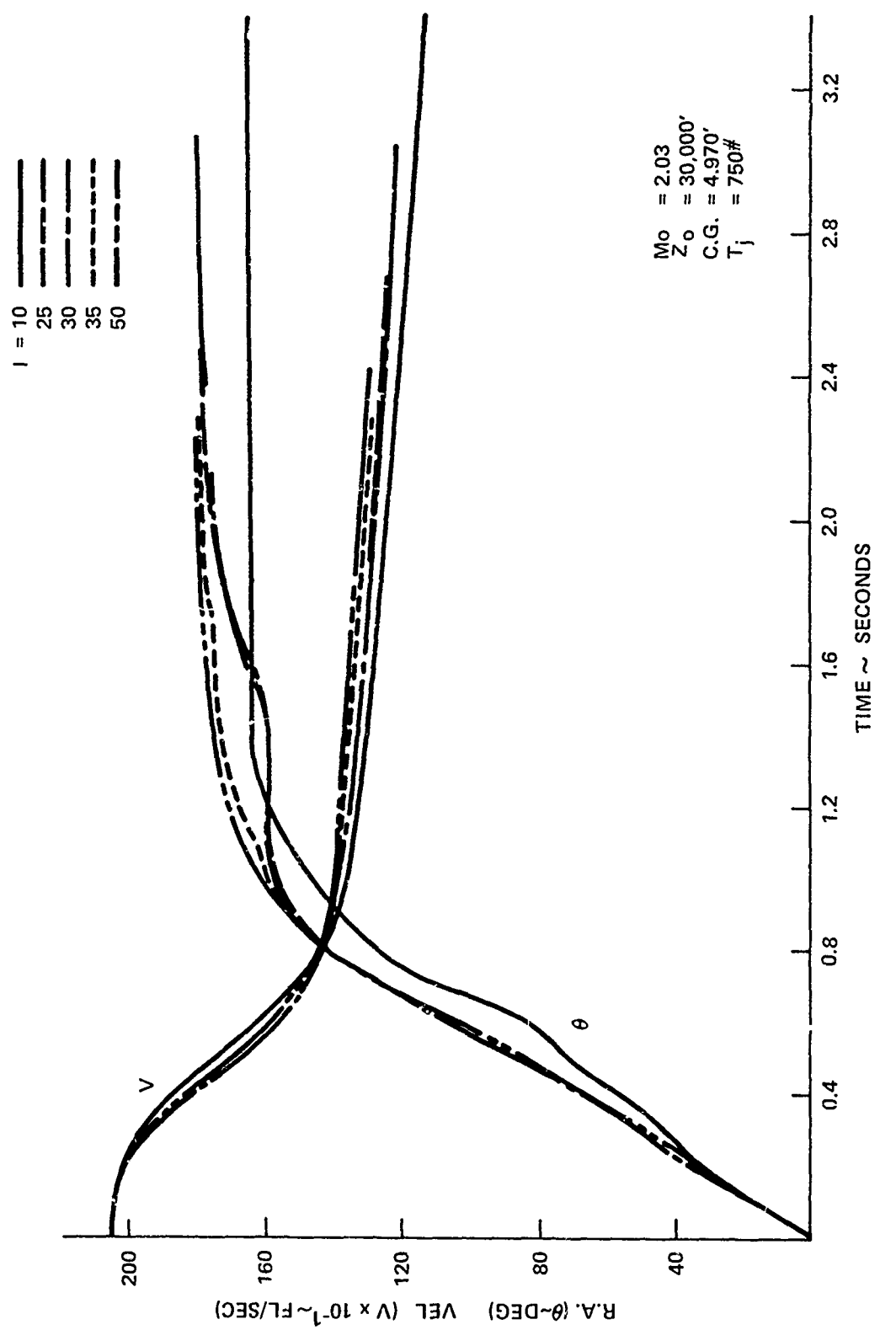


Fig. 8 Rotation Angle & Velocity Versus Time (U)

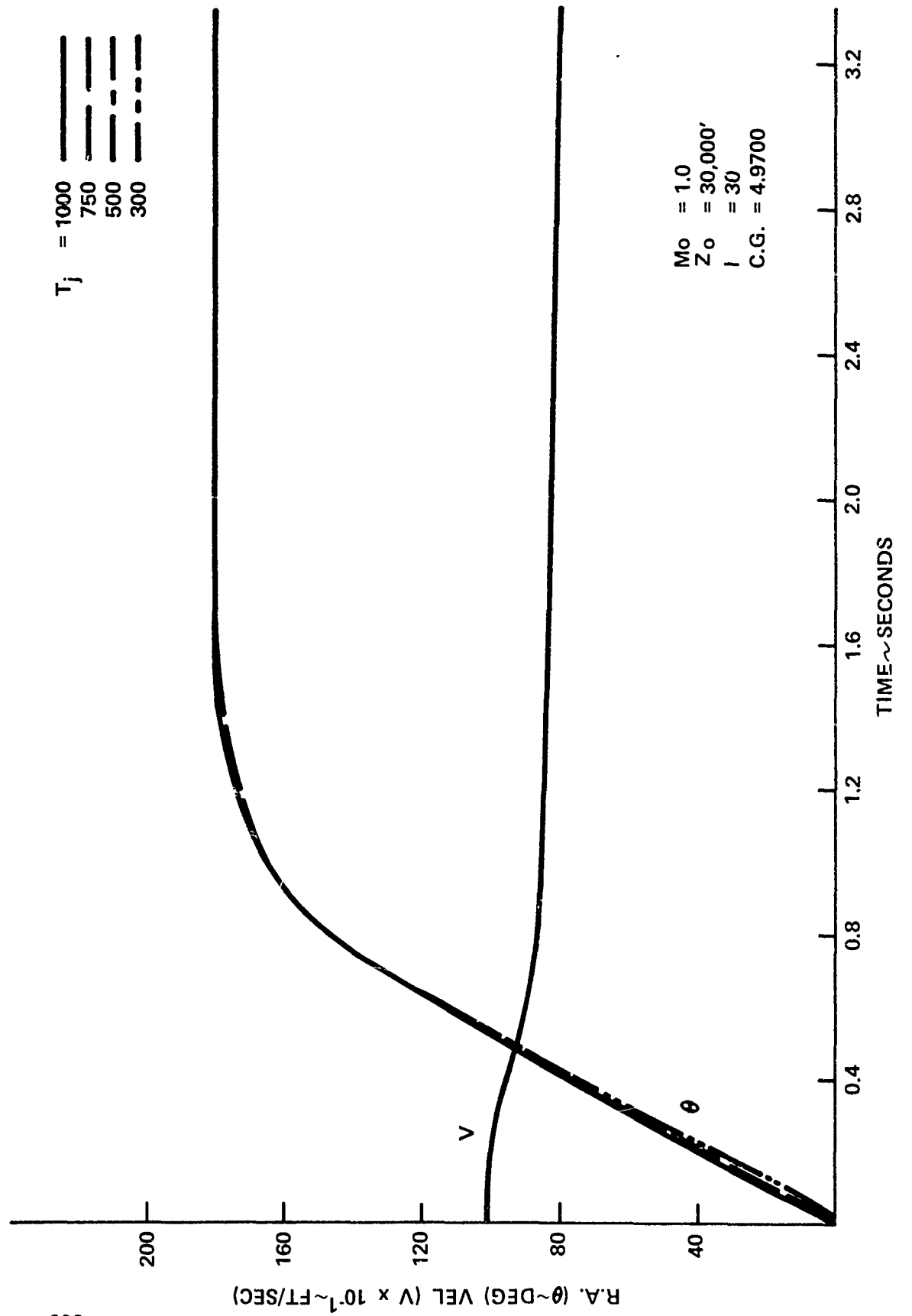


Fig. 9 Rotation Angle & Velocity Versus Time (U)

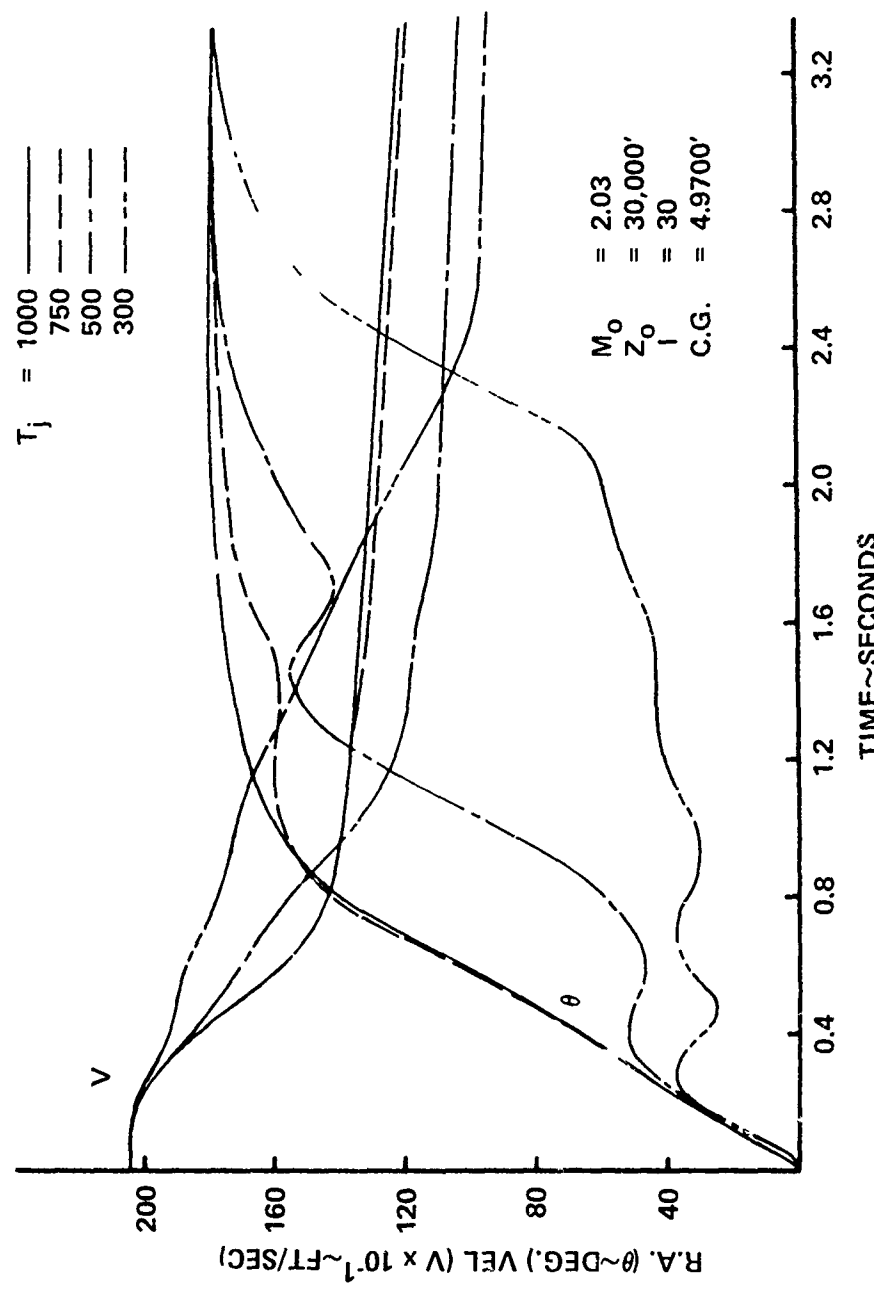


Fig. 10 Rotation Angle & Velocity Versus Time (U)

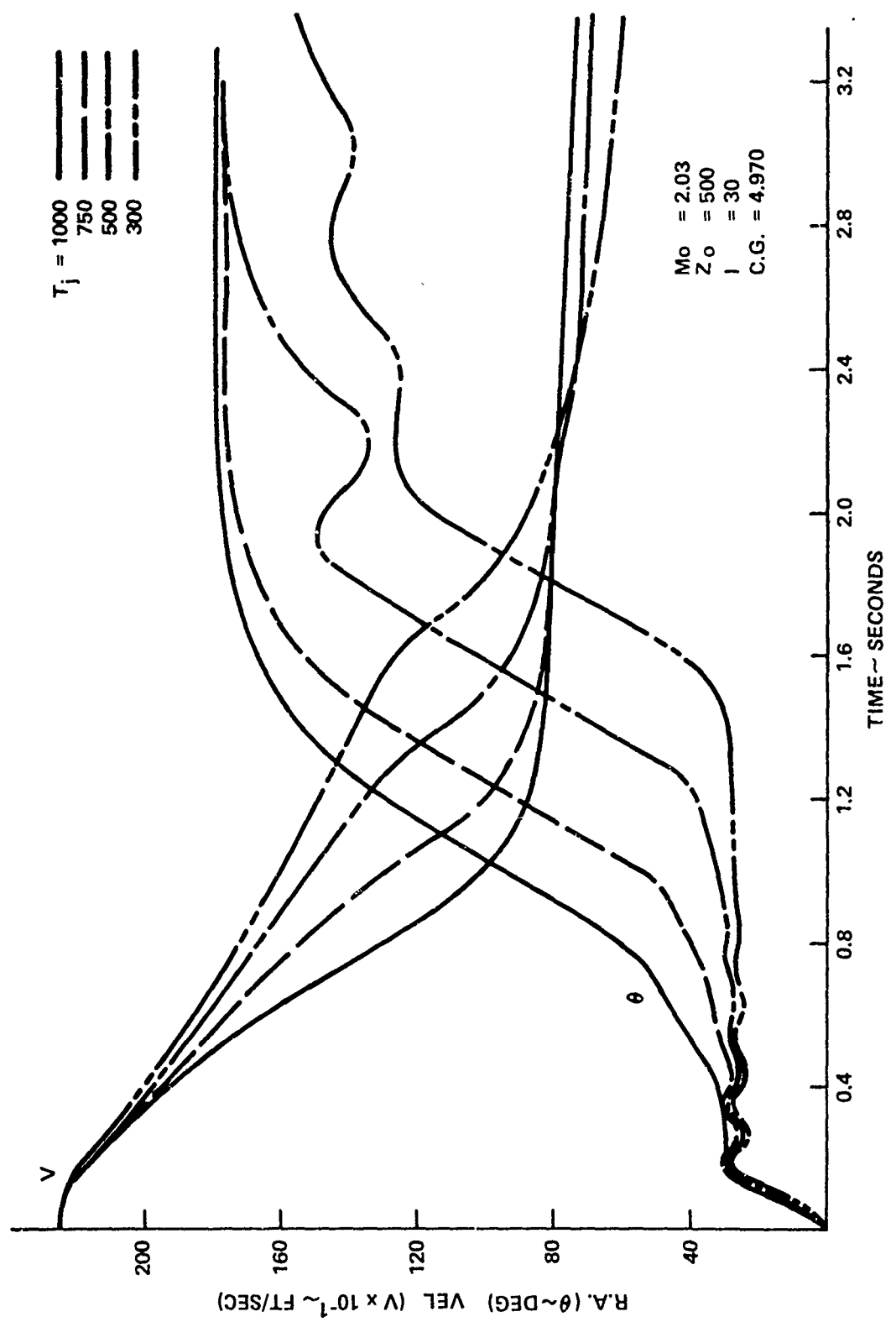


Fig. 11 Rotation Angle & Velocity Versus Time (U)

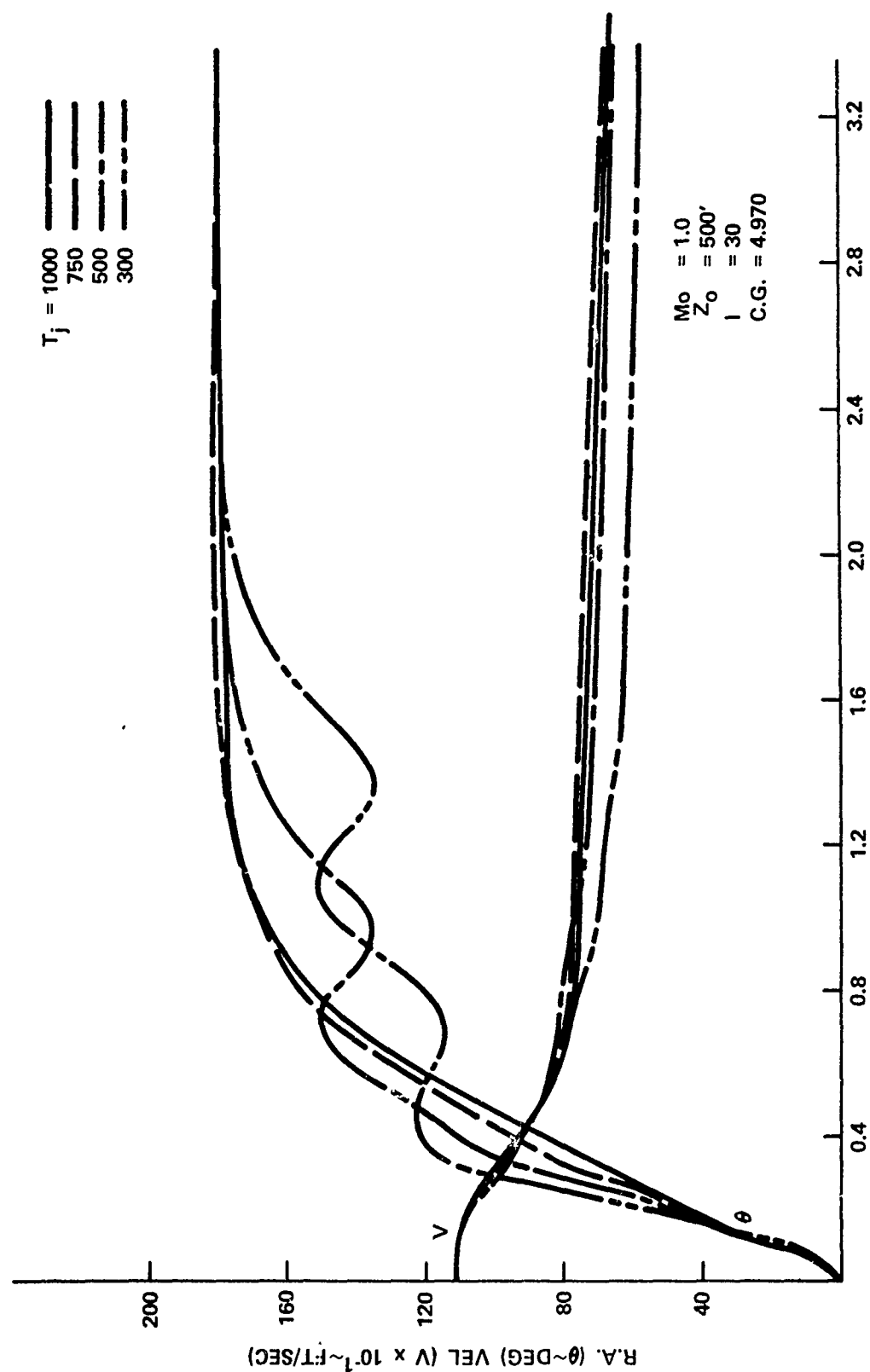


Fig. 12 Rotation Angle & Velocity Versus Time (U)

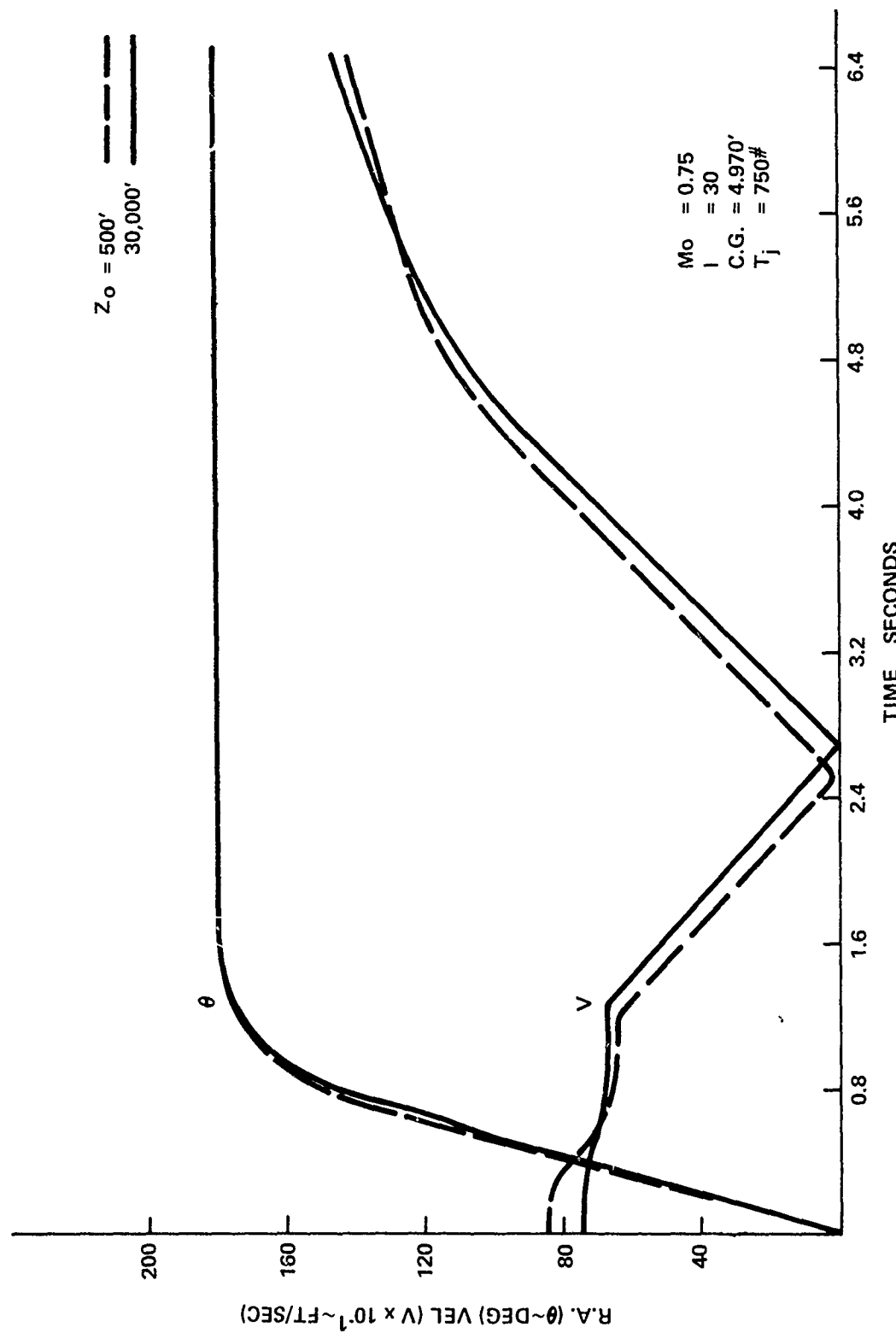


Fig. 13 Rotation Angle & Velocity Versus Time (U)

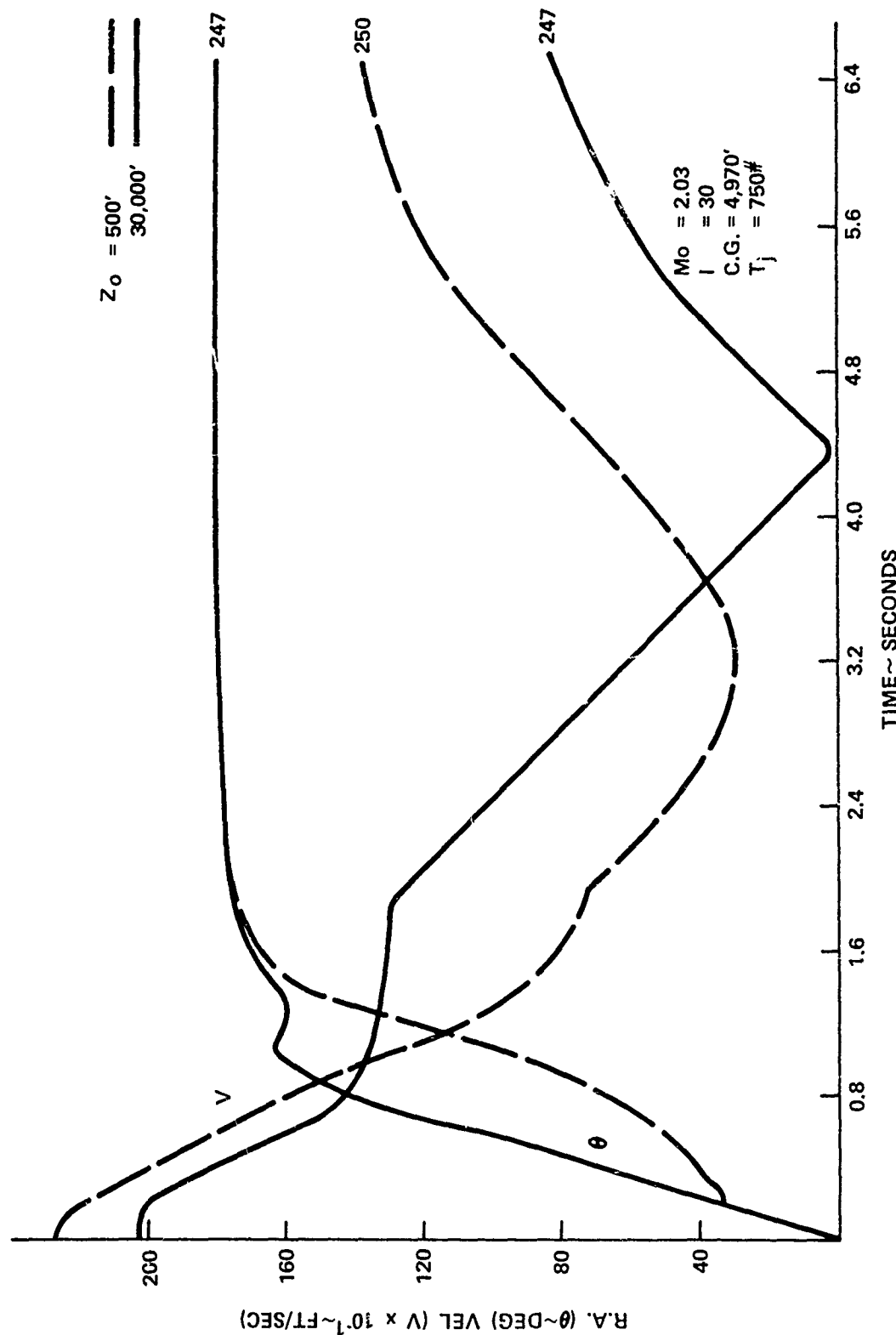


Fig. 14 Rotation Angle & Velocity Versus Time (U)

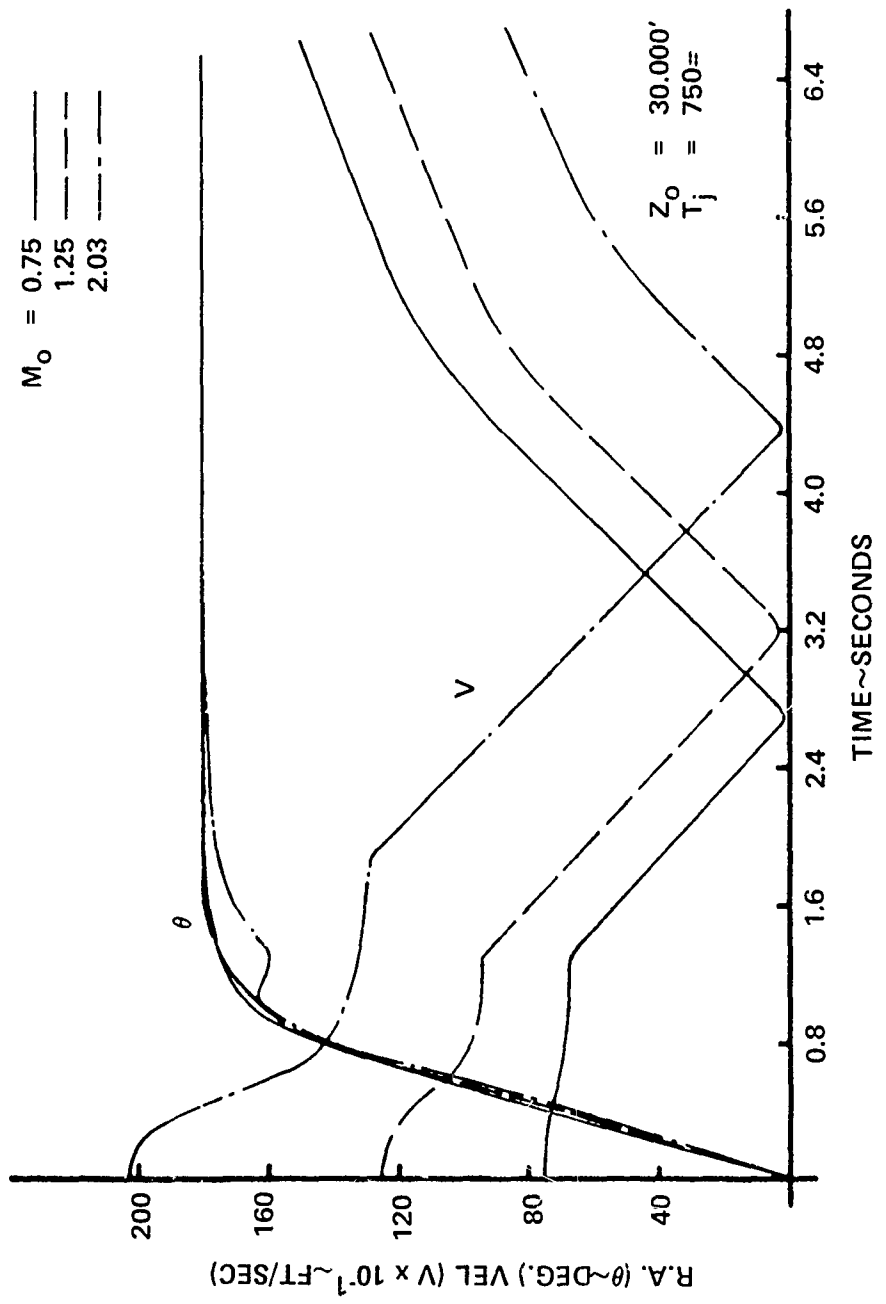


Fig 15 Rotation Angle & Velocity Versus Time (U)

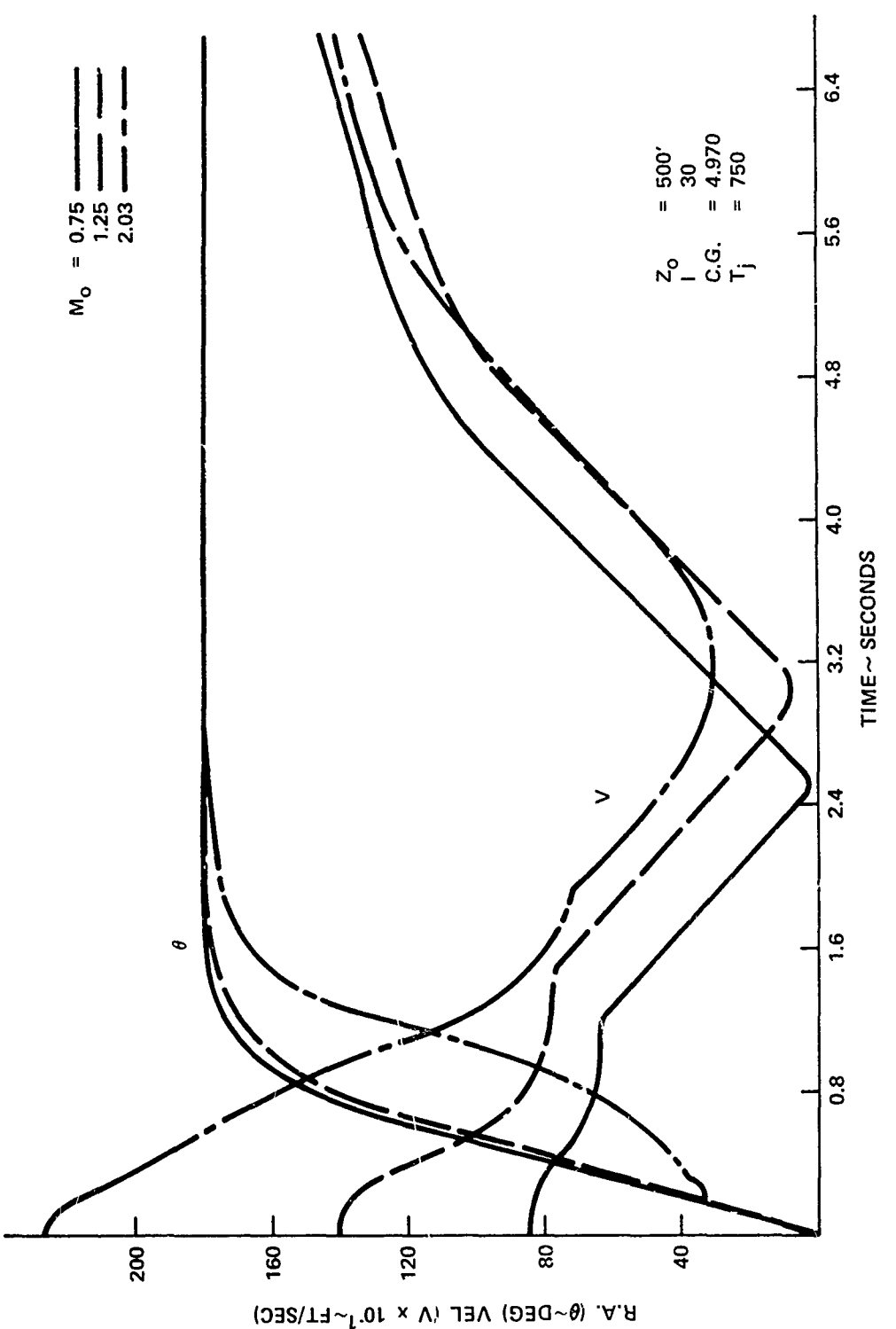


Fig. 16 Rotation Angle & Velocity Versus Time (U)

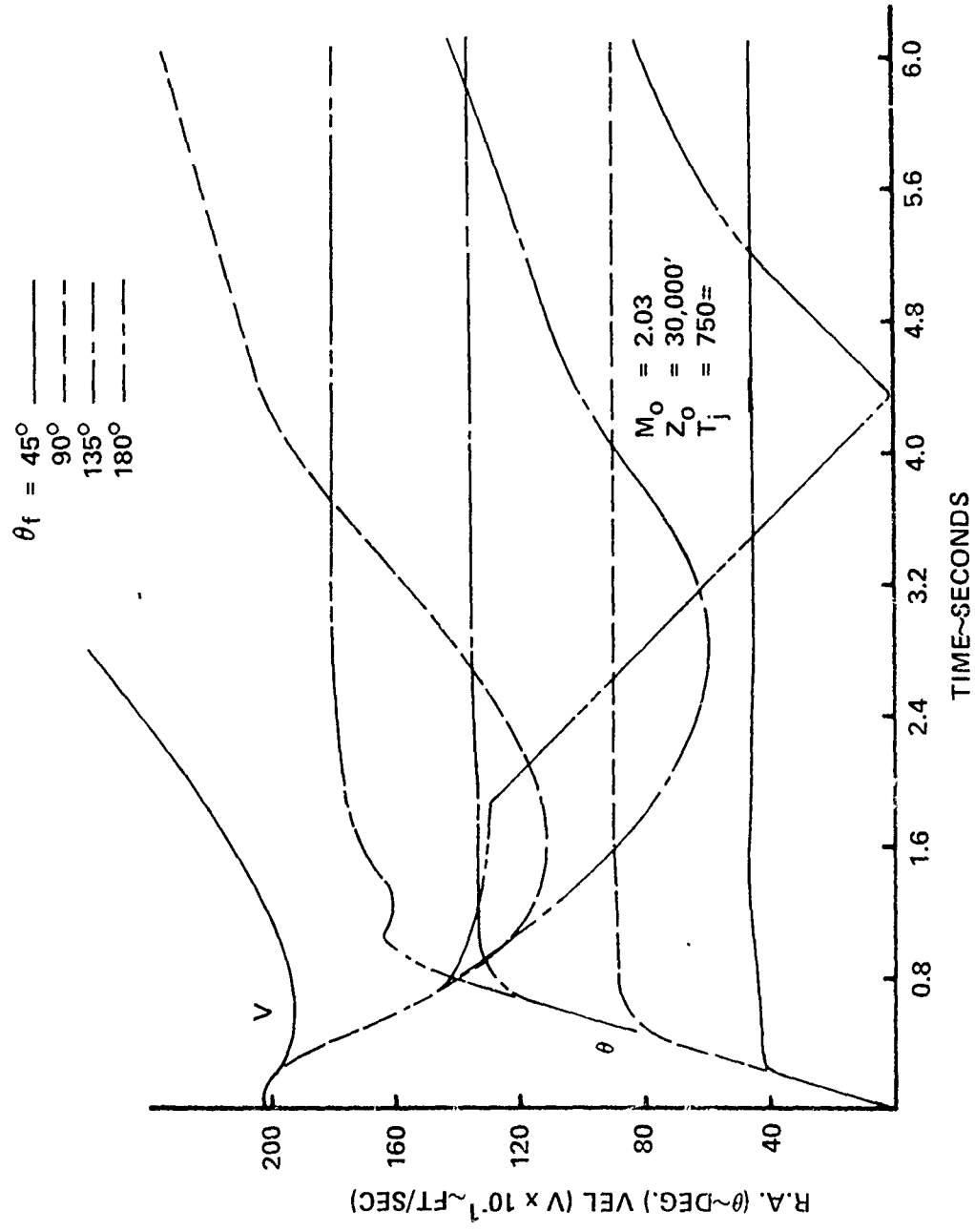


Fig. 17 Rotation Angle & Velocity Versus Time (U)

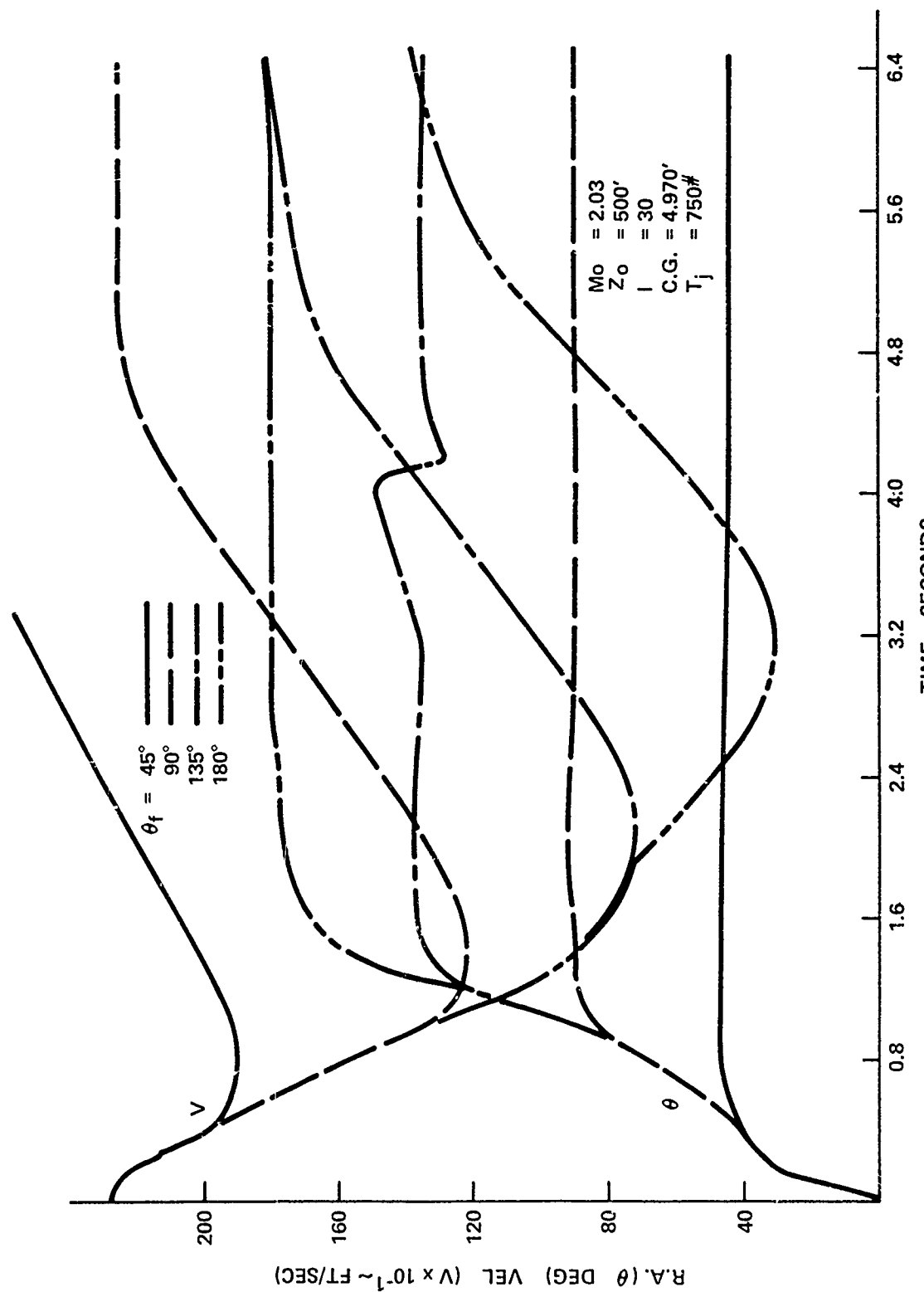


Fig. 18 Rotation Angle & Velocity Versus Time (U)

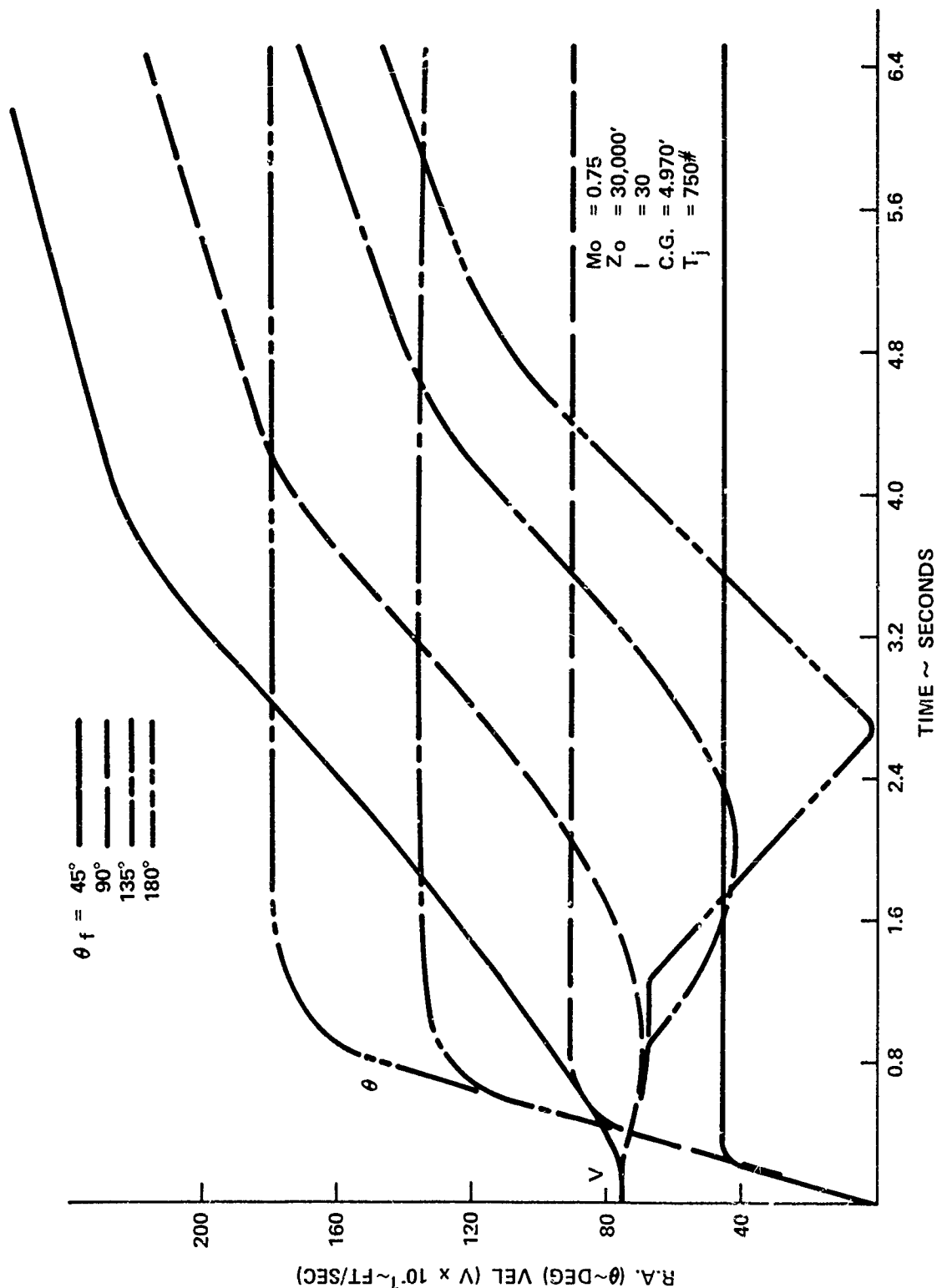


Fig. 19 Rotation Angle & Velocity Versus Time (U)

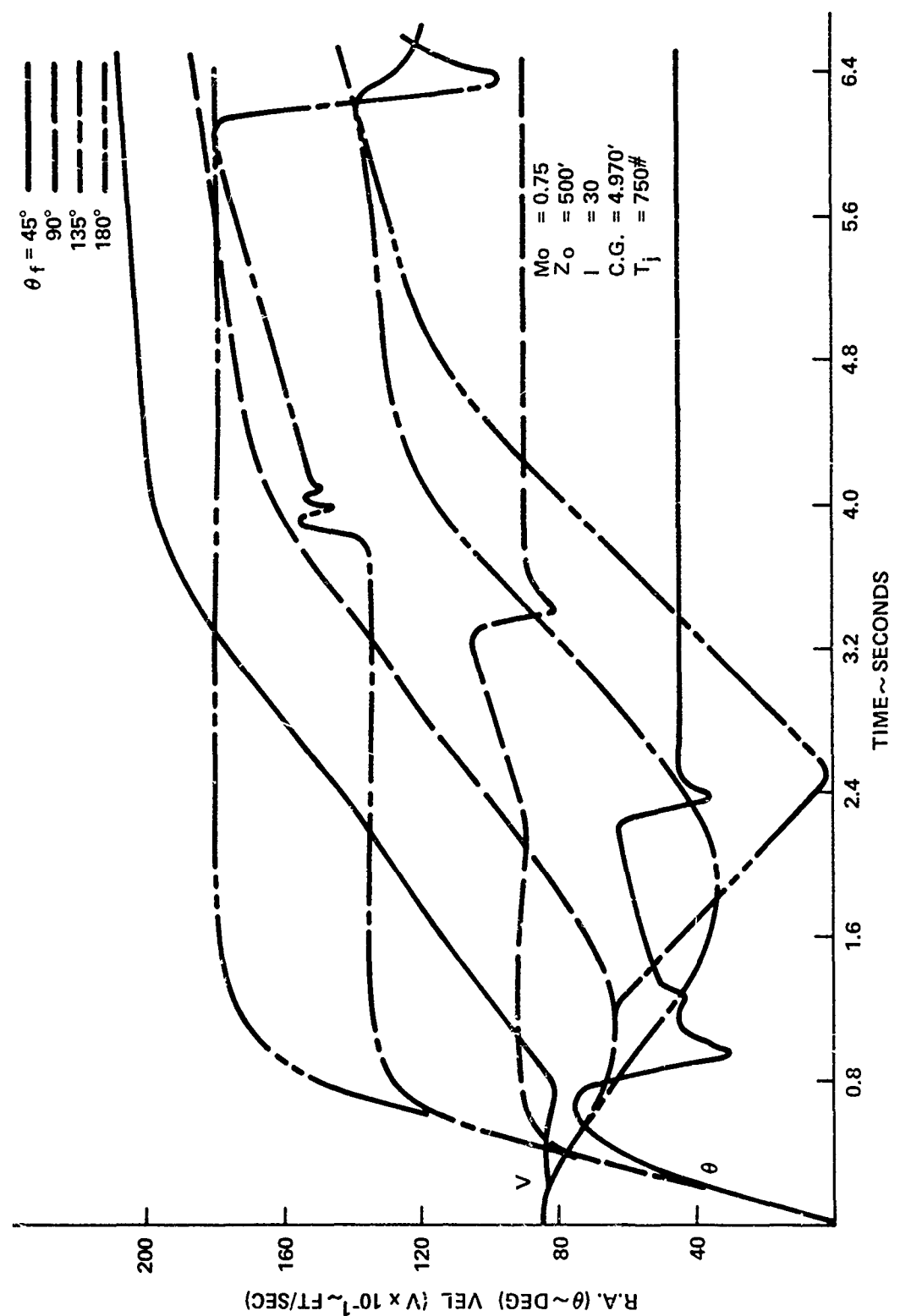


Fig. 20 Rotation Angle & Velocity Versus Time (U)

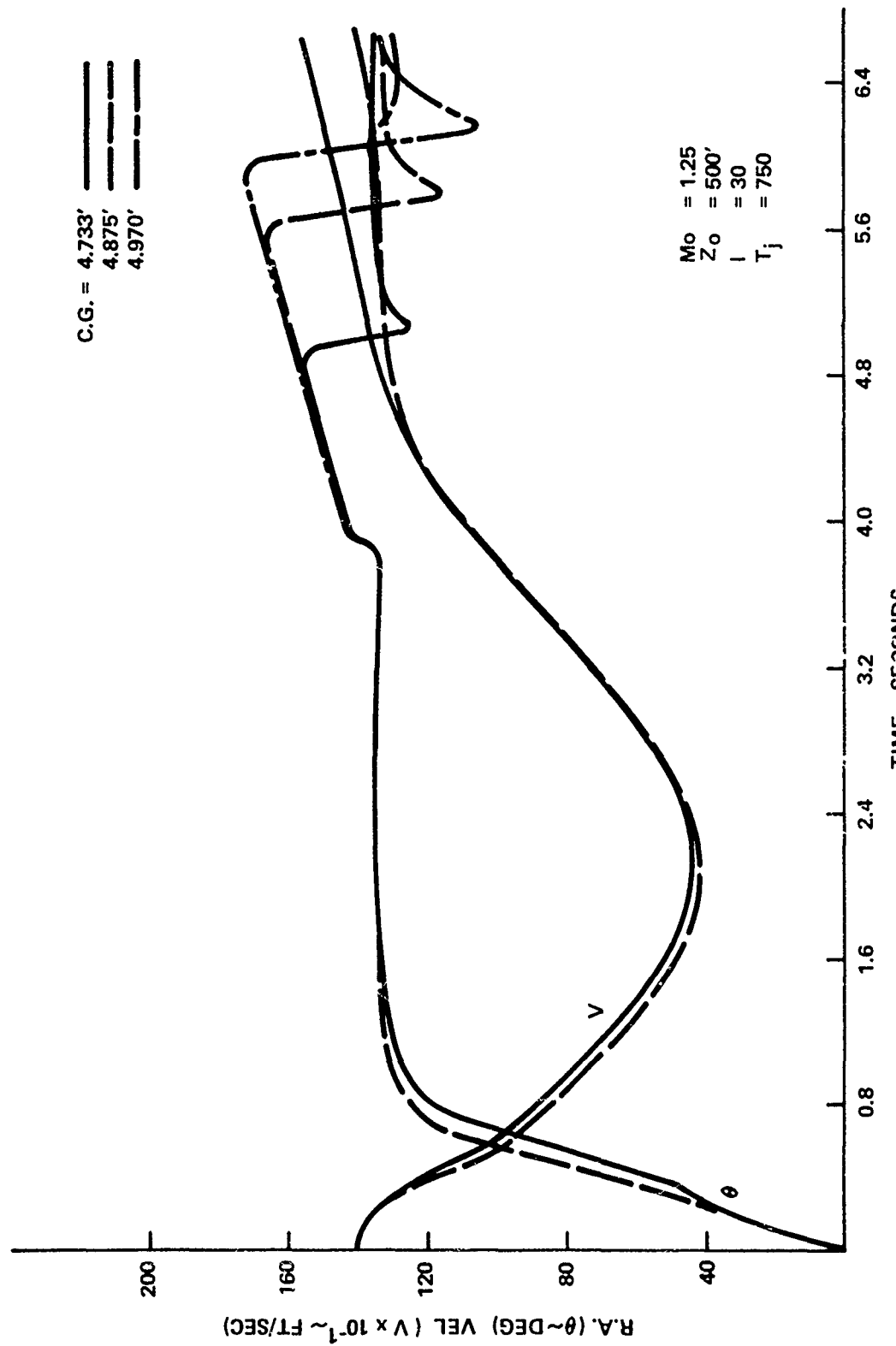


Fig. 21 Rotation Angle & Velocity Versus Time (U)

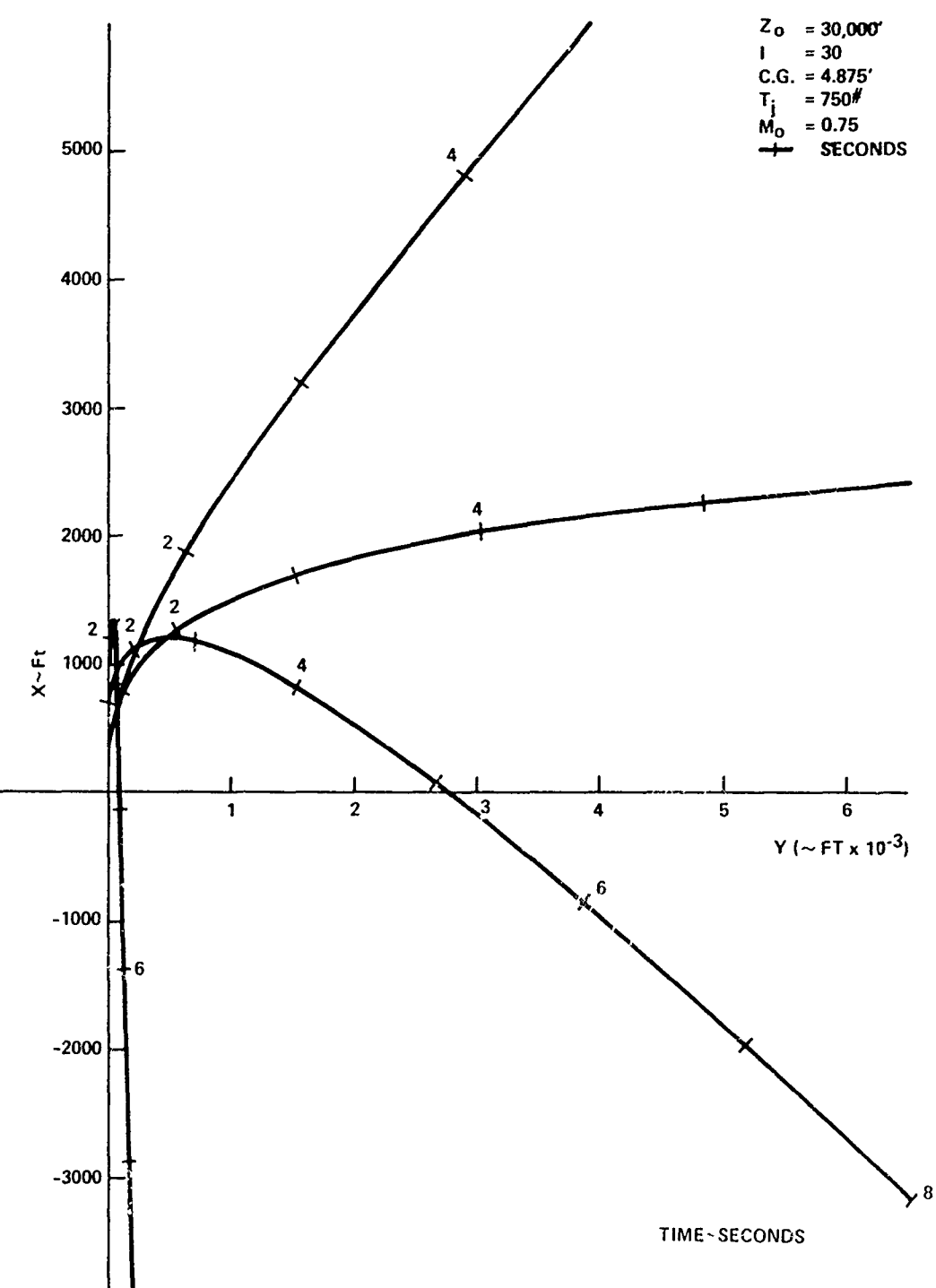


Fig. 22 Missile Position as a Function of Time (U)

8th Navy Symposium on Aeroballistics

Vol. 3

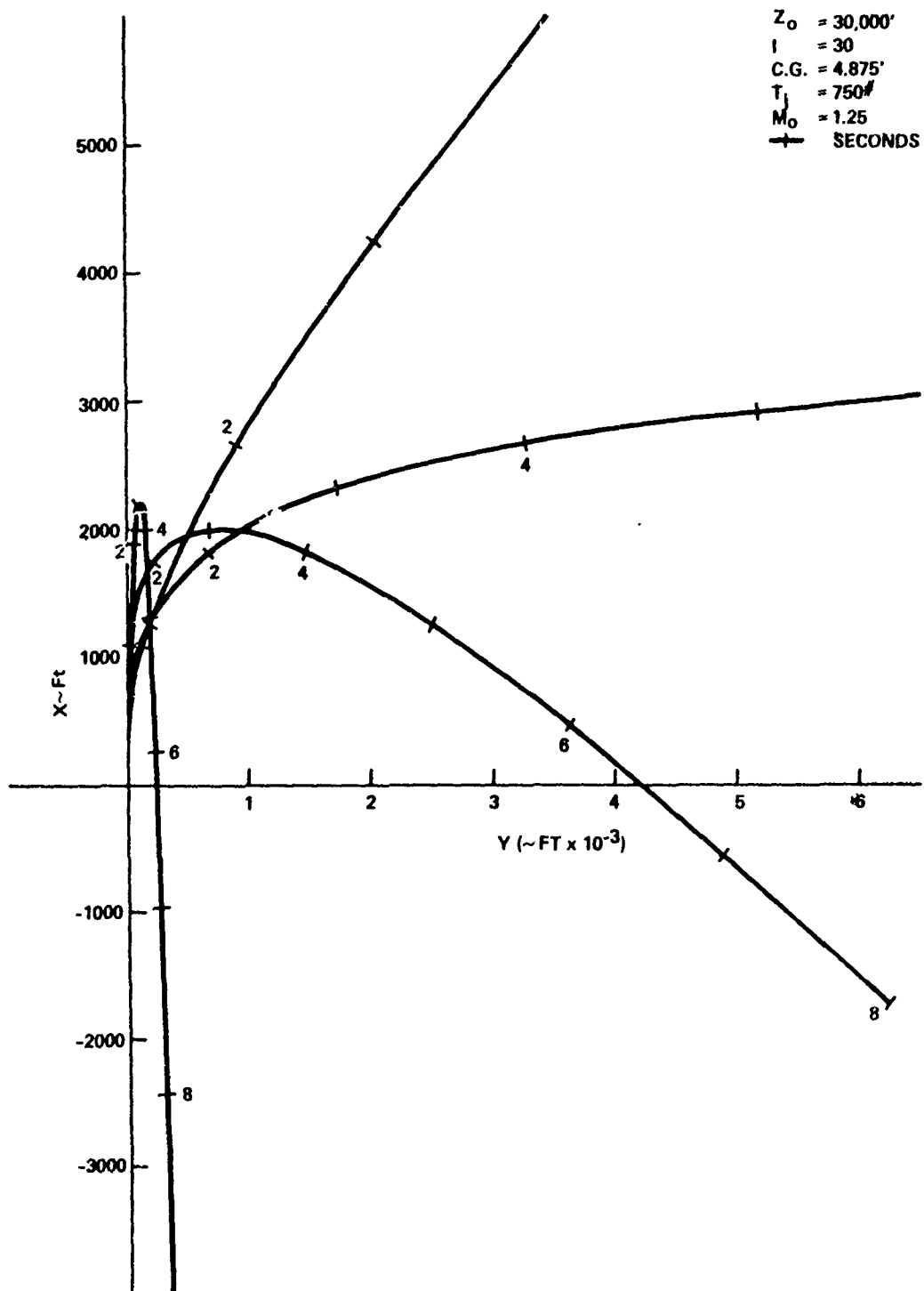


Fig. 23 Missile Position as a Function of Time (U)

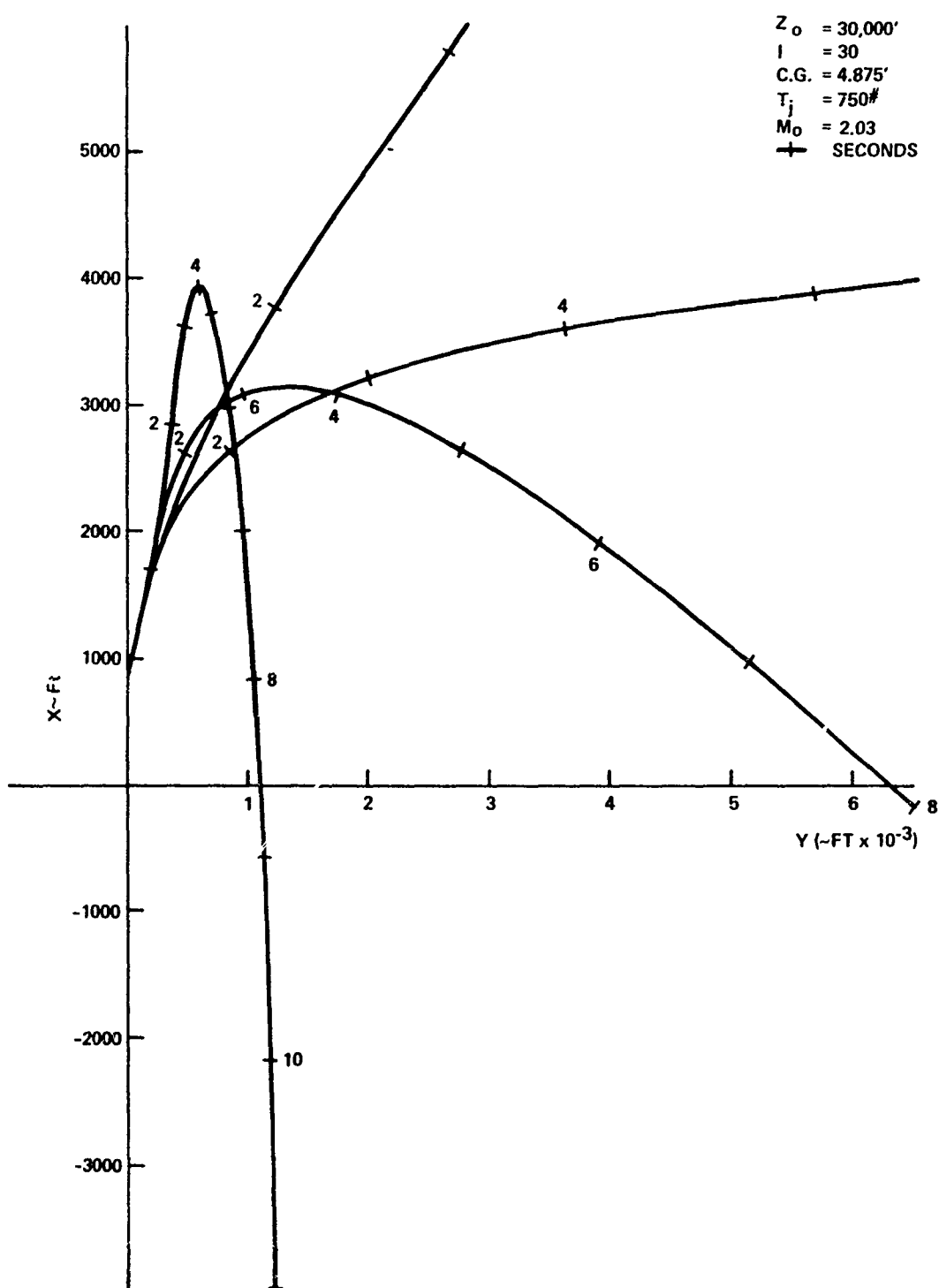


Fig. 24 Missile Position as a Function of Time (U)

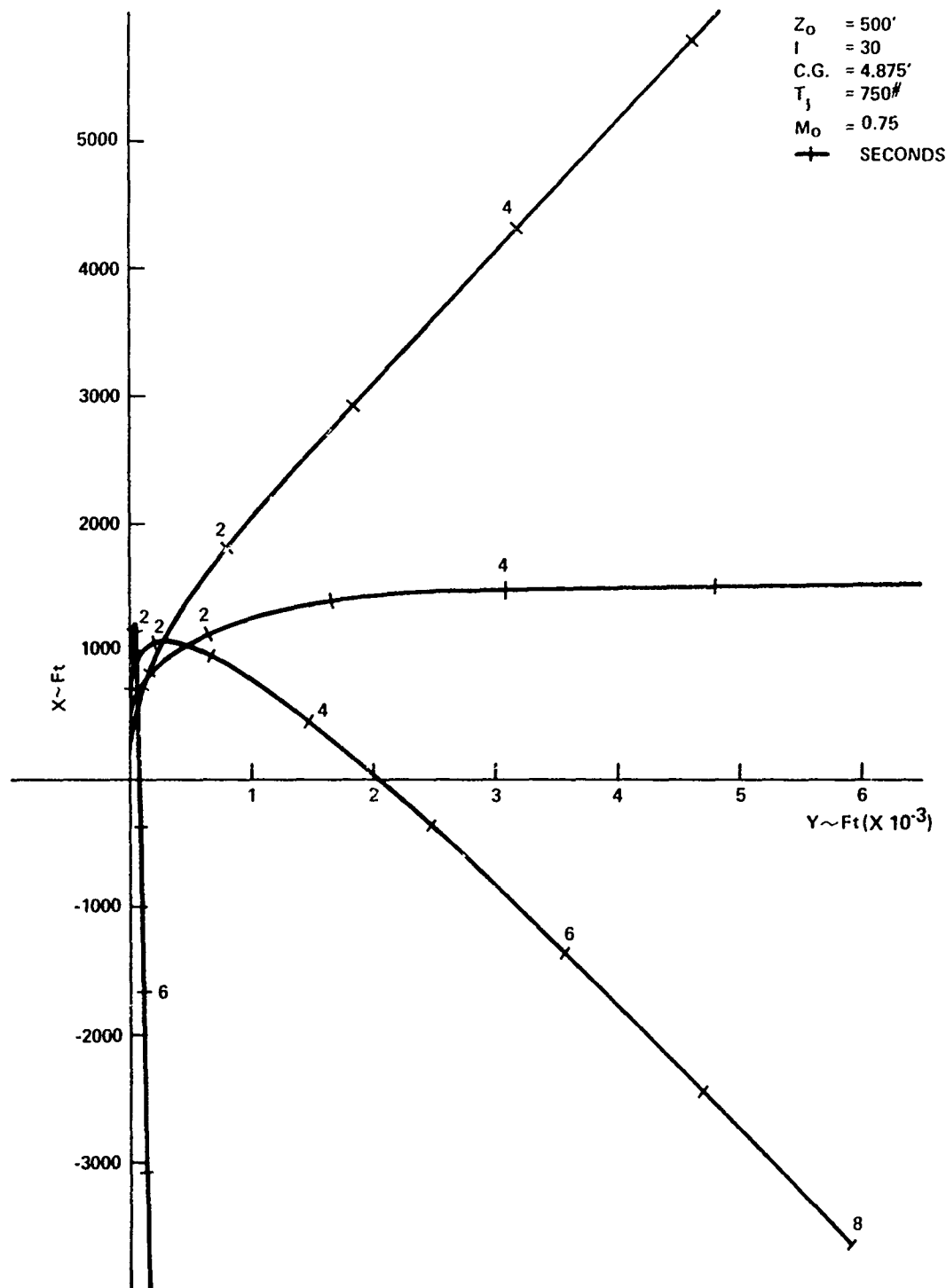


Fig. 25 Missile Position as a Function of Time (U)

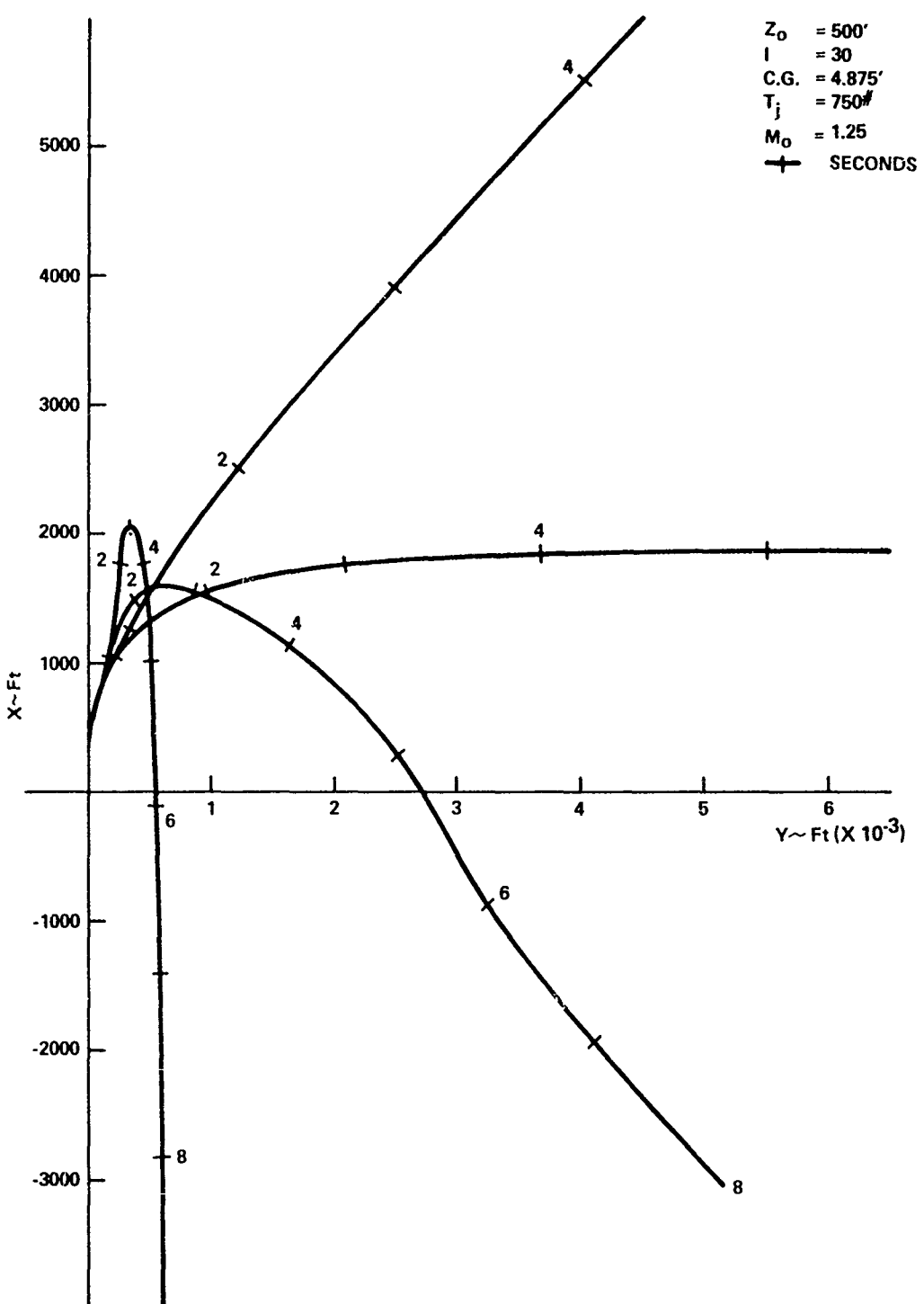


Fig. 26 Missile Position as a Function of Time (U)

8th Navy Symposium on Aeroballistics

Vol. 3

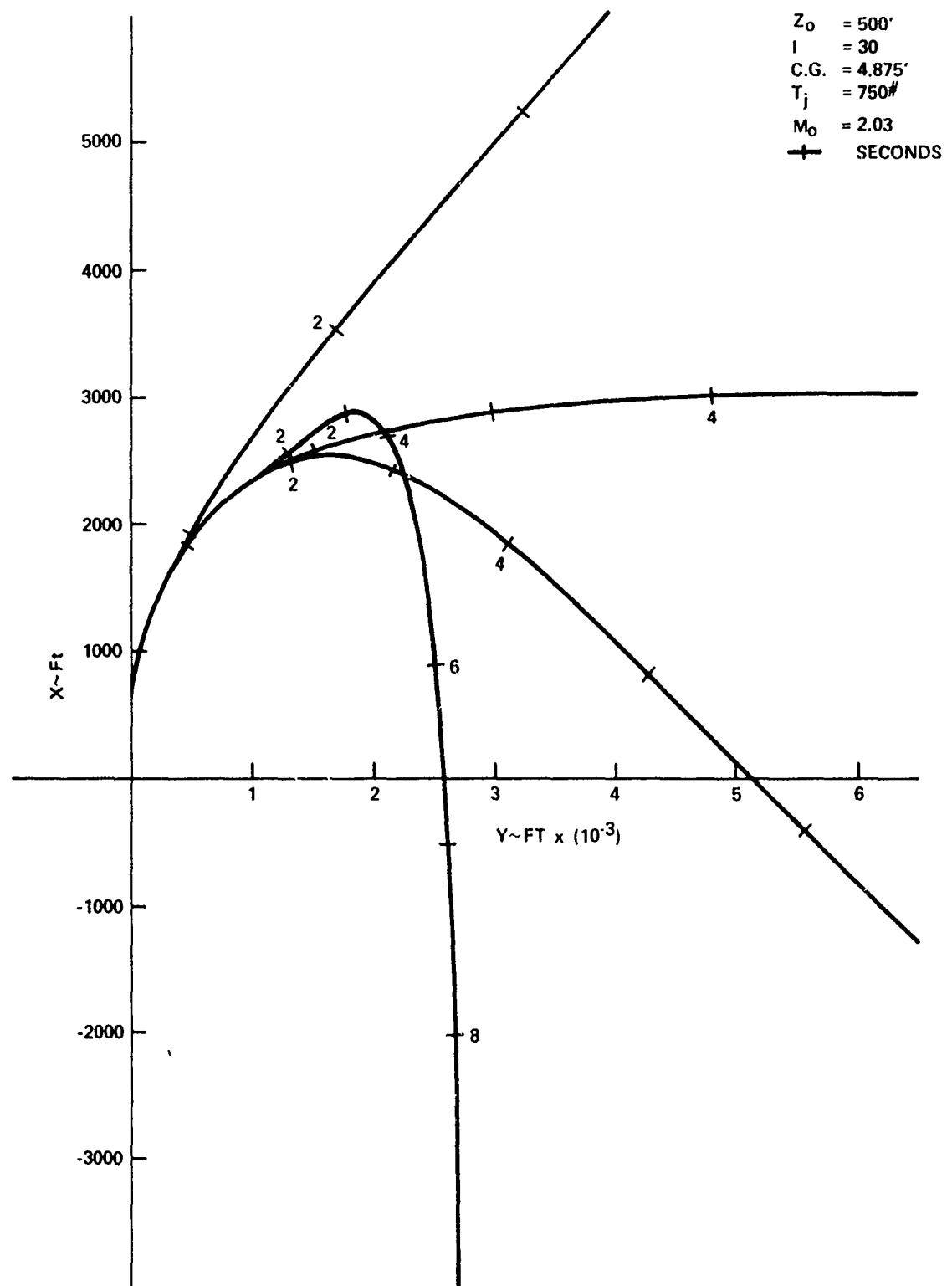


Fig. 27 Missile Position as a Function of Time (U)

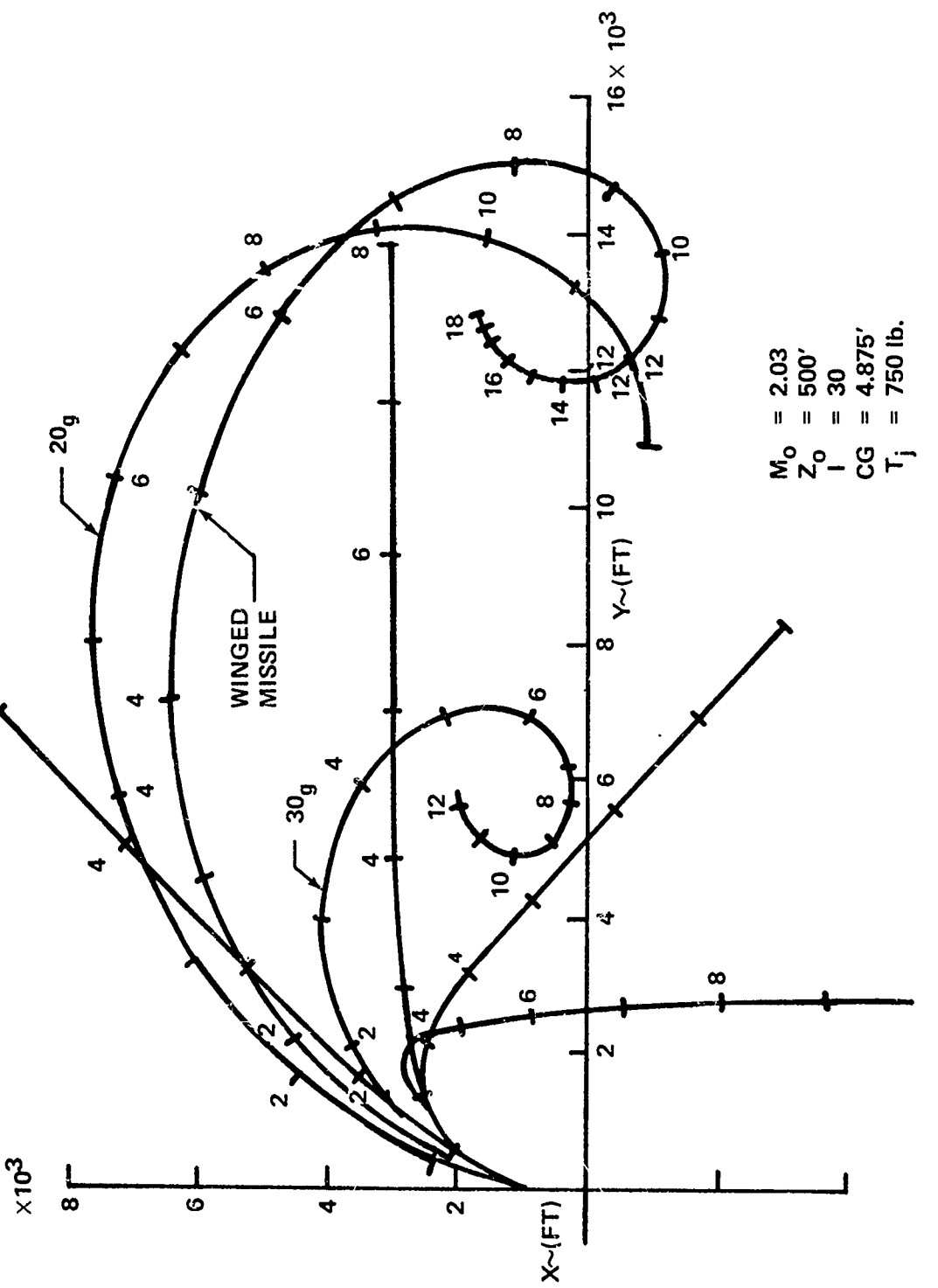


Fig. 28 Mission Position Versus Time (s)

BLANK PAGE

Paper No. 26

STABILIZATION OF A LIQUID-FILLED SHELL BY INSERTING
A CYLINDRICAL PARTITION IN THE LIQUID CAVITY
(U)

(Paper UNCLASSIFIED)

by

John T. Frasier and William P. D'Amico
U.S. Army Ballistics Research Laboratories
Aberdeen Proving Ground, Md. 21005

ABSTRACT. (U) "Ad hoc" techniques for the stabilization of liquid-filled shell are frequently not successful, nor are they based on well-founded theory. On the other hand, the rationale for using a cylindrical partition to stabilize a spinning shell can be justified by analytical methods. Cavities typical to liquid-filled shell have non-cylindrical walls, are 95 percent filled, and use central bursters. If test firings demonstrated that a shell-liquid instability exists, a projectile can usually be stabilized without a drastic aerodynamic redesign or a payload reduction through the use of a cylindrical partition. Emplaced concentrically to the longitudinal shell axis, the partition allows for free movement of the liquid. Consider that the liquid has achieved a rigid body rotation. Two independent cavities are exhibited: an outer cavity with non-cylindrical wall and a rigid core and an inner cavity with a cylindrical wall and an air core. The liquid eigenfrequencies for both cavities must be calculated to determine if they are sufficiently close to the nondimensional nutation frequency of the shell to cause an instability. For an inviscid liquid and for small angles of yaw, the inner cavity is the problem treated by Stewartson and later expanded by Frasier. The outer cavity can be considered by a combination of techniques established by Wedemeyer and by Frasier and Scott. It is possible to portray graphically a range of shell nutational frequencies and complementary partition radii that will not produce resonant conditions for the outer cavity. This means that usually a cylinder radius can be selected that produces stable conditions for both of the cavities. The designer now has partial control over the liquid eigenfrequencies. Viscous corrections to the procedures can be made according to Wedemeyer. The question of transient resonances that occur during the spin-up of the liquid cannot be answered explicitly. An approach that estimates the yaw growth rate while passing through a transient instability gives satisfactory results, however.

8th Navy Symposium on Aeroballistics

Vol. 3

INTRODUCTION

(U) Over the past decade investigators at the U.S. Army Ballistics Research Laboratories have conducted theoretical and experimental studies of the causes of flight instability of liquid-filled projectiles. Recently, these studies led to a rationale for the stabilization of such projectiles by incorporating within their payload compartment, an axially aligned cylindrical partition [1a]*. A limited, but successful, field test of the design rationale was made in July 1968.

(U) The XM 613, a 107mm, spin stabilized, WP (white phosphorous) mortar shell, was range tested at Yuma Proving Ground. The projectile had a history of flight instabilities when the WP was in the liquid state. Specially modified rounds incorporating cylindrical partitions experienced stable flights. Limited resources allowed the testing of only two rounds, and therefore conclusive proof testing of the rationale cannot be claimed. However, the insertion of cylindrical partitions in liquid-filled projectiles is a straight-forward and flexible method to produce stable flight by means of well-founded design procedures. In fact it is the most flexible means for "a priori" design of a stable liquid-filled-projectile available to munitions designers today. This method is not seen as a panacea, but it does represent a major improvement over previous "ad hoc" procedures.

(U) Our intention in the present paper is to explain the rationale for using a cylindrical partition to achieve well-behaved flights of liquid-filled shell. This is a simple task if we assume our audience is familiar with the work done at the BRL over the past ten years. This assumption is not likely to be valid, however. We will begin our presentation with a brief discussion of the problem of liquid-filled projectiles and our current understanding of the causes of their ills. Having done this, the use of cylindrical partitions in the payload compartment to achieve stability will be explained.

LIQUID-FILLED PROJECTILE STABILITY

(U) WP rounds, one of the most common types of liquid-filled projectiles, have long been infamous for their poor flight behavior, (WP melts at 112°F). A major step toward understanding the physical realities of this behavior was achieved by Stewartson when he published

* Numbers in square brackets denote references found at the end of the paper.

an analysis of the stability of a spinning top containing liquid in a cylindrical cavity [2]. This work provided a clear definition of the basic mechanisms causing flight instabilities of liquid-filled projectiles and was the basis for further analytical and experimental research. A summary description of the current level of knowledge concerning liquid-filled projectiles is given very conveniently by using the conditions, assumptions, and results of Stewartson's analysis as a foundation. Theoretical and practical advances are, in large measure, the consequence of relaxation of the assumptions of Stewartson's analysis.

STEWARTSON'S THEORY OF STABILITY

(U) Stewartson's theory concerns the flight stability of a spinning shell with a right circular cylindrical cavity either wholly or partially filled with liquid. Results of the theory show that growth of the nutational component of the projectile's yaw is possible under adverse combinations of the geometrical and physical characteristics of the projectile and its liquid filler. Instabilities are a consequence of the nutational frequency of the shell being hazardously close to certain natural frequencies of the liquid. This can be described as a condition of resonance. When this condition occurs, oscillations of the liquid produce a periodic moment (couple) on the shell casing and lead to a growth in yaw.

(U) The theory is valuable for several reasons. First, it provides a clear understanding of the physical phenomena through which liquids produce instabilities in spinning projectiles, namely, the resonance type behavior mentioned above. This basic mechanism of instability applies to cavities of all geometries and not just cylinders. Second, the assumptions and conditions of the theory supply a useful framework to discuss the work at the BRL. The advances represented by the latter efforts are, in many instances, the consequence of modifications or relaxation of Stewartson's assumptions and conditions.

(U) Stewartson's theory is based upon assumptions and stipulations that define the situations for which it is valid. Here we will review the most important of these factors and attempt to point out their physical significance. When appropriate, research advances by other investigators will be mentioned and references to their work cited. Certain of the stipulations are absolute requirements in that if they are not satisfied the theory is invalid. Others are taken as a matter of convenience to simplify the analysis and to clarify the role of the liquid in causing flight instability. An example of an assumption of the latter type is that the overturning moment is the only significant aerodynamic force or moment acting on the shell. Drag, etc., can be included in the analysis but are not essential to its development. Therefore, we shall neglect them to maintain focus on the basic features of interactions between the shell and its liquid. Distinctions between the two types of assumptions will become clear in the course of discussion.

8th Navy Symposium on Aeroballistics

Vol. 3

Assumptions of Stewartson's Analysis

(U) The Cavity in the Shell is a Right Circular Cylinder Whose Axis is Parallel to the Spin Axis of the Projectile. Immediately we see that the theory is restricted to shell with cylindrical cavities. Hence, direct quantitative application of its results is limited to a single geometrical shape. Wedemeyer, however, has achieved a modification of Stewartson's theory through which it is possible to design for other shapes; specifically, cavities whose radii change slowly along their length [3a]. As a consequence, we are able to perform analyses on many practical cavity geometries. To use Wedemeyer's modification, one must have a working knowledge of the basic Stewartson analysis.

(U) The Aerodynamic Overturning Moment is the Only External Force or Moment Affecting the Flight of the Shell. We explained above that this assumption is taken for convenience. Gravity and other aerodynamic effects can be taken into account through conventional procedures but are not essential to the theory.

(U) The Shell Flies with Constant Translational Velocity and Spin. This assumption is consistent but implies that the liquid does not influence the spin rate of the projectile. In practice these conditions are never satisfied. For a period after the projectile leaves the gun, the shell's spin decreases because it must spin-up the liquid. Subsequent to liquid spin-up, the shell experiences spin decrease due to drag. Furthermore, the projectile encounters translational drag. In general however, once the transient phase of liquid spin-up complete, the drag effects are sufficiently small for the current assumption to be reasonable for most projectiles.

(U) Finally, we remark that this assumption deals with the shell casing - not with the liquid - and relates to the equation of motion written for the projectile. Assumptions below concern the motion of the liquid.

(U) The Gross Motion of the Liquid is a Rigid Body Translation and Spin Identical to the Translation and Spin of the Projectile. This assumption, in conjunction with the one above, restricts our considerations to the full spin condition of the liquid. The theory does not consider situations where the shell casing and liquid have unequal rigid body spins, nor does it take account of variations in the spin of the liquid.

(U) Wedemeyer [3b] and Scott [4] have performed analyses that allow us to calculate the time required for the liquid to spin-up after a projectile leaves the muzzle. Hence, in practical situations, we can determine when Stewartson's full-spin assumption becomes valid. Usually, it is soon after exit from the muzzle. Furthermore, a semi-empirical analysis is available to determine whether instability is likely to occur during the transient spin-up process [5].

8th Navy Symposium on Aeroballistics

Vol. 3

(U) The Spin of the Liquid and the Dimensions of the Cylindrical Cavity Satisfy the Condition.

$$\underline{a^2\Omega^2 \gg qc} \quad (1)$$

where a = cavity radius, inches,

Ω = spin rate of the projectile (and therefore the liquid),
rad/sec,

q = magnitude of the resolved gravity and drag vectors, in/sec²,

$2c$ = height of the cavity, inches.

The physical significance of this assumption is that centrifugal forces exerted on the liquid due to its spin far outshadow any forces imposed by gravity or drag. A consequence of the assumption is that the liquid (except when the cavity is completely filled) has the shape of a cylinder with a hollow, cylindrical core*.

(U) Equation (1) must be satisfied for Stewartson's theory to be used. If a shell experiences high drag along with a low spin rate there is a possibility the relation will be violated. Then the liquid will not have a cylindrical core, but will develop a paraboloidal surface. Designers should always verify Equation (1) is satisfied to avoid imprudent application of the theory.

(U) It should be understood that the current assumption is not the external forces assumption. The former condition concerns external forces and moments acting on the shell casing and their effect on the motion of the shell. The present assumption concerns the effect of gravity and drag on the behavior of the liquid.

(U) The Mass of the Liquid is Small Compared to the Total Mass of the Shell. This assumption is one of convenience. It is satisfied for many shell and simplifies the equations of motion for the liquid-shell system. We use it here for these reasons.

(U) The Liquid is Incompressible and Inviscid. The assumption of incompressibility is reasonable for the liquids encountered in actual projectiles. Viscous effects, however, can influence the behavior of liquid-filled projectiles. Fortunately, Wedemeyer has provided an analysis to account for these effects [3c]. His analysis involves a boundary layer correction to the basic, inviscid theory of Stewartson.

(U) The Final Assumptions Concern the Nature of any Variations to the Rigid Body Translation and Spin of the Shell and Liquid. Any Disturbance to the Shell's Motion is Restricted to Small Amplitude Perturbations Superposed on its Gross Translation and Spin. Correspondingly, the Liquid is Assumed to Experience only Small Amplitude Perturbations to its Large Scale Translation and Spin. The assumption about the shell is the familiar small yaw situation associated with the linearized equations of yawing motion.

*Actually a paraboloid whose vertex is far from the shell.

8th Navy Symposium on Aeroballistics

Vol. 3

Similarly, the assumption imposed on the liquid linearizes the equations describing its behavior. By virtue of linearization, the equations for the liquid motions can be solved and their result incorporated into the equations of the motion for the shell.

Results of Stewartson's Analysis

(U) All the basic assumptions and conditions underlying Stewartson's theory were presented above. From these assumptions, we can make a qualitative statement of our problem. Namely, determine the conditions for which a symmetric, rapidly spinning projectile will experience a flight instability as a consequence of having liquid (at full spin) in a cylindrical, axially symmetric cavity. Stewartson attacked this problem in two phases, and it seems most effective to describe his analysis in a similar fashion. First, he considered the behavior of the liquid in a state of rapid rotation within a container that could perform motions similar to those of the yawing motion of a shell. He then combined the problem solution he found for the liquid with the equations of motion for a shell. Upon analysis of the resulting equations it was found that under certain adverse conditions the yaw of the shell will grow without limit.

(U) To describe the behavior of the liquid, we remember that it is confined in a container and that its basic motion involves rigid body spin about an axis with fixed direction. Upon assuming that the axis of the container is subjected to a small disturbance similar to the yawing motion of a shell, it is necessary that the liquid also experiences a disturbance to its basic motion because it must follow the walls of the cavity. Stewartson's solution shows that the liquid conforms to the cavity motion through the excitation of small amplitude oscillations superposed on the rigid body motion. There is an infinite number of discrete frequencies for these oscillations - the natural frequencies (or eigenfrequencies) of the spinning liquid. For an arbitrary motion of the container all the natural frequencies will be excited, but in varying degrees. If, however, the container performs a yawing motion at certain of the eigenfrequencies of the liquid, oscillations at this frequency become predominant, that is, a condition of resonance is established. As we shall describe later, it is this resonance that leads to the instability of a liquid filled projectile.

(U) We should emphasize that the oscillations performed by the liquid are of small amplitude. Sloshing does not occur, but a wave pattern is established in the longitudinal, radial, and circumferential directions of the cavity and there are mode numbers* associated with each direction. For problems of projectile stability, an infinity of the possible longitudinal and radial modes are significant theoretically, but only the first circumferential mode is important. This circumstance is a result of the fact that the pressure fluctuations produced in the

* These can be thought of as fundamental wave patterns and harmonics.

liquid by this mode lead to a periodic couple (with the same frequency as that of the oscillating liquid) on the walls of the container. It is this couple which renders a projectile unstable.

(U) Now, we must explain how the natural frequencies of the liquid are determined. Stewartson's theory gives these frequencies in a complicated relation of the form

$$\tau_{nj} = \frac{\omega_{nj}}{\Omega} = f_n \left[\frac{c}{a(2j+1)}, \frac{b^2}{a^2} \right]; \quad n = 1, 2, 3, \dots \quad (2)$$

$j = 0, 1, 2, \dots$

where n = radial mode number (the number of nodes in the radial wave pattern),

j = longitudinal wave number ($2j+1$ = number of nodes in the longitudinal wave pattern),

ω_{nj} = natural frequency of the nj^{th} node,

τ_{nj} = the non-dimensional eigenfrequency of the nj^{th} mode,

$2a$ = diameter of the cavity,

$2b$ = diameter of the cylindrical air core,

$2c$ = cavity length.

(U) Several aspects of Equation (1) should be noted. First, the eigenfrequencies of the liquid are dependent upon the cavity geometry through the ratios c/a and b^2/a^2 . The ratio b^2/a^2 is the air volume in the cavity expressed as a fraction of the total cavity volume. Hence $(1 - b^2/a^2)$ is the fraction of the cavity occupied by liquid. Next, we note that the eigenfrequencies depend upon the longitudinal mode number through the ratio $c/a(2j+1)$ appearing as a variable in f_n . This is a fortunate circumstance, because once τ_{nj} is known for a set of fixed values of $c/a(2j+1)$, b^2/a^2 , and n , the eigenfrequencies are known for all longitudinal modes for which $c/a(2j+1)$ equals the set value. Finally, Equation (2) shows the frequencies are linearly related to Ω , that is, τ_{nj} is independent of Ω .

(U) As mentioned above, the function of f_n in Equation (1) is a complicated one, and it must be evaluated numerically through machine determination of the poles (singularities) of another equation appearing in the Stewartson analysis. This has been done and the results, the liquid eigenfrequencies, tabulated so that it is possible to make quantitative use of Stewartson's and subsequent work [1b].

(U) This completes our discussion of the natural frequencies of the spinning liquid, which are dependant upon the cavity geometry, i.e., $(c/a$ and b/a). Now, we turn to the questions of how and when

8th Navy Symposium on Aeroballistics

Vol. 3

an instability of a liquid-filled shell is produced by the oscillating liquid. To begin we recall our assumptions that the overturning moment is the only significant aerodynamic force or moment acting on the shell and that we are dealing with small yaws. Under these conditions, the motion of the shell (without the liquid) is governed by the relations

$$\lambda = \lambda_0 e^{i\Omega\tau t} \quad (3)$$

$$I_y \tau^2 - I_x \tau + \frac{I_x^2}{4I_y s} = 0 \quad (4)$$

where I_x and I_y are, respectively, the axial and transverse moments of inertia of the shell, and

λ is the complex yaw,

t is time,

τ is the non-dimensional frequency of the motion of the shell,

s is the gyroscopic stability factor.

(U) Equation (3) represents the form of the motion of the shell and the values of τ are provided by solution of Equation (4). Since Equation (4) is quadratic, the latter are found easily:

$$\tau_n = \frac{1}{2} \frac{I_x}{I_y} (1 + \sigma) \quad \text{Nutational frequency} \quad (5)$$

$$\tau_p = \frac{1}{2} \frac{I_x}{I_y} (1 - \sigma) \quad \text{Precessional frequency} \quad (6)$$

where $\sigma = \sqrt{1 - \frac{1}{s}}$,

$$s = \frac{v^2}{4M} \quad ,$$

$$\bar{v} = \frac{I_x}{I_y} \frac{2\pi}{n} \quad ,$$

$$M = \frac{\rho_a S d}{2m} K_t^{-2} C_{M_\alpha} \quad ,$$

ρ_a = air density ,

S = reference area of shell, usually the cross-sectional area,

n = twist of rifling, calibers per turn,

d = diameter of the shell ,

m = mass of the shell ,

$$k_t^{-2} = md^2/I_y ,$$

C_{M_α} = aerodynamic overturning moment coefficient .

(U) It is advantageous to recall here that the shell is stable (the yaw does not grow with time) so long as τ_n and τ_p are real quantities. To achieve this situation we must have s greater than one, a familiar condition for the gyroscopic stability of a projectile. If s is less than one, σ and therefore τ_n and τ_p become imaginary, and an exponential growth of yaw occurs.

(U) Earlier, we stated that the oscillating liquid produces a moment on the casing of the projectile. Now we must describe that moment in functional form and modify Equation (4) to include its effect. Stewartson showed that when the frequency, τ , of the projectile is near any one of the natural frequencies, τ_{nj} , of the liquid, the moment applied to the shell casing is given by

$$\frac{M_L}{\Omega^2} = - \frac{\rho a^6 [2R(\tau_{nj})]^2 / 4c}{\tau - \tau_{nj}} , \quad (7)$$

where M_L = the moment exerted on the shell by the liquid,

τ = the frequency of motion of the shell,

ρ = the density of the liquid,

$R(\tau_{nj})$ = a (small) constant depending upon τ_{nj} and is always positive, "the residue".

The quantity R_{nj} is available in the tabulation of liquid eigenfrequencies referred to above [lb]. We see from Equation (7) that it governs the magnitude of the liquid-moment for a given cavity and frequency, τ_{nj} . Each possible frequency and modal configuration of the liquid involves a specific value of R_{nj} . With regard to the residue, it is convenient to point out a significant feature of its behavior. Namely, for any specific value of frequency, τ_{nj} , the residue decreases greatly for each successively larger value of n (i.e., R_{nj} decreases with increasing radial mode number). Thus, the higher radial modes produce relatively weak liquid-moments. In practice it has been found that modes beyond $n = 2$ are seldom strong enough to cause projectiles to be unstable.

8th Navy Symposium on Aeroballistics

Vol. 3

(U) The moment due to the liquid is a forcing function on the motion of the shell. Thus to account for the presence of the liquid in the equation of motion of the shell we add Equation (7) to the right-hand-side of Equation (4) and obtain

$$I_y \tau^2 - I_x \tau + \frac{I_x^2}{4I_y s} = - \frac{\rho a^6 [2R(\tau_0)]^2 / 4c}{\tau - \tau_0} , \quad (8)$$

where for convenience, τ_0 has been written in place of τ_{nj} to emphasize that we are now thinking of a specific fluid frequency. By solving Equation (8) for τ , the frequency of the shell's motion and the conditions under which the liquid can produce an unstable flight are determined, (that is, the conditions for which τ has an imaginary part assuming, of course, that $s > 1$). Here, we shall only summarize the results of this solution. It is found that when τ_0 is close to τ_p , the precessional frequency, no instability occurs. However, if τ_0 is near the nutational frequency, τ_n , Equation (8) has the roots

$$\tau = \left(\frac{\tau_n + \tau_0}{2} \right) \pm \sqrt{\left(\frac{\tau_n - \tau_0}{2} \right)^2 - \frac{\rho a^6 [2R(\tau_0)]^2}{4c I_x \sigma}} \quad (9)$$

The condition for instability is provided immediately by Equation (9). When the quantity under the radical is negative, τ has a negative imaginary part as we see by substituting Equation (9) into Equation (3):

$$\begin{aligned} \lambda &= \lambda_0 \exp \left\{ i\Omega \left(\frac{\tau_n + \tau_0}{2} \right) t - i\Omega \sqrt{\left(\frac{\tau_n - \tau_0}{2} \right)^2 - \frac{\rho a^6 (2R)^2}{4c I_x \sigma}} t \right\} \quad (10) \\ &= \lambda_0 \exp \left[i\Omega \left(\frac{\tau_n + \tau_0}{2} \right) t \right] \exp (\alpha \Omega t) , \\ \text{where } \alpha &= \sqrt{\frac{\rho a^6 (2R)^2}{4c I_x \sigma} - \left(\frac{\tau_n - \tau_0}{2} \right)^2} \end{aligned}$$

Thus, an exponential growth of the nutational component of yaw occurs when

$$\left(\frac{\tau_n - \tau_0}{2} \right)^2 - \frac{\rho a^6 (2R)^2}{4c I_x \sigma} < 0 ,$$

or, written more conveniently, when

$$-1 < (\tau_o - \tau_n)/S^{1/2} < 1 \quad \text{The condition for instability} \quad (11)$$

where S , "Stewartson's Parameter", is

$$S = \frac{\rho \sigma^5 (2R)^2}{I_x \sigma (c/a)}$$

When Equation (11) is satisfied, the rate of growth of yaw is [Equation (10)].

$$\alpha = \frac{1}{2} \sqrt{S - (\tau_o - \tau_n)^2} \quad (12)$$

or

$$\frac{2}{\sqrt{S}} \alpha = \sqrt{1 - \left(\frac{\tau_o - \tau_n}{\sqrt{S}} \right)^2}$$

(U) Figure 1 is a plot of $(2/S^{1/2})\alpha$ against $(\tau_o - \tau_n)/S^{1/2}$. This curve, as well as examination of Equations (11) and (12), shows the yaw growth rate to be largest when $\tau_o = \tau_n$. For non-zero values of $\tau_o - \tau_n$, the yaw growth rate decreases until it vanishes for $|\tau_o - \tau_n| = S^{1/2}$.

(U) Equations (11) and (12) are the basic results of the Stewartson theory. They permit us to calculate the conditions producing instability in a given projectile (and therefore a means to avoid these instabilities) and to calculate the strength of the instability, provided, of course, that the assumptions of Stewartson's analysis are satisfied. More accurately, we should say "provided that these conditions are satisfied or that advantage is made of the advances of Karpov [5], Wedemeyer [3] and Scott [4] to relax these restrictions." The work of these investigators was referenced during discussion of the assumptions of Stewartson's analysis. This work is extremely important in that it demonstrated the strengths and weaknesses of the original analysis and made the necessary advances for the practical application of the theory. Space does not permit any discussion of the details of this work. It can be summarized quickly, however, by pointing out that this work considers three points of concern that must be included in the analysis of any genuinely practical situation. Namely,

- Viscous effects in the liquid filler [3c],
- Certain types of non-cylindrical cavities, including those with profiles similar to the ogival shape of conventional artillery projectiles [3a],
- Liquid spin-up effects [3b].

8th Navy Symposium on Aeroballistics

Vol. 3

STABILITY OF A SHELL WITH A CENTRAL ROD ALONG ITS PAYLOAD COMPARTMENT

(U) The preceding discussion has centered about the problem of the stability of a projectile with a payload cavity that is either partially or completely filled with liquid. For the original Stewartson case this cavity is a right circular cylinder. However, owing to the efforts of Wedemeyer this restriction can be relaxed to treat cavities where a profile radius varies slowly with axial distance [2]. An important feature of these analyses, however, is that when the cavity is partially filled, a cylindrical air core runs along the axis of the cavity. A problem very similar to this and one that is important to the rationale for projectile design involves a core of rigid material along the center of the cavity rather than a flexible air core.

(U) Let us substitute an axially rigid core for Stewartson's flexible air core. Analytical treatment of the problem of flight stability of a projectile carrying liquid in a payload compartment consisting of a right circular cylinder with an axially aligned rigid core is quite similar to that of the Stewartson problem. This problem has recently been solved by Frasier and Scott and has results completely analogous to those discussed earlier [1c]. Namely, yaw of the projectile grows without limit if the nutational frequency of the projectile is sufficiently close to certain of the eigenfrequencies of the spinning liquid payload. More specifically, the constraints apply to the analysis; and the results expressed by Equation (1) through (12) apply with only one qualification. That qualification is that the dimension b used in those equations should be replaced by d , where d is the radius of the rod in the cavity. The residues for this case are numerically distinct from the air core solution.

(U) We should emphasize that the analysis involving the rod requires that all the volume of the cavity after the rod is inserted is completely filled with liquid. Hence, the side walls, end faces, and rod are wetted by liquid at all times. We will now explain how all of the preceding methods can be combined into procedures for the insertion of a cylindrical partition.

RATIONALE FOR THE INSERTION OF A CYLINDRICAL PARTITION

(U) The rationale for inserting cylindrical partitions in liquid-filled shell is an integrated use of Stewartson's theory and the subsequent extensions to techniques that account for non-cylindrical cavities, rigid central cores, and liquid spin-up. Once castings for a liquid-carrying projectile are made, it is not an easy task to modify the round for the elimination of shell-liquid resonances. Several "ad hoc" approaches for stabilization, longitudinal baffles being the most common, are frequently not successful. It is desirable to establish techniques that make possible "a priori" design control. A concept satisfying this criterion involves the insertion of a cylindrical partition in the payload cavity.

(U) Flight instabilities due to liquid payloads are a consequence of resonance between liquid eigenfrequencies and the shell nutational frequency. This matching can occur during liquid spin-up or at a full spin condition. To alleviate such a resonant condition, the shell geometry, the percent of fill, or the shell nutational frequency must be changed. Normally, the liquid payload cannot be significantly altered. A redistribution of mass could shift the shell nutational frequency, but this results in a complete aerodynamic redesign. It appears that a variation in cavity geometry is the best route. This geometry modification should not be a haphazard one.

(U) An intelligent change in geometry can be made by using a cylindrical partition. To illustrate this method, consider the two common shell cavities shown in Figure 2. Non-cylindrical cavities are shown with a burster located in the nose and with a central burster. Assume that the cavity is 95 percent filled with liquid. A cylindrical partition could be mounted about the longitudinal center line, as indicated by the broken lines. These cylinders must be fastened in such a way as to allow the liquid to move over the cylinder edges when it is thrown outward by centrifugal force. Since the spinning liquid will seek the outermost position, the outer cavity will be 100 percent filled after the liquid spin-up process is completed.

(U) Effectively two cavities result from the insertion of a cylinder in a shell cavity. For Figure 2a, the outer cavity takes up boundary conditions of a non-cylindrical wall and a rigid core (100 percent full). The inner cavity is the case treated by Stewartson, consisting of a partially filled cylindrical cavity [2]. A similar double cavity results in Figure 2b except that the central burster may act as a rigid core [1c] or as a partially wetted rod [6]. If the percent fill is not high enough to cause liquid-burster interference, then both Figure 2a and 2b have the same boundary conditions. Usually a cylinder radius can be selected that will result in a stable flight.

(U) Assume that an analysis of some non-cylindrical cavity reveals a resonant condition. (How could a cylindrical partition be selected to stabilize the projectile?) In the case of the XM613, a 107mm, WP mortar shell, an unstable flight was caused by a transient resonance. The XM613 geometry is shown in Figure 3, with a cylindrical partition in place. It is possible to generate a table of nutational frequencies and rigid core radii that produce resonant conditions for the outer cavity [3a, 1c]. This is done for rigid core, full spin modes. Considering only the first radial mode, Table I lists the longitudinal modes ($u = 2, 3, 4, \text{ and } 5$) for a fill ratio of 100 percent over a range of frequencies close to the XM613 nutational frequency of 0.067.

(U) TABLE I

τ	$d_{j=2}$ inches	$d_{j=3}$ inches	$d_{j=4}$ inches	$d_{j=5}$ inches
0.00	0.568	0.891	1.036	1.138
0.02	0.616	0.910	1.052	1.156
0.04	0.653	0.927	1.066	1.166
0.06	0.686	0.944	1.081	1.179
0.08	0.718	0.961	1.096	1.194
0.10	0.745	0.978	1.111	1.208

(U) A graphical representation of Table I is shown in Figure 4. The selection of a nonresonant cylinder radius, d , can easily be made. Logical choices would be 0.85" or 1.025". If values of 0.70" or 0.95" were selected, a resonant condition is produced. Once d and a cylinder wall thickness are chosen then the geometry of the inner cavity is fixed. For the XM613, a cylinder outside radius of 1.025" and a wall thickness of 0.10" were selected. The slenderness ratio (height/diameter) of the inner cavity for the $j = 0$ mode was 5.27. The resulting percent of fill for the inner cavity was 62.5 percent.

(U) The new design was checked for viscous effects and transient resonances [3,7]. Conditions for the XM613 were such that no viscous corrections needed to be made. Transient resonances can occur in either of the cavities. Transient eigenfrequencies cannot be explicitly calculated, but the yaw growth while passing through a transient instability can be approximated by the following equation [5,7].

$$\log\left(\frac{\alpha_1}{\alpha_0}\right) = - \left(\frac{\pi\Omega}{4}\right) \frac{S}{d\tau_0/dt}$$

where α_0 = yaw angle before transient resonance,

α_1 = yaw angle after transient resonance,

Ω = shell spin rate,

S = Stewartson's parameter,

τ_0 = time dependent, non-dimensional eigenfrequency,

t = time.

If $d\tau_0/dt$ is computed correctly, viscous effects in the spin-up process are taken into account. Assumptions made to extend the above equation to partially filled cylinders or to non-cylindrical, solid core cavities are not overly restrictive. For the inner cavity of the XM613, a transient resonance was located for an effective percent fill of 0.597. Since α_1/α_0 was calculated to be 1.35, no serious problems were expected.

(U) It is quite possible the cylinder radii available from plots such as Figure 4 could still yield serious resonances for either spin-up or full spin conditions. It might then be possible to use more than one cylinder, especially in some of the larger rounds. A multi-cylinder design should still allow for fluid movement, while not decreasing the payload capacity or impairing the manufacturing process. This was not needed for the XM613, which was flown just as shown in Figure 3.

(U) Firings held in July 1968 at Yuma Proving Ground were part of a project termination that included the expenditure of available hardware. Since the XM613 had a history of flight instabilities, blamed upon shell-liquid resonances, this afforded the design engineers a test vehicle for "ad hoc" stabilization methods. At the invitation of personnel from the Artillery and Mortar Section of Picatinny Arsenal and the Weapons Development and Engineering Laboratory of Edgewood Arsenal, the BRL suggested the use of a cylindrical partition. Other modifications made by the MUCOM agencies included the insertion of several types of longitudinal baffles, the use of a gel filler representing thickened WP, and the addition of a sponge material into the shell cavity in an attempt to suspend the WP, i.e., reduce fluid movement. Firings were made from a single tube for a single charge and elevation. Thirty projectiles were thermally cured to a surface temperature of 145°F for a period of twenty-four hours. Four to five rounds were removed from the conditioning oven and fired within thirty minutes until all ammunition was expended. This insured that the filler was in a liquid state. Of the thirty rounds fired only the two rounds that employed cylindrical partitions flew well. These two rounds fell ten meters apart at 6,000 meters.

CONCLUSIONS

The small number of rounds that have actually been field tested does not represent statistical proof or conclusive verification of the overall ability of a cylindrical partition to stabilize liquid-filled shell. It does, however, produce a high level of confidence in the technique and in the combined use of many theoretical methods. The use of a cylindrical partition is the only available procedure that has a well-understood theoretical foundation for "ad hoc" stabilization.

8th Navy Symposium on Aeroballistics

Vol. 3

Some of the theoretical methods used to insert a cylindrical partition can be improved. The spin-up techniques are a prime example. The entire design procedure is based upon linear theory. It is quite possible that many shell will experience levels of yaw where the fluid mechanics becomes non-linear. Projectile behavior at summittal yaw is a specific example. Many questions, other than the above two, need to be addressed.

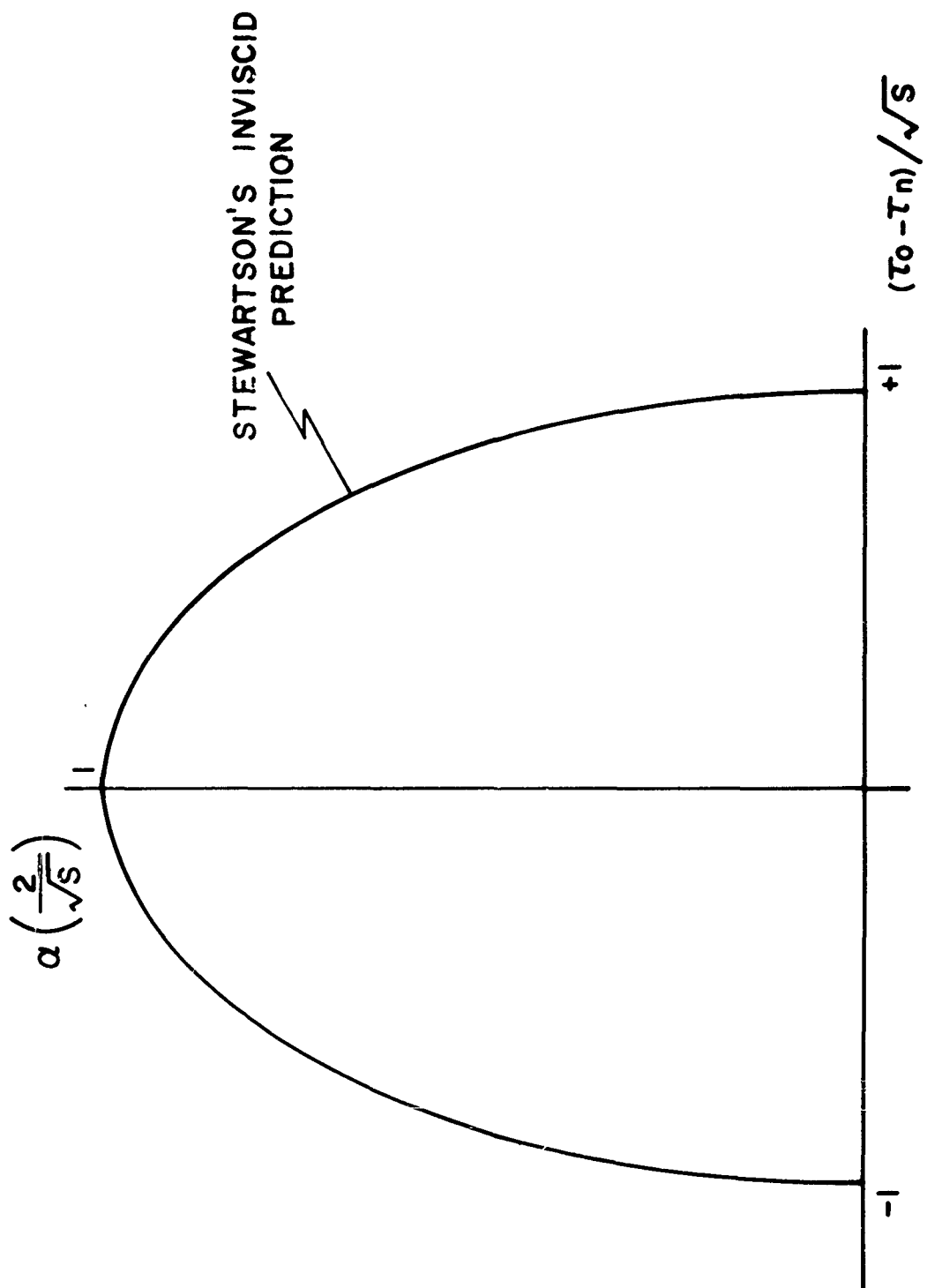
REFERENCES

- 1a. Ballistic Research Laboratories. Stabilization of a Liquid-Filled Shell by Inserting a Cylindrical Partition in the Liquid Cavity, by J. T. Frasier and W. P. D'Amico. Aberdeen Proving Ground, Md., Technical Note to be published.
- b. Ballistic Research Laboratories. Dynamics of Liquid-Filled Shell: Aids for Designers, by J. T. Frasier. Aberdeen Proving Ground, Md., BRL, December 1967. (BRL Memorandum Report 1892) AD 665356.
- c. Ballistic Research Laboratories. Dynamics of Liquid-Filled Shell: Cylindrical Cavity with a Central Rod, by J. T. Frasier and W. E. Scott. Aberdeen Proving Ground, Md., BRL February 1968. (BRL Report 1391) AD 667365.
2. On the Stability of a Spinning Top Containing Liquid, by K. Stewartson. J. of Fluid Mech., Vol. 5, Part 4, 1959, pp 577-592.
- 3a. Ballistic Research Laboratories. Dynamics of Liquid-Filled Shell: Non-Cylindrical Cavity, by E. H. Wedemeyer. Aberdeen Proving Ground, Md., BRL August 1966. (BRL Report 1326) AD 489899.
- b. Ballistic Research Laboratories. The Unsteady Flow Within a Spinning Cylinder, by E. H. Wedemeyer. Aberdeen Proving Ground, Md., BRL October 1965. (BRL Report 1225) AD 431846.
- c. Ballistic Research Laboratories. Viscous Corrections to Stewartson's Stability Criterion, by E. H. Wedemeyer. Aberdeen Proving Ground, Md., BRL June 1966. (BRL Report 1325) AD 489687.
4. Ballistic Research Laboratories. A Theoretical Analysis of the Axial Spin Decay of a Spin-Stabilized Liquid-Filled Shell, by W. E. Scott. Aberdeen Proving Ground, Md., BRL August 1962. (BRL Report 1170) AD 287605.
5. Ballistic Research Laboratories. Dynamics of Liquid-Filled Shell: Instability During Spin-Up, by B. G. Karpov. Aberdeen Proving Ground, Md., BRL January 1965. (BRL Memorandum Report 1629) AD 465926.

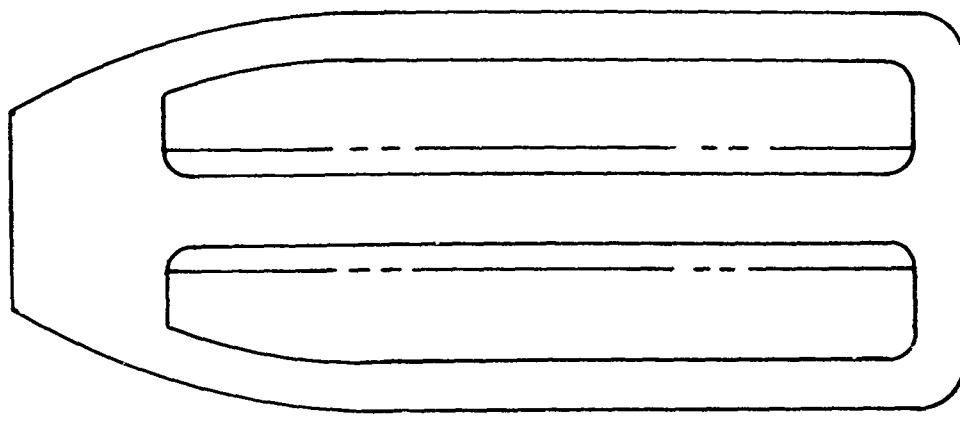
8th Navy Symposium on Aeroballistics

Vol. 3

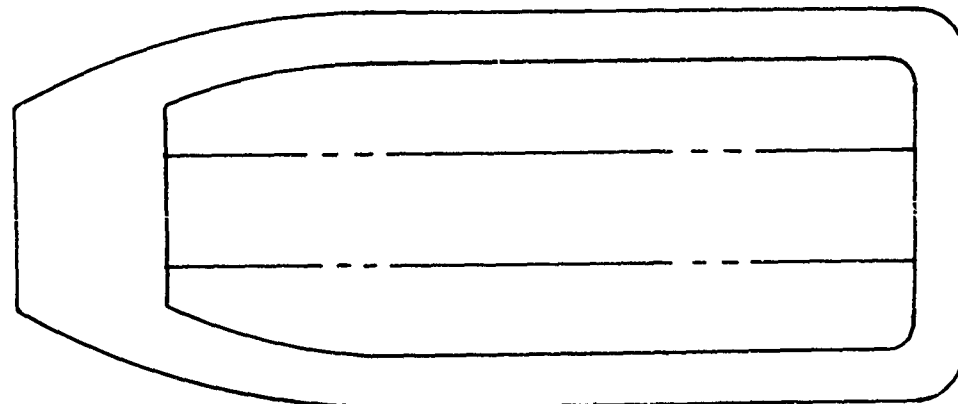
6. Ballistic Research Laboratories. Dynamics of a Liquid-Filled Shell: Rod-Liquid Interference, by W. P. D'Amico. Aberdeen Proving Ground, Md., BRL Memorandum Report in publication.
7. U.S. Army Materiel Command. Liquid-Filled Projectile Design Handbook, Engineering Design Handbook of the Army Materiel Command, in publication.



(U) FIG. 1. Resonance Curve for Liquid-Filled Projectile.



(b)

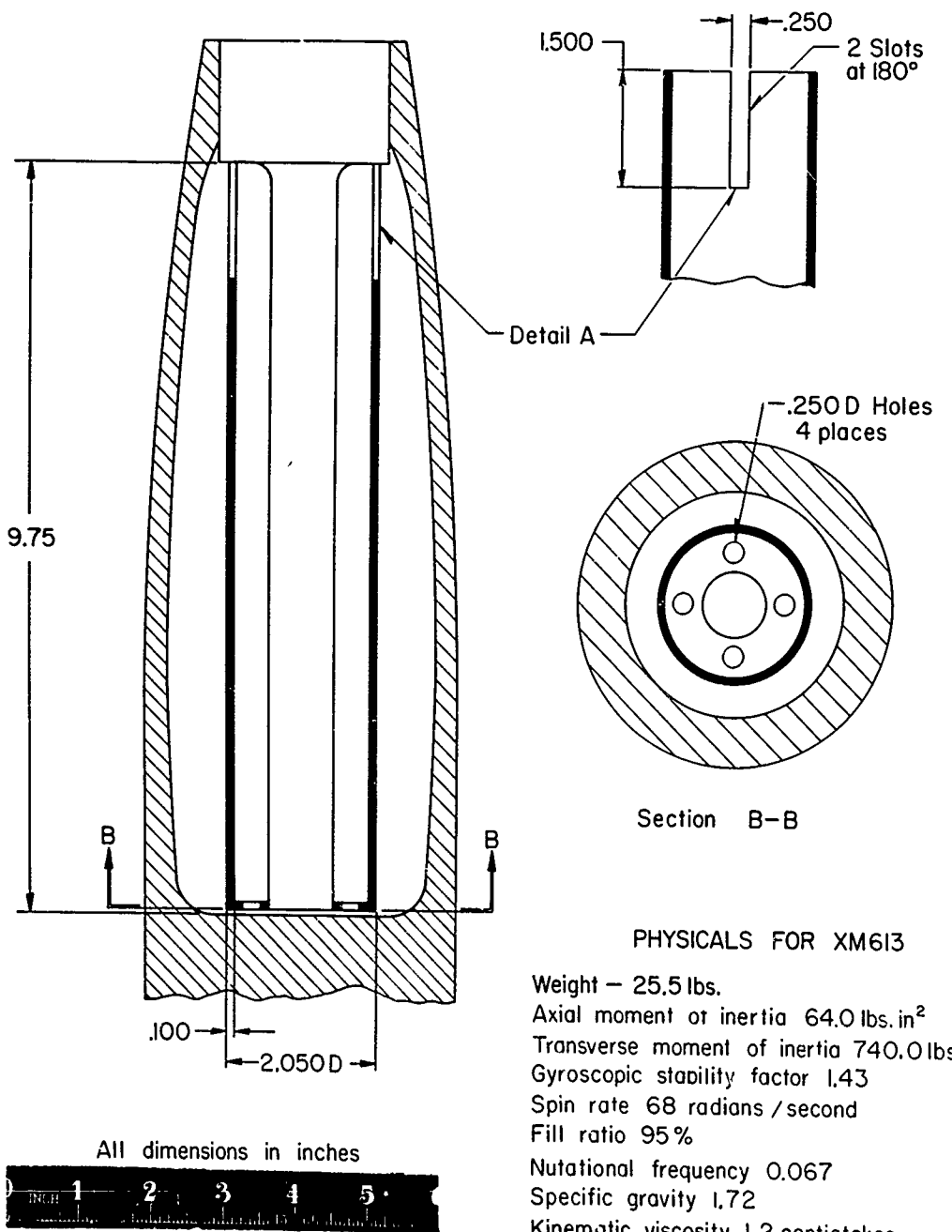


(a)

(U) FIG. 2. Typical Shell Cavities.

8th Navy Symposium on Aeroballistics

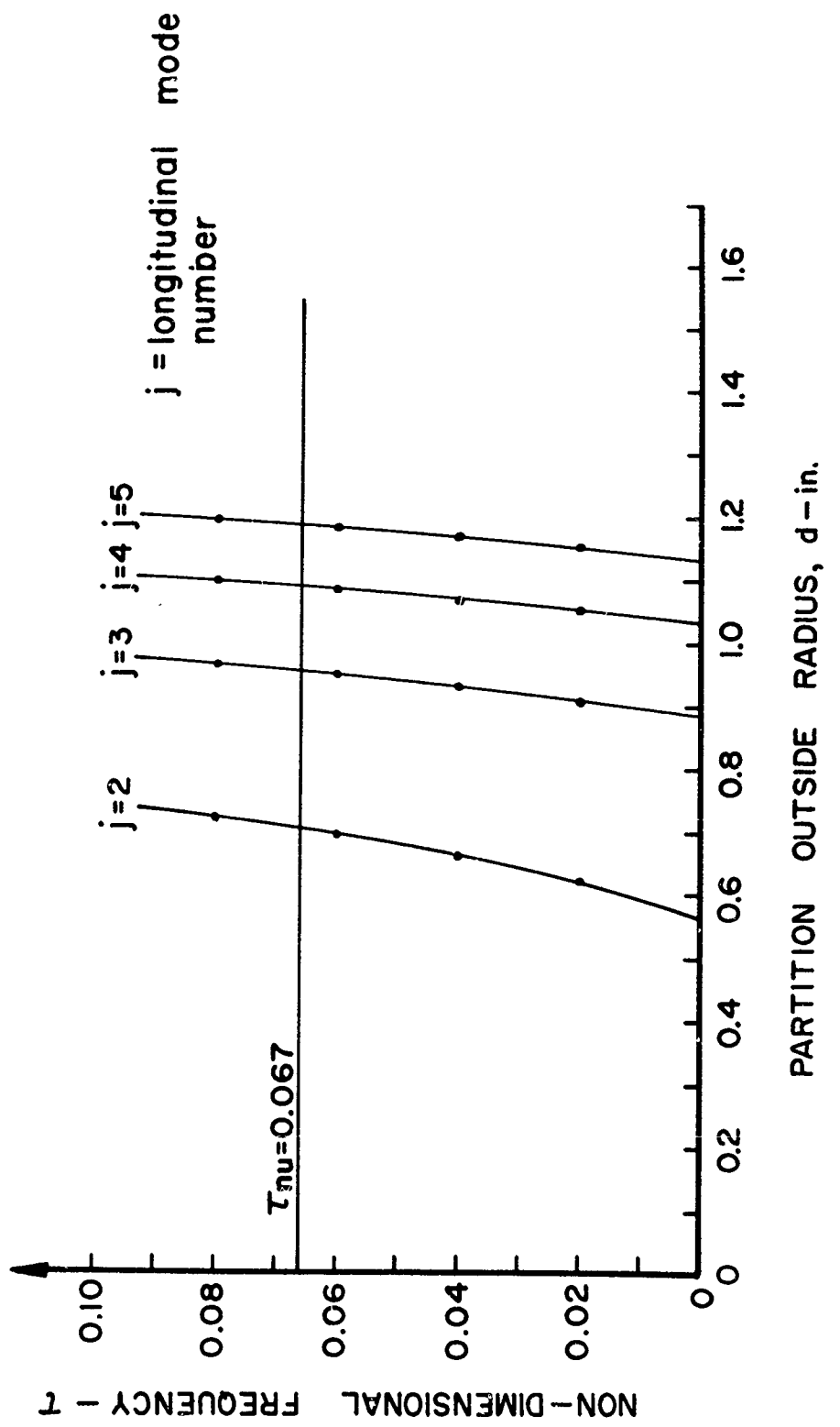
Vol. 3



PHYSICALS FOR XM613

Weight - 25.5 lbs.
 Axial moment of inertia 64.0 lbs. in²
 Transverse moment of inertia 740.0 lbs. in²
 Gyroscopic stability factor 1.43
 Spin rate 68 radians /second
 Fill ratio 95%
 Nutational frequency 0.067
 Specific gravity 1.72
 Kinematic viscosity 1.2 centistokes

(U) FIG. 3. Physical Characteristics of the XM613.



(U) FIG. 4. Nondimensional Frequencies Versus Partition Outside Radii.

BLANK PAGE

Paper No. 27

EFFECTS OF ROLL ON THE FREE-FLIGHT
MOTION OF BODIES
(U)

(Paper UNCLASSIFIED)

by

C. J. Welsh and R. M. Watt
ARO, Inc.
Arnold Air Force Station, Tenn. 37389

ABSTRACT. The effects of a roll velocity on the free-flight yawing motion of axisymmetric bodies, having linear force and moment characteristics, are discussed. Expressions for the frequency and the damping of the motion vectors are given as explicit functions of the roll velocity and the inertia and aerodynamic characteristics of the bodies. Stability boundaries defined by these expressions are noted, and the significance of the various aerodynamic parameters of a rolling body that can contribute to a dynamic instability is discussed. The correspondence between the damping, frequency, and amplitude of the nutational and precessional motion vectors is noted.

The research reported in this paper was sponsored by the Arnold Engineering Development Center (AEDC), Air Force Systems Command (AFSC), under Contract F40600-69-C-0001 with ARO, Inc. Further reproduction is authorized to satisfy the needs of the U. S. Government.

NOMENCLATURE

C_D	Drag coefficient
$C_{L\alpha}$	Lifting coefficient derivative
$C_{m\alpha}$	Static-stability derivative
$C_{m_{p\alpha}}$	Magnus-moment derivative
$C_{m_q} + C_{m_{\dot{\alpha}}}$	Damping-in-pitch derivatives, $\frac{\partial C_m}{\partial q(l/v)} + \frac{\partial C_m}{\partial \dot{\alpha}(l/v)}$
C_{N_G}	Normal-force derivative
H, M, P, T	Constants in Eq. (1)
I_x	Model moment of inertia (relative to the longitudinal axis)
I_y	Model moment of inertia (relative to a transverse axis)
K_1, K_2	Constants in Eq. (2)
k_1, k_2	Absolute values of K_1 and K_2 , respectively
k_a	Radius of gyration relative to the longitudinal axis/ l
k_t	Radius of gyration relative to a transverse axis/ l
l	Reference length
m	Model mass
p	Model roll rate (with respect to distance traveled)
S	Reference area
v	Model velocity
x	Distance traveled
α, β	Components of the complex yaw angle

δ	$\sqrt{\beta^2 + \alpha^2}$
θ_1, θ_2	Constants in Eq. (2)
μ_1, μ_2	Damping rates of the motion vectors in Eq. (2)
ξ	Complex yaw angle
ρ	Mass density of the range air
ϕ'_1, ϕ'_2	Rates of rotation of the motion vectors in Eq. (2)
ψ	Precession angle, see Fig. 1

SUPERSCRIPTS

'	First derivative with respect to distance
"	Second derivative with respect to distance

SUBSCRIPTS

n	Nutational vector
o	Corresponding to the start of a motion pattern
p	Precessional vector

8th Navy Symposium on Aeroballistics

Vol. 3

INTRODUCTION

In free-flight testing in either an aeroballistic range or in a wind tunnel, certain stability derivatives can be evaluated from the measured yawing motion of the model. Hence, a knowledge of the relationship between the motion of the model and the constants of the equation that describes its motion can be particularly useful.

For the case of a nonrolling, axisymmetric model, the two motion vectors have identical damping parameters and have identical rotation rates. As the roll velocity of a model increases from a zero value, the damping parameters of the motion vectors can change appreciably. For example, a combination of the Magnus-moment and yawing-moment terms can exist in conjunction with an adequate roll rate to cause a dynamic instability in one of the two vectors.

The purpose of this paper is to present a discussion of rolling-yawing motion including some stability limitations related to such motion.

DISCUSSION

BASIC MODEL MOTION

The yawing motion equation examined in this paper is referenced to a nonrolling axis system, as is the custom in aeroballistic range work. The differential equation describing general rolling-yawing motion of an axisymmetric model can be written

$$\xi'' + (H - iP) \xi' - (M + iPT) \xi = 0 \quad (1)$$

where

$$H = (\rho S/2m) [C_{L\alpha} - C_D - k_t^{-2} (C_{m\dot{q}} + C_{m\dot{\alpha}})]$$

$$M = (\rho S/2m\ell) k_t^{-2} C_{m\alpha}$$

$$T = (\rho S/2m) [C_{L\alpha} + k_a^{-2} C_{m\dot{p}\alpha}]$$

$$P = (I_x/I_y)p$$

Derivations of this equation have been presented previously, for example Refs. 1 and 2. The solution of Eq. (1) for a model having linear variations of force and moment with yaw angle and a constant p can be written

$$\xi = K_1 \exp(\theta_1 x) + K_2 \exp(\theta_2 x) \quad (2)$$

where

$$\theta_j = \mu_j + i\phi'_j$$

The θ 's are roots of the auxiliary equation corresponding to the differential equation designated Eq. (1). It should be noted that the damping of the motion corresponding to the θ_j root is defined by the real part of the root and that the frequency of the motion is defined by the imaginary part of the root. Hence, for oscillatory motion to exist the root must have a nonzero imaginary part.

The roots expressed as functions of the coefficients of Eq. (1) are

$$\begin{aligned} \mu_1 + i\phi'_1 & \quad (3) \\ & = 1/2 \left[-H + iP + \sqrt{4M + H^2 - P^2 + i2P(2T - H)} \right] \end{aligned}$$

and

$$\begin{aligned} \mu_2 + i\phi'_2 & \quad (4) \\ & = 1/2 \left[-H + iP - \sqrt{4M + H^2 - P^2 + i2P(2T - H)} \right] \end{aligned}$$

In range testing, values for the K 's and θ 's of Eq. (2) are obtained by fitting Eq. (2) to the measured variations of the α and β components of the angular motion of the model with distance traveled. This equation is nonlinear in terms of the θ 's, and the use of an iterative, differential correction-type curve-fitting procedure is necessary. The desired H , M , P , and T parameters can then be determined as functions of the evaluated θ 's with use of the expression for the sum and the product of $(\mu_1 + i\phi'_1)$ and $(\mu_2 + i\phi'_2)$ and can be written

$$H = -(\mu_1 + \mu_2) \quad (5)$$

$$P = \phi'_1 + \phi'_2 \quad (6)$$

8th Navy Symposium on Aeroballistics

Vol. 3

$$T = -(\phi'_2 \mu_1 + \phi'_1 \mu_2)/P \quad (7)$$

$$M = \phi'_1 \phi'_2 - \mu_1 \mu_2 \quad (8)$$

$$\approx \phi'_1 \phi'_2$$

The assumption in the approximate relationship for M , that the product of the damping parameters is small relative to the product of the frequencies, is quite reasonable for a typical aerodynamic configuration.

The above procedure, permitting large roll velocities, is very adequate in the analysis of yawing motion. It is difficult for one to appreciate the significance of the roll effects that the procedure accounts for; however, considerable insight to the problem of roll effects can be obtained by examining the related equations. If P is set equal to zero (implying a zero roll rate) in Eqs. (3) and (4), the corresponding μ 's and ϕ 's are

$$\mu + i\phi' = 1/2 \left[-H \pm \sqrt{4M + H^2} \right] \quad (9)$$

Considering that oscillatory motion requires complex or imaginary roots and that H is a real number, the term $(4M + H^2)$ must be less than zero or $4M < -H^2$. From the definition of M listed previously,

$$4M = 4 (\rho S/2ml) k_t^{-2} C_{m\alpha}$$

and it follows that $C_{m\alpha}$ must be negative. An aerodynamic configuration is defined as being statically stable when it has a negative $C_{m\alpha}$ value. Hence for oscillatory motion (nonrolling model), it is apparent from Eq. (9) that the model must be statically stable.

The two terms on the right side of Eq. (2) defining the complex yaw angle, ξ , correspond to rotating vectors in the α, β plane (see Fig. 1). The model yawing motion defined by the two vectors is obviously dependent on the values of the K 's and θ 's. Values of the θ 's are functions of the aerodynamic and inertia characteristics of the model and the rolling velocity; the K 's are dependent on the initial disturbances of the model. For general rolling-yawing motion, K_1 , K_2 , θ_1 , and θ_2 are general complex numbers; however, roll effects on the yawing motion of a model become more apparent from first examining the more restricted types of model motion.

With use of the motion sketches shown in Fig. 1, the basic types of model motion corresponding to assigned

restrictions on the K 's and θ 's of Eq. (2) are demonstrated in the following examples, in which zero damping is assumed:

- a. If K_1 and K_2 , and θ_1 and θ_2 , are complex conjugates, then the motion is planar and along the real axis. This type corresponds to the angular motion of a one-degree-of-freedom dynamic balance system as used in a wind tunnel. A basic point to be noted here is that for the θ 's to be complex conjugates, the roll velocity, p , must necessarily be zero, which is apparent from Eqs. (3) and (4). It should be noted that the restriction on the θ 's dictates that the angular frequencies, ϕ 's, are equal in magnitude and have opposite signs.
- b. Let the restriction of θ_1 and θ_2 being complex conjugates be retained ($p = 0$). If K_1 and K_2 are not required to be complex conjugates but $|K_1| = |K_2|$, then general planar motion exists. This is indicated in the sketch in Fig. 1a where the yawing motion is along a line displaced from the α and β axes.
- c. If the restrictions of item (b) are retained except that $|K_1| \neq |K_2|$, then elliptic motion exists as indicated in Fig. 1b. The limiting case here is circular motion corresponding to one of the K 's being zero.
- d. If K_1 and K_2 are general complex numbers as in item (c) and the restriction of θ_1 and θ_2 being complex conjugates is removed, the resulting motion is of the precessing elliptic type shown in Fig. 1c.

Removing the restriction of θ_1 and θ_2 being complex conjugates corresponds to a nonzero roll velocity (see Eqs. (3) and (4)). Hence, the precessing elliptic motion of item (d) is caused by model roll, and the motion patterns of items (a, b, and c) are characteristic of nonrolling yawing motion.

The relationship between the roll velocity of a model and the direction and magnitude of the precession of the corresponding elliptic motion is obtained in the following derivation. In Fig. 1c the angle of precession, ψ , is defined as the angle between two adjacent peaks, as indicated in the sketch. The peak at (a) corresponds to a point in flight where both vectors are aligned, and at peak (b) the vectors are aligned again after each vector has rotated approximately 360 deg. As previously noted, the two vectors rotate in opposite directions, and since $|\phi_1| \neq |\phi_2|$, for ($p \neq 0$), then ψ must have a nonzero value. The sign of ψ is defined consistent with rotating vector notation; hence,

if the motion precesses counterclockwise, ψ is positive. It is apparent from the above that the motion will precess in the direction of the rotation of the larger absolute frequency. From Eq. (6) it follows that the larger absolute frequency will have the same sign as the roll velocity of the model. Consistent with the notation of Fig. 1c, and for $\psi < 120$ deg or $1/2 < |\phi'_1/\phi'_2| < 1$,

$$(360 + \psi)/\phi'_2 = (-360 + \psi)/\phi'_1$$

which corresponds to the roll rates of interest here; hence,

$$(\phi'_1/\phi'_2) = (\psi - 360)/(\psi + 360) \quad (10)$$

With use of Eqs. (6) and (10) an expression for P can be written as

$$P = [2\psi/(\psi + 360)]\phi'_2$$

Thus,

$$p = (I_y/I_x)[2\psi/(\psi + 360)]\phi'_2 \quad (11)$$

and

$$\psi = 360 p/[2(I_y/I_x)\phi'_2 - p], \quad (again for \psi < 120 deg) \quad (12)$$

For these expressions, ψ is in degrees; hence, p and the ϕ' 's are in deg/ft units. Equations (11) and (12) show explicitly the correspondence between the measured precessing elliptic motion of a test model, the inertia ratio (I_y/I_x) , and the roll velocity of the model.

A further point of interest related to an α, β plot is roll resonance, which can be of concern in testing an asymmetric configuration. Roll resonance occurs when $p \approx \phi'_2$ (ϕ'_2 is the larger absolute angular velocity), considering that the condition of resonance is slightly dependent on the damping of the system. The precession angle corresponding to resonance, ψ_{res} , can be obtained from Eq. (12):

$$\psi_{res} \approx 360/[2(I_y/I_x) - 1] \quad (13)$$

Although Eq. (13) is restricted to $\psi < 120$ deg, it has a wide range of use in that the inertia ratio (I_y/I_x) of many configurations is greater than two.

In the above examples of model motion defined by Eq. (2), it should be noted that when $|K_1| \neq |K_2|$, the motion sketches are for the case where the vector having the larger amplitude corresponds to the larger absolute frequency. The correspondence between the frequency, damping, and amplitude of the vectors is discussed in a later section of this report.

GENERAL ROLLING-YAWING MOTION

As noted above, the desired aerodynamic parameters H , P , T , and M can be evaluated, in experimental tests, with use of Eqs. (3) and (4) without solving these equations for the individual μ 's and ϕ' 's. However, in determining how particular parameters of Eq. (1) affect general rolling-yawing motion, it is useful to examine the individual frequency and damping equations for the two motion vectors. Although Eqs. (3) and (4) define the frequency and damping of the motion, they involve complex radicals which limit the use of the equations in this form. In the past, such complex radicals have usually been evaluated by using a binomial expansion or other approximate methods (see, for example, Ref. 3). However, complex radicals can be evaluated precisely by working with the general polar form of a complex number and can be written

$$\sqrt{a + ib} = \pm \left[\pm \sqrt{\frac{\sqrt{a^2 + b^2} + a}{2}} + i \sqrt{\frac{\sqrt{a^2 + b^2} - a}{2}} \right] \quad (14)$$

The sign preceding the real term on the right side of Eq. (14) is positive if (b) is positive and is negative if (b) is negative. From Eqs. (3) and (4), $a = 4M + H^2 - P^2$ and $b = 2P(2T - H)$.

In evaluating the complex radical of Eqs. (3) and (4), it should be noted that the term $(2T - H)$, in general, can be expected to be negative; however, it is quite possible for the term to be positive for certain configurations in consideration of the wide variations in the Magnus-moment term (T) that have been reported. It follows for a positive roll rate (P is positive) that the sign of (b) will be positive for $(2T - H) > 0$ and negative for $(2T - H) < 0$. With use of Eq. (14), the following expressions can be written for the μ 's and ϕ' 's:

$$\mu_1 = 1/2 \left[-H + e_1 \sqrt{\frac{\sqrt{(4M + H^2 - P^2)^2 + [2P(2T - H)]^2} + (4M + H^2 - P^2)}{2}} \right] \quad (15)$$

$$\phi'_1 = 1/2 \left[P + e_1 \sqrt{\frac{\sqrt{(4M + H^2 - P^2)^2 + [2P(2T - H)]^2} - (4M + H^2 - P^2)}{2}} \right] \quad (16)$$

8th Navy Symposium on Aeroballistics

Vol. 3

$$\mu_2 = 1/2 \left[-H - e_1 \sqrt{\frac{\sqrt{(4M + H^2 - P^2)^2 + [2P(2T - H)]^2} + (4M + H^2 - P^2)}{2}} \right] \quad (17)$$

$$\phi_2' = 1/2 \left[P - \sqrt{\frac{\sqrt{(4M + H^2 - P^2)^2 + [2P(2T - H)]^2} - (4M + H^2 - P^2)}{2}} \right] \quad (18)$$

where

$$e_1 = \frac{P(2T - H)}{|P(2T - H)|}$$

The above expressions indicate that ϕ_1' corresponds to the nutational vector for a positive roll rate and that this nutational vector has the larger damping when $(2T - H) < 0$; whereas, for configurations where $(2T - H) > 0$, the nutational vector has the smaller damping. Note that for a negative roll rate the nutational vector corresponds to ϕ_2' and will have the larger damping value when $(2T - H) < 0$. Note that the above equations permit the generation of model motion (using Eq. (2)) that corresponds to specifically assigned values of H , M , P , and T . Relationships for the frequency and damping of the nutational and precessional vectors can be written

$$\phi_{n,p}' = 1/2 \left[P \pm e_2 \sqrt{\frac{\sqrt{(4M + H^2 - P^2)^2 + [2P(2T - H)]^2} - (4M + H^2 - P^2)}{2}} \right] \quad (19)$$

where

$$e_2 = \frac{P}{|P|}$$

$$\mu_{n,p} = 1/2 \left[-H \pm e_3 \sqrt{\frac{\sqrt{(4M + H^2 - P^2)^2 + [2P(2T - H)]^2} + (4M + H^2 - P^2)}{2}} \right] \quad (20)$$

$$\text{where } e_3 = \frac{(2T - H)}{|(2T - H)|}$$

Equations (15) through (18) defining the ϕ' 's and μ 's are quite useful in observing how particular aerodynamic parameters are involved in rolling motion. In the case of the damping equations (Eqs. (15) and (17)), it is apparent

that if the radical term has a nonzero value, the damping of one motion vector is increased by the contribution of the radical term, whereas the damping of the other vector is decreased. The significance of the different terms within the radical becomes more apparent when the damping equation for the less damped vector is written as

$$\mu = 1/2 \left[-H + \sqrt{\frac{\sqrt{(-A)^2 + \Delta^2} + (-A)}{2}} \right] \quad (21)$$

where

$$-A = 4M + H^2 - P^2$$

and

$$\Delta = 2P(2T - H)$$

Here (A) is a positive number for a statically stable body or a spin stabilized body. For the radical term to have a nonzero value, Δ must have a nonzero value; hence, since P is a direct function of the roll rate (see Eq. (1)), it follows that a body must be rolling before the radical term can contribute to the damping. Further, the radical term has a zero value for the unique case of $(2T - H) = 0$. It should be noted that T is the Magnus-moment term, and H is the basic dynamic stability parameter, which for purposes of this paper is considered to be positive (see Eq. (1)).

It is apparent from Eq. (21) that the destabilizing effect of the radical term increases as Δ increases; hence, it is important to observe that the Magnus-moment term has a stabilizing effect on the less damped vector, if $T < H$ and is positive. If T is negative or greater than H , the Magnus-moment term has a destabilizing effect. Further, for a body for which the Magnus-moment term can be assumed zero and which has a zero static margin ($M = 0$), then the damping is independent of the roll rate, and one of the motion vectors will always have zero damping.

It has been noted previously (see, for example, Refs. 1 and 2) that for many conditions of interest the effects of the H and T parameters in the frequency equations are small. With this assumption, approximate frequency equations are usually written as

$$\phi''s \approx 1/2 [P \pm \sqrt{P^2 - 4M}] \quad (22)$$

It can be observed that a statically unstable body ($M > 0$) can be made stable with a sufficiently high roll rate and is referred to as gyroscopic stability. The condition for

8th Navy Symposium on Aeroballistics

Vol. 3

gyroscopic stability, as used in the past by ballisticians, is where $P^2 - 4M > 0$.

The above expressions for the μ 's permit the definition of a dynamic stability boundary corresponding to any arbitrary limitation placed on the μ of the less damped motion vector. In Fig. 2 a curve of the ratio, $4M/P^2$, is shown as a function of the ratio, T/H , and defines the dynamic stability boundary corresponding to the case in which one of the motion vectors has zero damping. It is of interest to note that Fig. 2 indicates that within a band of the T/H ratio of $0 < (T/H) < 1$, a statically unstable body can be dynamically stabilized with a sufficiently high roll rate; however, outside of this T/H band it is impossible to dynamically stabilize a statically unstable body. Further, a body that is both statically and dynamically stable and has a T/H ratio outside of the above band can be dynamically destabilized with a sufficiently high roll rate.

The relationship between the frequency of a vector and its amplitude is dependent on the initial disturbances of the model and can be examined with use of the sketches in Fig. 3, in which the yawing motion has the same initial displacement, ξ_0 . Note that the ξ vector is rotating counter-clockwise in Sketch (a) and clockwise in Sketch (b). It is apparent that the ξ vector will rotate, in the case of precessing elliptic motion, in a direction consistent with the rotation direction of the motion vector having the larger amplitude (K_n or K_p). As previously discussed, the elliptic motion will precess in the direction of the rotation of the nutational vector (direction of the model roll); hence, the nutational vector will have the larger amplitude only if the ξ vector rotation is in the same direction as that of the nutational vector. The direction of rotation of the ξ vector and the ratio of the amplitudes of the two vectors corresponding to the elliptic motion are defined by the initial velocity disturbance of the ξ vector (ξ_0'). From the correspondence between the μ 's and ϕ 's and between the ϕ 's and the amplitudes of the vectors, it follows that a model can be disturbed such that the larger amplitude vector can have either the larger or smaller damping value.

ANALYSIS OF MOTION VIEWED IN ONE PLANE

An example in which the effects of model roll can be of particular concern is in free-flight testing in wind tunnels, where the model motion may be monitored in only one plane. The orthogonal components (β and α) of the yawing motion of a nonrolling model can be described by an equation defining damped sinusoidal motion, with both components having identical frequencies and damping parameters. It follows that

in such tests the stability derivatives can be adequately evaluated from either component. In the case of a rolling body the complexity of the motion of each orthogonal component increases as the roll velocity increases from zero, and each component consists of two subcomponents having different damping parameters and different frequencies.

In the case of wind tunnel testing, some model roll arising from the launching of the model or from small asymmetries that are either accidental or designed into the model may exist. In the past, stability data from such wind tunnel tests have usually been analyzed assuming negligible roll effects; hence, the concern in this type of testing is the sensitivity of the components of the yawing motion to model roll. To aid in examining this problem, the β and α components of Eq. (2) can be separated and written as

$$\begin{aligned}\beta = & (a \cos \phi'_1 x - b \sin \phi'_1 x) \exp (\mu_1 x) \\ & + (c \cos \phi'_2 x - d \sin \phi'_2 x) \exp (\mu_2 x)\end{aligned}\quad (23)$$

and

$$\begin{aligned}\alpha = & (b \cos \phi'_1 x + a \sin \phi'_1 x) \exp (\mu_1 x) \\ & + (d \cos \phi'_2 x + c \sin \phi'_2 x) \exp (\mu_2 x)\end{aligned}\quad (24)$$

where a , b , c , and d are real constants.

From Eqs. (23) and (24) it is apparent that each component, for the case of a rolling model, is the sum of trigonometric terms containing different frequencies; hence, the resulting curve for the simplified case of zero damping will necessarily have an apparently varying frequency and a varying amplitude. Examples of such motion are shown in Figs. 4 and 5. The motion plots of Fig. 4 are representative of a small roll rate (the precession angle is 5 deg). Each component appears to represent sinusoidal motion with a constant damping value; however, the damping values for the two components are appreciably different. In the case of the model motion of Fig. 5 with a larger roll rate, the curves can be deceiving in that apparent nonlinearities are observed in both components. It follows that the primary concern in experiments is related to possible effects on the yawing motion existing at small roll rates where the apparent nonlinearities (roll effects) are not obvious from the motion plots when the model motion is monitored in only one plane. It was noted in Ref. 4, in discussing free-flight testing in wind tunnels, that for the range of small roll rates which could be expected in such tests, significant errors in the reduced damping values could exist when one motion component is analyzed assuming a zero roll rate.

In the conventional stability analysis used in aeroballistic range testing, the measured values of both α and β are fitted simultaneously, and hence, various types of motion from planar to patterns exhibiting large precession can be fitted adequately. However, a suggested approach discussed in Ref. 5 for analyzing model motion is of interest in relation to wind tunnel testing in which the motion is monitored in only one plane. It was noted in Ref. 4 that all of the equation constants in the expression for the complex yaw angle, ξ , are present in each component of ξ (α or β). Further, it was stated, in view of this, that the unknown constants could be determined by fitting either the α or β values separately or both simultaneously. In examining this approach, it is believed that evaluating equation constants corresponding to general motion patterns by fitting one component of the motion is infeasible. Recent work concerned with fitting generated motion patterns, using either α or β values, has supported this conclusion. Considerable difficulty was experienced in satisfactorily fitting motion patterns having precession angles of about 5 deg or less. Unfortunately, a large portion of current stability testing involves models subject to roll rates corresponding to precession angles of 0 to 5 deg.

CONCLUDING REMARKS

The effects of a roll velocity on the free-flight yawing motion of axisymmetric bodies having linear force and moment characteristics have been discussed. Expressions for the frequency and the damping of the motion vectors have been given as explicit functions of the roll velocity and the inertia and aerodynamic characteristics of the bodies. Stability boundaries defined by these expressions were noted, and the significance of the various aerodynamic parameters of a rolling body that can contribute to a dynamic instability has been discussed. The dynamic stability boundary curve indicates that within a band of the T/H ratio of $0 < T/H < 1$, a statically unstable body can be dynamically stabilized with a sufficiently high roll rate, but outside of this band it is impossible to dynamically stabilize such a body. Further, a body that is both statically and dynamically stable and has a T/H ratio outside of the band can be dynamically destabilized with a sufficiently high roll rate. The correspondence between the damping, frequency, and amplitude of the nutational and precessional vectors has been discussed.

8th Navy Symposium on Aeroballistics

Vol. 3

REFERENCES

1. Ballistic Research Laboratories. On the Free Flight Motion of Missiles Having Slight Configurational Asymmetries, by J. D. Nicolaides. June 1953. (Report 858.)
2. Ballistic Research Laboratories. Advances in the Dynamic Analysis of Range Data, by C. H. Murphy. May 1960. (BRL-MR-1270.)
3. University of Notre Dame, Aerospace Engineering Department. Free-Flight Missile Dynamics, by J. D. Nicolaides. (1965.)
4. Arnold Engineering Development Center. Effects of Roll on the Free-Flight Motion of Statically Stable Bodies, by C. J. Welsh and R. M. Watt. September 1967. (AEDC-TR-67-156 (AD658433).)
5. Aerodynamics Testing Conference. Dynamic Wind Tunnel Testing Techniques, by J. D. Nicolaides and R. S. Eikenberry. Los Angeles, California, September 1966. (AIAA Paper No. 66-752.)

BLANK PAGE

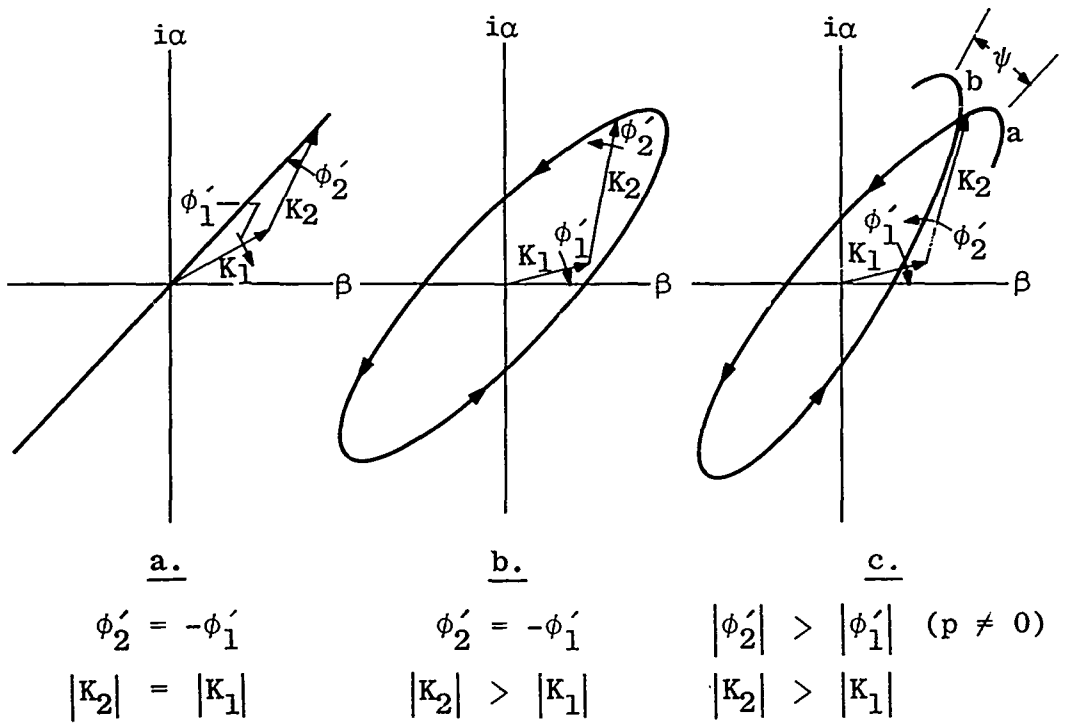


FIG. 1. Computed Motion Patterns as Functions of Initial Disturbances and Model Roll.

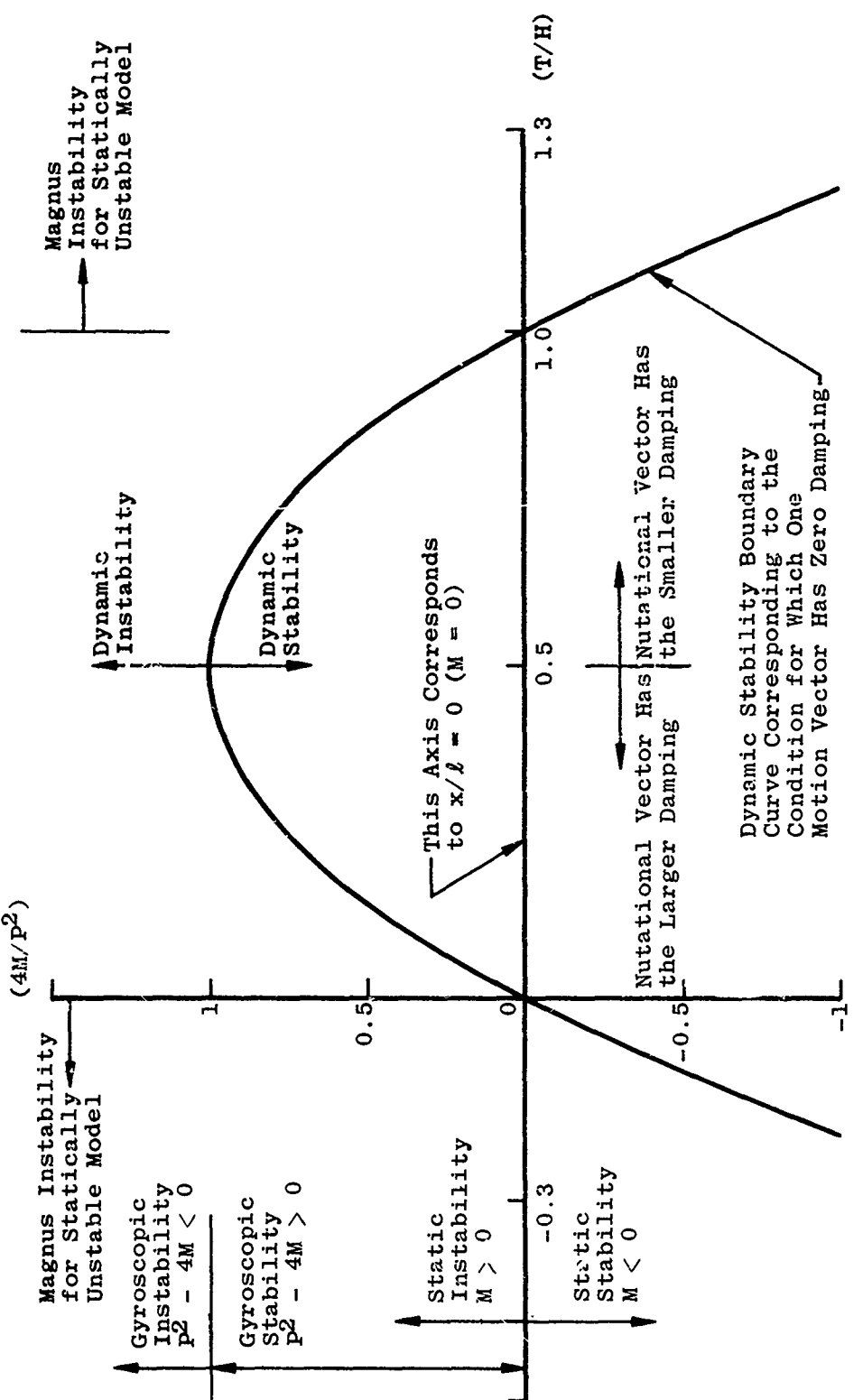
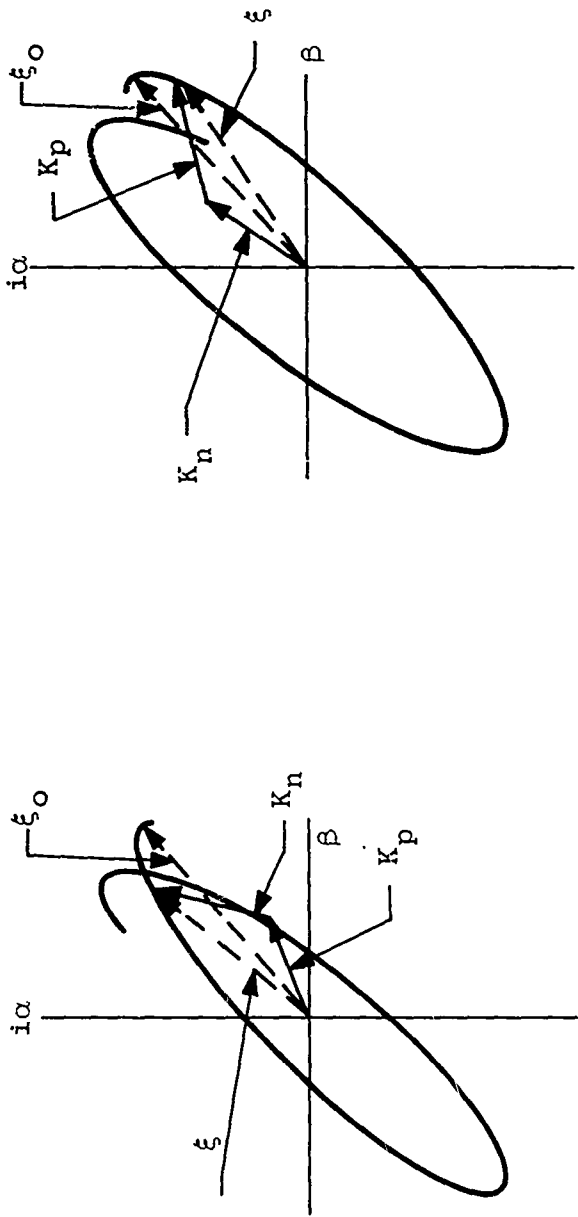


FIG. 2. Stability Boundaries.



a. Pattern When Nutational Vector Has the Larger Amplitude.
 b. Pattern When Precessional Vector Has the Larger Amplitude.

FIG. 3. Computed Motion Patterns as Functions of the Rotation Direction of the ξ Vector.

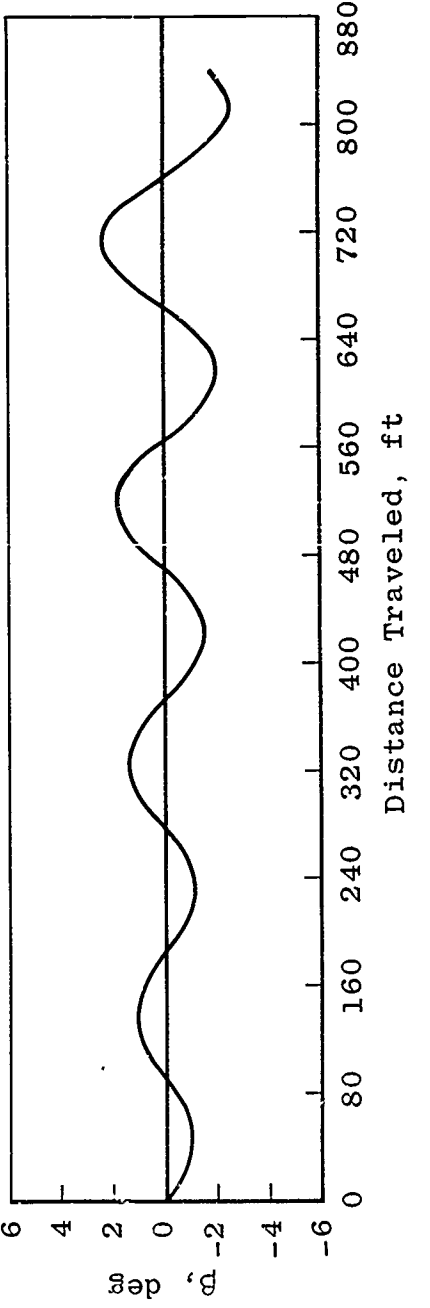
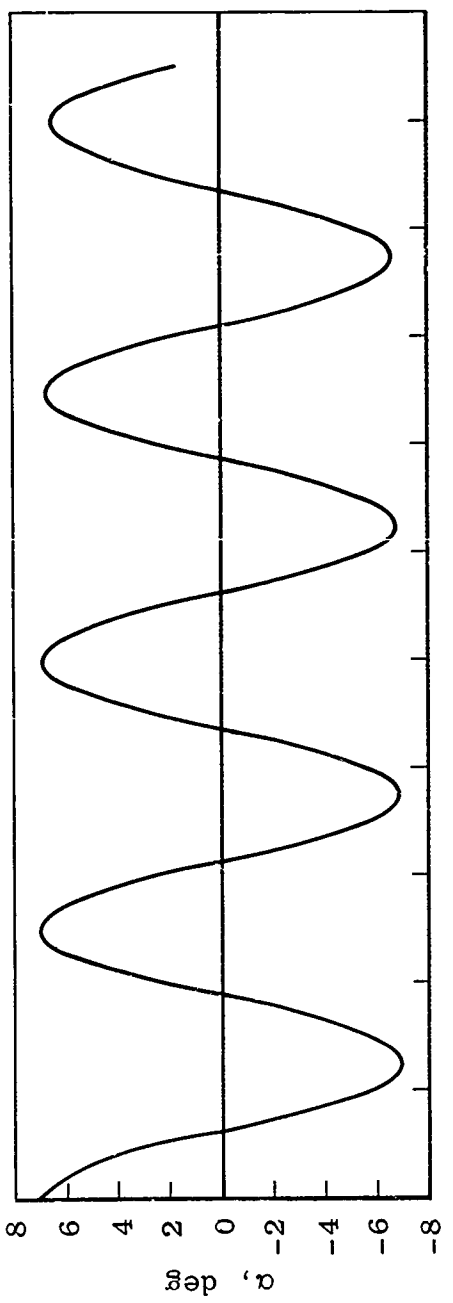


FIG. 4. Computed Motion for a Statically Stable Configuration,
 $\psi = 5$ deg.

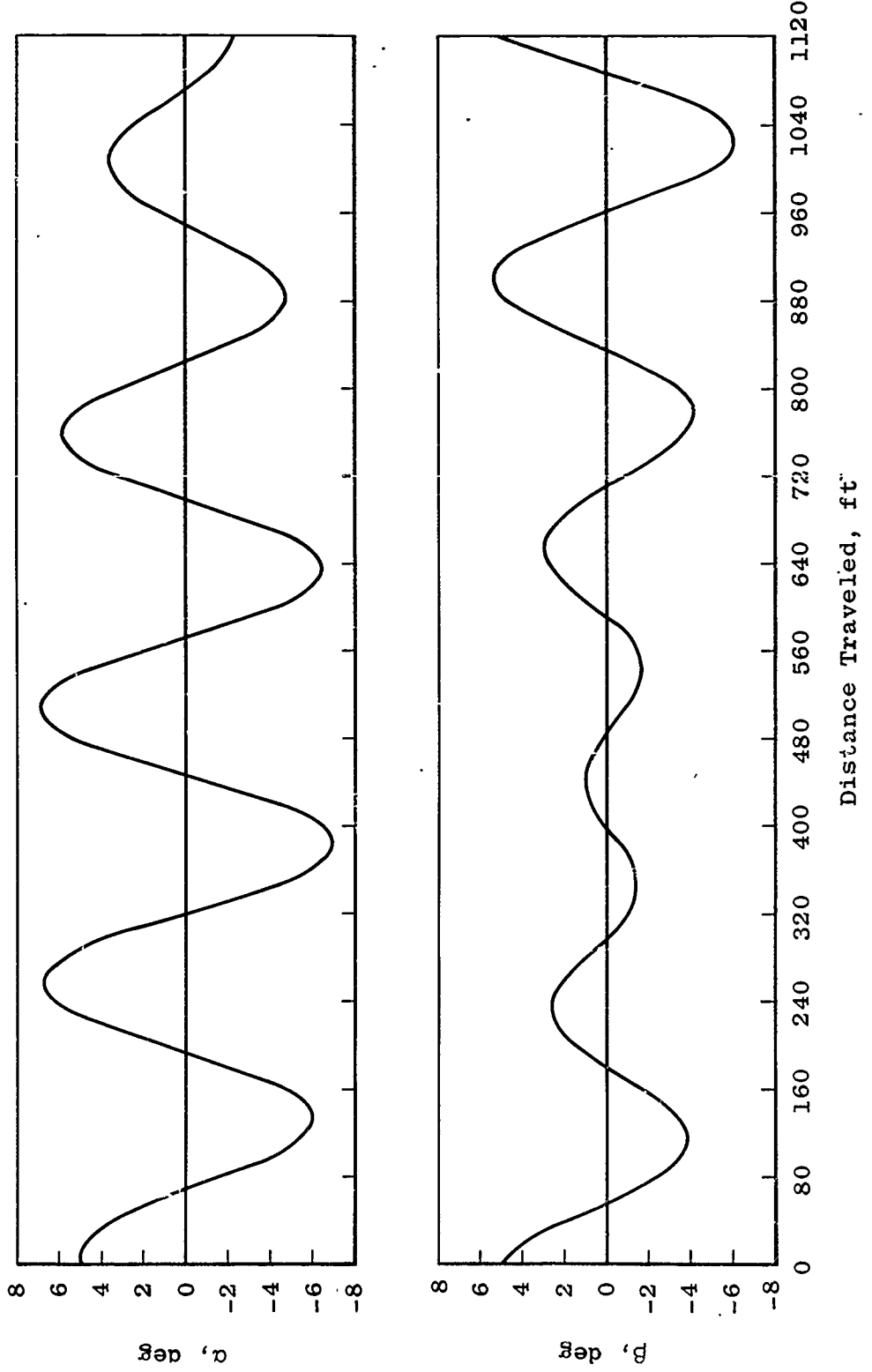


FIG. 5. Computed Motion for a Statically Stable Configuration,
 $\psi = 26.6$ deg.

Paper No. 28

DYNAMIC STABILITY OF THE
5-INCH/54 ROCKET ASSISTED PROJECTILE
(THE INFLUENCE OF A NON-LINEAR MAGNUS MOMENT)
FOR
EIGHTH UNITED STATES NAVY SYMPOSIUM ON AEROBALLISTICS
(U)

(Paper UNCLASSIFIED)

by

W. R. Chadwick
Naval Weapons Laboratory
Dahlgren, Va. 22448

ABSTRACT. (U) This note presents the results of a stability analysis of the 5-inch/54 Rocket Assisted Projectile. Aerodynamic data from the BRL spark ranges are used to determine the stability characteristics of the projectile at very small angles of yaw. The analysis then employs supplementary wind tunnel data which highlight the non-linear properties of the Magnus moment to investigate stability at larger angles of yaw.

(U) The 5-inch/54 RAP is shown to be highly stable at launch and to possess adequate gyroscopic stability over the entire spectrum of flight conditions. However, during descent from the vertex height of short-to-medium range trajectories the projectile may be expected to fly with a constant circular yawing motion of amplitude about two degrees. A more serious stability problem could develop during maximum range firings but only if the projectile is disturbed by winds to very large angles of yaw.

INTRODUCTION

(U) In order to increase the range performance of 5-inch Naval guns, the 5-inch/54 caliber and the 5-inch/38 caliber standard service projectiles have been redesigned to incorporate rocket assistance. The extended range projectiles are designated the 5-inch/54 RAP (see Figure 1) and the 5-inch/38 RAP respectively. This note presents the results of a dynamic stability analysis of the 5-inch/54 RAP.*

(U) Two slightly different 105mm artillery shells, which have physical properties somewhat similar to those of the 5-inch/54 RAP, are known to be dynamically unstable transonically at very small yaw (1, 2). However, owing to the influence of a highly non-linear Magnus moment, these 105mm projectiles recover their stability with increasing yaw, and fly with a constant circular yawing motion of amplitude about three degrees. From the outset of the RAP study it was therefore evident that the precise determination of possible limit cycle motions would require extensive information on the non-linear properties of the Magnus moment, particularly at transonic speeds where the Magnus moment depends not only on yaw but also on Mach number (2, 3, 4).

(U) The solution of the difficult Magnus moment problem demanded extensive spark range firings and wind tunnel testing. Complete low incidence aerodynamic properties were derived from motions recorded in the free-flight spark ranges at the Ballistic Research Laboratories. Supplementary wind tunnel data to establish the non-linear properties mentioned above were obtained from the David Taylor Model Basin and from the Naval Ordnance Laboratory.

* Since this analysis was conducted the sustainer motor (Figure 1) has been replaced by a short-period high-impulse booster having the same total impulse. Important stability characteristics are not affected by this change.

AERODYNAMIC PROPERTIES

The Assumed Drag Function

(U) Figure 2 shows the drag function for the standard 5-inch/54 MARK 41 projectile. This drag function was derived originally by slightly modifying spark range data based on comparisons between particle trajectory computations and results from several hundred full-scale range firings (5). Since the 5-inch/54 MARK 41 projectile is almost identical in external shape to the 5-inch/54 RAP this drag function has been assumed also for the 5-inch/54 RAP. Data from the more recent 5-inch/54 RAP spark range tests are also shown in Figure 2. Agreement with the assumed drag function is excellent. For reference purposes precise tabulated values of the above drag function are also given in Figure 2 together with results from particle trajectory computations on range performance.

(U) Figures 3 to 6 illustrate respectively the stability coefficient derivatives $C_{z\alpha}$, $C_{m\alpha}$, C_{mq} and C_{lp} as functions of Mach number. It is perhaps worth noting that the spark range data indicate a definite change from negative to positive values of C_{mq} as the Mach number falls below about 1.0 (see also reference 3).

Variation of Magnus Moment Coefficient Derivative with Mach Number

(U) The Magnus moment coefficient derivative for the 5-inch/54 RAP, of primary importance in the analysis which follows, is shown against Mach number in Figure 7. It is immediately obvious that the spark range data exhibit considerable scatter in the range $M = 0.7$ to 1.2 . Furthermore, a close preliminary examination of the average yaw for each of the rounds fired revealed no precise yaw dependence. However, as the data have been presented in Figure 7, corresponding to test rounds experiencing either 0.5 to 3.0 degrees or 3.0 to 5.5 degrees of average yaw, some yaw dependence does in fact seem to be present. In order to establish more definitely the true variation of $C_{np\alpha}$ with Mach number for identically zero yaw, use has been made of the excellent spark range data contained in reference 2. As mentioned previously, the 105mm projectile of reference 2 is somewhat similar to the 5-inch/54 RAP. A large number of these projectiles were fired at entirely subsonic speeds ($M = 0.4$ to 0.8) where, for present purposes, undesirable variations due to Mach number may reasonably be neglected. This is evidently not true in the case of the available RAP data which embrace the transonic speed range. The 105mm data are shown in Figure 8 and clearly illustrate a definite yaw dependence within the subsonic speed range. The Magnus moment coefficient derivative for the 105mm projectile, at average yaw levels approaching zero, evidently tends

Vol. 3

to large negative values as the speed becomes subsonic. At larger yaw this tendency is less pronounced. Based on the 5-inch/54 data, but influenced significantly by the 105mm data, the curve in Figure 7 was finally taken as the best probable representation of the variation with Mach number of the zero yaw stability coefficient derivative $C_{np\alpha}$. As will be shown later, this representation, from a dynamic stability standpoint, is also the most pessimistic representation possible based on the available data.

Variation of Magnus Moment Coefficient with Yaw and Mach Number

(U) Practically no data appear available which establishes conclusively the variation of the Magnus moment coefficient C_{np} with yaw for a fast spinning projectile passing through the transonic speed range. Attempts have been made, using data from spark range firings, to estimate this variation at subsonic speeds by neglecting the influence of Mach number - as discussed above. This approach, however, would certainly be unjustified within the range $M = 0.8$ to 1.2 , where Figures 7 and 8 indicate a strong and definite Mach number dependence. Furthermore, the variation of the Magnus moment with yaw at different Mach numbers is of considerable interest up to yaws in excess of those normally achieved during ballistic range tests. Accordingly, employing highly accurate machined models, full scale transonic and $2/5$ scale supersonic wind tunnel tests were conducted to measure the 5-inch RAP Magnus moment characteristics (6). The zero yaw derivative $C_{np\alpha}$, derived above from the ballistic range data, has been used in conjunction with this supplementary wind tunnel data to establish the variation of C_{np} with yaw up to 15 degrees over the range $M = 0.7$ to 2.5 . These results are presented in Figure 9. In estimating the trends shown in Figure 9 the zero yaw Magnus moment coefficient derivative $C_{np\alpha}$ was assumed to represent adequately the variation of C_{np} with α up to about two degrees of yaw. Above about four degrees of yaw the wind tunnel estimates of C_{np} were considered reliable.

(U) The Magnus moment is seen to exhibit a highly non-linear dependence on yaw within the range $M = 0.7$ to 1.15 . Within this range C_{np} also varies considerably with Mach number. For example, at $M = 1.05$ to 1.15 a large observed forward shift in the position of the center of pressure of the Magnus force gives rise to large negative values of the Magnus moment. This fundamental change in the Magnus moment-yaw relationship, which appears to occur with increase in Mach number transonically, will be shown later to have

important ramifications with regard to dynamic stability. It should be noted finally that at $M = 1.75$ the Magnus moment is almost linear with yaw (see also reference 7).

DYNAMIC STABILITY

(U) In order to establish the dynamic stability characteristics of the 5-inch/54 RAP, consideration must be given to the non-linearity of the Magnus moment. However, since this non-linearity is most likely to be important only when the projectile exhibits marginal stability at very small yaw, it is clearly desirable to first determine stability boundaries over a wide range of flight conditions based entirely on the zero yaw stability coefficient derivatives obtained from the BRL spark ranges. Accordingly, the results of the first part of the present investigation, a linear stability analysis, are outlined below in the first paragraph of the present Section. It is shown that the flight performance of the 5-inch/54 RAP will indeed be influenced by the non-linear properties of the Magnus moment. In the next paragraph, therefore, dynamic stability is discussed on the basis of the quasi-linear theory. Finally, in the last paragraph, numerical solutions of the complete six-degree-of-freedom equations of motion are considered and an indication is given of the effect of small instabilities on range performance.

Linear Analysis

(U) In non-rolling aeroballistic axes the tricyclic motion of a fast spinning axially symmetrical projectile, with appropriate initial conditions, is given by

$$\bar{\alpha} = \bar{\alpha}_N e^{(\lambda_1 + i\omega_1)t} + \bar{\alpha}_P e^{(\lambda_2 + i\omega_2)t} + \bar{\alpha}_R \quad (1)$$

where the total complex yaw $\bar{\alpha}$ consists of a high frequency nutation $\bar{\alpha}_N$, a slower precessional motion $\bar{\alpha}_P$ and a zero frequency term $\bar{\alpha}_R$ which represents the slowly changing steady state yaw of repose. The damping and frequency concepts, using standard notation, are

$$\lambda_{1,2} = \frac{QA}{2mV} \left[C_{z\alpha} (1 \pm \tau) + \frac{md^2}{2I_y} C_{m\alpha} (1 \pm \tau) \pm \frac{md^2}{I_x} C_{n\alpha} \tau \right] \quad (2)$$

$$\omega_{1,2} = \frac{pI_x}{2I_y} \left[1 \pm \frac{1}{\tau} \right] \quad (3)$$

where $S = \frac{p^2 I_x^2}{4I_y QAdC_{m\alpha}}$ and $\tau = \frac{1}{[1 - 1/S]^{1/2}}$ (4)

8th Navy Symposium on Aeroballistics

Vol. 3

The necessary and sufficient conditions for dynamic stability in the linear case are then

$$S > 1 \text{ and } \lambda_{1,2} < 0 \quad (5)$$

(U) The gyroscopic stability factor S for the 5-inch/54 RAP has a minimum value of 1.62 at launch. It increases during flight before decreasing finally to about 3.0 at graze for all Q_e . The projectile therefore exhibits adequate gyroscopic stability over the entire spectrum of flight conditions.

(U) Figures 10 and 11 indicate that from launch to vertex height the nutational and precessional motions of the 5-inch/54 RAP are stable at very small yaw for all possible Q_e . Indeed, at launch, $\lambda_1 = -0.9$ and $\lambda_2 = -1.2$ so that any transient yaw at the gun will damp out almost immediately. However, during descending flight in the case of the short-to-medium range trajectories ($Q_e = 25$ and 35 degrees) the linear theory predicts dynamically unstable precessional motions corresponding to the sustained positive values of λ_2 . For $Q_e = 35$ degrees, Figures 12 and 13 show the amount by which each of the stability coefficient derivatives appearing in Equation 2 contribute to the total values of λ_1 and λ_2 respectively. Clearly, the elimination of precessional instability at very small yaw requires a large reduction in the destabilizing influence of the Magnus moment. Reference to Figure 14 indicates further that the positive values of λ_2 occur in the high subsonic range $M = 0.9$ to 0.95 corresponding to the region of large negative $C_{n_{p\alpha}}$ discussed previously.

(U) At high subsonic speeds it seems most unlikely that the precessional motion of the projectile can be stabilized at very small yaw. Unacceptable changes in spin, center of gravity position and axial inertia would certainly be necessary. Within the range $Q_e = 25$ to 35 degrees, therefore, the 5-inch/54 RAP will probably be unstable in service at small yaw. The behavior of the projectile as the yaw increases is discussed in the following paragraph.

Non-Linear Analysis

(U) In the non-linear case projectile motions cannot be discussed in terms of zero yaw stability coefficient derivatives and a precise closed form solution for the complex yaw as a function of time is not possible. Criteria for dynamic stability in this case, however, which determine whether a given initial yaw will grow or decay with the passage of time, have been derived by Nicolaides (8). These are

$$\lambda_{1,2}^* = \frac{QA}{2mV} \left[\hat{C}_{z\alpha} (1 \pm \tau) + \frac{md^2}{2I_y} \hat{C}_{mq} (1 \pm \tau) \pm \frac{md^2}{I_x} \hat{C}_{np\alpha} \tau \right] \quad (6)$$

$$\lambda_{1,2}^* < 0 \quad (7)$$

where the quasi-linear damping factors λ_1^* and λ_2^* are estimated using variable secant slopes for the stability coefficient derivatives (the $\hat{}$ notation is used to denote non-linear quantities).

(U) Equation 7 is a necessary and sufficient condition for dynamic stability in the non-linear case, assuming adequate gyroscopic stability. It indicates whether the projectile will be dynamically stable at a given yaw (provided the motion is one of almost pure precession or pure nutation) and is in general independent of linear considerations. The wind tunnel data revealed no important non-linearity in C_z so that if C_{mq} is taken to be independent of yaw the only significant non-linear term in Equation 6 is the Magnus term $\hat{C}_{np\alpha}$. Figure 15 illustrates the time variation of λ_2^* assuming a constant circular yawing amplitude of two degrees ($Q_e = 25$ and 35 degrees). Thus it may be seen that while the 5-inch/54 RAP is unstable at very small yaw during descending flight over short-to-medium range trajectories the projectile may be expected to recover rapidly from this condition as the yaw increases. The amount by which $\hat{C}_{np\alpha}$ changes with increasing yaw during these descents ($M = 0.9$ to 0.95) is evident from Figure 9.

(U) The fundamental change which occurs in the Magnus moment-yaw relationship with transition from high subsonic to low supersonic speeds (Figure 9) has an important effect on stability. Within the range $M = 0.7$ to 0.95 increasing yaw stabilizes the precessional motion of the projectile, resulting in the stable limit cycle motions discussed above. Within the range $M = 1.05$ to 1.15, however, the reverse is true - increasing yaw has an adverse effect on precessional stability. Thus, although the 5-inch/54 RAP has been shown to be stable at very small yaw during descent from the vertex height of the maximum range trajectory, the projectile nevertheless flies within the higher terminal Mach number range $M = 1.0$ to 1.1 and will therefore become unstable if disturbed to sufficiently large yaw. Mach numbers within the above range are sustained from about 65 seconds to graze during long range firings ($Q_e = 50$ to 55 degrees) and it has been estimated that λ_2^* will tend to a small

8th Navy Symposium on Aeroballistics

Vol. 3

positive value if at any time during this period the projectile is disturbed suddenly to a total yaw in excess of about six degrees. Below $Q_e = 45$ degrees the post vertex Mach number never exceeds 1.0 and stability should increase with increasing yaw, as discussed previously.

Computed Motions

(U) The dynamic stability characteristics of the 5-inch/54 RAP have been studied also using a complete six-degree-of-freedom mathematical model. The results from this study confirm the theoretical predictions outlined previously. Figures 16 and 17, for example, show the response of the projectile following a large disturbance during descent from the vertex height of trajectories having $Q_e = 25$ and 35 degrees. Only the slowly changing yaw of repose and the precessional motion are shown - the small amplitude high frequency nutations are discussed later. Thus it may be seen that the precessional motion about trim, which is highly stable at large yaw owing to the non-linear Magnus term $C_{n,p\alpha}$ converges rapidly initially and that the projectile then flies with an almost constant circular yawing motion of amplitude about two degrees. The interesting nutations which follow the above disturbance are illustrated in Figure 18. As expected, these high frequency oscillations are very lightly damped at large yaw but become more stable as the yaw decreases.

(U) An indication of the loss in range caused by various limit cycle motions during descending flight is given in Figure 19. Clearly, the above stability problem will not seriously affect range performance.

(U) The response characteristics of the 5-inch/54 RAP following transient disturbances during descent from the vertex height of maximum range trajectories were also studied. The projectile was disturbed in flight 70 seconds after launch ($M = 1.05$) where previous considerations indicate dynamic instability at large yaw. The magnitude of the disturbance was of primary importance in these computations-Previously any disturbance would have resulted in the observed limit cycle motions. Precessional instability occurred at average disturbed yaw levels in excess of about six degrees. When the transient yaw was reduced to four degrees the projectile recovered completely. However, wind gusts are unlikely to result in transient yawing motions of amplitude six degrees and it seems most unlikely, therefore, that the maximum range performance of the 5-inch/54 RAP will be severely affected owing to flight within the terminal Mach number range $M = 1.0$ to 1.1.

CONCLUSIONS

(U) a. The 5-inch/54 RAP possesses adequate gyroscopic stability over the entire spectrum of flight conditions.

(U) b. Any small yawing motions at the gun will be highly stable. Time to half amplitude should be less than one second.

(U) c. From launch to vertex height, for all possible quadrant elevation angles, the projectile is dynamically stable at all reasonable yaw levels.

(U) d. During descent from the vertex height of short-to-medium range trajectories, the projectile will probably be unstable at very small yaw. This instability should disappear with increasing yaw and the projectile should continue to fly with a constant circular yawing motion of amplitude about two degrees.

(U) e. The effect of the above problem on range performance is negligible.

(U) f. Owing to a fundamental change in the Magnus moment-yaw relationship, at terminal Mach numbers which are sustained only during maximum range flight, the projectile could become completely unstable if disturbed by wind gusts to yaw levels in excess of about six degrees. Such severe disturbances, however, must be considered most unlikely.

8th Navy Symposium on Aeroballistics

Vol. 3

REFERENCES

1. Hayden, H. G., "Yaw Measurement Analysis", RARDE Memo 54/64, Dec 1964
2. Roecker, E. T., "The Aerodynamic Properties of the 105mm HE Shell, M1, in Subsonic and Transonic Flight", BRL Memo Report No. 929, Sept. 1955
3. Karpov, B. G. and Schmidt, L. E., "The Aerodynamic Properties of the 155mm Shell M101 from Free Flight Range Test of Full Scale and 1/12 Scale Models", BRL Memo Report No. 1582, June 1964
4. Schmidt, L. E., "Aerodynamic Properties of 4.9-Calibers Long, Square Based Shell at Transonic Speeds", BRL Memo Report No. 824, Aug 1954
5. Mulligan, J. E., "Preparation of Anti-Aircraft Range Tables for 5-inch 54-Caliber Gun MARK 41 MOD 0 Projectile", NPG Report No. 1463, May 1956
6. Regan, F. J., Holmes, J. E., and Falusi, M. E., "Magnus Wind Tunnel Test of the 5-inch/38 and 5-inch/54 RAP Projectile", NOL Tech Report No. 65-198, March 1966
7. Whyte, R. H., "Effects of Boattail Angle on Aerodynamic Characteristics of the 175mm M437 Projectile at Supersonic Mach Numbers", Picatinny Arsenal Memo Report No. 1646, Sept 1965
8. Nicolaides, J. D., "Two Non-Linear Problems in the Flight Dynamics of Modern Ballistic Missiles", IAS Report No. 59-17, Jan 1959

8th Navy Symposium on Aeroballistics

Vol. 3

PARAMETER	WEIGHT (1b)	I_x (slug-ft 2)	I_y (slug-ft 2)	C. G. (calibers from nose)	THRUST (1b)
LAUNCH	59.9	0.0451	0.521	3.184	55.8
BURN OUT	53.3	0.0424	0.472	3.060	55.8

VELOCITY AT LAUNCH - 2768.00 Ft/sec

SPIN AT LAUNCH - 266.00 rps

TIME AT BURN OUT - 24.00 sec

7.5 DEGREE BOATTAIL

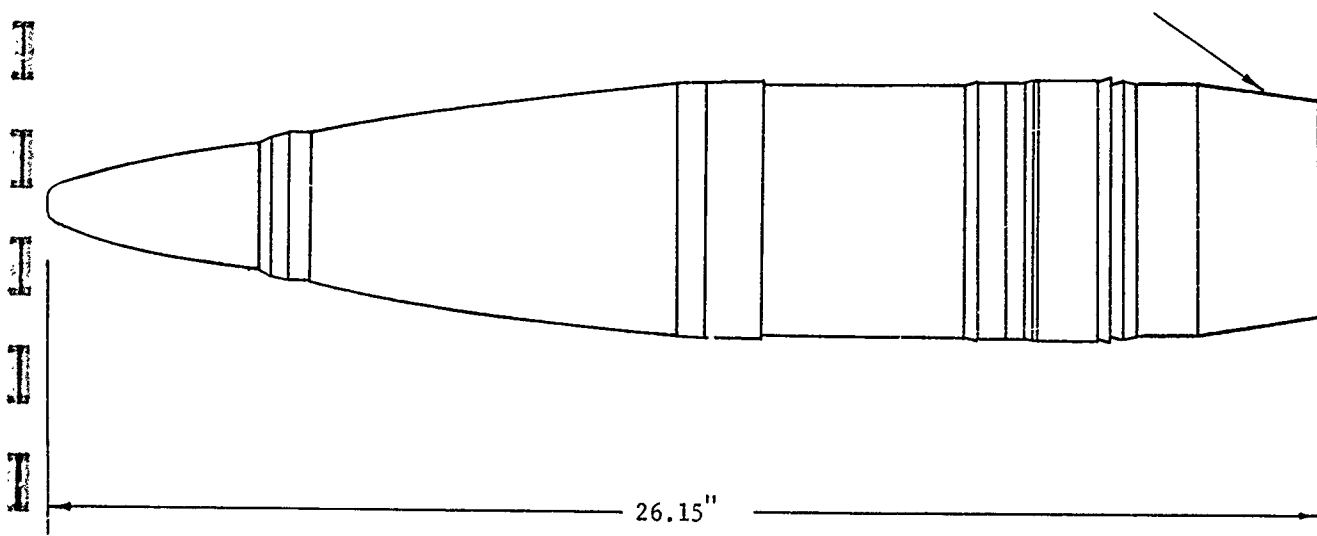


FIGURE 1 OUTLINE DIAGRAM AND PHYSICAL PARAMETERS OF THE 5-INCH/54 RAP.

8th Navy Symposium on Aeroballistics

Vol. 3

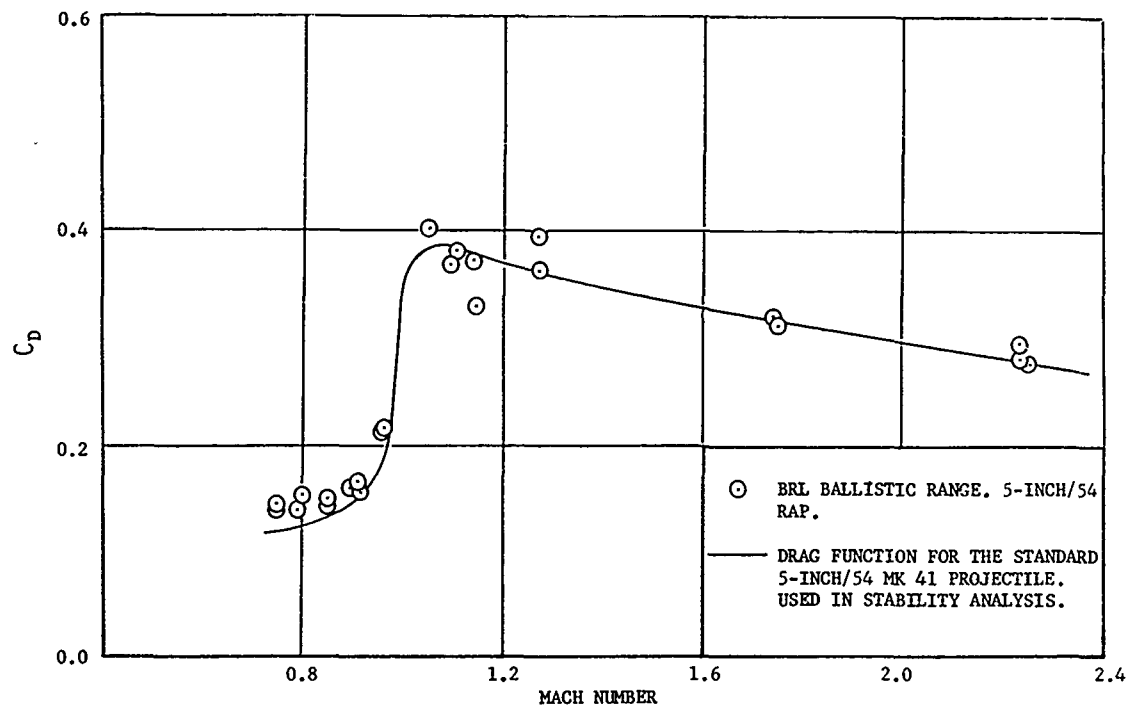


FIGURE 2 DRAG FUNCTION ASSUMED FOR THE 5-INCH/54 RAP.

TABULATED VALUES OF C_D

MACH NUMBER	0.70	0.80	0.90	1.00	1.05	1.10	1.15	1.50	1.75	2.00	2.50
C_D	0.1215	0.1215	0.1450	0.325	0.375	0.380	0.385	0.335	0.305	0.285	0.250

RANGE ESTIMATES BASED ON PARTICLE THEORY

Q_e (DEGREES)	25.0	35.0	45.0	55.0
RANGE (YARDS)	24234	28345	31119	32472

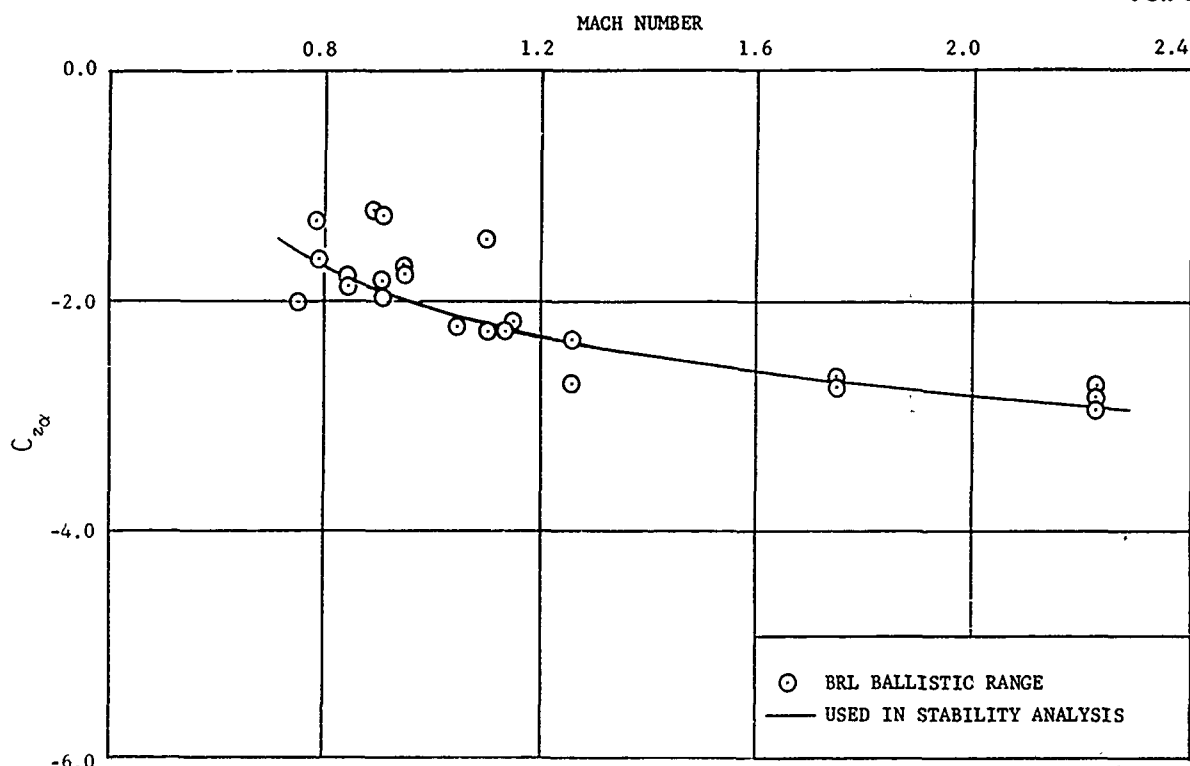


FIGURE 3 VARIATION OF NORMAL FORCE COEFFICIENT DERIVATIVE WITH MACH NUMBER. 5"/54 RAP.

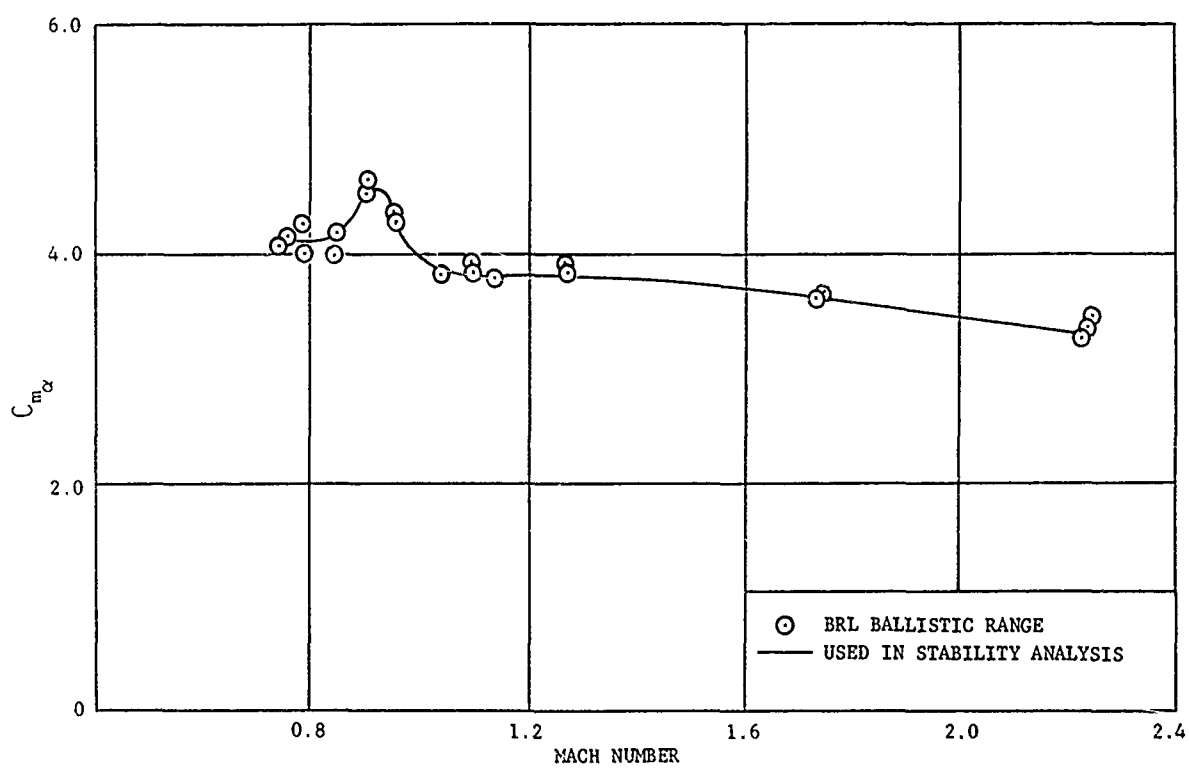


FIGURE 4 VARIATION OF OVERTURNING MOMENT COEFFICIENT DERIVATIVE WITH MACH NUMBER. 5"/54 RAP

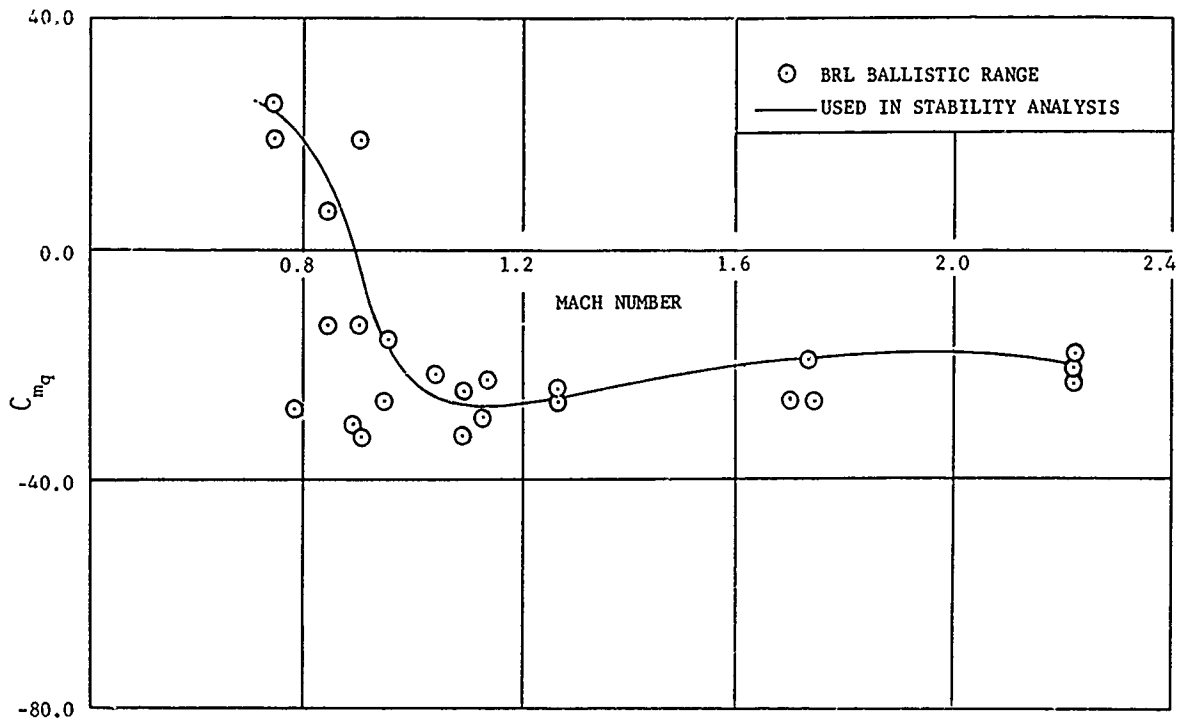


FIGURE 5 VARIATION OF PITCH DAMPING MOMENT COEFFICIENT DERIVATIVE WITH MACH NUMBER. 5"/54 RAP.

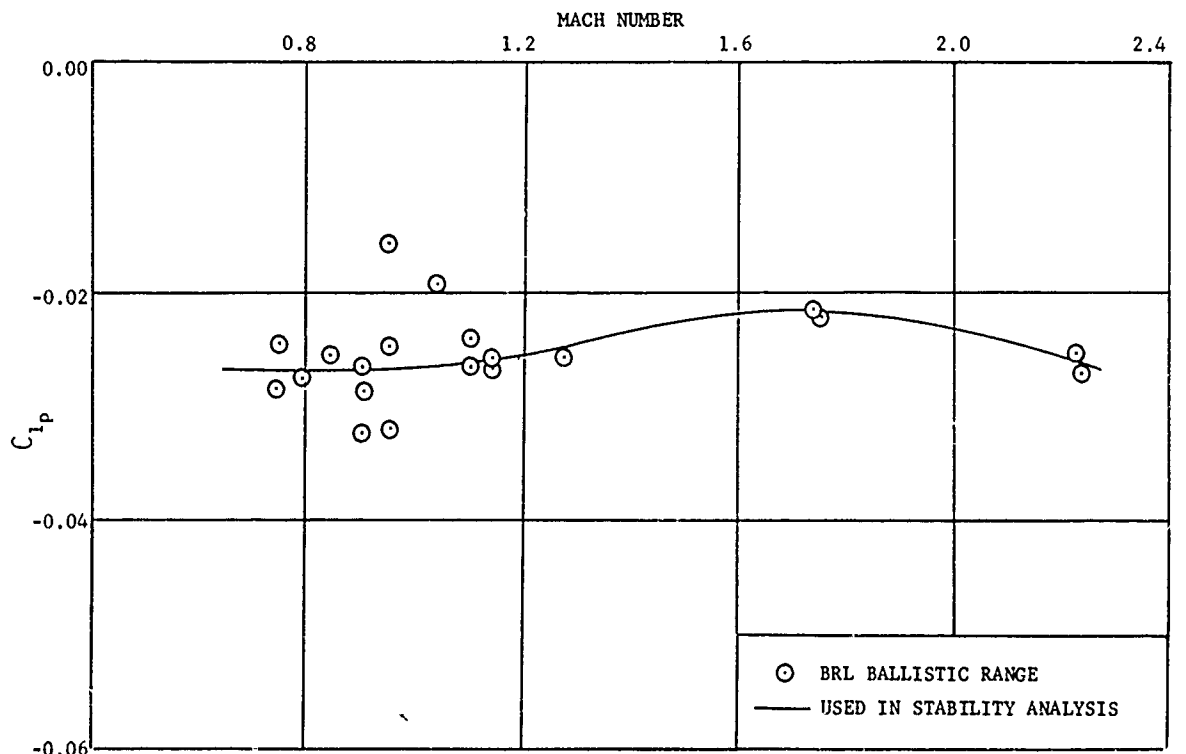


FIGURE 6 VARIATION OF SPIN DAMPING COEFFICIENT DERIVATIVE WITH MACH NUMBER. 5"/54 RAP.

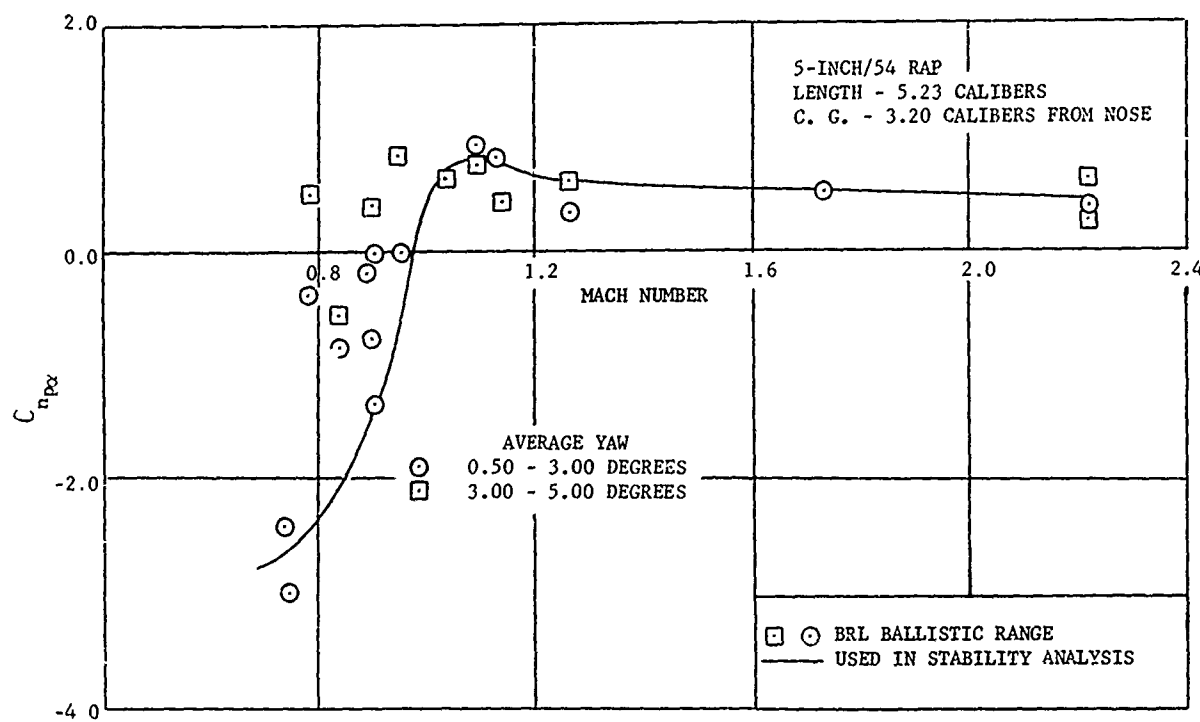


FIGURE 7 VARIATION OF MAGNUS MOMENT COEFFICIENT DERIVATIVE WITH MACH NUMBER. 5"/54 RAP.

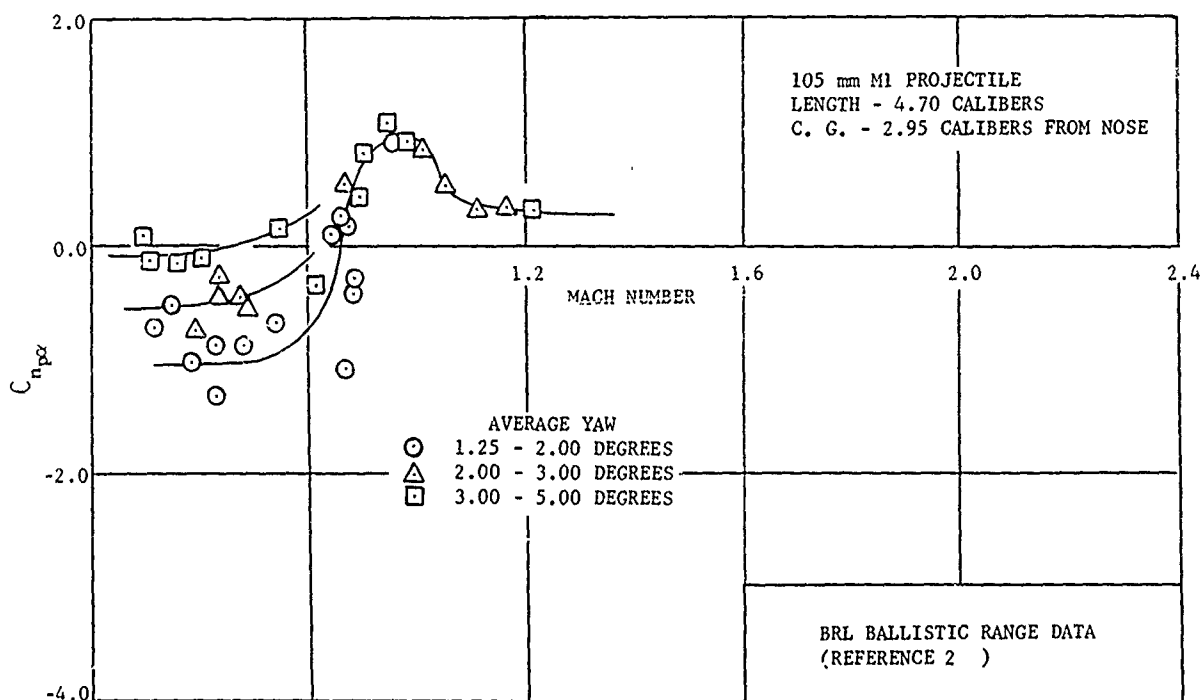


FIGURE 8 VARIATION OF MAGNUS MOMENT COEFFICIENT DERIVATIVE WITH MACH NUMBER. 105 mm M1 PROJECTILE.

8th Navy Symposium on Aeroballistics

Vol. 3

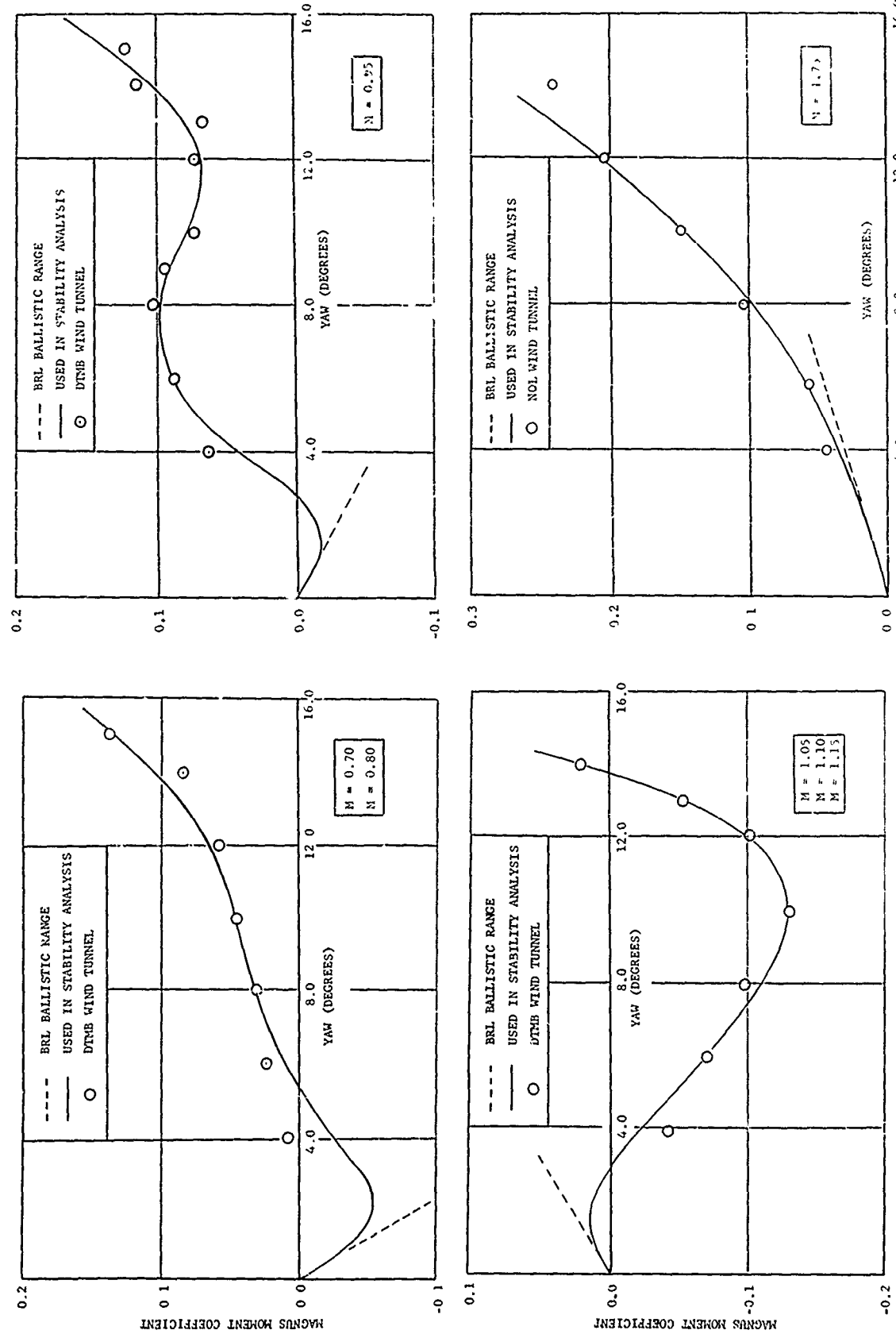


FIGURE 9 VARIATION OF MAGNUS MOMENT COEFFICIENT WITH YAW AND MACH NUMBER. 5° 5° RA?

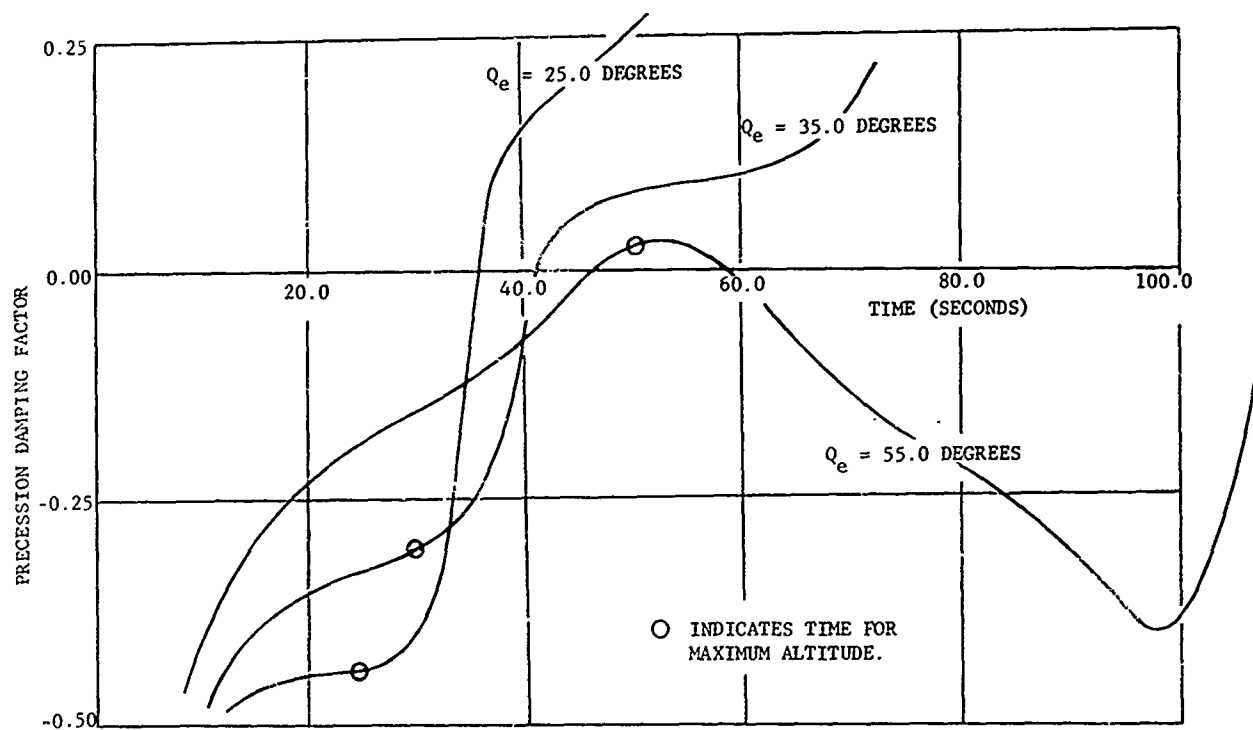


FIGURE 10 VARIATION OF PRECESSION DAMPING FACTOR (LINEAR) WITH TIME OF FLIGHT. $Q_e = 25.0$, 35.0 AND 55.0 DEGREES. 5"/54 RAP.

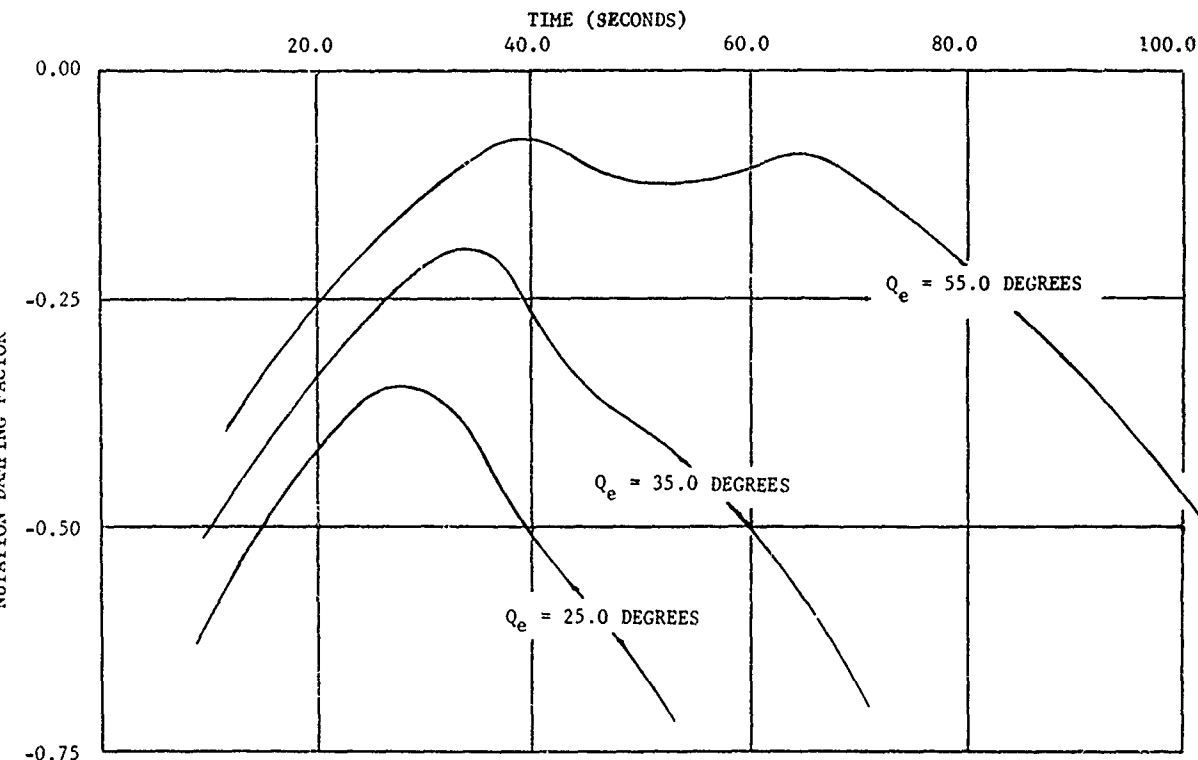


FIGURE 11 VARIATION OF NUTATION DAMPING FACTOR (LINEAR) WITH TIME OF FLIGHT. $Q_e = 25.0$, 35.0 AND 55.0 DEGREES. 5"/54 RAP

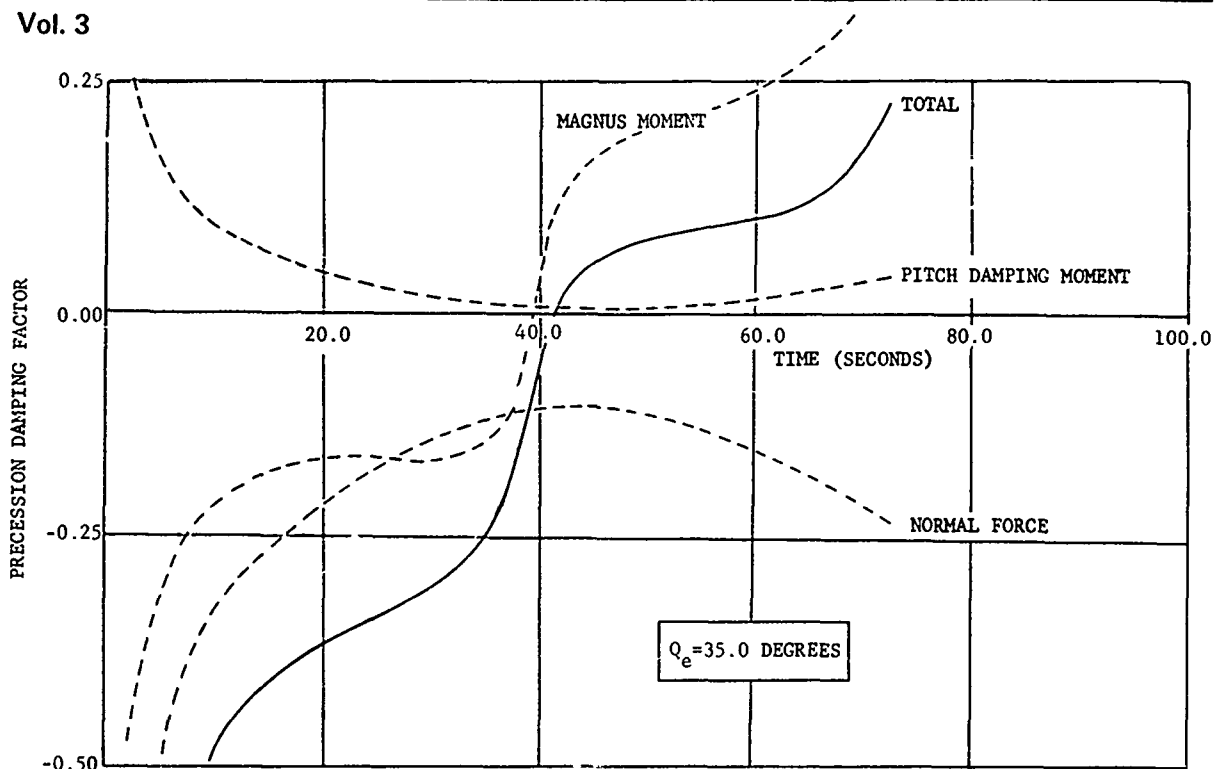


FIGURE 12 VARIATION OF COMPONENTS OF PRECESSION DAMPING FACTOR (LINEAR) WITH TIME OF FLIGHT.
 $Q_e = 35.0$ DEGREES. 5"/54 RAP.

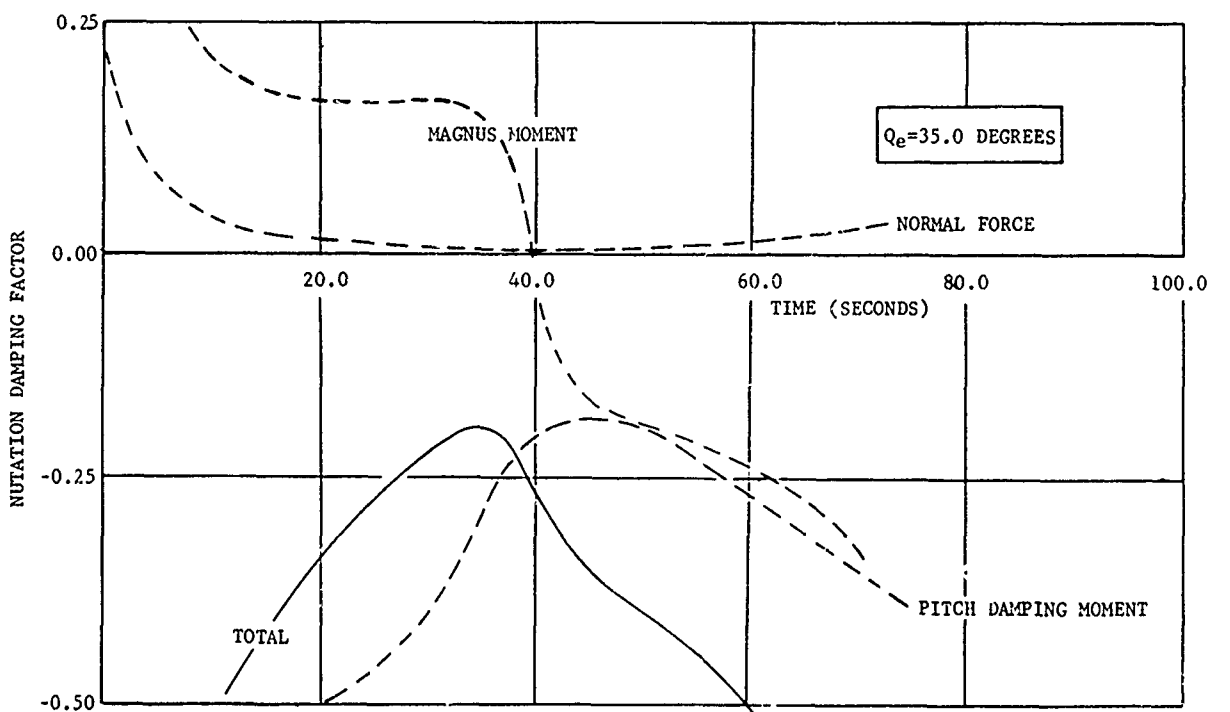


FIGURE 13 VARIATION OF COMPONENTS OF NUTATION DAMPING FACTOR (LINEAR) WITH TIME OF FLIGHT.
 $Q_e = 35.0$ DEGREES. 5"/54 RAP.

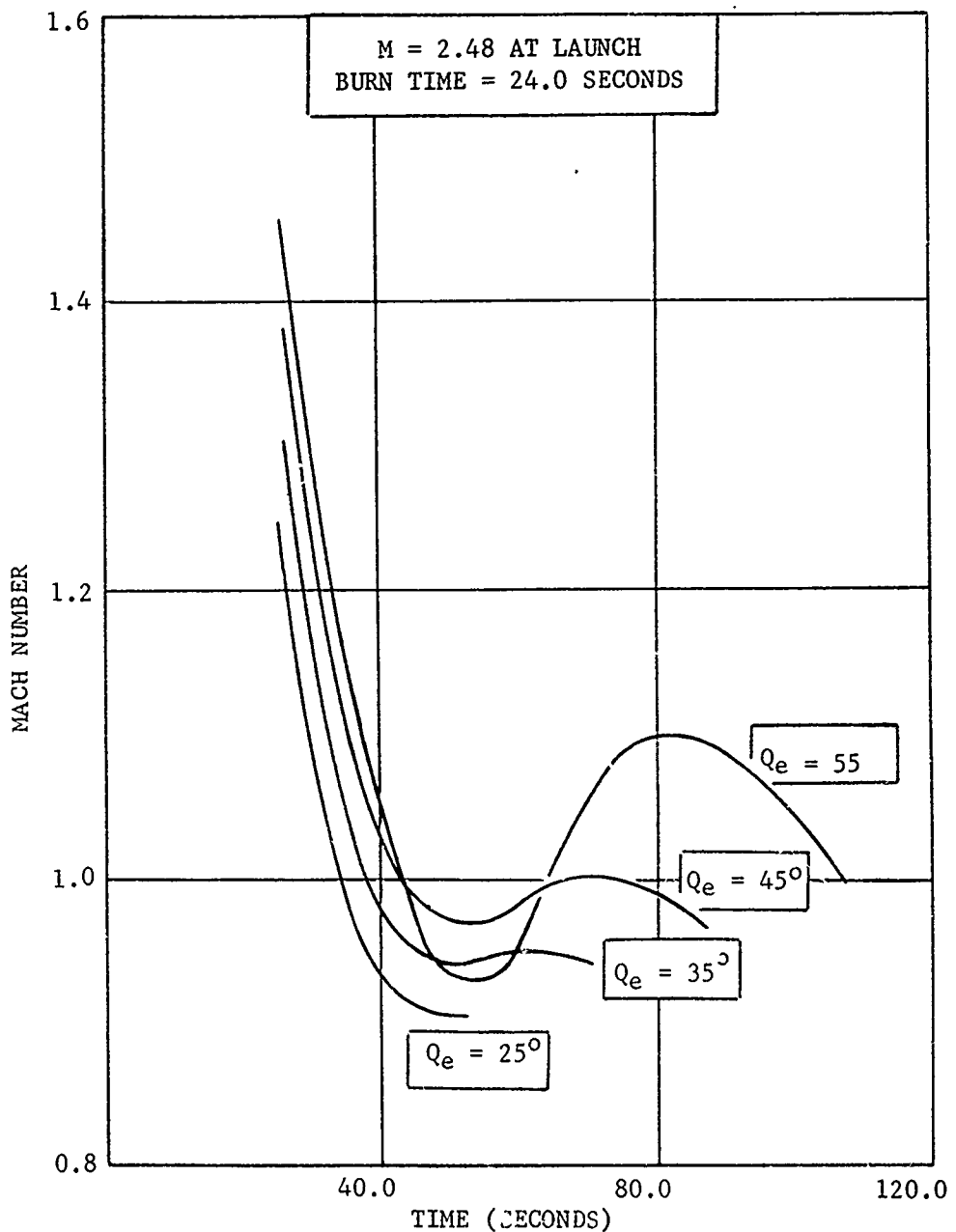


FIGURE 14 VARIATION OF MACH NUMBER WITH TIME OF FLIGHT FROM END OF BURNING. $Q_e = 25.0, 35.0, 45.0$ AND 55.0 DEGREES. 5"/54 RAP

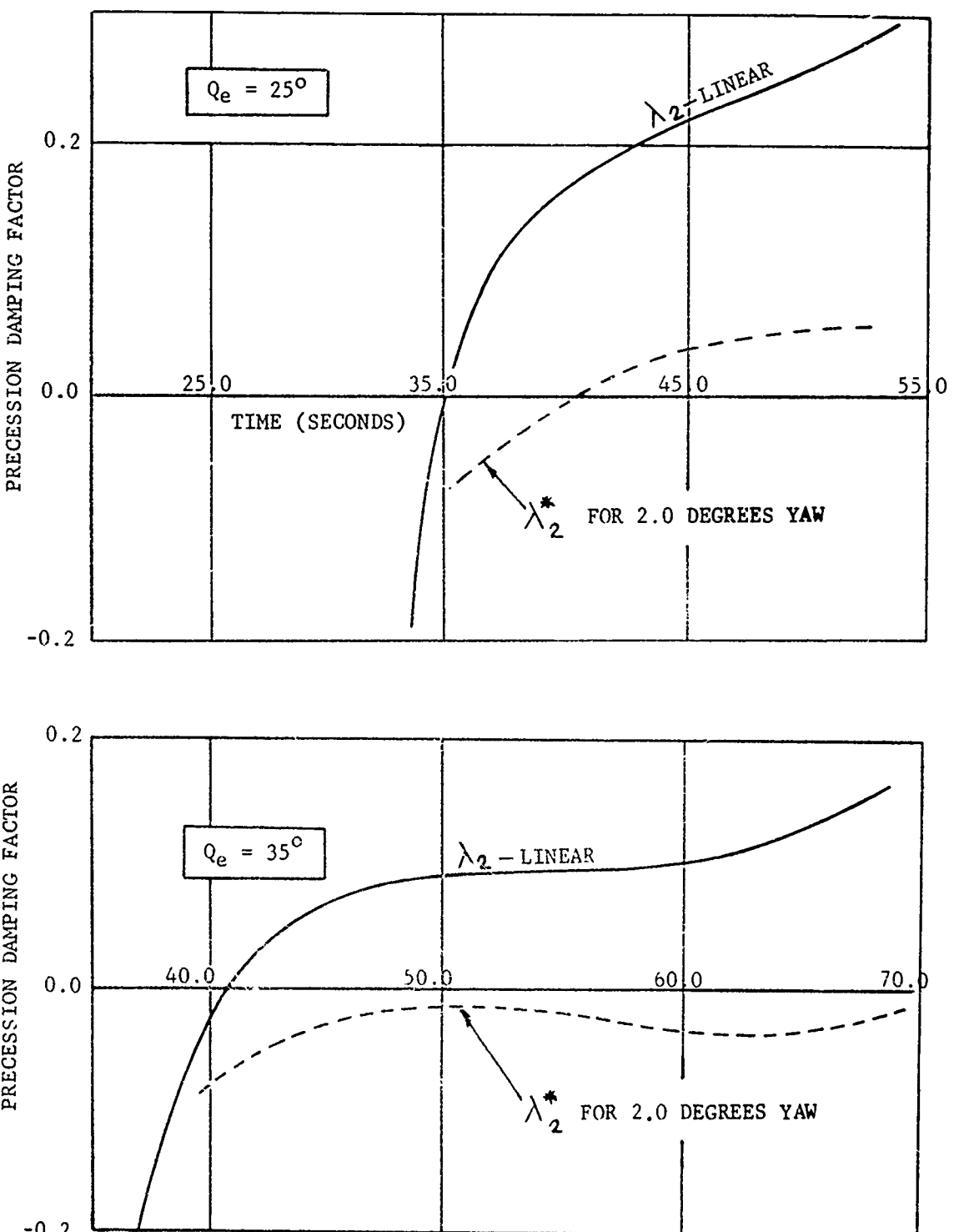


FIGURE 15 VARIATION OF LINEAR AND QUASI-LINEAR PRECESSION DAMPING FACTORS WITH TIME OF FLIGHT. $Q_e = 25.0$ AND 35.0 DEGREES. 5"/54 RAP

8th Navy Symposium on Aeroballistics

Vol. 3

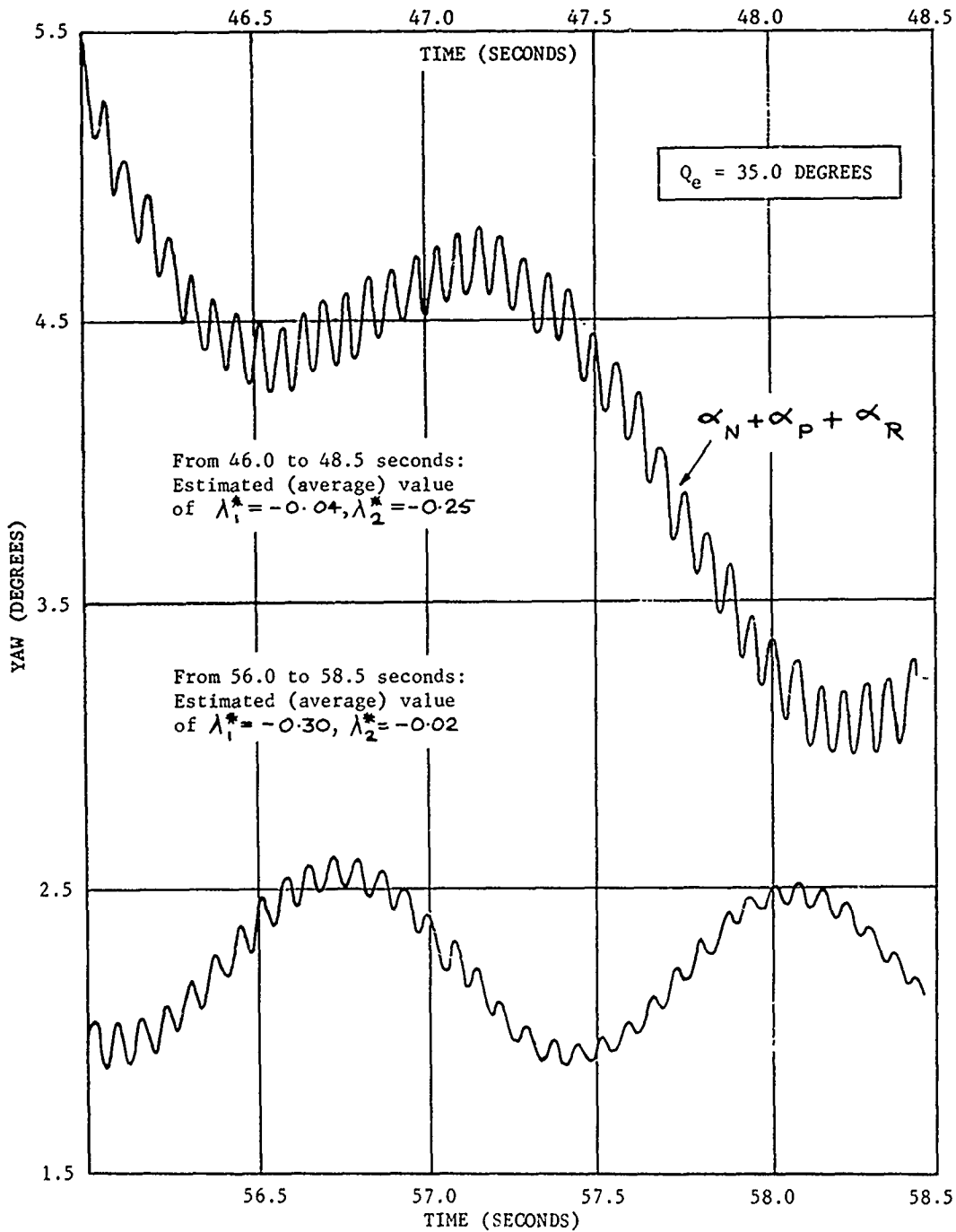


FIGURE 18 NUTATIONAL AND PRECESIONAL MOTION FOLLOWING TRANSIENT DISTURBANCE AT 18000 FT (DESCENDING). $Q_e = 35.0$ DEGREES. 5"/54 RAP.

8th Navy Symposium on Aeroballistics

Vol. 3

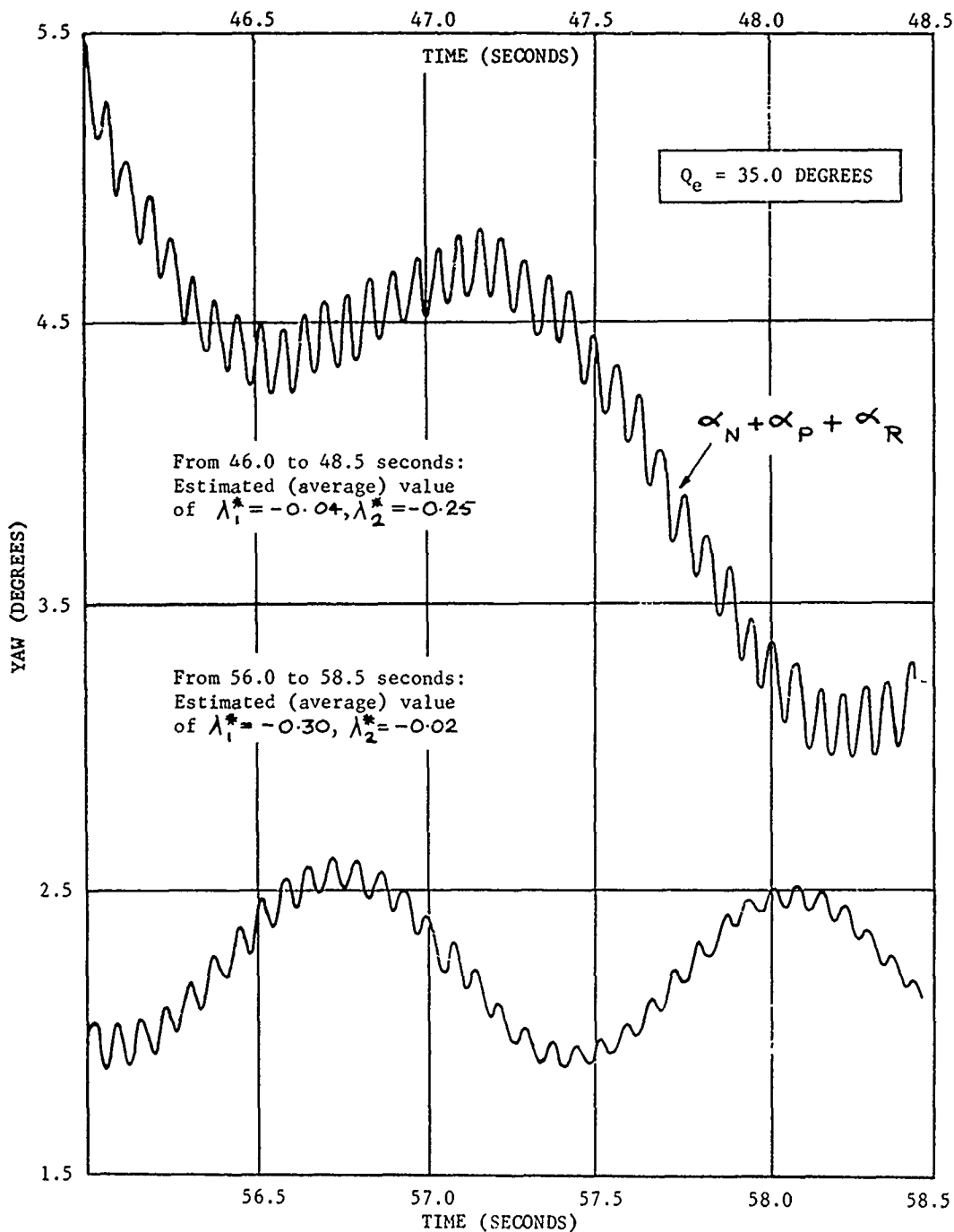


FIGURE 18 NUTATIONAL AND PRECESSIONAL MOTION FOLLOWING TRANSIENT DISTURBANCE
AT 18000 FT (DESCENDING). $Q_e = 35.0$ DEGREES. 5"/54 RAP.

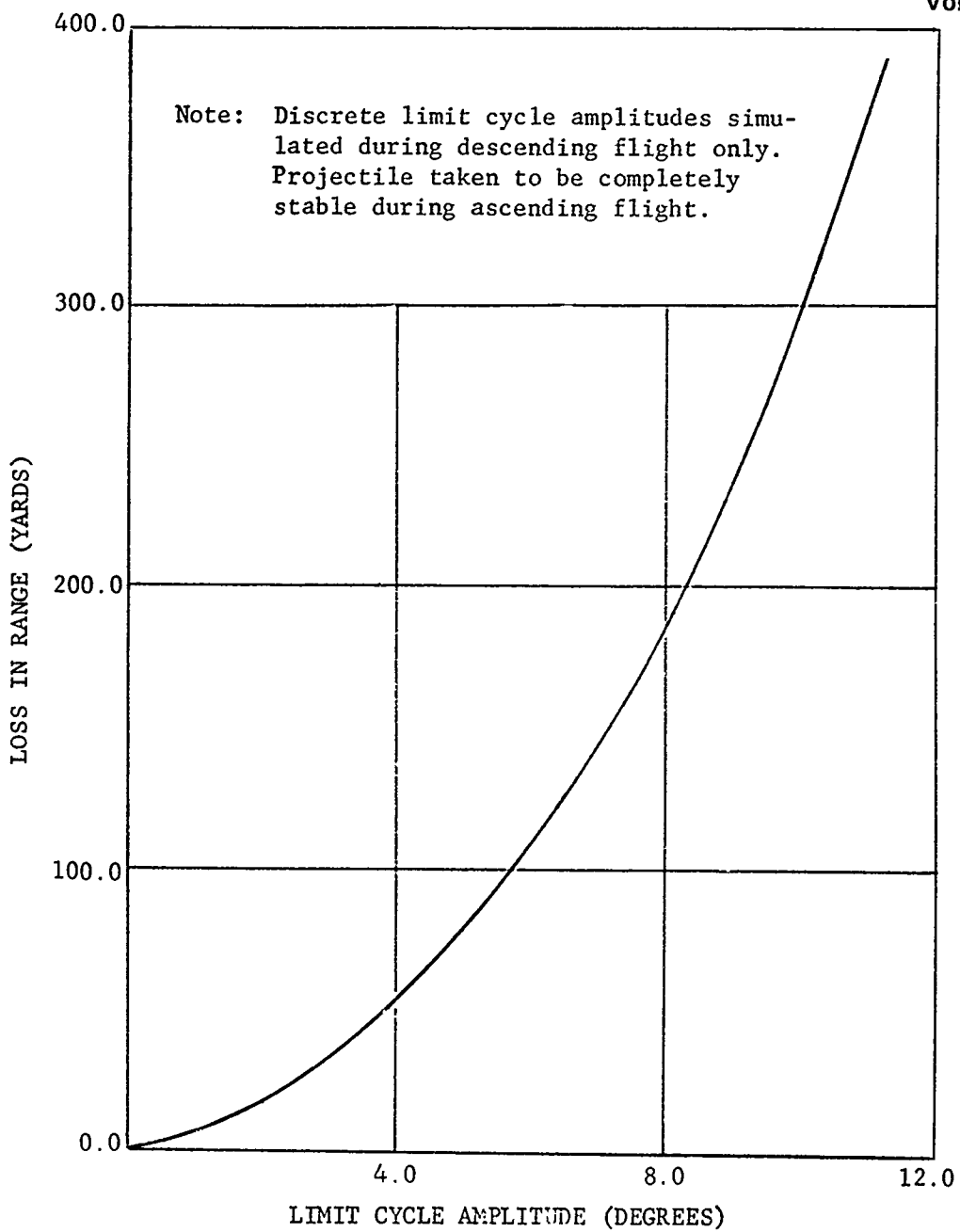


FIGURE 19 VARIATION OF LOSS IN RANGE WITH LIMIT CYCLE AMPLITUDE. $Q_e = 35.0$ DEGREES. 5"/54 RAP.

Paper No. 29

THE UNIVERSITY OF VIRGINIA
COLD MAGNETIC WIND TUNNEL BALANCE
(U)

(Paper UNCLASSIFIED)

by

Hermon M. Parker and Ricardo N. Zapata
Department of Aerospace Engineering and Engineering Physics
University of Virginia
Charlottesville, Va. 22901

ABSTRACT. (U) A three-degrees-of-freedom electromagnetic balance, using stabilized superconductor coil systems, is being assembled at the University of Virginia. The cold balance, together with a 6" Mach 3 blow-down wind tunnel, will be a unique aerodynamic experimental facility. The major potential of the system is considered to be the investigation, with reasonable and improved accuracy, of the dynamic stability characteristics of a model. The two major goals of the prototype system are a) verification of the approach to dynamic stability studies and b) to provide a confident extrapolation of the system to a larger size. Though the system will not have been in full operation, preliminary operating characteristics and current status will be presented. A summary and current status of the investigations of "experiment configuration" will be given.

8th Navy Symposium on Aeroballistics

Vol. 3

GENERALITIES

(U) About a dozen years ago, a three dimensional magnetic suspension arrangement (1) was discovered at the University of Virginia. The supported magnetic body was spherical, or near spherical. The possible, practical application of this technique to support a model in a wind tunnel was recognized at that time. Since that time considerable development has occurred. Currently a group at U.Va., under the sponsorship of NASA Langley*, is engaged in assembling and putting into operation a 6", Cold Magnetic Balance Wind Tunnel System (the cold balance prototype). The Virginia group and the NASA sponsors believe that the U.Va. system and approach will provide a significant advance in the experimental measurement of dynamic stability characteristics of aerodynamic configurations.

(U) In this paper the intention is to describe the current situation. After a brief discussion of a few U.Va. balance generalities; the current status of the prototype facility is described. Then a qualitative but fairly detailed discussion of the U.Va. approach to dynamic stability is given.

OPERATING PRINCIPLE AND PHILOSOPHY

(U) The basic operating principle of the U.Va. magnetic balance is readily explained with the help of Figs. 1 and 2. A perfect sphere of isotropic ferromagnetic material, when placed in a uniform magnetic field, becomes uniformly magnetized. Since the magnetizing field is uniform no force acts on the magnetized sphere. A force on the sphere does result if a magnetic field with a gradient is added. A magnetic field gradient is efficiently produced by a pair of coils, with a common symmetry axis, placed symmetrically about the sphere, and with equal but opposing currents. Such an arrangement produces no field but maximum field gradient at the sphere center proportional to the current for air core coils.

(U) The direction of the force on the sphere depends on the angle ϕ between the gradient coil pair axis and the direction of magnetization of the sphere. The magnitude of the force on the sphere also changes as

*The Langley Research Center of NASA has supported, beginning in 1964, the U.Va. magnetic wind tunnel balance program which is primarily directed toward dynamic aerodynamic stability investigation. NASA Grant No. NGR-47-005-029.

ϕ changes for a given current in the gradient coil pair. These quantities may be readily calculated starting with the fundamental expression

$$d\vec{F} = (d\vec{M} \cdot \nabla) \vec{B}$$

for the element of force $d\vec{F}$ which acts on an element $d\vec{M} = \vec{M} dV$ of magnetized material in an external field \vec{B} . On the ideal assumption that the gradient field is axially symmetrical about the gradient coil axis which passes through the center of the sphere, it results that no moment of force acts on the sphere and the force on the sphere is in the plane defined by the direction of the sphere magnetization (the main field) and the gradient coil axis. Further, the direction and magnitude of the force, as a function of ϕ , are as is shown in Fig. 2.

(U) For the wind tunnel magnetic balance the arrangement is as follows. The main, magnetizing field is parallel to the tunnel axis. Three gradient coil pairs with their axes at $\phi = \tan^{-1}\sqrt{8} \approx 70.5^\circ$ are equally spaced, at 120° , around \vec{M} or the tunnel axis. The three orthogonal force directions lie along the edges of a cube whose major diagonal lies along the tunnel axis. It is considered that this arrangement gives the maximum space to place the wind tunnel.

(U) Magnetic support systems of this sort are unstable and must be servo-controlled to stability. Thus a system to sense the sphere position is a necessity. And, of course, for the wind tunnel application one envisions a model of some aerodynamic configuration constructed of some non-conducting material around the sphere. The sphere position sensing system must operate independently of the model built around the sphere.

(U) The basic, primitive situation is that the model, with a magnetic sphere imbedded in it, is rotationally free - the balance exerts only forces on the sphere. Further, the balance system is limited in frequency response, i.e., it responds to and tries to reduce low frequency translational oscillations of the sphere - just enough to retain the model in the tunnel. At higher frequencies the translational oscillations are free. This mode of operation has been called Quasi-6 mode of operation, and is intended to indicate that at the higher frequencies the model has six degrees of freedom.

POTENTIAL USE

(U) The particular character of the magnetic wind tunnel balance which gives it a unique potential is (1) no physical connection to the model is required, i.e., the sting effect is eliminated and (2) a high degree of motion freedom is retained. The possible rewards due directly to (1) undoubtedly are significant but will not be considered in this paper. However, the second characteristic opens an avenue of investigating the motion induced forces and moments which act on an aerodynamic configuration, i.e., the dynamic aerodynamic stability characteristics of a configuration.

8th Navy Symposium on Aeroballistics

Vol. 3

(U) Here it is interesting to note that the one other magnetic wind tunnel balance system being developed, which basically supports a rod rather than a sphere, and which has been in development at MIT for some time, also can, in principle, investigate the dynamic stability case. The approach is significantly different. In the MIT approach the motion of the model is commanded and forced, thus there can be quite simple motions, and the aerodynamic forces and moments due to the motion must be extracted from the forces and moments required to force the motion. In the U.Va. approach the model motion is essentially caused by the aerodynamic forces and moments--ideally the balance applies the minimum forces (accurately measurable forces) to retain the model in the tunnel--and the forces and moments are to be inferred from the observed motion. The motion in this case can be and usually is quite complex. The two approaches are so different that they are considered to be complementary rather than competitive.

(U) Given that the prime ultimate goal of the U.Va. magnetic wind tunnel balance is dynamic stability, they are still two, sometimes not easily separable, points of view to take. First, there is the design point of view in which (to exaggerate a little) one might measure the stability characteristics of series and families of aerodynamic shapes to compile reams of "design data." Second, and at the other extreme, one can imagine a white haired academician (surely the hair could be some other color) who is interested in understanding the unsteady aerodynamics on a spinning missile configuration. If NASA ever builds a 4' or an 8' cold magnetic balance wind tunnel system--and many of us think this is a very real possibility--one might expect its use to correspond to a mark somewhat toward the design end of the above scale. On the other hand, the prototype which will (hopefully) remain at Virginia will (again hopefully) make a little mark more toward the fundamental research end of the scale.

SCALING

(U) When a stability expert is asked: "How large a model and tunnel (U.Va. magnetic, naturally) do you need to get the stability information you want?", the answer usually is: "what size did you have in mind?"

(U) The scaling problem is complex primarily because some of the subsystems e.g., the gradient coil power supplies, simply do not scale very well. Interestingly enough, the basic magnetic interaction scales very readily, as follows.

(U) Given a non-ferromagnetic cored coil system of any complexity if the system is scaled by the factor λ (i.e., all linear dimensions multiplied by λ) and the current density is held constant then at any point the magnetic field strength is multiplied by λ and the gradient of the magnetic field remains unchanged. Thus one can see that at sufficiently large sizes the problem of producing the gradient fields dominates the problem of producing the main field.

8th Navy Symposium on Aeroballistics

Vol. 3

(U) There are a series of facts or relationships which are involved in the total scaling problem. A few of these will be listed.

(1) For a given balance, the gradient coil currents required to support (against gravity) a sphere of a given magnetic material is independent (to a very high order) of the size of the sphere. The magnetic force is proportional to the total magnetic dipole moment of the sphere, i.e., to its volume. The sphere weight is also proportional to its volume.

(2) Since balance forces are proportional to the volume (ℓ^3) of the sphere and since aerodynamic forces and moments are proportional to a characteristic area (ℓ^2) of the model, the ratio of balance forces to aerodynamic forces is proportional to ℓ . Thus less product of magnetization M (magnetic dipole moment per unit volume) and magnetic field gradient is required as the size increases. In a very real sense a large balance is easier to design than a small one.

(3) The gradient coil power supply systems, which represent a considerable fraction of the cost of the total system, do not scale well because the optimum methods of producing electrical power capacity at a given frequency range change drastically from one power and frequency range to another. Apparently rather detailed studies are required to optimize at a given size.

(4) At a constant Reynolds number per foot, the natural aerodynamic frequency decreases inversely as the first power of the scale.

(5) The balance design and scaling considerations to date have been based on the assumption of ferrite as the magnetic sphere material. Because of its low electrical conductivity and low magnetic rotational hysteresis the condition of rotational freedom is assured. The penalty is that the maximum magnetization is not large.

(6) The extrapolation of designs to large tunnel sizes (4' to 8') assuming conventional water cooled copper coil systems becomes unfeasible. Megawatts of electrical power are not frightening, but the sheer volume and weight of copper coils at this scale are. A more efficient method of producing magnetic fields becomes necessary for the larger sizes.

(U) The word "cold" in "cold balance prototype" indicates 4.2°K. The current 6" cold balance prototype is cryogenic, using superconducting gradient coils, drag augmentation coils and a main field coil, refrigerated with liquid helium. The gradient coils are servo controlled and thus must carry time varying electric currents. The general problem of AC losses in superconductors is not yet solved.

(U) The two prime objectives of the current cold magnetic wind tunnel balance prototype program at U.Va. are (1) to verify the validity of the U.Va. approach to dynamic stability and (2) to provide as much information as possible to enable a confident extrapolation of the

8th Navy Symposium on Aeroballistics

Vol. 3

system to larger sizes. An item of vital concern is whether or not the restriction to ferrite spheres (certainty of rotational freedom) can be relaxed, or, specifically, whether iron in some non-electrically conducting form can be used for the support element. If the damping moments on a model due to the magnetic rotational hysteresis of iron are not large enough to prevent the measurement of aerodynamic damping moments, then the cost of a large system is likely to be about an order of magnitude less. Unfortunately, the ratio of hysteresis damping to aerodynamic damping increases as the first power of the scale. This problem will receive early attention in the prototype.

CURRENT STATUS OF THE PROTOTYPE FACILITY

(U) According to the current schedule, the assembly of the prototype cold balance facility will begin in the summer of 1969. At the time of this writing all of the major components have been designed and are either in house or on order. The design of this facility has been quite challenging in the sense that in many key decisions state-of-art technology had to be invoked. In what follows a brief discussion on the design and status of the principal balance components is given. Reference is made to Fig. 3 where the overall facility is sketched.

THE COIL SYSTEM

(U) The support system comprises 9 superconducting coils. One of them (main field coil) produces a uniform magnetic field at the point of suspension. The other 8 are grouped in four pairs that produce pure magnetic field gradients at that point. The coil system is sketched to scale in Fig. 4. The most important characteristics of the different coils are listed in Table I. It should be noted that there are 3 identical $\tan^{-1} \sqrt{8}$ gradient coil pairs of which one appears in the figure. The main field coil and the drag augmentation pair will operate in a DC mode. Until recently the AC operation of the gradient coils constituted the greatest uncertainty about the feasibility of the cold balance concept. For the original design fully stabilized superconducting cable, capable of carrying the maximum operating current in case of total transition to the normal mode of conduction, was specified. Two important developments were responsible for the switch to the present design. First, detailed calculations of the probable dissipation from eddy currents in the copper revealed that relatively high rates of liquid helium consumption should be expected. Second, preliminary results (2) from experiments at the Brookhaven National Laboratory, where AC losses in coils wound with superconducting tape were measured, indicated that stability could be achieved with far less copper than it had been possible for superconducting cables and, consequently, with much lower eddy current losses. The University of Virginia group recently confirmed these findings in experiments performed at the laboratories of Atomics International. It is fully expected that these developments have essentially

removed the key uncertainty referred to above.

THE CRYOSTAT

(U) The liquid helium dewar was designed with the following high priority constraints in mind:

- (a) Room temperature access for the supersonic wind tunnel and other system components;
- (b) Minimum distance between the coil system and the suspended model;
- (c) Minimum interference between the dewar and the magnetic fields produced by the coils;
- (d) Reasonable ease of assembly and of access to the critical components of the coils system.

(U) The resultant geometry can be observed in Fig. 4. It should be noted that the 4 inner walls (between the coils and the wind tunnel) are made of fiberglass while a more conventional stainless steel construction has been adopted for the outer walls. About 250 liters of liquid helium will be necessary to load the cryostat and operate the system.

MODEL POSITION INDICATOR

(U) For the successful operation of the prototype facility the need to determine the position of the aerodynamic model arises from three different sources:

- (a) The operator of the facility needs to "see" the model to properly coordinate the launching and the recovery of the model.
- (b) An error signal is needed to close the automatic control loop effecting stable support.
- (c) Model "trajectory" information is needed as data to compute the aerodynamic parameters of interest.

The practical difficulties of establishing a direct optical path between the aerodynamic model and an outside observer should be apparent upon examination of Fig. 4. It is fortunate that requirement (a) can be satisfied with a relatively low resolution system. A combination of a wide angle lens and fiber optics has been developed and is presently in the refinement stage. It is not yet known what degree of sophistication will be required to upgrade this type of system so that it has acceptable resolution for data acquisition. Requirements (b) and (c) can, in principle, be satisfied simultaneously by an electromagnetic position sensor presently in the final stages of development. This sensor is based on a concept originally developed at MIT utilizing the principle of the variable transformer. There are a total of 12 electromagnetic coils wound on a cylindrical form surrounding the test section of the wind tunnel (Fig. 4). By proper manipulation of the signals induced in

8th Navy Symposium on Aeroballistics

Vol. 3

the 10 pick-up coils (the other two coils are used for excitation at 30 k-Hertz) three translations and two angular displacements can be detected and recorded as a function of time. Preliminary calibrations revealed a linear response within a ± 2 cm range with typical sensitivities in the 100-500 mV/cm range. Current efforts are concentrated on improving the stability of the calibrations, optimizing the geometry of the sensing element imbedded in the model and minimizing the cross-talk between channels. It is anticipated that a detailed report on this system will be published as soon as the optimization work is finished and complete calibration and operational characteristics become available. In the meantime, Fig. 5 should help to clarify the preceding discussion.

THE CONTROL SYSTEM

(U) Stabilization of the aerodynamic model will be effected by controlling the current through the $\tan^{-1} \sqrt{8}$ gradient coils. A minimum time or bang-bang control law for large disturbances and a linear control law for small disturbances have been chosen. The stability of the control system has been demonstrated through analog computer simulations using the real values of the parameters of the power supplies and coils.

THE POWER SUPPLIES

(U) The power supplies for the $\tan^{-1} \sqrt{8}$ coil pairs, designed by Oerlikon Engineering Co. (Switzerland), consist of an energy storage device and fast switching circuits to permit rapid modulation of the purely inductive loads. A schematic diagram of the basic circuit is shown in Fig. 6. There are three possible modes of operation depending on the condition of the silicon controlled rectifiers (SCR).

- (a) Both SCR's on: Voltage across coils is +250V
- (b) One SCR off: Coils clamped by the other SCR and a DIODE. Voltage across coils is dropped across DIODE + SCR ($\approx 3V$)
- (c) Both SCR's off: Both diodes conduct, clamping the voltage across coils to -250V.

The principal advantage of this solution to the switching problem is that the SCR's have practically zero dead time and, consequently, require a relatively modest maximum voltage (250V). It should be noted that there is no provision for current reversal in the power supply circuit. It is planned to operate the coils at a DC level of one half the maximum current i.e., 175A., thus making a $\pm 175A$ variation with respect to the steady state value possible. The circuits are designed to be capable of a complete current cycle (175A-350A-0 A-175A) in 32 msec.

THE WIND TUNNEL

(U) The aerodynamic testing facility will be a Mach 3 blowdown wind tunnel with a nominal test section diameter of 6 inches. The principal design constraints are:

- (a) Severe limitations in geometry imposed by the presence of the cryostat (Figs. 3 and 4).
- (b) Need to maximize run time. This has been approached from two ends: double the existing air storage capacity and maximize the efficiency of the tunnel by optimizing the variable second throat configuration.
- (c) Need to support the model by mechanical means before the start of the tunnel and effect a transfer to magnetic support as soon as steady state conditions are reached.
- (d) Exclusion of electrically conducting or ferro-magnetic materials from any of the tunnel components and mechanisms in the vicinity of the supporting coils.

THE U.VA. APPROACH TO DYNAMIC STABILITY

(U) Though some other technique eventually may be found to be more efficient in classifying and communicating stability information, this article will use the conventional and traditional method, i.e., the determination or specification of aerodynamic derivatives, static and dynamic. Further, in the interest of clarity, a derivative will be termed static if it can, in principle, be measured by holding a model fixed in a wind tunnel; the measurement of a dynamic derivative requires that the position and/or orientation of the model in the tunnel change with time.

(U) As indicated earlier one can foresee two general uses of a U.Va. magnetic balance tunnel facility, namely, design and fundamental research oriented activities. The basic process of acquisition of stability information is independent of whether the objective is design or research. One could speculate that there might be considerable difference in the detailed character of the information required in the two cases. Nevertheless, in the remainder of this article, whether the ultimate objective is design or research will not be considered.

BASIC APPROACH

(U) The basic U.Va. approach to dynamic stability is as follows:

- (a) A model in the wind tunnel executes oscillatory translational and rotational motion under the influence of gravity, forces and moments applied by the magnetic balance, and aerodynamic forces and moments.

8th Navy Symposium on Aeroballistics

Vol. 3

(b) The force and moment due to gravity may be easily and accurately determined.

(c) The balance forces and moments may be measured with good accuracy.

(d) The motion of the model, in all six degrees of freedom, can be measured.

(e) With information (b), (c), (d) and the model geometric and inertial parameters, the equations of motion allow, by one of several techniques, the determination of the aerodynamic forces and moments or the stability derivatives, static as well as dynamic.

(U) It is interesting that in the early phases of the project it was assumed for simplicity that the balance would hold the magnetic sphere center in a fixed position in the tunnel. Later more detailed design showed this to be unfeasible and the current concept, called Quasi-6 operation, is that the balance will apply those low frequency control forces required simply to hold the model in the tunnel and that higher frequency transiational oscillations are essentially free.

(U) It is, of course, basic to the entire philosophy that the model is rotationally free, i.e., that the balance exerts, or can be made to exert, no moments on the model. Thus the prototype design is based on the use of a ferrite for the magnetic support element since a perfect sphere of uniform ferrite would experience (engineeringly) zero spring-like and damping moments due to the balance. A spring-like (conservative, static) balance induced moment on the model is not serious; indeed such a static moment can be advantageous and simply adds to the usually large aerodynamic static moment. Balance induced damping moments (due to eddy current effects and/or rotational magnetic hysteresis) are much more serious. Aerodynamic damping (dynamic) moments are usually small and the danger is that they may be swamped by balance induced damping moments.

(U) One of the interesting aspects of the U.Va. approach to dynamic stability is the large range and variety of motions or motion characteristics that can be arranged for a given model (see below). As a result the question of "experiment design" becomes important. In order to extract a particular piece of stability information, a particular dynamic derivative, with maximum accuracy what is the optimum experiment or motion state? It is anticipated that this problem can be successfully studied theoretically.

INFORMATION EXTRACTION METHODS

(U) One can imagine that the optimum method of extracting stability information from the data gathered from a particular experiment depends upon many things, and in particular the accuracy of the data is surely an important one. Perhaps two rather extreme cases illustrate the point.

(U) Consider a spinning axisymmetric missile executing the transient after having been perturbed from a steady, trimmed, non-oscillatory

reference flight condition. Further, imagine that the measurements of the kinematic motion variables have not been very accurate, perhaps the random noise is on the order of 1/4 to 1/2 of the value of a variable for the best portion of the data. It would not seem unreasonable that a least squares fit of the data to a linearized solution of the problem would be the optimum information extraction method for this problem.

(U) As a really imaginary limit, suppose that for a model in the tunnel the kinematic variables, the balance forces and moments, and all the other input to the extraction problem have been measured with very great accuracy--say, to one part in 10^8 , to have a number. With such extremely accurate data, it seems reasonable to assume that a direct inversion of the equations of motion (i.e., by substitution of the kinematic variables and their derivatives, geometric and inertial parameters and, balance forces and moments to convert the full equations of motion into an appropriate set of inhomogeneous linear algebraic equations for the chosen force and moment derivatives) could well be the optimum method of extracting stability information. The authors are aware of no instance in which this direct method of data reduction has been used and are inclined to suspect that insufficiently accurate data has been the reason. The U.Va. group has not yet abandoned the prospect that this direct inversion method may work well for the U.Va. approach to dynamic stability.

(U) It seems that essentially every dynamic stability group has evolved its own--presumably reasonably optimum for them--method of extracting information. The problem is certainly non-trivial. One can foresee that many methods will be tried at U.Va. before a best or a few best methods are found.

PERTURBING TECHNIQUES

(U) There are various kinds of force and moment (or equivalent) inputs to the model in a magnetic balance wind tunnel which can be arranged. These perturbations change the motion of the model and in general change the sensitivity of the motion to the individual force and moment derivatives, or more importantly change the relative accuracy of extracted derivative and motion data inputs.

(U) Here we list and briefly discuss several of the perturbing techniques which have been considered and in some cases analyzed in some detail. The reader should note that the following discussion will tacitly assume that the model is (effectively) axially symmetrical and likely to be spinning (roll control is not expected to be added to the system in the near future).

(a) Passive Techniques

(i) Prolate Ellipsoid. Imagine that the spherical magnetic support element, assumed to be ferrite for the present discussion, is replaced with a prolate ellipsoid with the long axis parallel to the model symmetry

8th Navy Symposium on Aeroballistics

Vol. 3

axis. A conservative moment (due to shape anisotropy and the main field) tends to return the ellipsoid to alignment with the main field, effectively adding to the static aerodynamic restoring moment acting on the model. The frequency at which the model will oscillate will be increased. Considerable control of the oscillation frequency (as well as choice of the center of mass position) results. For example, one could operate with a model which is aerodynamically unstalbe but which in the tunnel is stabilized by a prolate ellipsoid-balance induced moment.

(ii) Built-in Damping. It is easy to build damping into the system. One easy way is to build a copper shorted turn in a plane perpendicular to the model symmetry axis. Eddy currents induced in the loop by rotation about a lateral axis interact with the main field and produce a viscous damping moment, i.e., a resisting moment proportional to the rotation rate. Another way is to use for the support element a magnetic material which has a large rotational hysteresis which gives a coulomb-type damping moment. The possible use of some form of iron, the most efficient support material, is contingent on the damping due to rotational hysteresis not being too large. The usual concern is very likely to be that the balance induced damping is small enough that the aerodynamic damping may be efficiently measured. Of course, one can imagine a situation in which the aerodynamic damping is very negative and a large positive balance induced damping is required for good operation.

(iii) Mass Unbalance. If the model were perfectly balanced and trimmed then the steady state condition ideally is no motion of the model with respect to the tunnel. A direct way to produce a more interesting steady state motion is to unbalance the model by judicious addition or removal of some mass. Though a perfectly balanced initial condition is not to be expected, changes in the inertial parameters can be made with considerable percision.

(iv) Prolate Ellipsoid and Varying Main Field. A rather particular but interesting possibility is that with a prolate ellipsoid as in (i) above the model oscillation frequency can be changed by changing (slowly by necessity) the magnitude of the main magnetic field. Thus, with a spinning missile type model a portion of the classic roll-pitch resonance response could be observed in a single run.

(b) Active Techniques

(i) Impulsive Force. The magnetic balance may be commanded to apply an impulsive force on the support element embedded in the model. "How impulsive" will depend on the magnitude required since the basic limitation is how rapidly the current in a gradient coil pair may be changed. Of course, if the magnetic sphere is not at the model center of mass then a corresponding moment about the C.G. is also applied to the model. It can be anticipated that such an impulsive perturbation which would produce a transient motion mode, could be very helpful in measuring damping derivatives.

(ii) Periodic Forces. In a similar way, the balance will be capable of applying commanded steady state oscillatory forces on the sphere at frequencies at least up to 100 Hertz. This sort of balance operation corresponds to a gradient coil pair, power supply system operating in a linear mode as distinct from the basic large amplitude bang-bang control. In general one expects that the amplitude of these higher frequency forces to be limited (and to decrease with increasing frequency) but significant perturbations up to about 100 Hertz are expected to be possible.

(iii) RF Induced Moments. To this point the methods discussed involve essentially no additional hardware. In the last two items radio frequency (RF) induced current arrangements similar in principle to the model position sensing system but designed to produce moments on the model, are considered. Imagine a copper shorted turn placed in the model with its plane at 45° with the model symmetry axis. Assume that the model is spinning and that its symmetry axis remains essentially parallel to the tunnel axis. Then a uniform, axial RF magnetic field gives rise to a moment of force on the model about a lateral axis fixed in the model (in the plane of the shorted turn) which has a DC component and a double frequency RF component. At several tens of Kilohertz the double frequency RF component can be neglected. A uniform lateral RF field gives rise to 1) an oscillatory moment about the tunnel axis (model symmetry axis) at twice the model spin frequency, 2) an oscillatory moment at twice spin frequency about a lateral inertial axis perpendicular to the RF field, and 3) a DC lateral moment about the same axis. At the present time the effect of such moments on the efficiency with which various interesting derivatives can be measured from the motion produced (or even what effect these moments have on the model motion) are not known.

(iv) Pulsed or Programmed RF. In (iii) above the amplitude of the impressed RF field is considered to be constant. It ought not to be difficult to arrange for the amplitude of the impressed RF field to vary with time in an arbitrary manner on the time scale of the model motion, i.e., the time interval for significant RF field amplitude change to be simply smaller than, say, one tenth of the period of the model motion. If the possibilities for constant amplitude RF in (iii) could not be foreseen, the possibilities for arbitrary RF amplitude vs. time are even less evident.

ERROR ANALYSIS AND EXPERIMENT DESIGN

(U) A rather obvious, theoretical method of assessing quantitatively the potential of the U.Va. approach to dynamic stability is in progress. Unfortunately the status is such that no results can be presented at this time. The interest here is to describe the method. Essentially it consists of two parts as follows:

(a) the full (non-linear) equations of motion of a rigid body (aero-elastic effects are neglected) may be set up and numerically integrated with input forces and moments in agreement (hopefully) with

8th Navy Symposium on Aeroballistics

Vol. 3

the experimental situation. In essence, one hopes and expects to calculate the motion of a model in the tunnel subject to the actual forces and moments to which the model is subjected. Thus one hopes to calculate by a direct numerical procedure, the motion of a real model in the tunnel and arrive at "perfect" motion data.

(b) Given the "perfect" motion data of a) above, one expects to invert the equations of motion and "regurgitate" the values of the force and moment derivatives (an algebraic problem) which were inserted into the calculation. One hopes to obtain good accuracy, say, 4 to 6 digits of accuracy for the recovery of the force and moment derivatives.

(U) Essentially the combination of a) and b) above (note that no specifications of detailed methods has been given) constitutes a basic, circular, "greasy pig," method of evaluating the U.Va. approach to dynamic stability. The basic methods of analysis are:

(a) The influence on accuracy of recovered derivatives of systematic and/or random errors superposed on the perfect data. Presumably this is the best one can do with respect to error analysis.

(b) The influence of choosing a different set of derivatives to "recover" then the set used to calculate the perfect data. This simulates the real life situation of not knowing the set of derivatives a model "has."

(c) Most important (one can speculate) is the rather undefined and vague problem of finding what sort of motion, corresponding to what sort of boundary conditions or what sort of perturbations, results in the most accurate or efficient extraction of a particular derivative. It is expected that this area of experiment design will be very interesting.

CONCLUSIONS

(U) It is undoubtedly premature to arrive at conclusions with respect to what stability information with what accuracy may be obtained via the U.Va. cold balance system and the U.Va. approach to stability. Nevertheless it must be admitted that the U.Va. group, at least, is optimistic. We believe that we will take significant steps forward in the problem of determining the dynamic stability characteristics of aerodynamic configurations.

(U) Table I. Design Characteristics of the Coils.

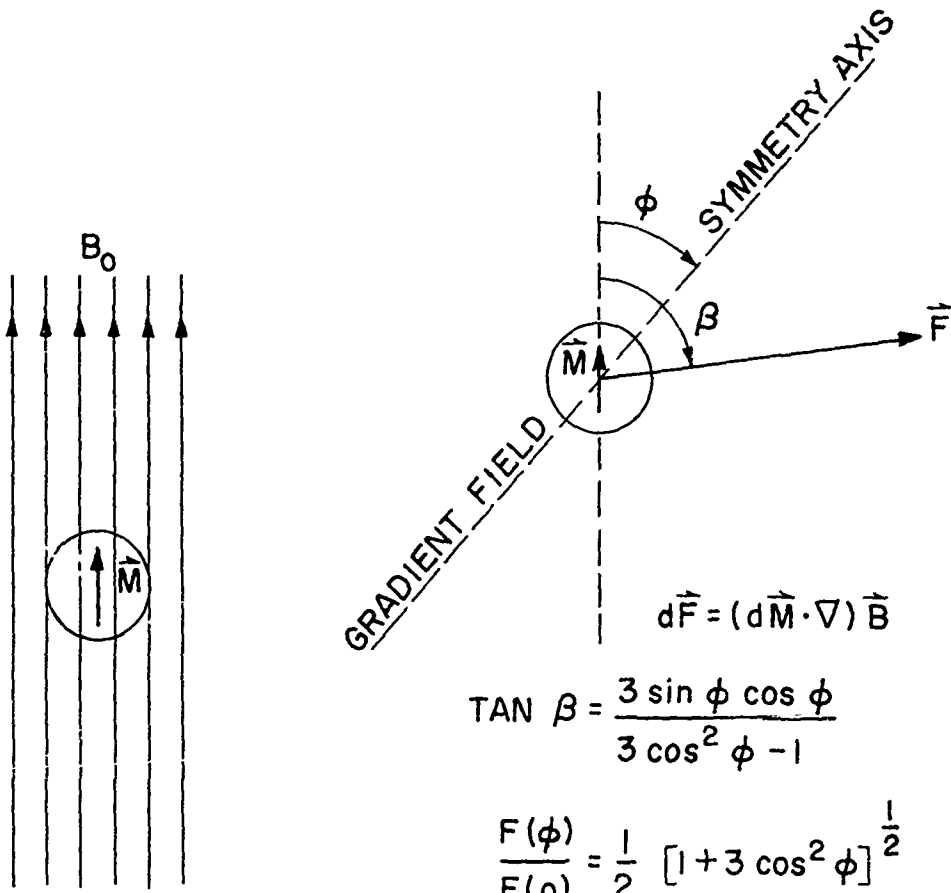
	<u>$\tan^{-1}\sqrt{8}$ pair</u>	<u>Drag Augmentation Pair</u>	<u>Main Field</u>
Number of turns	133	3000	2500
Maximum current	350 A.	100 A.	100 A.
Maximum voltage	250 V.	-----	-----
Type of wire	1/2" Nb-Sn tape	0.030" copper clad NbTi	0.030" copper clad NbTi
Type of operation	unsteady	steady state (DC)	steady state (DC)
Maximum average current density	10,800 A/cm ²	8000 A/cm ²	8000 A/cm ²
Inductance	0.008 henries	6.0 henries	5.1 henries
Central field	0 (nominal)	0 (nominal)	5×10^3 Gauss
Maximum field gradient at 0	80 Gauss/cm	420 Gauss/cm	0 (nominal)

8th Navy Symposium on Aeroballistics

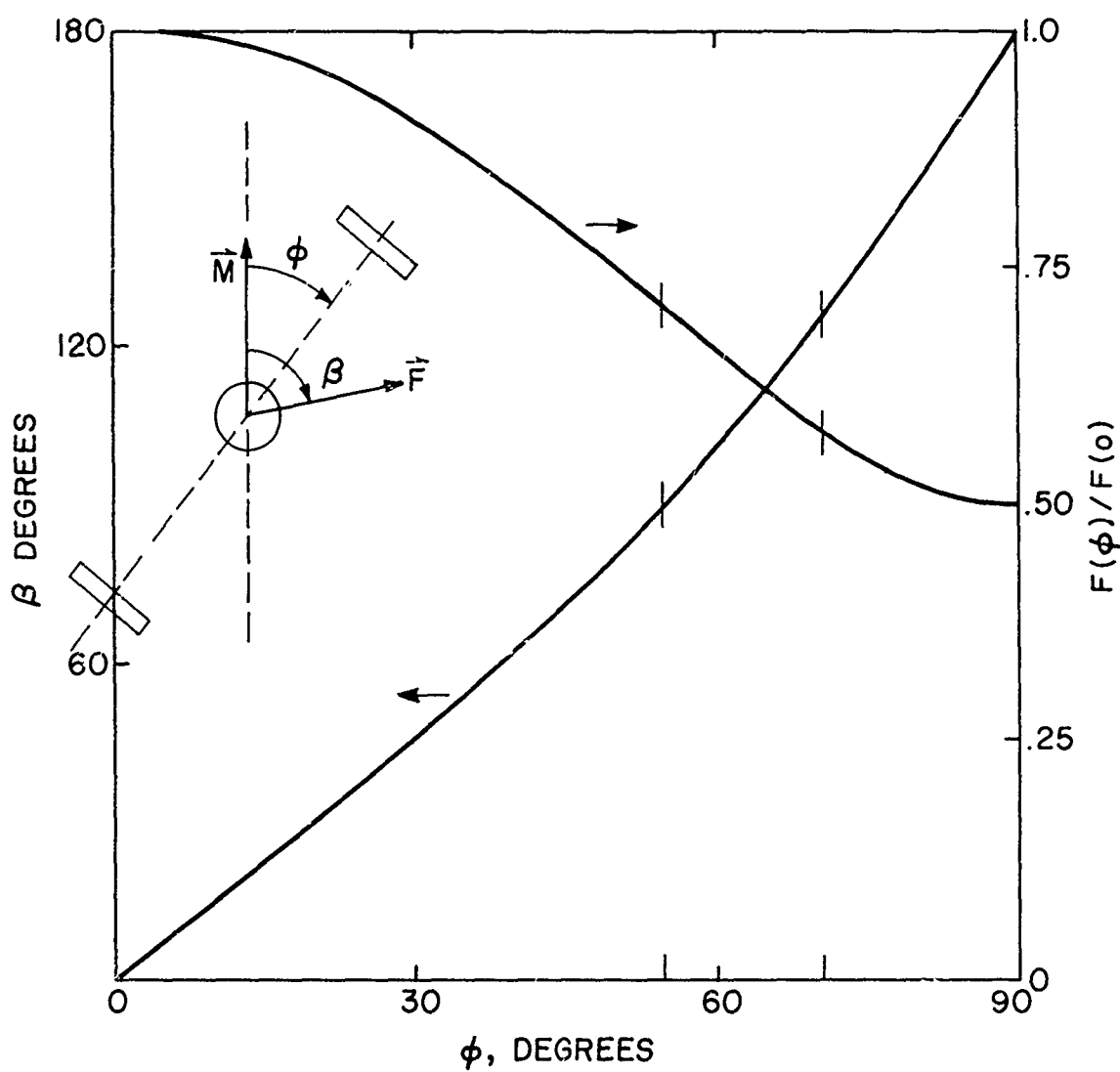
Vol. 3

REFERENCES:

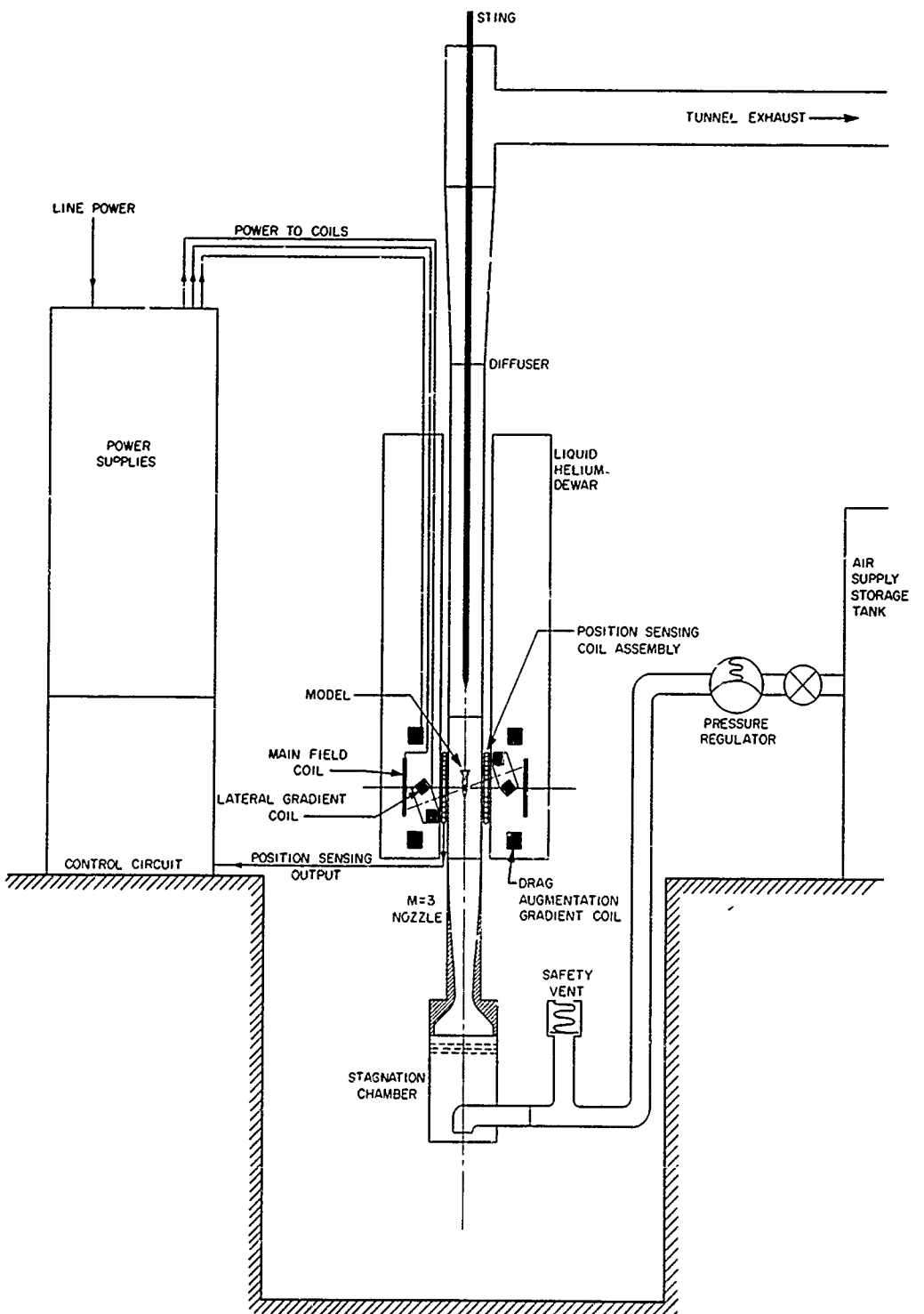
- [1] Journal of Applied Physics. Electromagnetic Support Arrangement with Three-Dimensional Control. I. Theoretical (U), by A. W. Jenkins and H. M. Parker, vol. 30, No. 4, pp. 2385-2395, April 1959.
- [2] Brookhaven National Laboratory. Measurements of Energy Losses in Pulsed Superconducting Magnets (U), by G. H. Morgan, P. F. Dahl, W. B. Sampson, and R. B. Britton (BNL 12586 R).



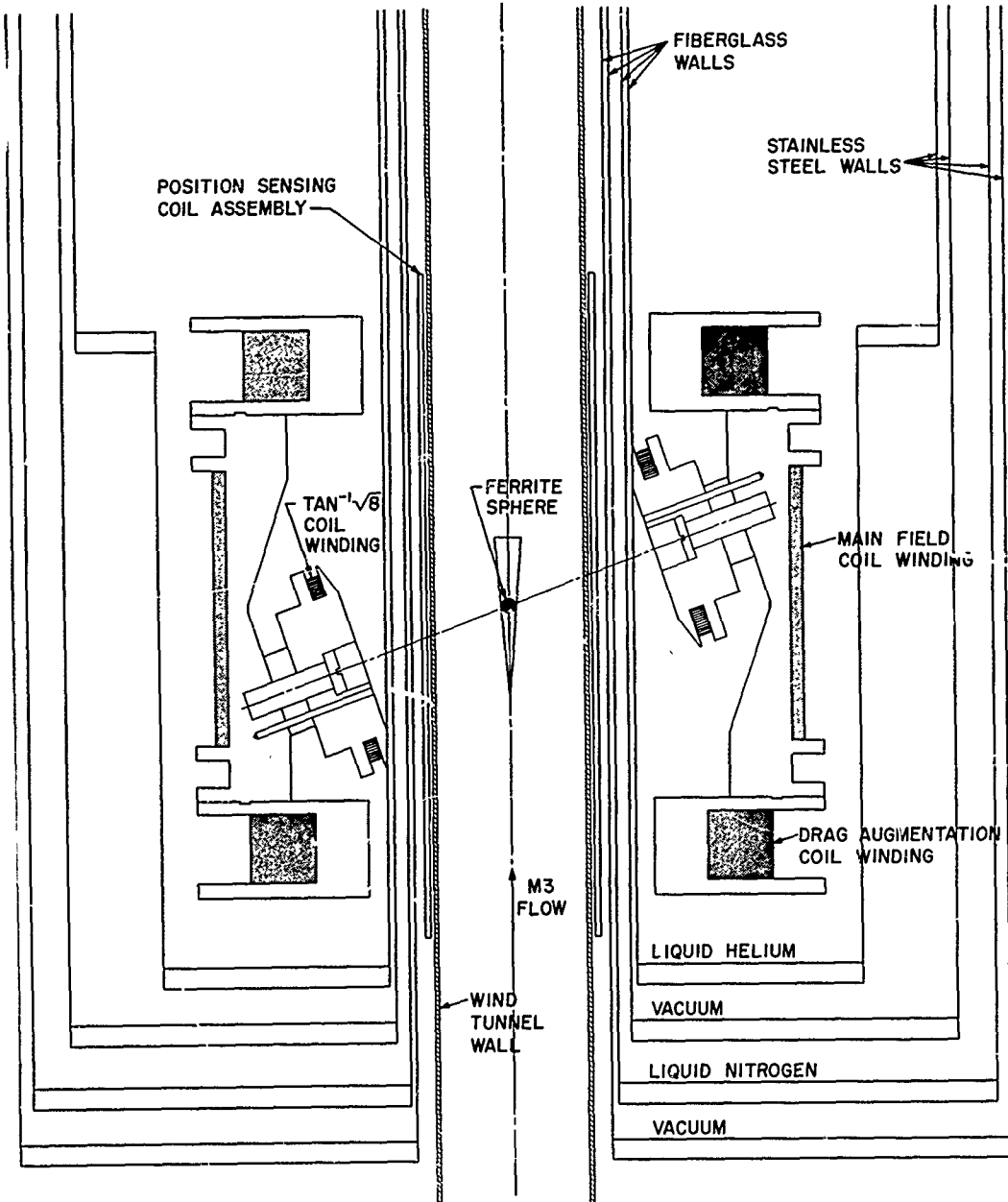
(U) FIG. 1. U.Va. Magnetic Balance Support Principle.



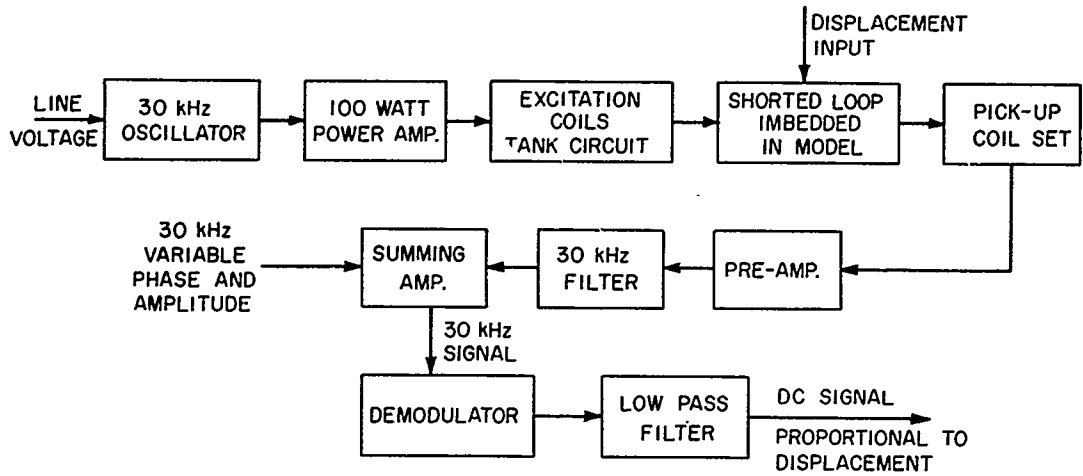
(U) FIG. 2. Force Direction and Magnitude vs ϕ .



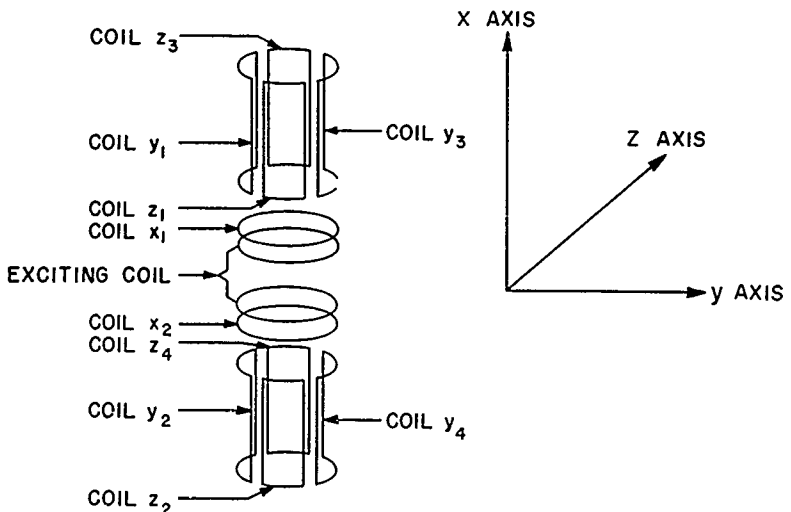
(U) FIG. 3. The Prototype Facility.



(U) FIG. 4. Sketch of Superconducting Coil System.

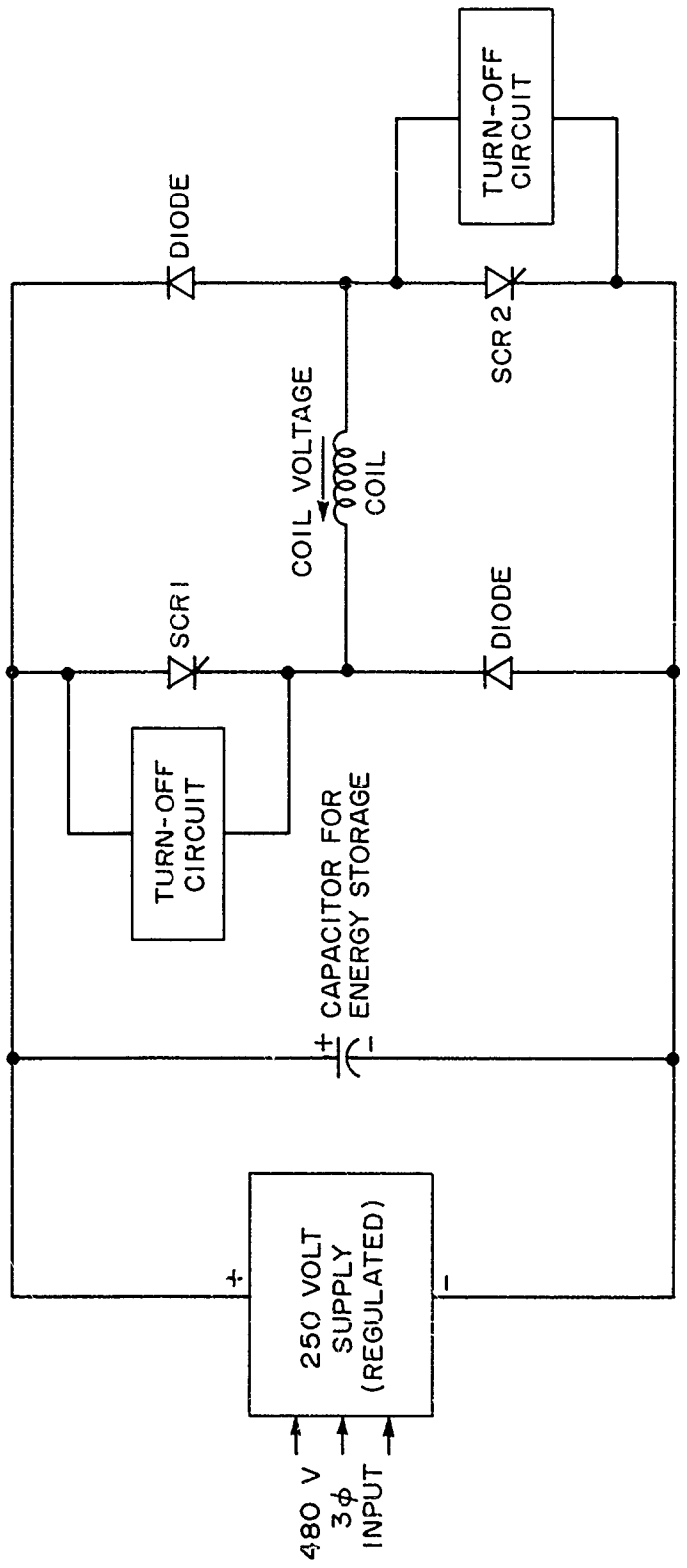


a) BLOCK DIAGRAM



b) COIL ASSEMBLY

(U) FIG. 5. Electromagnetic Position Sensing System.



(U) FIG. 6. Basic Schematic of $\tan^{-1}\sqrt{8}$ Coils Power Supplies.

Paper No. 30

WIND TUNNEL MEASUREMENTS OF THE AERODYNAMIC
CHARACTERISTICS OF THE 2.75 WRAPAROUND FIN
ROCKET USING A MAGNETIC SUSPENSION SYSTEM

(U)

(Paper UNCLASSIFIED)

by

Milan Vlajinac
Massachusetts Institute of Technology
Cambridge, Mass. 02139

ABSTRACT. (U) Wind tunnel data on damping in roll, damping in pitch, as well as lift, drag and pitching moment coefficients at a Mach number of 4.25 is presented for the 2.75 wrap-around fin configuration for angles of attack from zero to nine degrees. Force and moment data were obtained using a pneumatic calibration technique developed for magnetic suspension systems. Recommendations for future dynamic stability testing using magnetic suspension systems are discussed.

INTRODUCTION

(U) An experimental study was conducted to obtain the aerodynamic characteristics of the 2.75 wrap-around fin rocket using a magnetic suspension system. The aerodynamic parameters under investigation were roll damping moment, damping in pitch as well as the static forces and moments.

(U) The magnetic balance and suspension system* and the 3" x 4", $M = 4.25$, open jet wind tunnel at the M.I.T. Aerophysics Laboratory were used in the tests. The tests on the model were conducted over an angle of attack range from zero to nine degrees. Static force and moment data are compared with results obtained at N.O.L.

MODEL DESCRIPTION

(U) The model configuration as tested is shown in FIG.1. This corresponds to configuration No. 1 on BUWEPS Drawing No. SK675192. The model bodies were made of magnetic-ingot-iron. The fins were made of heat treated beryllium-copper and were soft-soldered to the body using a fixture that would orient their position with respect to the body as well as space them 120° apart. The bourrelets were made of brass rings soft-soldered in place and then machined down to size.

(U) The fin cant on the models was checked with an indicator after they were soldered, and maximum acceptable run-out over the chord (2.48) was .001 inch (0.1°).

(U) Prior to wind-on tests each model was suspended magnetically and the fin orientation was noted. Stock was removed from the fins until no preferred orientation in roll was observed. This provided an accurate way of statically balancing the model in roll.

* This balance was developed under the sponsorship of the USAF Aerospace Research Laboratories under Contract Nos. AF33(616)-7023 and AF33(615)-1470.

(U) The model diameter of .218 inches was chosen for two reasons: 1) it allowed the model to remain inside the tunnel Mach rhombus at the angle of attack range tested, and 2) the diameter was compatible with existing equipment used for damping in roll measurements. The model location with respect to the Mach rhombus is shown in FIG. 2. Note that the model was angulated about a point near the tail to insure that the model remained within the Mach rhombus.

TEST TECHNIQUES AND INSTRUMENTATION

MAGNETIC SUSPENSION SYSTEM

(U) The tests made in this study involved the use of a magnetic balance suspension system. The magnet configuration is shown in FIG. 3. The balance is capable of controlling the model position and attitude in six degrees of freedom. For these tests the roll moment coils were not installed, so the model was controlled in only five degrees of freedom (Ref 1). A photograph of a suspended model is shown in FIG. 4. The performance of the suspension system in positioning the model in the desired location during wind tunnel tests is as follows:

Absolute position in drag, lift, and slip with respect to the wind tunnel axis at the time of position adjustment is ± 0.001 inch; maximum amplitude of moderate fluctuations (3-30 cps) is 0.001 inch; angular position with respect to the wind tunnel axis at time of position adjustment is $\pm .1$ degree. Note that the angular position includes the maximum amplitude of moderate fluctuations (3-30 cps) 0.1 degree.

DESCRIPTION OF TESTS

Damping in Roll Measurements

(U) Damping in roll data was obtained using a spin decay technique (Ref 2). Since the magnetically suspended model is free to rotate about its longitudinal axis, a rolling torque was applied to the model in the wind tunnel with air jets orthogonal to the flow direction and forward of the model fins to change its steady state roll rate. This system is shown in FIG. 5. The rotation of the model is sensed by having the fins interrupt a beam of light striking a photocell whose output is recorded on a Sanborn optical oscilloscope.

8th Navy Symposium on Aeroballistics

Vol. 3

(U) The procedure followed during damping in roll tests was follows:

1. The difference between nozzle static and test section pressures was checked and set to approximately 1 inch of silicone manometer fluid.

2. The model's absolute position was checked and the magnet currents were recorded in wind-off damping tests.

3. The air injectors were moved forward and located approximately 1/2 inch ahead of the model fins. The air jets were turned on and the roll rate of the model was observed.

4. When a substantial change in roll rate was observed, the jets were shut off, retracted, and the Sanborn recorder was started.

5. The Sanborn trace was stopped approximately 10 seconds after the start of the run. This procedure was repeated for each run and angle of attack.

(U) Due primarily to eddy currents introduced by the magnetic field on a rotating model, a magnetic roll damping is produced. This damping must be measured and subtracted from the wind-on data in order to obtain the aerodynamic damping in roll. An air bearing was used to support the model in the same location as during wind-on test and is described in Ref. 2. The magnet currents were set to the values recorded during wind-on tests. The test section was evacuated to .05 psia, the model was spun up with the air jets and the roll rate decay was recorded. The damping due to the air bearing was measured with the magnet currents turned off.

Damping in Pitch Tests

(U) Damping in pitch ($C_{M_q} + C_{M_\alpha}$) data was obtained using a forced oscillation technique (Ref 3). A sinusoidal current was superimposed independently on the direct current of each of the two lift magnet coils to control the pitching and plunging motion of the model. The relative phase and amplitude of the two sinusoids determines the axial location of the center of rotation of the model. The circuit shown in FIG. 6 provides two sinusoids of equal frequency, with variable amplitude and phase adjustments of $180^\circ \pm 90^\circ$. The phase and amplitude of the two sinusoids was varied until a photocell indicated the model was pitching about its center of mass, i.e. a minimum signal was observed. The photocell was illuminated by a thin parallel light beam that was partially interrupted by the suspended model at its center of mass. Since the light beam was only .020 in. thick the accuracy of the point of rotation of the model is estimated to be .005 in.

(U) The magnet currents from the two coils were read differentially ($I_{L_1} - I_{L_2}$) from current shunts and were amplified using the circuit shown in FIG. 7. This signal is proportional to the magnetic forcing moment in pitch. The model pitching motion was determined from the difference between the forward and aft lift optics output. A phase shift was introduced to the optics output and adjusted to give the same phase shift as the magnet current amplifier circuit. The complete pitch position sensor is shown in FIG. 7.

(U) Since eddy currents flow in the model, an additional damping was present. The magnitude of this effect was estimated by repeating the experiment, with the wind off, while maintaining the same model motion. This evaluation of magnetic damping includes all effects except that due to the drag field, which is smaller than other fields. The difference between the wind-off and wind-on phase shift is the aerodynamic damping torque.

(U) The procedure followed during damping in pitch tests was as follows:

1. The difference between nozzle static and test pressure was checked and set to approximately 1 in. of silicone manometer fluid.
2. The model absolute position was checked.
3. The frequency at which the model would be forced was set and recorded.
4. The amplitude of the forcing signal was increased until the model oscillated with approximately 2° peak-to-peak amplitude.
5. The relative phase and amplitude of the forcing signal were adjusted until the model's center of gravity motion produced no change in photocell output.
6. The magnet currents producing the pitching motion and the model's position in pitch were recorded on the Sanborn recorder for approximately 5 seconds.

This procedure was repeated for each run.

Static Tests

Static forces and moments were obtained from the currents by a new technique developed for use with magnetic balance and suspension systems and is described in Appendix A.

DATA REDUCTION AND RESULTS

DAMPING IN ROLL DATA

(U) The equation of motion for a finned configuration in the roll degree of freedom is as follows:

$$\frac{I_{xx}}{qSD} \ddot{\phi} - C_{\ell_p}(\alpha) \left(\frac{D}{2V} \right) \dot{\phi} - C_{\ell_i}(\alpha) \sin n \phi = C_{\ell_{\delta}}(\alpha) + C_{\ell_o}(\alpha) \quad (1)$$

The motion described by this equation can be both a periodic variation in roll rate about a steady state value as well as a damped oscillation about an equilibrium roll angle (usually referred to as "locked in"). The roll rate during spindown was obtained by averaging the rolling velocity $P(t)$ in a time interval Δt such that

$$\tau \gg \Delta t \gg \frac{1}{P} \quad (2)$$

where τ is the time constant of the spindown and P is the rolling velocity. Equation (1) can be linearized at

α if $\frac{C_{\ell_i} qSD}{I_{xx}} \ll 1$ and $\frac{C_{\ell_i}}{C_{\ell_p} \left(\frac{D}{2V} \right)} \ll 1$. This assumption is

further justified by the data. Equation (1) including the magnetic damping then becomes:

$$\frac{I_{xx}}{qSD} \ddot{\phi} - [C_{\ell_p}(\alpha) + C_m(\alpha)] \frac{D}{2V} \dot{\phi} = C_{\ell_{\delta}} + C_{\ell_o} \quad (3)$$

where $C_m(\alpha)$ is the coefficient of roll damping due to the magnetic fields. The homogeneous solution to this equation is of the form

$$\phi = \phi_0 e^{-t/\tau} + \phi_1 \quad (4)$$

where $\tau = \frac{2I_{xx}V}{qSD^2 (C_{\ell_p} + C_m)}$ (5)

(U) The roll-damping data was taken from the Sanborn optical oscilloscope records by counting the peaks of the roll sensor output during an interval of 0.1 sec. The intervals were spaced 0.2 sec. apart. The time constant for Eq. (5) was determined using a method developed in Ref. 4. An exponential equation of the form

$$P(t) = a + be^{-t/\tau} \quad (6a)$$

becomes at $(t + \Delta t)$

$$P(t+\Delta t) = a + be^{-t/\tau} \quad (6b)$$

(U) Solving, we obtain:

$$[P(t+\Delta t)] = [P(t)]e^{-\Delta t/\tau} + a(1-e^{-\Delta t/\tau}) \quad (6c)$$

This is a linear equation with slope $m = e^{-\Delta t/\tau}$
Solving for τ we obtain

$$\tau = \frac{-\Delta t}{\log m} \quad (6d)$$

(U) A typical plot of $P(t)$ versus $P(t+\Delta t)$ is shown in FIG. 8 and further justifies the assumption made in linearizing Eq. (1).

(U) The mean slope \bar{m} was obtained from

$$m = \frac{\frac{n}{n} \sum_{i=1}^n P(t_i)P(t_i + \Delta t) - P(t_i) \sum_{i=1}^n P(t_i + \Delta t)}{\frac{n}{n} \sum_{i=1}^n P(t_i) - (\sum_{i=1}^n P(t_i))^2} \quad (7)$$

where n is the number of points taken. The damping in roll coefficient C_{p} versus angle of attack is shown in FIG. 9.

(U) The steady state roll rate of the models was recorded for different angles of attack and is shown in FIG. 10. One of the models tested had a steady state roll rate $\frac{PD}{2V} = 6.98 \times 10^{-5}$ and locked in at approximately 2° angle of attack. Unfortunately, further data could not be obtained on this model due to a power failure in the magnet power supplies and subsequent loss of the model. The projected curves indicate that lock-in can be expected at approximately two degrees when $0 < \frac{PD}{2V} < 3.4 \times 10^{-4}$ at zero degrees angle of attack.

8th Navy Symposium on Aeroballistics

Vol. 3

DAMPING IN PITCH DATA

(U) The equation describing the motion in one degree of freedom rotation about the center of mass of an axisymmetric configuration is:

$$I_{yy}\ddot{\alpha} - \frac{qSD^2}{2V}(C_{M_q} + C_{M_\alpha})\dot{\alpha} - qSDC_{M_\alpha}\alpha = M_f \quad (8)$$

(U) If the model is forced to maintain pure sinusoidal oscillation about its center of gravity then the lumped parameter $C_{M_q} + C_{M_\alpha}$ can be solved in the following manner.

$$(U) \text{ Substituting } M_f = M_0 e^{j(\omega t + \psi)} \quad (9)$$

$$\alpha = \bar{\alpha} e^{j\omega t}$$

Eq. (8) becomes

$$[-I_{yy}\omega^2 - j\omega C - M_\alpha]\bar{\alpha} = \bar{M}e^{j\psi} \quad (10)$$

where

$$C = M_q + M_\alpha$$

The phase difference (ψ) between the forcing moment (\bar{M}) and the angular position ($\bar{\alpha}$) is

$$\psi = \tan^{-1} \frac{C\omega}{M_\alpha + I_{yy}\omega^2} \quad (11)$$

where ω is the frequency of oscillation in radians per second. The value of the lumped parameter C can be found by measuring the phase angle between the forcing moment and the angular position.

$$C = \frac{M + I_{yy}\omega^2}{\omega} \tan \psi \quad (12)$$

(U) In order to obtain the aerodynamic damping, the magnetic damping due to eddy currents must be subtracted from the measured value C during a wind-on test. The wind-on model motion was duplicated, wind off, to determine magnetic damping. The magnetic damping is:

$$C_m = I_{yy}\omega \tan \psi' \quad (13)$$

where ψ' is the phase difference between the forcing moment and model position with wind off. The aerodynamic damping

(U)
 $(M_q + M_\alpha)$ is then

$$C_A = C - C_m \quad (14)$$

The data was obtained by simultaneously recording the magnet currents forcing the model and the model position in pitch. The zero crossing on the trace of each signal was obtained by integrating the areas above and below the axis of the signal. Once the axes of the two signals were obtained, the phase difference between them was averaged over 20 cycles.

(U) The damping in pitch measurements show that, for the configuration tested, the aerodynamic damping at the model's center of mass is comparable in magnitude to the magnetic damping. The error in the reduced data was therefore amplified since the aerodynamic damping in pitch coefficient was the difference of two comparable quantities. The accuracy of the data could have been improved by moving the model center of mass forward of its present location, thereby increasing the value of the aerodynamic damping about the axis of oscillation. This would have involved additional modifications in the present optical position sensors which were beyond the scope of this work.

(U) The damping coefficients $C_{M_q} + C_{M_\alpha}$ are plotted versus frequency $\frac{\omega D}{2V}$ in FIG. 11. It should be noted that the damping in pitch data was obtained for a point $\frac{x}{l} = 0.531$ corresponding to the model's center of mass. Note that the center of pressure moves forward at $\alpha \approx 7^\circ$. This suggests that the fins may be near stall. The effects of stall could not only be destabilizing in damping but could also account for the chopoff in roll damping at higher angles of attack.

(U) During damping in pitch measurements, the model roll rate was approximately ten times the maximum pitch frequency tested. Thus a coupling between damping in pitch and roll rate is definitely possible.

(U) The damping in pitch data shows a destabilizing trend at both higher angles of attack and higher reduced frequencies of oscillation in pitch. This variation in damping coefficient is several times the standard deviation of the data.

FORCE AND MOMENT DATA

(U) The force and moment data was obtained using the pneumatic force measuring apparatus described in Appendix A. Using this technique the forces and moments in six degrees

8th Navy Symposium on Aeroballistics

Vol. 3

(U) of freedom acting on a model supported in the apparatus can be measured independently with respect to the latter's coordinates. The interactions of orthogonal forces measured with this apparatus are less than .5%. The aerodynamic forces and moments on the model can therefore be measured by positioning the model in the same location with respect to the magnet coils as during wind-on testing and setting the magnet currents to the values recorded during the tests. The data thus obtained is shown in Table 3. The forces and moments in the model's yaw plane are not shown since their values are zero within the accuracy of the measurements.

(U) The drag, lift, and pitching moment coefficients versus angle of attack at $x/l = .401$ are shown in FIG. 12, 13 and 14. Comparison with values from Ref. 5 at smaller Mach numbers is shown. The value of the coefficients obtained in this study appears to agree with the trend due to Mach number. At $\alpha = 3^\circ$, the center of pressure is 2.93 diameters aft of the reference point with a standard deviation of 0.10 diam. The maximum scatter in the drag coefficient data is 1.6%. No correction for horizontal buoyancy was made since it was less than 1%.

(U) In estimating the over-all accuracy of the data, the following sources of error were considered:

$\Delta p/p = .16\%$, $\Delta M/M = 0.4\%$ for wind tunnel parameters.

$\Delta S/S = 0.6\%$ for model geometry.

$\Delta C/C = 0.2\%$ for system calibration.

$\Delta I/I = 0.4\%$ for current measurement.

Combining these parameters on an equi-probability basis

$$\frac{\Delta \text{coeff}}{\text{coeff}} = \sqrt{\left(\frac{\Delta p}{p}\right)^2 + \left(2 \frac{\Delta M}{M}\right)^2 + \left(\frac{\Delta C}{C}\right)^2 + \left(\frac{\Delta I}{I}\right)^2 + \left(\frac{\Delta S}{S}\right)^2} = 1.2\%$$

The error due to ΔM could be eliminated by calculating the horizontal buoyancy effects in the usual way. If this were done the estimated error would be $\pm 0.8\%$.

(U) The detailed values for drag, lift and pitching moment coefficients are presented in Table 3.

(U) It should be noted that the force and moment coefficients obtained in this study are for a model with reduced roll rate $PD/2V \sim 6 \times 10^{-4}$ and should represent average coefficients independent of model roll angle.

MAGNUS FORCES AND MOMENTS

(U) Attempts were made to measure the change in Magnus force and moment due to a change in model roll rate by

(U) recording the sum and difference of the two lateral magnet currents on the Sanborn recorder during a roll spin-down. The attempt failed because the maximum Magnus force expected over the angle of attack range used here is approximately 10^{-3} oz. The magnet currents required to produce this force are less than .010 amperes which is of the same order of magnitude as the magnet power supply noise level. In addition, the change in yaw angle required to produce a .010 change in current is $.02^\circ$ which is a factor of five below the low frequency fluctuations in model yaw angle during a four second spindown.

CONCLUSIONS AND RECOMMENDATIONS FOR FUTURE WORK

(U) The damping in roll coefficients for the 2.75 wrap-around fin rocket configuration have been measured over an angle of attack range from zero to nine degrees using a magnetic suspension system. Repeat measurements have a maximum scatter of 4% and are within the expected scatter based on roll damping data obtained in previous studies using the magnetic suspension system.

(U) The variation in steady state roll rate versus angle of attack obtained indicates the possibility of roll lock-in for models with sufficiently small steady state roll rate at zero degrees angle of attack. This was qualitatively observed on one of the models tested.

(U) Drag, lift and pitching moment coefficients were obtained successfully over an angle of attack range from zero to nine degrees, using the pneumatic calibration system. Comparison with data at lower Mach numbers as well as repeatability of the measurements gives confidence in this new technique for magnetic suspension system calibration.

(U) Damping in pitch measurements were obtained using a forced oscillation technique. The accuracy of the data could have been improved by moving the model center of motion further forward. The damping in pitch coefficients obtained indicate the possibility of an unstable dynamic behavior at higher angles of attack due to fin stall, or may be due to an unsuspected coupling between roll rate and pitching rate (Ref 8). This point warrants detailed study.

(U) An attempt was made to measure a change in Magnus force and moment during roll spindown. It is apparent that modifications in both the lateral optical system as well as noise reduction in the lateral magnet power supply must be made before successful Magnus testing can be performed.

APPENDIX A

(U) The Pneumatic Calibration System was used in this study to obtain aerodynamic forces and moments on the model during wind tunnel tests. A detailed report of this technique will appear in Ref. 6.

(U) The Pneumatic Calibration Rig consists of an array of six pairs of air bearing pads located on a fiberglass frame. The pads are so located that air injected through an orifice in each pad supports an inner frame in six degrees of freedom. A pressure tap located on each pad measures the air pressure between the inner and outer frames. A force applied on the inner frame will cause a differential pressure change to occur in the pairs of bearing pads. By properly arranging the air bearing pads a given applied force will produce a pressure change on each pair of pads that is proportional to the magnitude of the component of the applied force in the calibration rig's coordinate system (orthogonal-Cartesian). Forces are determined by taking the sum of two pairs of bearing pad pressures and moments as the difference of these pressures. By applying known forces and moments on the calibration rig the relationship of pressures to pneumatic applied forces and moments is obtained. An arbitrary force and moment applied to the inner frame can therefore be reduced to both magnitude and direction by measuring six pressures on the Pneumatic Calibration Rig. The calibration curves of pressures versus known applied forces show a maximum force and moment interaction of 0.5% between orthogonal components with the exception of roll on yawing moment which is on the order of 5%. The Pneumatic Calibration System at this time has a force resolution of $\pm 1/128$ oz over a 2 lb range and a moment resolution of .015 in.-oz over a 64 in.-oz range.

(U) During the force and moment calibration, the model was rigidly attached to the inner frame of the Pneumatic Calibration Rig. The latter was then positioned in the magnetic balance until the model was in the same location as during wind-on tests. The magnet currents were set to their wind-on values and the six pressure changes were recorded. This was repeated for each angle of attack tested.

8th Navy Symposium on Aeroballistics

Vol. 3

(U) The technique adopted here represents a substantial simplification over previous methods used in measuring aerodynamic forces and moments using a magnetic suspension system. (See Ref. 7.)

8th Navy Symposium on Aeroballistics

Vol. 3

REFERENCES

1. Chrisinger, J. E., et al., "Magnetic Suspension and Balance System for Wind Tunnel Application," Journal of the Royal Aeronautical Society, Vol. 67, 1963, pp. 614-724
2. Copeland, A. B., "Wind Tunnel Measurements of the Roll Aerodynamics of the Iroquois Sounding Rocket and the Basic Finner Using a Magnetic Model Suspension System," MIT Aerophysics Lab Rept TR 137, February 1967 (See also Ref 7)
3. Tilton, E. L., III, "Dynamic Stability Testing With a Wind Tunnel Magnetic Model Suspension System," M.S. thesis, Massachusetts Institute of Technology, January 1963
4. Mangelsdorf, P. C., Jr., "Convenient Plot for Experimental Functions with Unknown Asymptotes," J. Appl. Phys., March 1953
5. Preliminary Wind Tunnel Data from "Naval Ordnance Laboratory WTR 1037 Tunnel Axis, Configuration BN₁F₁C₁"
6. Massachusetts Institute of Technology - Summary Rept to Aerospace Research Laboratory (to be published)
7. Copeland, Alan B., Covert, Eugene E., and Petersen, Robert A., "Wind Tunnel Measurements at M = 4.28 of Some Static and Dynamic Aerodynamic Characteristics of Finned Missiles Suspended Magnetically," J. Spacecraft and Rockets, 5, 7, July 1968, pp 838-842

TABLE II
DAMPING IN PITCH DATA
 $P_O = 30$ psia $T_O = 759.7^\circ R$

α Degrees	ω Rad/sec	ψ Degrees	C_m in oz sec rad	M_α in oz rad	ψ Degrees	$M_\alpha + M_\theta$ in oz sec rad ²	$C_m + C_{M_\alpha}$ 1 (rad) ²
0	62.20	8.05	.01163	-.8996	6.88	-.0008	-.1.012 x 10 ³
0	60.94	7.93	.01124	-.8996	6.76	-.0007	-.886 x 10 ³
0	97.76	11.59	.0265	-.8996	10.92	-.0002	-.253 x 10 ³
0	97.76	11.59	.0265	-.8996	10.40	+.0011	+1.392 x 10 ³
0	124.40	14.02	.0412	-.8996	18.56	-.0165	-20.882 x 10 ³
2	94.3	12.82	.0284	-.8996	13.20	-.0031	-3.923 x 10 ³
2	123.1	14.99	.0436	-.8996	21.20	-.0226	-28.603 x 10 ³
2	141.5	21.04	.0719	-.8996	24.41	-.0161	-20.376 x 10 ³
4	123.1	13.22	.0384	-1.656	18.84	-.0220	-27.843 x 10 ³
4	153.3	22.18	.0827	-1.656	23.70	-.0109	-13.795 x 10 ³
6	123.1	17.18	.0505	-1.031	17.53	-.0038	-4.809 x 10 ³
6	153.3	23.77	.0893	-1.031	20.07	+.0125	-15.820 x 10 ³
8	123.1	12.60	.0365	+.573	13.90	-.0028	-3.544 x 10 ³
8	154.8	20.13	.0751	+.573	15.07	+.0209	+26.451 x 10 ³
0	96.13	11.59	.0261	-.8996	13.69	-.0072	-9.112 x 10 ³

TABLE III
(σ = Standard Deviation)
 $P_O = 30.0$ psia $T_O = 759$
 $P_1 = 4.25$

α Degree	C_D	(C_D) avg	σ_{C_D}	C_L	(C_L) avg	σ_{C_L}	C_m	C_m avg	σ_{C_m}
0	.7732			-.0055			-.0471		
	.7592			-.0034			-.2378		
	.7592	.761	.0069	-.0030	-.0056	.0171	-.0995	-.1245	.0087
	.7592			-.0005			-.2220		
	.7518			-.0013			-.1579		
3	.7913			.332			-.9588		
	.7936			.287			-.8769		
	.7855	.789	.0036	.300	.305	.0164	-.9033	-.904	.0094
	.7855			.300			-.9033		
5	.8220			.575			-.1.779		
	.8214			.582			-.1.851		
	.8167	.817	.0043	.560	.567	.0094	-.1.630	-.1.684	.014
	.8099			.552			-.1.554		
	.8167			.560			-.1.630		
7	.8683			.899			-.2.629		
	.8673	.863	.0003	.892	.895	.0032	-.2.676	-.2.660	.019
	.8673			.892			-.2.676		
9	.914			1.360			-.3.607		
	.915			1.353			-.3.662		
	.922	.918	.0009	1.376	1.371	.011	-.3.763	-.3.710	.066
	.921			1.376			-.3.763		
	.920			1.383			-.3.832		
Mean standard deviation		± 0.0032			± 0.011				± 0.029

NOMENCLATURE

C	Total damping in pitch ($C_A + C_m$)
C_A	Aerodynamic damping in pitch ($M_q + M_\alpha$)
C_D	Drag coefficient
C_L	Lift coefficient
C_{ℓ_i}	Induced roll moment coefficient
C_{ℓ_o}	Roll moment coefficient due to fin curvature
C_{ℓ_p}	Roll damping moment coefficient $\frac{\partial C_\ell}{\partial (\frac{PD}{2V})}$
C_{ℓ_δ}	Fin cant roll moment coefficient
C_m	Magnetic damping
C_M	Pitching moment coefficient
C_{M_α}	Pitching moment coefficient due to rate change of angle of attack, $\frac{\partial C_M}{\partial (\frac{\dot{\alpha}D}{2V})}$
C_{M_q}	Pitching moment coefficient due to pitch rate, $\frac{\partial C_M}{\partial (\frac{\dot{\theta}D}{2V})}$
D	Model diameter
I_{xx}, I_{yy}	Moment of inertia about roll axis, moment of inertia about pitch axis, respectively
I_{L_1}, I_{L_2}	Lift 1, lift 2 coil current, respectively
j	$\sqrt{-1}$
l	Model length
M, M_f	Pitching moment, forcing moment, respectively
M_∞	Mach number

8th Navy Symposium on Aeroballistics

Vol. 3

NOMENCLATURE (continued)

M_α	Slope of pitching moment vs angle of attack
$M_{\dot{\alpha}}$	Pitching moment due to rate change of angle of attack
M_q	Pitching moment due to pitching velocity
\bar{M}	Moment in frequency domain
m	Slope
\bar{m}	Average slope
n	Number of fins
P_o	Stagnation pressure
P	Roll rate
q, q'	Dynamic pressure, pitching velocity ($\frac{\partial D}{2V}$), respectively
Re_l	Reynolds number based on model length
S	Reference area based on model diameter
T_o	Stagnation temperature
t	Time, seconds
Δt	Time interval
V	Flight velocity
x	Distance from nose of model
$\alpha, \bar{\alpha}$	Angle of attack, angle of attack in frequency domain, respectively
δ	Fin cant angle
τ	Time constant of exponential decay
θ	Pitch angle
ϕ	Roll angle

NOMENCLATURE (concluded)

ψ Phase angle wind on
 ψ' Phase angle wind off
 ω Angular frequency
 a, b, ϕ_0, ϕ_1 Constants

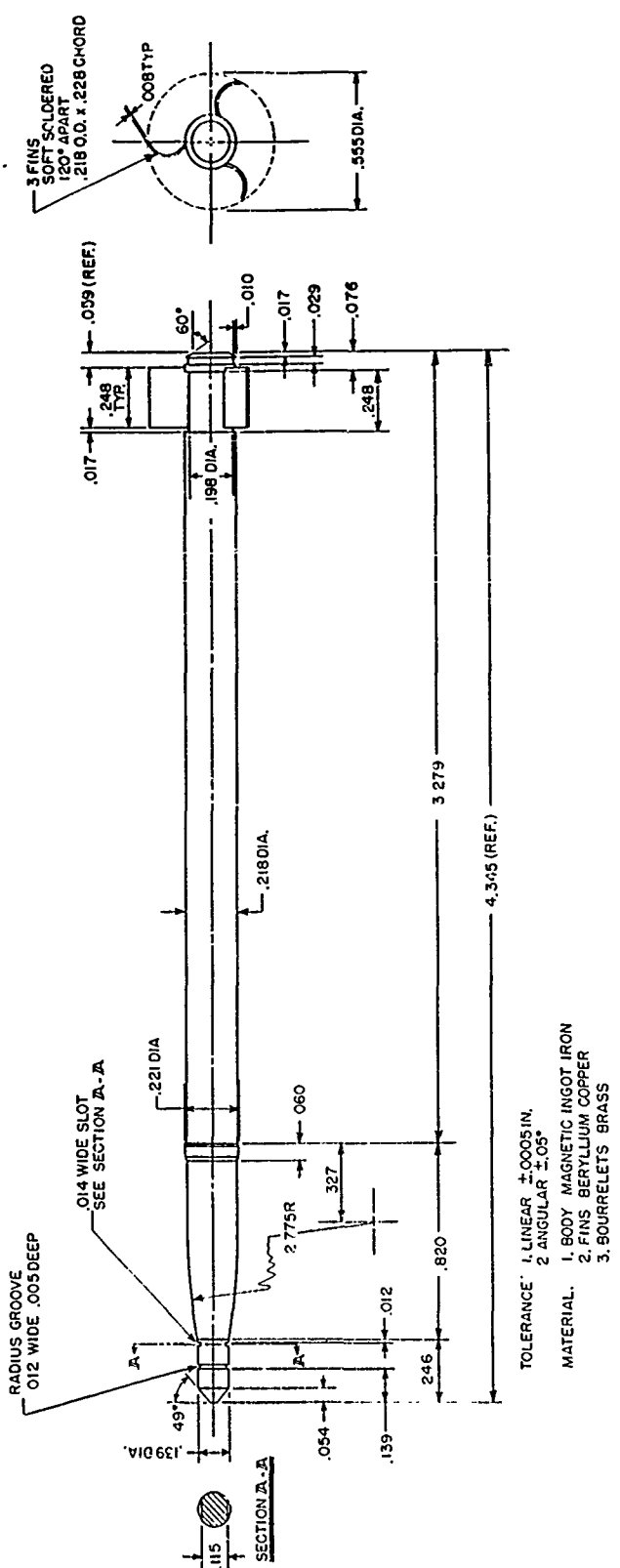


FIG. 1. 2.75 Wrap-Around Fin Model

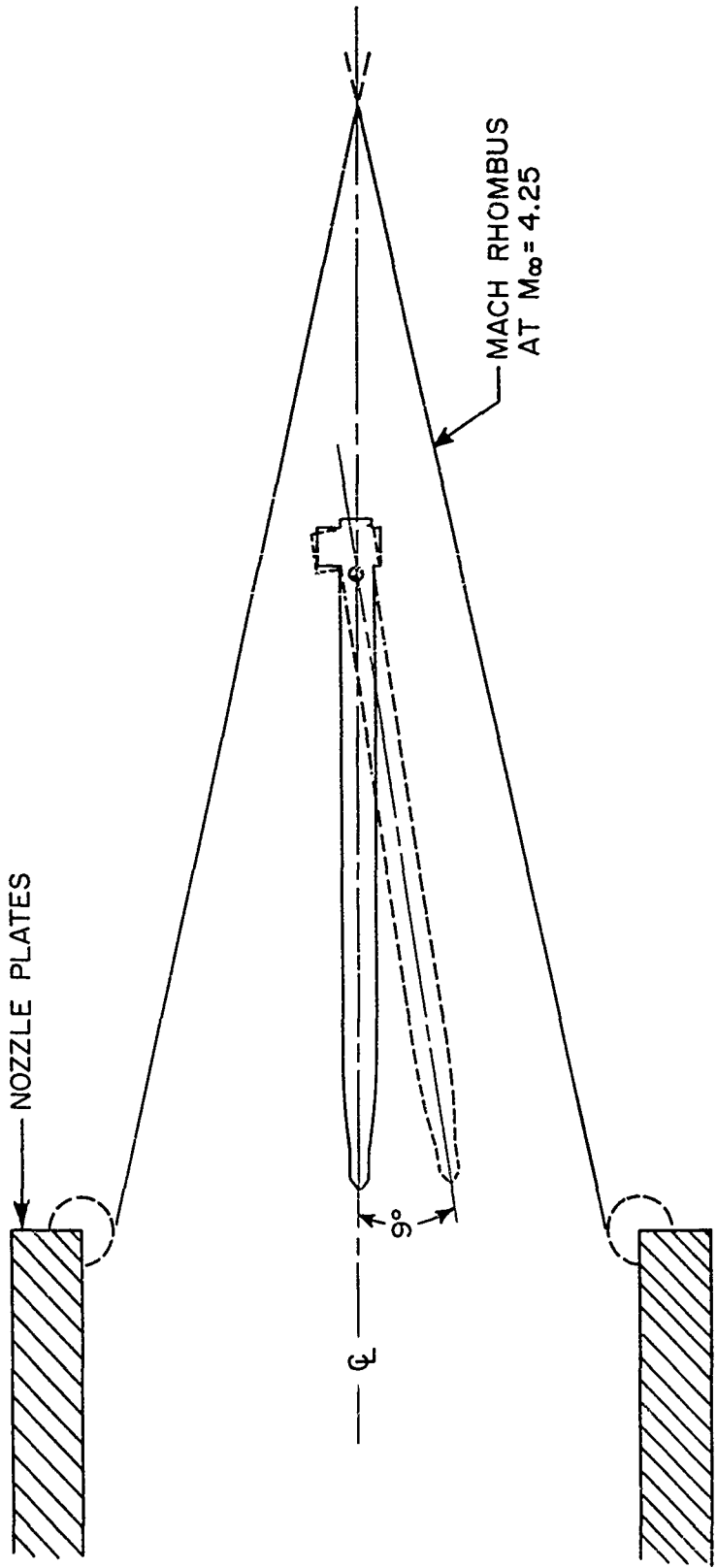


FIG. 2. Model Location in Tunnel During Tests

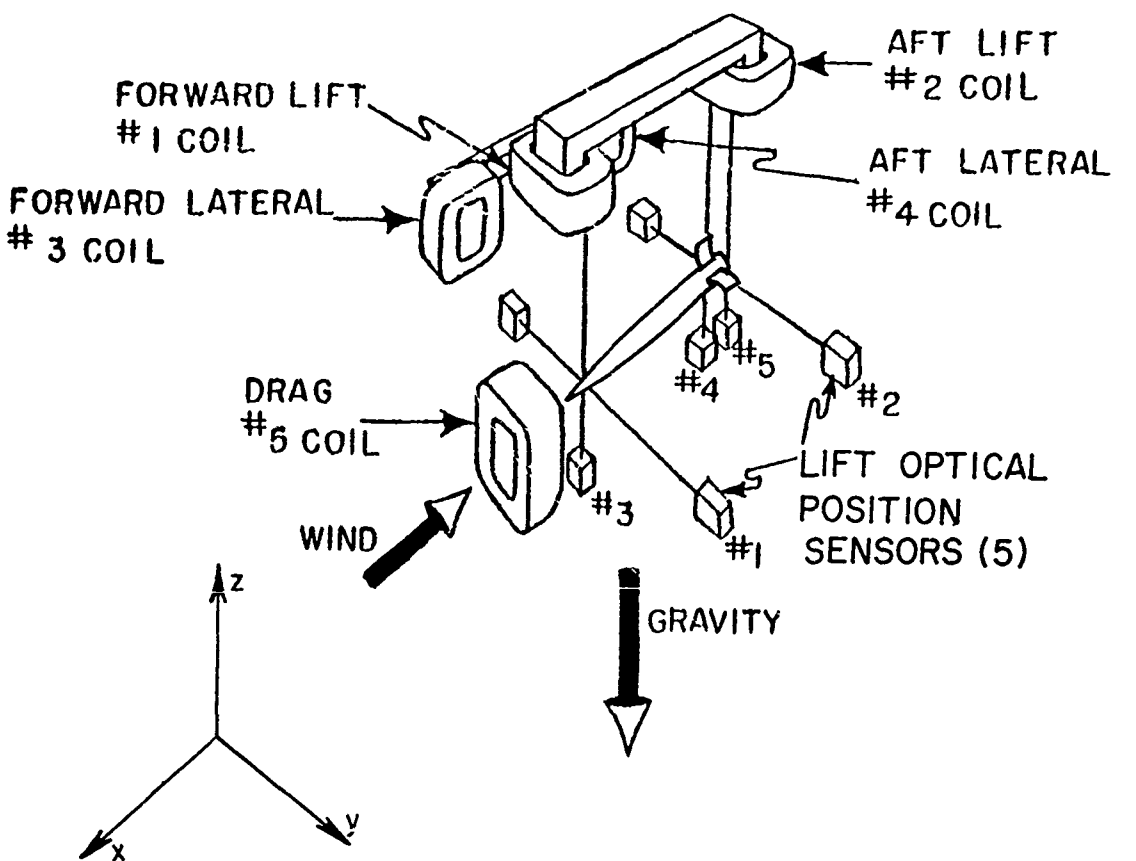


FIG. 3. Magnet Configuration Showing Model and Optical Position Sensors



FIG. 4. Model Suspended in Magnetic Balance.

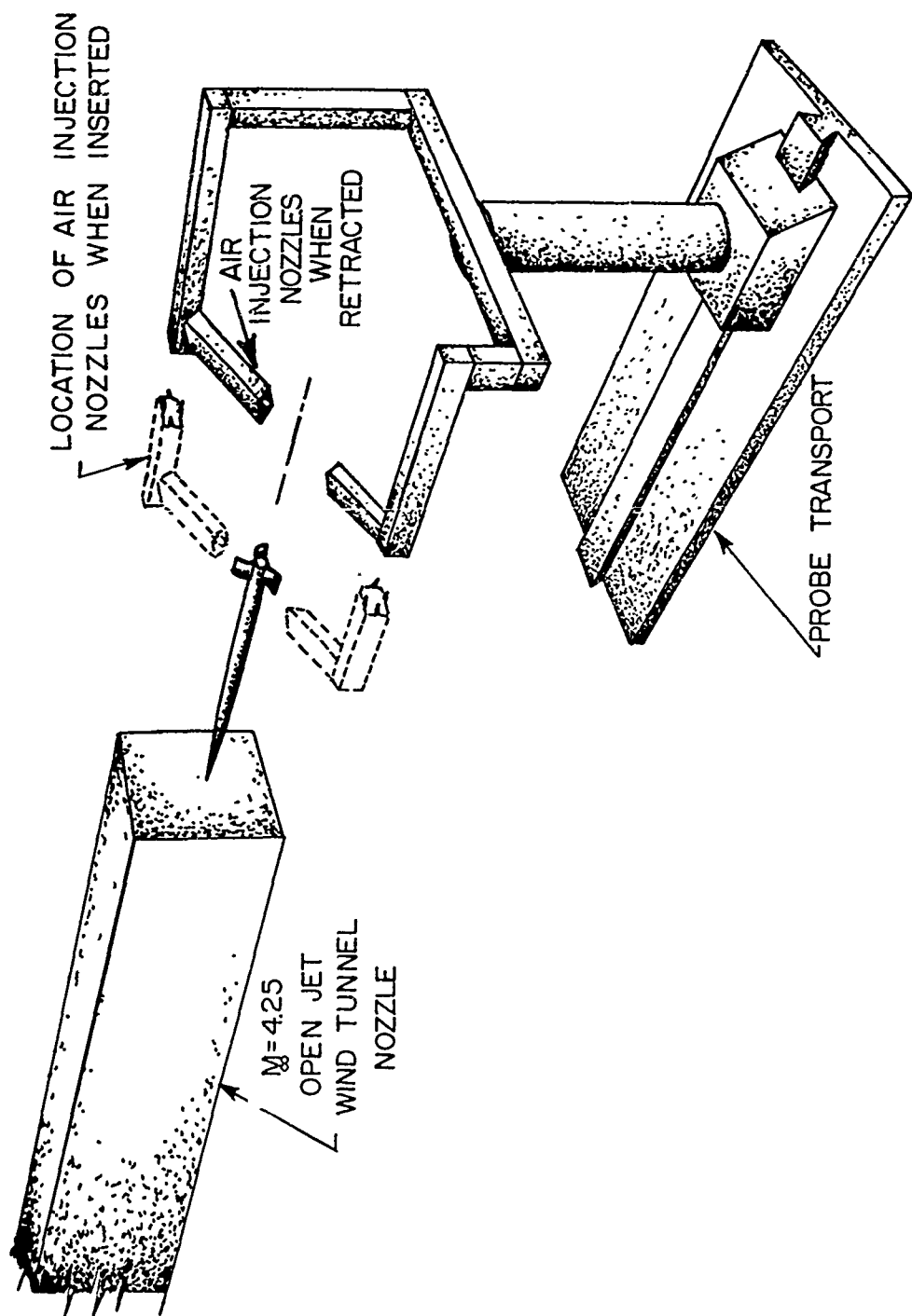


FIG. 5. Air Injection System for Producing Roll Torque

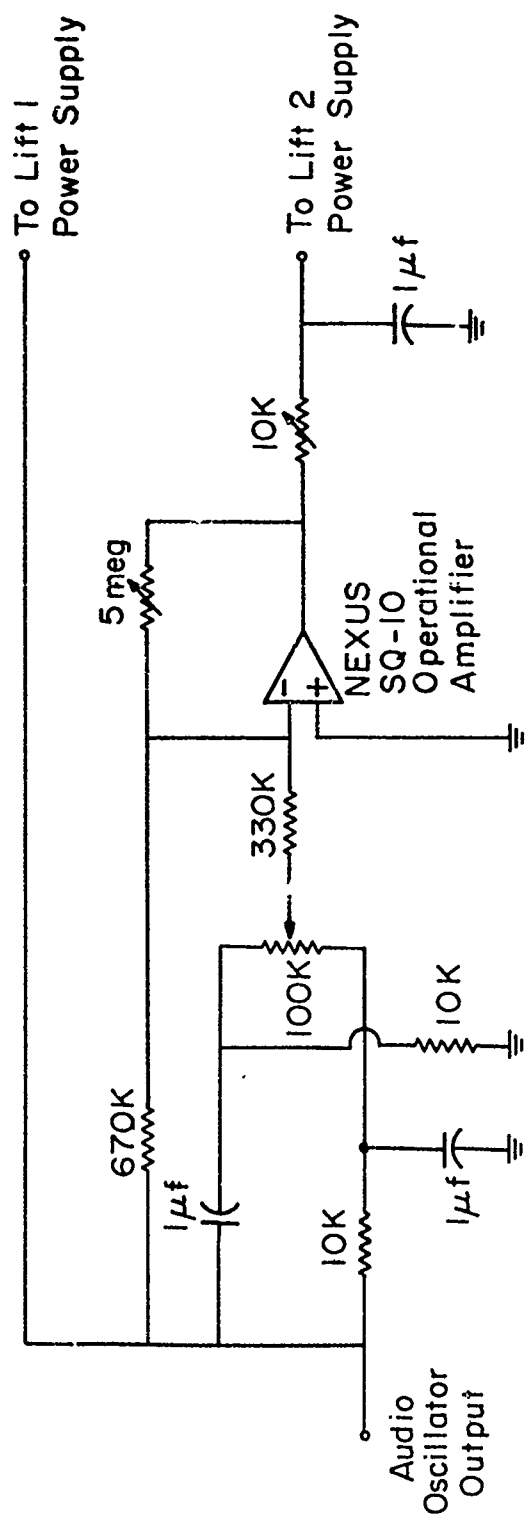


FIG. 6. Pitching Motion Forcing Circuit

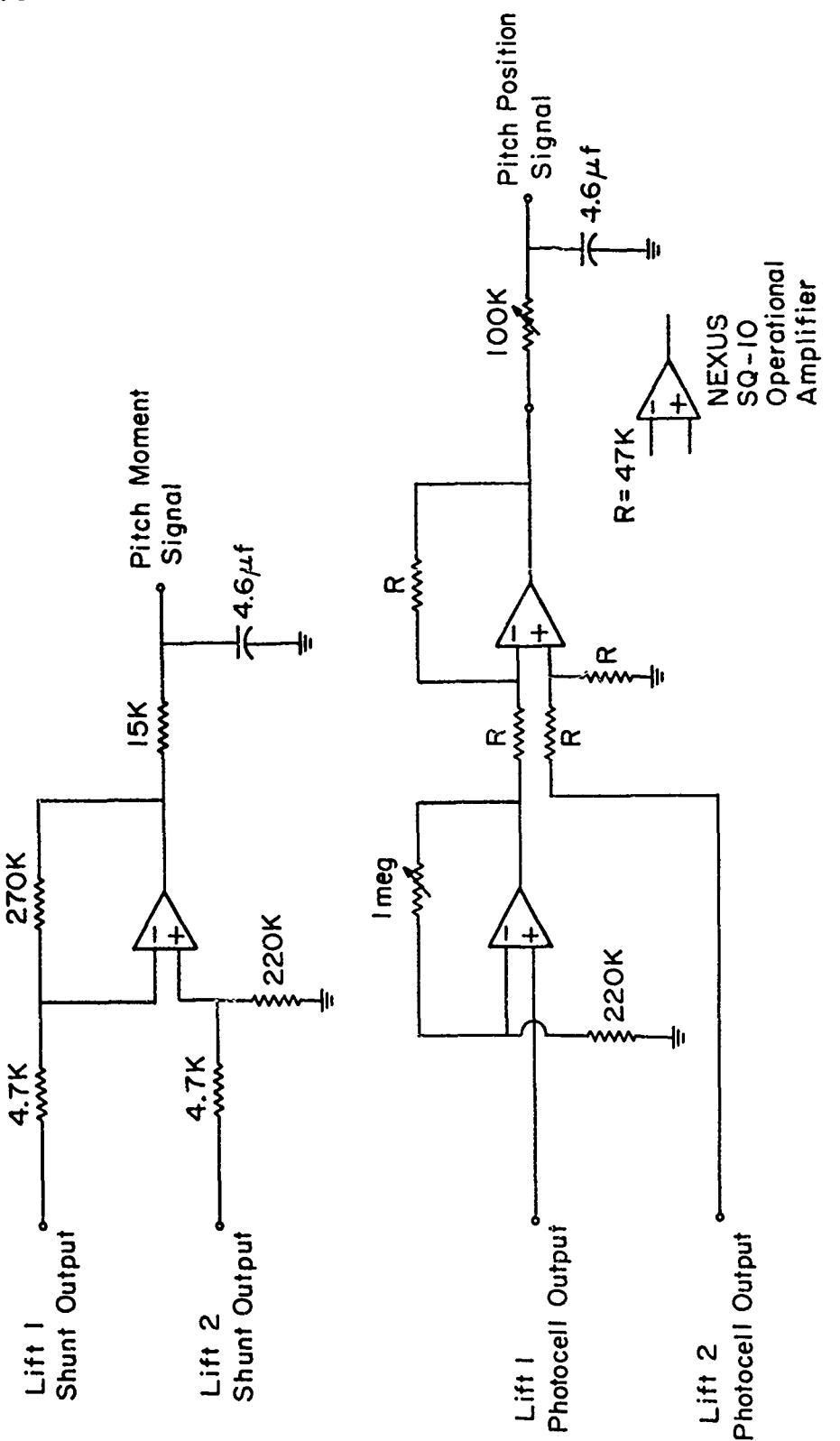


FIG. 7. Pitch Current and Pitch Position Measuring Circuits

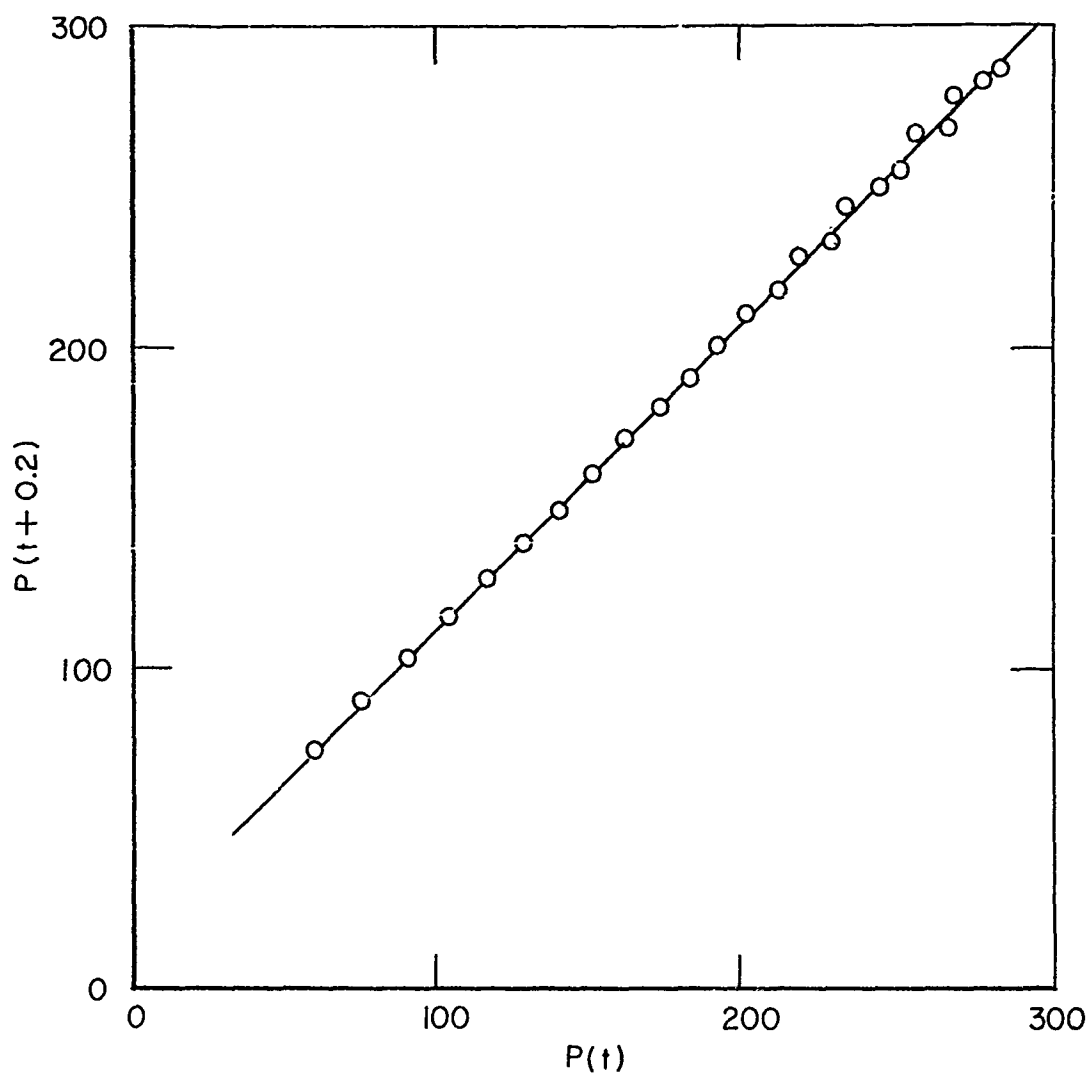


FIG. 8. Typical Roll Rate Plots Used in Determining the Damping in Roll Coefficient (see text)

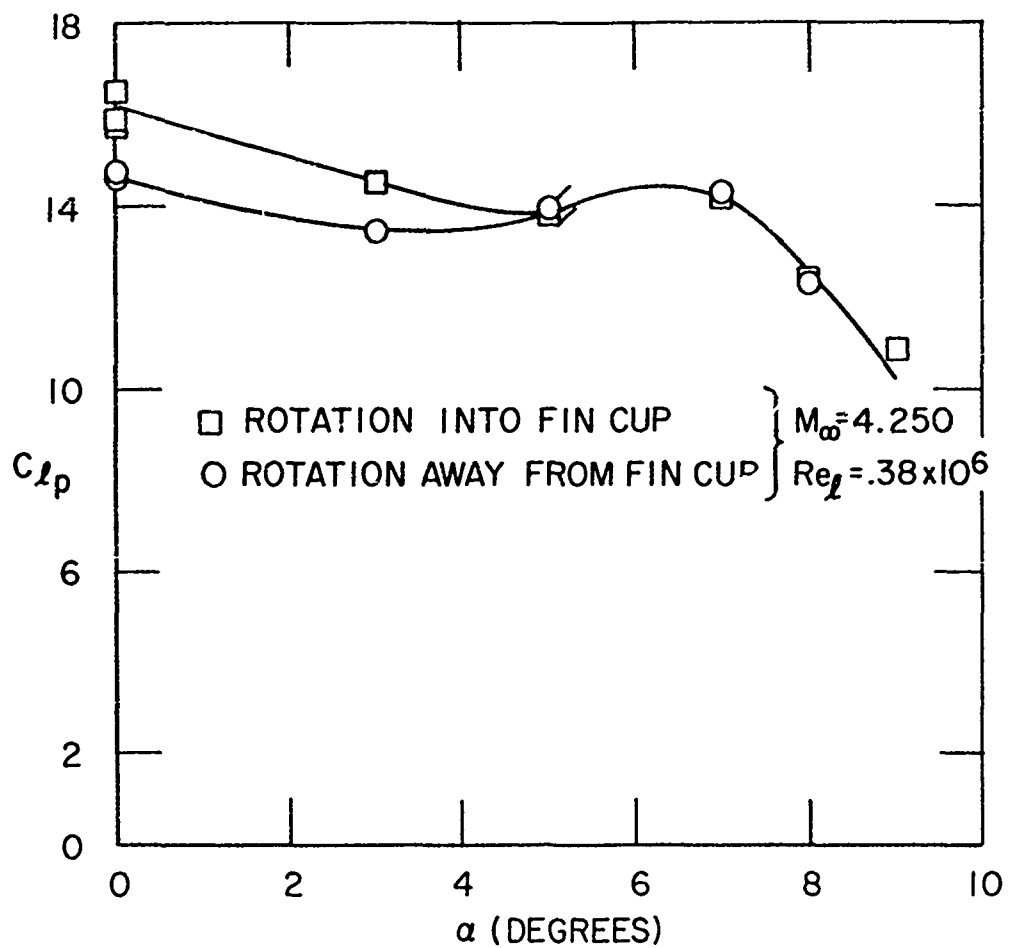


FIG. 9. Damping in Roll Coefficient Vs. Angle of Attack

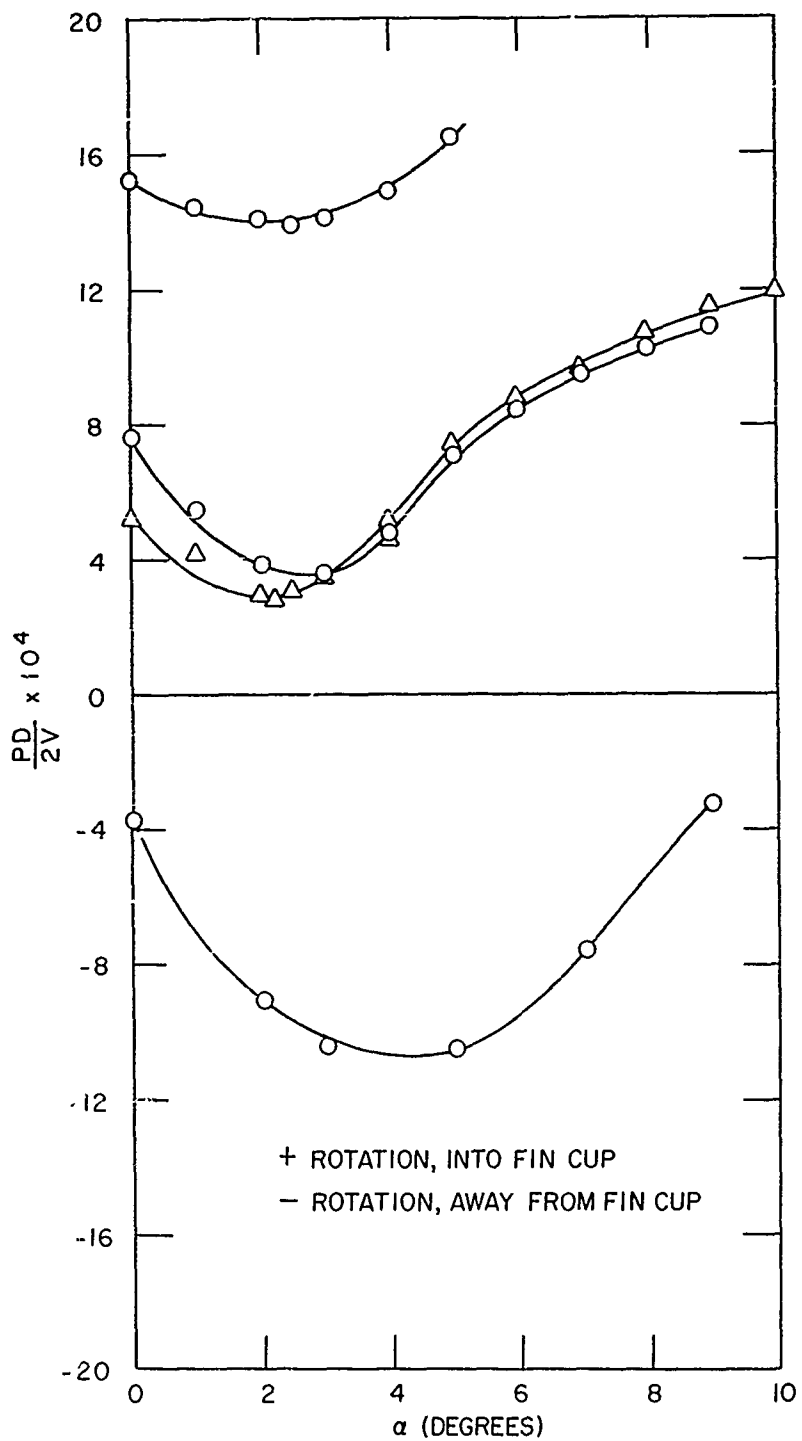


FIG. 10. Equilibrium Reduced Rolling Velocity Vs. Angle of Attack of Four Different Models Tested

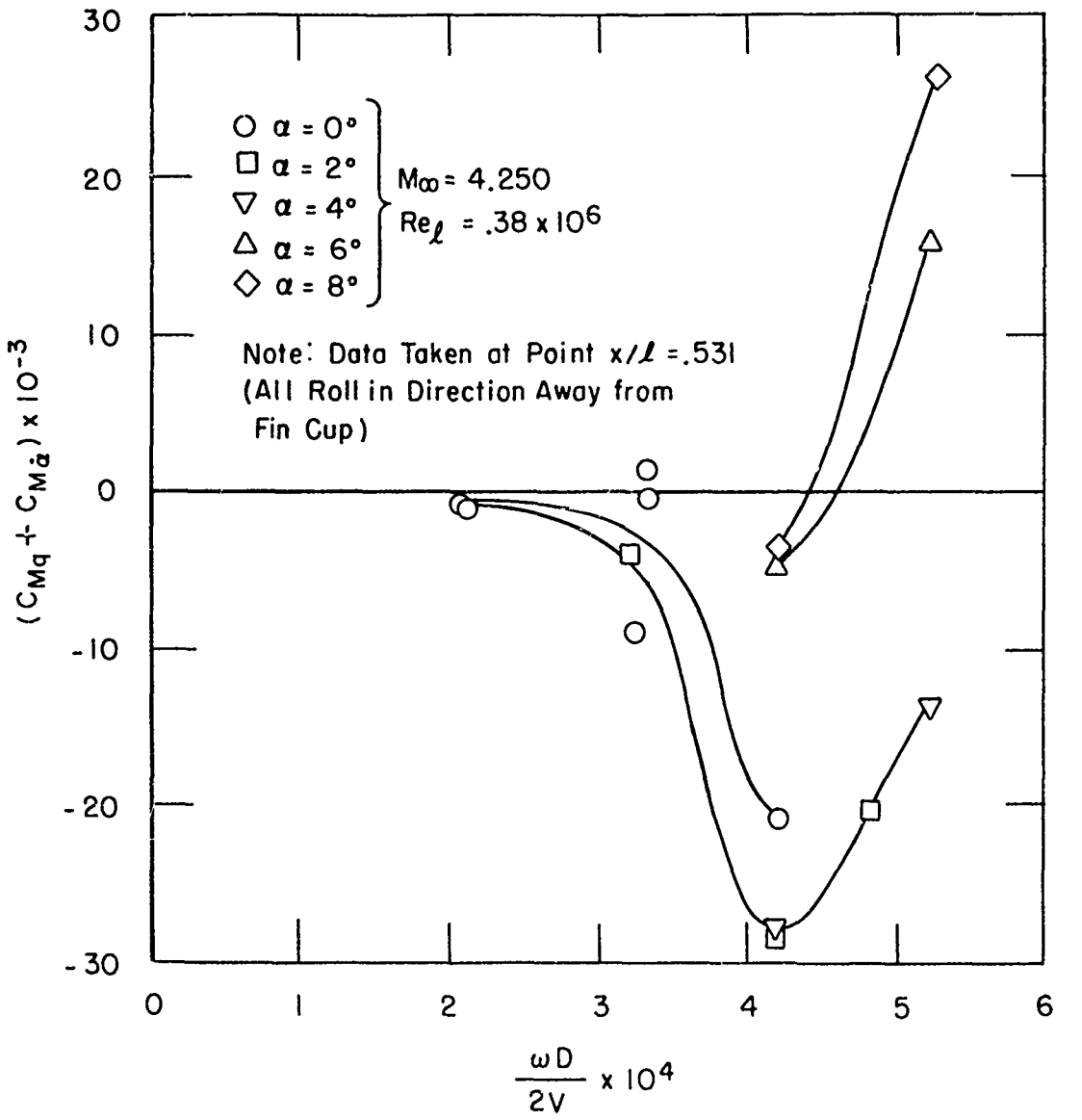


FIG. 11. Damping in Pitch Coefficient Vs. Reduced Oscillation Frequency

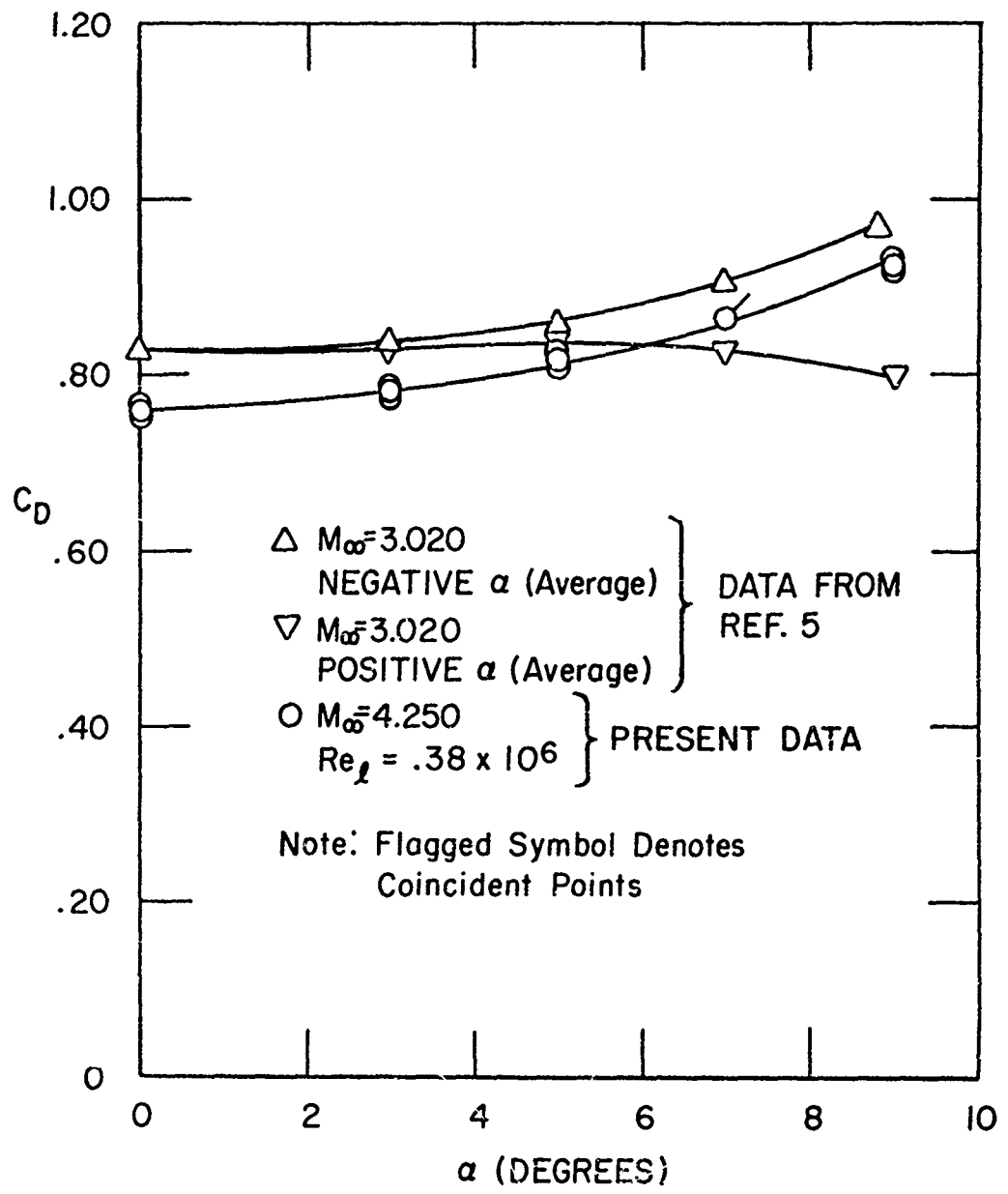


FIG. 12. Drag Coefficient Vs. Angle of Attack

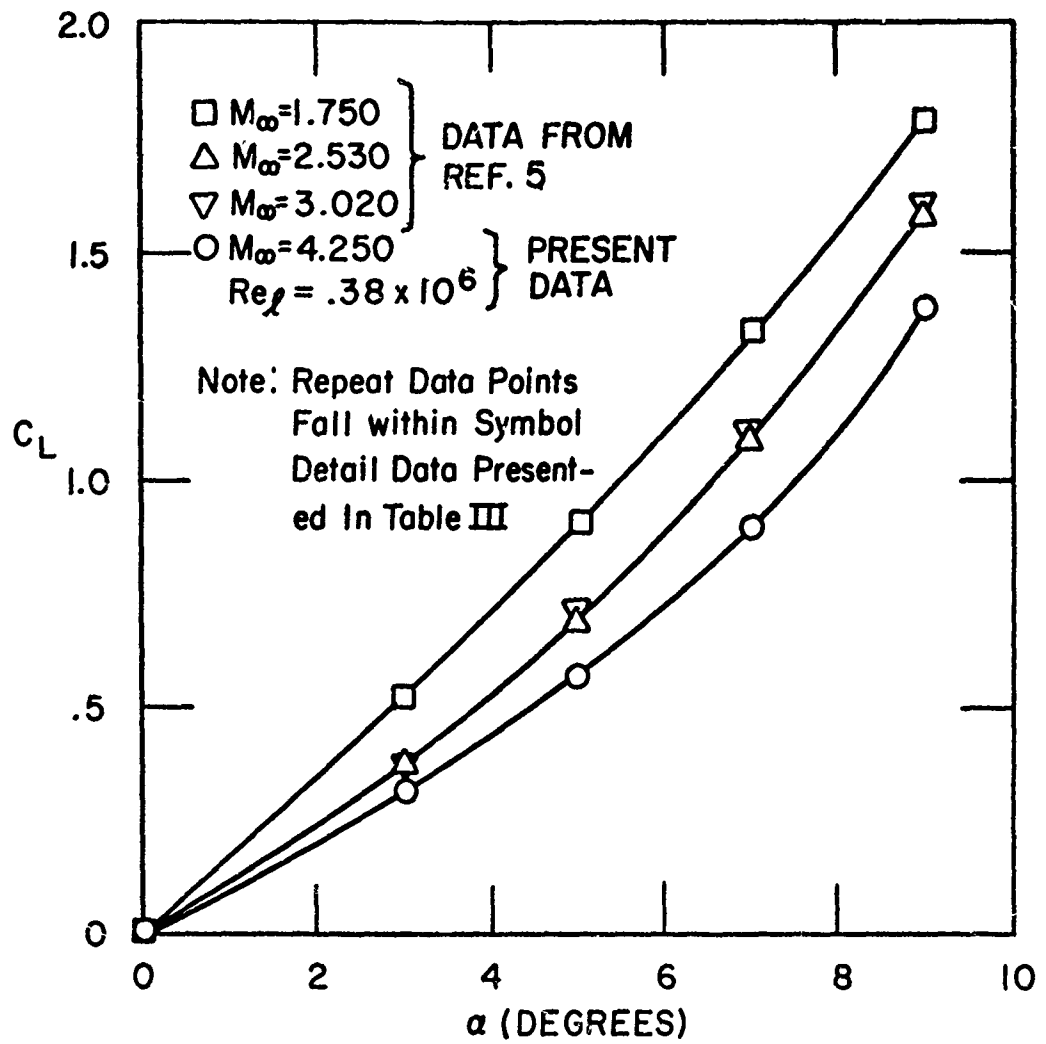


FIG. 13. Lift Coefficient Vs. Angle of Attack

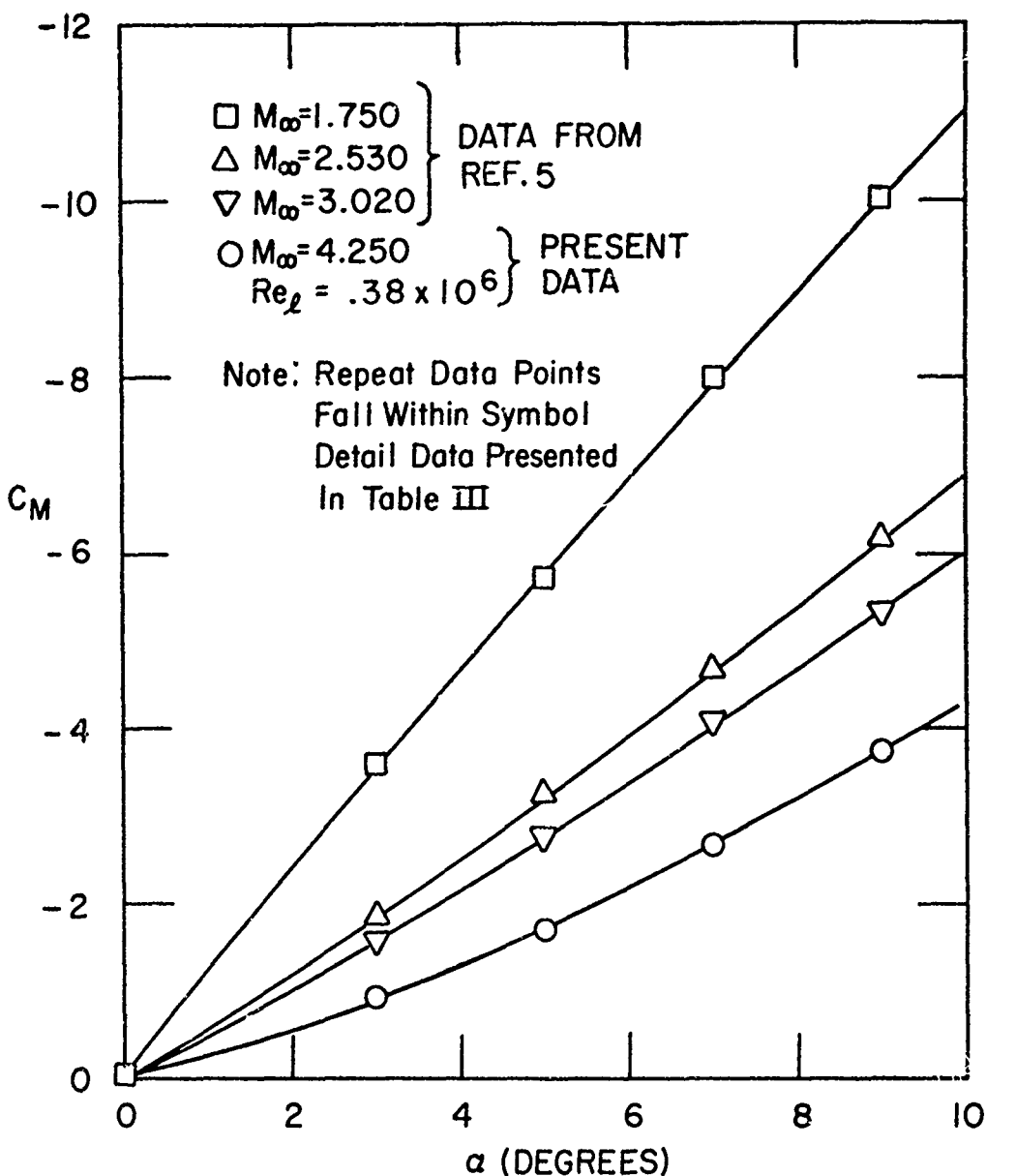


FIG. 14. Pitching Moment Coefficient Vs. Angle of Attack

BLANK PAGE

Paper No. 31

NONLINEAR AERODYNAMIC STABILITY CHARACTERISTICS OF THE
2.75 WRAP-AROUND FIN CONFIGURATION
(U)

(Paper UNCLASSIFIED)

by

John D. Nicolaides*, Charles W. Ingram**, James M. Martin***,
and Alfred M. Morrison***
University of Notre Dame
Department of Aero-Space Engineering
Notre Dame, Ind. 46556

ABSTRACT. (U) An analysis is presented of dynamic wind tunnel tests and stability evaluation for a wrap around fin configuration of the 2.75 rocket. The program consisted of one-and three-degree-of-freedom subsonic wind tunnel tests in which angular oscillations were obtained through the use of a sapphire jewel bearing support system. In addition, angular data was obtained from supersonic free flight wind tunnel tests conducted by the Jet Propulsion Laboratory. Using the Notre Dame Nonlinear Reduction Procedure, these angular oscillations were fitted to yield the restoring, damping and Magnus moment stability coefficients as nonlinear functions of angle of attack. The 3-D, and free flight wind tunnel investigations indicated that both a precession limit cycle at subsonic velocities and an instability at supersonic velocities were due to the nonlinear Magnus coefficient. Furthermore, stability evaluations for the full scale configuration indicated that a Magnus instability would occur for roll rates above the nutation frequency.

Supported by Naval Weapons Center under Contract No. N00123-68-C-2280.

* Chairman and Professor, **Instructor, *** Research Assistant.

INTRODUCTION

(U) At present tubular launched finned rockets employ high^{1,2} aspect ratio rectangular fins. To overcome the severe mechanical and structural requirements the tubular type launching apparatus imposes on the rectangular finned rockets, a wrap-around fin design has been developed by the U. S. Naval Ordnance Station, Indian Head, Maryland. This new fin configuration is currently being adapted to the 2.75 rocket. As part of the 2.75 program, the U. S. Naval Weapons Center, China Lake, California, requested the University of Notre Dame to perform wind tunnel tests and stability evaluations for this new configuration.

(U) The program, which will be presented in this report, consisted of a series of free-flight supersonic and dynamic subsonic wind tunnel tests. The free-flight tests were conducted by the Jet Propulsion Laboratory.³ The angular data resulting from these tests was reduced by the University of Notre Dame to determine the nonlinearity of the restoring, damping and Magnus moment stability coefficients with angle of attack.

(U) The dynamic tests consisted of three-degree-of-freedom and one-degree-of-freedom subsonic wind tunnel evaluations carried out at the University of Notre Dame. These tests furnished the necessary angular motions from which the nonlinearity of the restoring, damping and Magnus moment stability coefficients were determined as functions of angle of attack.

(U) A comparison of the stability coefficients resulting from the free-flight and dynamic wind tunnel tests was made with static strain gage data obtained by the U. S. Naval Ordnance Laboratory.⁴

(U) In conducting constrained dynamic wind tunnel tests, one consideration of vital importance is the type and nature of the support system utilized. In the past ball bearings were primarily used to^{5,6,7} obtain the desired oscillations, but subsequent analysis showed the results to be affected by bearing friction in the system. Consequently a

sapphire jewel system was recently designed, and ensuing analyses^{1,2,8} have shown it to be effective in reducing friction interference. With such a system, the 2.75 model is mounted on metal pins that are set into sapphire jewel cups. The sapphire jewels are synthetically fabricated, and their inherent hardness permit the pins to freely rotate on their surface with a minimum of friction. Both pitch and yaw oscillations rely on these jewel cup bearings while ball bearings are utilized for roll oscillations. This sapphire jewel bearing support system was employed for the 3-D subsonic wind tunnel tests while a system modified to constrain the model in roll and pitch was used for the 1-D tests.

(U) Numerous wind tunnel tests were conducted at subsonic and supersonic velocities so that the repeatability of the aerodynamic stability coefficients with angle of attack could be evaluated. The actual steps of the analysis used to determine the coefficients consisted of: 1) photographing the angular motions of the 2.75 rocket in the wind tunnel; 2) reducing the motions to digital values of angle of attack or angle of attack and angle of sideslip; 3) fitting the Aeroballistic Theory to the angular data to obtain the stability parameters, K_1 , λ_1 , ω_1 or $K_{N,P}$, $\lambda_{N,P}$, $\omega_{N,P}$; 4) using the stability parameters, mass parameters of the model, wind tunnel velocity, roll velocity where applicable and density, the aerodynamic stability coefficients were computed from linear and nonlinear techniques. The coefficients determined were: the pitching moment, $C_{m\alpha}$, the damping moment, $C_{mq} + C_{m\dot{\alpha}}$, and the Magnus moment, $C_{mp\alpha}$.

(U) Using the aerodynamic coefficients obtained from these tests, stability evaluations were carried out for the full-scale configuration. Employing typical inertias, thrust and launch conditions, numerical computations of the Aeroballistic Theory were made in conjunction with numerically integrated trajectory parameters and roll rate. These data furnished the pertinent stability parameters from which the flight performance of the full-scale 2.75 wrap-around fin rocket was evaluated.

AEROBALLISTIC THEORY

(U) The dynamic behavior of free-flight missiles, as well as constrained three-degree-of-freedom wind tunnel models is governed by the same differential equation, provided the normal force effects in free-flight are neglected.

LINEAR THEORY⁹

(U) For aerodynamic moments which are assumed to vary linearly with angle of attack,

$$M + iN = -iM_a \bar{\alpha} + M_Q \bar{Q} + -iM_a \dot{\bar{\alpha}} - PM_{Pa} \bar{\alpha} - iM_S \delta_e e^{iPT} \quad (1)$$

For the case where the angular displacements are referred to a fixed coordinate system, as in free flight, the solution to the governing angular equation can be written as

$$\bar{\theta} = K_N e^{(\lambda_N + i\omega_N)T} + K_P e^{(\lambda_P + i\omega_P)T} + K_T e^{iPT} + K_R \quad (2)$$

$$\text{where } \lambda_{N,P} = \frac{Q S d^2}{2V} \left[\frac{C_{Za}}{M_d} (1 \mp T) + \frac{C_{M_Q} + C_{M_a}}{2I} (1 \pm T) \pm C_{M_P} \frac{T}{I} \right] \quad (3)$$

$$\omega_{N,P} = \frac{P I_x}{2I} (1 \pm \frac{1}{T}) \quad (4)$$

$$T = \frac{1}{(1 - \gamma_s)^{1/2}} \quad (5)$$

$$S = \frac{(I \times P)^2}{4I C_{M_a} Q S d} \quad (6)$$

$$K_T = \frac{C_{M_a} \delta \epsilon Q S d}{I [i(P - \omega_N) - \lambda_N] [i(P - \omega_P) - \lambda_P]} \quad (7)$$

NONLINEAR THEORY^{10,11}

(U) For the situation where the aerodynamic moments are assumed to be nonlinear functions of the magnitude of the angle of attack,

$$-i(M+iN) = M_a(|\bar{\alpha}|)\bar{\alpha} + M_Q(|\bar{\alpha}|)\bar{\alpha} + M_{\dot{\alpha}}(|\bar{\alpha}|)\bar{\alpha} + M_{P\bar{\alpha}}(|\bar{\alpha}|)P\bar{\alpha} \quad (8)$$

where

$$M_a(|\alpha|) = M_{a0} + M_{a2}|\bar{\alpha}|^2 \quad (9)$$

$$M_Q(|\alpha|) = M_{Q0} + M_{Q2}|\bar{\alpha}|^2 \quad (10)$$

$$M_{\dot{\alpha}}(|\alpha|) = M_{\dot{\alpha}0} + M_{\dot{\alpha}2}|\bar{\alpha}|^2 \quad (11)$$

$$M_{P\bar{\alpha}}(|\alpha|) = M_{P\bar{\alpha}0} + M_{P\bar{\alpha}2}|\bar{\alpha}|^2 \quad (12)$$

The solution for the complex angle of attack is given by.¹² (It should be noted that this nonlinear theory assumes an approximate solution of the same form as the Linear Theory; however, the stability parameters now reflect the nonlinearity in the stability coefficients.)

$$\bar{\Theta} = \Theta + i\psi \quad (13)$$

$$\bar{\Theta} = K_N e^{i\phi_{NT}} + K_P e^{i\phi_{PT}} \quad (14)$$

$$K_N = K_{N0} e^{\lambda_{NT}^*}, \quad K_P = K_{P0} e^{\lambda_{PT}^*} \quad (15)$$

$$\lambda_{N,P}^* = \lambda_{N,P} + \lambda_{N,P}^V \quad (16)$$

$$\lambda_{N,P}^V = \frac{Q S d^2}{2 V} \left[\frac{2 I V}{d(P I_x)} \right]^2 C_{M a_2}^2 I_{N,P}^2 (K_{N,P} K_{N,P} + 2 K_{N,P} \dot{K}_{N,P}) \quad (17)$$

$$\begin{aligned} \lambda_{N,P} = \frac{Q S d^2}{2 V} & \left\{ \frac{[C_{M Q} + C_{M a_1}]}{2 I} \right. (I \pm I_{N,P}) + \frac{[C_{M Q} + C_{M a_1}]}{2 I} \\ & \left[[K_{N,P}^2 + K_{P,N}^2] (I \pm I)_{N,P} + K_{P,N}^2 I_{N,P} \left(\frac{1}{I_{P,N}} \pm I \right) \right] \\ & \left. \pm \left[C_{M P a_0} + C_{M P a_2} \delta_{\epsilon N,P}^2 \right] \frac{I_{N,P}}{I_x} \right\} \quad (18) \end{aligned}$$

$$\phi_{N,P} = \frac{P I_x}{2 I} (I \pm \frac{1}{I_{N,P}}) T + \phi_{N_0, P_0} \quad (19)$$

$$\omega_{N,P} = \phi_{N,P} = \frac{P I_x}{2 I} (I \pm \frac{1}{I_{N,P}}) \quad (20)$$

$$I_{N,P} = \left(1 - \frac{1}{S_{N,P}} \right)^{-\frac{1}{2}} \quad (21)$$

$$S_{N,P} = \frac{(P I_x)}{4 I (C_{M a_0} + C_{M a_2} \delta_{\epsilon N,P}^2) Q S d} \quad (22)$$

$$\delta_{\epsilon_{N,P}}^2 = K_{N,P}^2 + 2K_{P,N}^2 \quad (23)$$

(U) From references 9, 10 and 13, it has been found that a frequency variation, resulting from a nonlinear restoring moment, varying density or velocity, or any combination thereof will cause the modal amplitudes to vary in the following manner:

$$K_{N,P}(T) = \left(\frac{\omega_{N,P}(0)}{\omega_{N,P}(T)} \right)^{\frac{1}{2}} K_{N,P}(0) \quad (24)$$

COMPUTATION OF AERODYNAMIC STABILITY COEFFICIENTS

(U) To obtain aerodynamic stability coefficients from the free-flight motions, the Aeroballistic Theory is fitted to the angular orientation data, Θ , ψ . The fitting is accomplished by employing the "Wobble" computer program.¹³ This program fits the theory to short segments of the data in overlapping sections so that the stability parameters, $K_{N,P}$, $\lambda_{N,P}$, $\omega_{N,P}$, are determined as functions of time. It should be noted that the "Wobble" program fits the epicyclic equation which is assumed to be applicable for linear, as well as the nonlinear situation.

COMPUTATIONS OF LINEAR COEFFICIENTS

(U) Using $\lambda_{N,P}$ and $\omega_{N,P}$ with the velocity, dynamic pressure, roll rate, and mass parameters of the missiles the aerodynamic stability coefficients, $C_{M\alpha}$, $C_{Mq} + C_{M\dot{\alpha}}$ and $C_{MP\alpha}$ were computed as functions of time in the following manner:

$$C_{M\alpha} = \frac{\omega_N \omega_P 8 I}{\pi \rho d^3 V^2} \quad (25)$$

$$C_{Mq} + C_{M\dot{\alpha}} = \frac{2 I V}{Q S d^2} (\lambda_N + \lambda_P) \quad (26)$$

$$C_{MPa} = \pm \frac{Ix}{T} \left[\frac{2V}{QSd}^2 (\lambda_N, \lambda_P) - \frac{1}{2I} (C_{MQ} + C_{M\dot{a}}) (I \pm T) \right] \quad (27)$$

COMPUTATION OF NONLINEAR COEFFICIENTS

(U) The nonlinear aerodynamic stability coefficients $C_{M\dot{a}}(|\dot{\alpha}|)$, $C_{MQ}(|\dot{\alpha}|) + C_{M\dot{a}}(|\dot{\alpha}|)$ and $C_{MPa}(|\dot{\alpha}|)$ were computed as polynomial functions of angle of attack from the stability parameters as follows:

$$\omega_N \omega_P = \left[\frac{C_{M\dot{a}0}}{I} + \frac{C_{M\dot{a}2}}{I} \delta_a^2 \right] QSd \quad (28)$$

where

$$\delta_a^2 = K_N^2 + K_P^2 + \frac{K_N^2 \omega_N - K_P^2 \omega_P}{\omega_N - \omega_P} \quad (29)$$

Using a least squares technique to fit a straight line to $\omega_N \omega_P$ versus δ_a^2 yields $C_{M\dot{a}0}$ as the intercept and $C_{M\dot{a}2}$ as the slope.

(U) Correcting λ_N^* and λ_P^* by determining λ_N^V and λ_P^V from a logarithmic technique developed in reference 13, the actual damping rates λ_N and λ_P are fitted simultaneously with a least squares procedure to yield $(C_{MQ} + C_{M\dot{a}})_0$, $(C_{MQ} + C_{M\dot{a}})_2$, C_{MPa0} and C_{MPa2} .

1-D MOTIONS

(U) For one-degree-of-freedom pitching or yawing motion the solution for the angular response is given as:

$$\Theta = \Theta_T + K e^{\lambda T} \cos(\omega T + \delta) \quad (30)$$

The restoring and damping stability coefficients are computed as:

For the linear case

$$C_{M\dot{a}} = -\frac{2I\omega^2}{\rho V^2 S d} \quad (31)$$

$$C_{MQ} + C_{M\dot{a}} = \frac{8I\lambda}{\rho V S d} \quad (32)$$

For the nonlinear case,

$$\omega = \left\{ QSD \left\{ \frac{C_{M\dot{a}0}}{I} - \frac{3}{4} \frac{C_{M\dot{a}2}}{I} K^2 \right\} \right\}^{\frac{1}{2}} \quad (33)$$

$$\lambda = \frac{QSD^2}{2\nu} \left\{ \frac{\{C_{MQ} + C_{M\dot{a}}\}_0}{2I} + \frac{\{C_{MQ} + C_{M\dot{a}}\}_2}{8I} K^2 \right\} \quad (34)$$

The non-linear stability coefficients are determined by a least squares fitting procedure applied to the above equations for λ and ω . It should be noted that the damping rate, λ , has been corrected as in the complete non-linear case.

(U) The Aeroballistic Theory was fitted to the angular oscillations of both the wind tunnel and free-flight configurations by using the

"WOBBLE" computer program. By employing over-lapping sectional fits of small segments of data, the non-linearity of the stability coefficients is determined. The nonlinear computation assumes that the sectional fits are chosen such that the stability parameters, $K_{N,p}$, $\lambda_{N,p}$, and $\omega_{N,p}$, are relatively constant over this portion. For the case where the stability coefficients are nonlinear functions of the magnitude of the angle of attack, as specified in Eq. 8, this procedure has proven to yield extremely accurate results.

(U) In the following sections the Non-Linear Theory and data reduction technique is applied to angular oscillations of missiles in the wind tunnel as well as free flight wind tunnel tests.

EXPERIMENTAL TECHNIQUE¹⁵

(U) The model tested had a curved or wrap around fin configuration. A schematic representation of this configuration is given in Fig. 1.

INERTIA MEASUREMENT¹⁶

(U) The torsional pendulum method was used to determine the transverse and longitudinal moments of inertia, I and I_x for the model. Using the torsional technique, the inertial moments were first computed for a test mass of known density and cross section. These results were then compared to inertial moments computed strictly from theoretical considerations, with errors of small magnitude resulting. The accuracy of the experimental results was thereby confirmed.

1-D WIND TUNNEL TESTING PROCEDURE^{1, 15, 16}

(U) The Notre Dame low turbulence subsonic wind tunnel was used for the 1-D tests. A wind tunnel velocity of approximately 57 ft. /sec. was used throughout these tests, and an initial angular displacement of approximately 30° was imposed. Three wind tunnel tests were conducted at each of three different roll orientations so that repeatability of the aerodynamic data with angle of attack could be evaluated.

(U) The model was supported in the wind tunnel, as pictured in Fig. 2 on a one-degree-of-freedom jewel bearing support system which allowed it to freely oscillate. This support system was mounted on the floor of a 2 by 2 ft. test section.

(U) To obtain the 1-D angular motion in the wind tunnel a moving camera technique was employed. This technique consisted of a still camera, with its shutter open, propelled along a stationary track. A schematic of the wind tunnel set up is shown in Fig. 3, 4. The model

was illuminated by a strobe light which flashed every 0.5 seconds.

1-D DATA REDUCTION PROCEDURE

(U) The 1-D angular oscillations were converted to digital values of angle of attack on the optical comparator from the still negative pictures, a print made from one of these negatives is shown in Fig. 5. Two reference marks were painted on a rod inserted into the side of the wind tunnel, as can be seen in Fig. 6. The distance between the two fixed reference marks on the rod was actually measured. This measurement furnished the necessary factor for converting picture units to wind tunnel units.

3-D WIND TUNNEL TESTING PROCEDURE^{2,8}

(U) The Notre Dame low turbulence subsonic wind tunnel was used for the 3-D tests of the model. Small fin tabs were added, in order to obtain uniform roll rate during the 3-D testing. The addition of these tabs resulted in steady state rolling velocities which ranged in magnitude from 29 to 31 rad/sec. A wind tunnel velocity of 57 ft/sec was used for all the tests, and initial angular displacements of 10 to 12 degrees were imposed. Under these conditions numerous wind tunnel tests were made so that the repeatability of the aerodynamic data with angle of attack might be effectively evaluated.

(U) The model was mounted in the wind tunnel on a three-degree-of-freedom jewel bearing support system. Such a support allowed the model to pitch freely on two sapphire jewel bearings and simultaneously yaw on a sapphire cup, as indicated schematically in Fig. 7. Steady-state rolling motions were obtained by allowing fore and after body sections of the model to oscillate on roller bearings, while the middle section of the model was completely constrained on the mounting apparatus. The entire support system was mounted on the floor of a 2 by 2 ft. test section.

(U) To obtain 3-D angular motions in the wind tunnel, the model was displaced to an initial angle of attack and then released. The subsequent oscillations were recorded by a Fastex motion picture camera, and for this purpose a mirror was mounted at the rear of the test section at a 45 degree angle to both the model and the camera. Film speeds of 300 to 400 frames/sec were used to photograph the tunnel

Vol. 3

motions throughout the testing. This entire test setup is diagrammed in Fig. 8 and on an actual photograph shown in Fig. 9.

3-D DATA REDUCTION PROCEDURE

(U) The 3-D angular oscillations were converted to digital values of angle of attack and angle of side slip from the motion pictures. Two reference marks were painted on a thin wire suspended from the test section structure at the rear of the model, and a reference mark was painted on the tail of the model. The distance between the two fixed reference marks or the suspended wire was accurately measured. This measurement furnished the necessary factor for converting picture units to wind tunnel units. Likewise the distance from the C.G. of the model to the tail reference point was measured. The distance provided a means of computing angle of attack and angle of sideslip from the optical comparator readings. A diagram of the actual distances used in determining these angles is presented in Fig. 10. The recorded angular data were marked as functions of time by exposing the film to a timing mark every .01 sec while the moving pictures were being taken. The definition of forces and moments and an outline of the reduction procedure are presented in Figs. 11 and 12.

THREE-DEGREE-OF-FREEDOM TEST RESULTS

(U) The primary objective of the test program was to determine the aerodynamic stability coefficients for the wrap around configuration under the imposed testing conditions, and to examine the repeatability of these coefficients with angle of attack.

OBSERVED 3-D WIND TUNNEL MOTION

(U) The wrap around configuration used for testing was designed without fin cant; hence it was necessary to employ small tabs on the trailing edge of the fins to induce a rolling velocity. A schematic of these tabs is presented in Fig. 1. As a result of the rolling velocity, the wrap around configuration could be excited such that a nutation, K_N , limit cycle existed at higher angles of attack while a precession, K_p , limit cycle existed at low angles. In order to obtain reduceable motions, the model was excited into a predominately nutation mode

and allowed to damp to the precession limit cycle. The amplitude of this cycle was approximately 3 degrees. The limit cycle consisted of a single mode of oscillation. In such an oscillation the nutation mode approached zero while the precession remained constant. The precession damping rate must approach zero, while the nutation damping rate will maintain a relatively large negative value.

ANALYSIS OF 3-D SYSTEM

(U) Because of the construction of the 3-D jewel bearing support system, the pitch and yaw oscillations are obtained on individual bearings. The pitch oscillations depend on two jewel cup bearings which rest on sensitive pins. The yaw oscillations depend upon one jewel bearing located at the base of the strut support. This arrangement is illustrated in Fig. 7.

(U) It was found that the most advantageous mode for initial displacement was obtained when the yaw plane contained the larger component of the complex angular motion. With such modes of excitation one bearing primarily carried the large angular oscillations; hence the frictional interference effects were minimized while subjecting the fins to the strut-wake region for a minimal amount of time. Consequently only the yaw-mode oscillations were used for the evaluation of the nonlinear stability coefficients.

3-D DATA REDUCTION

(U) The Wobble computer program was used to fit the Aeroballistic Theory to the 3-D oscillations obtained from the wind tunnel tests. The angular data for the wrap around fin configuration was digitized at every 0.5 sec. This data was fitted in segments of 2.3 cycles of the elliptical motion, with each segment containing approximately 90 data points. Each test consisted of approximately 210 points. By employing fits of overlapping sections of data the nonlinear variation of the stability parameters was obtained as a function of time. The stability parameters, $K_{N,p}$, $\lambda_{N,p}$, were determined by the Wobble program at a time interval of 0.1 sec. The average percent error of fit of the theory to the data indicated that the epicyclic equation, Eq.(14), represented the recorded wind tunnel motions to within an accuracy of 2.5%. Representative complex angle of attack probable error of fit and stability parameters are presented in Figs. 13 through 15.

ANALYSIS OF 3-D STABILITY PARAMETERS

(U) The stability parameters shown in Fig. 15 indicate the presence of a precession limit cycle at approximately 4 degrees angle of attack. This is shown by the fact that the nutation mode, K_N , damps more rapidly than the precession mode, K_p . Also the trends in the damping rates, $\lambda_{N,P}$, show that the precession damping rate will maintain a negative value. As shown in these stability parameters the damping rates are nonlinear functions.

3-D LINEAR STABILITY COEFFICIENTS

(U) In order to obtain an indication of the nonlinearity of the stability coefficients with angle of attack, the aerodynamic stability coefficients were computed from the stability parameters using the Linear Aeroballistic Theory, Eq. 1 through 6. These coefficients are presented in Fig. 16.

(U) The computed values of the pitching moment stability coefficients, $C_{M\dot{a}}$, are shown to vary nonlinearly with time. Very good repeatability was noted in $C_{M\dot{a}}$ for all runs. An average value of $C_{M\dot{a}}$ was computed for an 8 degree mean angle of attack indicating that the maximum duration was less than 3%.

(U) The damping moment coefficient exhibited a lesser degree of repeatability. The damping moment coefficient seemed to be more sensitive to the frictional characteristics associated with the individual bearings of the support system than was $C_{M\dot{a}}$. The repeatability with angle of attack was still very good. $C_{Mq} + C_{M\dot{a}}$ was found to vary nonlinearly with angle of attack as is shown in Fig. 16. An average value of $C_{Mq} + C_{M\dot{a}}$ was computed for a mean angle of attack of 8°, and the corresponding maximum duration in the damping coefficient was less than 8%.

(U) The Magnus stability coefficient, $C_{MP\dot{a}}$ is also nonlinear with angle of attack, but it experiences scattering as the time increases. It was found that the calculation of the Magnus coefficient is more sensitive than that of the damping coefficient. This arises from the fact that $C_{MP\dot{a}}$ is determined from a difference in the damping rates, while $C_{Mq} + C_{M\dot{a}}$ is computed from the sum of the damping rates. Because the damping rates are of the same order of magnitude, the subtraction operation is more critical than the addition. The

determination of this difference in the damping rates in the vicinity of the precession limit cycle becomes even more critical, since the precession damping rate is approaching zero. Thus, scatter is experienced in the Magnus coefficient in the region of the limit cycle.

3-D NONLINEAR STABILITY COEFFICIENTS

(U) To get a more precise indication of the nonlinear variation of the stability coefficients with angle of attack, the Nonlinear Aeroballistic Theory, Eqs. 8 through 24 was employed. Using this nonlinear theory, the stability coefficients were determined as polynomial functions of the angle of attack, as defined in Eq. 8. The nonlinear evaluation of the stability coefficients is presented in Fig. 17 through 19. These plots represent C_{Mq} , restoring, $C_{Mq} + C_{M\dot{q}}$, damping, and C_{Mp} , the Magnus moment stability coefficients as functions of angle of attack. Also shown in these plots is the average of the coefficients for the two tests conducted.

(U) In comparing the linear and nonlinear coefficients computations, it was found that the linear results had the same trends with angle of attack as the nonlinear. However, a more pronounced variation of the nonlinear coefficients was seen in these data. C_{Mp} , the Magnus moment coefficient was seen to be highly nonlinear with angle of attack in this respect.

(U) By using overlapping fits, the linear evaluation of the stability coefficients will reveal nonlinear trends. However, to accurately determine the variation with angle of attack, the nonlinear theory must be employed.

3-D DYNAMIC BEHAVIOR

(U) As predicted by Eqs. 3 and 18, the degree of damping for each mode is dependent on the relative signs and magnitudes of the damping and Magnus moment stability coefficients, $C_{Mq} + C_{M\dot{q}}$ and C_{Mp} . At low angles of attack, the negative values obtained for both, act to stabilize the nutation mode; K_N , while destabilizing the precession mode, K_p . At larger angles of attack the Magnus coefficient predominates to assure damping of the precession mode; as well as the nutation mode. As the angle of attack is reduced, however, the Magnus coefficient assumes increasingly larger negative values, the

Vol. 3

damping coefficient becomes small negatively, until a point is reached at which the precession damping rate is zero. At this point the dynamic behavior is characterized by a precession limit cycle.

ONE-DEGREE-OF-FREEDOM TEST RESULTS

(U) The wrap around fin configuration was tested at three different roll orientation angles as shown in Fig. 20. During this phase of the testing the fin tabs were removed.

(U) The model was initially disturbed to an angle of attack of approximately 30° and then allowed to oscillate freely. The resulting angular motions were then recorded by the moving camera technique.

1-D DATA REDUCTION

(U) The "Wobble" computer program was used to fit the 1-D Aeroballistic Theory to the angular oscillations obtained from the moving camera technique. This data was fitted in segments of 1.8 cycles, with each segment containing approximately 28 points. The stability parameters $K_1, K_T, \lambda_1, \omega_1$ were determined by the Wobble program at a time interval of 0.2 sec. The average percent error of the theory to the data showed an error of less than 3%. A representative plot of probable error of fit vs time is shown in Fig. 22.

(U) The stability parameters were obtained from the fits as functions of time, representative angular oscillations, probable errors of fit, and stability parameters are presented in Fig. 21 through 26. The resulting stability coefficients versus time are presented in Figs. 27 and 28.

1-D NONLINEAR STABILITY COEFFICIENTS

(U) To get an indication of the nonlinearity of the stability coefficients with angle of attack, the 1-D Nonlinear Aeroballistic Theory was employed. Using this nonlinear theory, the stability coefficients were determined as polynomial functions of the angle of attack. Representative plots of runs made at a single roll orientation angle are presented in Fig. 29 and 30. Also shown in these plots is the average of the coefficients for three tests conducted at the given roll orientation.

(U) Both C_{Mq} , the pitching moment coefficient and $C_{Mq} + C_{M\dot{a}}$, the damping moment coefficient were found to vary linearly with angle of attack. Both were found to be highly repeatable. C_{Mq} varied no more than 1% about its mean, while $C_{Mq} + C_{M\dot{a}}$ varied less than 6% about its mean.

ROLL ORIENTATION EFFECTS

(U) A plot of C_{Mq} , the pitching moment coefficient as a function of roll orientation is presented in Fig. 31. The general trend of the coefficient is to decrease nonlinearly with increase in the roll orientation angle. A plot of $C_{Mq} + C_{M\dot{a}}$, the damping moment coefficient as a function of roll orientation is presented in Fig. 32. The general trend of the coefficient is to nonlinearly decrease then level off with increase in roll orientation angle.

COMPARISON OF 3-D, 1-D, STRAIN GAGE RESULTS

(U) Values for C_{Mq} from each phase of the testing program are presented in Fig. 33. The results are in agreement with a maximum deviation of less than 6%. Existing differences may be attributed to use of fin tabs during the three-degree-of-freedom test program which would cause an increase in fin plan form area, and to the higher Mach number at which the strain gage tests were performed.

(U) A plot of $C_{Mq} + C_{M\dot{a}}$ vs α is presented in Fig. 34 for both the one-and three-degree-of-freedom cases. Differences in the damping moment coefficient are seen to result for the two testing procedures.

FIN TAB EFFECTS

(U) Discrepancies in the damping moment coefficient data between the one and three-degree-of-freedom cases caused further investigation into the effects of fin tabs on the three-degree-of-freedom model. Fin tabs placed on the outermost tips of the three curved fins produced a precession limit cycle at small angles of attack. However, tabs placed on the innermost tip of the fins, at the edge of the body surface, caused a nutation limit cycle at small angles. Also, the size of the limit cycle could be regulated by the size of the fin tabs. This dependence of the aerodynamic stability coefficients upon the size and

8th Navy Symposium on Aeroballistics

Vol. 3

position of fin tabs reveals a need for further study of the aerodynamic characteristics of curved fins.

FREE FLIGHT WIND TUNNEL TEST RESULTS

(U) The wrap around fin configuration was fired supersonically with a compressed air gun in the Jet Propulsion Laboratory wind tunnel. The angular motions were recorded with a high speed camera and then converted with an optical comparator to angular oscillations as a function of time. These data were then sent to Notre Dame for nonlinear evaluation.

FREE FLIGHT DATA REDUCTION

(U) The Wobble computer program was again used to fit the aeroballistic theory to the free-flight oscillations. The average percent error of fit of the theory to the data indicated that the epicyclic equation, Eq. 14, represented the recorded free flight wind tunnel motions to within an accuracy of 2.8%. Representative complex angles of attack, probable error of fit and stability parameters are presented in Figures 35 through 42.

ANALYSIS OF FREE FLIGHT STABILITY PARAMETERS

(U) The free flight motion was characterized by a growing nutational mode, Fig. 37, and a damping precessional mode, Fig. 38. The nutation damping rate, λ_N , and frequency, ω_N , grew with increasing time, Fig. 39 and 41, while λ_P and ω_P tended to oscillate about a mean, Fig. 40 and 42. This oscillation was caused by the immediate damping of the precession mode to a negligible value. An over all look at the stability parameters reveals nonlinear trends in both the damping rates and frequencies.

FREE FLIGHT NONLINEAR STABILITY COEFFICIENTS

(U) The Nonlinear Aeroballistic Theory, Eqs. 8 through 24 was employed to define the nonlinear variation of the stability coefficients with angle of attack. According to the Nonlinear Theory, Eq. 8, the stability coefficients were determined as polynomial

functions of angle of attack. The nonlinear evaluation of the stability coefficients for the free flight data is presented in Figures 43 through 45. The plots represent C_{Mq} , pitching, $C_{Mq} + C_{M\dot{q}}$, damping, and $C_{Mp\dot{q}}$, Magnus, the stability coefficients, as functions of angle of attack.

(U) Fig. 43 shows a plot of C_{Mq} vs angle of attack. A comparison is made with strain gauge data, obtained by the Naval Ordnance Laboratory and free-flight results. The two sets of data exhibit similar hard spring restoring moments with a maximum deviation at 0° of 7.5 per cent.

(U) Fig. 44 shows a plot of $C_{Mq} + C_{M\dot{q}}$ versus angle of attack. The damping moment exhibits a small nonlinear variation with increased angle of attack.

(U) Fig. 45 represents a plot of $C_{Mp\dot{q}}$ versus angle of attack. It can be noted that the high positive values of the Magnus coefficient caused the nutation damping instability. $C_{Mp\dot{q}}$ is seen to be a highly nonlinear function of angle of attack. Since the free flight wind tunnel model exhibited a Magnus instability, a stability evaluation was carried out for the full-scale configuration.

ANOMALOUS ROLL BEHAVIOR

(U) The presence of possible Magnus problems indicated a need for some knowledge of the rocket's roll history. The rolling motion of the subsonic wind tunnel model was noted by holding the rocket at various angles of attack. As the angle of attack increased, the model's spin rate also increased. In the supersonic free flight case, roll rates were calculated from the data film. A typical free-flight roll history is plotted in Fig. 46 as a function of time and angle of attack. The curve indicates an increasing roll rate with both increasing angle of attack and time.

FULL SCALE STABILITY EVALUATION

(U) The translational equations were numerically integrated for typical ground to ground launch conditions. All mass and flight parameters plus a list of thrust as a function of time and drag coefficient as a function of Mach number are recorded in Table 1.

Vol. 3

These data were used to determine a typical flight trajectory. The resulting velocity profile and altitude are plotted as a function of range in Fig. 47. A thrust roll torque, roll damping and fin cant driving moment were chosen to produce the necessary roll histories. By varying the fin cant it was possible to roll the missile above or below resonance.

(U) For the typical flight situation, a fin cant was chosen such that the 2.75 rolled through resonance and maintained a steady state roll rate above the nutation frequency. For this case Fig. 48 shows plots of $\omega_{N,P}$, P and K_T versus time. The roll rate jumps above the nutation frequency immediately. At burnout, P decays to a terminal rate of $2\omega_N$. Also, the non-rolling trim of 0.5 degrees grows to 7.5 degrees at resonance. Fig. 49 represents K_T as a function of roll rate divided by the nutation frequency. This curve describes the magnification in the non-rolling trim at resonance, $P/\omega_N = 1$, and shows K_T damping to approximately 1.8 degrees as P approaches P steady state. The terminal point occurs at $P/\omega_N = 2$. Fig. 50 represents $\lambda_{N,P}$ as a function of time. Both damping rates grow initially as the configuration rolls through resonance. However, it can be noted that λ_N remains positive throughout the flight predicting a Magnus instability. This is completely analogous with the supersonic free flight case where the roll rate was greater than ω_N .

(U) The fin cant was then reduced to keep the roll rate below the resonance frequency. A typical trajectory for the reduced fin cant is described in Fig. 51 where $\omega_{N,P}$, P and K_T are plotted as functions of time. The roll rate reaches a maximum at burnout of 28 then damps to a terminal rate of approximately $\omega_N/3$. It is interesting to observe that the non-rolling trim magnifies from an initial amplitude of 0.5 degrees to about 7 degrees and retains this amplitude throughout the trajectory. This indicates the possibility of a resonance problem at low rolling velocities. Fig. 52 shows this magnification in K_T as a function of P/ω_N . Fig. 53 presents $\lambda_{N,P}$ as a function of time. It is important to note that the negative sign of λ_N indicates that the Magnus instability has been eliminated.

(U) So, for typical flight conditions, rolling velocities above the nutation frequency cause a Magnus instability. By reducing the rolling velocity below ω_N , the Magnus instability is eliminated, but a resonance problem arises which could give rise to Roll Lock-In and Catastrophic Yaw. However, if Roll Lock-In and Catastrophic Yaw can be avoided, the Resonance condition and resulting rolling trim could adversely effect the dispersion of the 2.75.

CONCLUSIONS AND RECOMMENDATIONS

(U) An analysis of dynamic wind tunnel tests and stability evaluation for a wrap around fin configuration of the 2.75 rocket has been presented. The restoring, damping, and Magnus moment stability coefficients were determined from both subsonic and supersonic wind tunnel data as nonlinear functions of angle of attack.

(U) The wind tunnel investigation indicated that:

- 1) the aerodynamic stability coefficients, particularly Magnus, are highly nonlinear functions of angle of attack.
- 2) a Magnus instability exists.
- 3) the Magnus instability can be changed with fin tabs.
- 4) roll speed up occurs for low values of angle of attack.

(U) Using full scale mass parameters and aerodynamic coefficients obtained from supersonic wind tunnel data, the Aeroballistic Theory was applied to a typical launch condition. The resulting stability evaluations indicated that a Magnus instability would be encountered for roll rates above Resonance. For roll rates below Resonance, there was no Magnus instability. However, a large magnification of the non-rolling trim resulted. The initial K_T of 0.5 degrees was amplified to approximately 7.0 degrees for the entire flight. Because of the variation in manufacturing asymmetries, the resulting non-rolling trim for actual flights could have severe effects on dispersion.

(U) It is felt that further subsonic and supersonic, 3-D and free-flight wind tunnel tests should be conducted to better establish the nonlinearity of the damping and Magnus moment coefficients. In addition, the effects of fin tabs should be explored as a possible means for controlling the Magnus characteristics. In these wind tunnel tests various fin configurations should be employed to better define

Vol. 3

an optimum fin design.

(U) The anomalous roll behavior associated with the wrap around fin and its possible adverse effects on the Magnus contribution to stability emphasize the urgent need for special investigations of roll histories. For these wind tunnel tests, a 2.75 model with wrap around fins should be designed for one-degree-of-freedom rolling motion only. In this manner, the transient roll behavior can be recorded and the associated roll moments can be obtained for the complete Mach number flight regime.

(U) Full scale free-flight tests should be performed to substantiate the wind tunnel and stability evaluations. Those flights should be instrumented to obtain the angle of attack and roll time-histories. Data reduction of these angular motions will then yield aerodynamic stability coefficients for the actual flight situations.

(U) Because of the mechanical and structural advantages of the wrap around fin for tubular launching, further wind tunnel and free-flight tests should be carried out to insure excellent flight performance.

REFERENCES

1. Butler, Carroll B., "2.75 FFAR Large Yaw Dynamics." Master's Thesis, Aero-Space Engineering Department, University of Notre Dame, 1967.
2. Ingram, Butler, Martin, Vazquez, "A Three-Degree-of-Freedom Wind Tunnel Testing Procedure." Presented at conference on Dynamics and Aerodynamics of Bomblets, Eglin Air Force Base, Florida, October 1968.
3. Jaffee, Peter, Unpublished Free Flight Wind Tunnel Tests of the 2.75 Wrap Around Fin.
4. Regan, Frank, Unpublished Static Aerodynamic Coefficients of the 2.75 Wrap Around Fin.
5. Nelson, Robert C., "On the Pure Pitching Motion of a Basic Finner Missile," Report-Aero-Space Engineering Department, University of Notre Dame, 1966.
6. Oras, J., "On the Combined Free Pitching and Yawing Motion of the Basic Finner Missile." Master's Thesis, Aero-Space Engineering Department, University of Notre Dame, 1967.
7. Lorenzen, C., "On the Determination of the Magnus Coefficient for the Basic Finner Missile." Master's Thesis, Aero-Space Engineering Department, University of Notre Dame, 1967.
8. Ingram, Martin, "A Three-Degree-of-Freedom Wind Tunnel Analysis of the Apache Sounding Rocket," DAAD 07-67-C-0298, Department of the Army, White Sands Missile Range, New Mexico, May 1968.
9. Nicolaides, J.D., Free Flight Dynamics, Text, Aero-Space Engineering Department, University of Notre Dame, 1961.

8th Navy Symposium on Aeroballistics

Vol. 3

10. Murphy, C.H., "Free Flight Motion of Symmetric Missiles," Ballistic Research Laboratories Report No. 1216, Ballistic Research Laboratories, July, 1963.
11. Murphy, C.H., The Measurement of Nonlinear Forces and Moments by Means of Free-Flight Tests. BRL Rept. No. 974, Feb. 1956.
12. Ingram, C., "An Approximate Solution of the Nonlinear Differential Equation for the Complex Angle of Attack of a Symmetrical Missile." Air Proving Ground Center, (Report pending publication). Eglin Air Force Base, Florida.
13. Eikenberry, R., "Wobble, Analysis of Missile Dynamic Data, Part I , Angular Motion." Aero-Space Engineering Department, University of Notre Dame (Pending publication as contractor report Sandia Corporation).
14. Ingram, Lando, "Flow Visualization and Dynamic Wind Tunnel Tests of Wind Measuring Instruments," ECOM C-0079-1, Atmospheric Sciences Laboratory, White Sands Missile Range, New Mexico, January 1969.
15. Nicolaides, Eikenberry, Ingram, Clare, "On the Flight Dynamics of the Basic Finner in Various Degrees of Freedom," AIAA paper No. 68-890, August 1968.

LIST OF SYMBOLS

$C_{M\alpha}$ pitching moment stability coefficient (rad^{-1})

$$C_{M\alpha} = \frac{M_d \alpha}{Q S d} = -C_{N\beta}$$

$C_{Mq} + C_{M\dot{\alpha}}$ damping moment stability coefficient (rad^{-1})

$$C_{Mq} = \frac{M_q Q}{(\frac{Qd}{2V}) Q S d} = C_{N\beta}$$

$$C_{M\dot{\alpha}} = \frac{M_d \dot{\alpha}}{(\frac{\dot{\alpha}d}{2V}) Q S d} = -C_{N\beta}$$

$C_{MP\alpha}$ Magnus moment stability coefficient (rad^{-2})

$$C_{MP\alpha} = \frac{N_p \alpha P_a}{\alpha (\frac{P_d}{2V}) Q S d} = \frac{M_p \beta P \beta}{\beta (\frac{P_d}{2V}) Q S d} = C_{MP\beta} = C_{NPA}$$

d
 $I = I_y = I$
 I_x
 K_N, K_P

reference length, missile diameter (ft)
pitching moment of inertia (slugs-ft²)
rolling moment of inertia (slugs-ft²)
nutation and precession vectors (deg)

8th Navy Symposium on Aeroballistics

Vol. 3

p, q, r	missile angular velocity in space (rad/sec)
Q	dynamic pressure, $Q = \frac{1}{2} \rho V^2$ (lb/ft ²)
S	reference area, $S = \frac{\pi d^2}{4}$ (ft ²)
V	total velocity (ft/sec)
$\vec{\alpha}$	complex angle of attack, (deg)
α	angle of attack (deg)
ψ	angle of sideslip (deg)
$\lambda_{N, P}$	nutation and precession damping rates (rad/sec)
ρ	density (slugs/ft ³)
$\omega_{N, P}$	nutation and precession frequencies (rad/sec)
ω	pitching frequency (rad/sec)
λ_1	damping rate (rad/sec)
K_1	model vector (deg)
K_T	Trim mode (deg)

8th Navy Symposium on Aeroballistics

Vol. 3

THRUST (LBS.)	TIME (SEC.)
1600	.00
1520	.10
1350	.20
1370	.30
1410	.40
1480	.50
1620	.60
1680	.70
1690	.80
1800	.90
1230	1.00

C_D	MACH NO.
.59	.00
.59	.60
.61	.90
1.04	1.75
.90	2.50
.80	3.00

Typical Full Scale Mass Parameters

$I = 1.08$ Slug/Sq. Ft.
 $I_x = .0059$ Slug/Sq. Ft.
Mass = .6930 Slugs
Quad. Elev. = 20 Deg.
Init. Veloc. = 890 Ft. /Sec.

TABLE 1

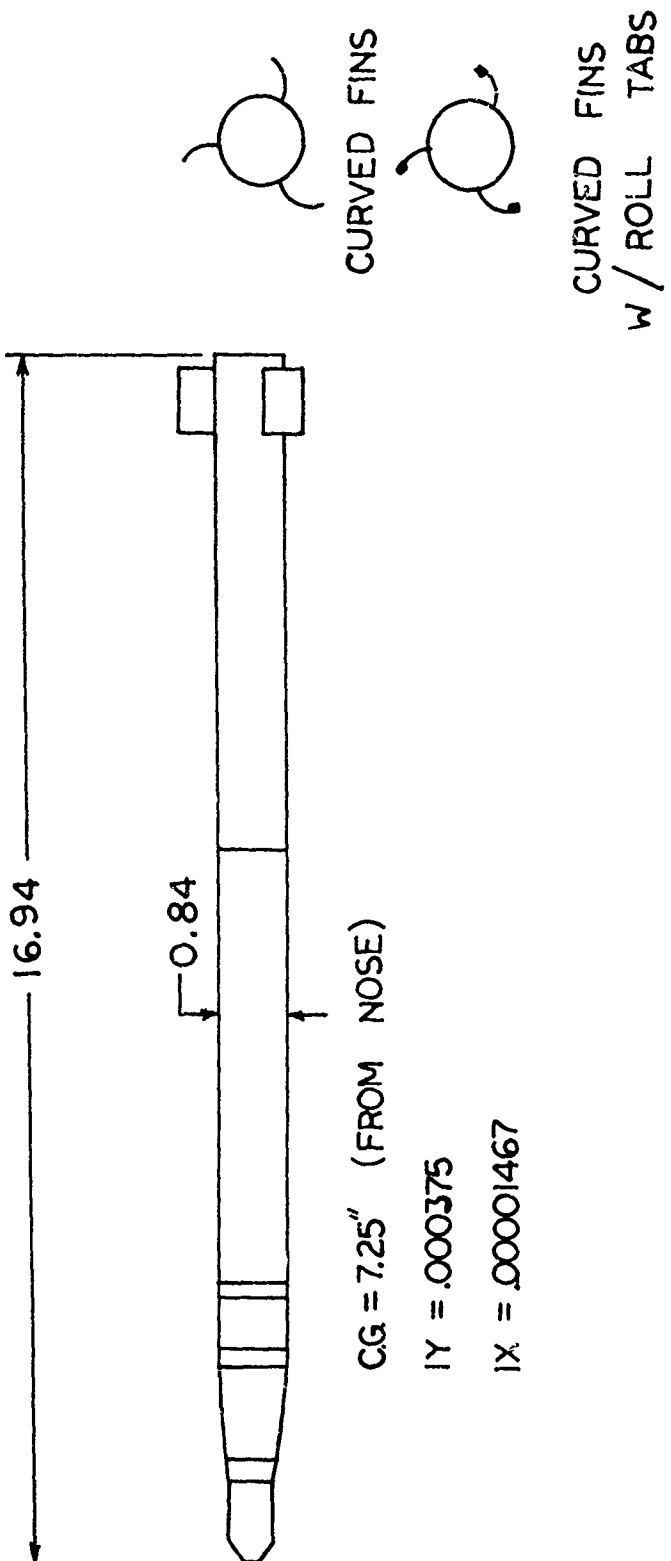


FIG. 1 SCHEMATIC OF MODEL

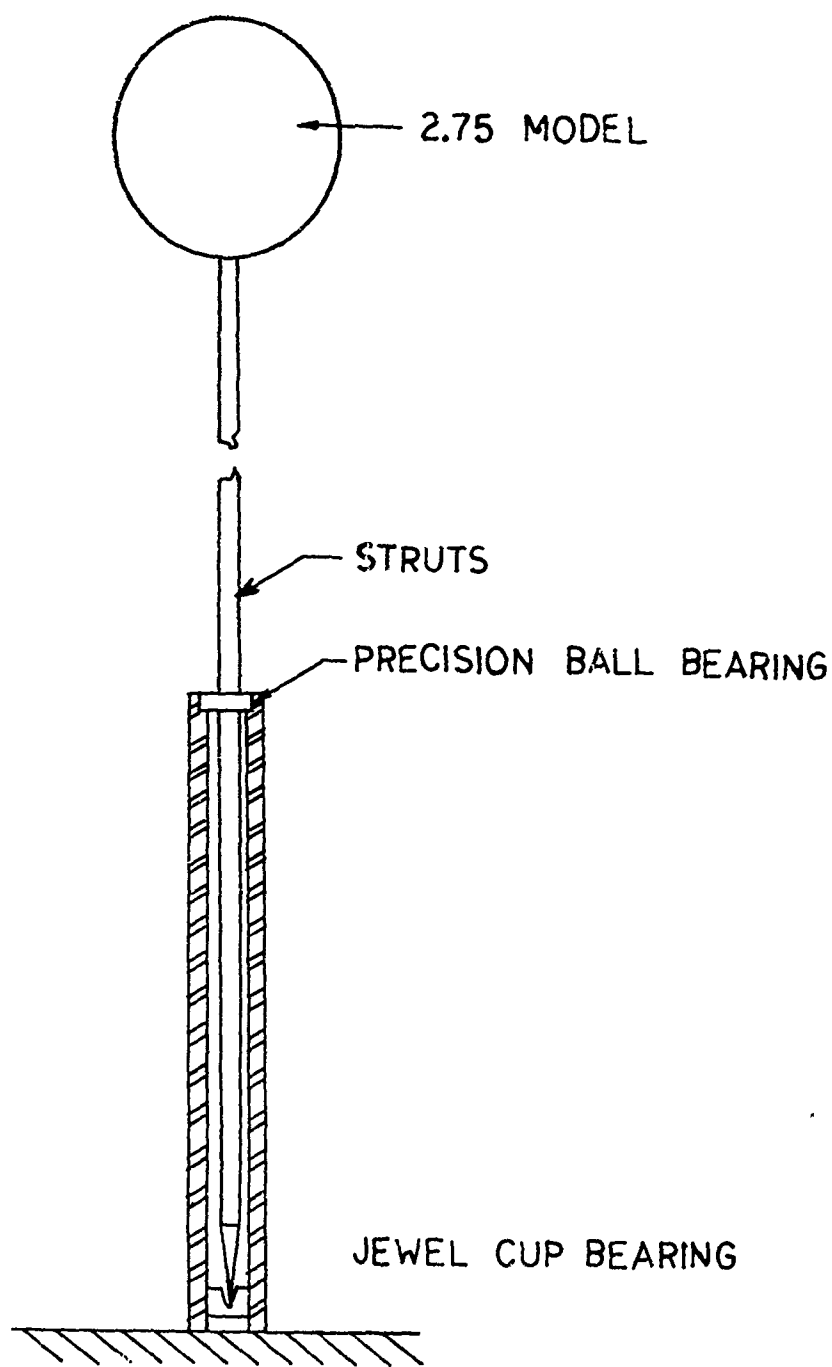


FIG.2 1-D SCHEMATIC OF SUPPORT SYSTEM

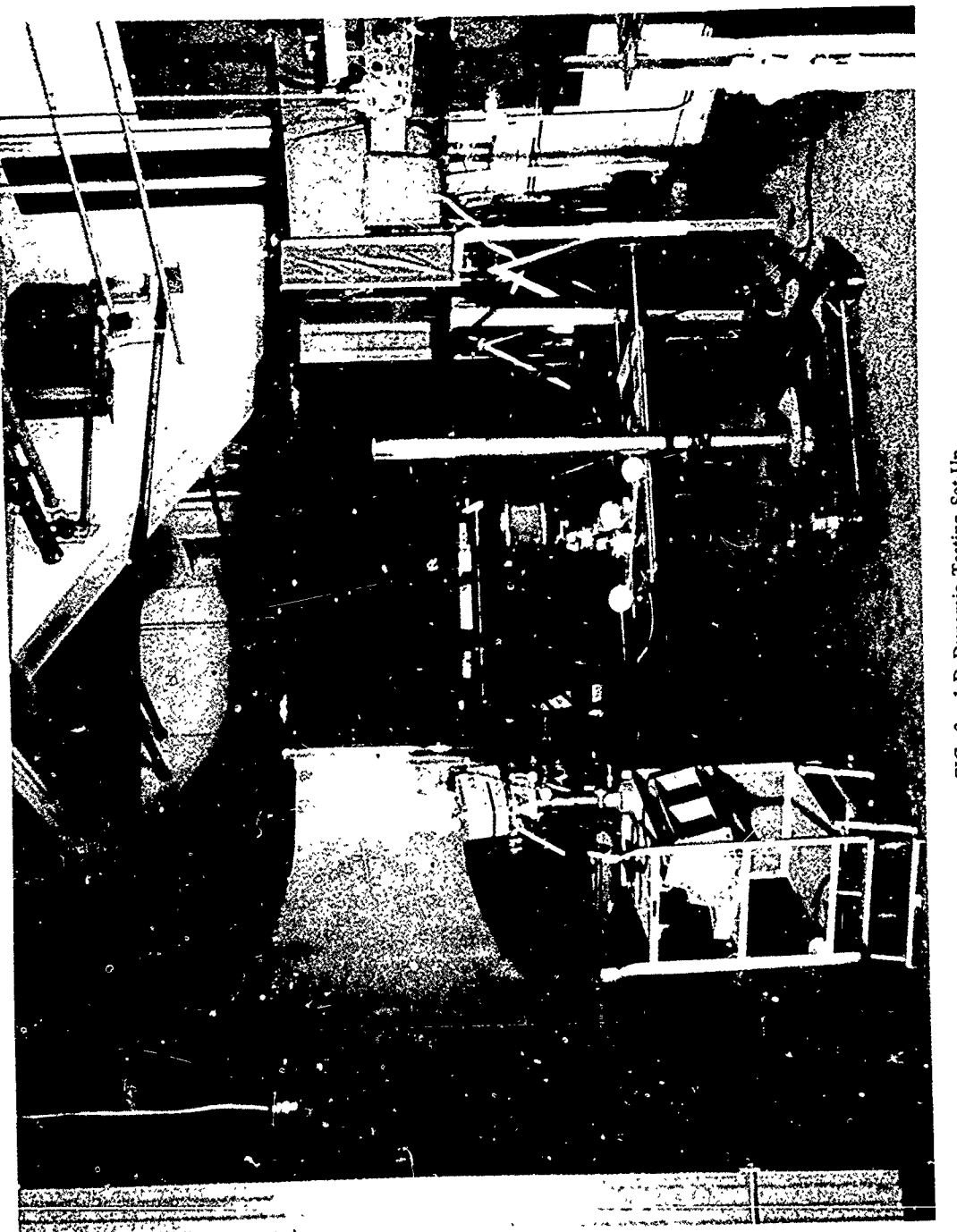


FIG. 3. 1-D Dynamic Testing Set-Up.

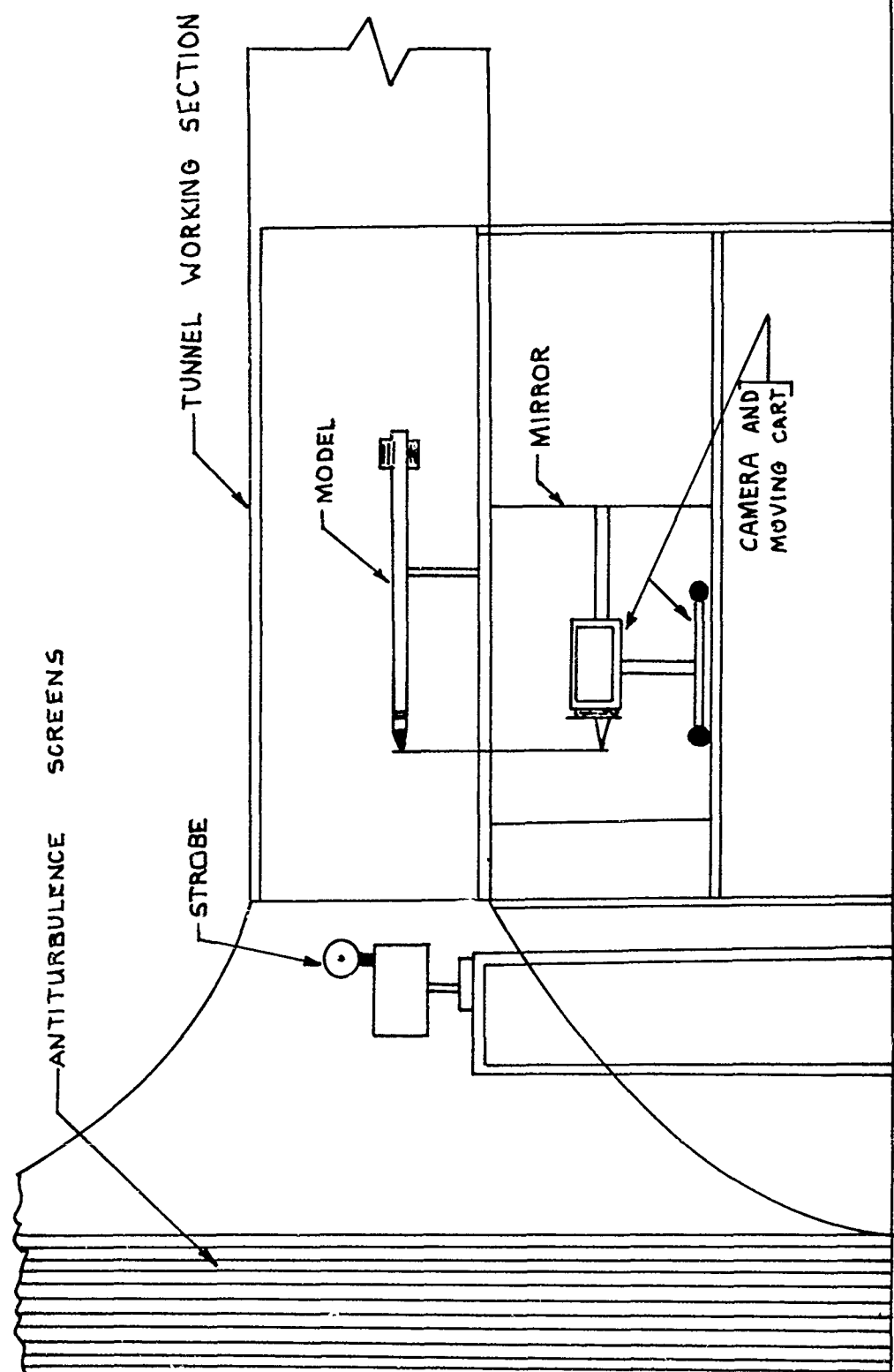


FIG. 4 1-D TEST SET-UP

8th Navy Symposium on Aeroballistics

Vol. 3



FIG. 5. 1-D Oscillations as Experimentally Obtained from Camera Cart Technique.

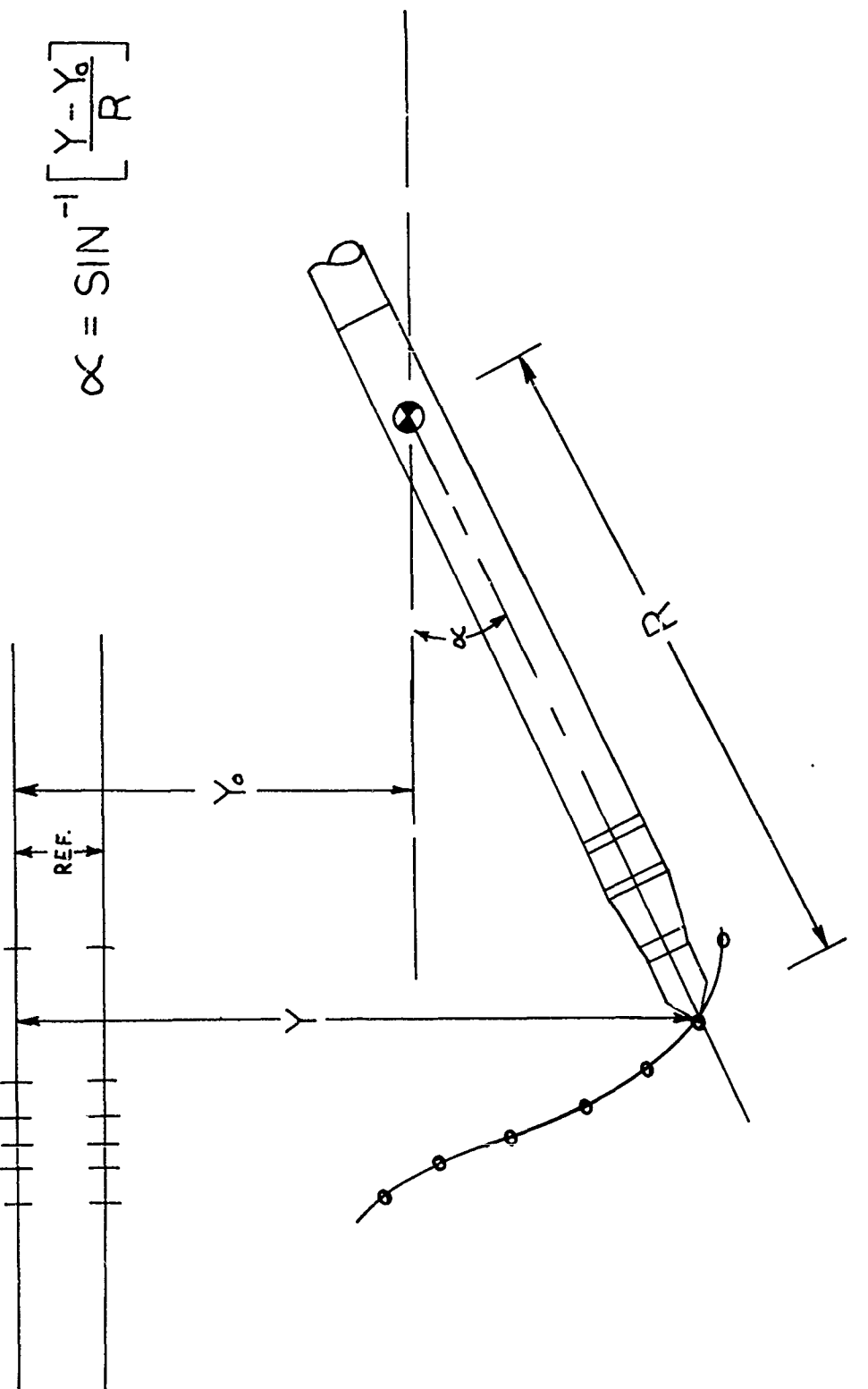


FIG. 6 DATA REDUCTION PROCEDURE

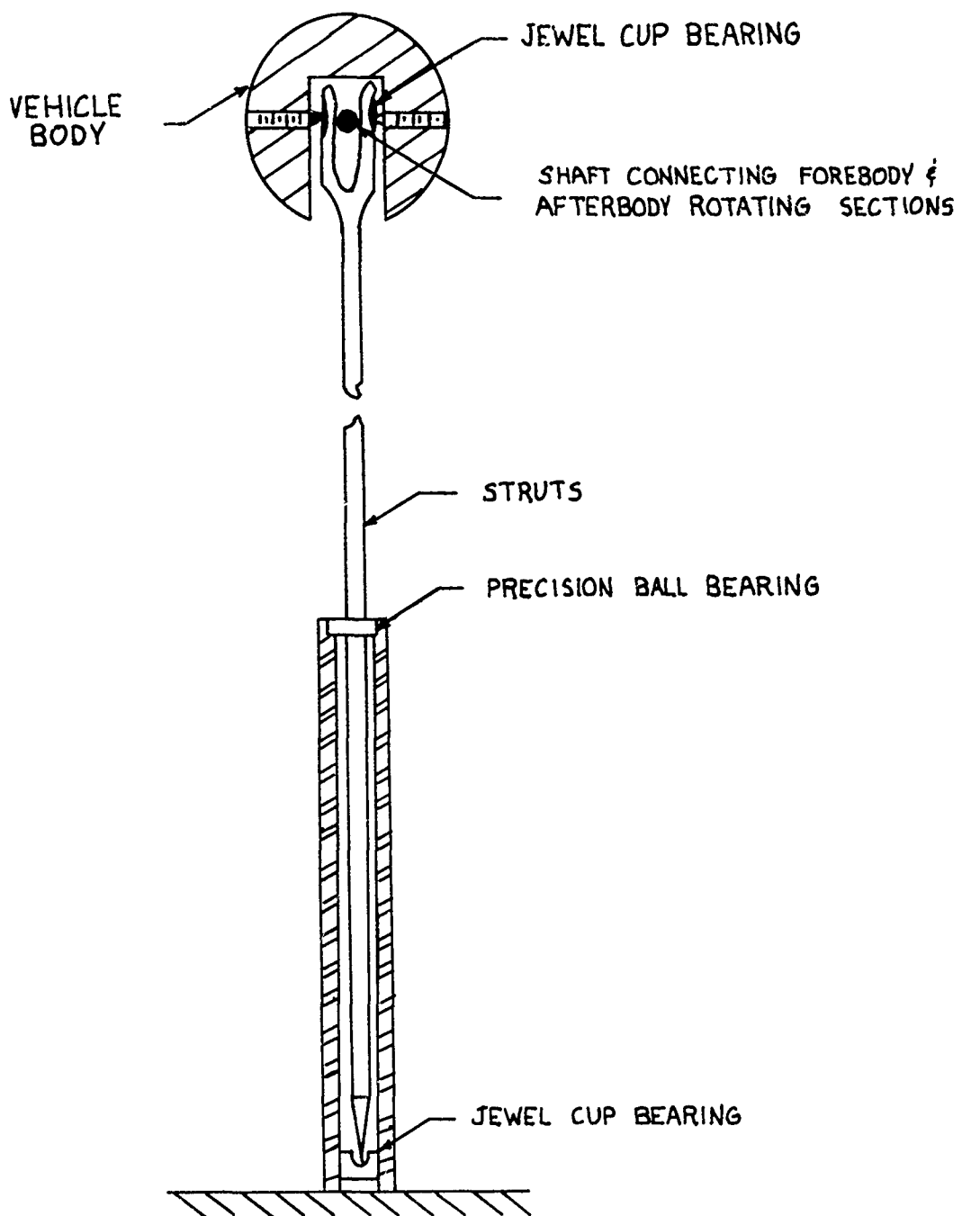


FIG 7 SCHEMATIC OF SUPPORT SYSTEM

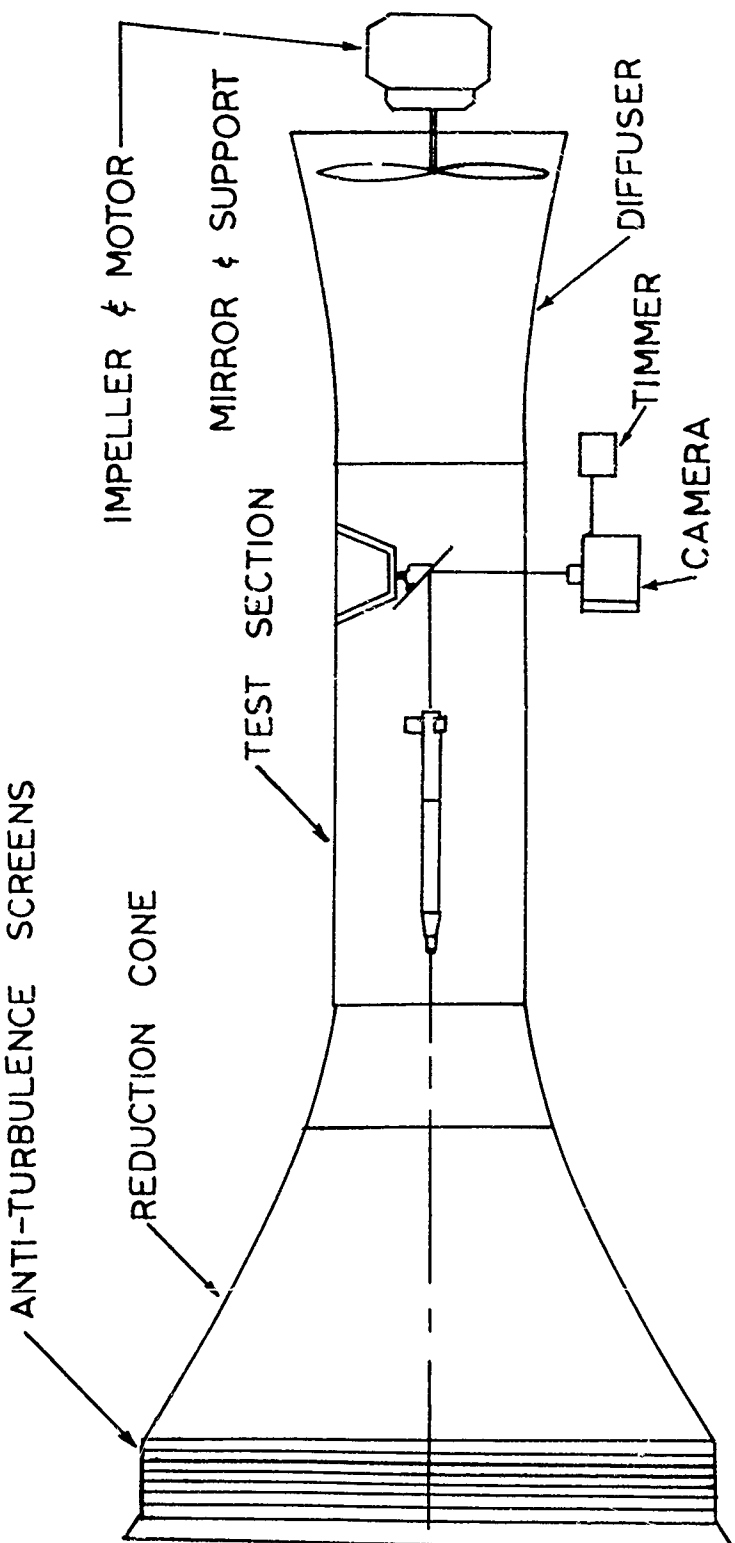


FIG. 8 SCHEMATIC OF WIND TUNNEL
(TOP VIEW)

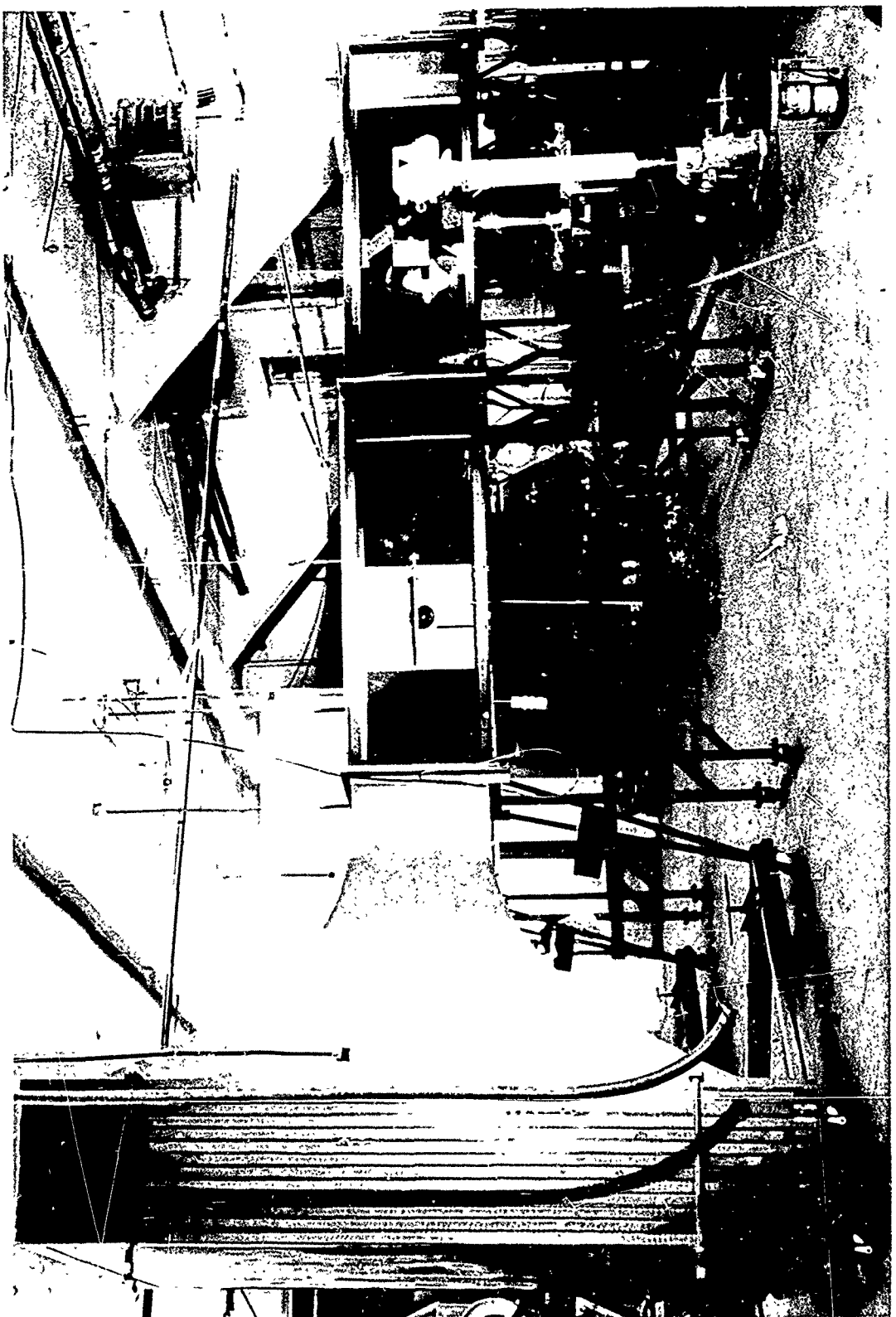


FIG. 9. 3-D Dynamic Testing Set-Up.

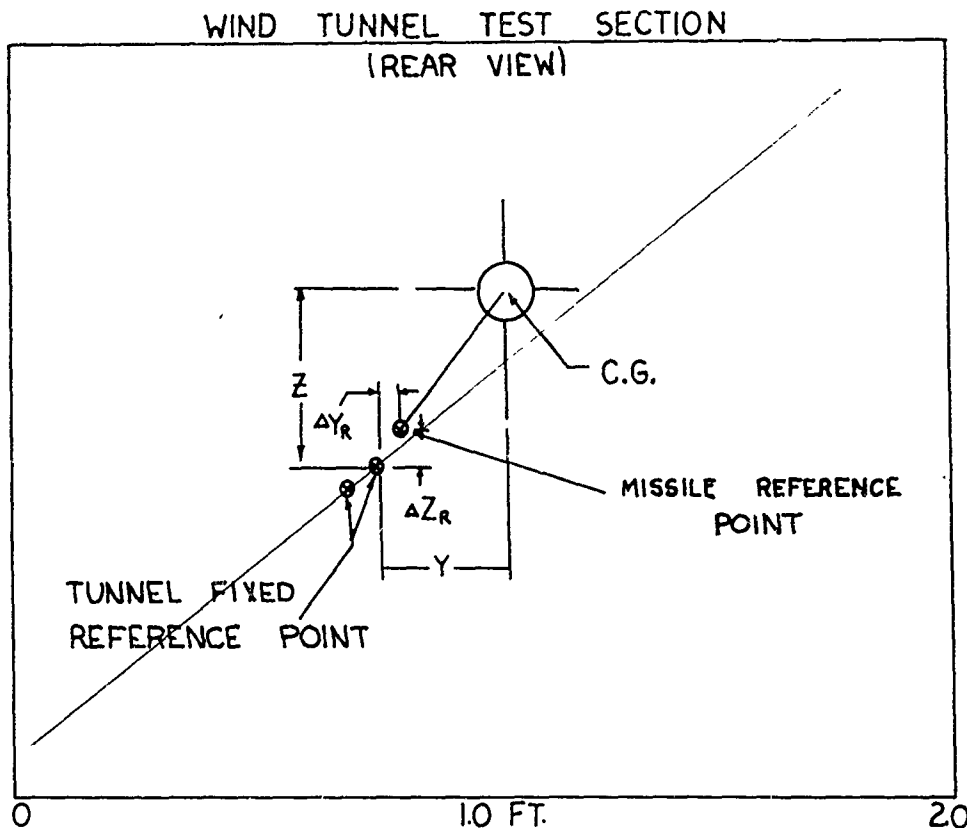
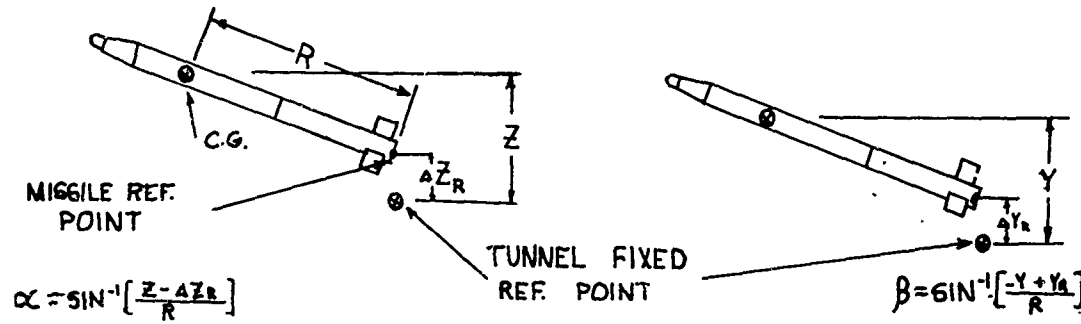


FIG. 10 REDUCTION OF TUNNEL MOTION TO ANGULAR DATA

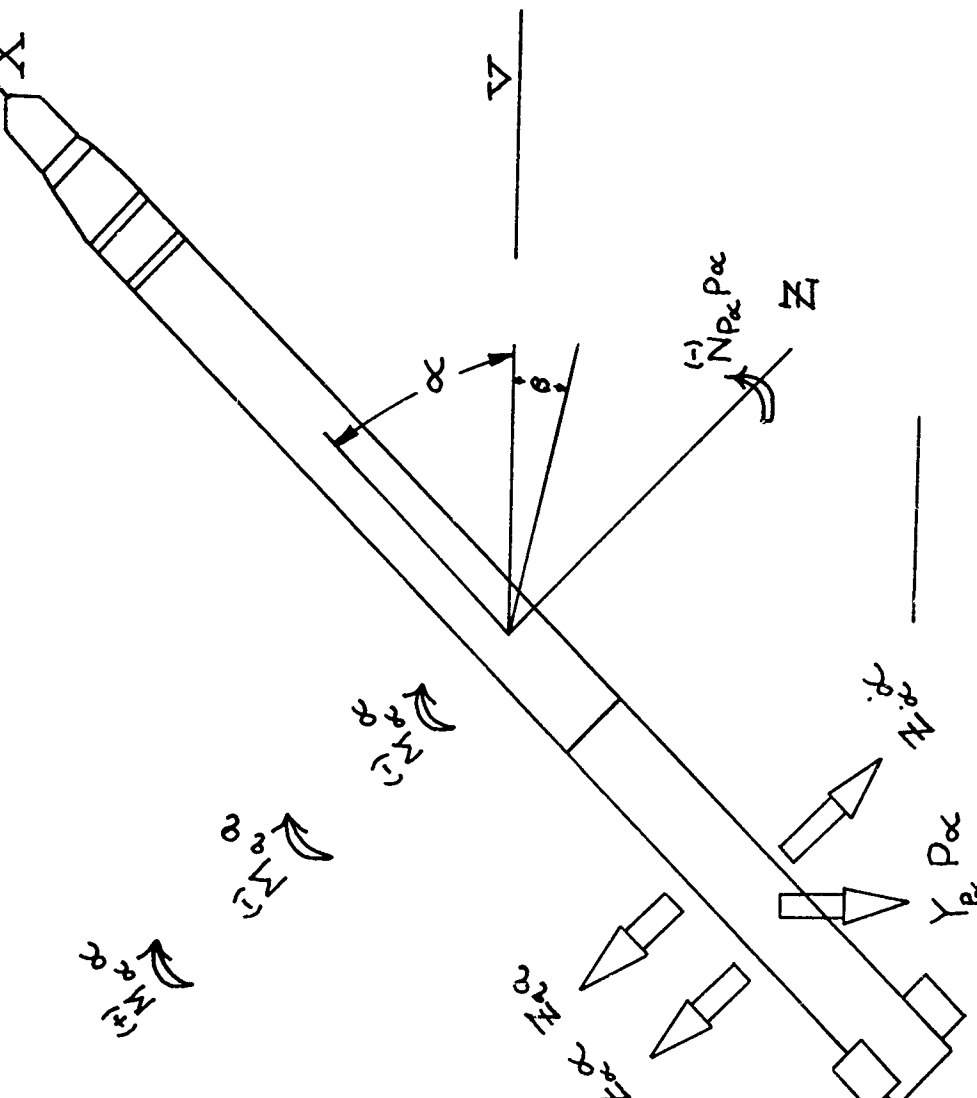
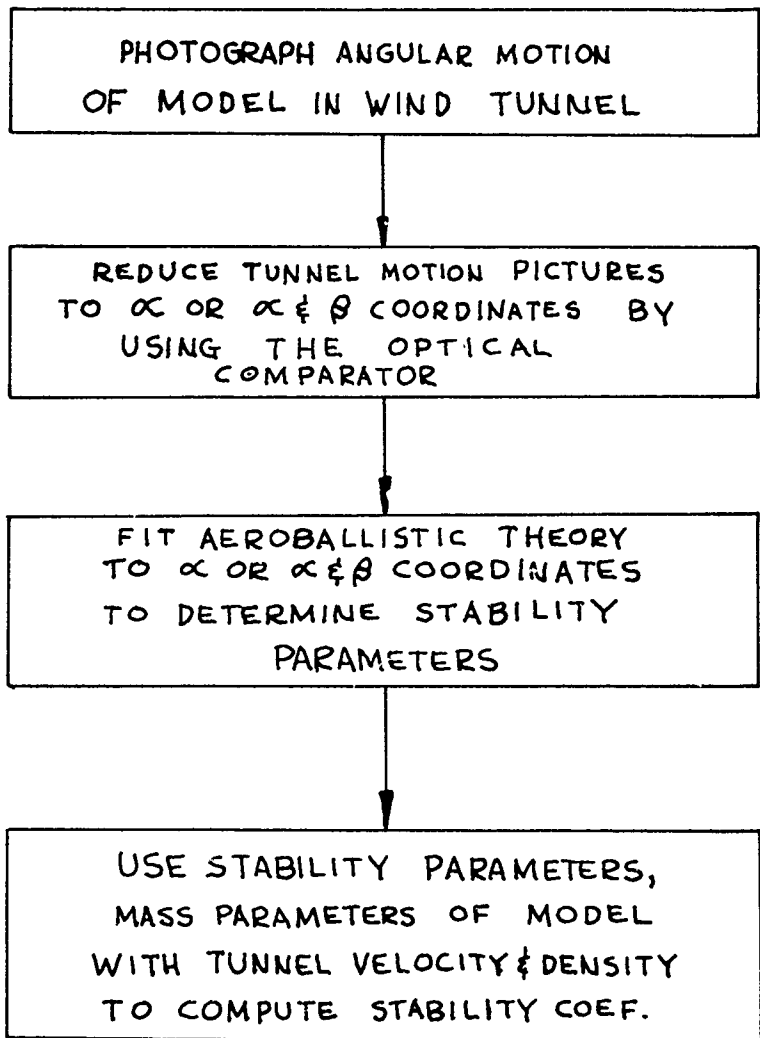


FIG II FORCE AND MOMENT SYSTEM



ANALYSIS PROCEDURE FOR OBTAINING AERODYNAMIC STABILITY COEFFICIENTS

FIG. 12

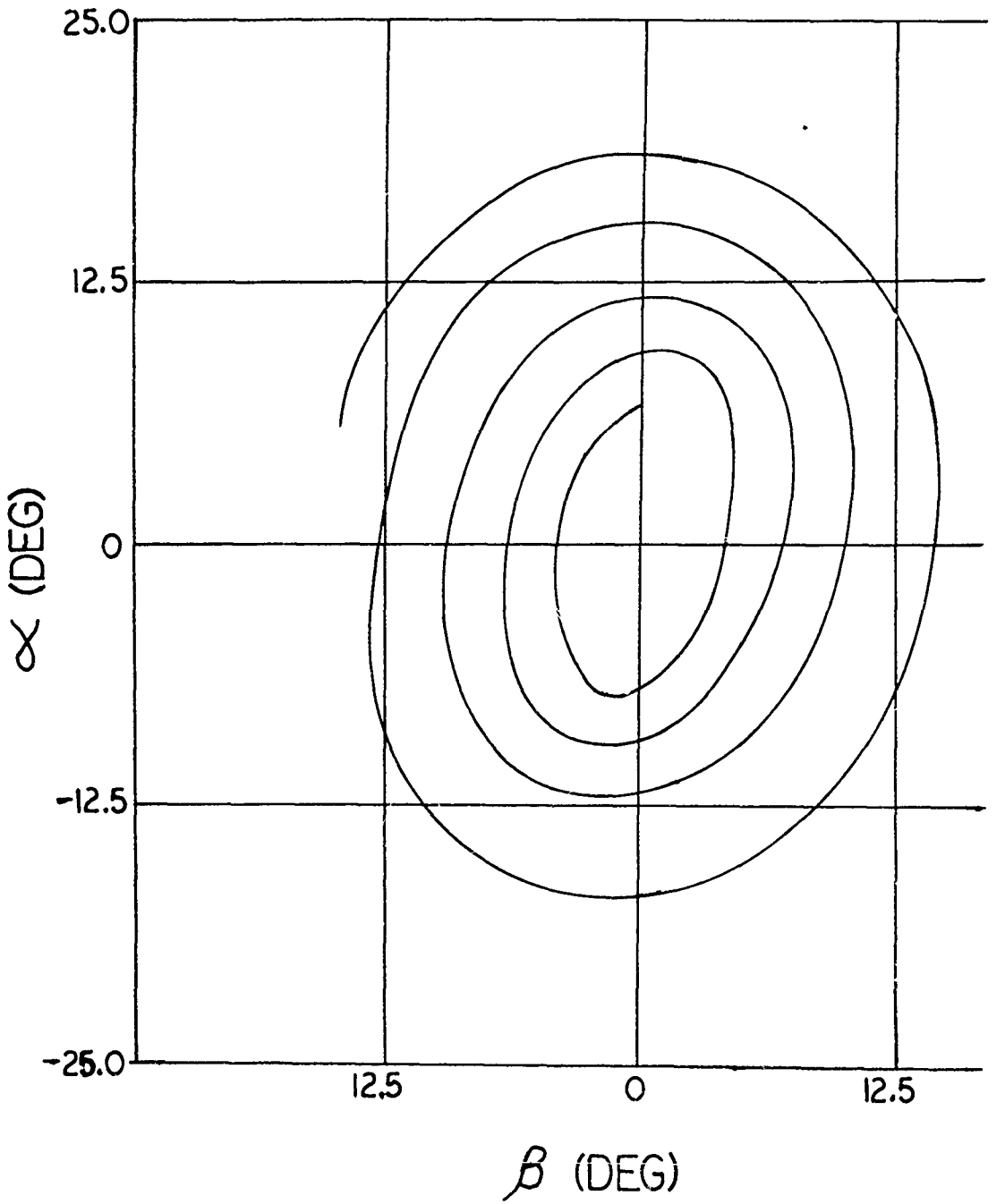


FIG 13 3-D COMPLEX MOTION

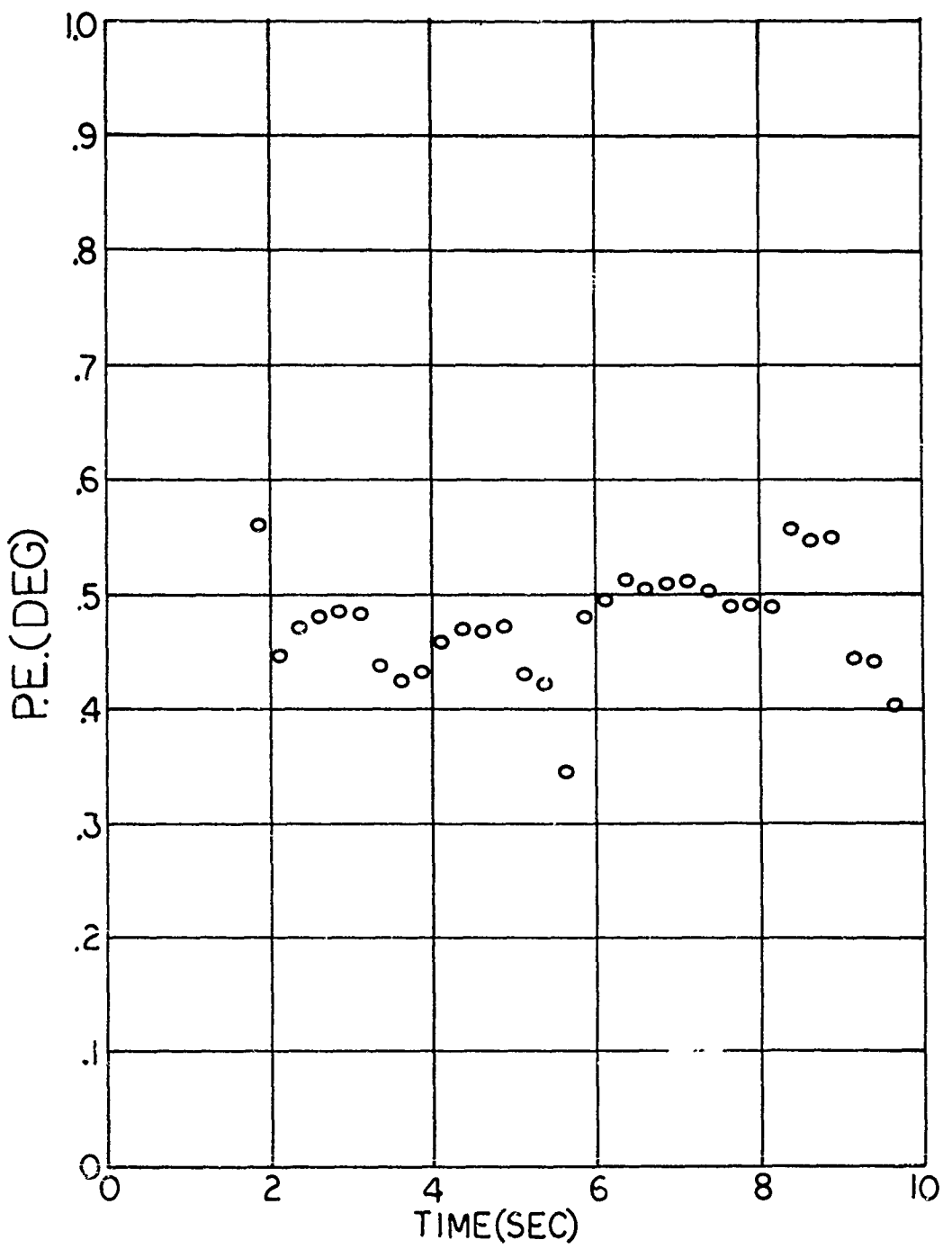


FIG. 14 PROBABLE ERROR VS TIME

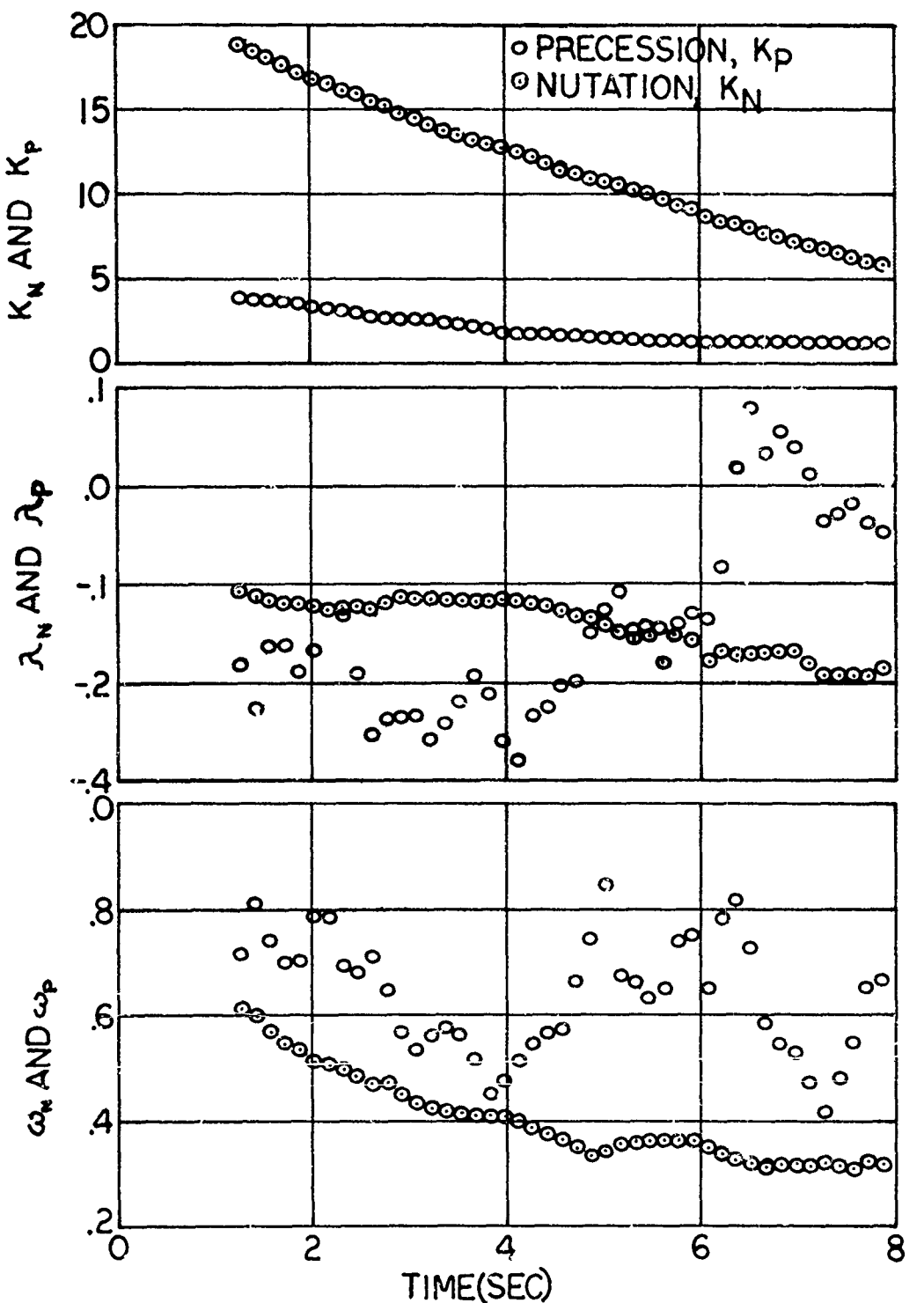


FIG. 15 3-D STABILITY PARAMETERS vs TIME

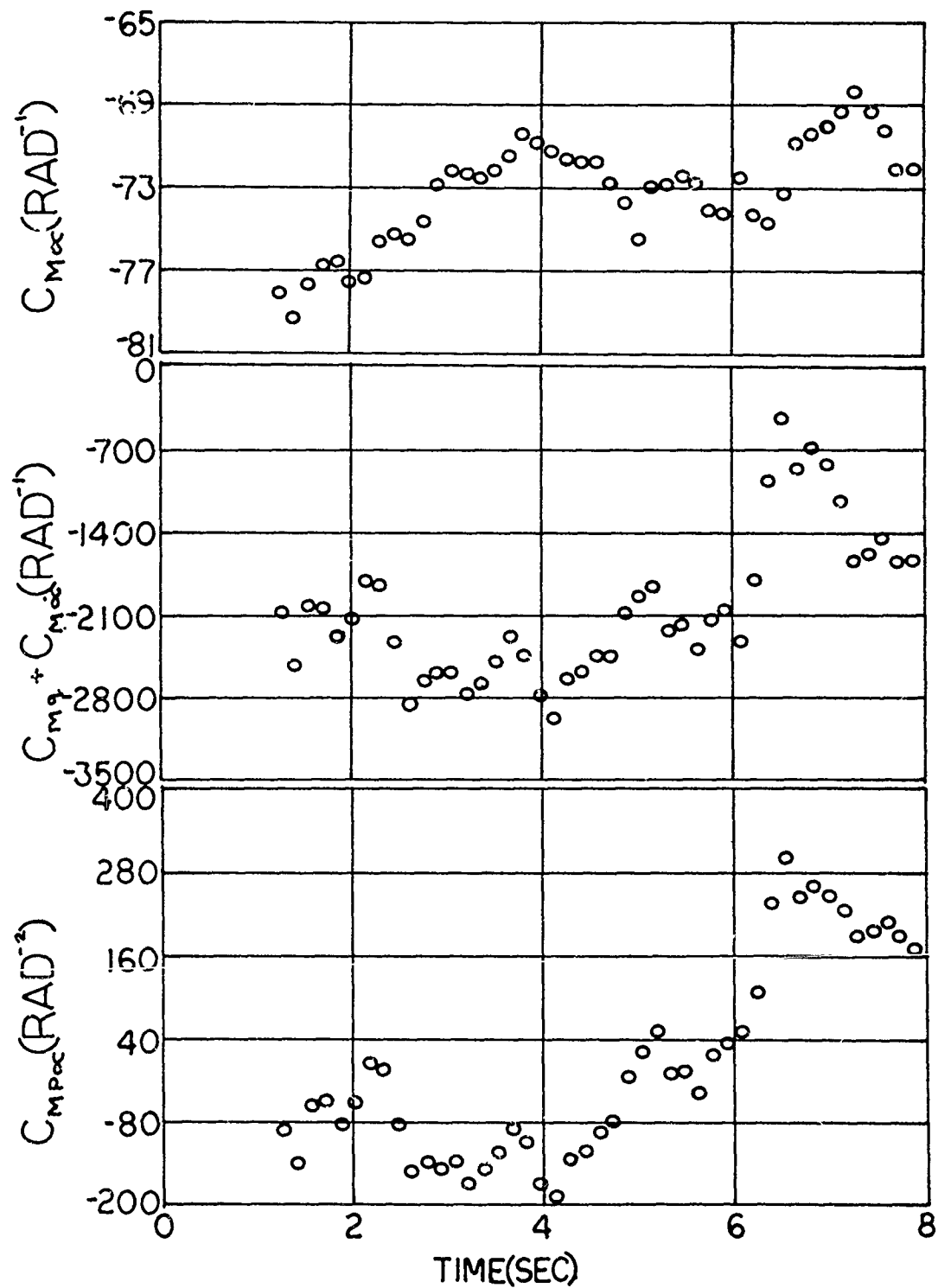


FIG. 16 STABILITY COEFICIENTS VS TIME

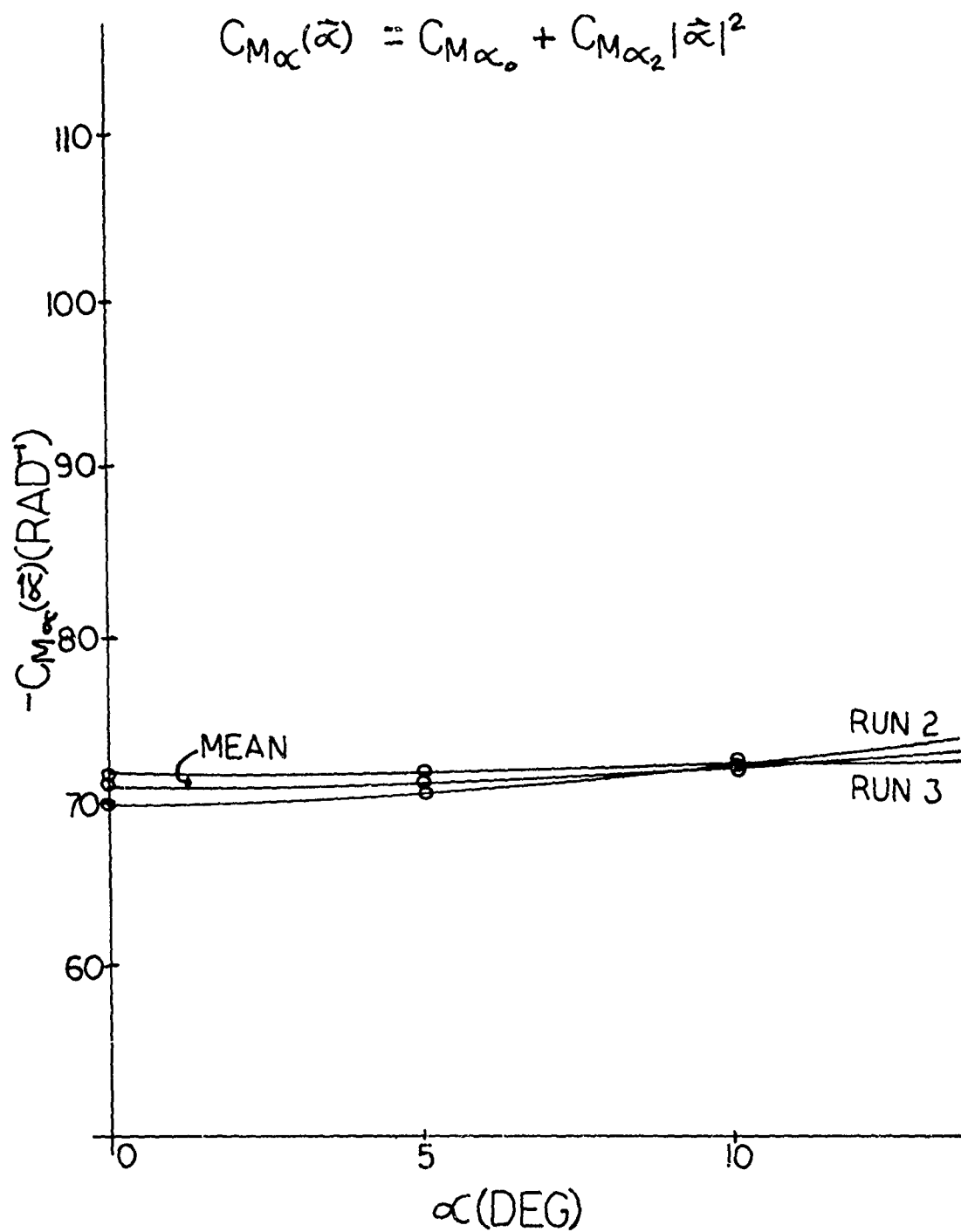
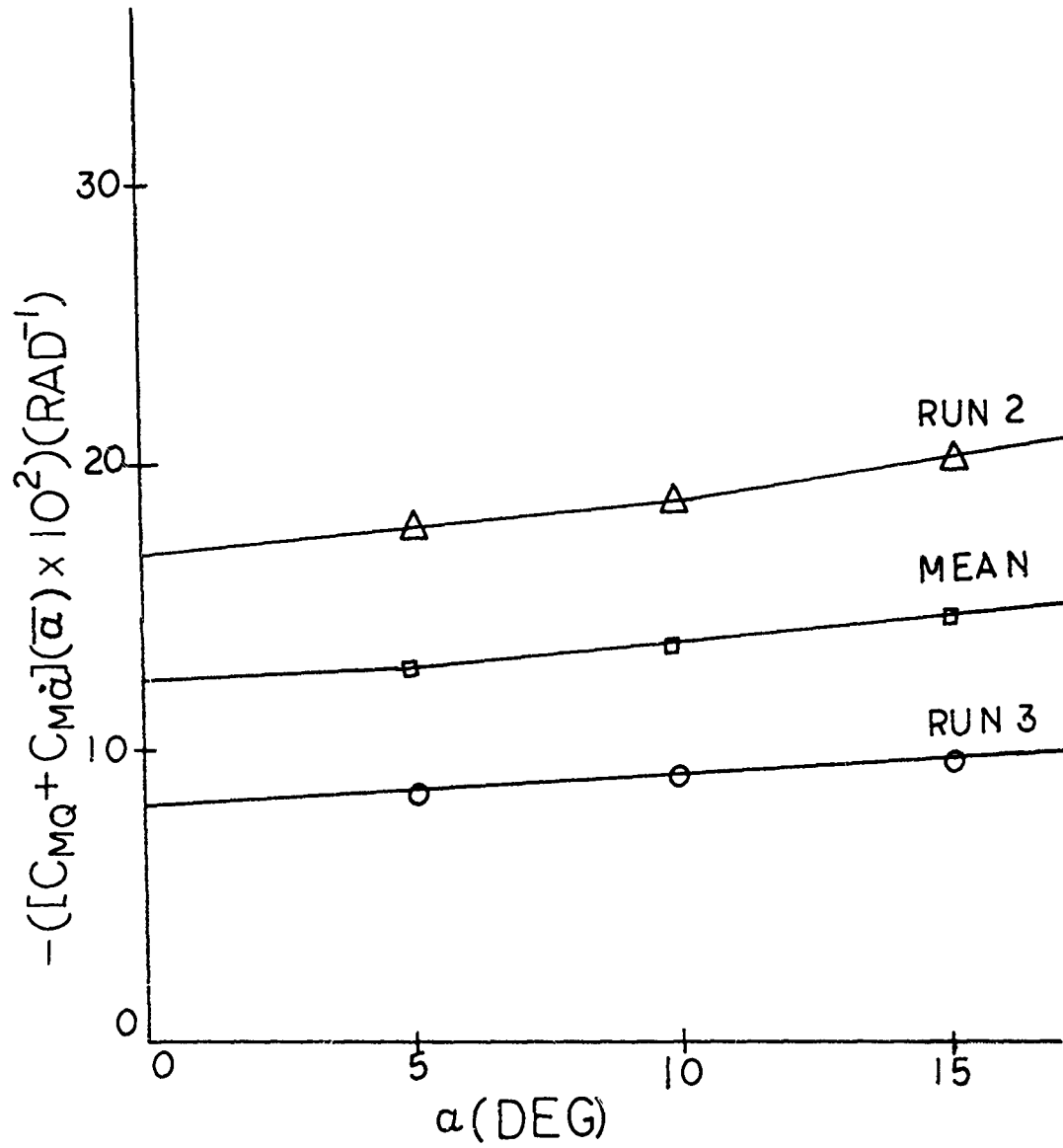
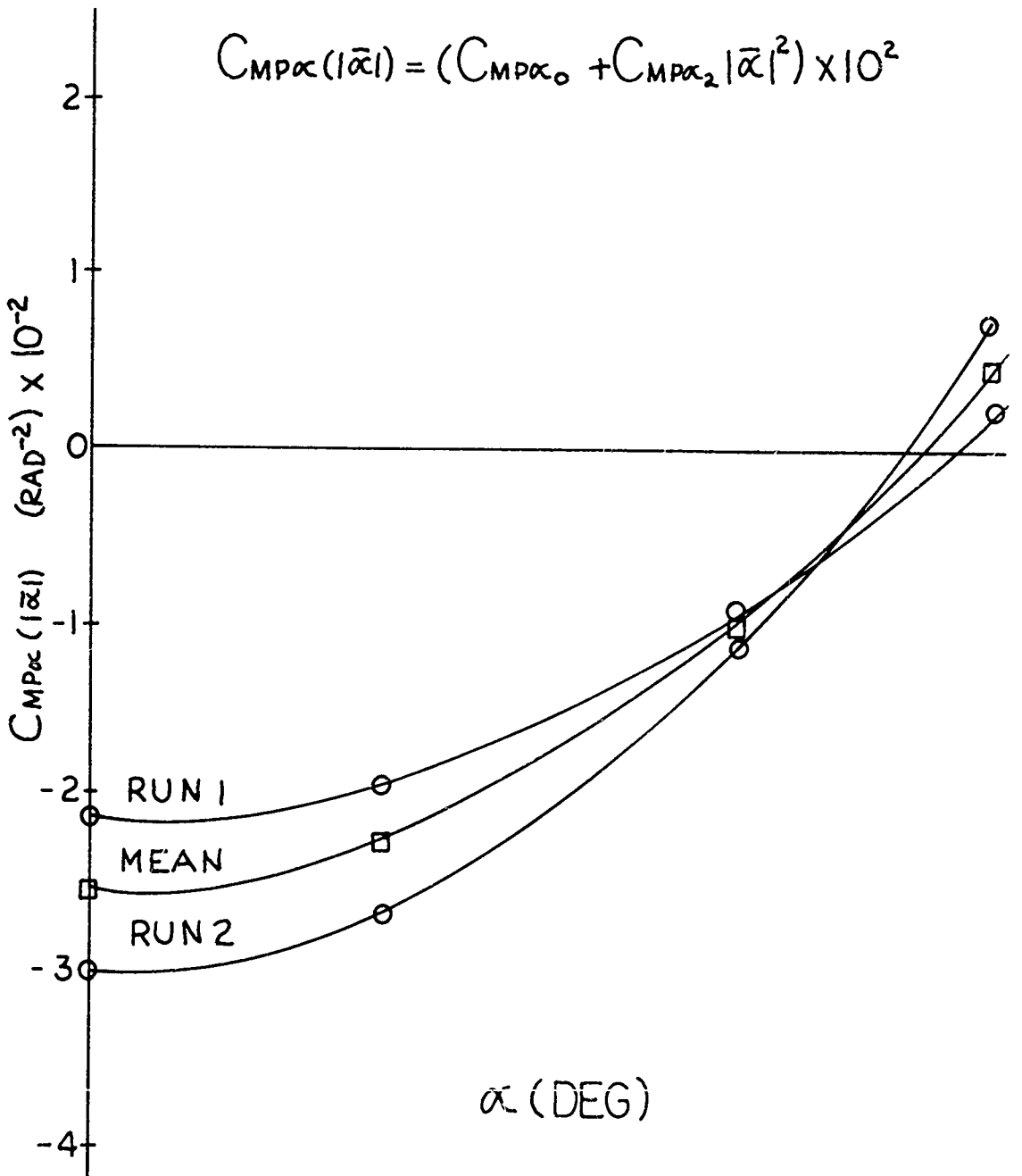


FIG. 17

 $C_{M\alpha}(\tilde{\alpha})$ VS α

$$C_{MQ}(\bar{\alpha}) + C_{M\dot{\alpha}}(\bar{\alpha}) = (C_{MQ} + C_{M\dot{\alpha}})_0 + (C_{MQ} + C_{M\dot{\alpha}}) |\bar{\alpha}|^2$$

FIG. 18 $C_{MQ}(\bar{\alpha}) + C_{M\dot{\alpha}}(\bar{\alpha})$ VS. α

FIG. 19 $C_{M\bar{\alpha}}(1\bar{\alpha})$ vs. ANGLE OF ATTACK

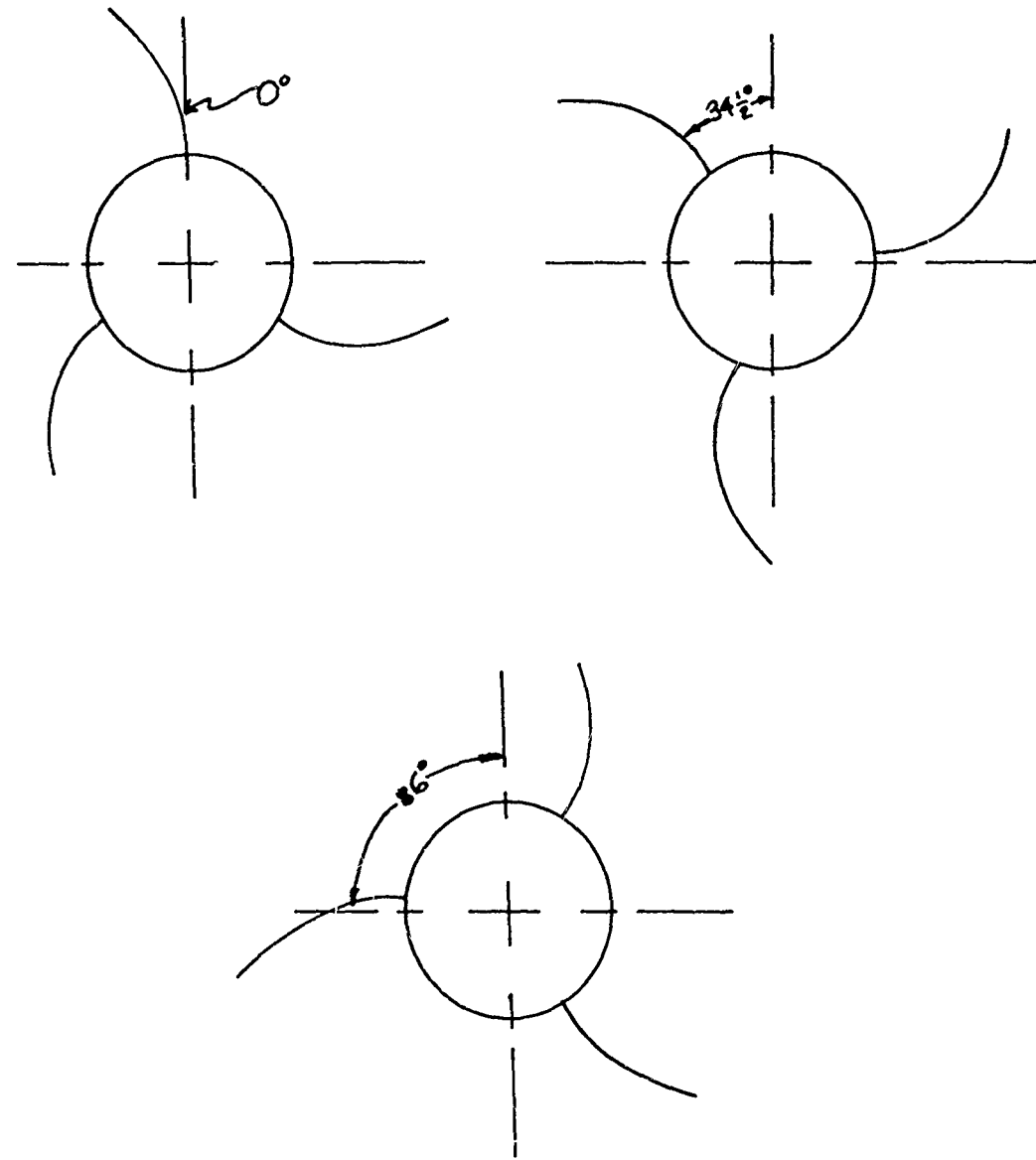


FIG. 20 ROLL ORIENTATION

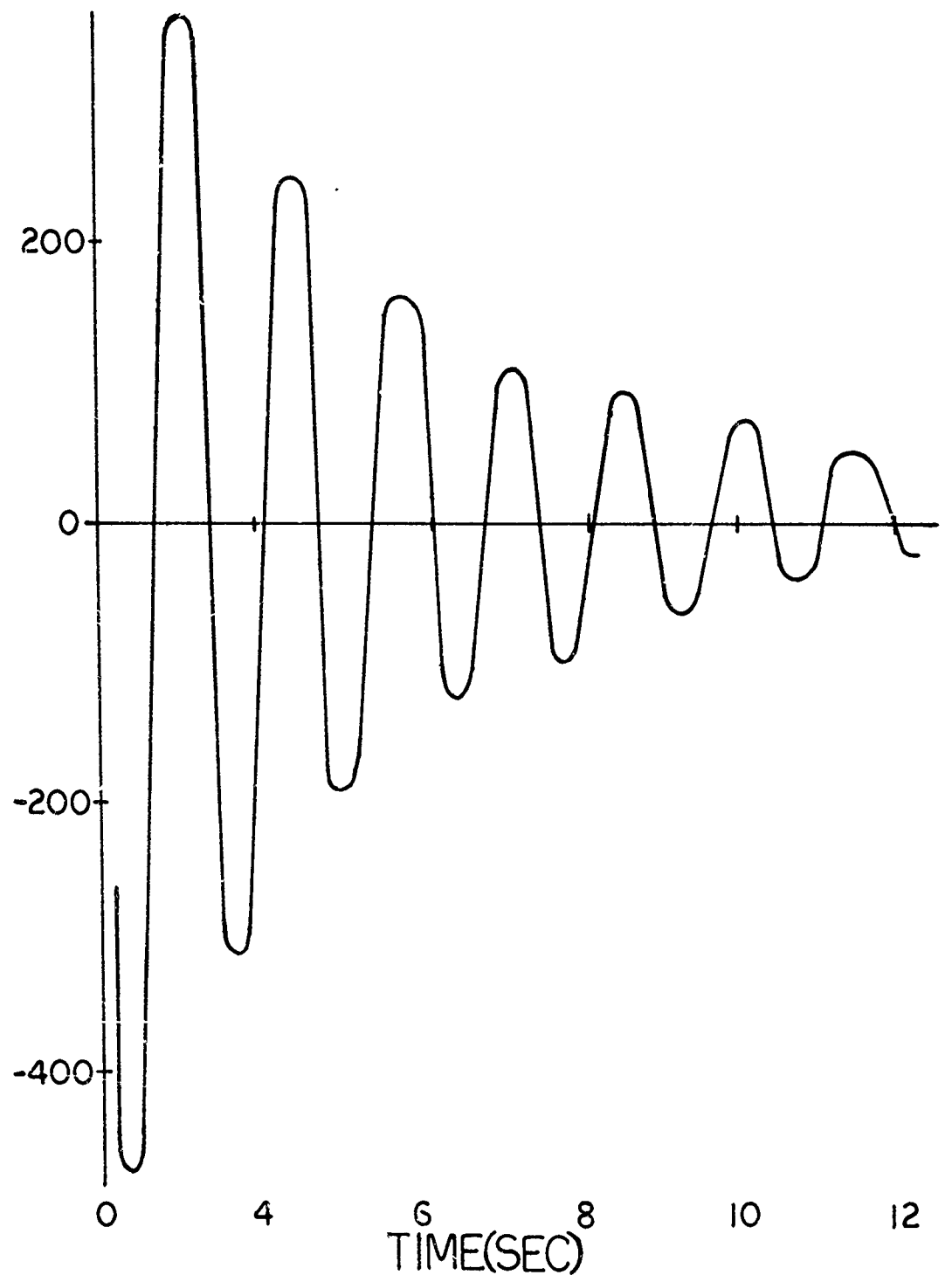


FIG. 21 1-D OSCILLATORY MOTION

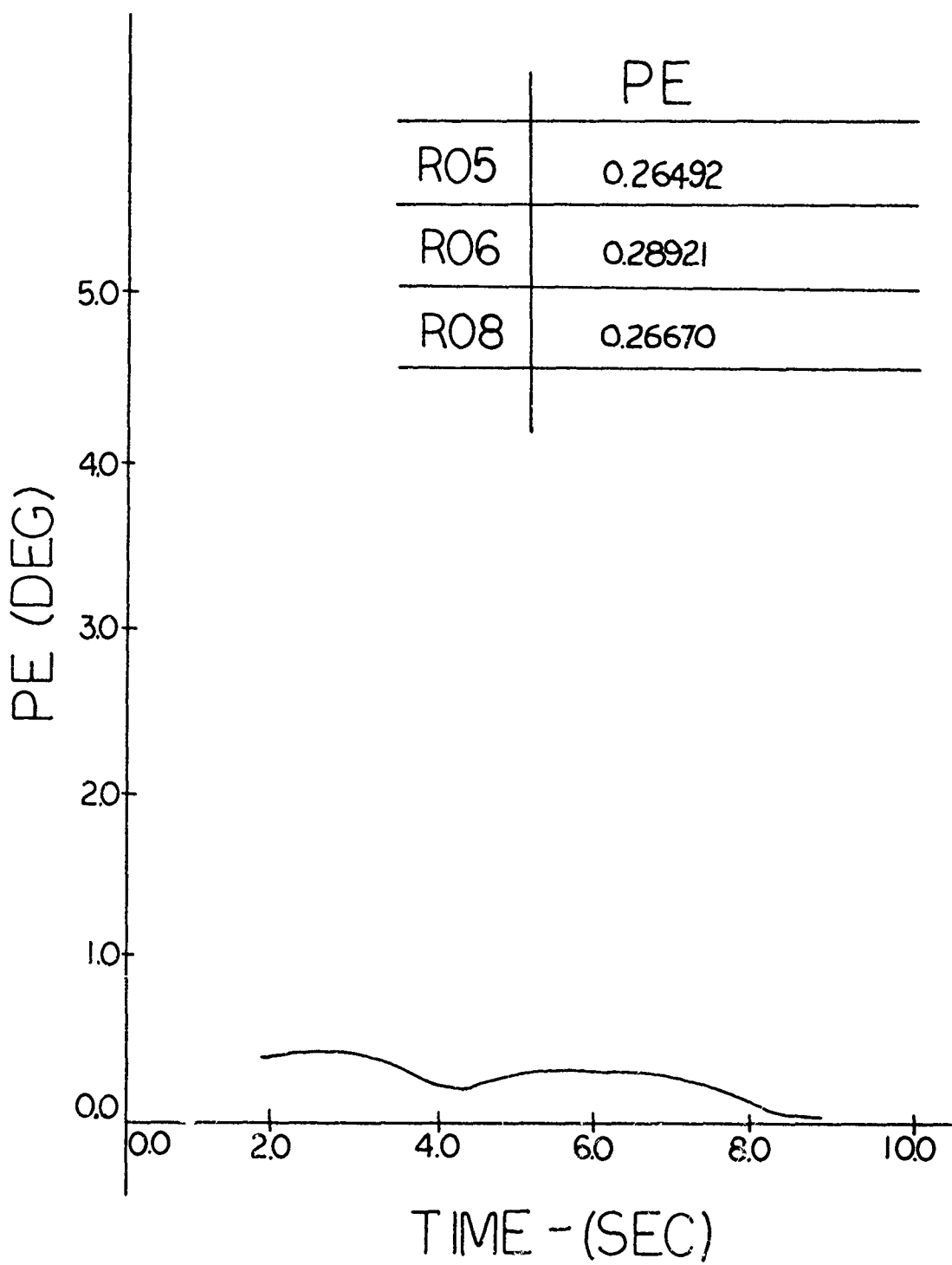


FIG. 22 PROBABLE ERROR OF FIT vs TIME

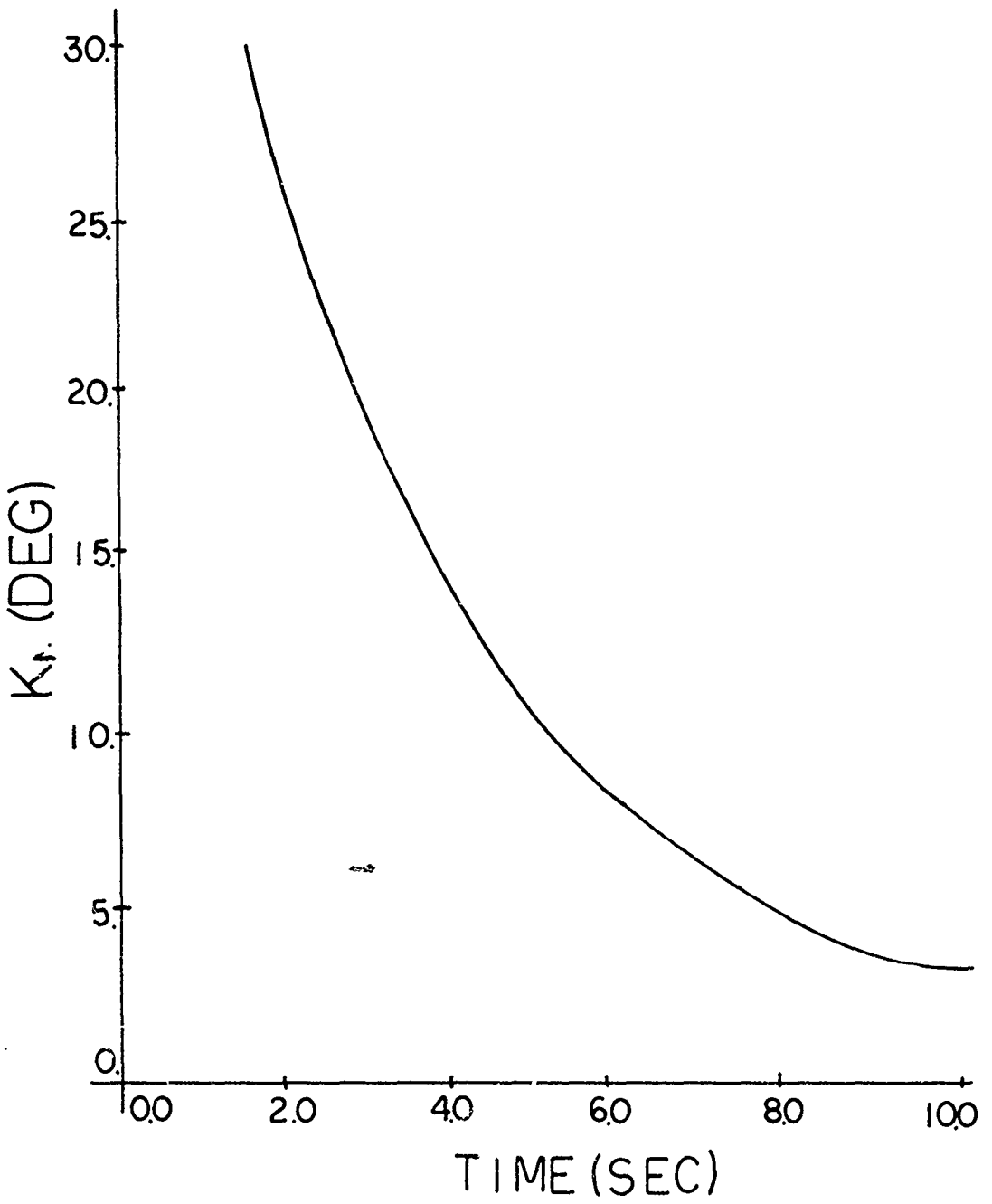


FIG. 23 K_r vs TIME

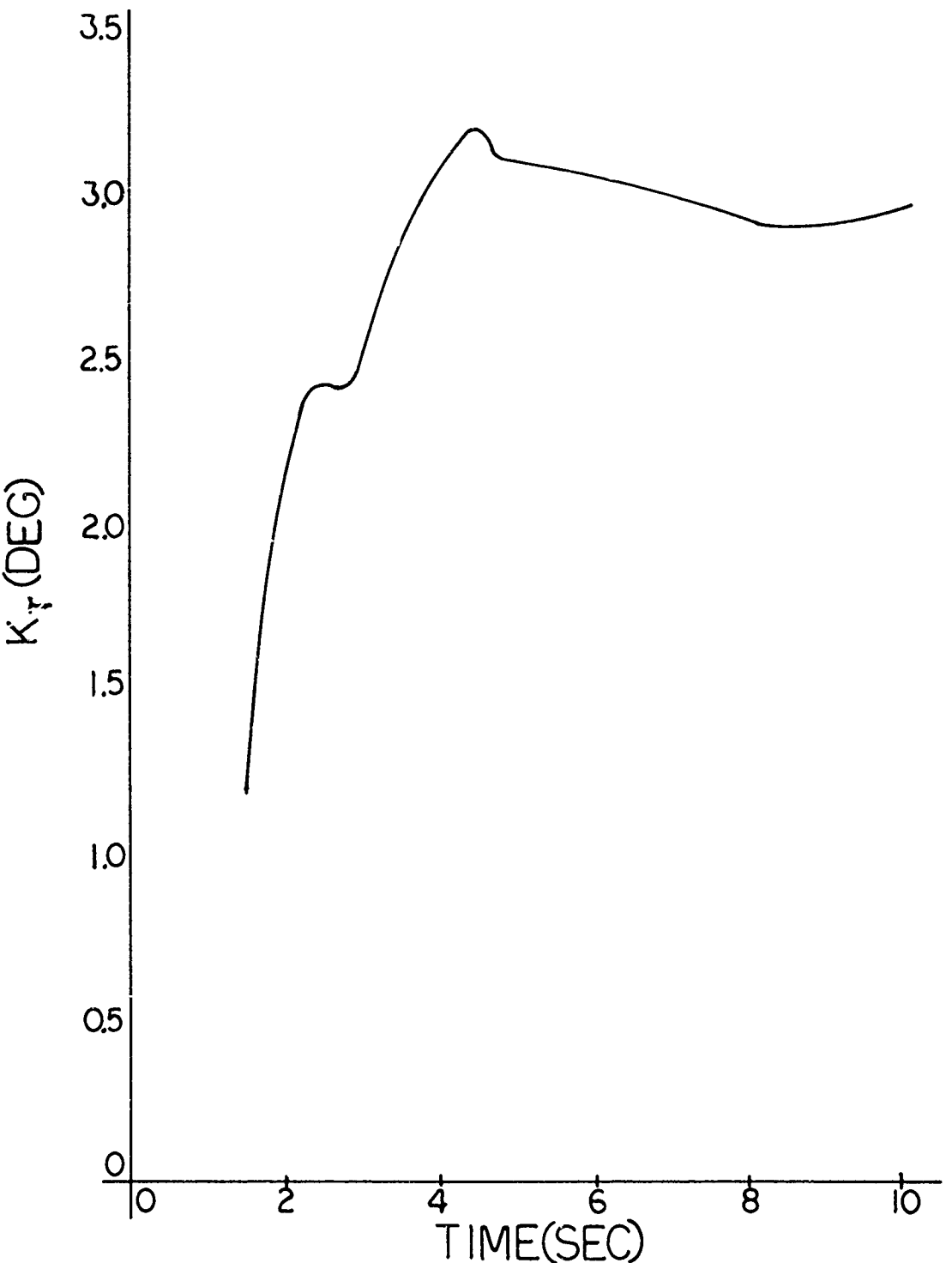


FIG. 24 TRIM MODE VS TIME

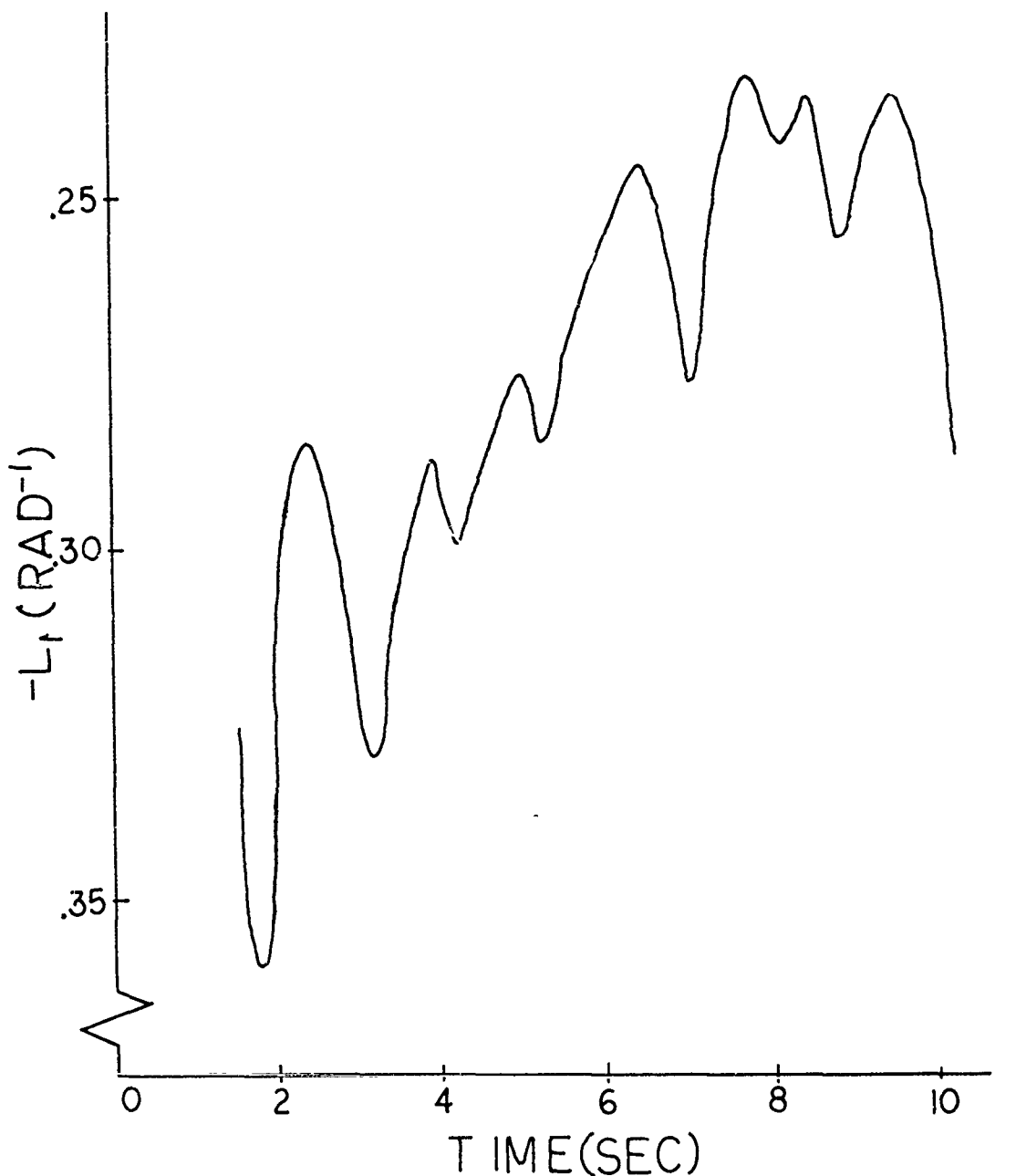


FIG. 25 L_1 VS. TIME

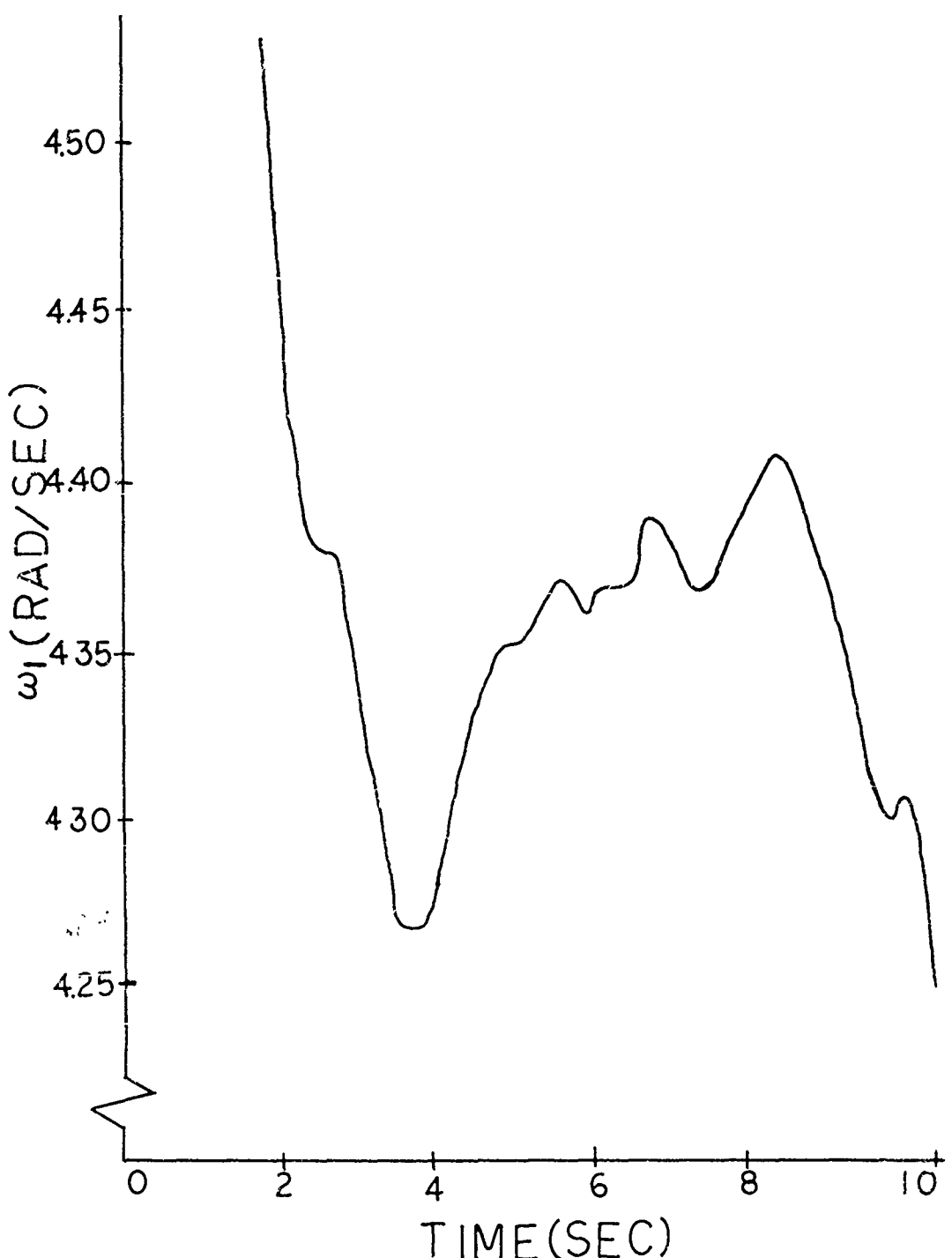


FIG. 26

 ω_1 VS. TIME

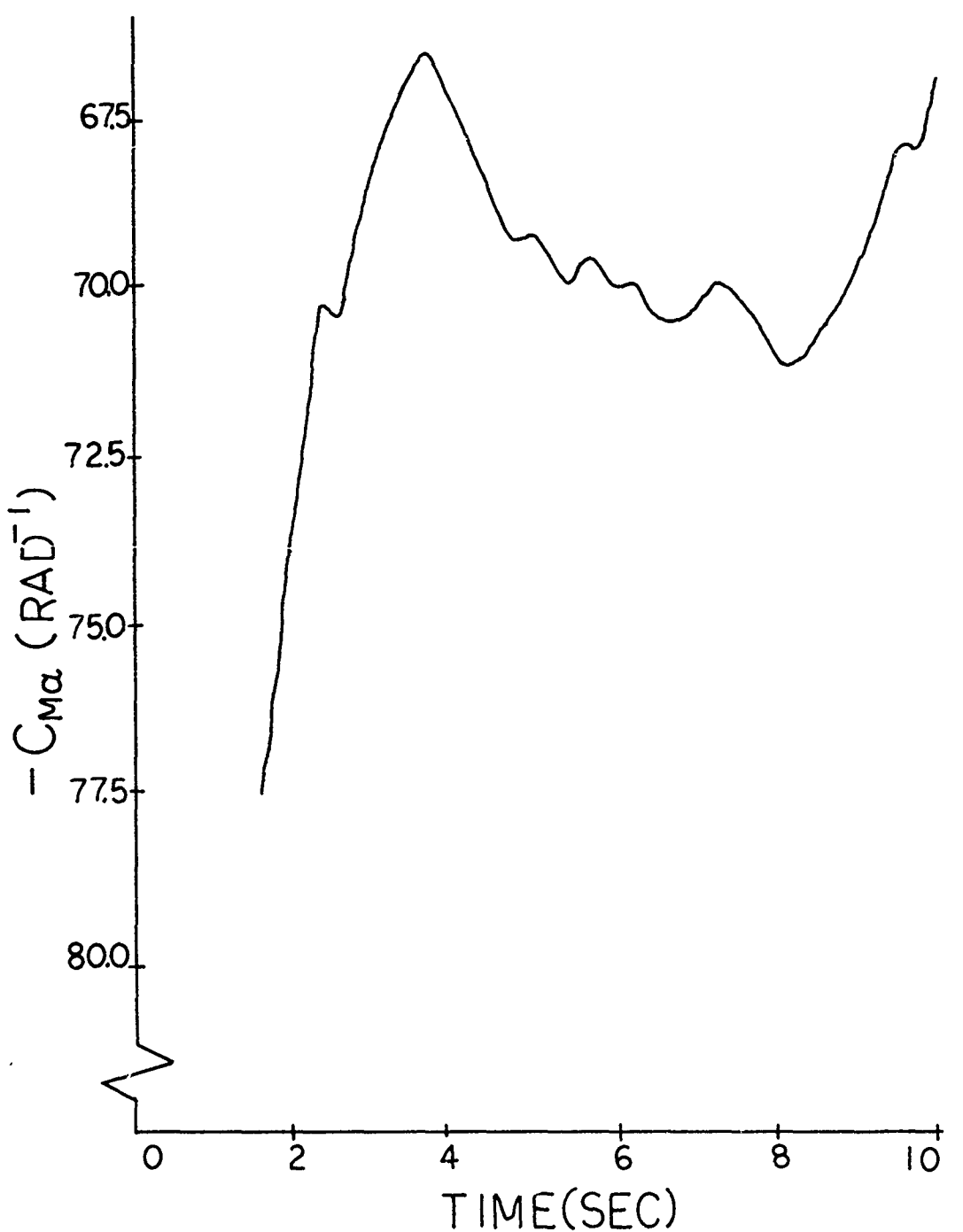
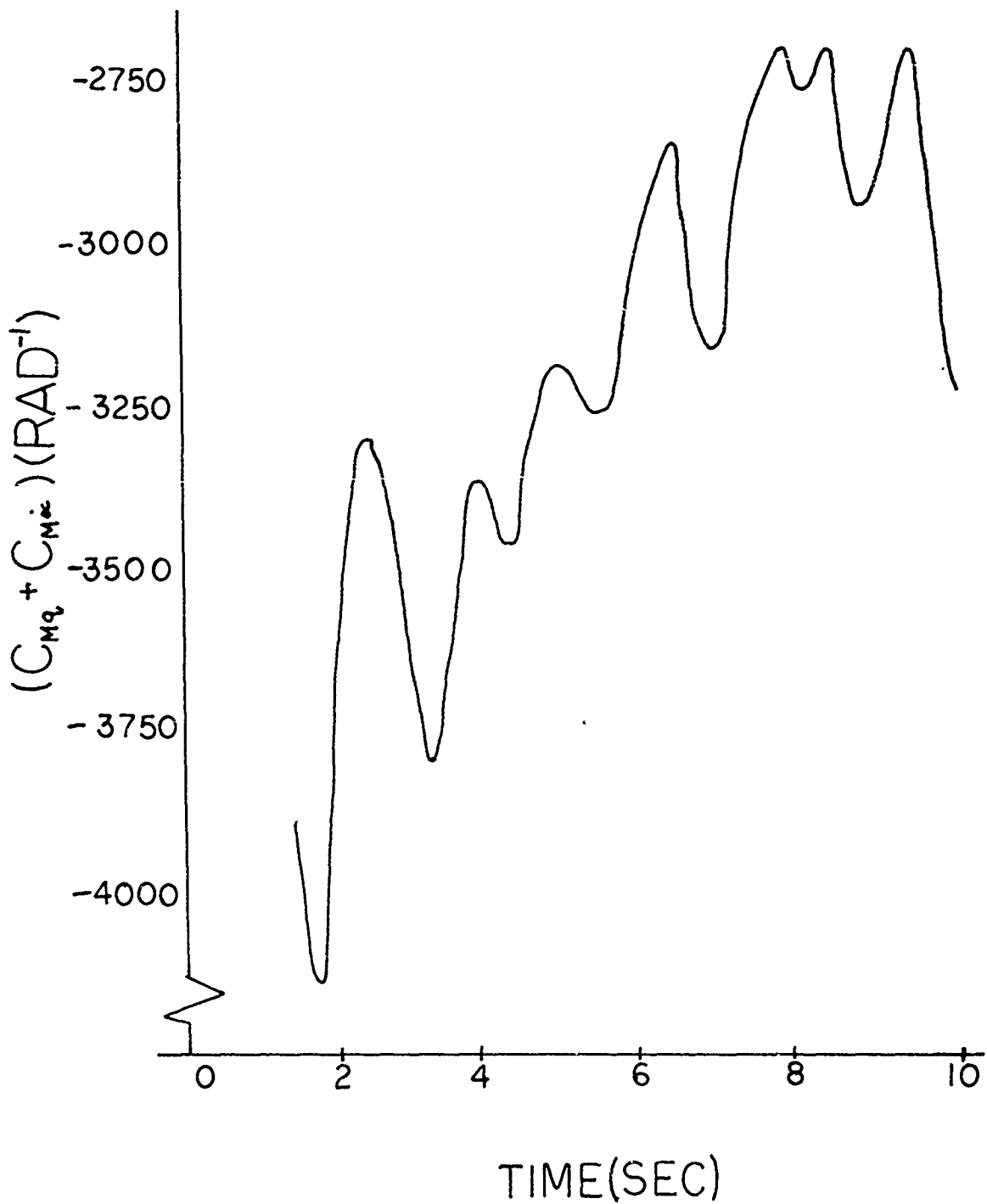
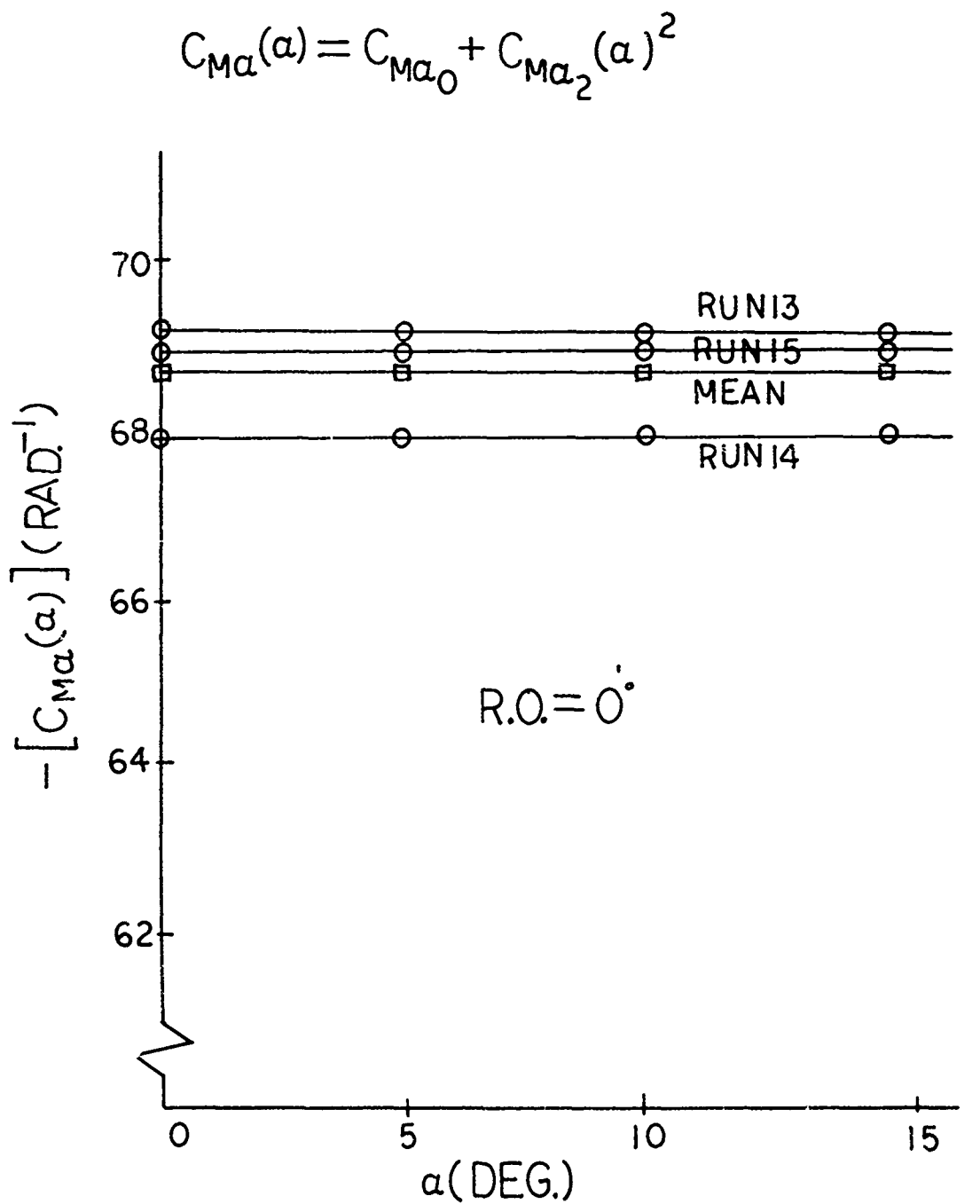
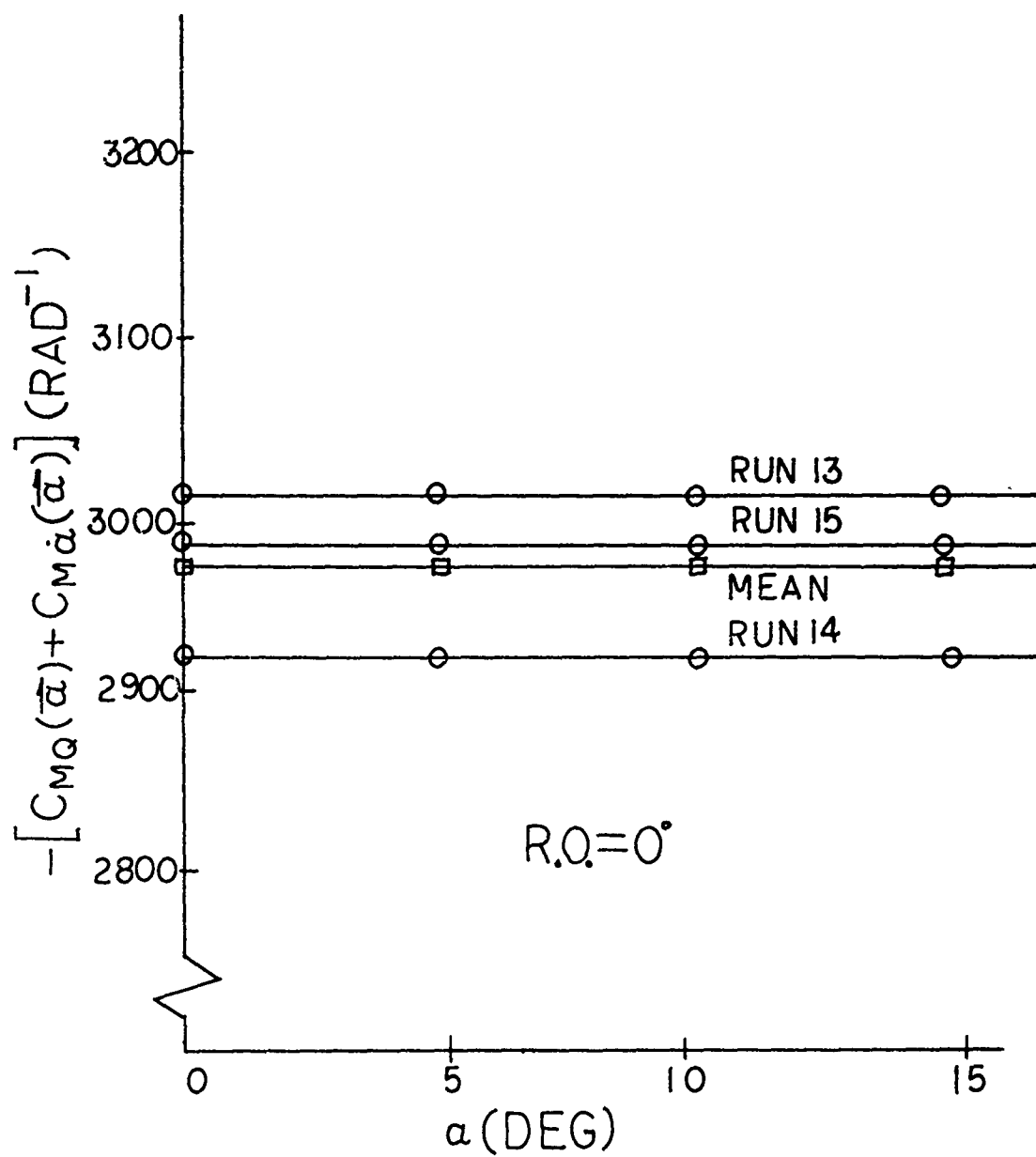


FIG. 27 C_{Ma} VS. TIME

FIG.28 $(C_{Mq} + C_{M\alpha})$ VS TIME

FIG. 29 $C_{Ma}(\alpha)$ VS. α

$$C_{MQ}(\alpha) + C_{M\dot{\alpha}}(\alpha) = [C_{MQ} + C_{M\dot{\alpha}}]_0 + [C_{MQ} + C_{M\dot{\alpha}}]_2 (\alpha)^2$$

FIG. 30 $-[C_{MQ}(\bar{\alpha}) + C_{M\dot{\alpha}}(\bar{\alpha})]$ VS. α

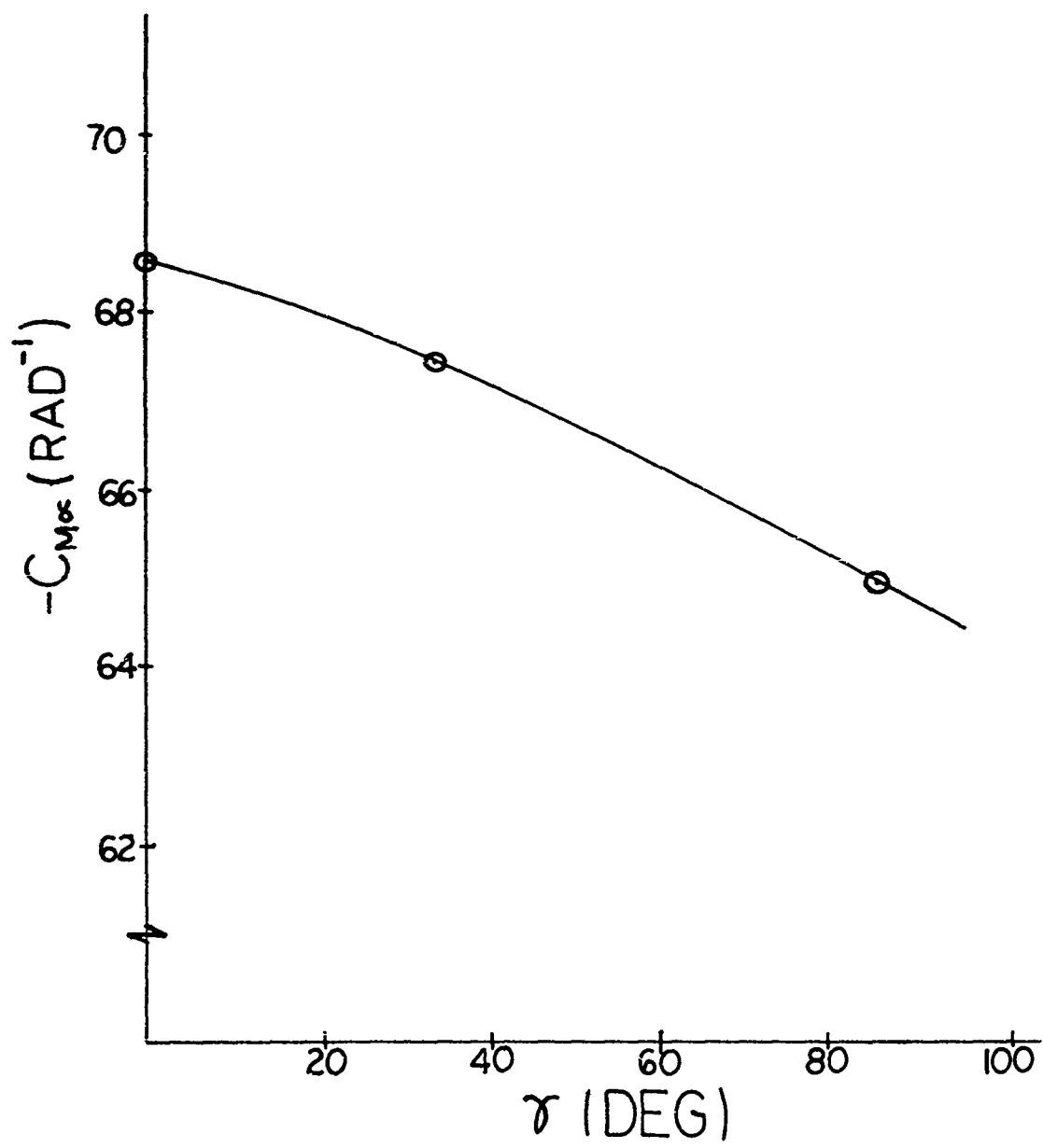
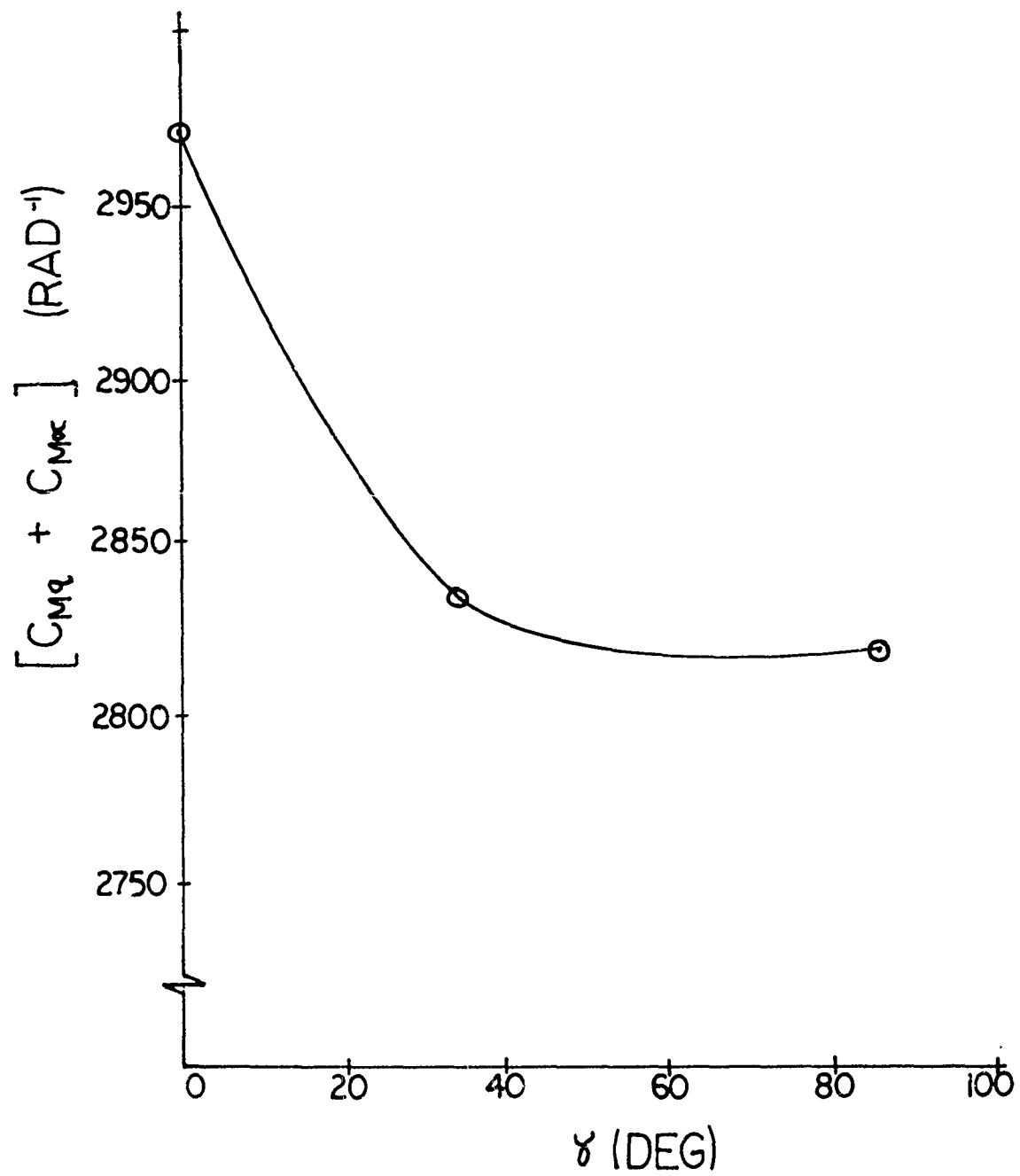


FIG. 31 $C_{M\alpha}$ vs ROLL ANGLE

FIG. 32 $C_{Mq} + C_{M\infty}$ vs ROLL ANG.

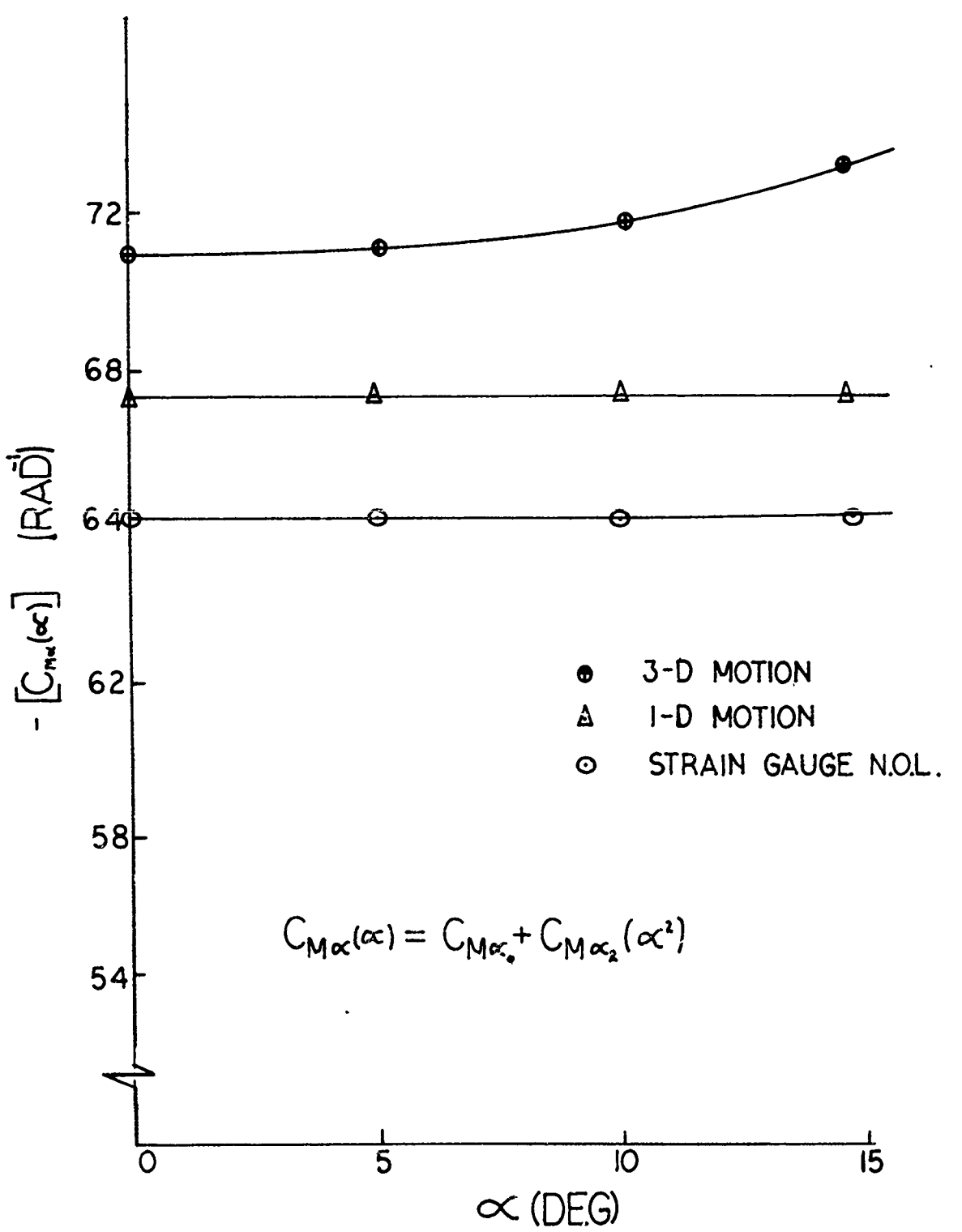
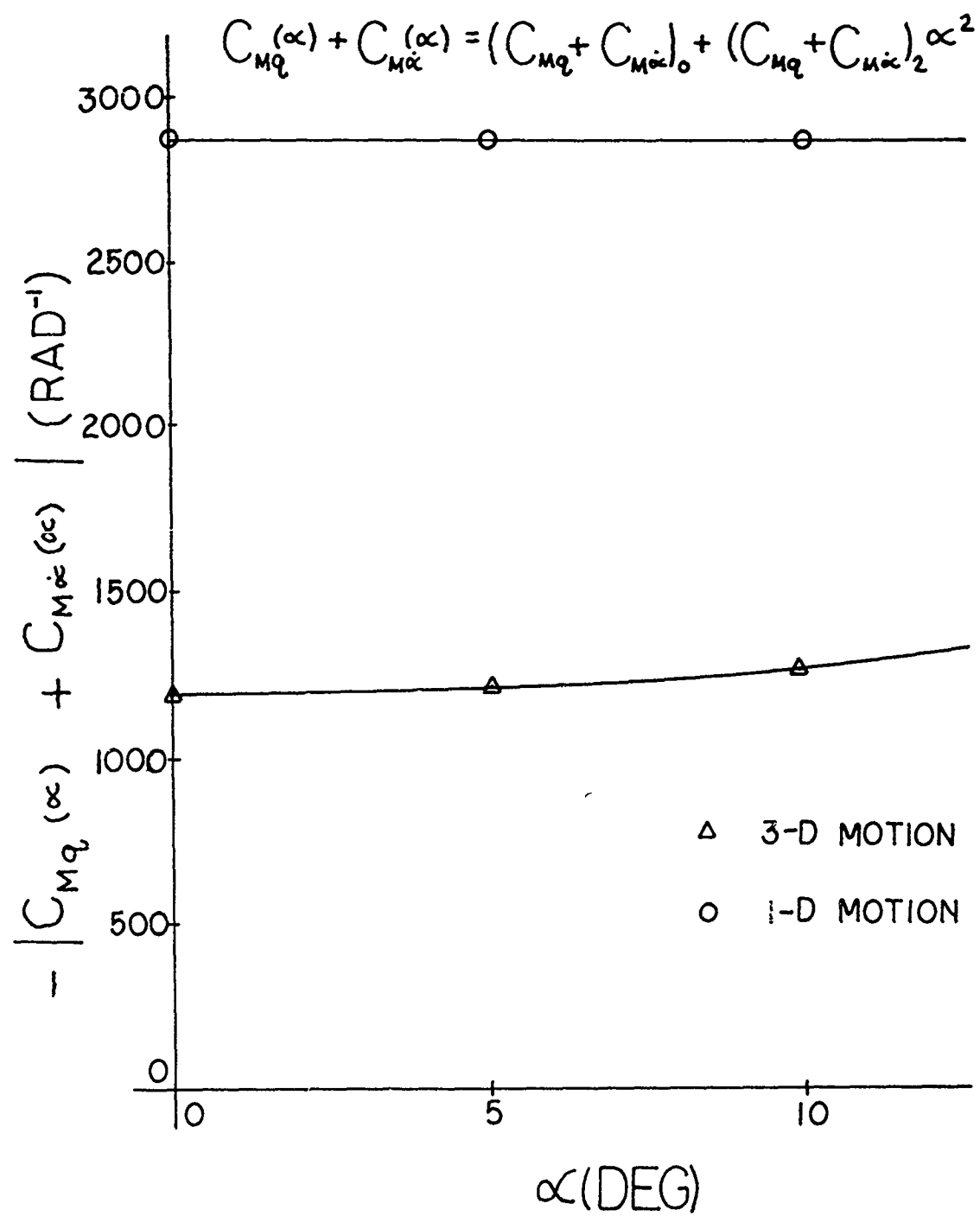


FIG. 33

MEAN $C_{M\alpha}$ VS α

FIG. 34 MEAN $C_{Mq} + C_{M\dot{\alpha}}$ VS α

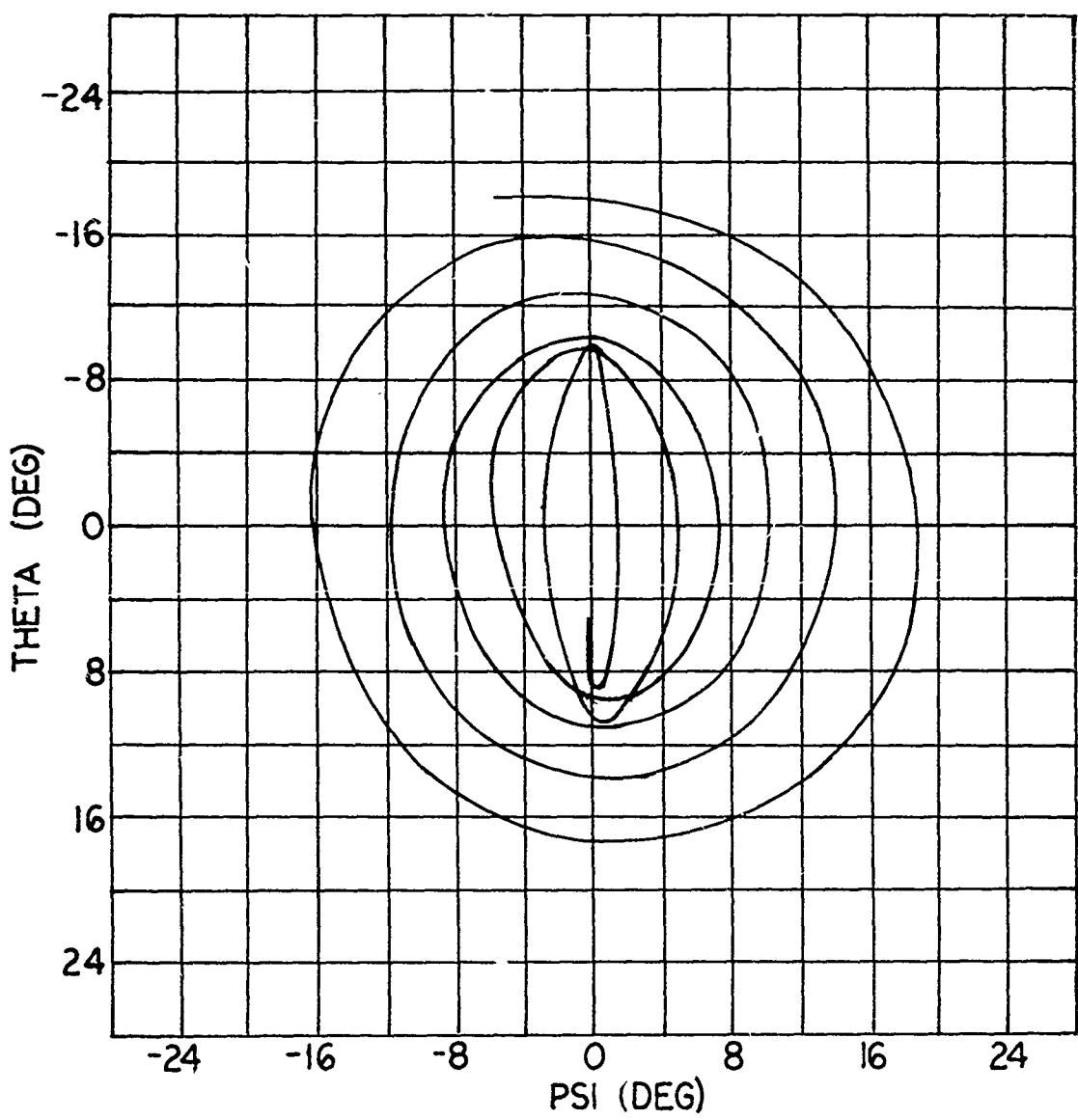


FIG. 35 6-D COMPLEX MOTION

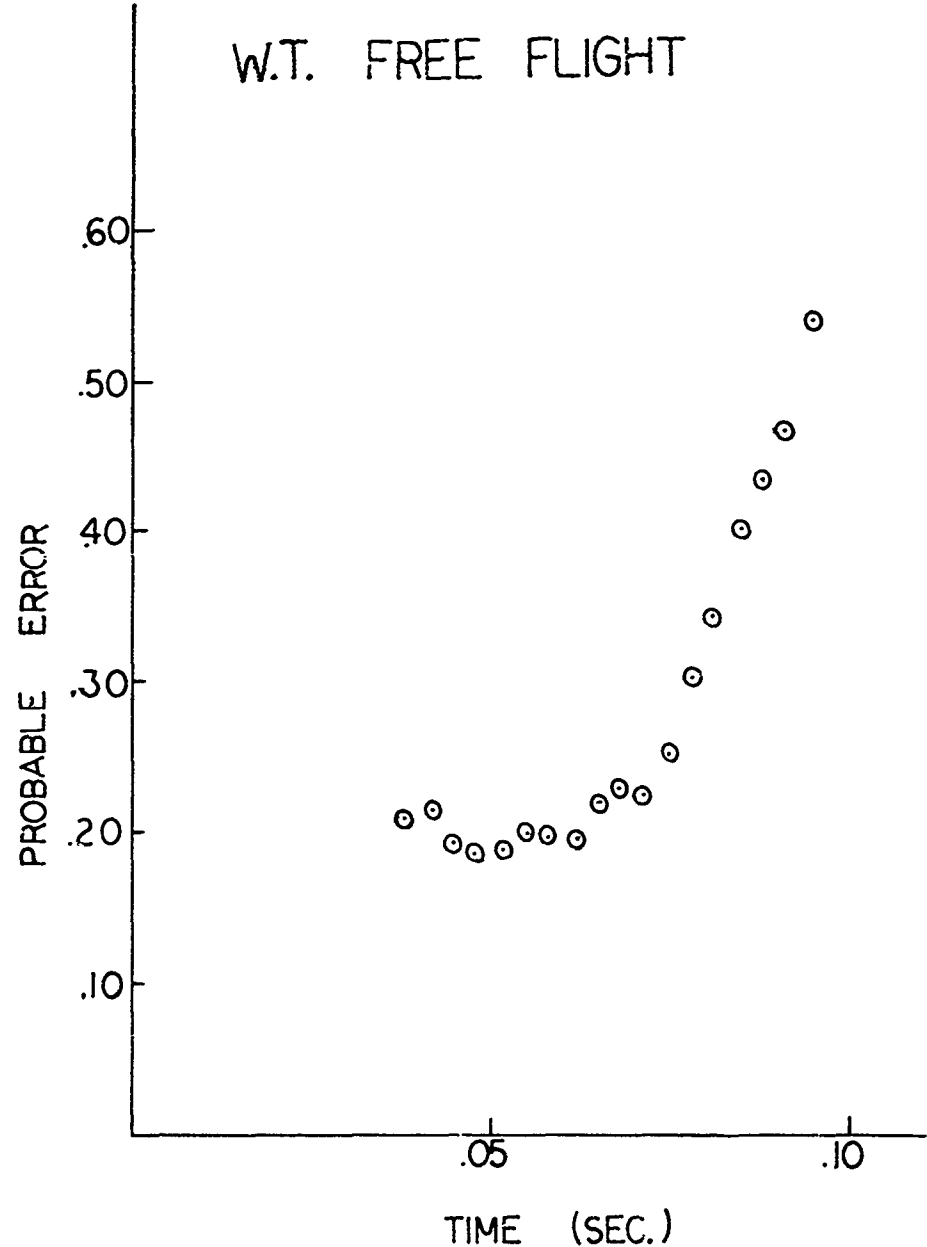


FIG. 36 PROBABLE ERROR vs TIME

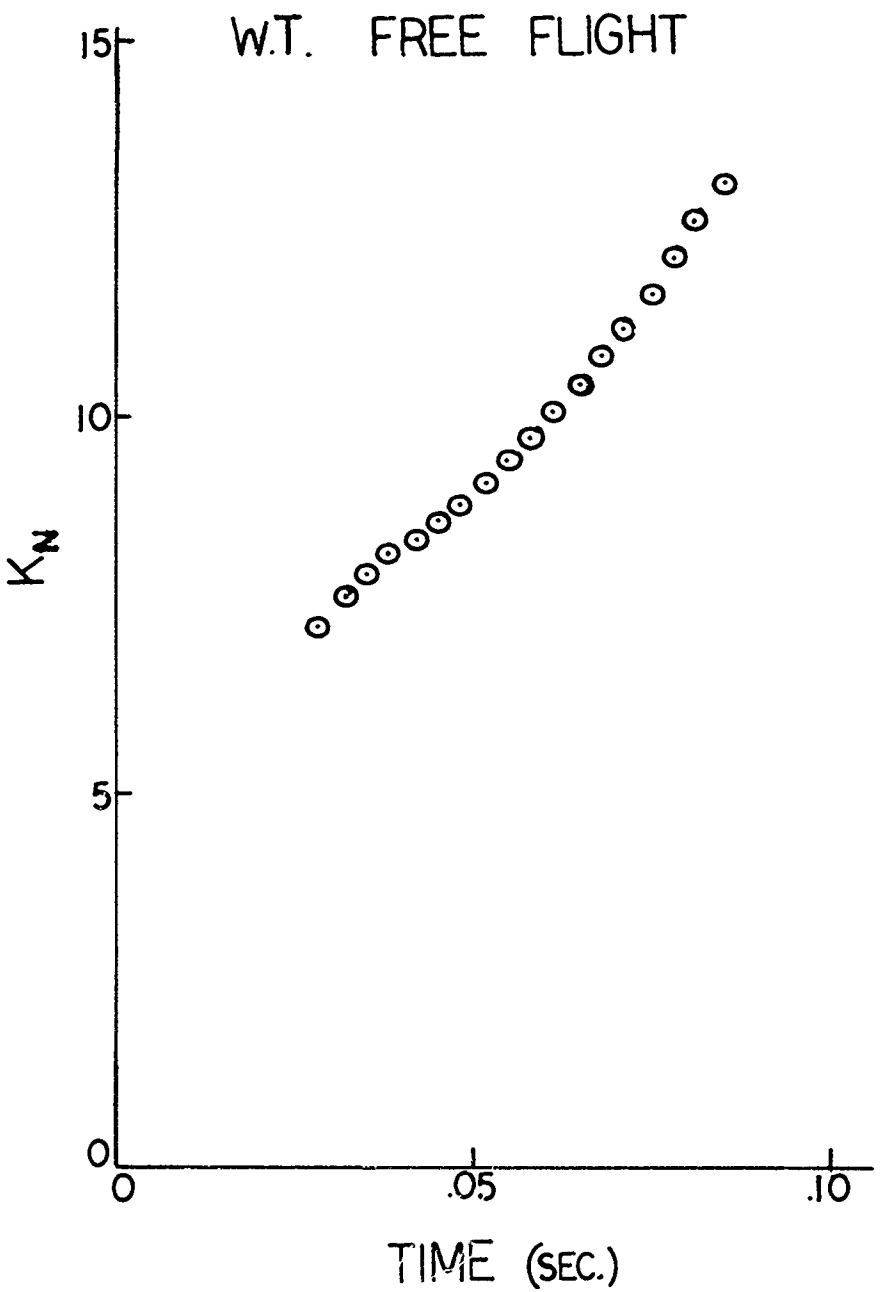


FIG 37 K_N vs TIME

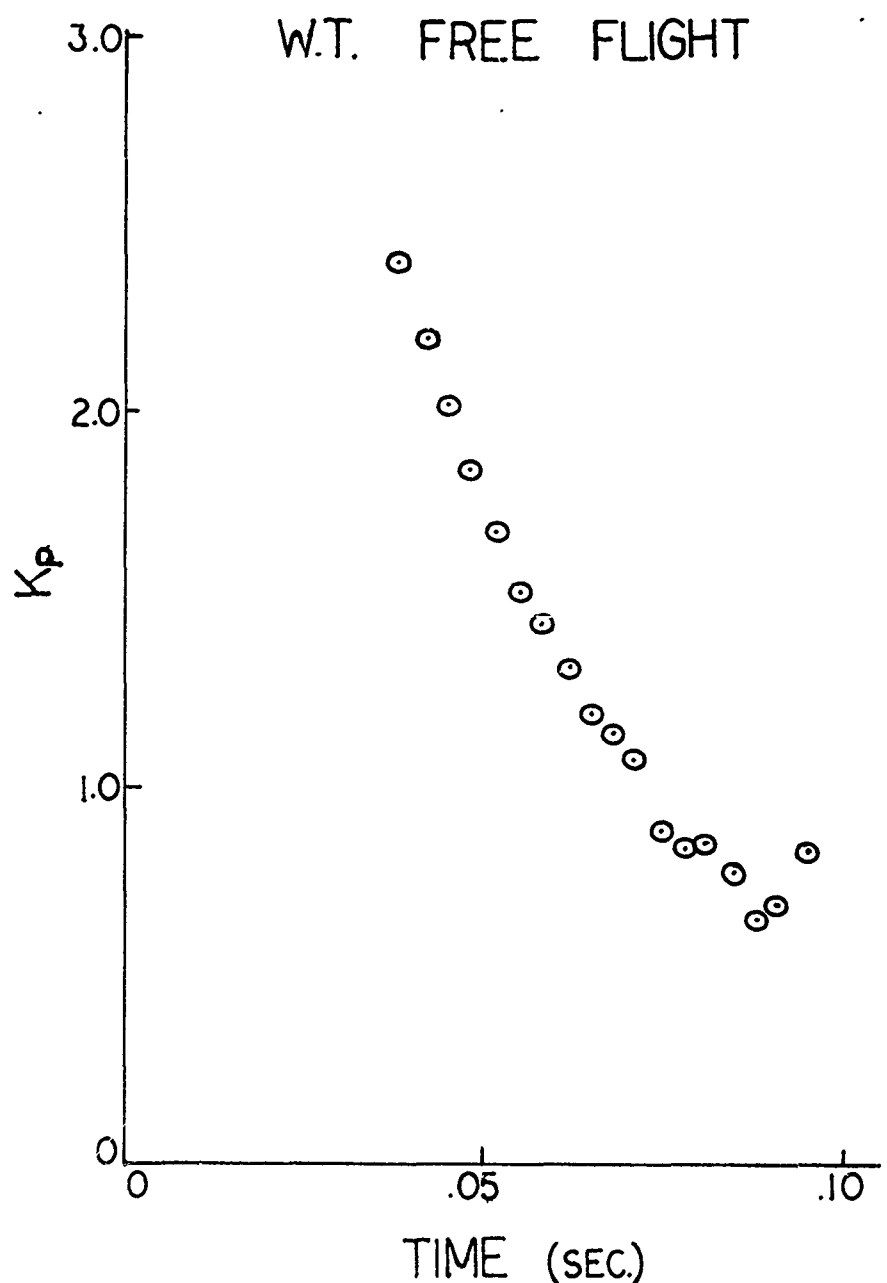


FIG 38 K_P vs TIME

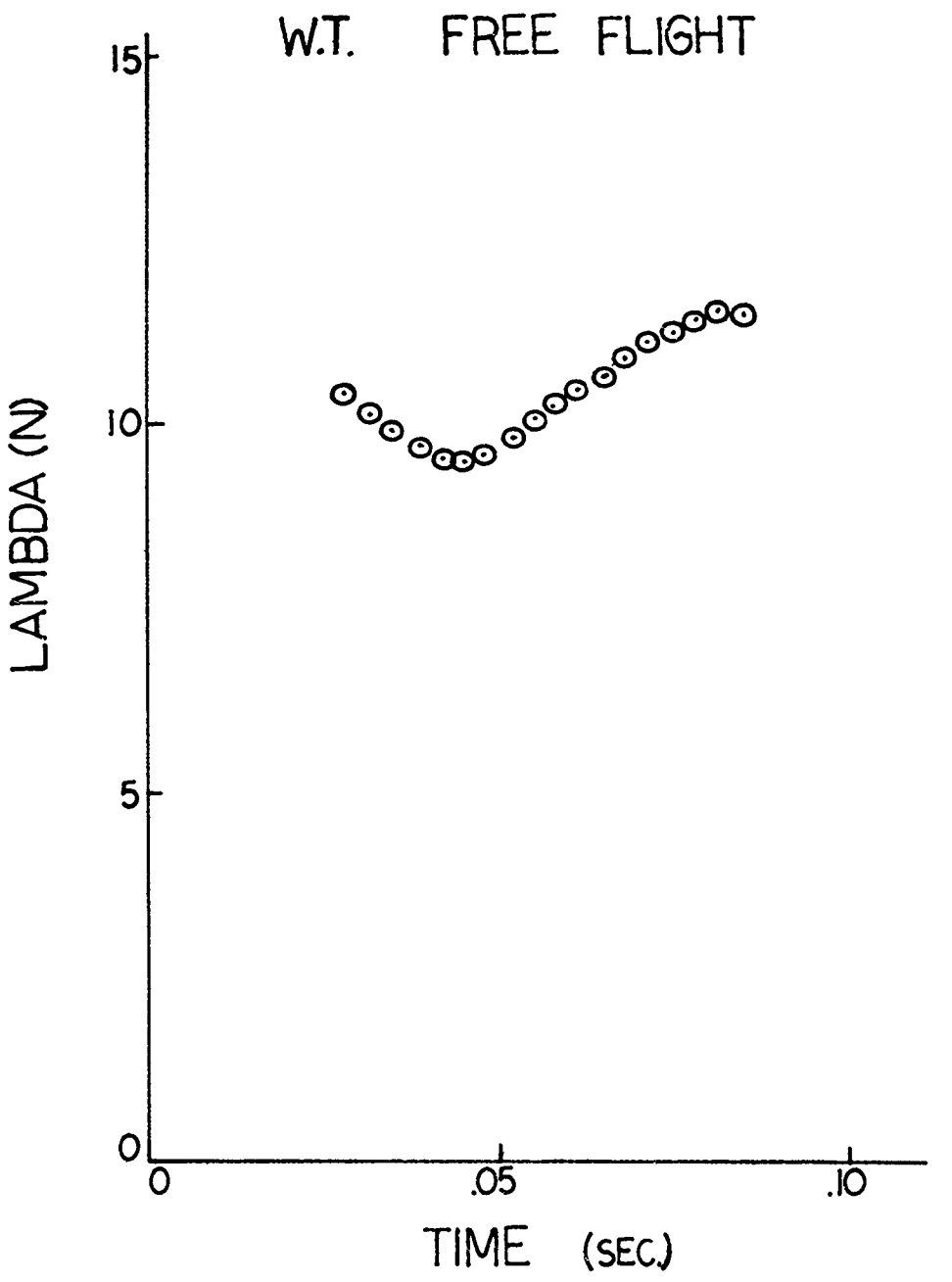


FIG 39 LAMBDA(N) vs TIME

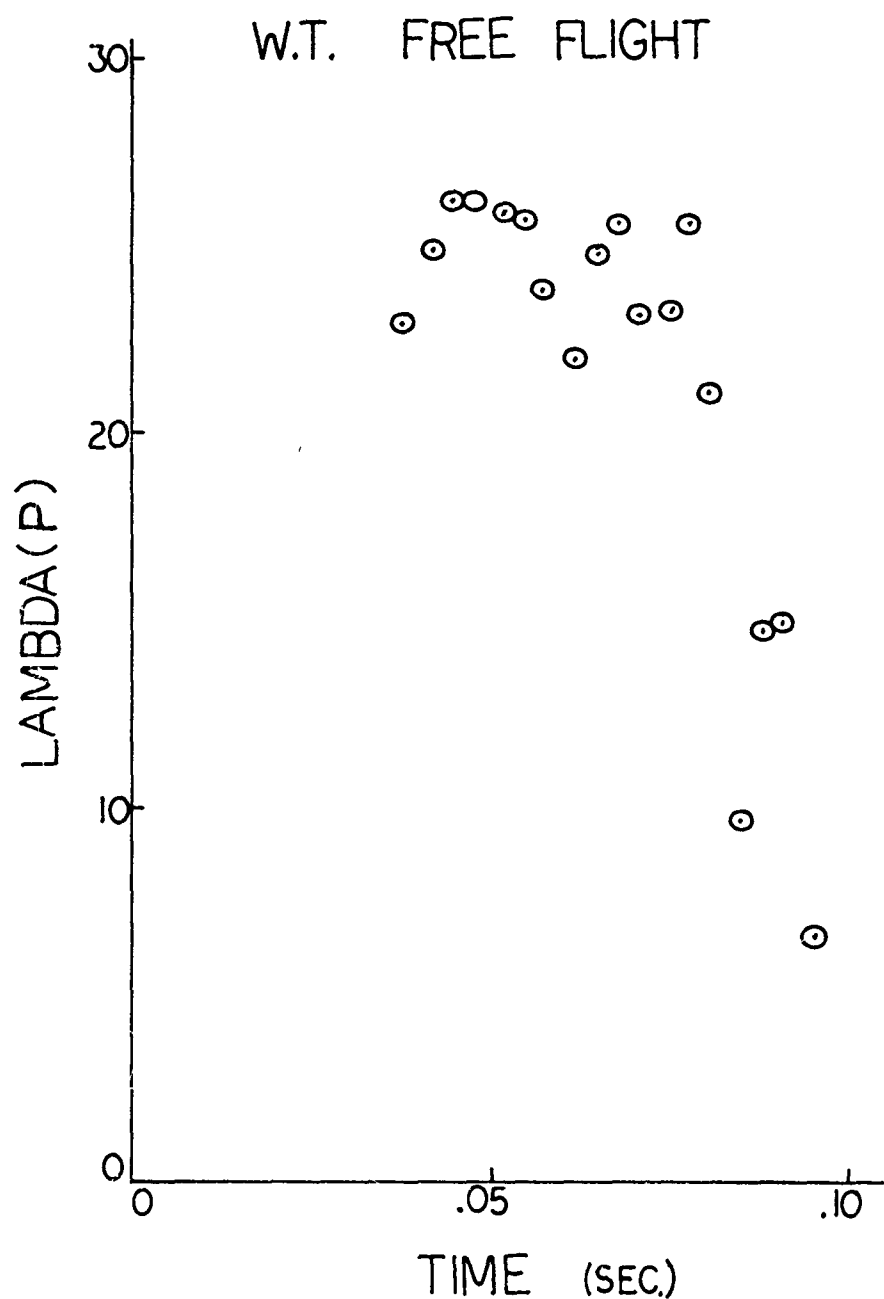


FIG. 40 LAMBDA(P) VS TIME

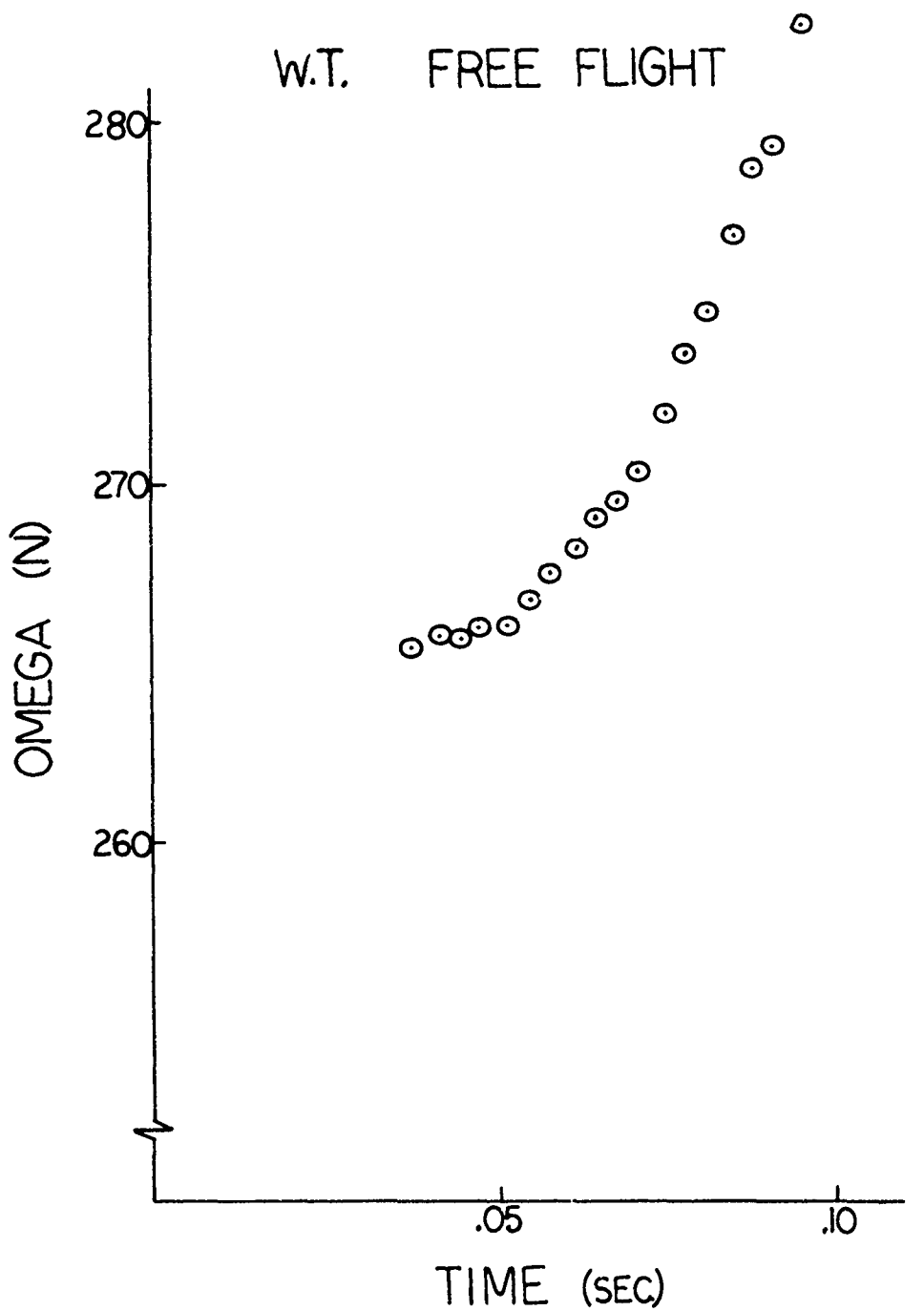


FIG 41 OMEGA (N) vs TIME

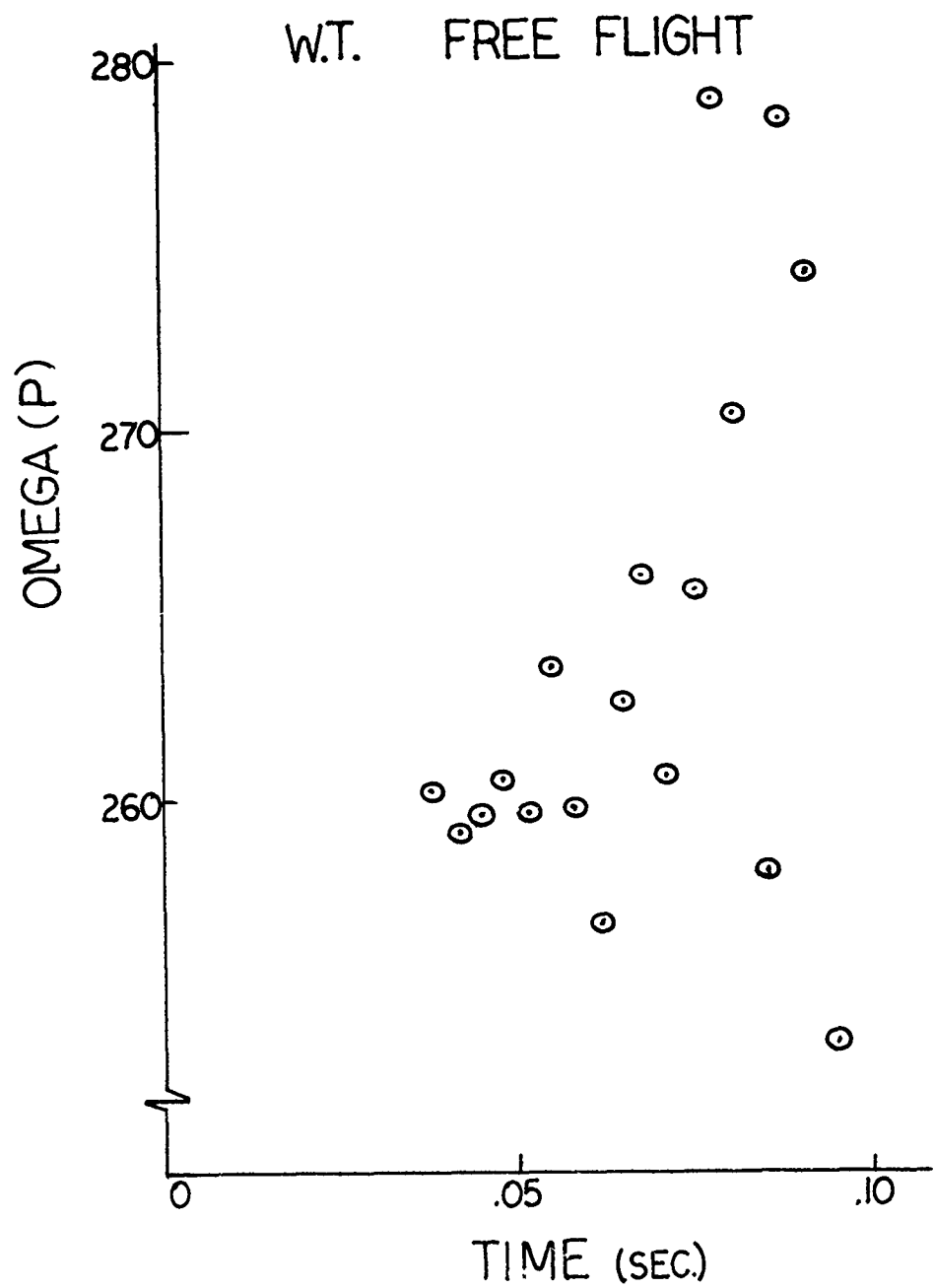


FIG. 42

OMEGA(P) vs TIME

W.T. FREE FLIGHT

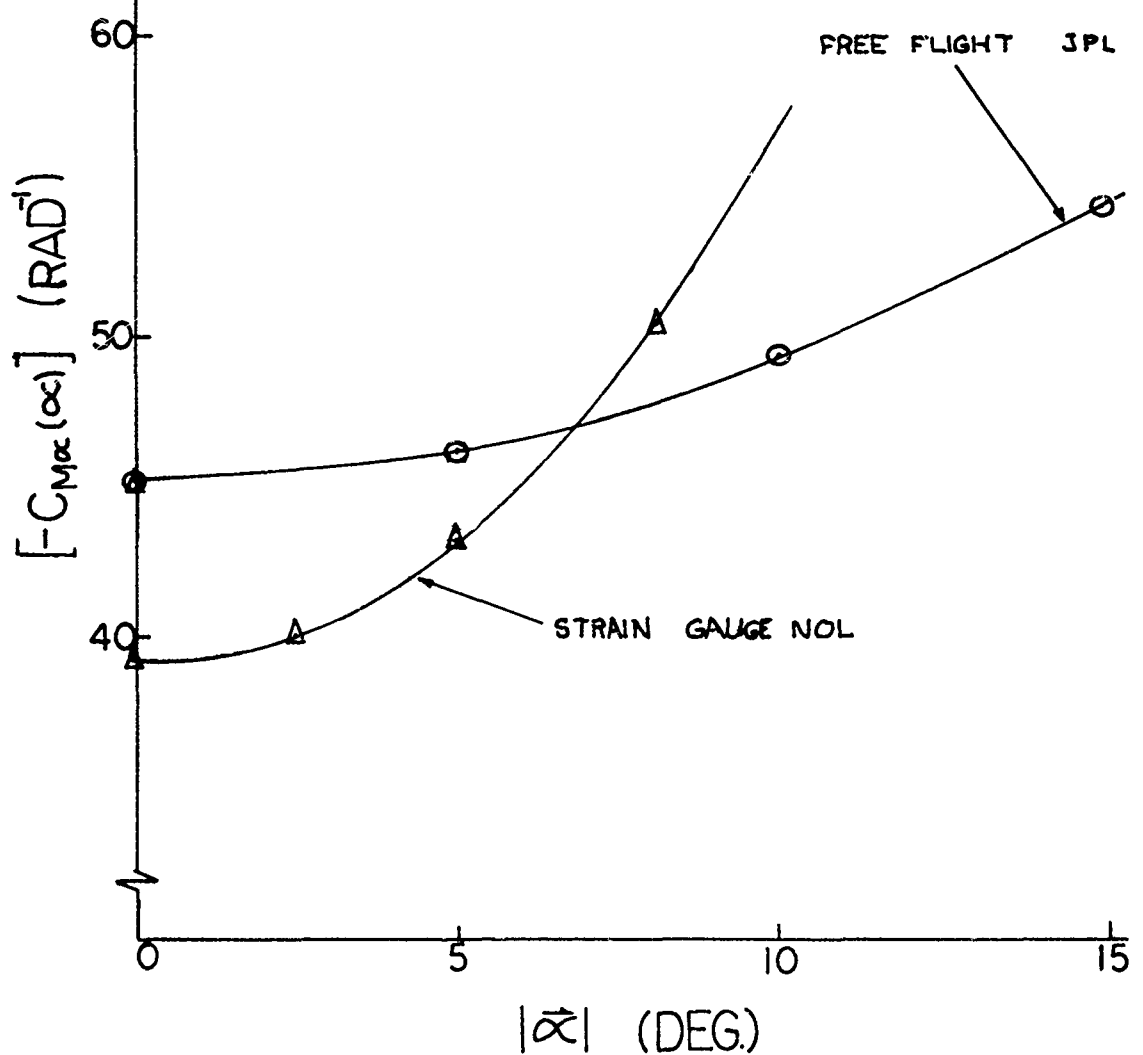
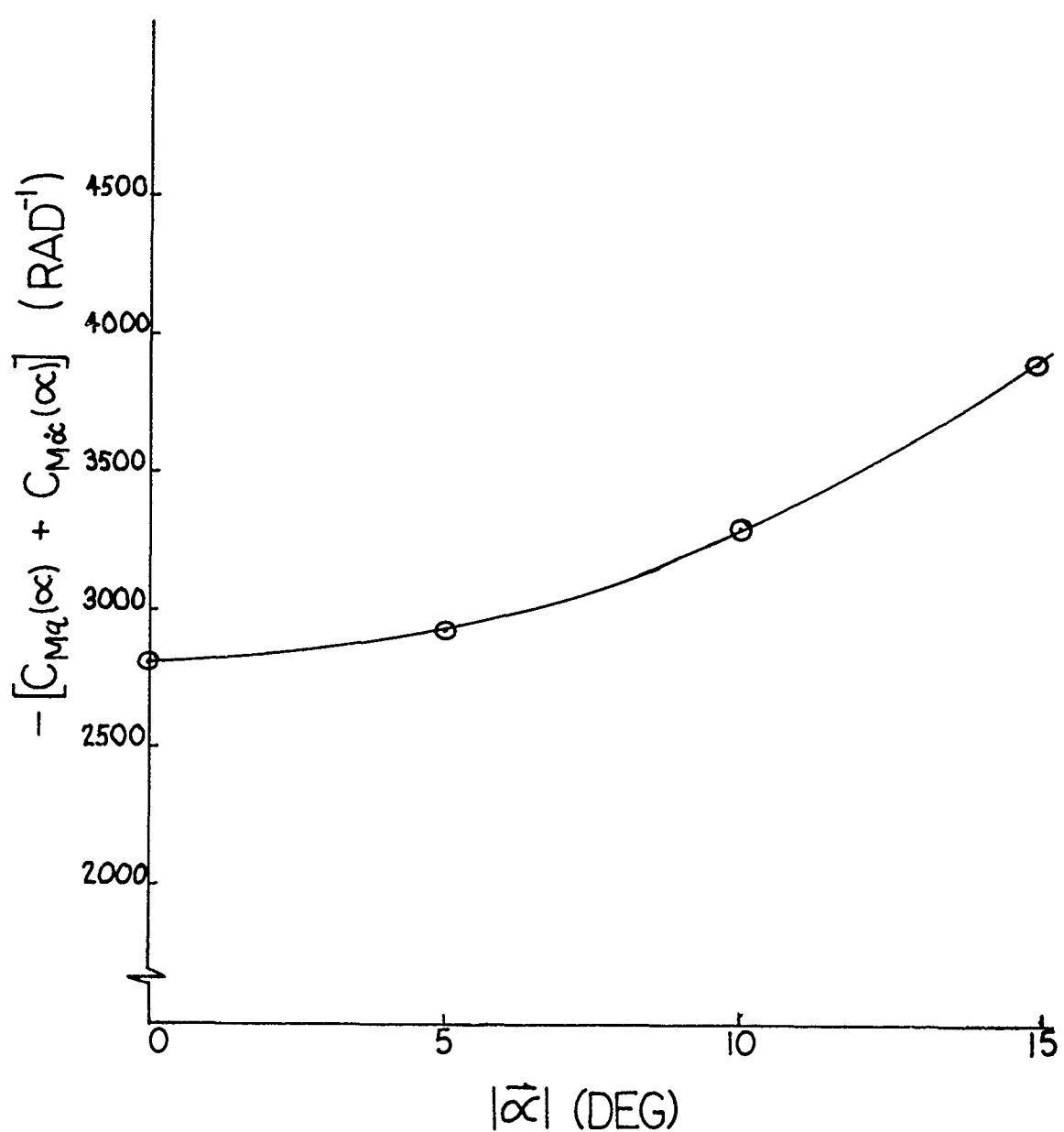


FIG. 43 $-C_{M\alpha}(\alpha)$ vs $|\bar{\alpha}|$

W.T. FREE FLIGHT

FIG. 44 $-[C_{Mq}(\alpha) + C_{M\alpha}(\alpha)]$ vs $|\bar{\alpha}|$

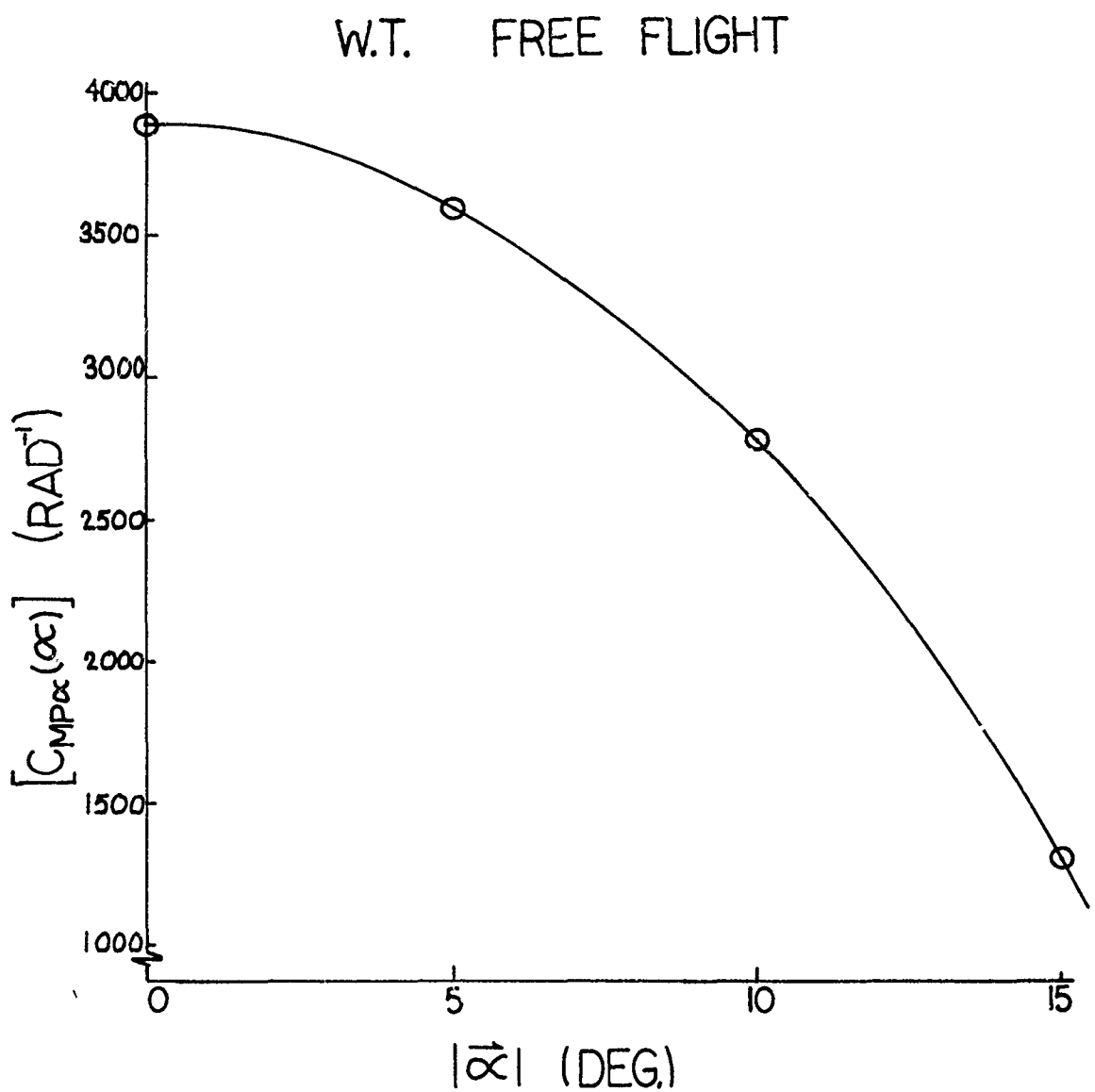
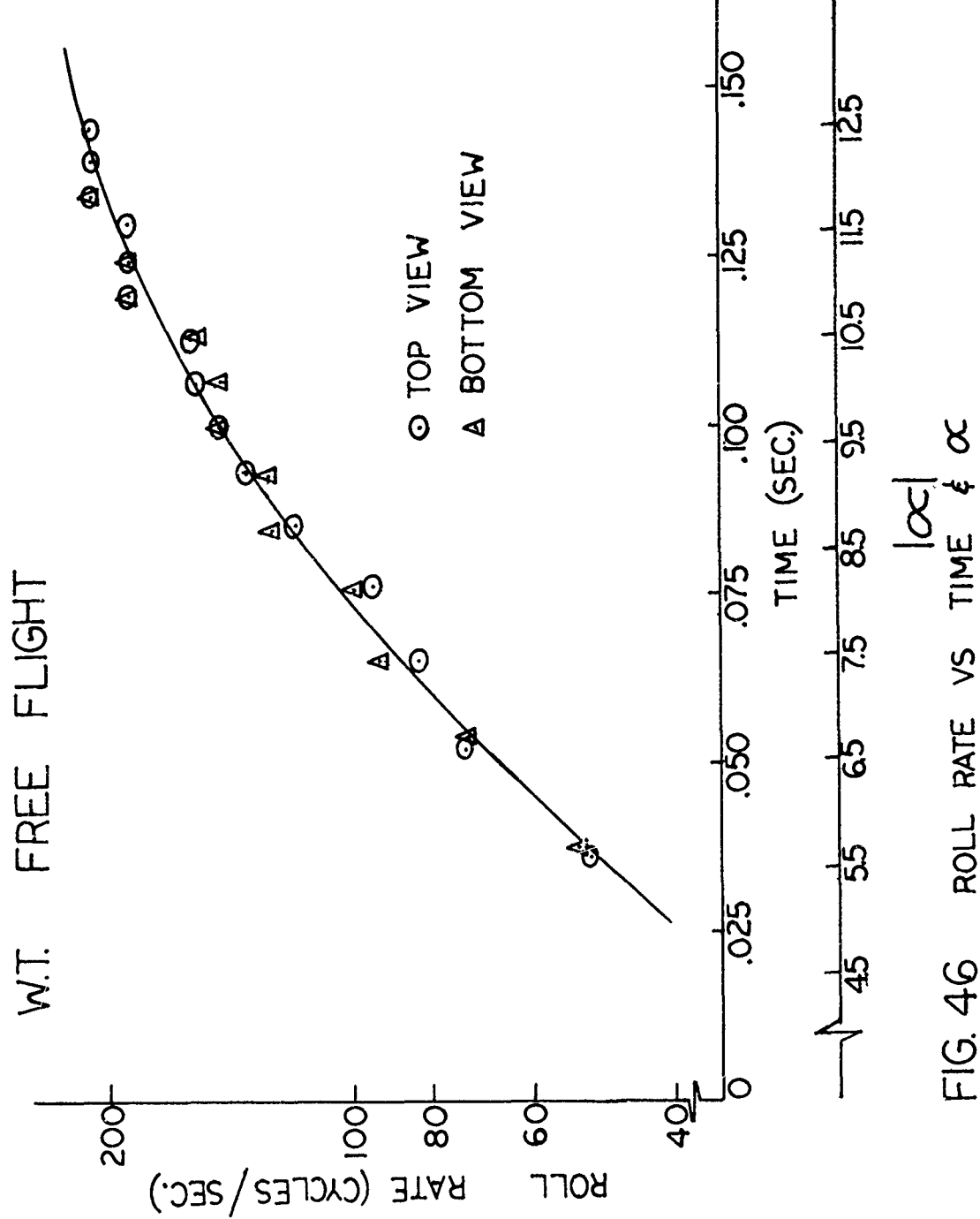


FIG. 45 $[C_{Mp\alpha}(\omega)]$ vs $|\omega|$



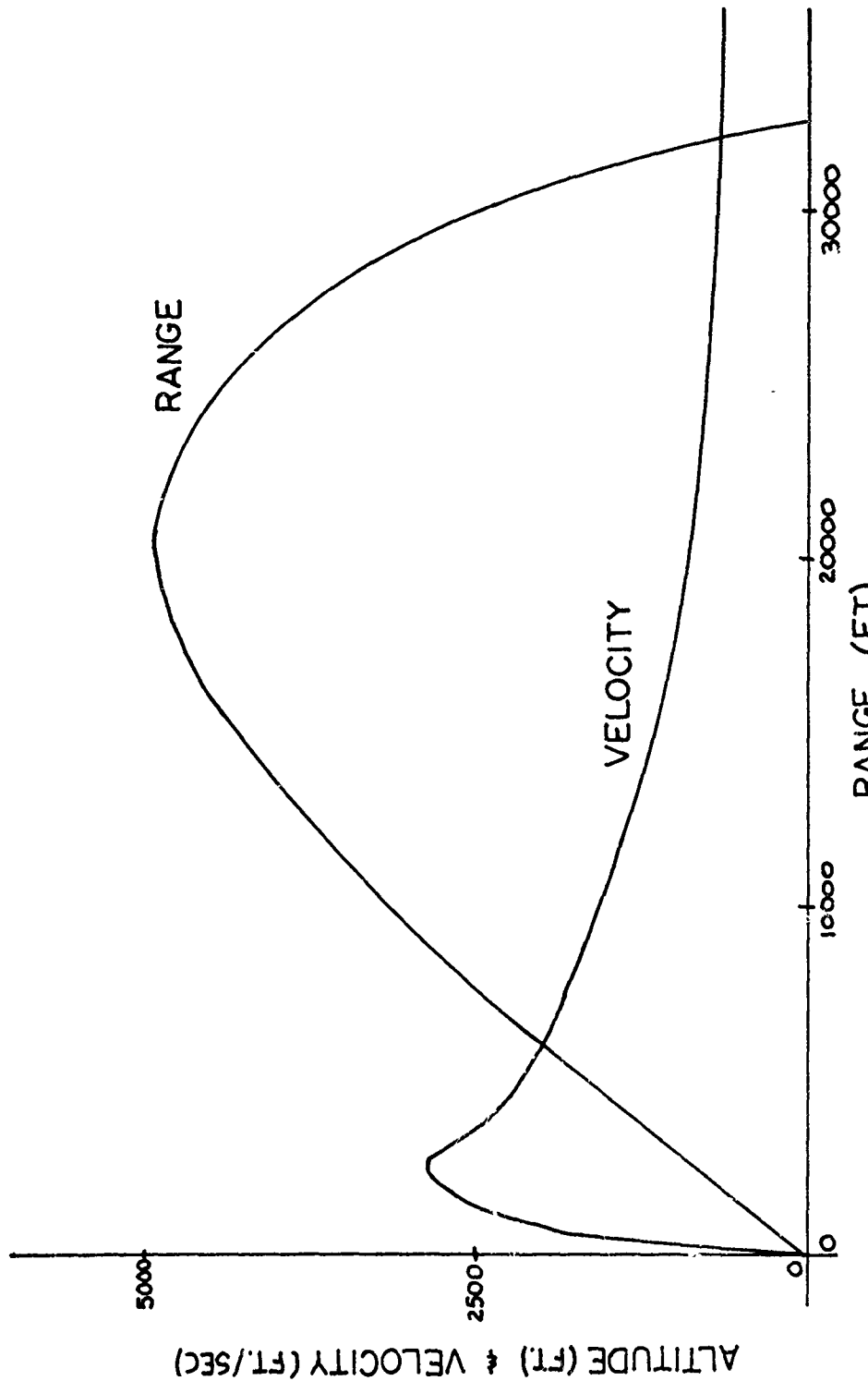


FIG. 47 TYPICAL FLIGHT PERFORMANCE

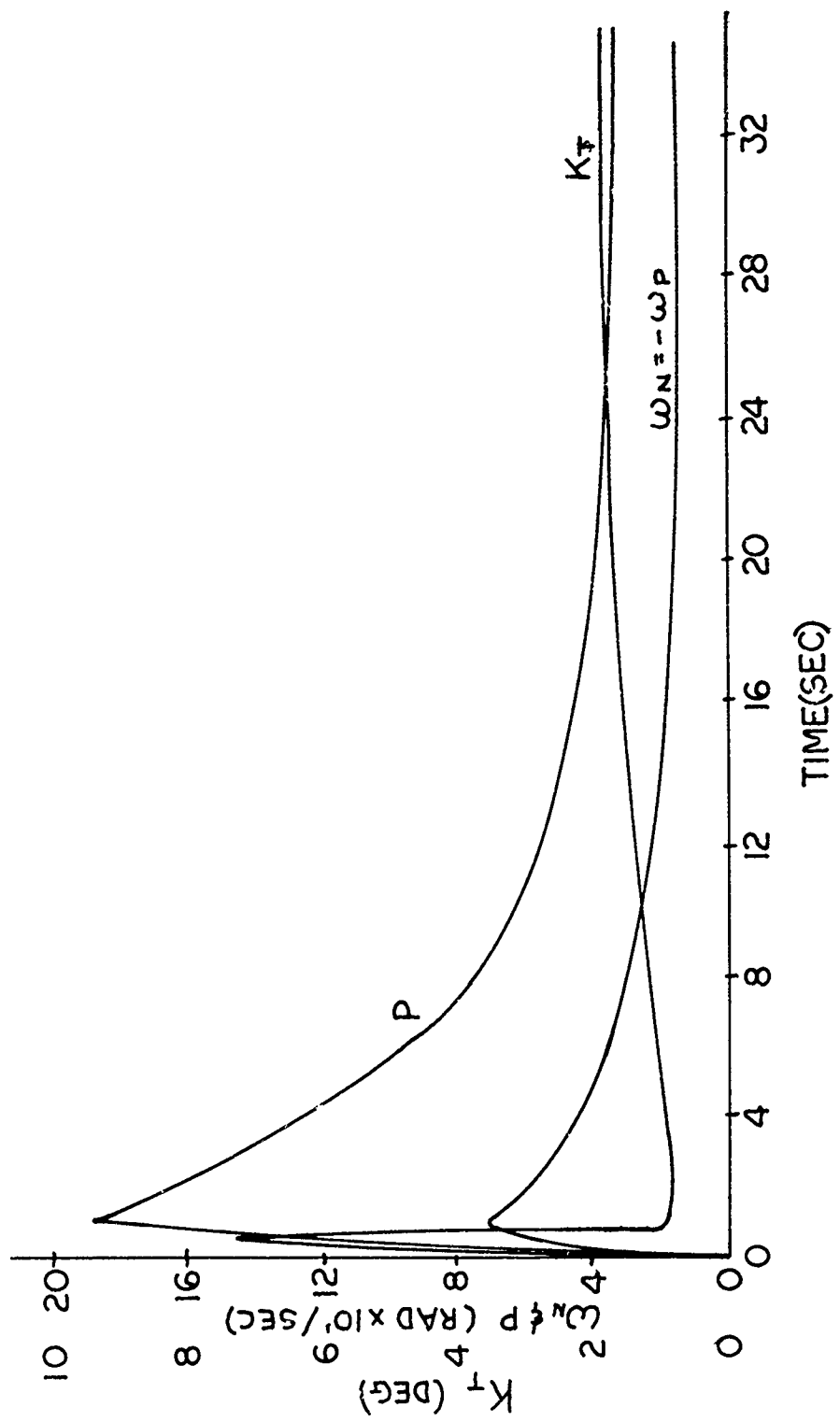


FIG. 48 TYPICAL FLIGHT PERFORMANCE 1

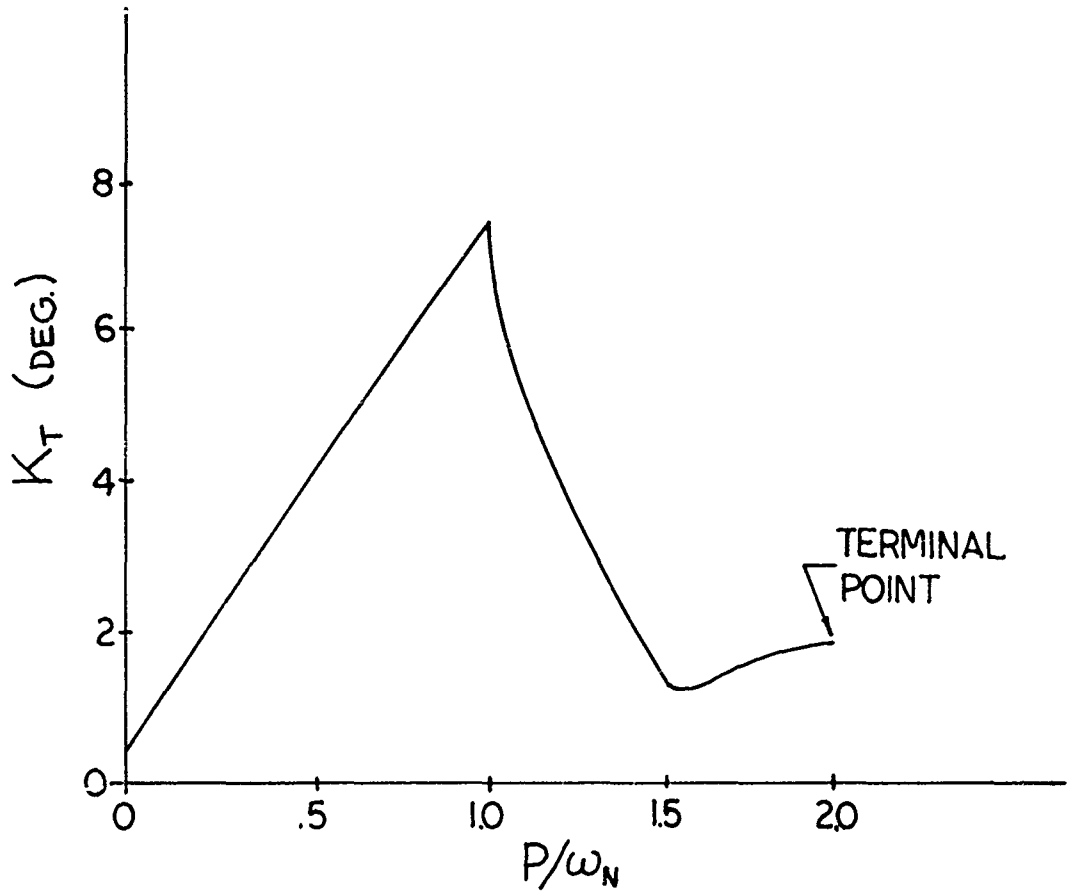


FIG. 49 TYPICAL FLIGHT PERFORMANCE 1

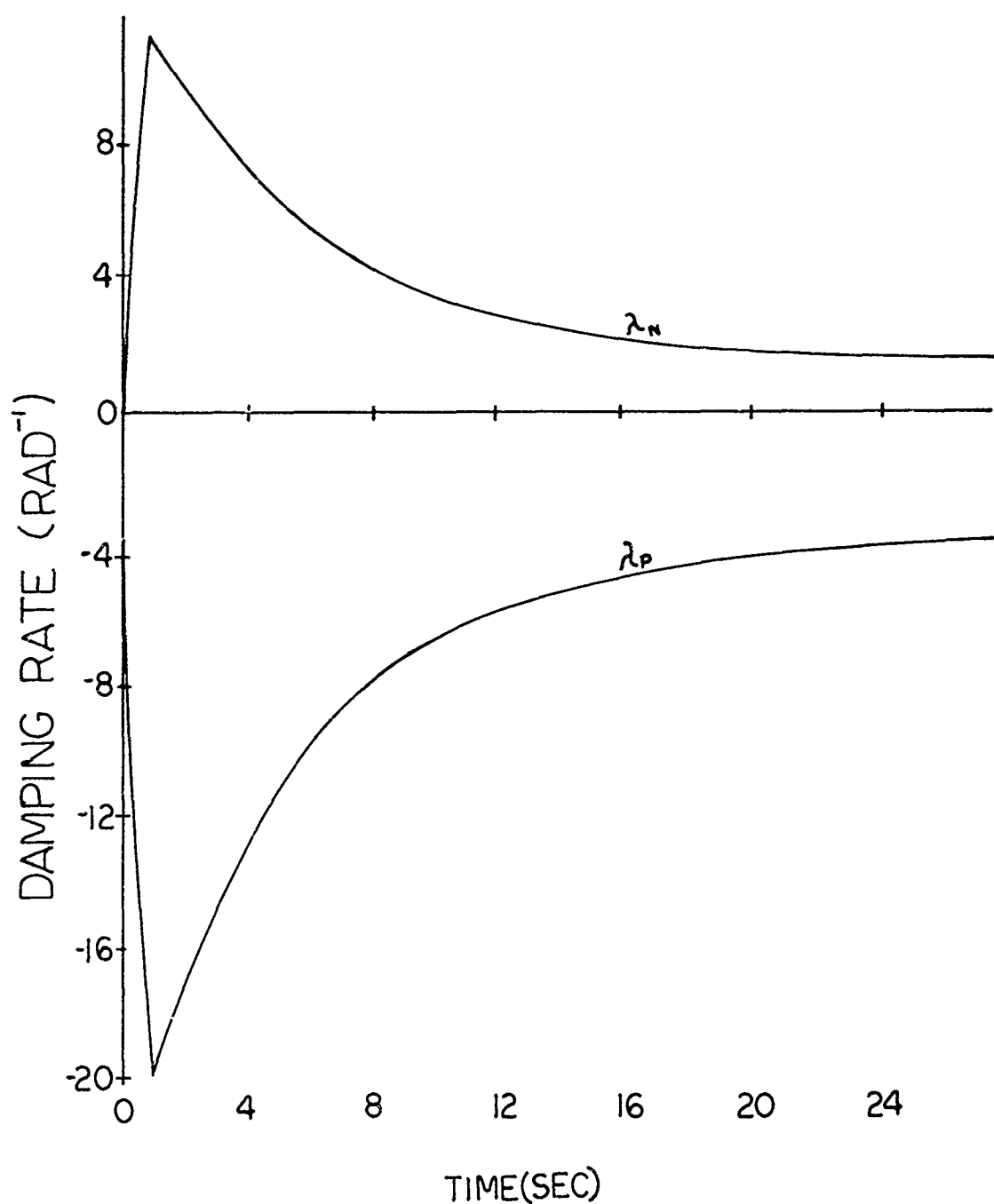


FIG.50 TYPICAL FLIGHT PERFORMANCE 1

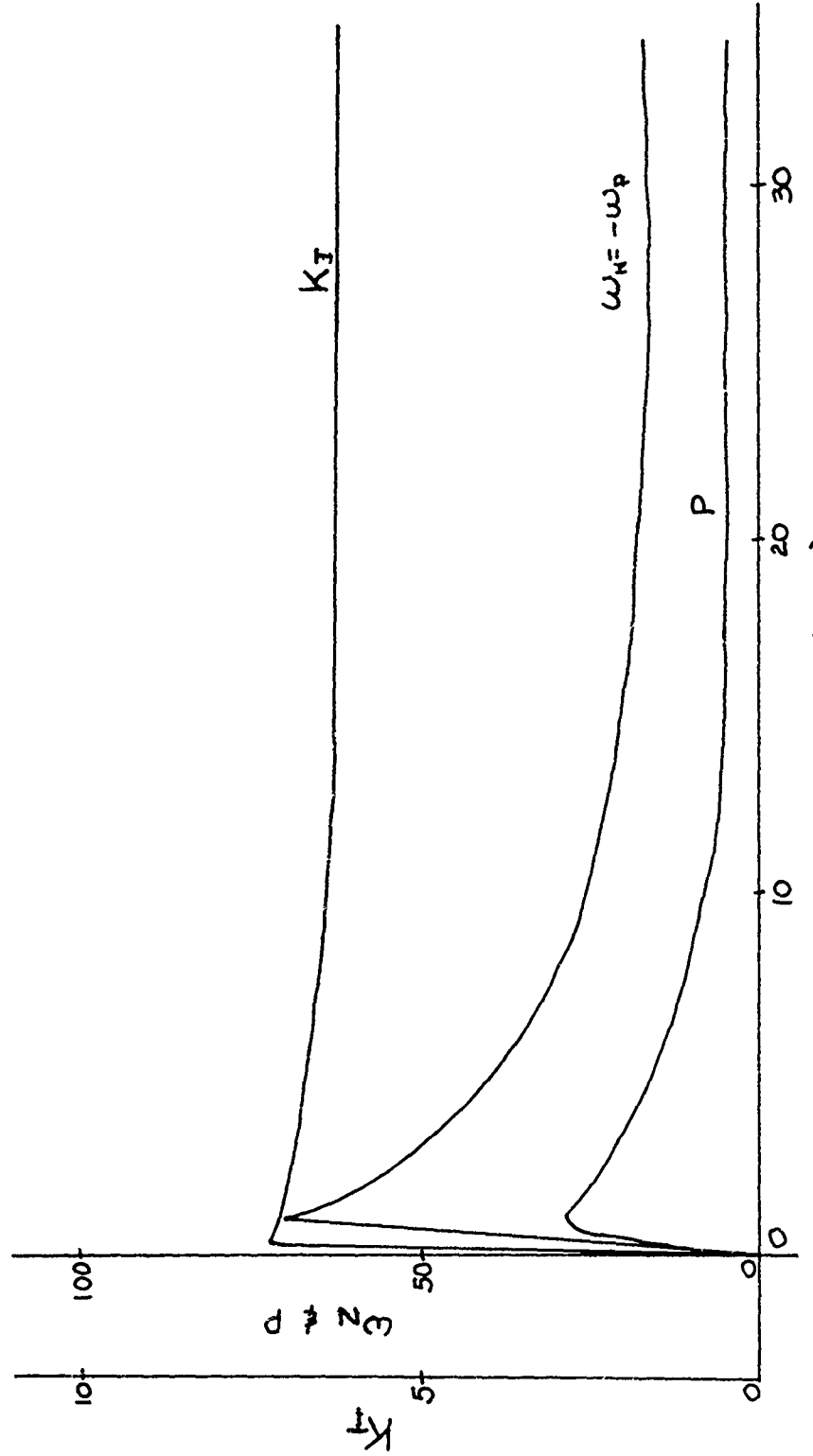


FIG. 51 TYPICAL FLIGHT PERFORMANCE 2

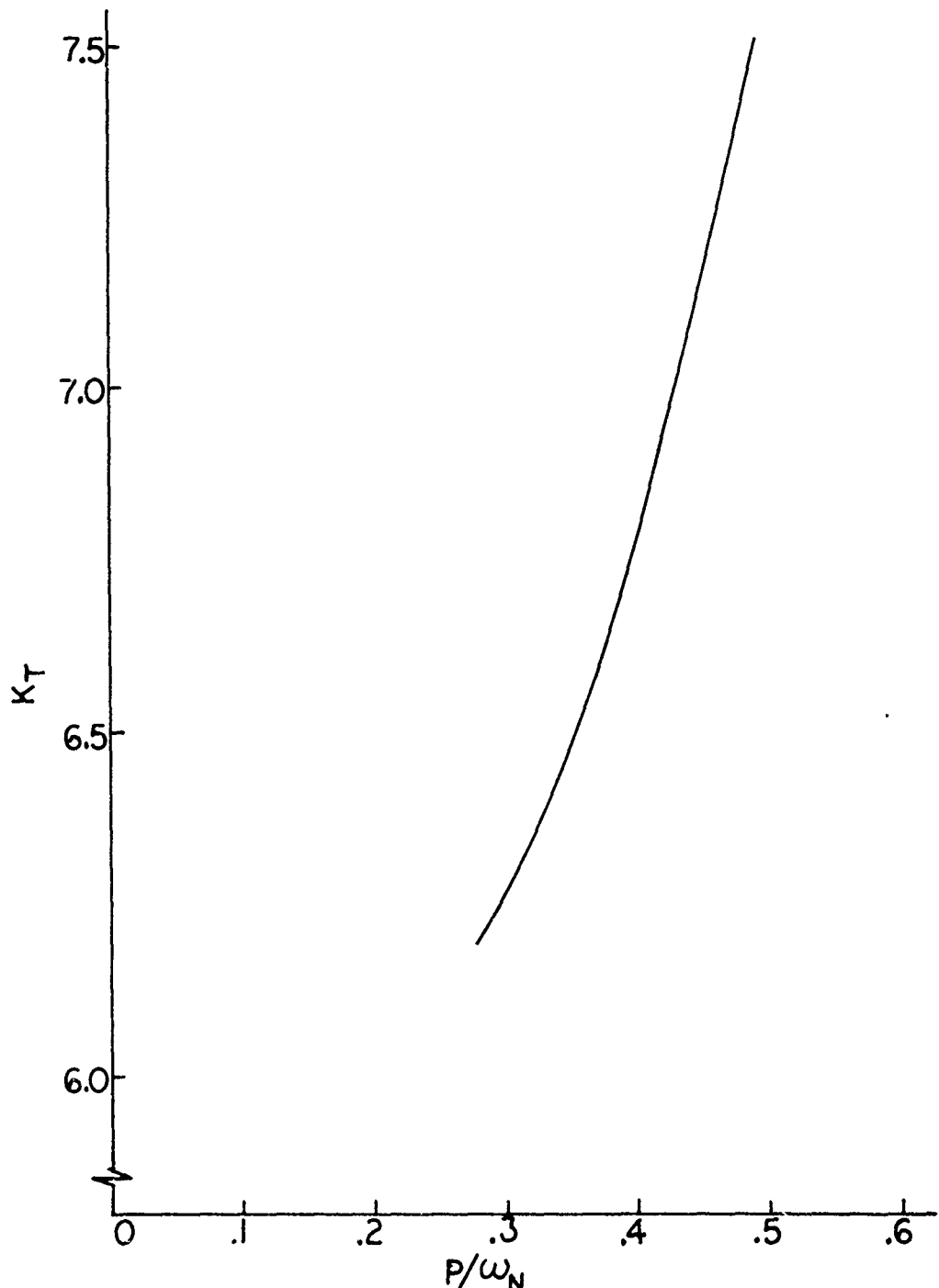


FIG. 52

TYPICAL FLIGHT PERFORMANCE 2

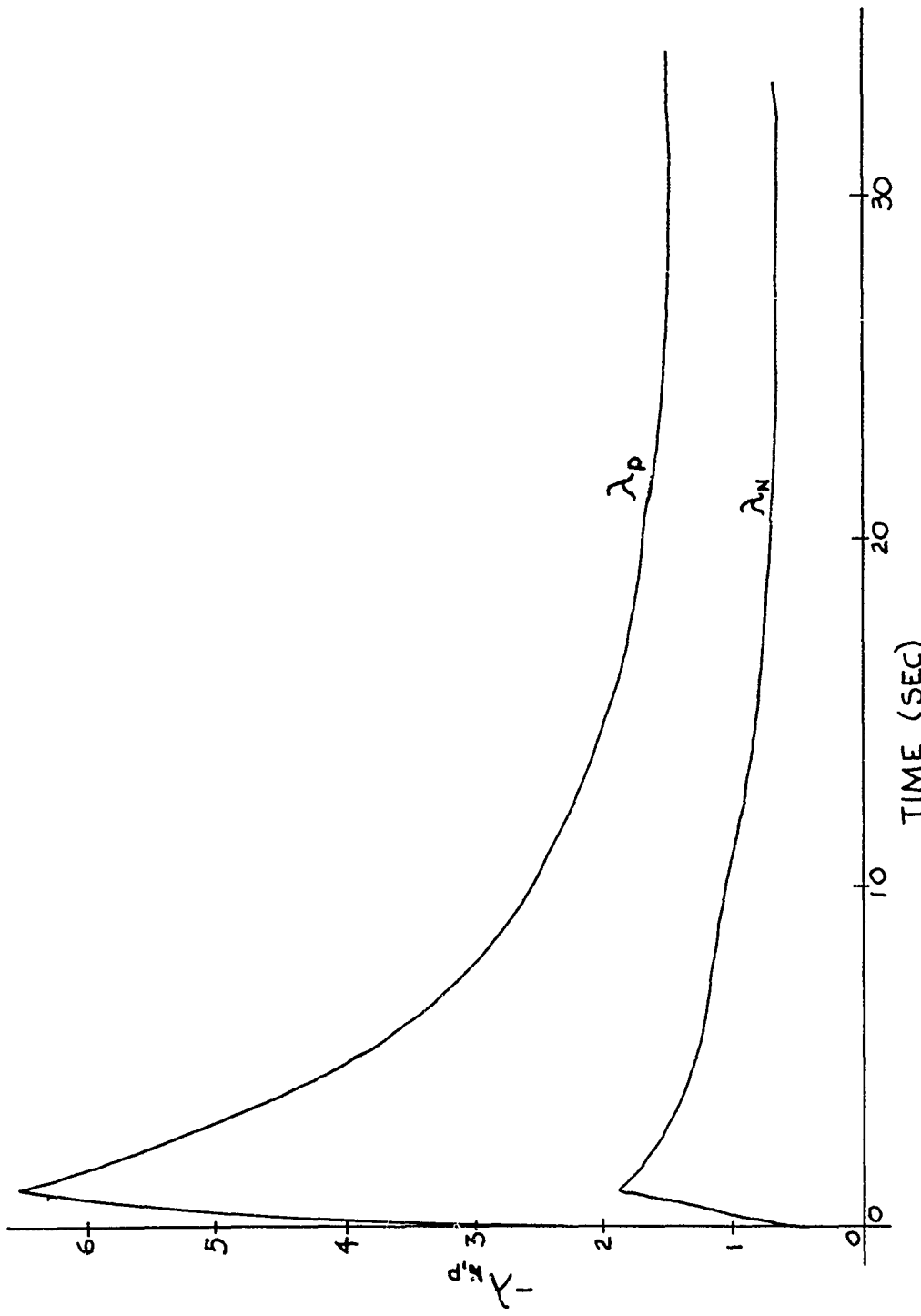


FIG. 53 TYPICAL FLIGHT PERFORMANCE
2

Paper No. 32

A STUDY TO ELIMINATE FLIGHT
INSTABILITIES ON A HIGH-DRAG AIR DELIVERED MINE*
(U)

(Paper UNCLASSIFIED)

by

Jack C. Hopps
Ordnance Division
Honeywell Inc.
Hopkins, Minn. 55343

ABSTRACT. (U) Analysis of flight test film, obtained in a high drag air delivered mine, revealed a type of coning motion in which the pitch and yaw frequencies were coincident with the roll frequency. This motion, which the literature refers to as "lunar motion", is the characteristic motion of catastrophic yaw instability. Two easily implemented solutions were selected to eliminate this instability. They were: (1) reduce roll producing asymmetries and (2) cant fins for spin.

(U) Data obtained from wind tunnel and flight tests revealed the existence of a strong unstable magnus moment and areas of questionable planar damping developed in the coning mode. Non-linear solutions to the tricyclic equation governing this motion were obtained using a stability criteria technique developed by Dr. J. D. Nicolaides. Final results dictated the first of the above solutions to be the most promising.

*This work was sponsored by the U. S. Air Force, Eglin Air Force Base, under contract AF08(635)-5954.

DEFINITION OF SYMBOLS

C_l	-	roll moment coefficient
C_{l_i}	-	induced roll moment coefficient
C_{l_p}	-	roll damping moment coefficient
$C_{l_{\varphi_A}}$	-	induced roll moment at $\varphi_A = 22.5^\circ$
C_m	-	pitch moment coefficient
$C'_{m_{\alpha}}$	-	secant slope of pitch moment coefficient vs angle of attack
$C'_{m_{\alpha_{\text{TRIM}}}}$	-	tangent slope of pitch moment coefficient at a trim angle of attack
$C_{m_q} + C_{m_{\dot{\alpha}}}$	-	pitch damping moment coefficient.
C_N	-	normal force coefficient
$C'_{N_{\alpha}}$	-	secant slope of normal force coefficient vs angle of attack
C_{n_i}	-	induced yaw moment coefficient
$C'_{n_{\varphi_A, \alpha}}$	-	secant slope of induced yaw moment at $\varphi_A = 22.5^\circ$
$C'_{n_{p, \alpha}}$	-	secant slope of magnus moment coefficient vs angle of attack
D	-	reference diameter, 0.373 ft.
I_x	-	mine roll moment of inertia, 0.01385 slug \cdot ft ²
I_y	-	mine pitch moment of inertia, 0.0867 slug \cdot ft ²
M	-	mach number

8th Navy Symposium on Aeroballistics

Vol. 3

m	-	mine mass, $\frac{W}{g}$, 0.625 slugs
p	-	roll rate, radians/sec.
Q	-	dynamic pressure, $1/2 \rho V^2$, lb./ft. ²
q	-	mine pitch rate, radians/sec.
S	-	reference area, $\frac{\pi D^2}{4} = 0.1094 \text{ ft}^2$
S_g	-	gyroscopic stability factor
V	-	mine flight velocity, ft./sec.
α_T	-	total angle of attack measured in a plane passing through the longitudinal axis of the body and the velocity vector.
δ_F	-	fin angle relative to body longitudinal axis of symmetry
φ_A	-	mine roll angle relative to total angle of attack plane
$\lambda_{N,p}^*$	-	nonlinear nutation and precession damping factor
ω_p	-	precession frequency, rad/sec.

INTRODUCTION

(U) Unsatisfactory flight behavior has been observed on many present day bombs and missiles. Possibly the most common of these in recent years is a roll-yaw resonance phenomenon which has been termed "catastrophic yaw" instability and which has been most often linked with configurations having low stability margins. In an effort to describe this behavior, a few authors (see references) have developed useful techniques which attempt to present an understanding of the motion and provide some method for a solution. The present study utilizes these techniques with some major modifications to obtain a solution for the instabilities observed during flight tests on a high drag air delivered mine.

DESCRIPTION OF THE PROBLEM

(U) Among the many requirements for successful operation of this particular air delivered weapon is the requirement for burial in a wide variety of soils. During development flight tests, however, unsatisfactory burial was observed. An examination of the impact data revealed that some of the mines partially buried at angles not coincident with their flight path and others failed to bury at all.

(U) All conceivable factors were examined in an effort to pinpoint the cause of weapon instability. These included possible fin angle asymmetries developed during fin opening at launch (see Figure 1), mine physical characteristics pertaining to product of inertia and lateral CG offset, and all aerodynamic forces and moments. While all of these areas may enhance the problem by contributing in part to the instability, the dominant area was discovered to exist in the aerodynamic forces and moments of the mine.

(U) Examination of the flight test film established the presence of a large amplitude (limit cycle) coning motion (α_T) of 25 degrees, in which the pitch and yaw frequencies were coincident with the roll frequency giving rise to the improper burial attitudes. The work of Nicolaides (Ref. 1) has demonstrated, when magnus moments are neglected, that the growth of this coning motion results from highly non-linear induced roll and yaw moments produced by fin leading edge vortices characteristic of all cruciform-finned flight vehicles. The effect of these induced moments produce a roll lock-in or lunar motion behavior which is known to be the characteristic motion of catastrophic yaw instability.

(U) Because this characteristic motion was also observed in the flight tests of the vehicle in this study, it was assumed that the problem was one of catastrophic yaw. (It was later found, however, that this assumption was incorrect and that the problem was actually one of gyroscopic stability.) The solution seemed simply to reduce or eliminate the effects of the induced moments. Consequently, four means were considered to accomplish this task:

1. Reduce the induced roll moment to prevent the strong tendency for roll lock-in.
2. Reduce the induced yaw moments.
3. Eliminate all configurational asymmetries producing roll.
4. Spin the mine by canting the fins to provide a driving moment greater than the induced roll moment.

(U) While all four solutions deserve merit in correcting the problem, the last two seemed to be the most practical and the most easily implemented. The elimination of all configurational asymmetries, however, would require extremely tight dimensional tolerances on the fin and fin assembly and would result in increased production costs. Canted fins, on the other hand, could be adapted easily without this tolerance restriction.

(U) The purpose of this study was, therefore, to examine the effects of these two solutions on the flight dynamics of the mine and to determine which of the two contained the most promise.

VEHICLE DESCRIPTION

(U) A description of the mine along with other important information is shown in Figure 1. In general, the mine may be described as being 14.25 inches in length, having a 4 inch square cross section at its maximum thickness and nominally weighing 19.7 pounds. A vertical stack of three mines laid horizontally is launched in a pack into the air stream from an aircraft-carried dispenser system.

(U) Folding drag fins located at the aft section not only provide the necessary aerodynamic retardation and stability but also terrodynamic drag to prevent deep burial in soft soils. The fins are folded against the body to provide minimum packing volume during carriage and opened at launch by means of the free-stream velocity and the assistance of small coil springs.

(U) The nose boss and aft square sections ride in vertical tracks, which assist in containing the mine prior to and during launch.

AERODYNAMIC DATA ANALYSIS

(U) Static and dynamic wind tunnel tests were conducted to collect estimated aerodynamic data at two fin angles and to determine the amount of fin cant required to satisfy the solution of mine spin. Due to the rather unconventional shape of the fins, an effective fin cant was realized by simply providing an asymmetry to the sides of the "V" shape on each fin, i. e., trimming one side of the "V" on each fin to a specified dimension.

(U) In addition to the usual pitch plane static aerodynamic data collected were roll damping and pitch damping. However, the method used to obtain values of pitch damping were found to be inadequate in analyzing most of the dynamic behavior in this study. Consequently, extreme caution was exercised in the application of those values.

WIND TUNNEL DATA

(U) Estimated static aerodynamic force and moment data was obtained from transonic wind tunnel tests conducted at the Ling-Temco-Vought Aeronautics Division facility, Dallas, Texas. This data is presented in Figures 2 through 6 in the non-rolling axis system at fin angles of 24 degrees and 26.5 degrees. Because the analysis of catastrophic yaw is associated with the roll lock-in orientation (45 degrees for the vehicle in this study), the curves of normal force and pitching moment are shown only at this roll orientation. The data are also shown extrapolated to permit a dynamic analysis at the higher angles.

(U) The pitching moment curve given in Figure 2 shows the effect of reducing the fin angle from 26.5 degrees to 24 degrees at the equilibrium Mach number of 0.3. Aside from the obvious increase in the static stability, a significant change in the local tangent slope from positive to negative occurs in the vicinity of $\alpha_T = 30$ degrees. Although these slopes are very small indeed, the resulting effect on stability was found to be two-fold. First, local pitch damping values ($C_{m_q} + C_{m_{\dot{\alpha}}}$) are extremely nonlinear with near zero or even positive values existing within the angle of attack region. Second and most important is the fact that a gyroscopic instability ($1/s_q > 1$) is produced by the positive slope region of the curve and the moderate roll rate encountered in the roll lock-in condition (see Dynamic Stability Equation paragraph). Because gyroscopic stability is the first condition to be satisfied in a dynamic analysis, the solution was again to either accept the positive slopes produced by the present fin angle of 26.5 degrees and spin the mine or reduce the fin angle to 24 degrees and control the roll rate by introducing a geometric tolerance to the fin.

(U) Reducing the fin angle to 24 degrees, however, does not eliminate the nonlinearities occurring at Mach numbers above equilibrium. This is illustrated in Figure 4 and provides additional

evidence to support the fact that spinning the mine could be the correct solution.

(U) Estimates of the induced roll moment, yaw moment and side force were also obtained and are presented in Figures 5 and 6 at a roll angle of 22.5 degrees. The induced force and moments approximate a simple $\sin 4\varphi A$ function and exhibit a nonlinear dependence on angle of attack.

(U) A constant value of roll damping was obtained for all angles of attack tested in the subsonic Mach number range. This value was calculated at the terminal roll rate and was found to be -1.38.

CALCULATED ESTIMATES

(U) Estimated values of pitch damping were obtained from a subsonic wind tunnel test in which a freely oscillating technique was utilized. This method is generally quite acceptable for configurations exhibiting a static moment which is linearly dependent on angle of attack. However, due to the nature of catastrophic yaw in which a quasi-trim angle of attack is attained in the roll-yaw resonance region, configurations exhibiting an extremely nonlinear static moment with angle of attack change their damping characteristics at each quasi-trim condition and cannot effectively use this method. Consequently, the pitch damping values used in the present study were calculated from the following equation:

$$(C_{m_q} + C_{m_{\dot{\alpha}}}) = -KC_{N_{\alpha}} \frac{(C.P.)^2}{D_{FIN}}_{FIN}$$

A value of $K = 4$ was obtained from flight tests in which nearly pure pitching motion was observed at the terminal velocity.

(U) Solutions to this equation are shown in Figure 7 and were assumed constant at Mach numbers in the subsonic range.

DYNAMIC ANALYSIS

(U) Evaluation of the canted fin configuration was conducted along parallel paths of a flight test, a dynamic wind tunnel test, and an analytical analysis. Due to the discussion regarding the possible stability effects of the moment curve local slope, configurations containing two different fin angles were included. The first had a fin angle of 26.5 degrees with a positive local slope between $\alpha_T = 0^\circ$ and $\alpha_T = 35^\circ$ and, the second had a fin angle of 24 degrees with a negative local slope throughout the angle of attack range.

8th Navy Symposium on Aeroballistics

Vol. 3

FLIGHT TEST

(U) The flight test was conducted from an F-4 aircraft in straight and level flight with a four bay dispenser loaded with the following mine configurations:

- a. Six models configured to spin above the pitch frequency by removal of a 1/16 inch strip from one side of the "V" on each fin to produce a clockwise roll. ($\delta_F = 26.5$ degrees)
- b. Three models with symmetrical fins. ($\delta_F = 24$ degrees)
- c. Three models with symmetrical fins. ($\delta_F = 26.5$ degrees)

(U) The test was conducted in four passes. Subsequently, ground tracking film was viewed from the test in which two of the three mines in each bay were captured in flight and were observed from launch to ground impact. The results of these observations were as follows:

Pass #1. (U) Three models configured to spin; fin angle $\delta_F = 26.5$ degrees; launched at $M = 0.5$ and 2200 ft altitude. Both mines were observed to stabilize to near zero angle of attack before reaching terminal spin rate. Shortly after stabilization and terminal spin had been reached (estimated at 1 to 3 seconds), an unstable coning motion began which increased in amplitude very rapidly to an angle of 80 or 90 degrees. At this point, the spinning mode was damped very quickly to zero. The remainder of the flight resulted in first, a lunar mode of roll-yaw resonance in which a circular coning motion was observed and, second, a damped mode with the return of a spin rate below terminal and irregular pitching and yawing motions. This later motion persisted until ground impact was achieved.

Pass #2. (U) Three models configured to spin; fin angle $\delta_F = 26.5$ degrees; launched at $M = 0.9$ and 2600 ft altitude. The bottom mine in the bay showed similar results to those in pass 1. The second mine photographed, however, stabilized and reached terminal spin but did not show any instability. This mine continued to spin in a stable flight mode and achieved ground impact in perfect orientation.

Pass #3. (U) Three models with symmetrical fins; fin angle $\delta_F = 24$ degrees; launched at $M = 0.9$ and 2600 ft altitude. Both mines stabilized to near zero angle of attack soon after launch and continued in a stable mode with only slight spin until ground impact.

Pass #4. (U) Three models with symmetrical fins; fin angle $\delta_F = 26.5$ degrees; launched at $M = 0.5$ and 2200 ft altitude. The bottom mine in the bay stabilized soon after launch and continued in this stable mode until ground impact. The second mine, however, did not stabilize. Instead, its flight mode was characteristic of lunar motion and roll-yaw resonance seen in previous flights. This motion also persisted until ground impact.

DYNAMIC WIND TUNNEL TEST

(U) In addition to the flight test, a dynamic stability analysis (Ref. 2) was performed by Dr. J. D. Nicolaides who is currently on the faculty at the University of Notre Dame. His analysis included a collection of the required estimated aerodynamic moment data from a unique model support system which permitted three degrees of rotational freedom, i. e., roll, pitch, and yaw. The results of his analysis are shown in Table 1 for the full scale mine using the following stability coefficients:

$$C_{m\alpha} = -2.6$$

$$C_{n_p, \alpha} = +47.0$$

$$C_{mq} = -30$$

$$PD/2V = 0.04$$

Note that at zero spin rate ($P = 0$) both the nutation and precession damping rates are stable, but that a severely unstable condition occurs at the large spin rate as a result of the magnus moment.

(U) Although the model support mechanism would not permit a dynamic analysis at angles of attack greater than approximately 12 degrees, the analysis shows quite clearly the detrimental effects on stability from spin which is in excellent agreement with flight test results.

ANALYTICAL ANALYSIS

(U) Numerical solutions were obtained for a quasi-linear damping factor developed from the equation describing tricyclic motion and for the complete six degree of freedom equations of motion using a mathematical model in conjunction with a digital computer. Analysis of mine stability included conditions of catastrophic yaw, high spin rates and gyroscopic stability effects.

Dynamic Stability Equation

(U) In the non-rolling stability axis system, the tricyclic motion of an axially symmetric missile, with appropriate initial conditions, is

$$w = k_1 e^{(\lambda_N + \omega_N)t} + k_2 e^{(\lambda_p + \omega_p)t} + k_3$$

where w consists of a high frequency nutation arm (k_1), a slower precessional frequency arm (k_2) and a pure trim (k_3).

(U) In the non-linear case, a precise closed-form solution for $w(t)$ is not possible. However, a criterion for the dynamic stability of these non-linear cases was derived by J. D. Nicolaides (Ref. 1) and defines whether a given initial pitch or yaw will grow or decay.

8th Navy Symposium on Aeroballistics

Vol. 3

This criterion is $\lambda_{N, P}^* < 0$ where $\lambda_{N, P}^* = \frac{QS}{V} \left[-\frac{C_m^l \alpha}{2m \cos \alpha} (1 \pm \tau) + \frac{C_m^l D^2}{4I_y} (1 \pm \tau) \pm \frac{V\tau D}{pI_x} C_{n_{\varphi_A, \alpha}} \sin 4\varphi_A \pm \frac{D^2 \tau}{2I_x} C_{n_{p\alpha}} \right]$ and

$\lambda_{N, P}^* < 0$ is a necessary and sufficient condition for dynamic stability.

(U) In the solution of the Quasi-linear damping factor, $\lambda_{N, P}^*$, it was assumed that a roll-yaw resonance motion existed and that this motion was one of pure circular pitch and yaw. Therefore,

$$P = \omega_p = \left[\frac{C_m^l QSD}{I_y (1 - \frac{I_x}{I_y})} \right]^{1/2} \approx \left[\frac{C_m^l QSD}{I_y} \right]^{1/2}$$

The terms not defined are: $\tau = \sqrt{\frac{1}{1 - \frac{1}{S_g}}}$ where $S_g = \frac{I_y (\frac{pI_x}{2I_y})^2}{C_m^l \alpha_{TRIM} QSD}$

$$\text{and } \sin 4\varphi_A = - \frac{C_l + C_{l_p} \frac{PD}{2V}}{C_{l_{\varphi_A}}}$$

(U) It should be pointed out that the gyroscopic stability factor, S_g , was calculated using the local or trim tangent slope of the moment curve instead of the usual secant slope. This was done to define the gyroscopic effects at high angle trim conditions produced by the pure circular pitch and yaw motion. The condition for gyroscopic stability is $1/S_g < 1$.

(U) Solutions to the quasi-linear damping factor were obtained assuming a roll yaw resonance condition existing at the equilibrium velocity and negligible magnus moments. The results are shown in Figures 8 and 9 for both a 26.5 degree and 24 degree fin angle. Notice the gyroscopic instability region in Figure 8 which is due to the positive slope of the moment curve in this angle of attack range (see Figure 2).

(U) A simulation corresponding to the flight test models in which a 1/16 inch strip was trimmed from one side of each fin was obtained to determine the behavior of magnus moment on spinning

mine stability. This is shown in Figure 10 for a magnus moment coefficient of +46.6 and a calculated terminal spin rate of 32.5 radians per second.

(U) Although the magnus moment coefficient is known to be nonlinear with angle of attack, it was the only estimate available and was assumed to be linear in the study. The curve clearly shows magnus instability occurring above three degrees angle of attack and demonstrates a qualitative correlation with wind tunnel and flight test results.

Six Degree-of-Freedom Simulation

(U) A dynamic simulation program containing the full six degree-of-freedom equations of motion was used to obtain numerical solutions describing the dynamic behavior of the mine in flight. The simulations included an analysis of the gyroscopic stability produced by the local tangent slope of the static moment curve and a complete solution of the roll-yaw resonance behavior.

(U) To show this, each simulated case was initiated to describe lunar motion in the roll lock-in orientation at a high angle of incidence. Displays of the total angle of attack, roll rate, and precessional frequency time histories were examined to determine the resulting dynamic behavior.

(U) Estimates of the aerodynamic coefficients, shown in Figures 3 through 7, at a Mach number of 0.5 were programmed for the simulations. The standard pitching moment curve is illustrated separately in Figure 11 along with two random variations of a positive slope and a negative slope at $\alpha_T > 25$ degrees for use in demonstrating gyroscopic stability. The aerodynamic data at a Mach number of 0.5 was chosen to simulate as accurately as possible the dynamic behavior of the mine containing an extreme local slope reversal in the moment curve. Throughout this analysis magnus moments were assumed negligible and not programmed.

(U) The first case tested demonstrates the effect of a positive slope reversal on mine stability and is shown in Figures 12 and 13. Notice that a limit cycle of approximately 23 degrees angle of attack is attained at the roll lock-in orientation which continues throughout the flight times investigated. Qualitatively, this correlates quite well with the results obtained from the flight test in which a limit cycle coning motion was observed.

(U) In order to demonstrate the existence of a gyroscopic instability, two additional programmed simulations were necessary. The first contained the negative slope moment curve shown in Figure 11 and the second the positive slope. In addition, pitch damping was neglected, since it should have no effect on the final outcome except to retard the action.

Vol. 3

(U) The results are shown in Figures 14 through 16 and illustrate quite clearly the effect of a positive local slope on stability. In Figure 14, α_T is seen to increase from 45 degrees to 90 degrees (data limit) in 1.7 seconds.

(U) The effect of the negative local slope is shown in Figures 15 and 16. In this case, a limit cycle is achieved in both the nutation and precession mode which would be expected without the influence of damping.

(U) Figures 17 and 18 presents the last case, showing the effect of including damping on the negative local slope curve of Figure 11. This effectively represents the aerodynamics associated with reducing the fin angle from the previous 26.5 degrees to 24 degrees. Also included was the effect of providing a geometric tolerance restriction to the fin to prevent roll rates in the resonance region. Figure 18 shows that a roll lock-in condition exists initially, but that roll "break out" finally develops at about 9 seconds of flight time. Stability is noted in Figure 17, where the total angle of attack amplitude is decreasing with flight time.

CONCLUSIONS

(U) The results of this study which included a stability analysis of all nonlinearities associated with the planar aerodynamic forces and moments, the induced aerodynamic forces and moments, and the magnus moments, have demonstrated the following:

1. The influence of magnus moments on the spinning mine causes the development of a severe instability.
2. Roll rates are extremely sensitive to fin asymmetries. Very high spin was achieved with a fin asymmetry of only 1/16 inch.
3. The induced aerodynamic forces and moments do not appreciably influence mine stability.
4. The induced roll moments produce a roll lock-in condition at high angles of incidence.
5. Planar aerodynamic moments are affected by the fin angle at the equilibrium Mach number and relatively unaffected at Mach numbers above equilibrium.

(U) Under the assumption that magnus moments are negligible in the roll-yaw resonance case, it was concluded that the resonance instability discovered in the initial phase of the flight test program was not derived from the induced yaw moments as first thought. In fact, the term "catastrophic yaw" cannot be applied here, since it must be concluded from the results that a gyroscopic instability was the initial cause of the problem.

(U) The final solution to the resulting instability was as follows:

1. Maintain a maximum fin angle of 24 degrees at the maximum design center of gravity limit of 6.8 inches to ensure gyroscopic stability at the equilibrium Mach number.
2. Maintain a geometric tolerance between the sides of each fin of less than 0.01 inches to prevent roll rates in the resonance region.

REFERENCES

1. Nicolaides, J. D., "Two Non-Linear Problems in the Flight Dynamics of Modern Ballistic Missiles," IAS Report 59-17 (January 1959).
2. Nicolaides, J. D., "On the Determination of the Stability Coefficients of a Special Bomblet," (January 1968), (Unpublished Report for Honeywell Inc.).
3. Nicolaides, J. D., "A Review of Some Recent Progress in Understanding Catastrophic Yaw," AGARD Report 551, 1966.
4. Chadwick, W. R., "Flight Dynamics of a Bomb with Cruciform Tail," J. Spacecraft, (June 1967).

8th Navy Symposium on Aeroballistics

Vol. 3

(U) TABLE 1. Effect of Magnus Moment on the Dynamic Behavior of a Spinning Mine

		FULL SCALE	
		P = 0	P = 64.34 RAD/SEC
DAMPING RATE		-0.4566	3.067
NUTATION (λ_N)			
DAMPING RATE		-0.4566	-3.980
PRECESSION (λ_P)			
HALF LIFE	SEC.	1.515	
NUTATION	CAL.	1218.941	
HALF LIFE	SEC.	1.515	0.1738
PRECESSION	CAL.	1218.941	139.841
DOUBLE LIFE	SEC.		0.2256
NUTATION	CAL.		181.469
DOUBLE LIFE	SEC.		
PRECESSION	CAL.		



Weight = 19.7 pounds

Length = 14.25 inches

Width = 4.01 inches maximum from flat to flat.

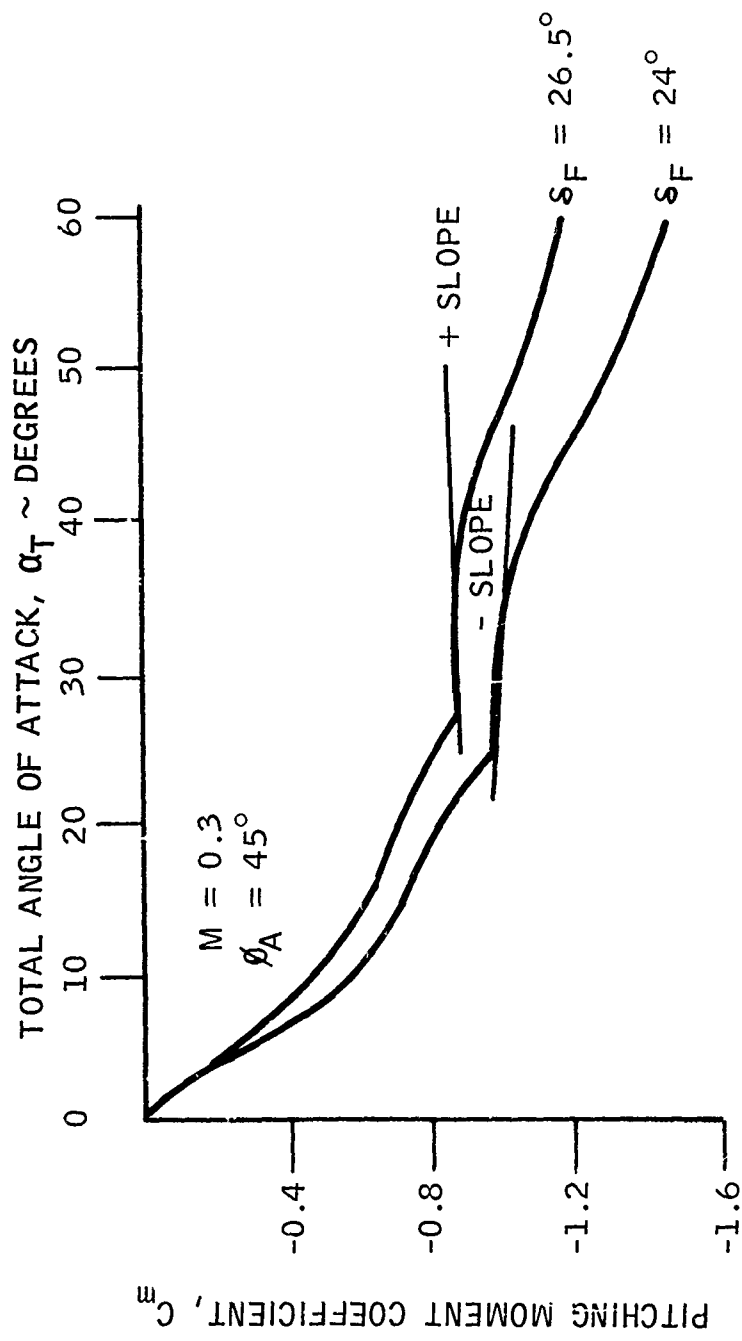
Pitch moment of inertia = 0.0863 slug-ft²

Roll moment of inertia = 0.0138 slug-ft²

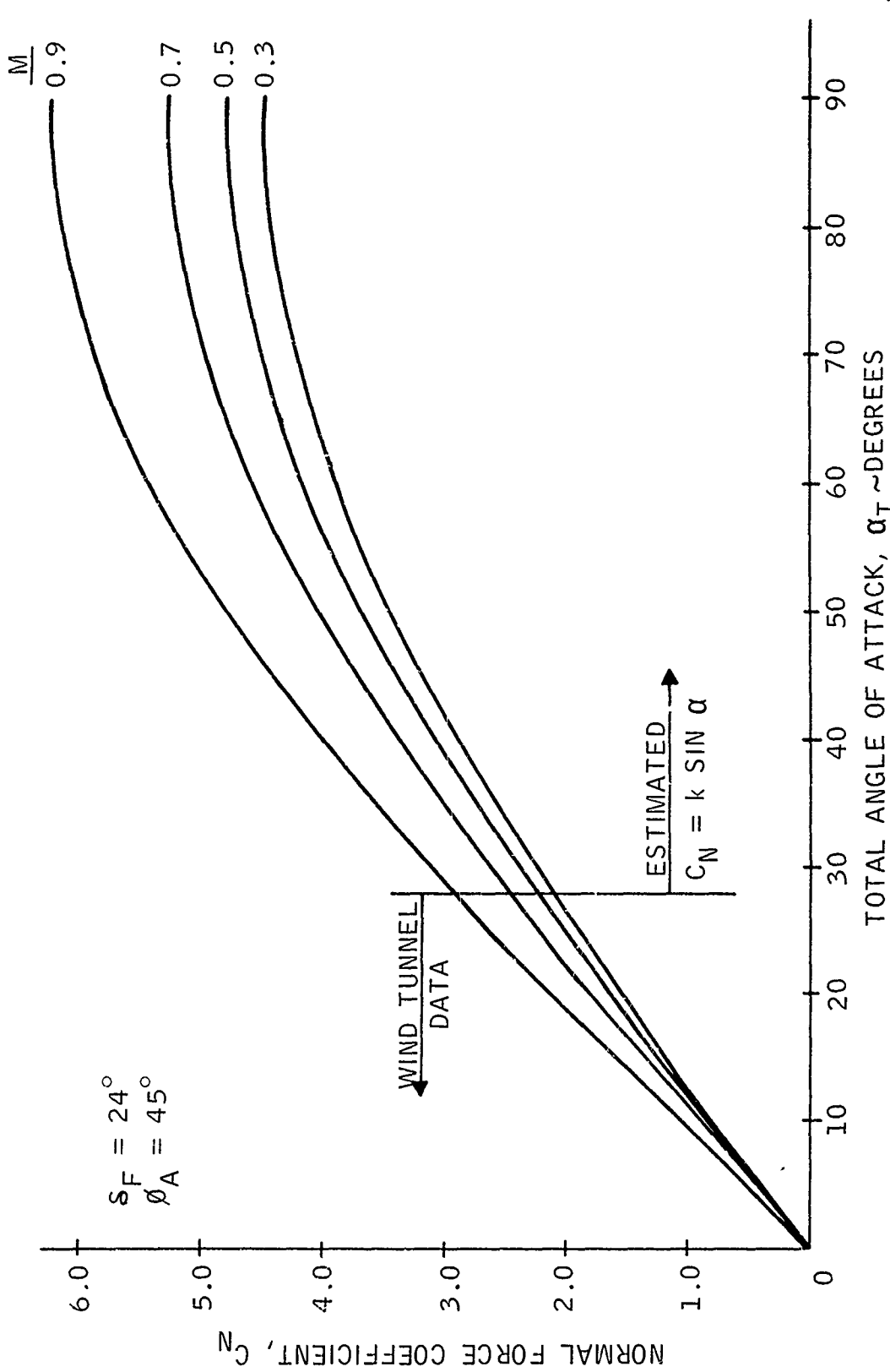
Fin angle = 24 degrees (centerline reference)

Center of gravity location = 6.8 inches (nose reference).

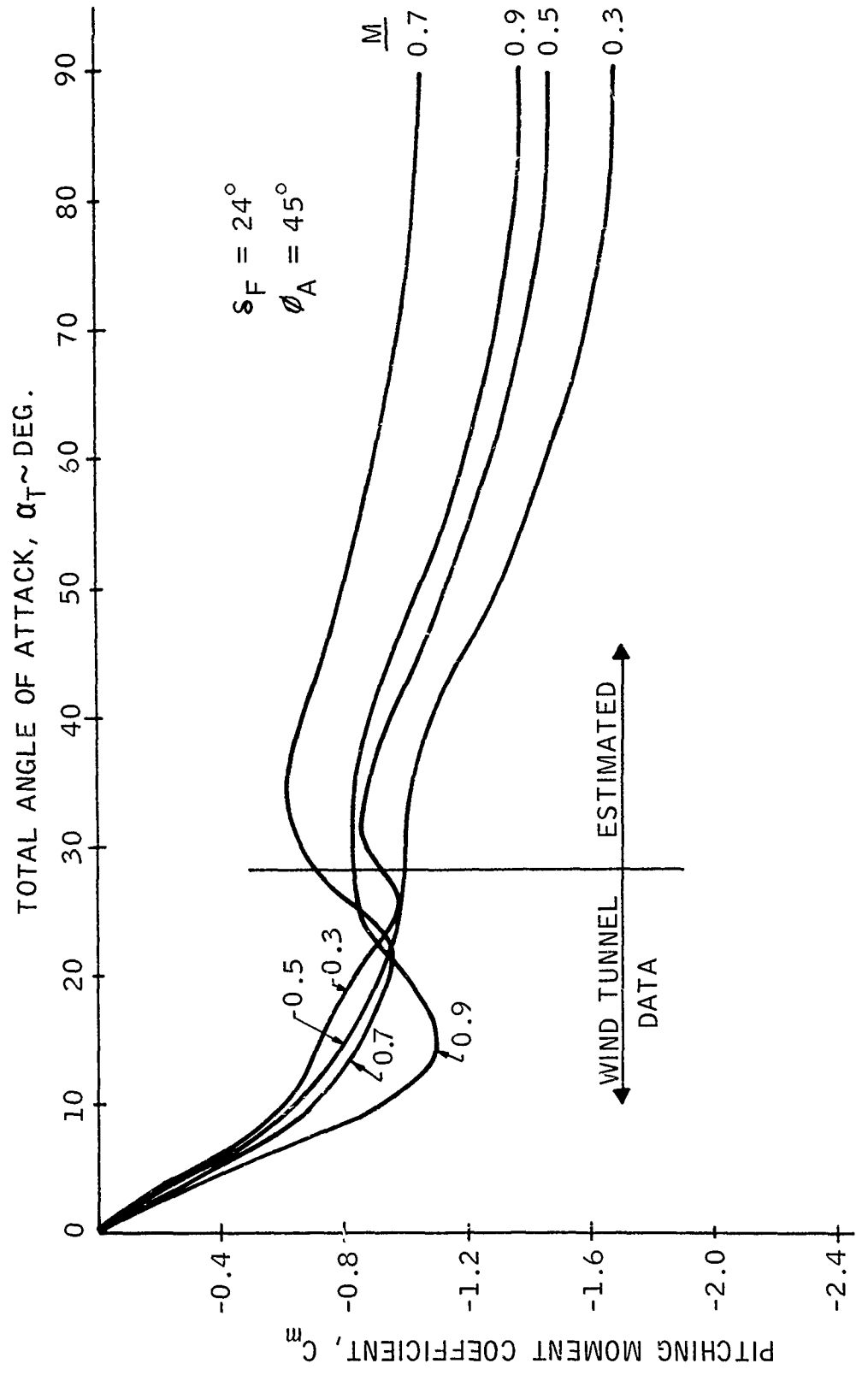
(U) FIG. 1. High Drag Mine



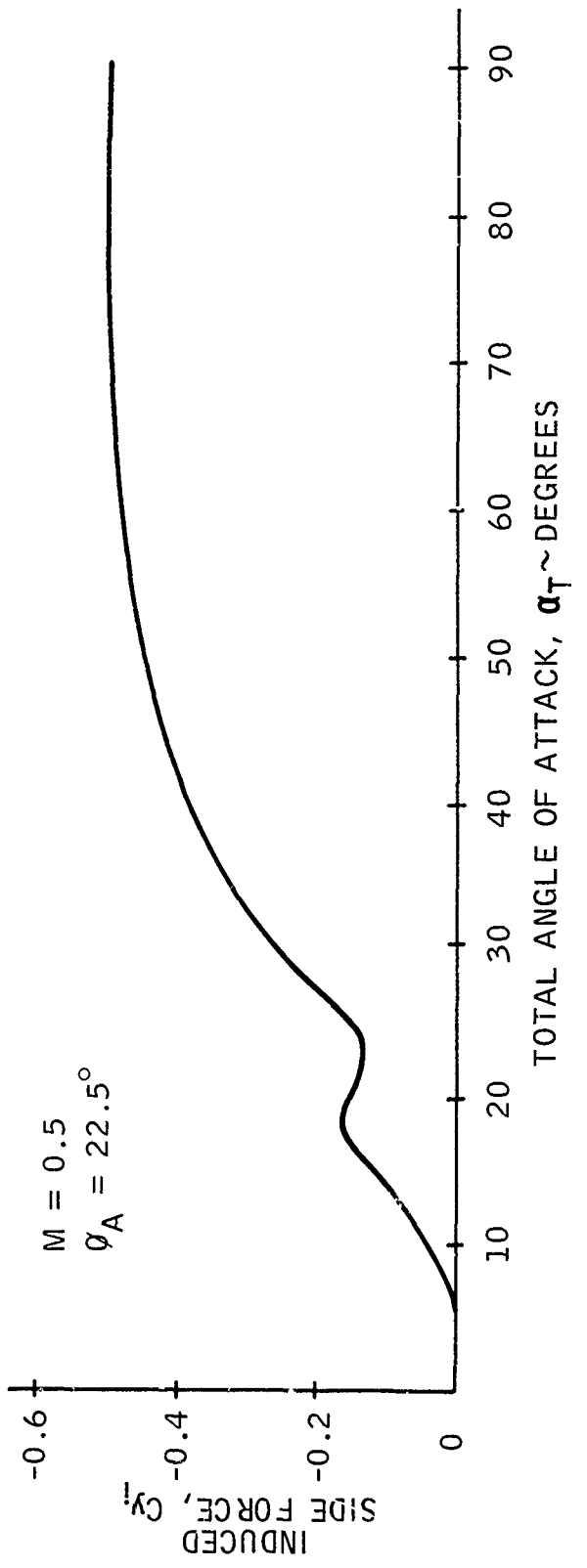
(U) FIG. 2. Pitching Moment Coefficient vs. Total Angle of Attack



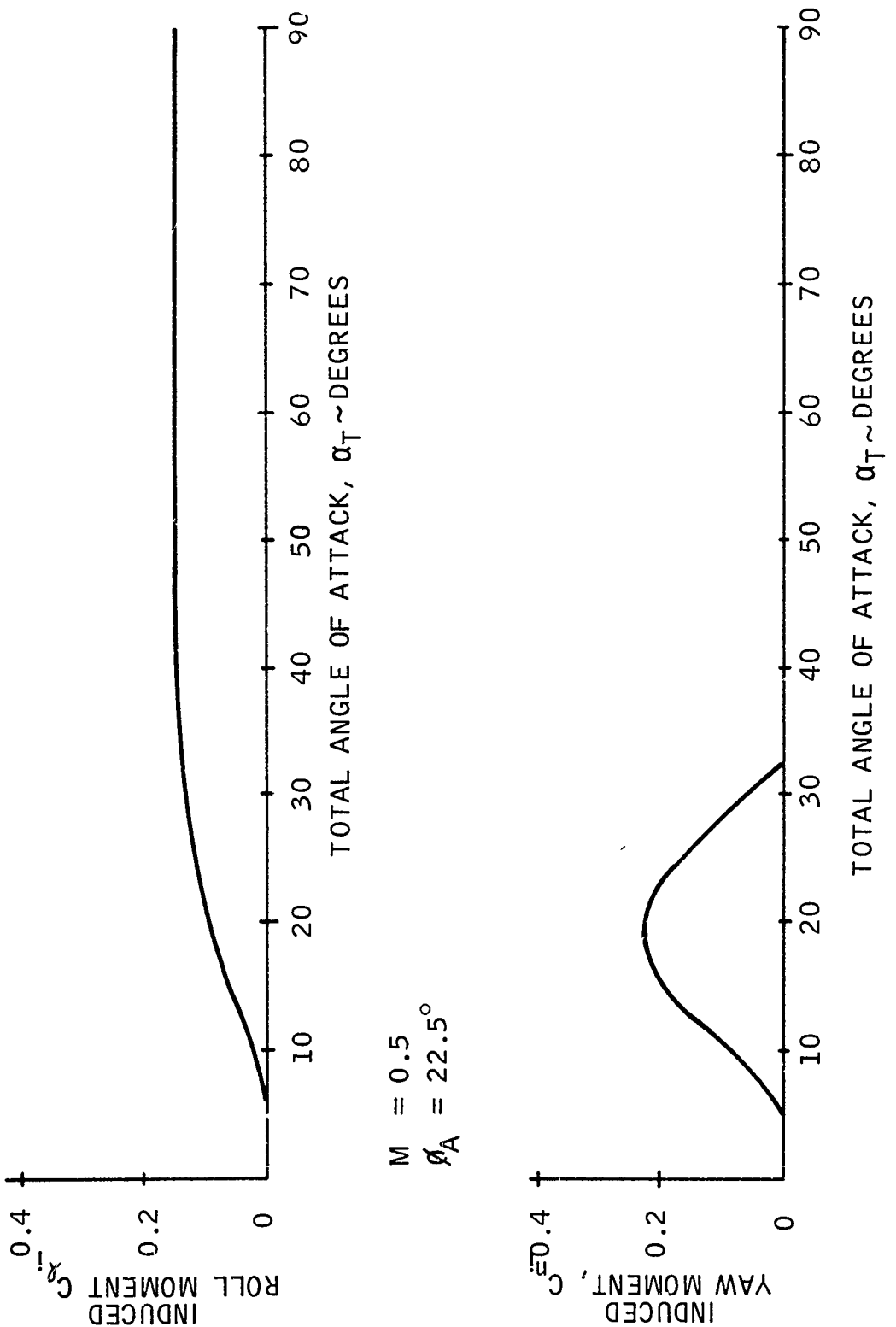
(U) FIG. 3. Normal Force Coefficient vs. Total Angle of Attack



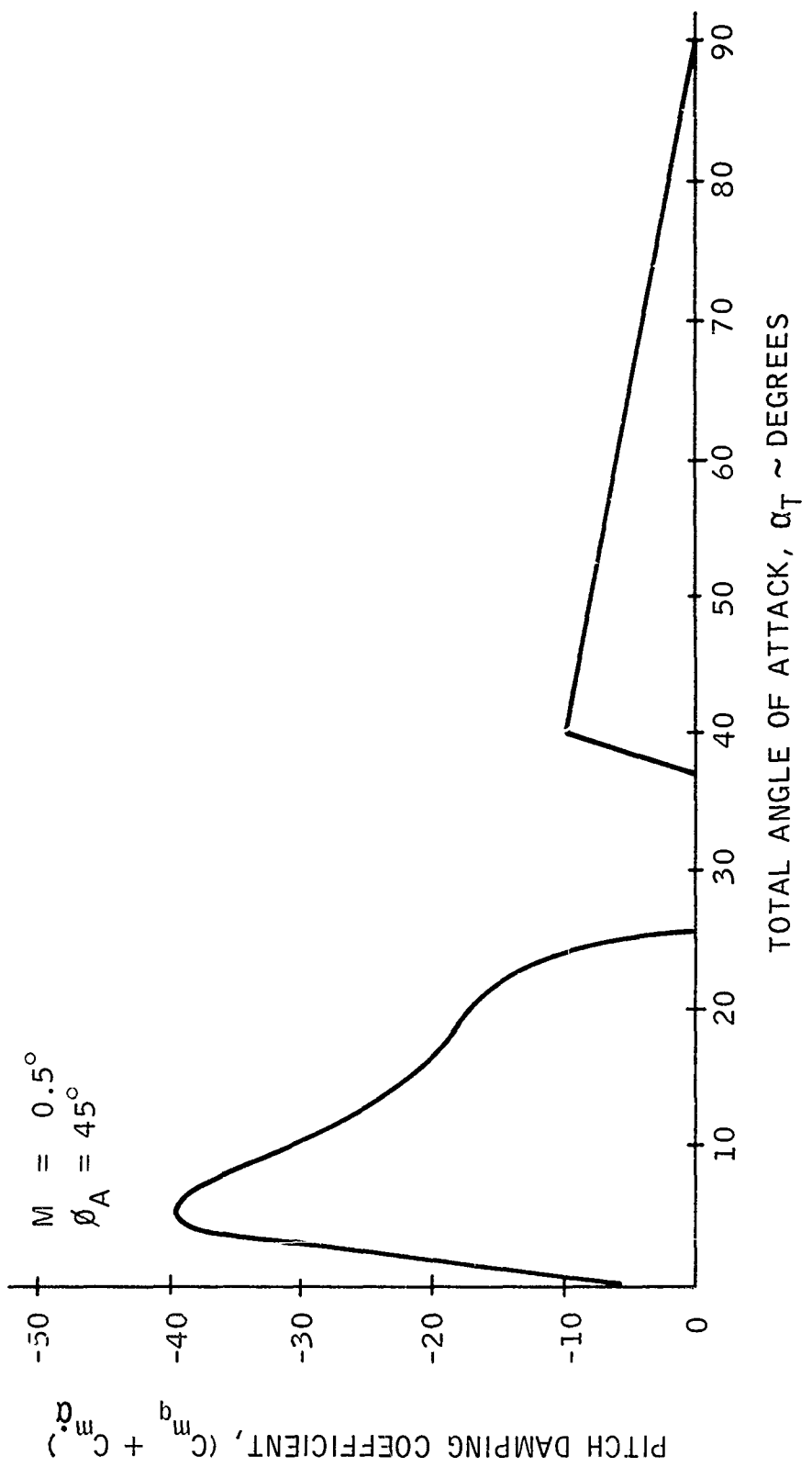
(U) FIG. 4. Pitching Moment Coefficient vs. Total Angle of Attack



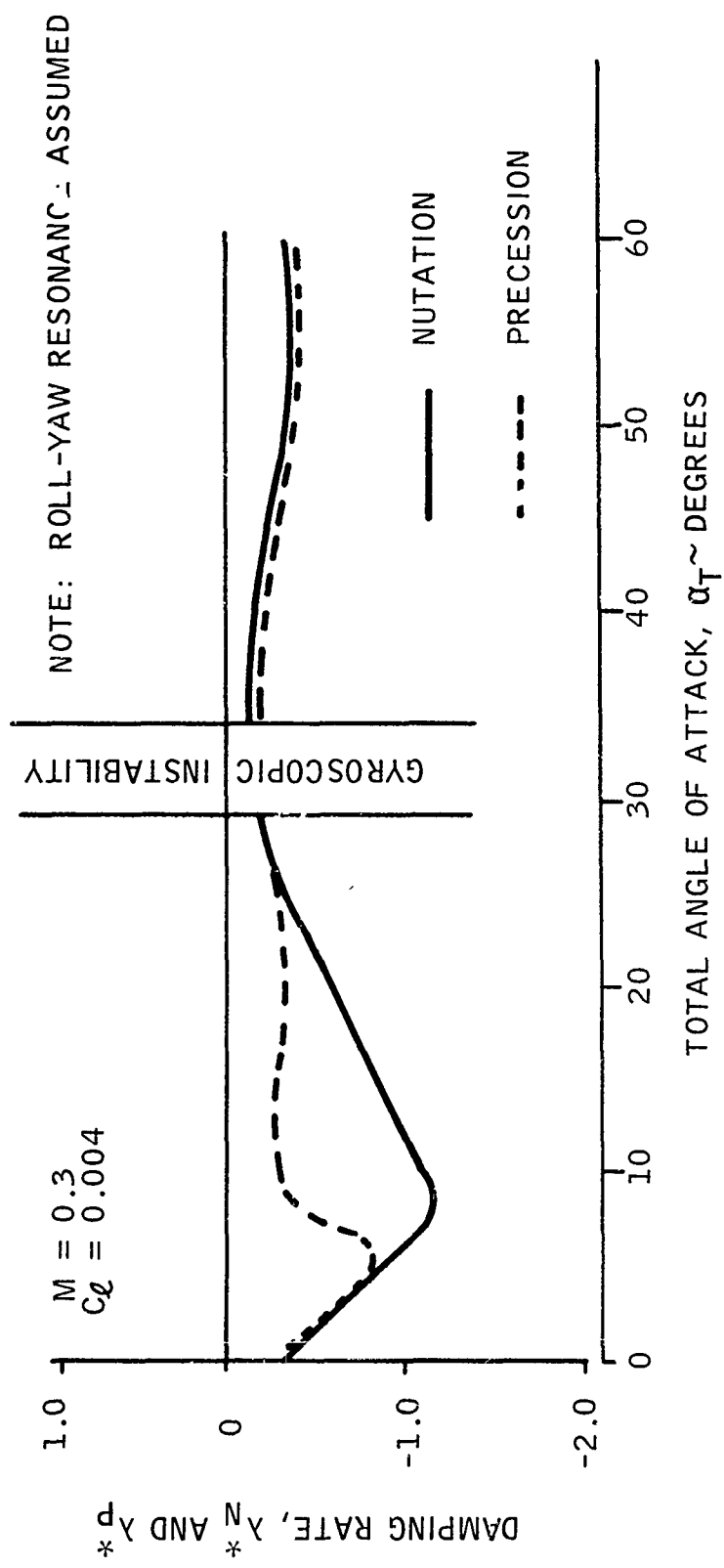
(U) FIG. 5. Induced Side Force Coefficient vs. Total Angle of Attack



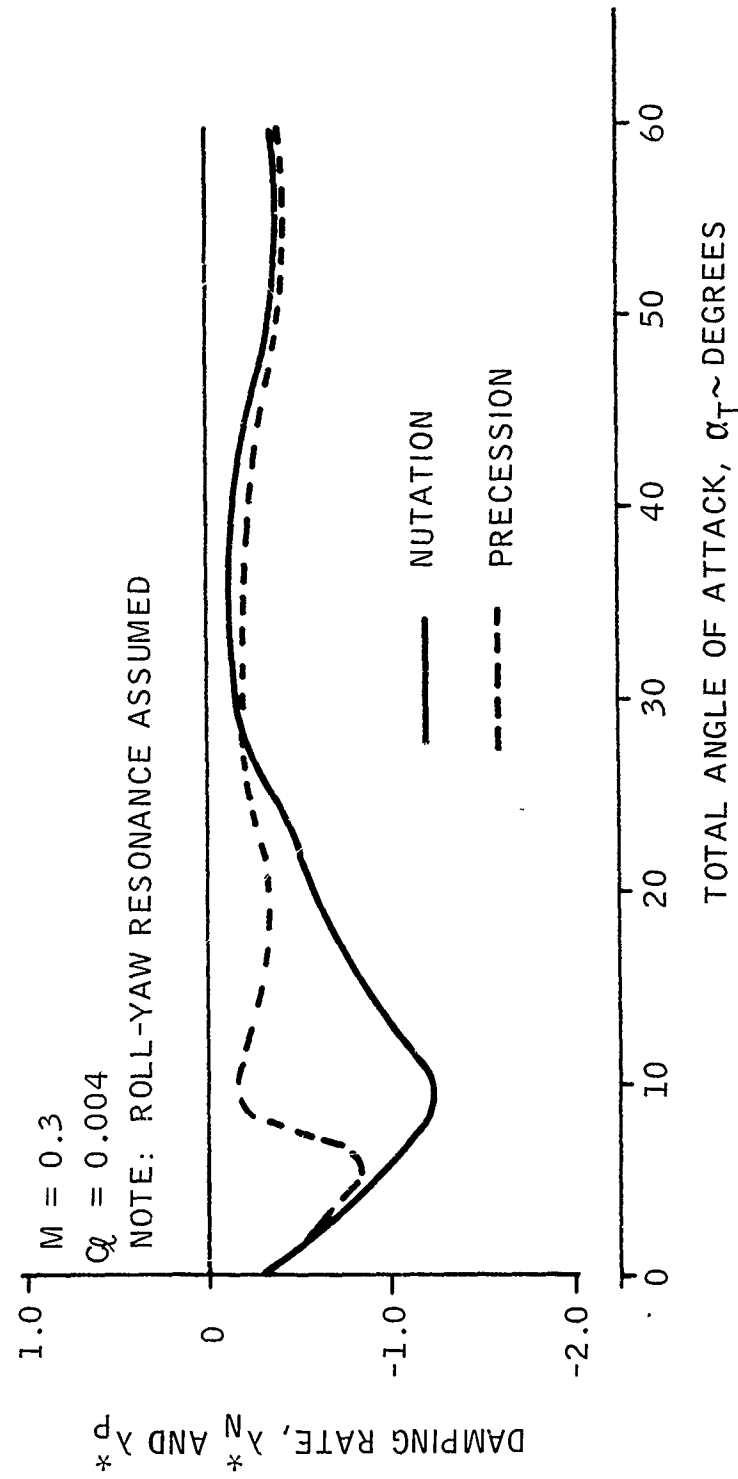
(U) FIG. 6. Induced Roll and Yaw Moment Coefficient vs. Total Angle of Attack



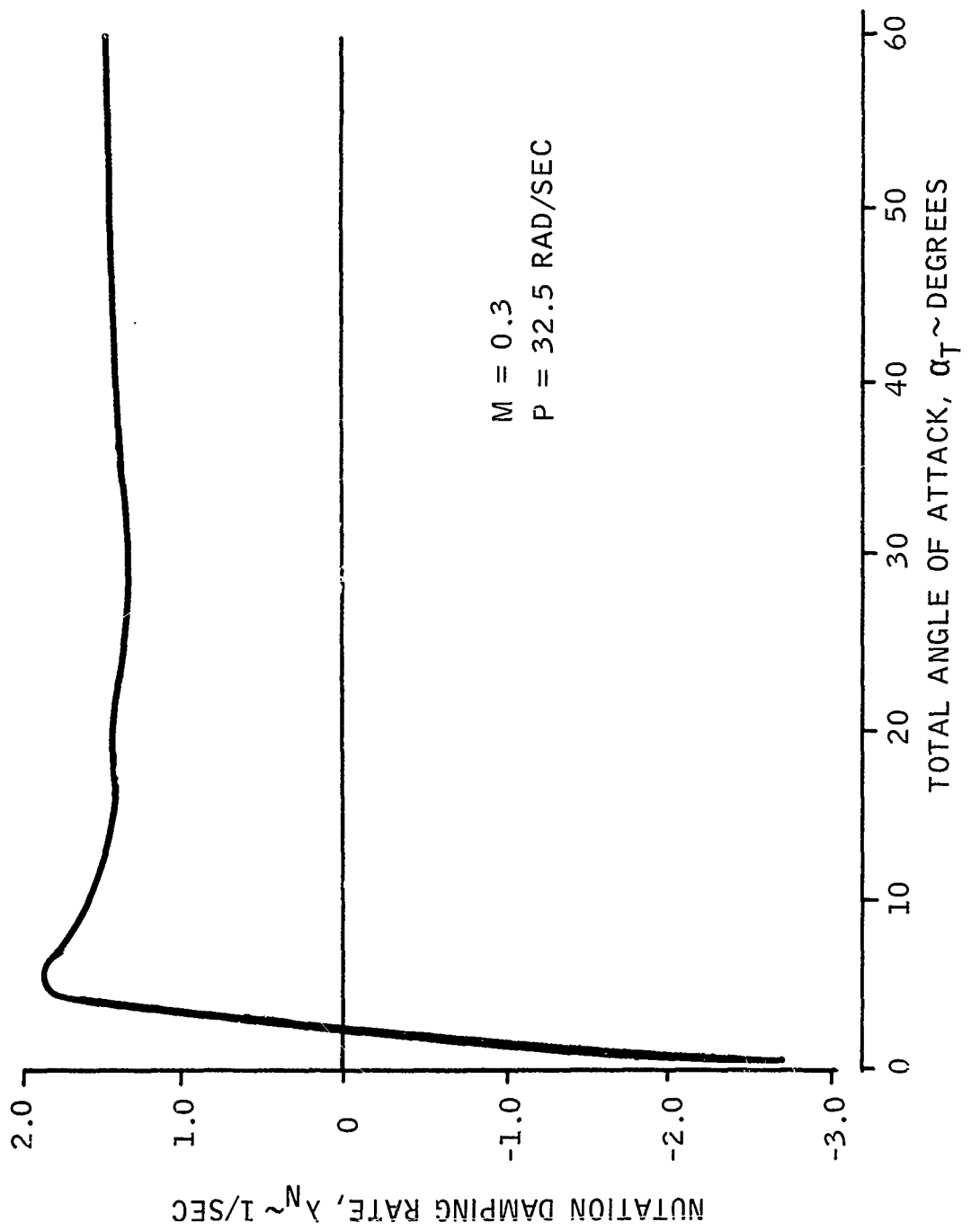
(U) FIG. 7. Pitch Damping Coefficient vs. Total Angle of Attack



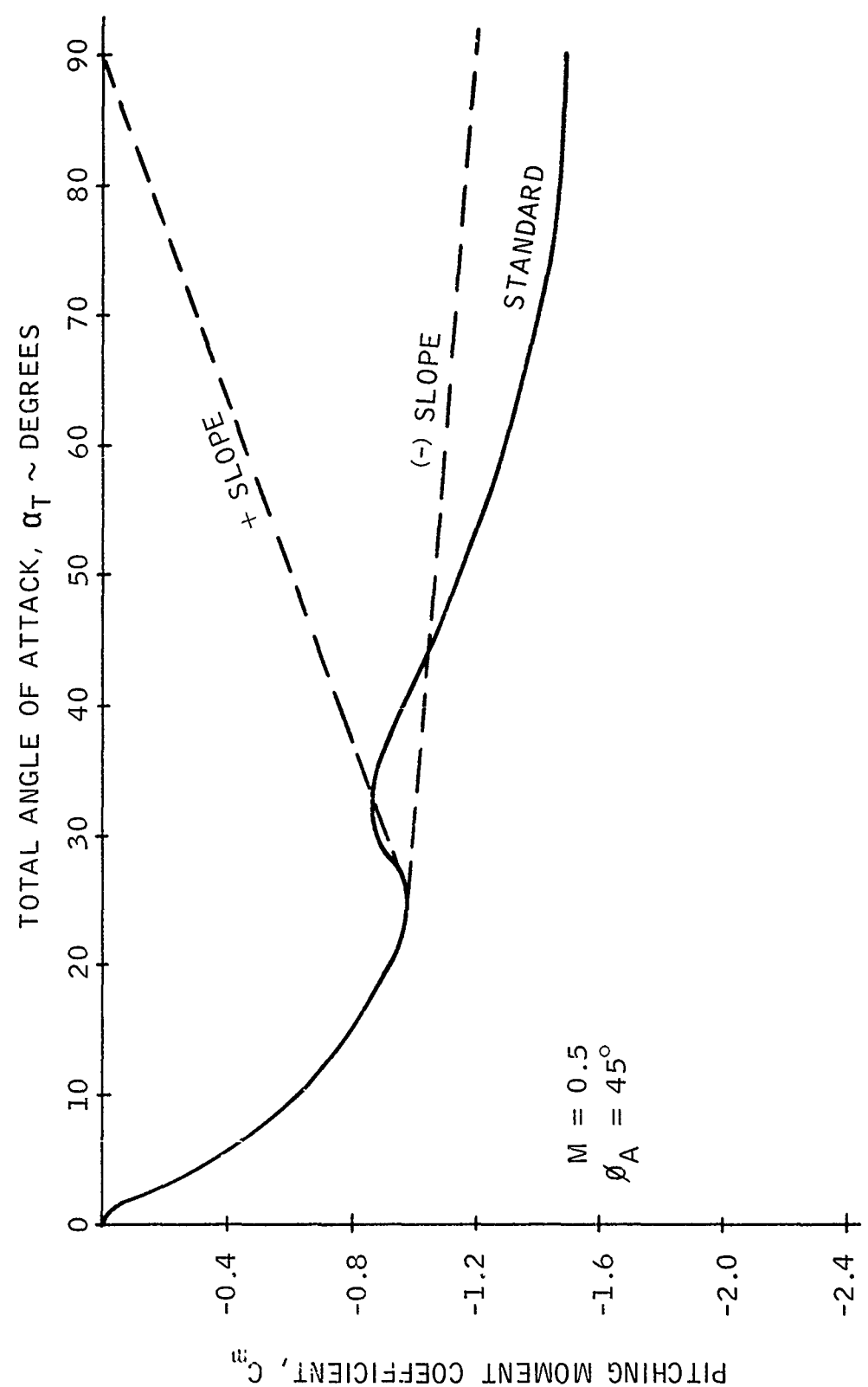
(U) FIG. 8. Effect of Damping Rates on Total Angle of Attack
 For a Fin Angle of 26.5 Degrees



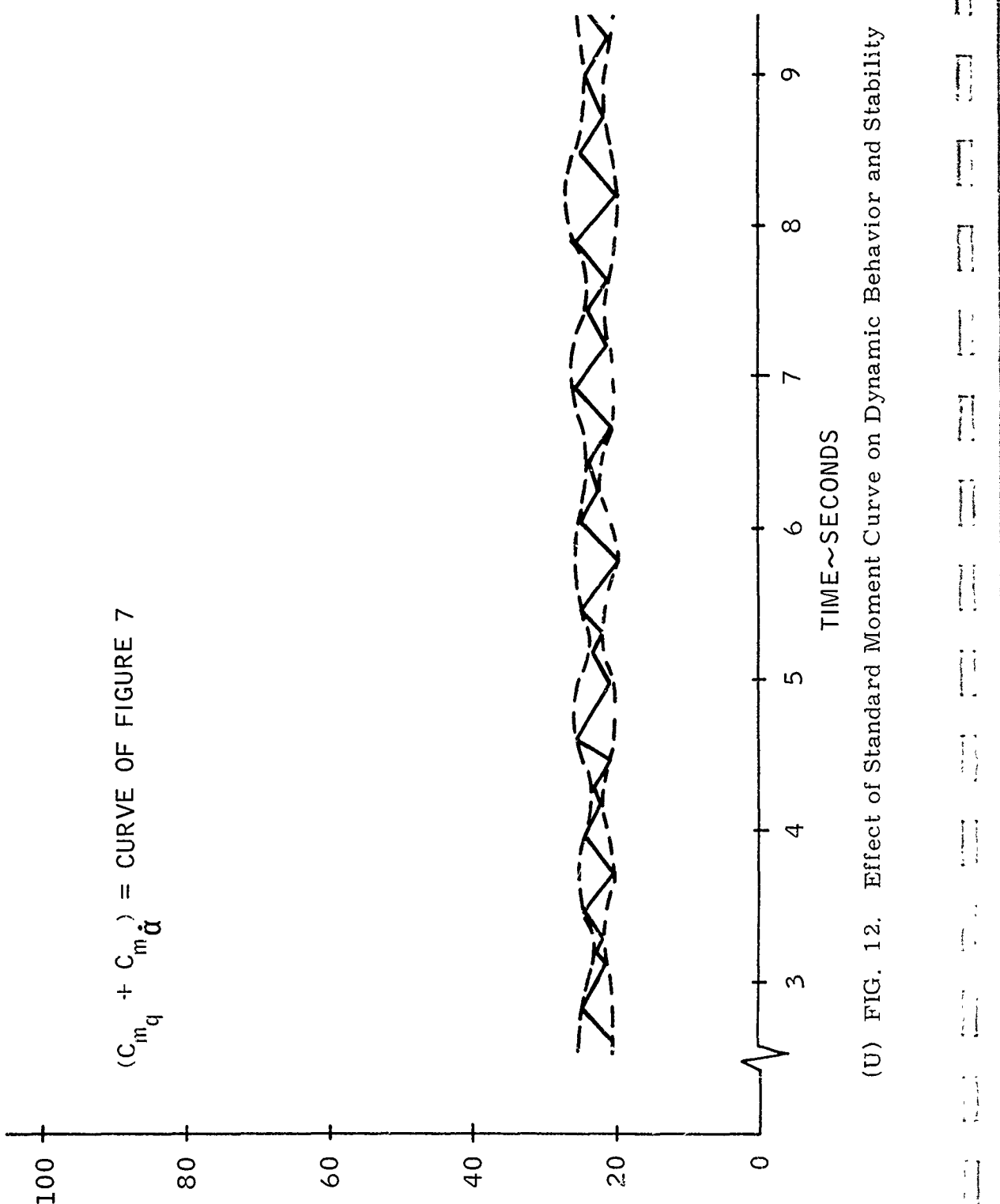
(U) FIG. 9. Effect of Damping Rates on Total Angle of Attack for a Fin Angle of 24 Degrees

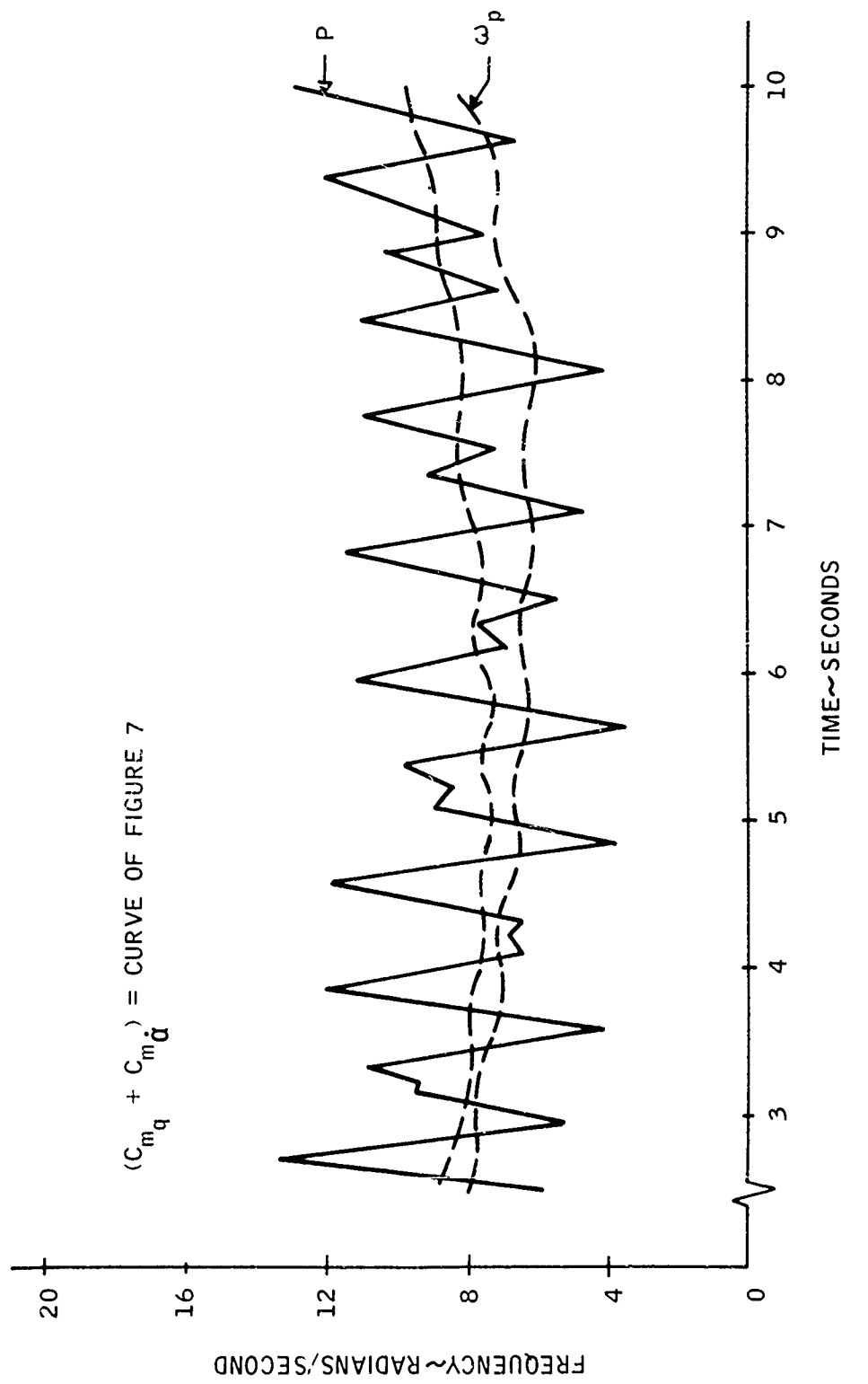


(U) FIG. 10. Effect of Mangus Moment on the Dynamic Damping Rate

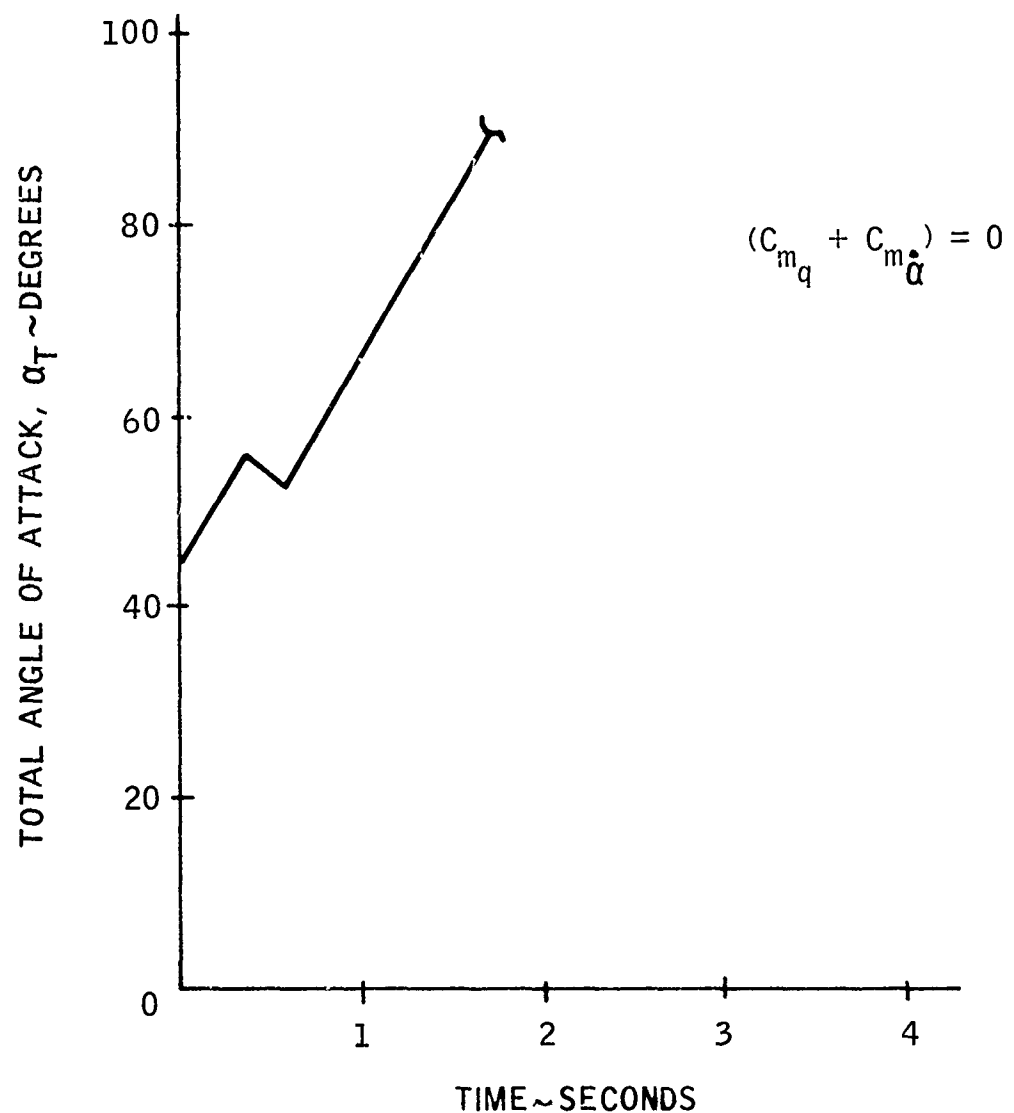


(U) FIG. 11. Pitching Moment Coefficient vs. Total Angle of Attack

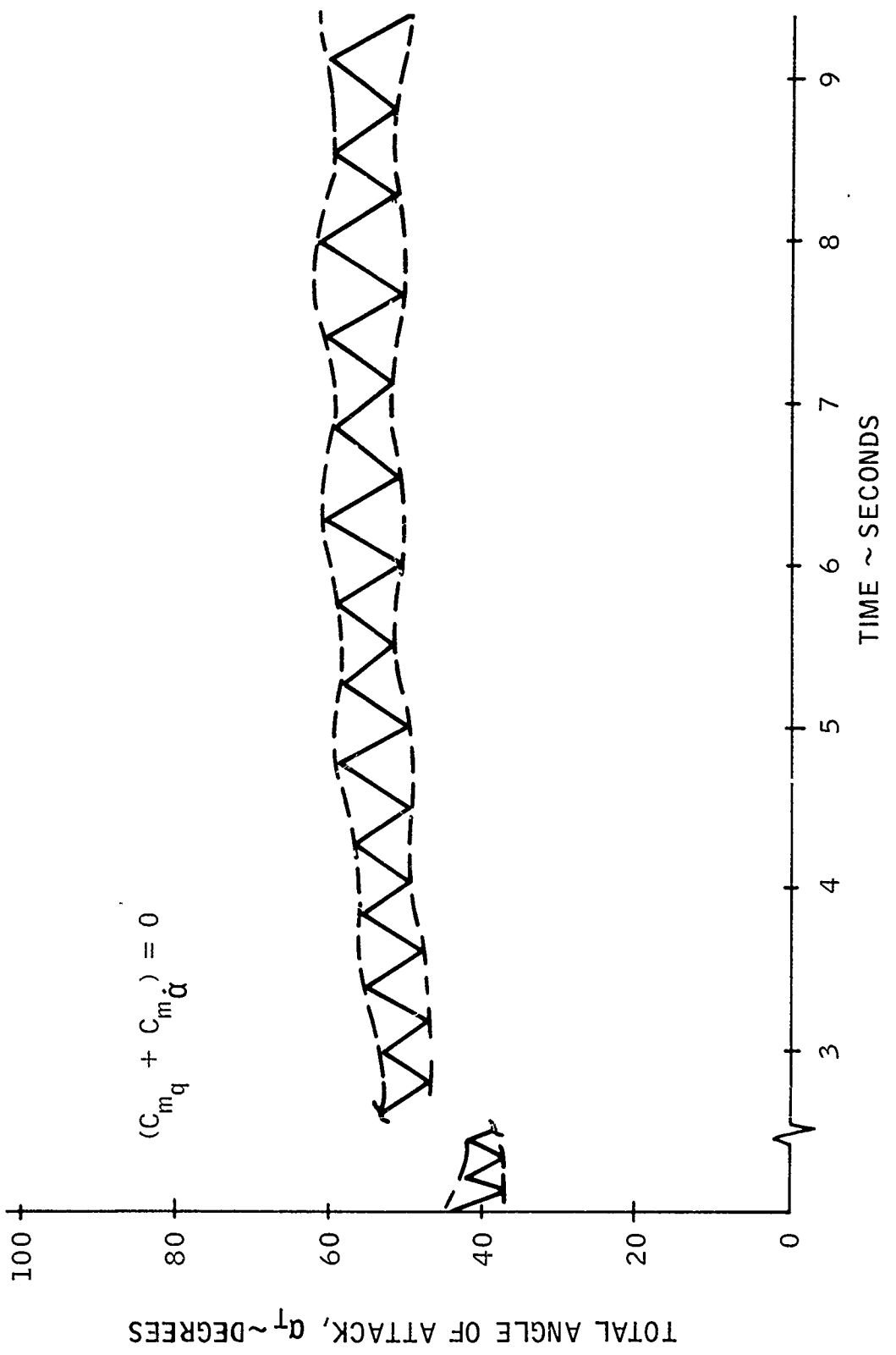


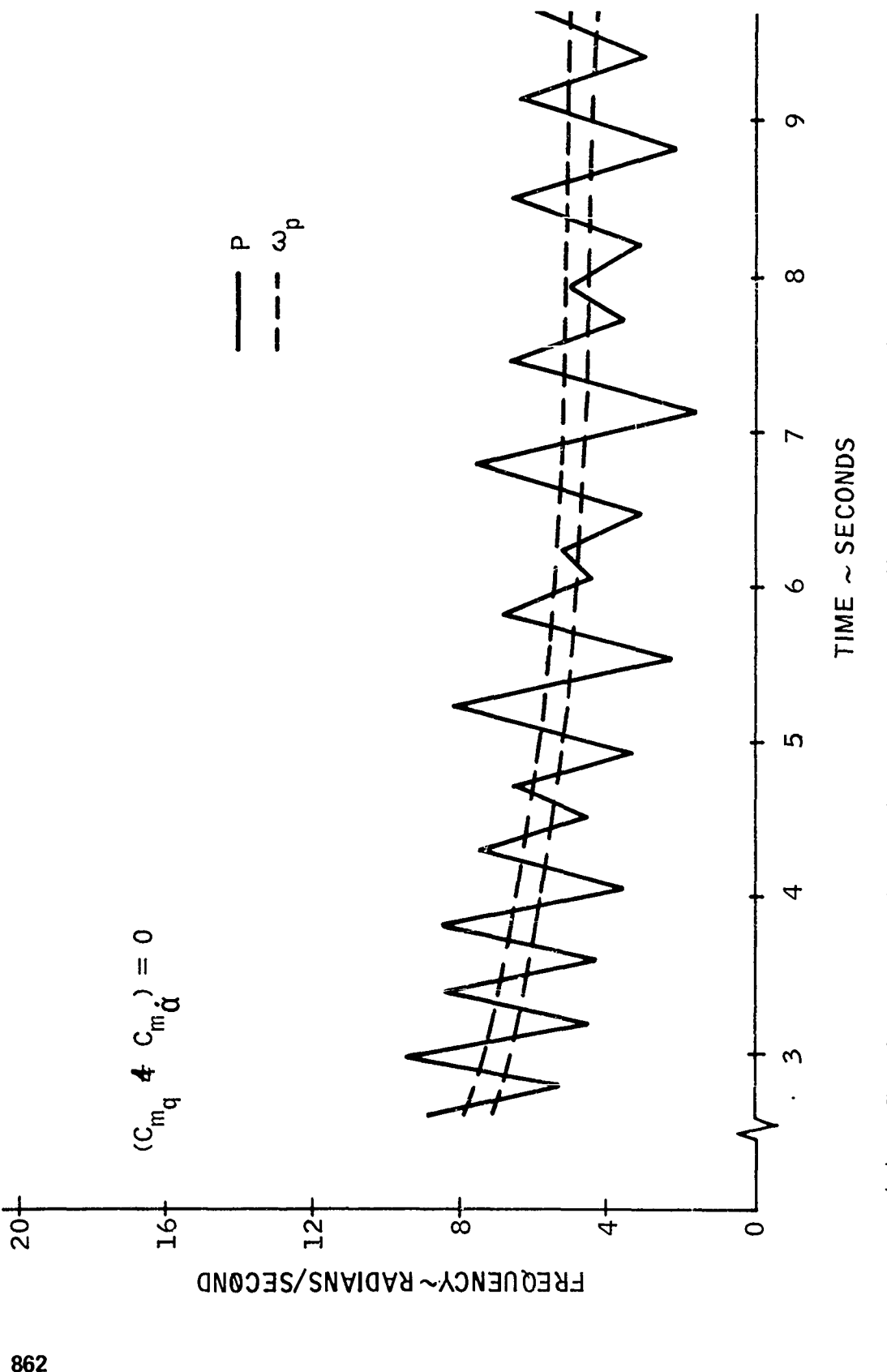


(U) FIG. 13. Effect of Standard Moment Curve on Roll Lock-In and Roll-Yaw Resonance

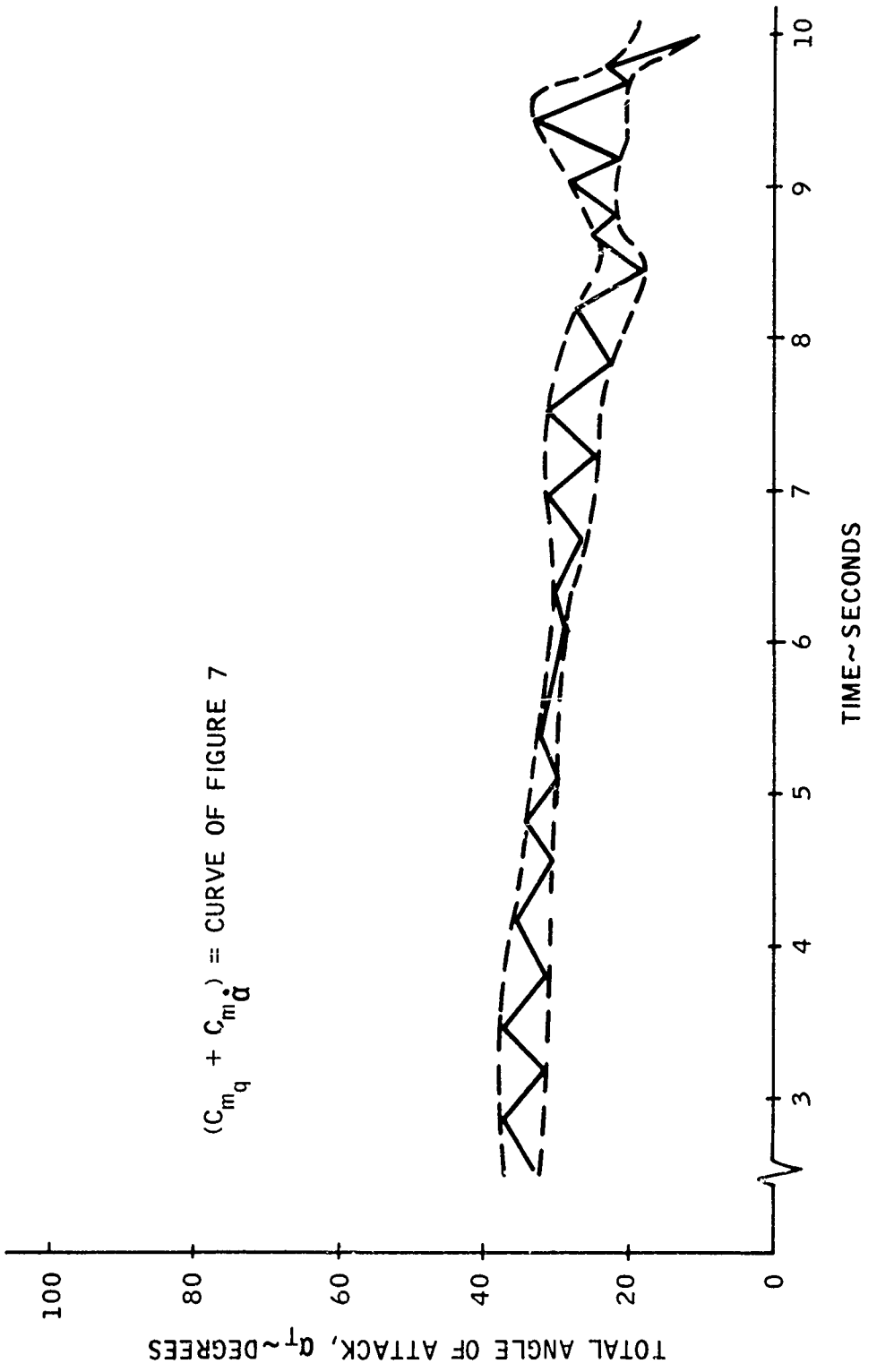


(U) FIG. 14. Effect of Positive Moment Slope on Dynamic Behavior and Stability



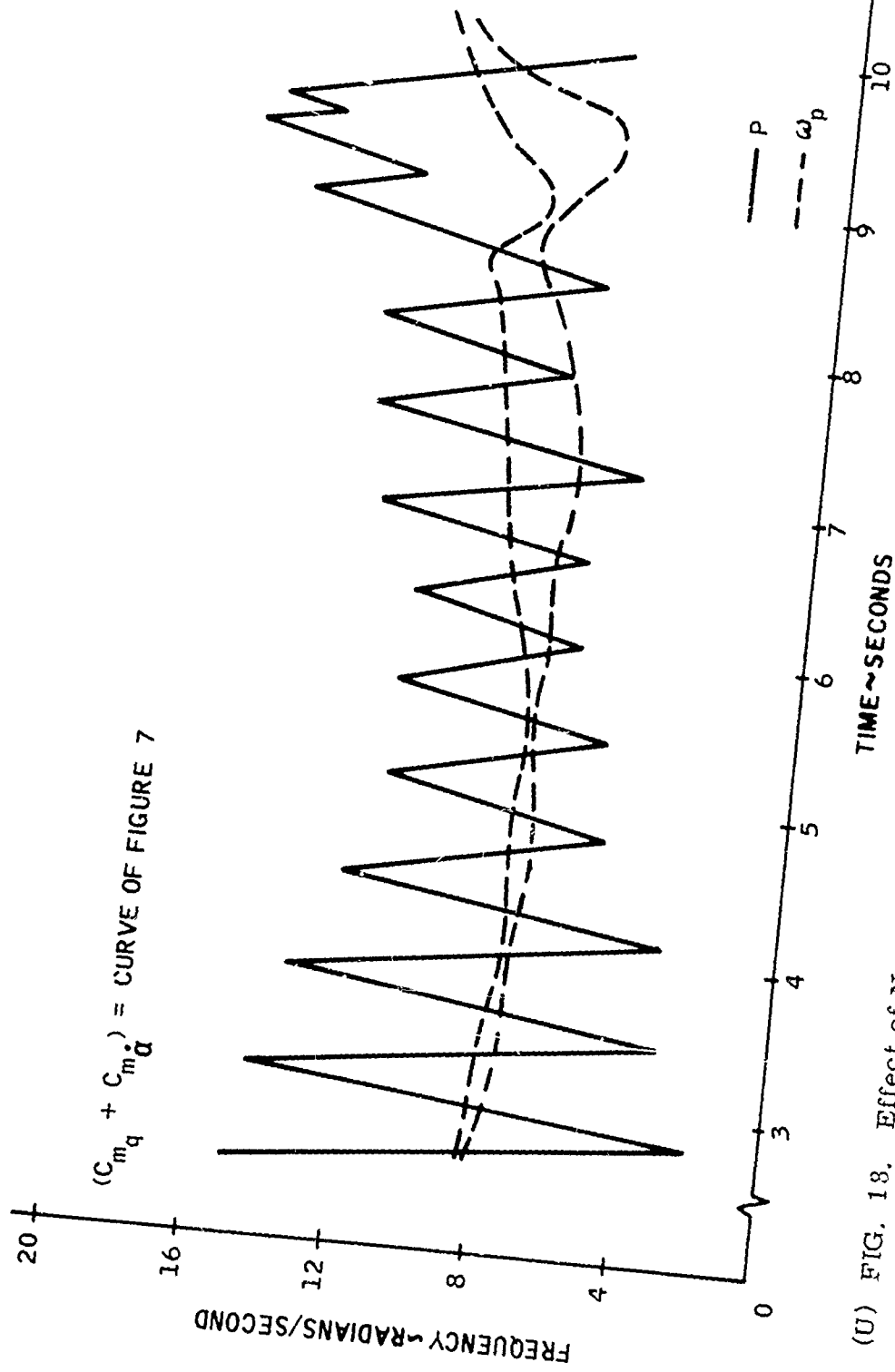


(U) FIG. 16. Effect of Negative Moment on Roll Lock-In and Roll-Yaw Resonance



(U) FIG. 17. Effect of Negative Moment Slope on Dynamic Behavior and Stability

$(C_{m_q} + C_{m\dot{q}})$ = CURVE OF FIGURE 7



(U) FIG. 18. Effect of Negative Moment Slope on Roll Lock-In and Roll-Yaw Resonance

Paper No. 34

TWO-DIMENSIONAL JET-INTERACTION EXPERIMENTS
RESULTS OF FLOW-FIELD AND SCALE EFFECT STUDIES
(U)

(Paper UNCLASSIFIED)

by

Michael J. Werle
Richard T. Driftmyer
David G. Shaffer
U.S. Naval Ordnance Laboratory
White Oak, Silver Spring, Md. 20910

ABSTRACT. This paper describes the results of two experimental studies concerning the injection of a gaseous secondary jet into an unbounded supersonic flow field which is uniform outside a turbulent boundary layer.

The first problem considered was that of mapping the streamline patterns for typical two-dimensional jet-interaction flow fields produced by sonic secondary jets. Tests were conducted at Mach 5 using a flat-plate model containing a sonic secondary jet directed normal to the mainstream. Local flow properties were measured throughout the flow field for jet strengths (ratio of jet gas stagnation pressure to mainstream static pressure) of 180 and 550. From these data and complementary shadowgraph studies, the streamline patterns and attendant shock structure have been formulated. The major qualitative features of these flows are compared with those that are assumed to exist in available analytical models.

The second problem considered in this paper is that concerned with the definition of the proper scale length to be associated with turbulent, two-dimensional jet-interaction flows. In support of this objective, results will be presented for a Mach 4 test conducted using the same flat-plate model described above. The secondary jet strength was varied from approximately 0 to 1000 for secondary jet throat sizes of 0.005 inch, 0.020 inch and 0.030 inch. Interaction normal forces were determined using the surface pressure distributions measured ahead of the secondary jet and comparisons of these results with available analytical predictions are presented.

INTRODUCTION

The general problem considered here is that of generating control forces in a supersonic environment through use of reaction-jet controls. NOL's present efforts are directed toward the development of a reliable analytical model for this type of fluidic system. An earlier study (Ref. 1) had indicated that while the general features of the jet-interaction phenomenon were reasonably well understood, there still exist areas of considerable confusion which seemingly negate all attempts to unify available data within the framework of existing analytical models, even for the two-dimensional problem. Apparently the only reliable statement that can be made about the forces generated by a two-dimensional jet-interaction system is that they will be somewhere around two to three times that of the jet thrust alone. Even this rather loose statement is largely based on empirical data of the type presented in Fig. 1, where experimental values of jet amplification (the ratio of the total force produced by the flow to that of the jet thrust alone) from several independent investigations are shown as a function of free-stream Mach number. The state of the art for theoretically estimating these amplification levels is well exemplified by the theoretical curves shown on Fig. 1 due to Spaid and Zukoski (Ref. 3) and NOL (Ref. 1). Both of these theories give order of magnitude estimates for the full range of Mach numbers shown but are completely incapable of explaining variations due to other parameters at a fixed Mach number - such as that due to variations in the secondary jet stagnation pressure (which is the major cause of the variations in A shown in Fig. 1 at any given M_∞). Interestingly enough, each of the data sources listed in Fig. 1 puts forth an analytical model none of which completely explains the data from the other sources listed. In an effort to clarify the picture, NOL has been conducting a series of limited scope experimental studies each directed at a single aspect of the interaction problem. The objective of this type of limited program is to provide isolated but well defined data points against which existing analytical models could be compared. The results of two such studies are reported in this paper.

The first of these, the flow-field study, presents the results of an attempt to define the detailed flow structure for two typical two-dimensional jet-interaction configurations. Mitchell (Ref. 7) had previously attempted the same using only shadowgraph studies whereas the present approach employed flow-field probe data as well. While the present study was not a complete success, it certainly gives reasonably accurate data that should provide a valid basis for comparison with analytical models.

The second study reported herein was concerned principally with the influence of the secondary jet-slot width on the forces produced by the jet-interaction process. The primary data taken were the surface pressure distributions fore and aft of several sonic slot jets blowing into a supersonic turbulent boundary layer. With careful attention given to each detail of the problem, the resulting data provide a much needed basis for comparison with theoretical jet-interaction force levels.

JET-INTERACTION FLOW-FIELD STUDY

In this study an attempt has been made to construct an accurate picture of the streamline pattern indicative of a typical two-dimensional jet-interaction flow field. The objective of this effort was to provide experimental results against which existing analytical models of the interaction process might be compared. To meet this objective, shadowgraph and flow-field probe studies were conducted using the flat-plate model shown in Fig. 2. The basic flat-plate model was 15.5 inches long and 10.0 inches wide. The plate was fitted with spherical boundary-layer trips located 0.75 inch from the leading edge. Glass ported side plates were mounted on the flat-plate surface so as to define a six-inch wide flow channel - the surface of which was instrumented with 78 static pressure taps. A six-inch span jet slot was flush mounted in the plate 7.25 inches (approximately the plate mid-chord) downstream of its leading edge. A sonic slot of nominal throat width, $b^* = 0.020$ inch was used throughout the test.

The three-pronged probe used to measure the local flow properties is shown in Fig. 2. The probe was used to simultaneously measure the local Pitot pressure, total temperature, angle of attack, and the surface pressure on a

Vol. 3

10-degree half-angle cone. From these quantities all local flow properties can be determined. The probe was mounted on the wind-tunnel angle-of-attack sector system with the line of probe tips lying on the system's center of rotation. This system arrangement permitted completely preprogrammed remote operation of the probe system throughout the test.

The tests were conducted at a free-stream Mach number, M_∞ , of 5 with a stagnation pressure, P_{O_∞} , of 660 psia and a stagnation temperature, T_{O_∞} , of 900°R; the resulting free-stream Reynolds number per foot was 18×10^6 . The secondary jet was supplied with high-pressure air at roughly ambient temperatures. Flow probing was done at two jet pressures, P_{O_j} , of 690 psia and 230 psia, resulting in jet strengths, $\frac{P_{O_j}}{P_\infty}$, of 550 and 180, respectively.

The streamline patterns resulting from this study are shown in Figs. 3(a) and 3(b). Concentrating first on the low-blowing rate data of Fig. 3(a), it is noted that the spherical boundary-layer trips produced a rather strong curved shock and thick boundary layer of the turbulent type. The boundary-layer thickness and type was determined from a separate Pitot pressure probe study. The trip shock was determined principally from shadowgraph pictures. Since a good deal of the flow field was not within the photographic field of view, the major portion of the boundary-layer trip shock shown could only be defined by a polynomial curve fit to the available data (the same holds true for all shocks shown in Fig. 3). Typical of this type of flow, the obstruction to the external flow created by the secondary jet resulted in a separated boundary layer and accompanying separation shock forward of the jet plume (the mixing region thicknesses shown in Fig. 3(a) was estimated from the shadowgraph studies). As shown in Fig. 3, the highly under-expanded secondary jet passes through a strong shock, usually assumed to be a normal

shock.¹ One striking feature of both Figs. 3(a) and 3(b), however, is the absence of the large angle deflections usually assumed to exist in the merging region of the separated mainstream and jet gas flow. Despite the appearance of a "strong-looking" bow shock wave no evidence was found of the "blunt body" type flow region proposed by Mitchell (Ref. 7), although it must be admitted that the severe fluctuations of the flow field observed in this merging region make it difficult to make a definitive assessment of the flow configuration. One further important observation that should be noted is that of the vertical displacement of the $\Psi = 0$ streamline above the jet shock. Numerous jet-interaction analytical models assume the $\Psi = 0$ streamline in the forward merging region intersects the jet plume at the jet shock. Actually it was found that the $\Psi = 0$ streamline intersects the jet gas well above the jet shock and further, at a point directly above the jet-slot location, the $\Psi = 0$ line is displaced to a position approximately 1.5 times the shock height, h_s , above the plate.

The jet gas, after passing through the jet shock, is turned downstream. This gas then reexpands to a supersonic state, passing over the separation bubble downstream of the jet plume. As the expanding gas turns towards the plate a recompression shock is formed which brings the flow back parallel to the plate surface.

Although not shown in Figs 3(a) and 3(b) it was found that virtually all of the flow for $\Psi < 0.2$ aft of the injection station was influenced by viscous effects - as evidenced by large variations in the local stagnation temperatures. It is not yet clear what direct influence this would have on analytical models of the problem at hand.

Both Figs. 3(a) and 3(b) contain similar information with two different jet strengths. This leads to one final significant point of interest. The flow field does not seem to scale linearly with the jet strength, P_{O_j}/P_∞ , (as implied

¹For the low jet blowing rate of Fig. 3(a), the jet shock was below the field of view of the ported side plates. The jet shock shown in Fig. 3(a) was determined by monitoring the decrease in the jet-shock height as the jet strength, P_{O_j}/P_∞ , was decreased and extrapolating the results to $P_{O_j}/P_\infty = 180$.

8th Navy Symposium on Aeroballistics

Vol. 3

in the analytical model of Refs. 1 and 3) but rather seems linearly dependent on the jet-shock height, h_s , which only doubled while P_{o_j}/P_∞ was increased by a factor of three.

The implication is that once a method is devised for estimating the jet-shock height, the major length parameter for the problem will be well in hand.

SCALE LENGTH STUDIES

GENERAL

The purpose of this phase of the study was to determine the influence of jet-slot width variation on the interaction forces produced ahead of a two-dimensional sonic slot. Previous NOL experimental results (Ref. 1) had indicated that the upstream force did not scale linearly with the slot width, (as predicted by the model proposed by Spaid and Zukoski in Ref. 3) nor did it correlate with the mass flow parameter of Hawk and Amick (Ref. 5). However, the data in question were taken with the large boundary-layer trips in Fig. 2, which, as shown in Fig. 3, produced an extremely thick boundary layer ahead of the jet slot. It was felt that part of the apparent discrepancy might well be attributed to the fact that available analytical models assume that the upstream boundary-layer thickness is small compared to the jet penetration - a restriction seemingly violated by the NOL data. In an effort to clarify the issue, a new experimental study was conducted using the flat-plate model of Fig. 2 but with the spherical trips replaced with a 0.025-inch-diameter wire. In addition, side plates with larger viewing ports were used to facilitate more extensive shadowgraph studies of the interaction flow field.

JET STUDIES WITH $M_\infty = 0$

Considerable useful data were obtained from a series of static tests ($M_\infty = 0$) made with the secondary jets exhausting into the evacuated tunnel. The primary purpose of these tests was to obtain accurate estimates to the jet-slot discharge coefficients under steady-state blowing conditions. The accompanying shadowgraph study provided apparently unique two-dimensional plume data for comparison with present analytical estimates of the jet-shock height. The results of this study are summarized in Fig. 4 which shows

that the nondimensional shock height, h_s/b_e , follows an expected linear variation with jet strength, P_o_j/P_b , and

that the constant of proportionality is approximately 0.54 (as opposed to estimates of 0.66 and 0.75 presented in Refs. 6 and 1, respectively). As shown in Fig. 4, b_e is the effective slot width computed using the measured slot width, b^* , and the mass flow discharge coefficient, C_d , of the slot as determined from a standard ASME orifice-type mass flow meter. Basically, three slots, with nominal widths of 0.005 inch, 0.02 inch and 0.03 inch, were tested. These slots though were built with two 0.05-inch-thick webs evenly spaced across the slot's six-inch span, the purpose of the webs being to try to prevent the slots from opening under pressurized conditions. A fourth slot of width 0.02 inch, but without webs was tested to allow an assessment of the webs' influence on the shock heights. From Fig. 4 it appears that the webs had no appreciable influence.¹ Also, as noted in Fig. 4, these static tests were performed with two separate settings of the back pressure at approximately 2 psia and 5 psia (these particular pressure levels were chosen as being roughly equivalent to the jet plume's effective back pressure during the subsequent jet-interaction tests). As shown in the figure, variations in P_b are completely accounted for in the jet strength, P_o_j/P_b .

j

JET-INTERACTION TESTS

Jet-interaction tests were performed in the NOL Supersonic Tunnel No. 2 at $M_\infty = 4$ and at free-stream Reynolds numbers per foot of 6×10^6 and 18×10^6 . A typical shadowgraph picture from this study is presented in Fig. 5 (in this case $R_e/\text{ft} = 18 \times 10^6$, $b^* = 0.02$ and $P_o_j/P_\infty = 500$) along with a table of the test conditions

j covered. Essentially, each of the four slots studied in the previously discussed static blows was run through a range of P_o_j/P_∞ until the forward separation bubble extended up

¹It should be pointed out that in order to achieve the excellent correlation of Fig. 4, it is necessary to admit to measured discharge coefficients greater than one. Apparently all the slots tested here opened under pressure and this fact was accounted for in all subsequent data reduction.

Vol. 3

to the leading edge or the maximum allowable $P_{o_j} = 1200$ psia was reached. The primary data taken here were the surface pressure distributions which have been integrated to give the upstream interaction forces. These results are summarized in Fig. 6 which shows the jet amplification as a function of the jet strength, P_{o_j}/P_∞ . It is immediately

apparent that there is no explicit slot-width or Reynolds number influence when the results are presented in this form. This result implies that correlations of jet ampli-

fication using the parameter grouping, $\frac{P_{o_j}}{P_\infty} b_e$, as proposed

in Refs. 2, 5 and 6, are incorrect. Further, the presence of a decrease in amplification for increased jet strengths in the present data directly contradicts the proposal of Ref. 3 that such a behavior is indicative of non-two-dimensional effects. Within the present data there was no evidence of any loss in two dimensionality as the jet strength was increased. Actually, the decreasing amplification shown in Fig. 6 can be traced to changes in the pressures occurring in the separation region upstream of the jet. To see this, it is first necessary to review the use of a step-flow analogy to model the upstream interaction region. In Refs. 1 and 3 it was pointed out that the normal forces produced by step-induced boundary-layer separation were linearly dependent on the step height. Virtually all analytical models for the jet-interaction problem have carried this concept over to jet-induced separation. Fig. 7 shows that this is apparently a valid approach for it shows that the upstream interaction force coefficient (based on b_e) is a linear function of the measured jet-shock heights. Apparently though, the effective step height is consistently about 1.5 times that of the jet-shock height (as predicted by Barnes et al, Ref. 6, and as supported by the streamline patterns of Fig. 3). The significant point though is that C_{N_i} varies linearly with

h_s/b_e so that it only remains to determine h_s/b_e . The shock height can be estimated through use of Fig. 4, once an effective back pressure, P_b , is decided upon. Kaufman (Ref. 8) has proposed use of the separation region plateau pressure as P_b and this assumption was applied to the present data.

Fig. 8 shows that, while the shock heights were well correlated among themselves with $P_b = P_{p_1}$, they were not predicted correctly by either Kaufman's correlation or the static results of Fig. 4. However, use of the separation region

second peak pressure to represent P_b definitely improved the agreement between the jet-interaction data and the static test results.¹ Apparently, then, the upstream force depends linearly on the shock height which in turn depends linearly on the second peak pressure P_{p_2} . This being the case it is

quite easy to show that the amplification must go as

$$A = 1 + \frac{K}{P_{p_2}/P_\infty} \quad (1)$$

where K is a constant. In the present test series P_{p_2}/P_∞ was observed to increase slightly with increasing P_{O_j}/P_∞ , thus causing the observed loss in A .

CONCLUSIONS

The results of two limited scope experimental studies were reported in this paper. The common objective of these works was to provide isolated but well-defined data points to serve as a basis of comparison for proposed analytical models of the jet-interaction phenomenon. As a result of these studies it has been found that the jet-slot width had no influence on the jet amplification for the case of thin upstream boundary layers. It was also found that the jet-shock height provided a valid scale length for the problem independent of the relative thickness of the upstream boundary layer. However, the effective penetration height of the jet stream (for use, say, in a step flow analogy) is somewhat greater than h_s and is given approximately as $1.5 h_s$. The shock height itself is not linearly dependent on the jet strength, as proposed in some analytical models.

¹Although not shown in Fig. 8, it was found that the shock-heights data taken at $M_\infty = 5$ in the streamline study (see Fig. 3) also correlated with the $M_\infty = 4$ data when the measured plateau and second peak pressures were used to represent the effective back pressure.

8th Navy Symposium on Aeroballistics

Vol. 3

Also, from the lack of high-turning angles encountered in the streamlines near the jet shock (see Fig. 3) it is apparent that the jet's effective back pressure is not that generated by a "blunt body"-type strong shock in the local flow. Rather, it seems to be a function principally of the pressure levels in the separation region ahead of the jet. It was found that the one correlation that gave reasonable consistency between the static and $M_\infty = 4$ data was that

which used the separation region second peak pressure as the jet plume's effective back pressure. It is recommended that future studies be directed toward determining the influence of jet conditions on the separation region second peak pressure - the end result of which should be a reliable model for the jet-interaction problem.

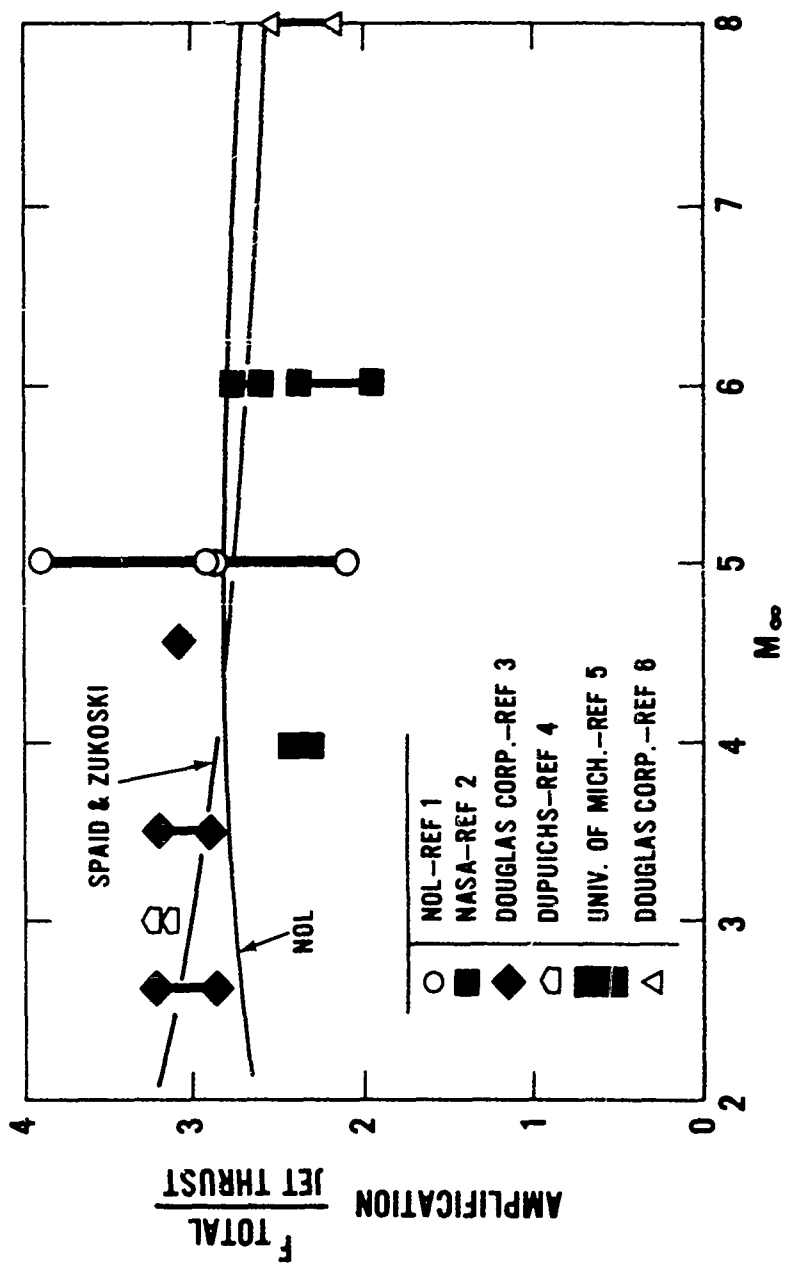
REFERENCES

1. U. S. Naval Ordnance Laboratory. A Critical Review of Analytical Methods for Estimating Control Forces Produced by Secondary Injection, by M. J. Werle. White Oak, Silver Spring, Md., NOL, January 1968. 94 pp. (NOLTR 68-5, publication UNCLASSIFIED.)
2. National Aeronautics and Space Administration. Experimental Investigation of Secondary Jets from Two-Dimensional Nozzles with Various Exit Mach Numbers for Hypersonic Control Applications, by J. R. Sterrett, J. B. Barber, D. W. Alston and D. J. Romeo. NASA, January 1967. (TN D-3795, publication UNCLASSIFIED.)
3. AIAA Journal. A Study of the Interaction of Gaseous Jets from Transverse Slots with Supersonic External Flows, by F. W. Spaid and E. E. Zukoski. February 1968. pp. 205-212. (Vol. 6, No. 2, publication UNCLASSIFIED.)
4. Office of Naval Intelligence Translation No. 2174 (translated from Publications Scientifiques et Techniques due Ministere de L'Air). Effect of a Transverse Jet on a Supersonic Flow, by G. Dupuichs. 1963. 151 pp. (No. 396, publication UNCLASSIFIED.)
5. AIAA Journal. Two-Dimensional Secondary Jet Interaction with a Supersonic Stream, by N. E. Hawk and J. L. Amick. April 1967. pp. 655-660. (Vol. 5, No. 4, publication UNCLASSIFIED.)

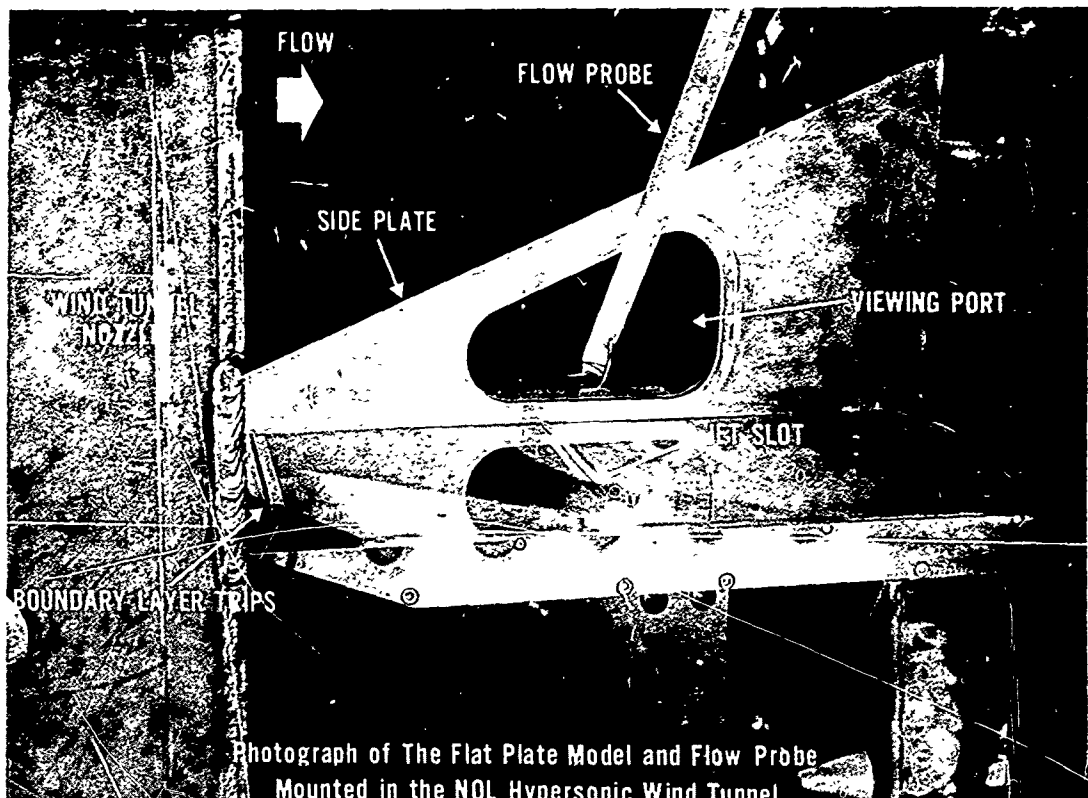
8th Navy Symposium on Aeroballistics

Vol. 3

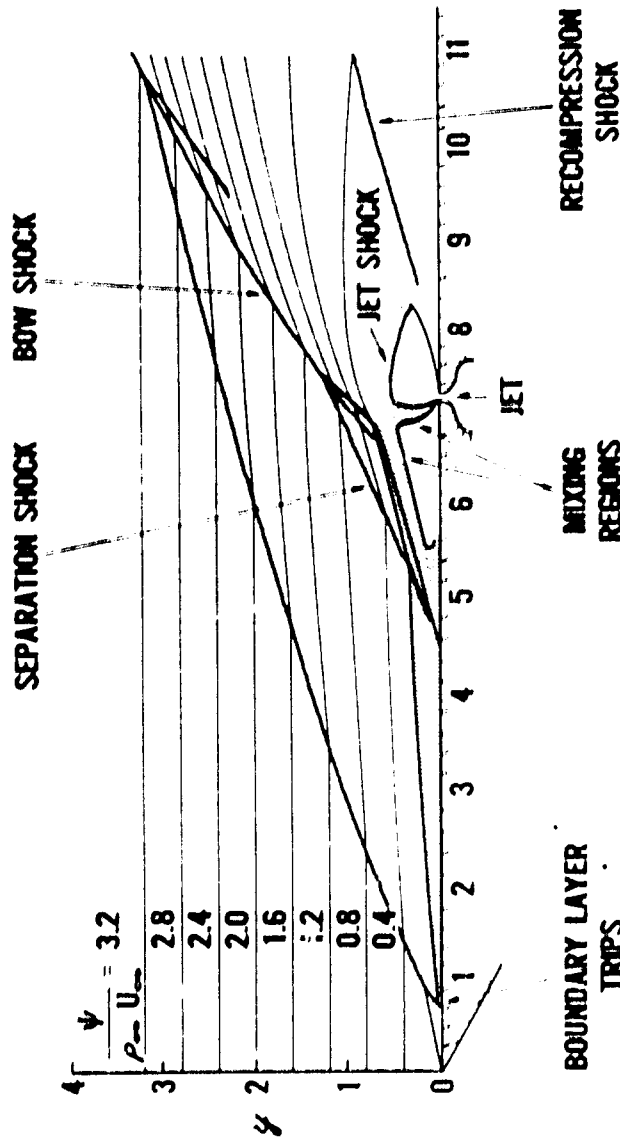
6. Control Effectiveness of Transverse Jets Interacting with a High Speed Free Stream, by J. W. Barnes, J. G. Davis and H. H. Tang. September 1967. 221 pp. (Technical Report AFFDL-TR-67-90, Vol. I, publication UNCLASSIFIED.)
7. An Analytical Study of a Two-Dimensional Flow Field Associated with Sonic Secondary Injection into a Supersonic Stream, by J. W. Mitchell. March 1964. 53 pp. (Technical Note, 9166-TN-2, publication UNCLASSIFIED.)
8. Grumman Research Department. High Speed Flows Past Transverse Jets, by L. G. Kaufman, II and F. Koch, II. October 1968. 73 pp. (Report RE 348, publication UNCLASSIFIED.)



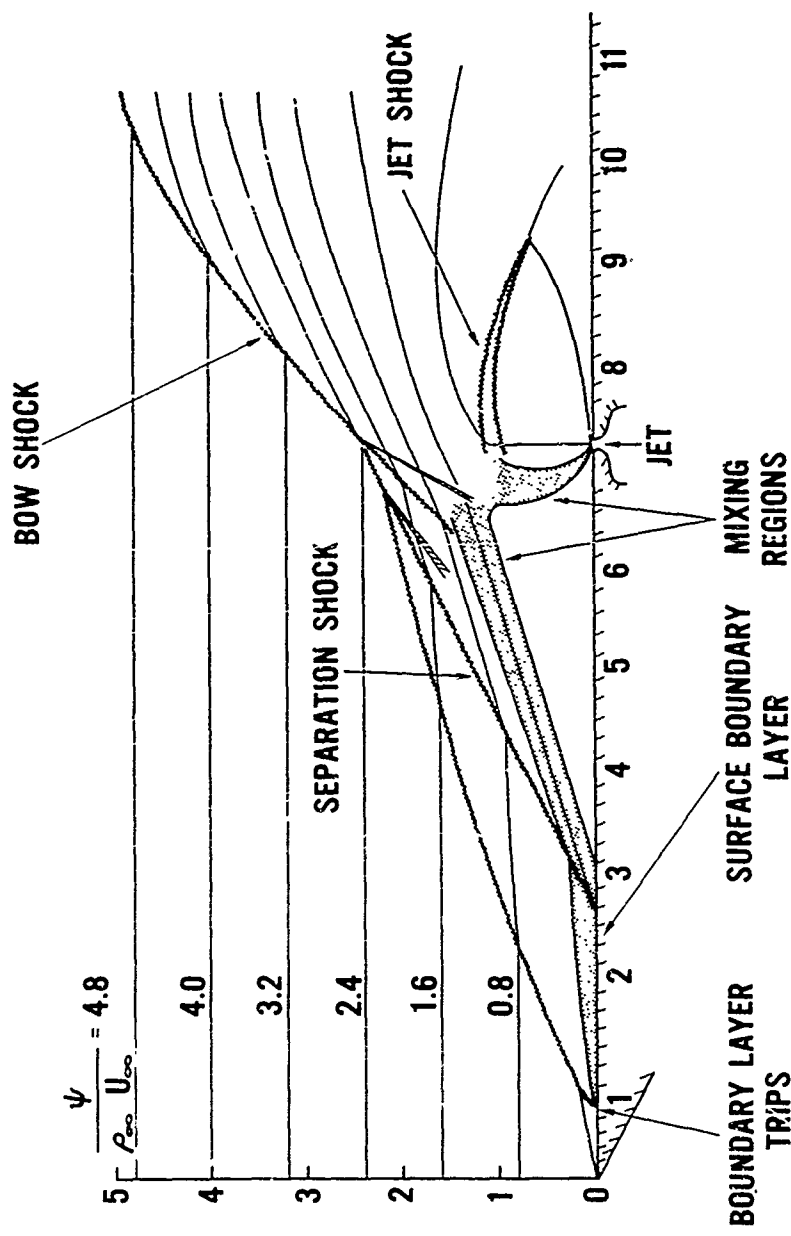
(U) FIG. 1 Two Dimensional Jet Interaction Results

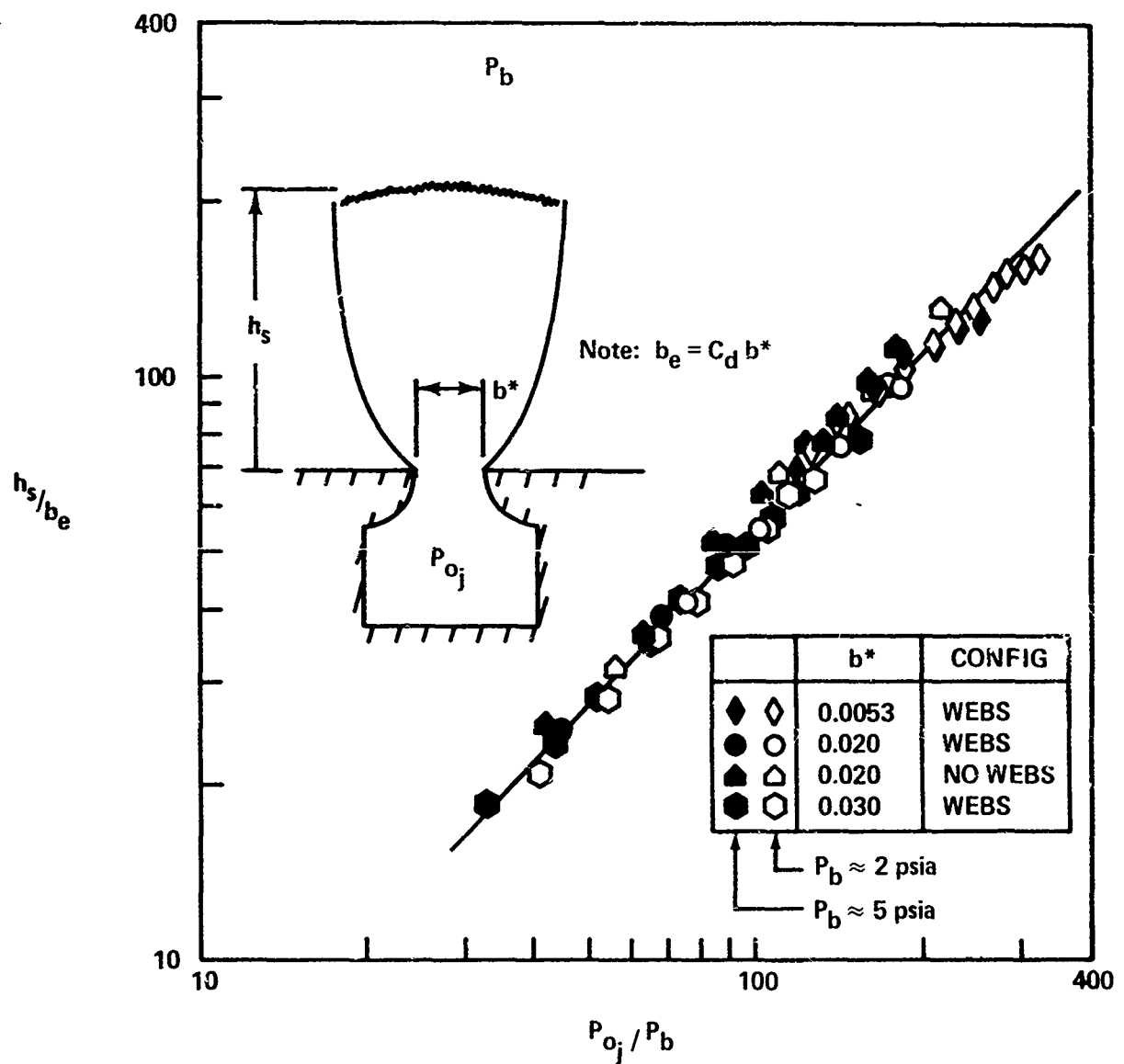


(U) FIG. 2.

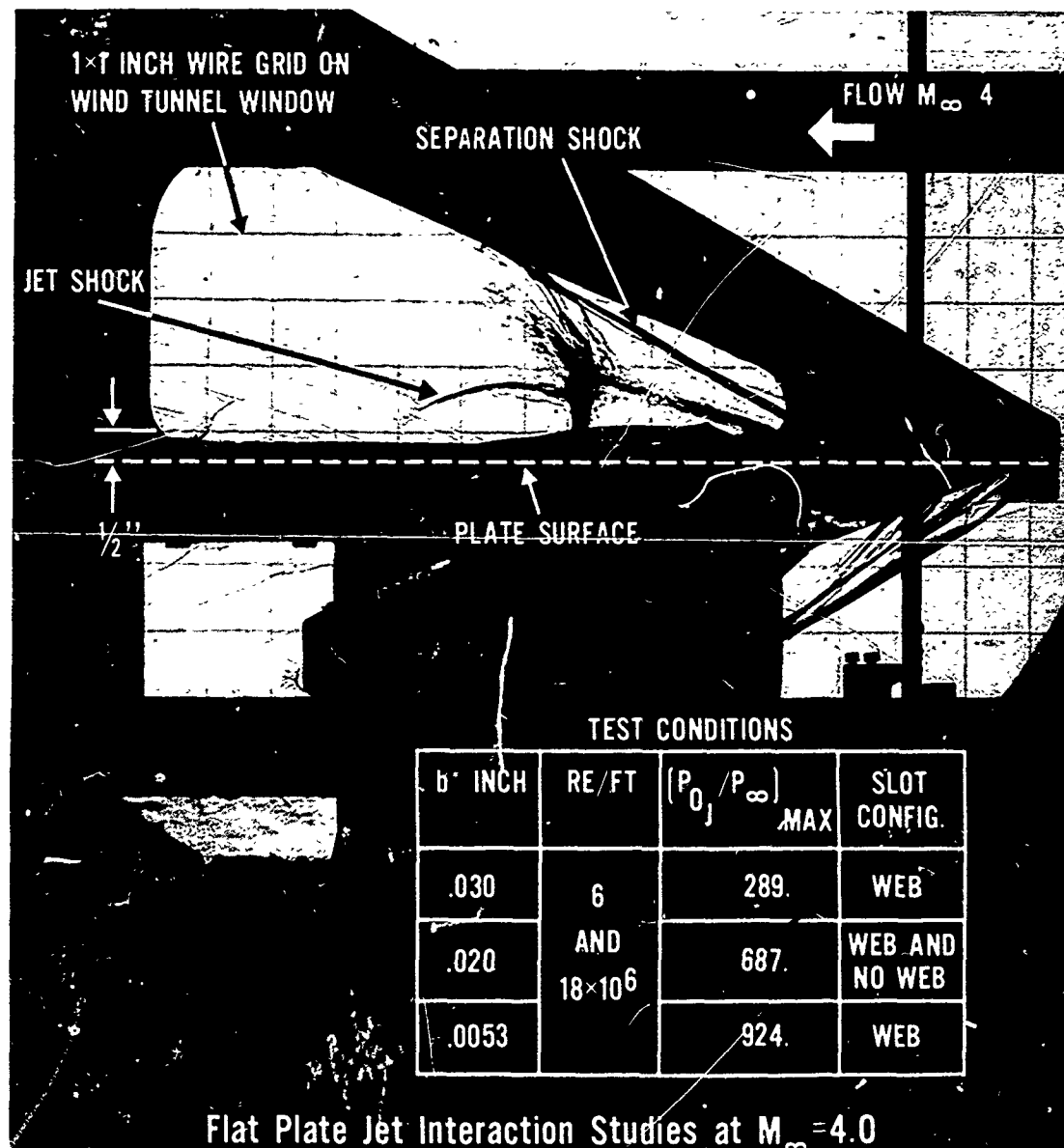


(U) FIG. 3[a] Interaction Flow Field for $P_j/P_\infty = 180$

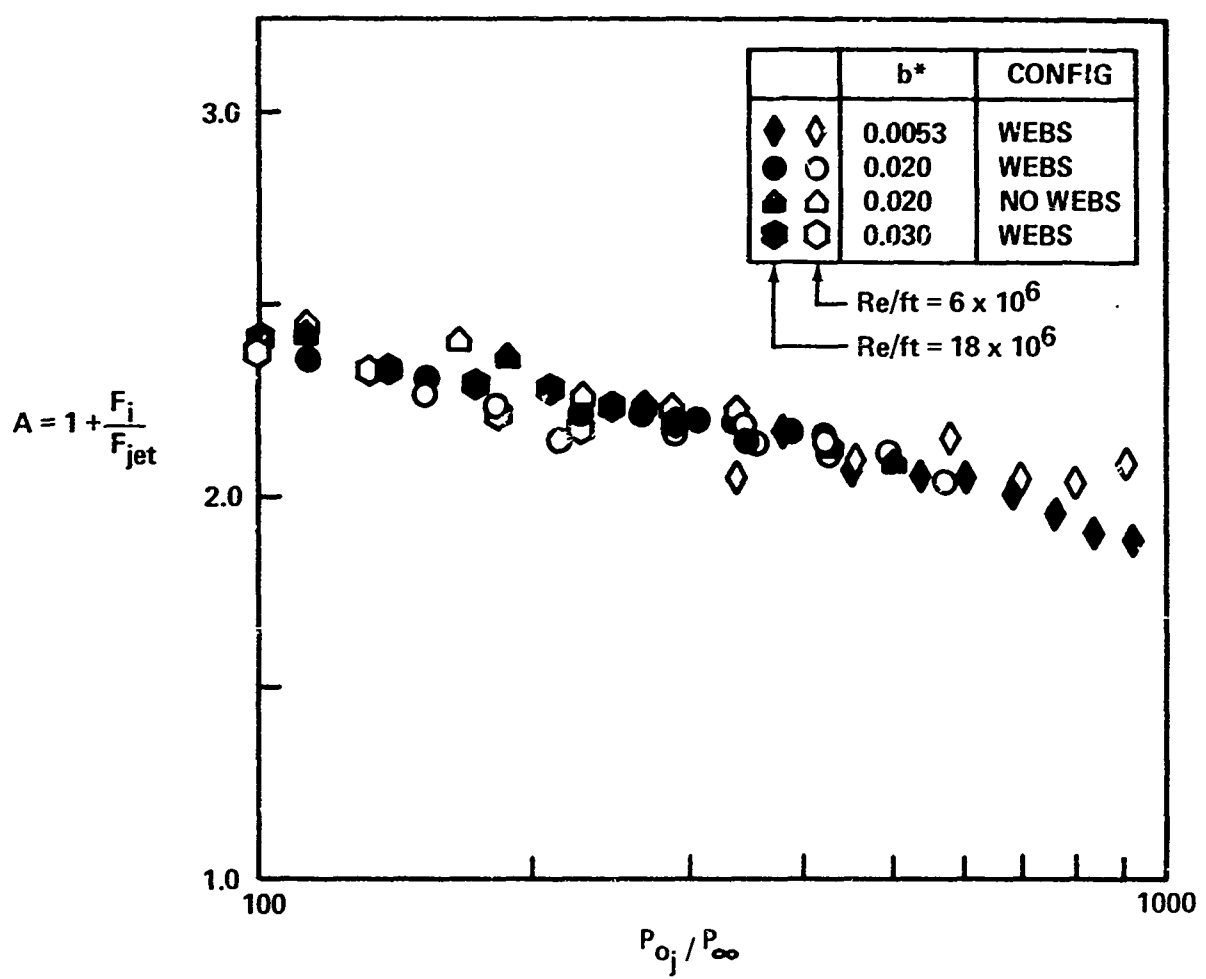
(U) FIG. 3(b) Interaction Flow Field for $P_{0j}/P_\infty = 550$

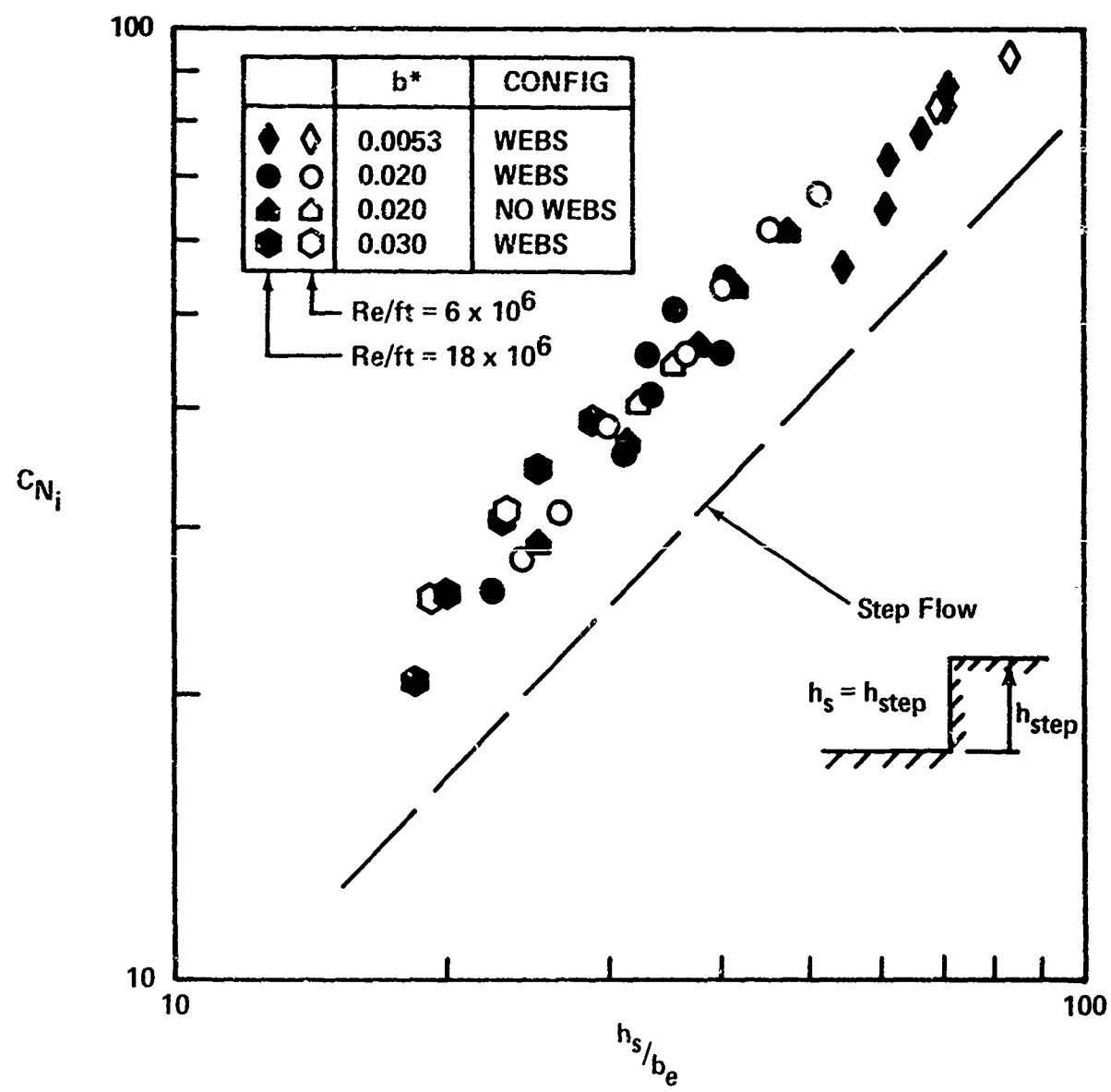


(U) FIG. 4 Shock Heights for Two Dimensional Underexpanded Jets

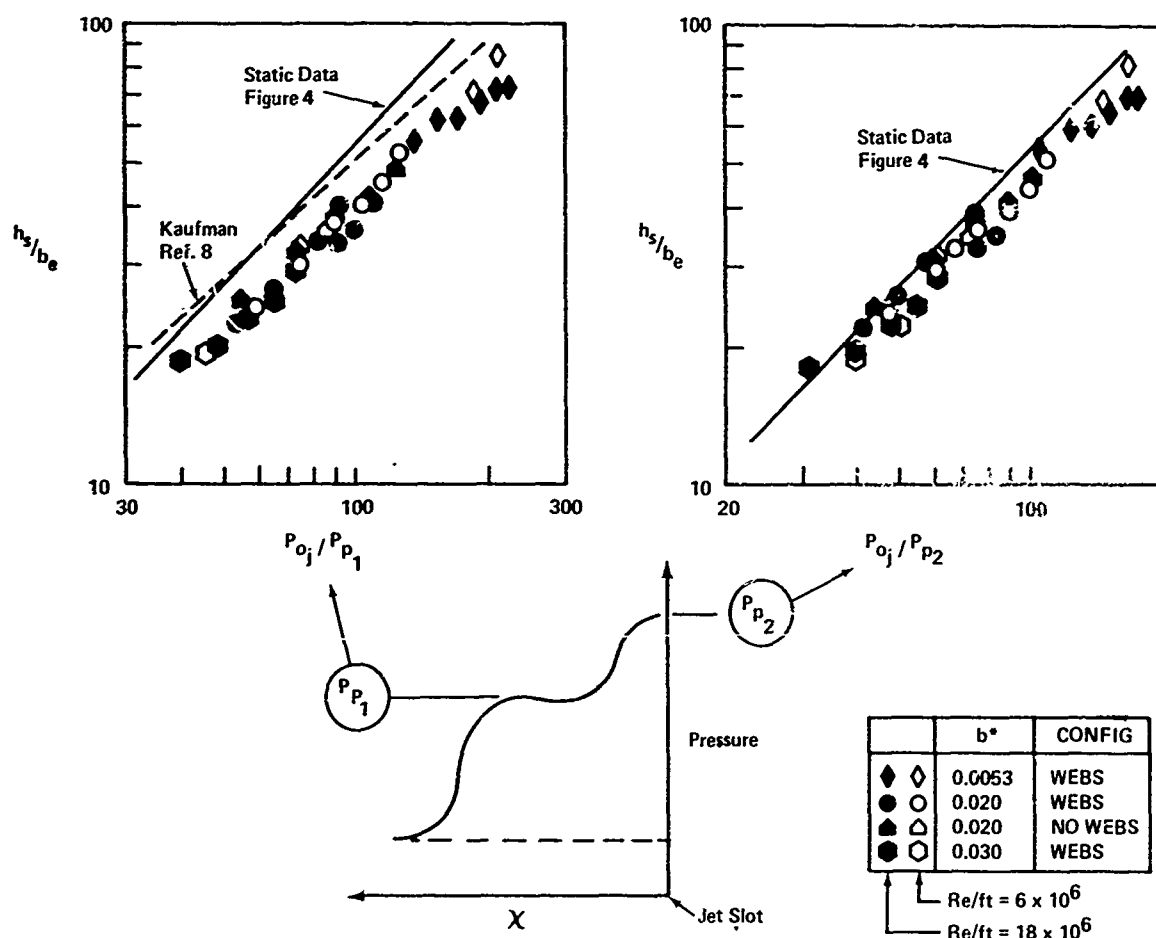


(U) FIG. 5.

(U) FIG. 6 Amplification Levels for $M_{\infty} = 4$



(U) FIG. 7 Interaction Force Dependence of Jet Shock Height



(U) FIG.8 Effective Back Pressures for Jet Interaction Shocks

Paper No. 35

INTERACTION BETWEEN HIGH SPEED FLOWS
AND TRANSVERSE JETS: A METHOD FOR PREDICTING
THE RESULTANT SURFACE PRESSURE DISTRIBUTION

(U)

(Paper UNCLASSIFIED)

by

Louis G. Kaufman II
Research Scientist
Grumman Aircraft Engineering Corporation
Bethpage, N.Y. 11714

ABSTRACT. (U) Reaction jets interact strongly with the local stream flow over a vehicle and can produce a force that is several times larger than the pure reaction force of the jet. Extensive data from many sources have been used to develop a method for calculating the increased force due to the interaction between high speed stream flows and jets issuing normally from slot-type orifices. Empirical relations are derived for estimating the effective distance the jet penetrates the stream flow in terms of the ratio of the jet total pressure to the "plateau" pressure in the separated flow region ahead of the jet. The penetration distance is then used in calculating the pressure distribution produced by the interaction for either laminar or turbulent boundary layer flows over the surface. The normal force and moment caused by the interaction can then be calculated with good engineering accuracy for a very wide range of jet and local airflow conditions in the supersonic-hypersonic speed range. The method is used to determine the effects of the various parameters influencing the interaction and their effects on the amplification factor (total force/jet reaction force).

8th Navy Symposium on Aeroballistics

Vol. 3

SYMBOLS

C_N	coefficient of interaction force using d as reference area (per unit span), $C_N \equiv \int [(p - p_1)/q_1 d] dx$
d	throat width of jet nozzle
h	effective jet penetration height
K	amplification factor (interaction force + reaction force)/(reaction force)
l_f	free interaction length
l_s	length of separated flow upstream of jet orifice ($l_s = x_s $)
L	length of (flat plate) surface upstream of jet orifice
M	Mach number
n	exponent in jet penetration height expression [Eq. (1)]
p	static pressure
p_p	plateau pressure
p_j	total pressure of jet flow
q	dynamic pressure
Re_L	Reynolds number based on undisturbed local flow conditions and upstream length L

Re_s	$Re_s \equiv [(L - \ell_s)/L]Re_L$
x	streamwise coordinate (origin at jet orifice location)
α	dividing streamline angle (cf. Fig. 1)
ξ	plateau pressure ratio, $\xi \equiv p_p/p_1$

Subscripts

1	undisturbed local flow conditions over flat plate surface with no jet flow
r	conditions at reattachment of jet flow on surface downstream of orifice
s	conditions at separation of stream flow from surface upstream of orifice

INTRODUCTION

(U) Reaction jets issuing normally from a surface can be used for control of high performance missiles or aircraft. These jets interact strongly with the local airflow over the surface and substantially increase the pressure loads on the surface both ahead of and behind the jet orifice. The additional surface pressure loads augment the simple reaction force of the jet and can result in a total control force several times larger than the reaction force, this depending on local flow conditions. The possibility of large additional forces and the many advantages of reaction jet control have prompted increasing interest in using transverse jets for a wide variety of applications. This has led to many experimental investigations of transverse jet interaction effects; however, there were no generally applicable analytical methods for predicting these effects reliably for a wide range of flow conditions.

(U) Several different types of jet-stream interactions have been observed experimentally and various flow models

Vol. 3

postulated. Many investigators sought correlation parameters and formulas for predicting the interaction force directly. However, the force correlation methods gave results, particularly for laminar boundary layers, that were in severe general disagreement. The results obtained from one series of experiments differed from those obtained from others. In part, the discrepancy arose from the fact that the force correlations do not account adequately for the local viscous flow conditions and jet geometry. To obtain reliable interaction force predictions it appears to be necessary to calculate the pressure distribution due to a particular jet and stream flow interaction as is done herein, and then integrate the resulting overpressures.

(U) The considerable interest in understanding transverse jet interactions has led to many recent experimental investigations and to several comprehensive reviews (e.g., Refs. 1-8). The availability of these extensive test results now provides a good basis for analyzing transverse jet interactions and for comparing analytical results with experiment for a wide variety of conditions.

(U) Although the analysis used herein is two dimensional, the results can be applied to jets issuing from large but finite aspect ratio, slit-type orifices. Further, several investigators (e.g., Refs. 9 and 10) have observed that some results of two dimensional jet interaction analyses can be applied to jets issuing from slit-type orifices in axisymmetric bodies.

ANALYTICAL FLOW MODEL

(U) Fundamentally, a jet issuing normally from a plate pushes the local stream flow away from the surface, and the jet flow is bent downstream by the stream flow. Although there are many self-induced flow effects and the interaction phenomena are quite complex, understanding of the phenomena has improved tremendously in the past several years, and certain features of jet interaction flows can now be described fairly reliably.

(U) The two dimensional stream flow separates from the surface (at x_s) ahead of the jet in a manner similar to

supersonic flow separation ahead of a forward-facing step (Fig. 1). The so-called dividing streamline indicates the boundary of the fluid trapped in the reverse flow region and can be taken as a new effective surface shape for the stream flow (the angle between the surface and the dividing streamline is α). The stream flow is compressed through the shock wave emanating from the separation point. The surface pressure rises to a "plateau" level and then remains fairly constant over the separated flow region. The length over which the pressure rise occurs is known as a free interaction length (l_f).

(U) Upon leaving the orifice (of width d), the jet flow initially expands but then passes through a strong, nearly normal shock wave. Thus most of the jet flow is subsonic when it is bent in the downstream direction. There is a strong interaction shock wave in the stream flow where the jet and stream flows meet, and there is a strong shear layer between the jet and stream flows. After passing through the nearly normal shock wave, the jet flow again expands and reattaches to the downstream surface (at x_r) through an oblique shock wave. The interaction pressure distribution on the surface downstream of the orifice is somewhat similar to pressure distributions behind rearward facing steps.

(U) The interaction sketched in Fig. 1 can be considered typical of "two dimensional" transverse jet interactions. For very weak jets, the jet behavior is similar to that occurring in the film cooling of a surface; thus there are no separated flow regions, and boundary layer analysis can describe the resulting flow. As the jet strength increases, laminar or turbulent separation occurs upstream of the orifice, the kind of separation depending on the nature of the boundary layer. The extent of the downstream separated flow region and the reattachment pressure rise depend primarily on the jet strength and local stream flow Mach number. For very strong jets with large penetration distances, the interaction shock is detached and moves far upstream.

JET PENETRATION HEIGHT CORRELATIONS

(U) Although many investigators have compared flows past transverse jets with flows over spoilers or forward

facing steps (cf. Ref. 3), there were no completely satisfactory ways to estimate the effective step height simply and reliably. As noted by Barnes et al. (Ref. 8), the total jet penetration height is not readily discernible in flow photographs. Many investigators have found, however, that the effective step height, representing the jet penetration distance, can be taken as the height of the strong shock in the jet flow.

(U) Various parameters have been used in correlating the effective step height. The lengths usually involved are the effective step height h , the width of the jet nozzle d , and possibly the upstream surface length L or a boundary layer thickness. The pressures most often used are the jet flow total pressure p_j , the pressure downstream of the strong jet shock, and the free stream static or total pressure. These parameters, along with the free stream Mach number and possibly the jet mass flow rate or total temperature, define the problem.

(U) Instead of choosing a particular parameter for correlating effective step heights, our approach was to examine methodically many different correlation schemes. A high speed digital computer was used to seek meaningful trends in about 500 sets of transverse jet interaction data from many different sources (data are tabulated in Ref. 3). The data were correlated by using a least squares fit to a power law variation of penetration height with 12 different parameters (composed of combinations of p_j , d , L , and a stream flow pressure). For each correlation the standard deviation, percentage of standard deviation, and correlation coefficient were calculated. From these, the computer could determine the goodness of fit for each correlation.

(U) The existence of meaningful trends in the data was investigated by restricting groups of data according to: the type of boundary layer separation occurring ahead of the jet, the free stream Mach number, the jet Mach number, the Reynolds number, the length of the flat plate ahead of the jet orifice, and the jet orifice aspect ratio (with and without end plates). The goodness of fit could then be calculated for each correlation of the chosen group of restricted data. For example, significant Mach number trends were sought by obtaining correlations only for the data within limited Mach number ranges.

(U) Those correlations that gave the best results (smallest percentage of deviation) were tabulated by: the correlation coefficient, the exponent, the standard deviation, the percentage of error, the amount of data included in the correlation, the type of data used (Mach and Reynolds number ranges, jet aspect ratio ranges), and the type of boundary layer separation. This tabulation was used to determine the more promising jet penetration distance correlations, which were then plotted and reviewed to select the best correlation parameter.

(U) The best correlation was achieved by using

$$\frac{h}{d} = 1.2 \left(\frac{p_j}{p_p} \right)^n \quad (1)$$

where n depends simply on the aspect ratio (AR) of the jet orifice:

$$n = \begin{cases} 0.70 & \text{for } AR < 300 \\ 0.75 & \text{for } 300 < AR < 500 \\ 0.80 & \text{for } AR > 500 \\ 0.85 & \text{for jet orifices with end plates.} \end{cases}$$

These correlations and data for the various ranges of aspect ratios are shown in Fig. 2; the data cover a very wide range of jet strengths and test conditions (cf. Ref. 3). In view of the very wide range of test conditions, the correlations approximate the data quite well. The computed constant for each range of aspect ratios was quite close to 1.20, and in each case the least squares fit calculated values of n were within 0.01 of the values shown in Eq. (1). Thus the values given in the equation and used herein (rounded for simplicity) give results well within the scatter of the experimental data.

(U) For jets exhausting into still air, the height of the jet shock depends simply on the jet nozzle throat width and the ratio of the jet total pressure to the still air pressure (Refs. 11-13). However, for jets exhausting transversely into high speed flows, the effective back pressure for the jet flow is considerably larger than the free stream static pressure. Reasoning on physical grounds leads one to expect that the plateau pressure immediately ahead of the jet may well be the effective pressure "felt" by the jet

8th Navy Symposium on Aeroballistics

Vol. 3

flow; thus one might seek to correlate h/d with the pressure ratio (p_j/p_p). This reasoning supports the statistical results presented in Eq. (1).

(U) An important conclusion is that no parameter other than jet aspect ratio was found to affect the correlation significantly. Thus the penetration distance data correlate well with p_j/p_p , independent of Mach number, Reynolds number, and type of separation. Schetz et al. (Ref. 12) and Spaid and Zukoski (Ref. 14) had earlier made similar observations. Although the correlation of penetration height with p_j/p_p does not depend on M_j , Re_L , or the type of separation, the interaction pressure distribution and resulting force do depend on these parameters.

INTERACTION PRESSURE DISTRIBUTIONS

UPSTREAM OF THE ORIFICE

(U) The effective jet penetration height can be used to determine the extent of separation ahead of the jet, but it is also necessary to know the type of boundary layer separation that can be expected. In some cases the jets are sufficiently strong to cause the stream flow to separate from the leading edge of the plate (cf: Ref. 8). A representative upstream pressure distribution resulting from this type of separation is sketched in the first part of Fig. 3. The interaction increases the pressure on the plate surface all the way from the jet location forward to the leading edge of the plate. In most cases, however, separation occurs downstream of the leading edge and the resulting interaction pressure distributions resemble those obtained, for example, by Chapman, Kuehn, and Larson (Ref. 15) for various types of boundary layer separation ahead of a step. Laminar separation occurs far upstream of the jet, and the pressure distribution has a characteristic "laminar plateau." Turbulent boundary layers do not separate until closer to the jet and reach a considerably larger "peak" or "plateau" pressure ahead of the jet. Transitional separation occurs when a laminar boundary layer separates but becomes turbulent in the separated flow region. The resulting pressure distribution combines the characteristics of purely laminar and purely turbulent separated flows (Fig. 3).

(U) The effective slope of the dividing streamline over the separated flow region is simply

$$\tan \alpha = \frac{h}{l_s} = \frac{h/d}{l_s/d} \quad (2)$$

where $l_s = |x_s|$ is the length of the separated flow region upstream of the orifice. The average pressure level (p_p) over the separated flow region can be obtained from oblique shock relations:

$$\tan \alpha = \frac{5(\xi - 1)}{7M_1^2 - 5(\xi - 1)} \sqrt{\frac{7M_1^2 - (6\xi + 1)}{6\xi + 1}} \quad (3)$$

where $\xi \equiv p_p/p_1$. From Eq. (2), $h/d = (l_s/d)\tan \alpha$; combining this with Eq. (3) and the expression for the effective jet penetration height [Eq. (1)], we have

$$1.2 \left(\frac{p_j/p_1}{\xi} \right)^n = \frac{l_s}{d} \frac{5(\xi - 1)}{7M_1^2 - 5(\xi - 1)} \sqrt{\frac{7M_1^2 - (6\xi + 1)}{6\xi + 1}} \quad (4)$$

where n depends on the jet orifice aspect ratio and the term (p_j/p_p) in Eq. (1) has been rewritten in the equivalent form $((p_j/p_1)/\xi)$.

(U) For leading edge separation, $l_s = L$ and Eq. (4) can be solved iteratively for the only unknown (ξ) by choosing successive values of ξ in the range $1 < \xi < p_j/p_1$.

(U) For laminar boundary layer separation, as noted by Chapman et al. (Ref. 15), the plateau pressure level depends solely on local flow conditions at the location of the separation point. Following Chapman's lead, Hill found

$$\frac{p_p}{p_1} - 1 = \xi - 1 = 1.22M_1^2 \sqrt{\left[(M_1^2 - 1)Re_s \right]^{\frac{1}{4}}} \quad (5)$$

to correlate laminar plateau pressures quite well for a wide range of Mach numbers (from 1.4 to 15) and for a very broad spectrum of experimental investigations and facilities (Ref. 16). In Eq. (5), Re_s is the Reynolds number based

Vol. 3

on undisturbed flow conditions and the running length of the boundary layer from the leading edge to the location of separation. Noting that $Re_s = ((L - \ell_s)/L)Re_L$, we can rewrite Eq. (5) as

$$\ell_s = L - \frac{L}{(M_1^2 - 1)Re_L} \left[\frac{1.22M_1^2}{\xi - 1} \right]^4 \quad (6)$$

Equations (6) and (4) can be solved iteratively (again by choosing successive values of ξ in the range $1 < \xi < p_j/p_1$ for the laminar plateau pressure ratio $\xi = p_p/p_1$ and the length of separation ℓ_s ahead of the jet.

(U) The length over which the pressure rises to the laminar plateau value is called the laminar free interaction length, ℓ_f (cf. Fig. 1). As described by Lewis et al. (Ref. 17), "... the flow field in the region of separation is dominated by the equilibrium interaction between the boundary layer and the external flow. Although the location of the point of separation depends strongly on the location and strength of the disturbance, the pressure distribution throughout the region away from the immediate neighborhood of the disturbance is governed by local interaction, and in this sense is independent of the disturbing mechanism. This phenomenon is commonly referred to as 'free interaction.'" These authors present universal curves by which the laminar pressure rise distributions can be scaled, "S"-shaped curves that approach p_1 and p_p asymptotically. Using the maximum slope intercepts to define ℓ_f , one obtains

$$\frac{\ell_f}{L + x_s} \approx \frac{2}{M_1^2} \left(\frac{T_w}{T_1} \right) \sqrt{\bar{\chi}_s} \quad (7)$$

where T_w is the wall temperature, T_1 the static temperature of the undisturbed local flow, and $\bar{\chi}_s = M_1^3 / \sqrt{Re_s}$. The free interaction length can be used to estimate the pressure distribution shape simply by fairing the universal "S"-shaped curve presented by Lewis et al. from p_1 at $x = x_s$ to p_p at $x = x_s + \ell_f$. (Here $x_s < 0$; thus $L + x_s$ is simply the distance from the leading edge to the location of separation.)

(U) For turbulent boundary layer separation, the following relations, due to Love and to Sterrett and Emery (cf. Ref. 18), give excellent agreement with experimental pressure levels in turbulent separated flow regions ahead of the jet:

$$\frac{p_p}{p_1} = \xi = \begin{cases} 1 + \frac{2.24M_1^2}{8 + (M_1 - 1)^2} & \text{for } M_1 < 3.38 \\ \text{or} \\ 1 + 0.7 \left(0.13M_1^2 - 1.5 + \frac{9.1}{M_1} \right) & \text{for } M_1 > 3.38 \end{cases} \quad (8)$$

where the value 1.4 has been used for the ratio of specific heats for air. These relations give p_p/p_1 explicitly in terms of M_1 . Therefore, for turbulent separation, the penetration height and separation location can be calculated directly [using Eqs. (1) through (3)], and are independent of Reynolds number. As noted by several investigators (cf. Ref. 3), the slope of the dividing streamline is insensitive to changes in the jet strength for turbulent separation. This observation agrees with the above; in this case the slope can be calculated directly [using Eq. (3)], independently of the jet penetration height. Therefore, for turbulent separation, the upstream pressure distributions scale with h and would be similar if plotted versus x/h (or, equivalently, versus x/x_s).

(U) Interaction pressure distributions for transitional boundary layer separation are most difficult to predict accurately. The dividing streamline is curved and the pressure increases throughout the separated flow region (cf. Fig. 3). However, an estimate of the pressure distribution for transitional separation can be taken simply as the average of those pressure distributions corresponding to laminar and turbulent separation: $P_{trans}(x) = \frac{1}{2} P_{lam}(x) + \frac{1}{2} P_{turb}(x)$. A weighted average can be used if the location of transition is known accurately, but at best the procedure results only in an engineering estimate for the interaction pressure distribution.

DOWNSTREAM OF THE ORIFICE

(U) The interaction pressures downstream of the orifice characteristically have a low pressure region followed by a pressure rise to the reattachment value (Fig. 1). At reattachment, the pressure can be either larger or smaller than the undisturbed stream pressure; downstream of reattachment, the pressure approaches its undisturbed value asymptotically.

(U) The downstream pressure distributions have frequently been compared with those behind rearward facing steps, and various base flow analyses have been used in estimating the pressure distributions (cf. Refs. 3 and 8). It is difficult, however, to determine the proper start conditions for the base flow analyses. The jet flow passes through a normal shock and is subsonic as it starts to expand downstream. There are large gradients in the flow, and there are no detailed flow field measurements in this region to guide the selection of the proper jet flow conditions to use as initial conditions in the base flow analyses.

(U) Alternatively, a purely empirical approach can be followed for estimating the downstream pressures. Although downstream pressure data have recently been obtained by many investigators for a wide range of flow conditions, inconsistencies have been observed among the various sets of data as well as disagreement on some aspects of the downstream pressure distributions. (The various trends that have been observed are described in Ref. 3.) The method presented here was developed from many sets of data and gives fair over-all agreement with experimental pressure distributions for many different test facilities and a wide range of flow conditions.

(U) As observed by Volz and Werle (Ref. 19), for example, immediately downstream of the orifice there is an "S"-shaped pressure rise starting from a value of about $\frac{1}{2} p_1$. The method suggested here for estimating the first part of the downstream pressure distribution is simply to fair an "S"-shaped curve from $p = \frac{1}{2} p_1$ at $x = 0$ to $p = p_r$ at x_r . The "reattachment" location and pressure can be estimated by using

$$x_r = 4h \quad (9)$$

and

$$p_r = \frac{p_1}{2} + \frac{1 + \bar{\chi}_L}{5} \frac{p_j + p_1}{h/d} \quad (10)$$

where $\bar{\chi}_L = M_1^3 / \sqrt{Re_L}$. These expressions are basically the same as those obtained by Barnes et al. (Ref. 8), but they have been modified to agree with experiment for a wider range of test conditions. Downstream of reattachment, the pressure can be estimated by using

$$\frac{p}{p_1} - 1 = \sqrt{\frac{x_r}{x}} \left(\frac{p_r}{p_1} - 1 \right) . \quad (11)$$

This expression indicates the correct trends in the downstream pressure distribution data for either positive or negative values of $(p_r - p_1)$. Barnes et al. observed that the pressure distributions downstream of reattachment did not scale with penetration height but were dependent on stream flow conditions. Because of the dependence of x_r on h , Eq. (11) does indicate a certain scaling of the downstream pressure distributions with penetration height. The phenomena are certainly much more complex than indicated by Eq. (11), but the expression at least indicates the correct trends and gives results in fair agreement with experimental pressure distributions, particularly if experimental values are available for x_r and p_r instead of those values calculated by using Eqs. (9) and (10).

EXPERIMENTAL COMPARISONS

(U) Sample pressure distributions calculated by using the procedure described above are compared with experimental data from various sources in Figs. 4 - 9 for a wide variety of test conditions (Mach numbers from 1.3 to 10). For turbulent separation at the lower Mach numbers (Figs. 4 and 5), the procedure described above results in pressure distributions in good agreement with experimental data obtained for end-plated jet orifices. The procedure predicts quite adequately the location of separation and pressure rise upstream of the orifice as well as the general trend of the pressures downstream.

(U) In Fig. 6, analytical results are compared with

Vol. 3

experimental pressure distributions obtained by Strike. The upstream laminar plateau pressure levels are predicted adequately but not the extent of separation. Estimating the extent of hypersonic laminar separation based on an effective step height is a formidable problem. The dividing streamline leaves the surface at a shallow angle (2 or 3 degrees), and the boundary layer is relatively thick. Another problem in predicting laminar separation for hypersonic flows is that favorable pressure gradients (due to viscous interaction or blunting) can delay the onset of separation (see e.g., Ref. 5).

(U) The free interaction lengths shown in Fig. 6 were calculated with adiabatic wall temperatures

$$\frac{T_{aw}}{T_1} = 1 + 0.17 M_1^2 . \quad (12)$$

The free interaction lengths predicted by the analysis fall short of those indicated by the experimental data (Fig. 6). This is a direct result of the predicted separation length being larger than that obtained experimentally. If the experimental locations for x_r are used, Eq. (7) accurately predicts the free interaction lengths. The analysis somewhat overestimates the pressures downstream of the orifice but predicts well the trends of the downstream pressure distributions.

(U) Analytical results are compared in Figs. 7 and 8 with experimental data obtained by Barnes et al. The data were obtained for end-plated jet orifices. For leading edge separation, the upstream load is predicted accurately except in the region immediately ahead of the origin. The extent of separated jet flow downstream of the orifice, however, is underestimated for this strong jet case. For the laminar separation cases shown, the pressure levels upstream of the orifice are predicted adequately, but the extent of upstream separation is overestimated for all except the weakest jet shown. For the weakest jet, x_r is close to the experimental value, but the predicted p_r is less than that measured by Barnes et al. For the stronger jets, the predicted x_r values are somewhat larger than those observed experimentally. For the turbulent separation data (Fig. 8), the analysis overestimates the upstream interaction load (area

under the analytical curve) and underestimates the downstream interaction load.

(U) Finally, shock tunnel data (for end-plated jet orifices) are compared with the predicted pressures in Fig. 9 (Ref. 20). In this case the calculated free interaction length [using $T_w = 6T_1$ in Eq. (7)] extends from the separation point to $x = 0$.

(U) In every case the predicted pressure distributions were calculated by using Eqs. (4)-(8) alone, with no experimental values being required. If any feature of a particular interaction is known experimentally, such as x_s or x_r , then use of these values in the remaining equations considerably improves the agreement. Particular aspects that require improvement are the location of laminar separation ahead of the orifice and a better knowledge of the downstream flow field. Nevertheless, the over-all pressure distribution can be predicted fairly well by using the method described above; and knowing the complete pressure distribution, one can calculate the moments due to the interaction as well as the augmentation ratio.

(U) The procedure requires knowledge of the particular type of upstream separation that can be anticipated. If transition occurs near the leading edge for the undisturbed boundary layer flow over the surface, then turbulent separation can be anticipated; whereas if the undisturbed boundary layer flow ahead of the orifice is entirely laminar, laminar separation should be anticipated. In those cases where transitional separation is expected, the laminar and turbulent solutions must be merged to arrive at an engineering estimate for the interaction pressure distribution.

PARAMETRIC CURVES

(U) The analytical method described above was used to obtain parametric curves showing the variation of x_s , p_p/p_1 , x_r , and p_r/p_1 with jet strength and stream Mach number. The curves were calculated for a jet orifice aspect ratio of 1000, which gave $n = 0.80$ in the penetration height equation, and for values of $d = 0.01$ and $L = 10$.

(U) The trends of the interaction parameters with jet strength, for a free stream Mach number of 4 and Reynolds

number of one million, are given in Fig. 10. Laminar separation always occurs ahead of turbulent separation, and both move forward as the jet strength increases. For jet strengths greater than about 1500 and for these flow conditions, laminar separation occurs essentially at the leading edge. The turbulent plateau pressure level remains constant with increasing jet strength until the turbulent separation point reaches the leading edge; there is no turbulent solution for stronger jets.

(U) The location of reattachment moves further downstream and the pressure ratio at reattachment increases with increasing jet strength. In agreement with the observations of Strike (Ref. 5) and Barnes et al. (Ref. 8), the reattachment pressure is greater for turbulent than for laminar separation.

(U) Variations in the interaction parameters with stream Mach number are shown in Fig. 11 for $Re_L = 10^6$ and for a jet strength of 100. The extent of laminar or turbulent separation ahead of the orifice decreases with increasing Mach number. This follows from the increase in plateau pressure ratios with increasing Mach number, which decreases p_j/p_p and thereby decreases h/d and the extent of separation.

(U) As a result of the decrease in effective penetration height, the extent of separated jet flow downstream of the orifice decreases as M_1 increases. In agreement with the observations of Spaid and Zukoski (Ref. 4), and of Strike (Ref. 5) and others, the reattachment pressure increases strongly with increasing Mach number and is larger for turbulent than for laminar upstream separation. For laminar separation, p_r does not exceed p_1 until the stream Mach number exceeds 3.

(U) The curves shown in Figs. 10 and 11 are for $d = 0.01$ and $L = 10$. The separation and reattachment locations depend on the jet strength and the width d and are not simply dependent on either d/L or $p_j d/p_1 L$ (cf. Ref. 3).

INTERACTION FORCES

(U) The additional force due to the interaction results from the increased (or decreased) surface pressures both ahead of and behind the jet orifice. For a particular design and jet strength, the interaction force can be calculated simply by integrating the overpressures on the surface.

FORCE COEFFICIENT

(U) The upstream contribution to the interaction force can be readily calculated by integrating the overpressures on the surface ahead of the jet orifice. Thus the upstream interaction force coefficient can be defined as

$$(C_N)_{\text{upstr}} = \int_{\text{LE}}^0 [(p - p_1)/q_1 d] dx \quad (13)$$

where q_1 is the undisturbed stream flow dynamic pressure, and the jet nozzle throat width is used for the reference area (per unit span). By using d as the reference area, interaction force coefficients obtained from many different experimental programs can be compared directly, independent of the various upstream surface lengths. Because of the smallness of d , however, the values of C_N appear quite large compared with other interaction force coefficients, as indicated by the following relationship for the one used by Sterrett et al. (Ref. 21): $C_{N,A} = (d/L)C_N$.

(U) The general applicability of the proposed method for calculating the interaction pressure distribution can be assessed further by comparing calculated values of the upstream force coefficient with experimental results. Although the analytical method is based on empirical relations for the effective penetration height and plateau pressure level, the data used in obtaining these relations are different from the force coefficient data shown in Fig. 12 (Ref. 3). For each test, the free stream conditions (M_1 and Re_L), jet strength (p_j/p_1), and jet orifice aspect ratio are known. These are used to predict the overpressures and upstream force coefficient [Eq. (13)] that result

from the interaction. The experimental force coefficient values shown in Fig. 12 were obtained from many different sources and include direct force measurements as well as integrated centerline pressure distributions. As indicated by the dashed lines in Fig. 12, most of the calculated values are within 20 percent of the experimental values for a wide range of test conditions.

(U) The contribution of the downstream overpressures to the interaction force can be particularly large at hypersonic speeds and can exceed that due to the upstream overpressures, this depending on flow conditions and the length of the surface behind the orifice. Representing the "S"-shaped portion of the downstream pressure distribution with a curve $\sim (1 - \cos \pi x/x_r)$ and using Eq. (11) for $x > x_r$, we have the downstream interaction force coefficient

$$(C_N)_{dnstr} = \int_0^{TE} [(p - p_1)/q_1 d] dx$$

$$= \frac{(5p_1 - 6p_r)x_r + 8(p_r - p_1) \sqrt{x_r x_{TE}}}{4q_1 d} \quad (14)$$

for plates sufficiently long so that reattachment occurs before the trailing edge ($x_r < x_{TE}$). As an example of the possible importance of these downstream overpressures, consider a jet orifice located at mid-chord ($x_{TE} = L$) with an orifice aspect ratio of 1000 ($n = 0.80$). For the same conditions as shown in Figs. 10 and 11 ($d = 0.01$, $L = 10$, $M_1 = 4$, $Re_L = 10^6$ and $p_j/p_1 = 100$), Eqs. (13) and (14) indicate $(C_N)_{dnstr} = 1.22(C_N)_{upstr}$ for laminar separation and $(C_N)_{dnstr} = 2.45(C_N)_{upstr}$ for turbulent separation.

AMPLIFICATION FACTOR

(U) The amplification factor K , defined as (interaction force + reaction force)/(reaction force), is frequently used as a measure of the total efficiency of a transverse jet control (Ref. 1). The reaction force for a sonic air jet exhausting into a pure vacuum is (Ref. 3): $1.268 p_j d$ (the orifice area per unit span is d). Using this, we can

write the amplification factor as

$$K = 1 + \frac{C_N q_1 d}{1.268 p_j d} \quad (15)$$

$$= 1 + 0.552 M_1^2 C_N / (p_j / p_1)$$

Values of K calculated for laminar and turbulent upstream separation for $Re_L = 10^6$ and $M_1 = 4$ are plotted in Fig. 13 versus jet strength for an aspect ratio 1000 jet orifice ($n = 0.80$) located at the trailing edge ($x_{TE} = 0$), with $d = 0.01$ and $L = 10$. The amplification factors for this trailing edge jet case result from the increased pressures upstream of the jet only, and can be referred to as upstream amplification factors. As shown in Fig. 13, the upstream amplification factor is larger for laminar than for turbulent separation and is particularly large for the weaker jets (smaller p_j / p_1 values). In this sense, as many investigators have observed, the weaker jets are more efficient. Design requirements for a certain minimum total force can, however, limit the minimum jet strength value.

(U) Mach number effects on the upstream amplification factors calculated for $Re_L = 10^6$ and $p_j = 100 p_1$ are indicated in Fig. 14 for an aspect ratio 1000 jet orifice with $d = 0.01$ and $L = 10$. The laminar amplification factors depend more strongly on M_1 than the turbulent ones, but both increase with increasing Mach number.

(U) The curves shown in Figs. 13 and 14 are for a trailing edge jet with a particular aspect ratio and d/L and Re_L values. Somewhat larger upstream amplification factors result for end-plated jet orifices (larger value of n). The laminar amplification factors depend also on Reynolds number and the d/L ratio, increasing with increasing values of Re_L and decreasing values of d/L (Ref. 3).

(U) For turbulent separation ahead of trailing edge jets, the present analysis gives

$$K_{turb}^{upstr} = 1 + \frac{0.94}{\tan \alpha} \frac{\xi - 1}{\xi^n} \left[\frac{p_j}{p_1} \right]^{-(1-n)} \quad (16)$$

Vol. 3

where ξ and $\tan \alpha$ are given by Eqs. (8) and (3), respectively. For turbulent separation, ξ is a function only of M_1 and therefore $\tan \alpha$ is a function only of M_1 . Thus for a given jet aspect ratio, the upstream amplification factor for turbulent separation is a function only of M_1 and the jet strength and can be presented by parametric curves such as those given in Fig. 15 for jets with end plates ($n = 0.85$). Generally, for turbulent boundary layer separation, the upstream amplification factor decreases toward unity with decreasing Mach number, increasing jet strength, and decreasing jet orifice aspect ratio (smaller values of n). These trends, as well as the magnitude of the amplification factors, are similar to those observed experimentally (Ref. 3).

(U) If one uses the supersonic linear relationship $(p_p - p_1)/q_1 = 2 \tan \alpha / \sqrt{M_1^2 - 1}$ and sets $n = 1$, Eq. (15) reduces exactly to Werle's expression for turbulent amplification factors for strong jets (Ref. 6). The resulting expression is independent, however, of jet strength and is valid only for very strong jets ($p_j/p_1 \gg 1$) in supersonic streams.

(U) Although the upstream amplification factor is greater for laminar separation than for turbulent, the downstream interaction load is greater for turbulent separation, and, as shown by the example case following Eq. (14), the downstream load can be predominant at very high speeds. Thus the entire interaction pressure distribution should be considered in designing a particular transverse jet application.

CONCLUSIONS

(U) Several factors strongly affect the interaction between transverse jets and high speed stream flows: the stream Mach and Reynolds numbers, the character of the boundary layer upstream of the jet orifice, and the jet strength and geometry. The interaction can result in increased surface pressures both upstream and downstream of slit-type jet orifices. Because of the strong interplay among the many factors influencing the interaction, it is

unreasonable to expect simple force correlations to be universally valid. It appears to be necessary to consider each particular design separately and to estimate first the changes in the pressure distribution resulting from the interaction, after which the overpressures can be integrated to obtain a reliable estimate of the interaction force and its distribution.

(U) Interaction pressure distributions on the surface upstream of the jet are similar to those ahead of forward facing steps. Using extensive experimental results from many sources, we find that the effective jet penetration height data correlate well with $(p_j/p_p)^n$, where p_j is the total pressure of the jet flow and p_p is the pressure in the separated flow region immediately ahead of the jet. The exponent n varies from 0.70, for low aspect ratio jet orifices, to 0.85, for jet flows with end plates or very high aspect ratio orifices.

(U) The penetration height equation is solved simultaneously with well verified relations for the plateau pressures p_p in laminar or turbulent separated flow regions. The remaining features of the interaction pressure distributions can then be determined directly. Upstream pressure distributions and interaction forces can be estimated fairly reliably by using the analysis described herein. The downstream pressure distributions can be estimated only qualitatively; more thorough knowledge of the jet flow field is required before theoretical analysis can be applied to develop more reliable methods for predicting pressure distributions downstream of the jet orifice. Nevertheless, the interaction force downstream of the orifice can exceed that upstream; the downstream pressure distribution should certainly be considered and accounted for in any particular design.

(U) The method presented herein can be used to determine the effects of the various parameters influencing the interaction and to determine their effects on the amplification factor. Limited experimental data indicate that some results of the two dimensional method can be applied to jets issuing from slit-type orifices in axisymmetric bodies.

8th Navy Symposium on Aeroballistics

Vol. 3

REFERENCES

1. Nunn, R. H. and Ulrich, R. D., Jet Reaction Controls for Atmospheric Flight - A Review and Summary of the Literature (U), Naval Weapons Center, China Lake, Calif., NWC, February 1969. (NWC TP 4559, publication CONFIDENTIAL.)
2. Swanson, R. S., Parametric and Preliminary Design Comparison of Transverse Jet Controls and Flap-Type Aerodynamic Controls for Re-Entry Vehicles and High Speed Cruise Aircraft (U), AFFDL TR 68-98, December 1968.
3. Kaufman, L. G. II and Koch, F. II, High Speed Flows past Transverse Jets (U), Grumman Research Department Report RE-348, October 1968.
4. Spaid, F. W. and Zukoski, E. E., "A Study of the Interaction of Gaseous Jets from Transverse Slots with Supersonic External Flows," AIAA Journal, Vol. 6, No. 2, February 1968, pp. 205-212.
5. Strike, W. T. Jr., Analysis of the Aerodynamic Disturbances Generated on a Flat Plate Containing Lateral Jet Nozzles Located in a Hypersonic Stream (U), AEDC-TR-67-158, January 1968.
6. Werle, M. J., "A Critical Review of Analytical Methods for Estimating Control Forces Produced by Secondary Injection (U)," NOLTR 68-5, January 1968
7. Allan, W. L., "An Experimental Investigation of the Aerodynamic Force Characteristics of a Jet Issuing Transverse to a Wedge (U)," Jet Propulsion Center, Purdue University Report F-68-1, January 1968.
8. Barnes, J. W., Davis, J. G., and Tang, H. H., Control Effectiveness of Transverse Jets Interaction with a High-Speed Free Stream (U), AF FDL TR 67-90, September 1967.
9. Phinney, R. E., Werle, M. J., Knott, J., and Volz, W. C., "Slot Jet Interaction Studies of an Ogive Cylinder at $M_\infty = 4$ and 5 (U)," NOLTR 68-143, September 1968.

10. Zakkay, V., Erdos, J., and Calarese, W., "An Investigation of Three-Dimensional Jet Control Interaction on a Conical Body (U)," AGARD Conference on Hypersonic Boundary Layers and Flow Fields, AGARD CP No. 30, May 1968.
11. Sterrett, J. R. and Barber, J. B., "A Theoretical and Experimental Investigation of Secondary Jets in a Mach 6 Free Stream with Emphasis on the Structure of the Jet and Separation Ahead of the Jet (U)," Separated Flows Specialists Meeting Fluid Dynamics Panel, AGARD, May 1966
12. Schetz, J. A., Weinraub, R. A., and Mahaffey, R. E. Jr., "Supersonic Transverse Injection into a Supersonic Stream," AIAA Journal, Vol. 6, No. 5, May 1968, pp. 933-934.
13. Sheeran, W. J. and Dosanjh, D. S., Investigation of Interacting Jet Flows -- Part II (U), Syracuse University Research Institute Report Number ME 1058-6608 F, August 1966.
14. Spaid, F. W. and Zukoski, E. E., A Study of the Interaction of Gaseous Jets from Transverse Slots with Supersonic External Flows (U), Douglas Paper No. 4480, April 1967.
15. Chapman, D. R., Kuehn, D. M., and Larson, H. K., Investigation of Separated Flows in Supersonic and Subsonic Streams with Emphasis on the Effect of Transition (U), NACA Report 1356, 1958.
16. Hill, W. G., Jr., Analysis of Experiments on Hypersonic Flow Separation ahead of Flaps Using a Simple Flow Model (U), Grumman Research Department Memorandum RM-383, November 1967.
17. Lewis, J. E., Kubota, T., and Lees, L., "Experimental Investigation of Supersonic Laminar, Two-Dimensional Boundary Layer Separation in a Compression Corner with and without Cooling," AIAA Journal, Vol. 6, No. 1, January 1968, pp. 7-14.
18. Sterrett, J. R. and Emery, J. C., Extension of Boundary-Layer-Separation Criteria to a Mach Number of 6.5 by Utilizing Flat Plates with Forward-Facing Steps (U), NASA TN D-618, December 1960.

8th Navy Symposium on Aeroballistics

Vol. 3

19. Volz, W. C. and Werle, M. J., "Jet Interaction Studies," Paper No. 40, Proceedings of the 7th U.S. Navy Symposium on Aeroballistics (U), Pt. Mugu, Calif., June 1966.
20. Kaufman, L. G. II, "Hypersonic Flows Past Transverse Jets," Journal Spacecraft, Vol. 4, No. 9, September 1967, pp. 1230-1235.
21. Sterrett, J. R., Barber, J. B., and Alston, D. W., Experimental Investigation of Secondary Jets from Two-Dimensional Nozzles with Various Exit Mach Numbers for Hypersonic Control Application (U), NASA TN D-3795, January 1967.

1. Separation Shock
2. Dividing Streamline
3. Interaction Shock
4. Strong Shock in Jet Flow
5. Reattachment Shock

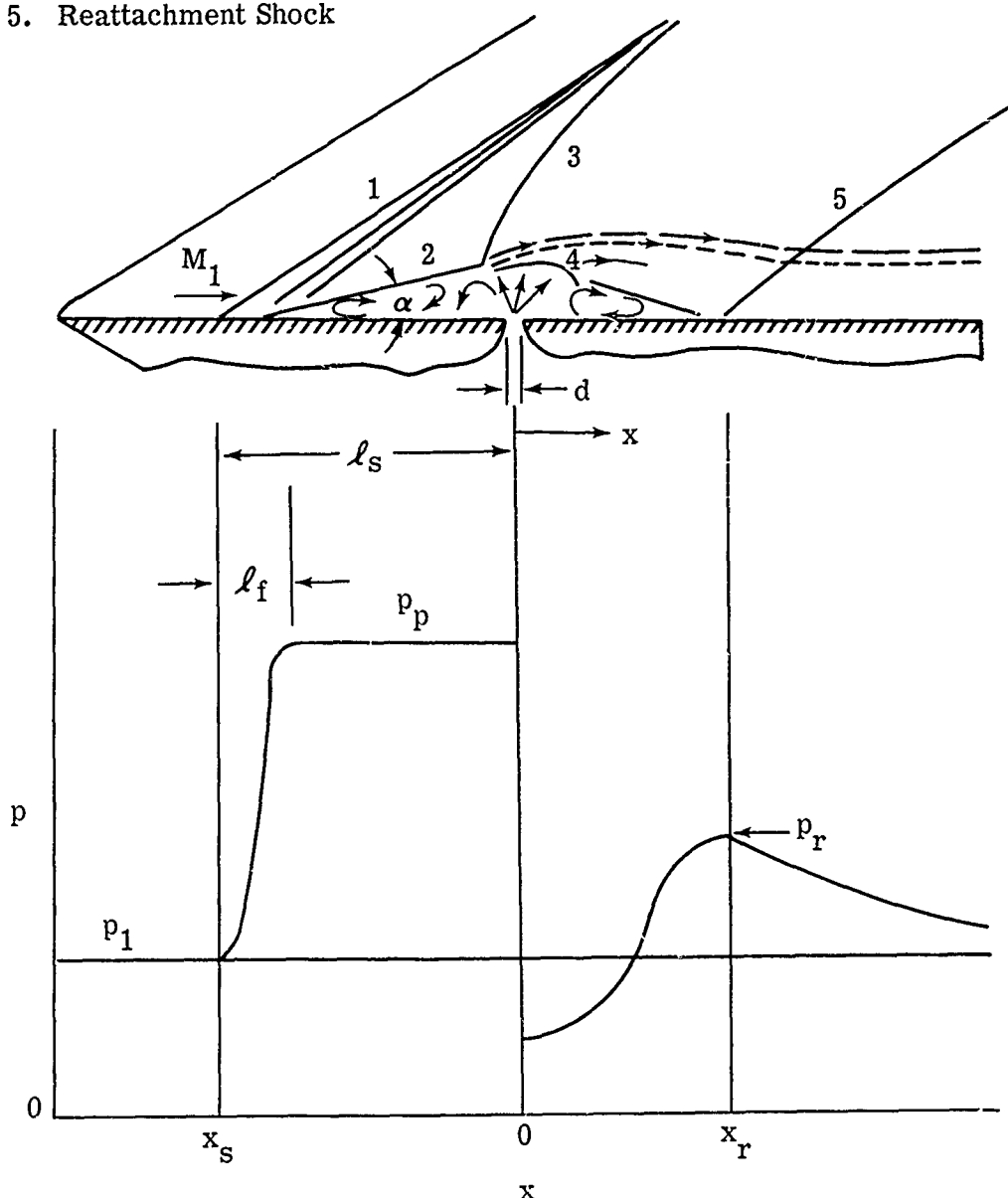


Fig. 1 Sketch of Flow Model and Corresponding Pressure Distribution for Laminar Separation

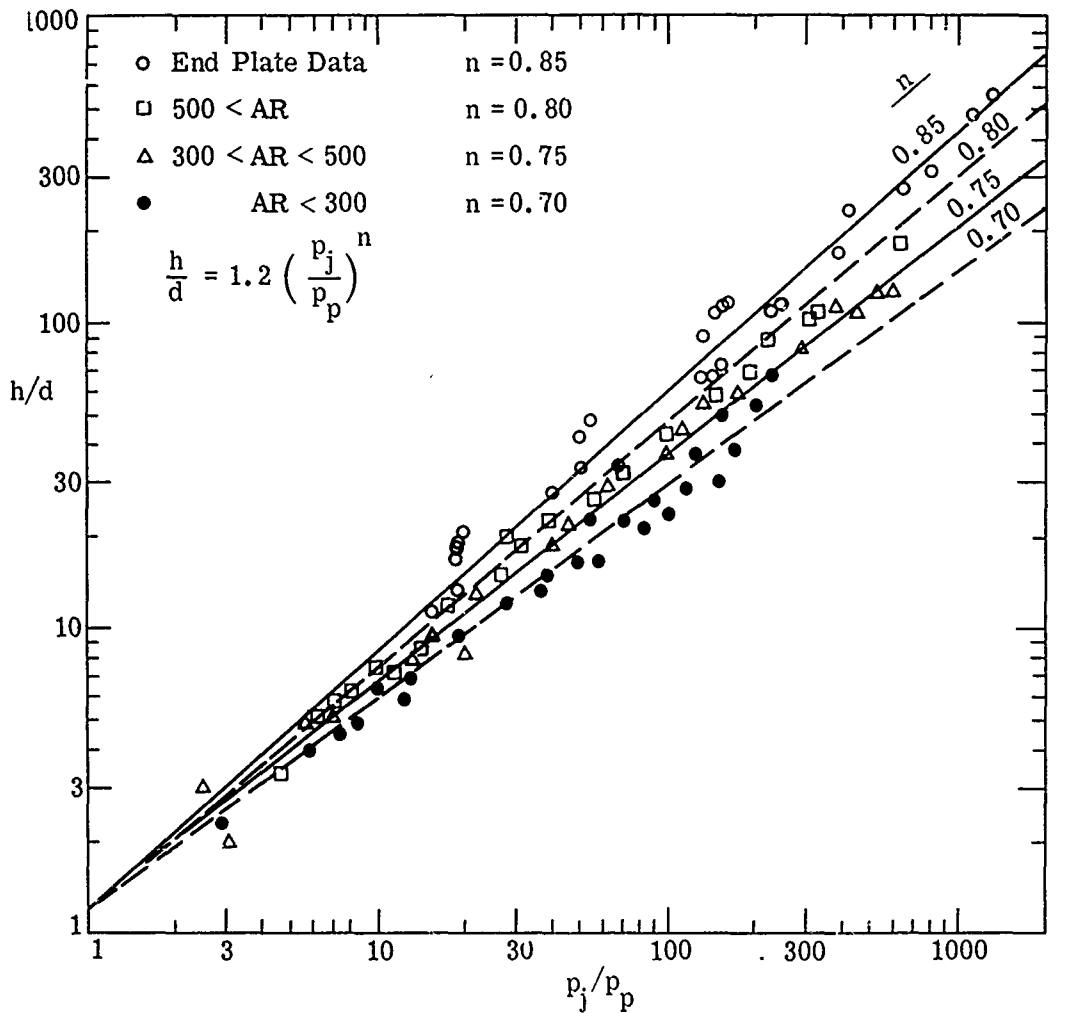


Fig. 2 Correlations of Effective Jet Penetration Heights

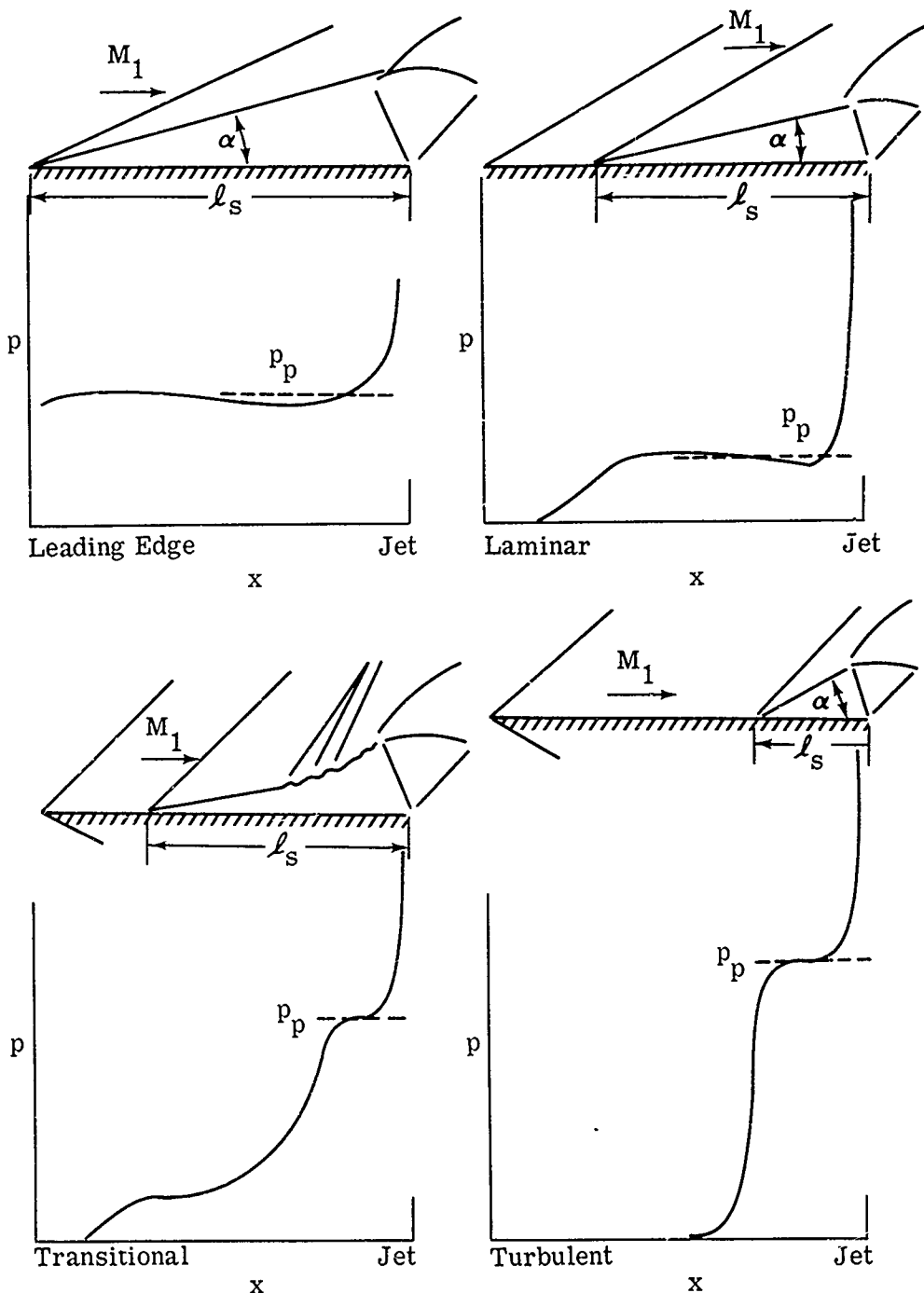


Fig. 3 Sketches of Different Types of Flow Separation ahead of Jet and Representative Upstream Pressure Distributions

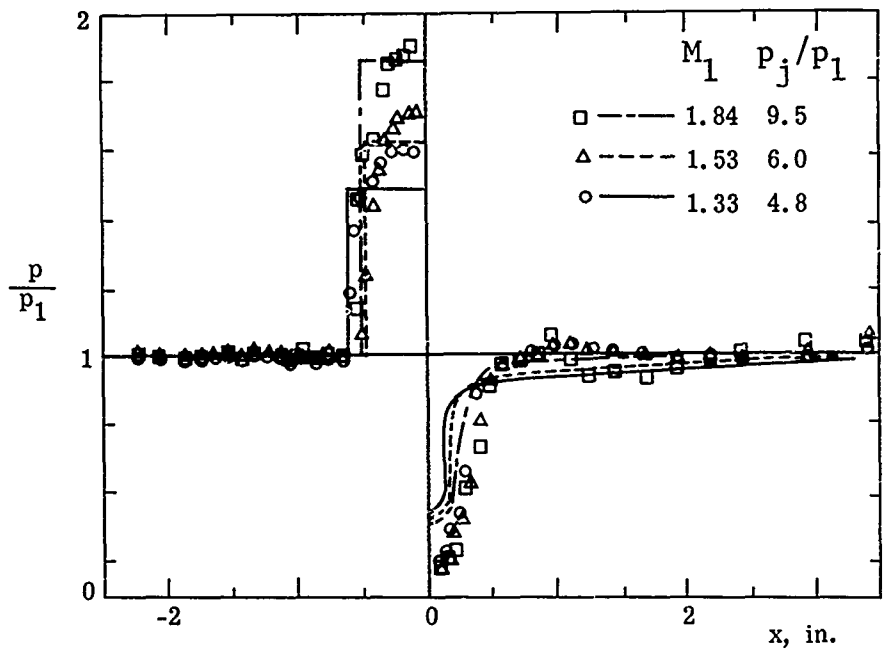


Fig. 4 Comparison of Turbulent Separation Pressure Distributions with Data from Ref 7 for $L = 3.1$ in. and $d = 0.024$ in.

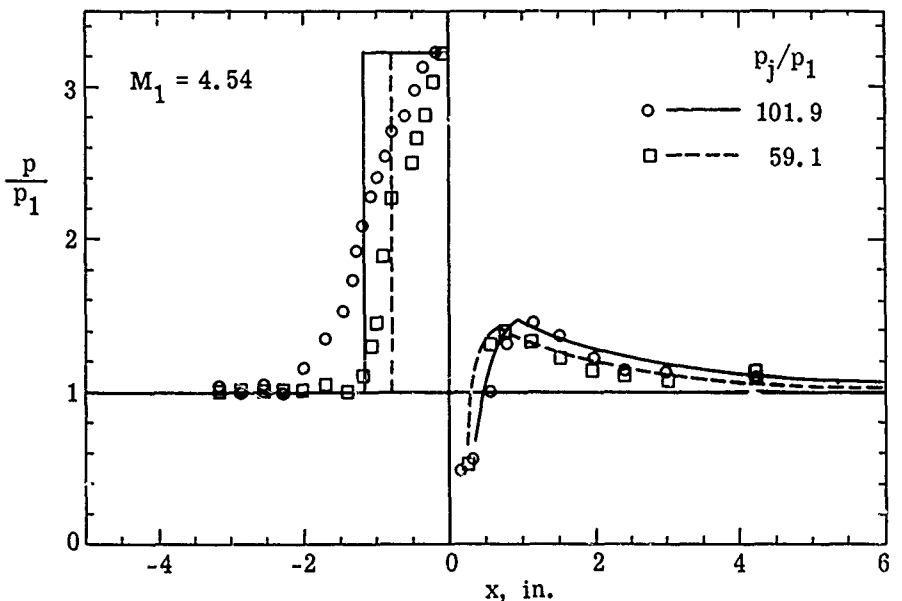


Fig. 5 Comparison of Turbulent Separation Pressure Distributions with Data from Ref 4 for $L = 9.0$ in. and $d = 0.0105$ in.

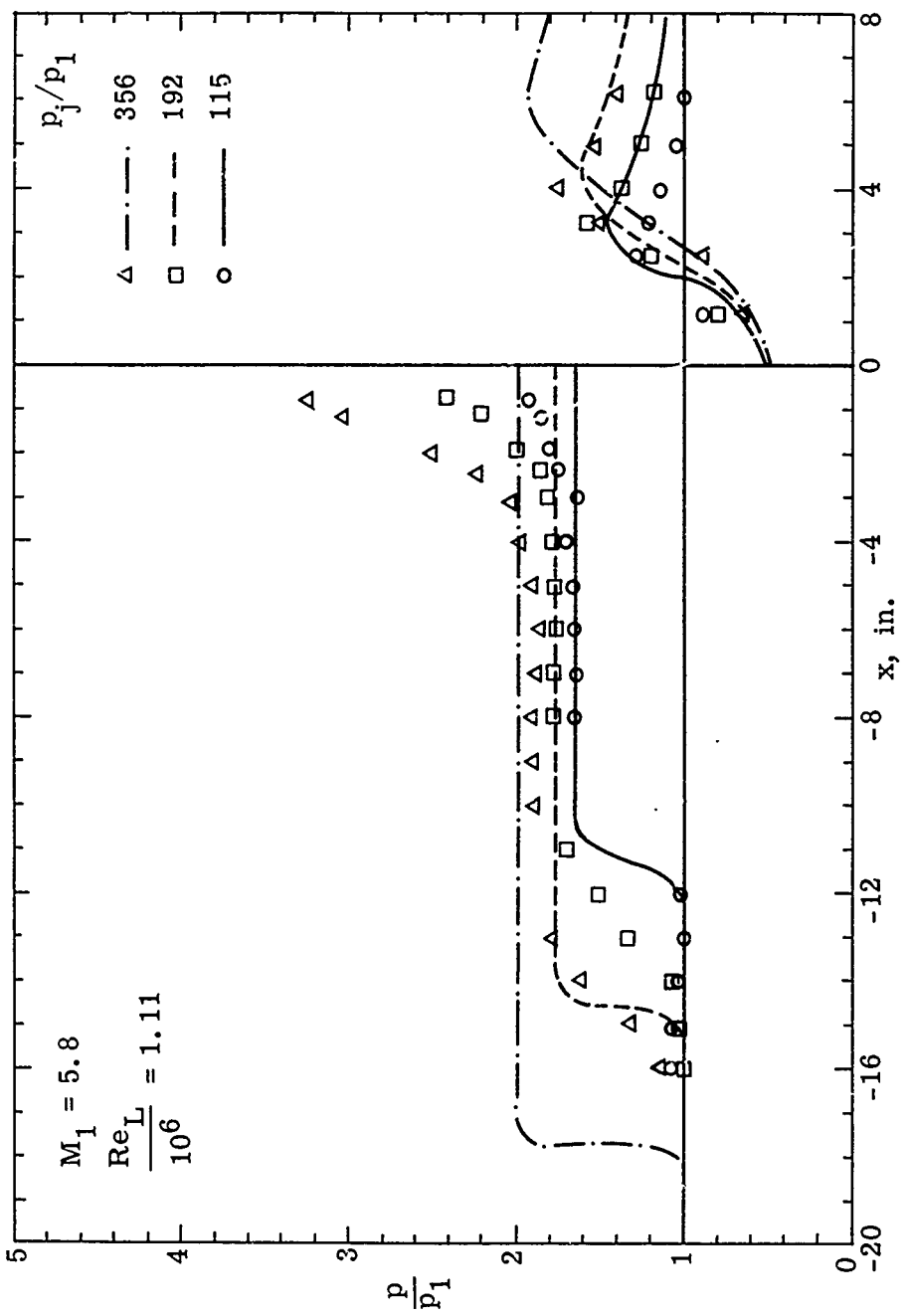


Fig. 6 Comparison of Laminar Separation Distributions with Data from Ref. 5 for $L = 19.86$ in. and $d = 0.028$ in.
Jet AR = 321.4 (No End Plates)

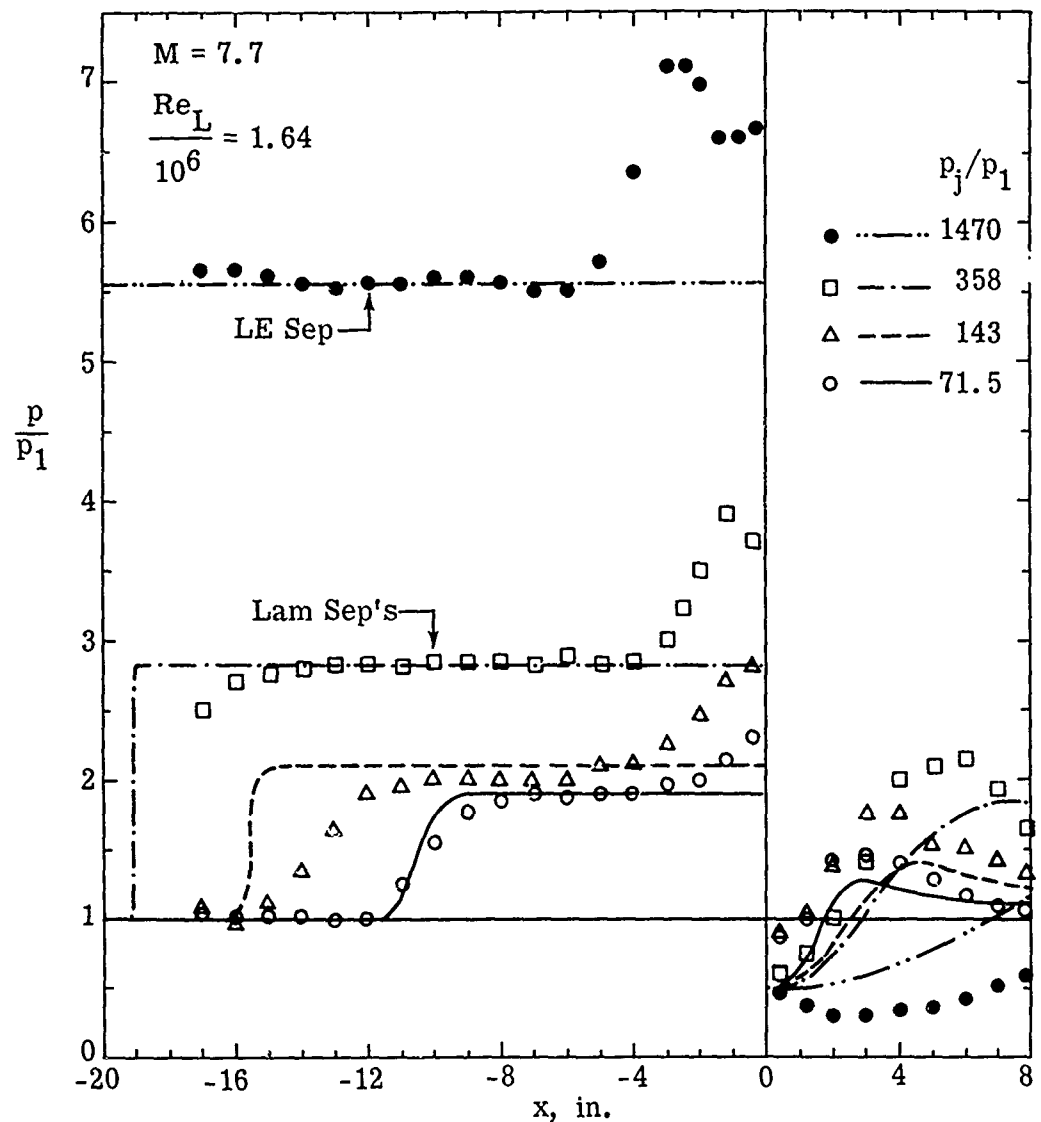


Fig. 7 Comparison of LE and Laminar Separation Distributions with Data from Ref 8 for $L = 19.86$ in. and $d = 0.028$ in.

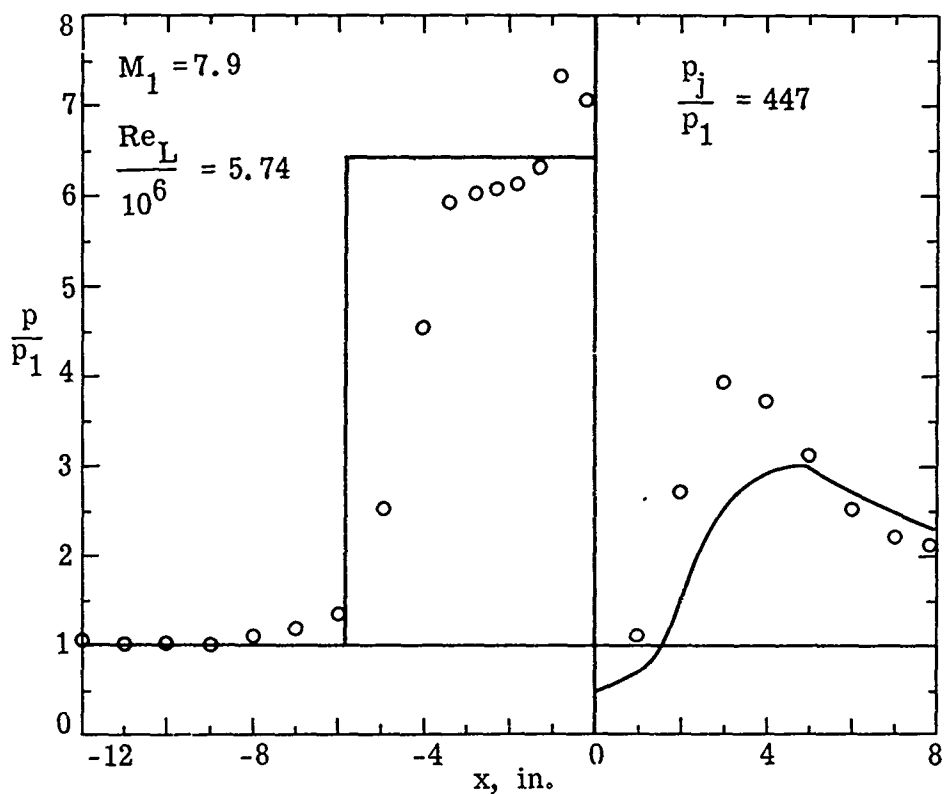


Fig. 8 Comparison of Turbulent Separation Pressure Distribution with Data from Ref 8 for $L = 19.86$ in. and $d = 0.028$ in.

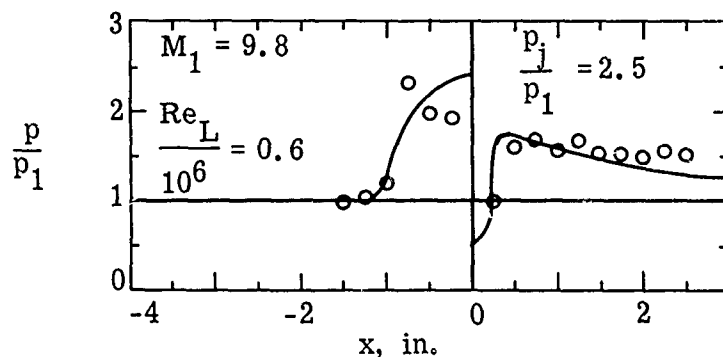


Fig. 9 Comparison of Laminar Separation Pressure Distribution with Data from Ref 20 for $L = 6.5$ in. and $d = 0.035$ in.

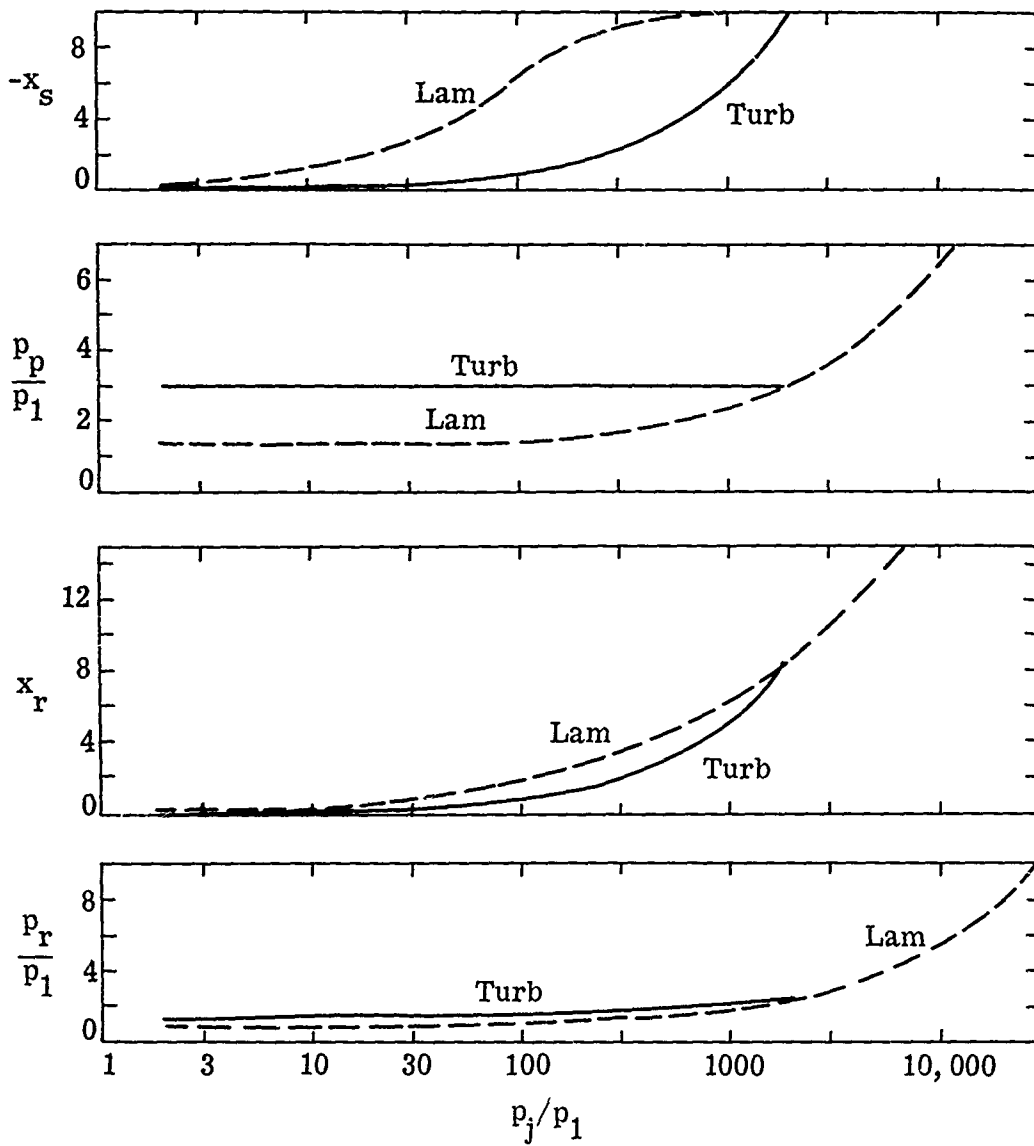


Fig. 10 Variation of Interaction Parameters with Jet Strength,
for $Re_L = 10^6$ and $M_1 = 4$

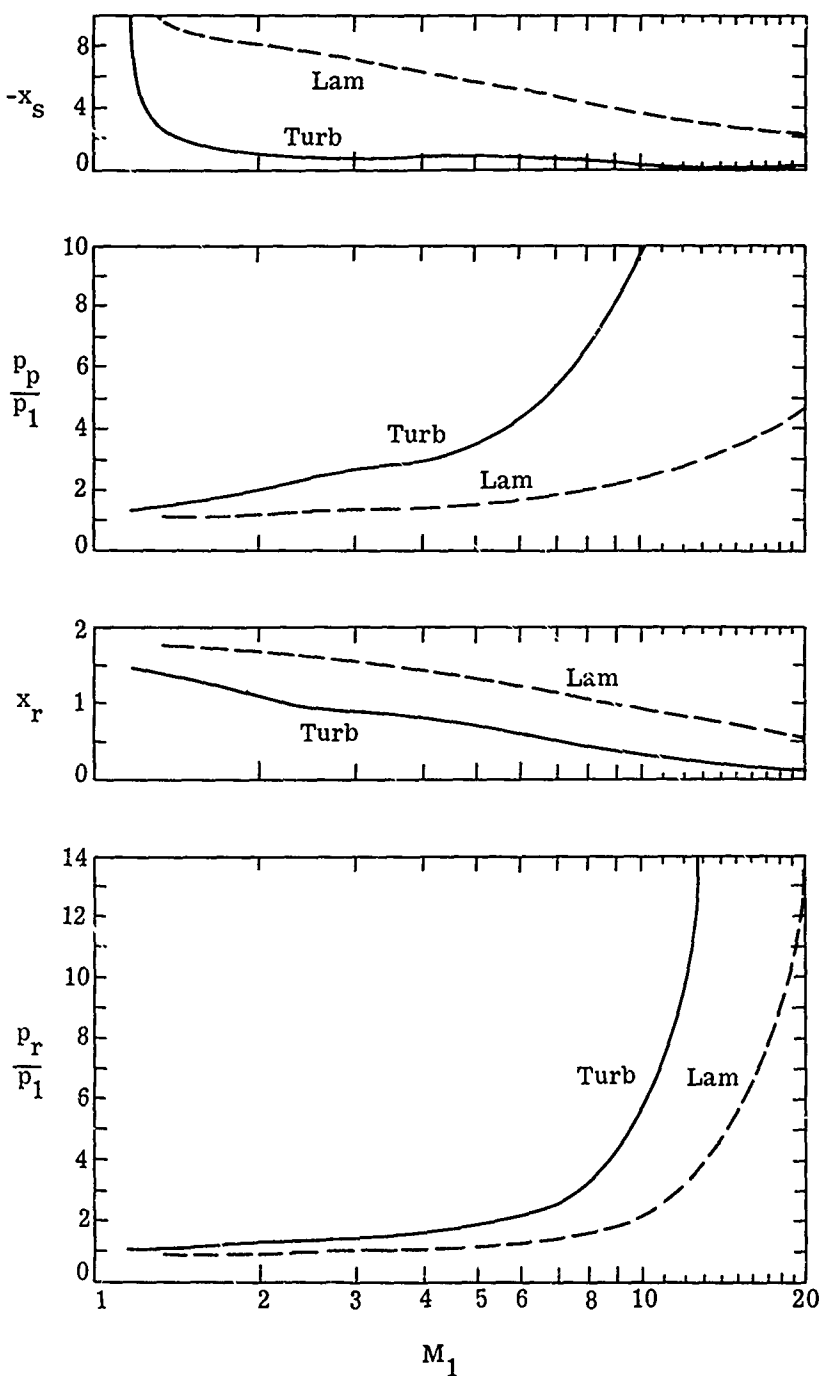


Fig. 11 Variation of Interaction Parameters with M_1 , for $Re_L = 10^6$
and $p_j/p_1 = 100$

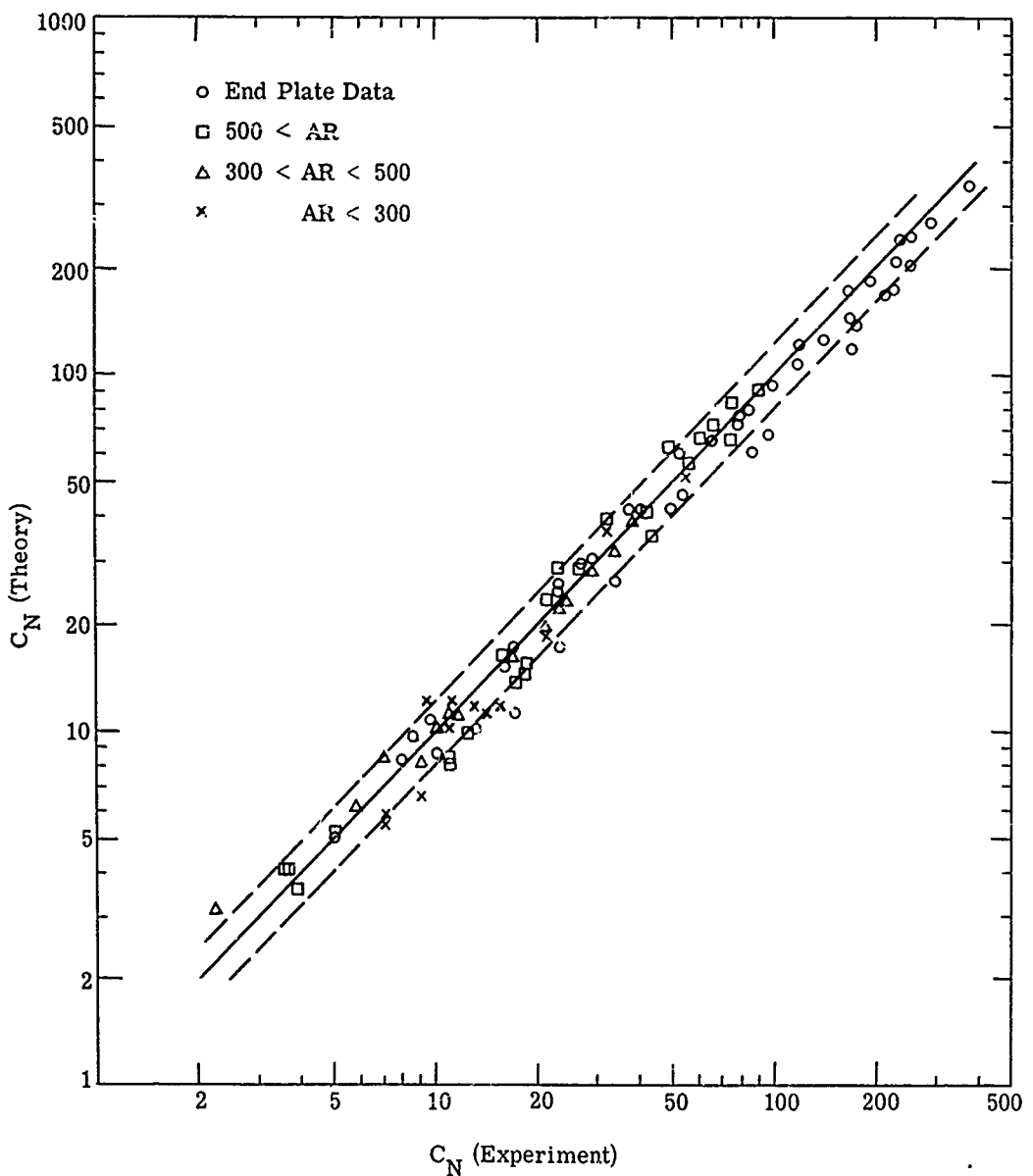


Fig. 12 Comparison of Calculated Upstream Force Coefficient with Data

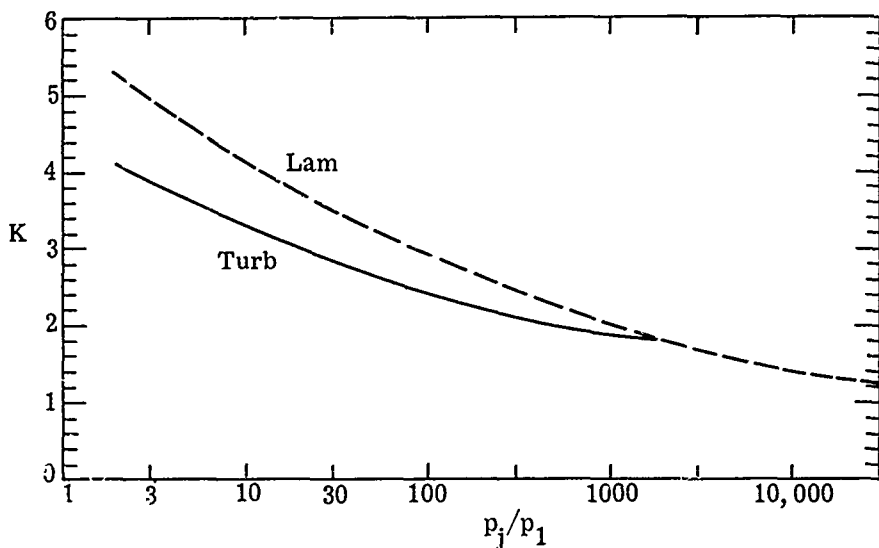


Fig. 13 Variation of Upstream Amplification Factor with Jet Strength,
for $Re_L = 10^6$ and $M_1 = 4$

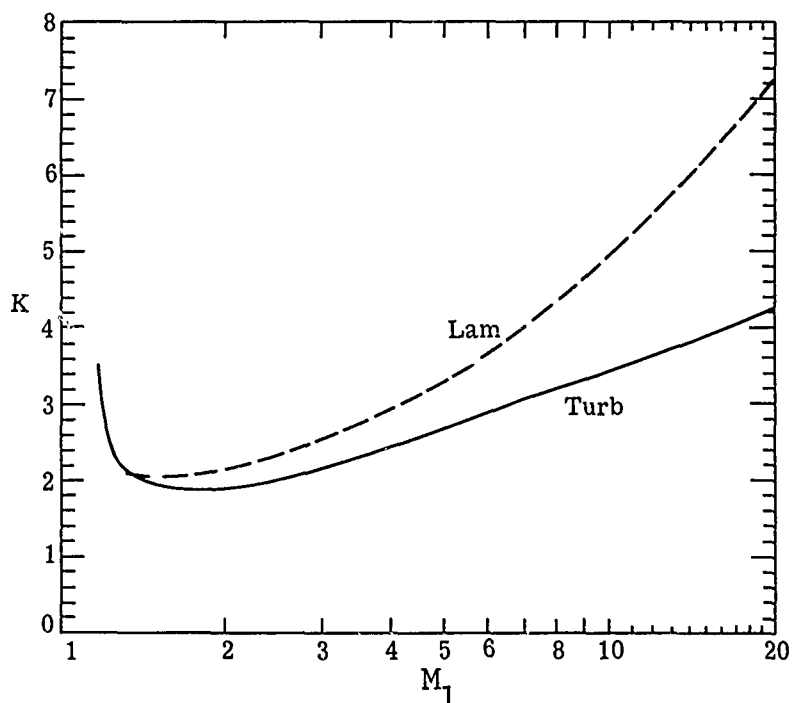


Fig. 14 Variation of Upstream Amplification Factor with Mach
Number, for $Re_L = 10^6$ and $p_j/p_1 = 100$

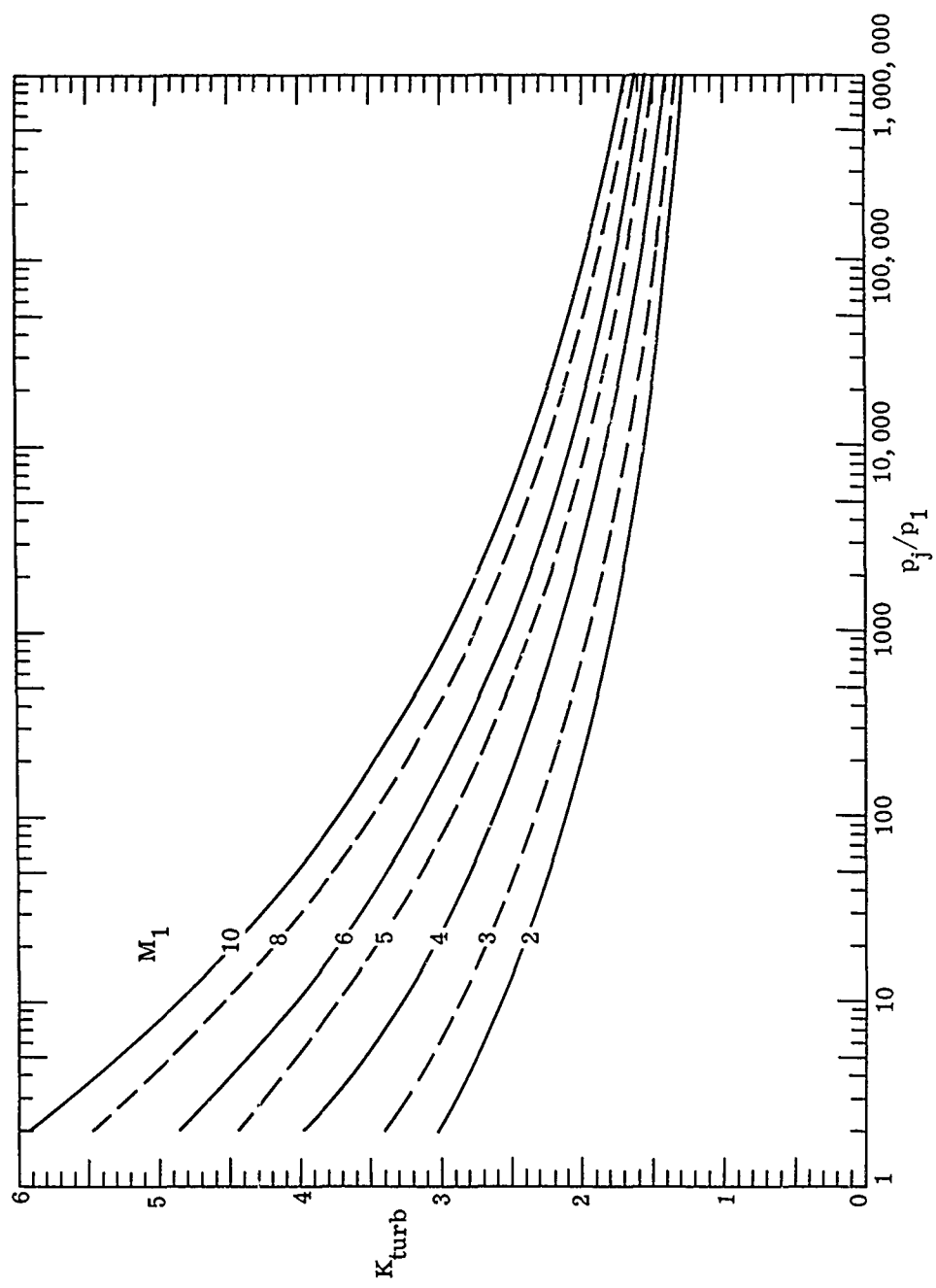


Fig. 15 Upstream Amplification Factors for Turbulent Separation ahead of Jets with End Plates

Paper No. 36

AERODYNAMIC AND HEAT TRANSFER EFFECTS
OF SATURN V PLUME-INDUCED FLOW SEPARATION

(U)

(Paper UNCLASSIFIED)

by

Calvin L. Wilkinson
The Boeing Company
New Orleans, La. 70100

ABSTRACT. (U) Saturn V photographic coverage and on-board instrumentation have provided information concerning the plume-induced flow separation (PIFS) phenomenon not previously available. Attempts to correlate the extent of PIFS on the Saturn V with data from flight and wind tunnel testing has shown that vehicle geometry significantly influences PIFS. Although the Saturn V has not been adversely affected, aerodynamic stability is reduced by PIFS as a result of shifting the center of pressure forward and non-linearizing aerodynamic coefficients. Flow separation usually results in a reduction in surface heating rates. Due to recirculated exhaust gases being drawn into the PIFS region on the Saturn V, surface heating rates are significantly increased. Methods for analytically predicting the occurrence and the effects of PIFS are not currently available and are needed.

INTRODUCTION

(U) When the ratio of engine exit plane static pressure to ambient static pressure is sufficiently large the exhaust gases will expand to form a plume whose dimensions are many times that of the vehicle itself. The presence of large exhaust plumes, which are likely to exist on aircraft (Ref. 1), missiles (Refs. 2,3,4), and launch vehicles (Ref. 5) operating at high altitudes, can result in flow separation which significantly affects aerodynamic stability and heat transfer. Flow separation resulting from the interaction of the exhaust plume and the free stream air is called plume-induced flow separation (PIFS).

(U) The Saturn V vehicle has experienced extensive flow separation and has provided a wealth of information of PIFS previously not available. This paper presents the current findings of a continuing study of PIFS on the Saturn V by The Boeing Company Launch Systems Branch.

(U) At the time this paper was written data from three Saturn V flights were available; denoted sequentially as AS-501, AS-502, and AS-503.

EXHAUST RECIRCULATION

(U) With a multi-engine configuration, engine exhaust plume expansion results in interaction between the plumes as shown by Figure 1a. Plume interaction creates shock patterns and attendant pressure gradients which the low-energy flow in plume boundaries cannot negotiate with the result that these low-energy gases turn and flow in the opposite direction and then outboard between the engines as shown by Figures 1b and 1c.

PLUME-INDUCED FLOW SEPARATION

(U) When exhaust plumes have assumed the shape dictated by engine exit plane and free stream conditions, the external flow field is affected as if the plumes were solid bodies attached to the base of the vehicle. As plume expansion continues, a point is reached when the momentum in the boundary layer is insufficient to overcome the adverse pressure gradient that exists forward of the plume-body intersection. Then, as shown by Figure 1d, separation occurs. This phenomenon is known as plume-induced flow separation; hereafter referred to as PIFS.

(U) As illustrated by Figure 1d, the combined effects of flow separation and exhaust recirculation cause engine exhaust products (usually fuel rich) to move forward from the plume interaction point to the base of the vehicle, outboard between the engines, forward along the vehicle surface to the separation point, and then outboard and aft. Continued plume expansion increases the strength of the adverse pressure gradient and causes the point where flow separation first occurs to move upstream.

(U) As shown by Figure 2, this flow separation phenomenon (PIFS) is similar in character to that which occurs upstream of a forward facing step or ramp or, more directly, over cylindrical bodies with conical tail flares (Refs. 6,7,8).

(U) PIFS has been detected during wind tunnel (Refs. 2,3,4,9,10) and flight (Refs. 2 thru 5) testing and has been treated analytically briefly but an exhaustive investigation of the subject remains to be done.

VISUAL FLIGHT OBSERVATIONS

(U) An examination of the 70mm movie film of the Saturn V flights taken from numerous ground stations and a Boeing C-135 aircraft revealed that, during the last one-third of first stage (S-IC) boost, PIFS occurs and envelopes as much as the aft one-half of the 365 ft. long vehicle at first stage separation. Selected frames from the AS-502 film taken from the C-135 aircraft are shown in Figures 3 through 7.

(U) As mentioned previously, most of the gases in the PIFS region emanate from the base region of the vehicle and are fuel-rich engine exhaust products. It is this fact that makes the PIFS region visible because of burning in the outer boundary of the region at lower altitudes or shielding from view the portion of the vehicle immersed in the region at higher altitudes (where combustion cannot be supported).

(U) In Figure 3 the vehicle is at an altitude of 97,269 feet and a Mach number of 3.68. Flow separation has reached a point 37.3 feet or 1.13 vehicle diameters (one diameter = 33 feet) forward of the exit plane. The fins at the base of the S-IC are almost completely immersed in the PIFS region. Combustion of the exhaust products is easily supported by oxygen from the free stream air. Figure 4 shows the vehicle at an altitude of 119,110 feet and a Mach number of 4.42. The flow separation point is now 2.69 diameters forward of the exit plane. Note that the extent of flow separation is greater on the lower side of the vehicle. This non-symmetry in the separated region will be discussed later. The plume has darkened considerably indicating that free stream oxygen is becoming less plentiful. Figure 5 shows the vehicle at an altitude of 143,396 feet and a Mach number of 5.18. The flow separation point has moved to 3.96 diameters forward of the exit plane. The

Vol. 3

darkened region that has become increasingly evident in the lower portion of the plume is thought to be exhaust products issuing outboard and aft from under the engine fairing in this area. Just above this dark area on the plume centerline is a bright area thought to be recirculated exhaust gases coming from between the fairings, part of which is drawn into the PIFS region. Figure 6 shows the vehicle at an altitude of 170,278 feet and a Mach number of 6.28. The PIFS region envelopes almost the entire first stage (S-IC); extending to a point 4.90 diameters forward of the exit plane. The plume is almost completely dark now and the gases in the separated region are no longer burning but block the immersed portion of the vehicle from view. The burning that is present is aft of the heat shield and is the combustion of recirculated gases flowing outboard between the fairings. In Figure 7 the vehicle is at an altitude of 193,809 feet and a Mach number of 7.48. The separated region extends 5.34 diameters forward of the exit plane onto the lower portion of the second stage (S-II). The center engine was cutoff about three seconds prior to the time this photograph was taken. The apparent increase in the amount of burning in the PIFS region and the plume is attributed to additional oxygen from boiloff of LOX in the center engine. First stage separation occurred shortly after this photograph was taken.

(U) The Saturn V flights, because of the vehicle size and the excellent photographic coverage, mark the first time it has been possible to visually observe flow separation taking place in flight and correlate these observations with on-board instrumentation and flight and wind tunnel results from other vehicles. Photographic data is invaluable because many doubts concerning the cause for the response of other instrumentation which appear to indicate PIFS are removed and the information extracted from this data can be more conclusive. For example, an increase in heating rate is not usually associated with flow separation (Ref. 11) but, because of the visual evidence, has a very obvious and accepted cause. This subject will be discussed in more detail later.

(U) The extent of flow separation (as determined from the film) in terms of vehicle diameters forward of the exit plane as a function of altitude for AS-501, -502, and -503 is shown in Figure 8. It will be noted that the extent of flow separation for these flights coincide quite well up to an altitude of 136,000 feet when the AS-503 curve drops below the others. This is due to a planned early center engine cutoff (CECO) on AS-503 to limit peak 'g' loads. It is expected that the change in the extent of flow separation resulting from cutoff of one engine will be invaluable in analytical studies of the relationship between PIFS, plume size, and exhaust mass flow rate.

(U) Figure 9 presents the angle between the PIFS region boundary and the vehicle surface, θ_s , as determined from the film for AS-502. The AS-503 film study has not progressed to the point of determining the effects of early CECO on θ_s but, since θ_s changes very little with altitude, the change resulting from early CECO is also expected to be minor.

CORRELATION BETWEEN VISUAL AND ONBOARD INSTRUMENTATION

(U) Visual observations of PIFS on the Saturn V have been substantiated by onboard instrumentation. As shown by Figure 10, surface pressure 0.73 and 0.88 diameters forward of the exit plane suddenly increased with respect to free stream pressure above 80,000 feet. It is well known (Refs. 12,13) that surface pressure starts to increase immediately upstream of the separation point, as shown by Figure 11, and continues to increase downstream of the separation point. The altitude at which PIFS was observed to occur coincides closely with the altitude where the difference between surface and free stream pressure reaches peak values. Six total calorimeters, located on the vehicle at points between 4.47 and 4.62 diameters forward of the exit plane, measure aerodynamic heating rates. At altitudes ranging from 134,500 to 170,000 feet, data from these calorimeters exhibited slope changes and spikes as exemplified by Figure 12.

(U) These increases in local heating rates are attributed to PIFS which, by visual observation, occurred in the area of these calorimeters at an altitude of 167,000 feet.

CORRELATION WITH OTHER FLIGHT AND WIND TUNNEL DATA

(U) As mentioned previously, PIFS has been detected on other vehicles in flight and has been studied using wind tunnel models. Visual observations of PIFS on other vehicles in flight have been primarily qualitative; that is, PIFS either occurred or did not occur. Quantitative information on PIFS for a flight vehicle has been obtained through the use of surface pressure measurements by Alpinieri and Adams (Ref. 3) who subsequently found excellent correlation between flight and wind tunnel data for a given configuration.

(U) The extent of flow separation expressed in vehicle diameters as a function of altitude is presented by Figure 13 for the Saturn I, Saturn V, and an envelope of data from three configurations studied by Adams and Holland (Ref. 2). "Step" increases in flow separation occur when the PIFS region moves beyond the point where vehicle diameter decreases. Once the adverse pressure gradient becomes strong enough to move up to the cone-cylinder juncture, it is often strong enough to move to or beyond the next juncture (if one exists). Since the first diameter change on the Saturn V is 6.65 diameters forward of the exit plane as shown by Figure 13, it does not experience this effect. The Saturn I first stage is made up of a cluster of nine cylindrical tanks which join a larger cylindrical section at a point about 0.8 diameters forward of the engine exit plane. It is evident in Figure 13 that flow separation hardly extends beyond this point. This fact raises the question whether Saturn I flow separation is plume-induced or is the result of the geometry change which may also result in extensive flow

separation as shown by numerous investigators (Refs. 6,7,8). It is evident that the extent of flow separation differs markedly as a function of altitude for various vehicles.

(U) Comparing flight and wind tunnel data, Alpinieri and Adams (Ref. 3) found that excellent correlation existed for a given configuration when correlating the extent of flow separation to the ratio of engine exit plane pressure divided by free stream dynamic pressure (P_j/q_∞). Figure 14 provides a comparison of the data from Alpinieri and Adams, the Saturn V, and the Saturn I when the extent of flow separation is expressed in vehicle diameters as a function of P_j/q_∞ . It is seen that the data from the various vehicles does not compare favorably except for low values of P_j/q_∞ . The sudden increase in separation distance from Alpinieri and Adams is due to geometry changes.

(U) Falanga et al (Ref. 10) have presented flow separation data from wind tunnel tests as a function of P_j divided by free stream static pressure (P_j/P_∞) for five models of slightly different configurations but all having a single nozzle. The crosshatched data band shown by Figure 15 includes all data for zero angle of attack for the configurations tested by Falanga. Saturn V data correlates with this data over a portion of the P_j/P_∞ range. Saturn I data does not correlate with the data from Falanga. This strengthens the belief that Saturn I does not experience PIFS. Wind tunnel tests on a very long, slender model ($L/D = 17.4$) by Hinson and Hoffman (Ref. 4) showed that significant PIFS occurred for values of P_j/P_∞ of 100 and, when $P_j/P_\infty = 200$, the separation region extended 13 diameters forward of the engine exit plane.

(U) In addition to a visual determination of the extent of flow separation during the Saturn V flights, it was also possible to determine the angle which the boundary of the separated flow region makes with the vehicle centerline; θ_s . Figure 16 provides a comparison of Saturn V data with data from Alpinieri and Adams (Ref. 3) and Falanga et al (Ref. 10) as a function of P_j/q_∞ . In this instance correlation is excellent. Hinson and Hoffman (Ref. 4) presented a Schlieren photograph showing PIFS at $M = 6.8$ and $P_j/P_\infty = 200$ from which θ_s was determined to be 7° .

EFFECTS OF PIFS ON STABILITY

(U) The dynamic pressure within a separated region is greatly reduced and, as shown previously, the flow direction in a large portion of a separated region is reversed. Control surfaces, flare-stabilizers, and fins located in a separated region experience loss of effectiveness (Refs. 1,3,4,6,8,9,10,14). PIFS, progressing forward from the aft area of the vehicle, results in the destabilizing effect of moving the center of pressure (CP) forward. However, at an angle of attack flow reattachment

is likely to occur on the windward side of the vehicle while separation increases on the leeward side. Such shifting separation introduces marked nonlinearity in the normal force coefficient (C_n) and center of pressure as functions of angle of attack. Falanga et al (Ref. 10) have studied the effects of varying angle of attack using wind tunnel models. Their conclusion was that, when PIFS exists, flare-stabilized vehicles could exhibit angle of attack limited oscillations. Hinson and Hoffman (Ref. 4) also showed through computer simulation of flight data that PIFS results in non-linearity in aerodynamic coefficients and marked reduction in flare effectiveness at angles of attack below 5° .

(U) Due to the small angles of attack experienced by the Saturn V and considering that this vehicle is aerodynamically unstable, even during the portion of flight when PIFS does not occur, it has been impossible to determine from flight data the destabilizing effects caused by PIFS. (Saturn V stability is controlled by gimballing the four outboard engines). Lowery (Ref. 15) has attempted to determine the effects of PIFS on Saturn V aerodynamics by assuming that the aerodynamic loads are negligible in the area where PIFS has been observed to occur. Examples of these results are shown by Figures 17 and 18 for C_n and CP respectively and are compared with wind tunnel results without PIFS (Ref. 16). Lowery did not account for the changes in the PIFS region on the windward and leeward sides of the vehicle as angle of attack increases; therefore, these results must be considered valid only for extremely small angles of attack. The nonlinearity in C_n resulting from flow reattachment at an angle of attack would be represented by a shift from the lower curve to the upper curve in Figure 17.

(U) Appreciable oscillations in the PIFS region have been visually observed during Saturn V flights; particularly AS-502 (or Apollo 6). A study of these oscillations is now in progress. Current findings reveal that the oscillations are in the 5 to 8 cps range and, when comparing separation extent on opposite sides of the vehicle, are generally not in phase. Maximum peak-to-peak amplitude of the oscillations is about one vehicle diameter. Due to the difference in pressures ahead and behind the separation point, it would be expected that, for time periods when the oscillations were 180° out of phase, appreciable loads in the lateral direction might result. An analysis of flight data from strain gages and accelerometers has shown that these loads, if they do exist, are small. Current plans are to add special instrumentation to the AS-505 vehicle to assist in determining these loads. The origin of these PIFS oscillations is unclear. An examination of the flight angle of attack data revealed no oscillations at these frequencies. The oscillations may be related to the fifth lateral bending mode which is known to have a natural frequency in the 5-8 cps range with a double-amplitude of 0.5 inches at 8.5 diameters. A study by Ericsson and Reding (Ref. 17) has shown the interrelationship of flow separation and vehicle dynamics and that large regions of separated flow are capable of dominating both the static and dynamic characteristics of an elastic vehicle. PIFS oscillations may also be related to thrust oscillations which, on AS-502, were as high as one percent of total vehicle thrust (these thrust oscillations are commonly known as

8th Navy Symposium on Aeroballistics

Vol. 3

the POGO phenomenon (Ref. 18). A direct relationship between PIFS and POGO seems unlikely since PIFS oscillations on opposite sides of the vehicle were generally out of phase.

HEATING EFFECTS

(U) It has been shown that heat transfer rates within a region of separated flow are generally about one-half (Refs. 7,11) that for attached flow. However, heating rates within the Saturn V PIFS region, as determined from thermocouple data, were considerably higher than heating rates for attached flow as shown by Figure 19.

(U) As discussed previously, on the Saturn V the adverse pressure gradient within the PIFS region draws recirculated exhaust gases from the base area forward along the vehicle surface. These gases are believed to be primarily turbopump exhaust products which are injected into the engine exhaust boundary layer to protect the nozzle from overheating. The estimated composition of the gases in the base region is shown by Table I.

(U) TABLE 1 Theoretical S-IC Base Gas Composition
Recirculated GG Exhaust Gas + Air

Species	Mole Fractions and Range Time						
	0 To 40 Sec	80 Sec	100 Sec	120 Sec	130 Sec	140 Sec	150 Sec
A	.00917	.00917	.00255				
CO ₂	.00030	.00030					
H ₂ O	.01598	.01598					
N ₂	.76840	.76814	.21293		.00001	.00001	
O ₂	.20615	.20588					
NO		.00052					
OH		.00001					
CH ₄		.00001	.00001	.00002	.00002	.00003	
C ₂ H ₂		.00002	.00001	.00001			
CO		.27420	.19892	.19892	.19892	.19892	
H		.00025	.00019	.00008	.00003	.00001	
H ₂		.38929	.49387	.49397	.49400	.49400	
H ₂ N		.00121					
C(s) 		.11953	.30697	.30700	.30701		

 (S) Refers to a condensed species

Since PIFS starts at a range time of 105 seconds it is apparent that these gases are fuel rich and without free oxygen.

(U) After flow in the PIFS region turns outboard and rearward the outer portion of the PIFS region mixes with free stream air and burning occurs, as shown by the photographs of Figures 3 through 7. The temperature of the gases drawn into the PIFS region is measured just before the gases leave the base region and, as seen in Figure 20, is considerably below the recovery temperature given by

$$T_r = T_\infty + r \frac{V_\infty^2}{2gJc_p} \quad (1)$$

(U) Since increased heating rates in the PIFS region cannot result from convective heating (excluding unrealistically high heat transfer coefficients which are generally significantly reduced in separated regions (Refs. 7,11) it is concluded that the increases are due to radiation from burning gases in the outer portion of the separated region.

CONCLUSIONS

(U) Once again, the value of the excellent photographic coverage given the Apollo-Saturn V flights has been proven. The PIFS phenomenon - though suspected based on other data - would have been difficult to prove without the photographs.

(U) Visual findings of the extent of PIFS and data from onboard instrumentation closely coincide.

(U) The extent of PIFS is strongly dependent on vehicle geometry thus making PIFS extrapolation from vehicle-to-vehicle impossible.

(U) PIFS has the effect of destabilizing a vehicle by moving the center of pressure forward and introduces marked nonlinearity in normal force coefficients.

(U) Heating rates in the PIFS region may be expected to be lower than for attached flow unless recirculated base region exhaust gases are drawn into the PIFS region and burning occurs as was the case for the Saturn V. Burning of exhaust products in the PIFS region significantly raises heating rates.

(U) Methods for estimating the aerodynamic and heating effects of PIFS for a given configuration without resorting to wind tunnel testing do not exist and are needed.

8th Navy Symposium on Aeroballistics

Vol. 3

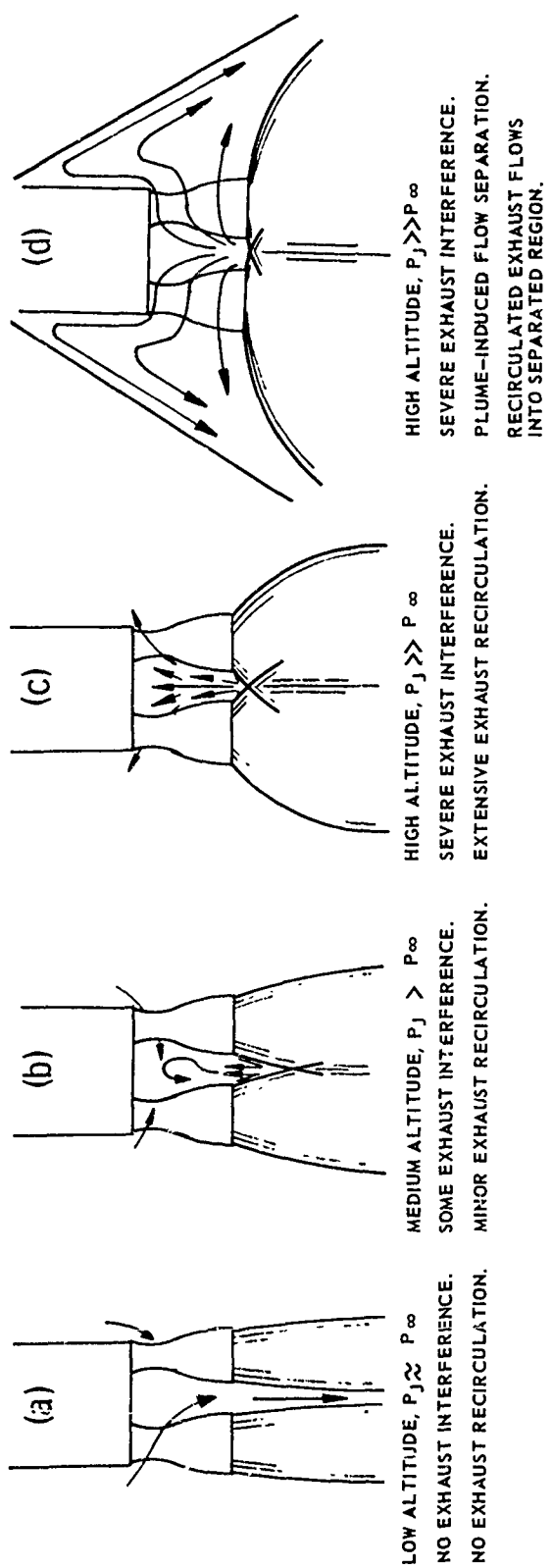
REFERENCES:

- (1) Preliminary Analysis of the Effect of Flow Separation Due to Rocket Jet Pluming on Aircraft Dynamic Stability During Atmospheric Exit (U), by M. Dryer and W. J. North, NASA MEMO 4-22-59E, June 1959, (UNCLASSIFIED)
- (2) Wind Tunnel Investigation of the LID Phenomenon (U), by R. H. Adams and A. C. Holland, AD-369531, December 1965, (CONFIDENTIAL)
- (3) Flow Separation Due to Jet Pluming (U), by L. J. Alpinieri and R. H. Adams, AIAA Journal, October 1966, (UNCLASSIFIED)
- (4) Analysis of Jet-Pluming Interference by Computer Simulation of Measured Flight Motions of Two RAM A Fourth Stages (U), by W. F. Hinson and S. Hoffman, NASA TN D-2018, December 1963, (UNCLASSIFIED)
- (5) S-IC-2 Flight Report (U), by Flight Evaluation Team, Boeing Document T5-7000-2, June 1968, (UNCLASSIFIED)
- (6) The Effects of Boundary Layer Separation Over Bodies of Revolution With Conical Tail Flares (U), by D. H. Dennis, NACA RM A 57130, 1957, (UNCLASSIFIED)
- (7) Heat Transfer and Pressure Distribution at a Mach Number of 6.8 on Bodies With Conical Flares and Extensive Flow Separation (U), by J. V. Becker and P. F. Korycinski, NASA TN D-1260, April 1962, (UNCLASSIFIED)
- (8) Turbulent Separation Associated With Axisymmetric Flared Bodies (U), by T. J. Goldberg, Journal of Spacecraft and Rockets, November 1967, (UNCLASSIFIED)
- (9) Effects of Simulated Rocket - Jet Exhaust on Stability and Control of a Research - Type Airplane Configuration at a Mach Number of 6.86 (U), by D. E. Fetterman, Jr., NASA TMX-127, 1959, (UNCLASSIFIED)
- (10) Exploratory Tests of the Effects of Jet Plumes on the Flow Over Cone-Cylinder-Flare Bodies (U), by R. A. Falanga, W. F. Hinson, and D. H. Crawford, NASA TN D-1000, February 1962, (UNCLASSIFIED)
- (11) A Theoretical Analysis of Heat Transfer in Regions of Separated Flow (U), by Dean R. Chapman, NACA TN3792, October 1956, (UNCLASSIFIED)
- (12) Boundary Layer Theory (U), by H. Schlichting, McGraw-Hill Book Company, Inc., 1955, 4th Edition, (UNCLASSIFIED)
- (13) Flow Separation in High Speed Flight A Review of the State-of-the-Art (U), by J. E. Wuerer, et al, AD 616 236, April 1965, (UNCLASSIFIED)

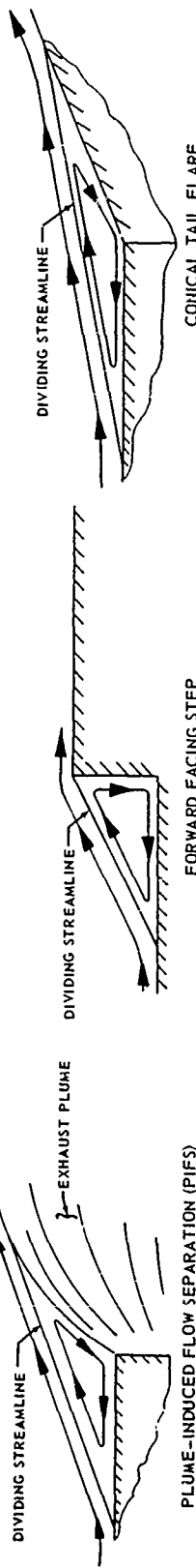
8th Navy Symposium on Aeroballistics

Vol. 3

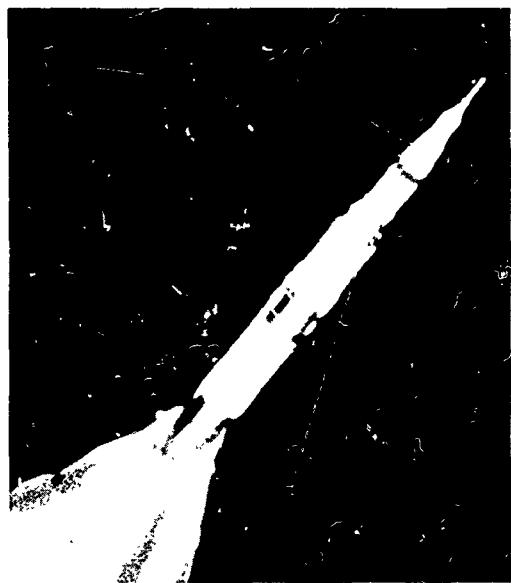
- (14) Rocket Exhaust - Plume Problems and Some Recent Related Research (U), by Allen R. Vick, James M. Cubbage, and Earl H. Andrews, Jr., AGARD Specialist Meeting on Fluid Dynamic Aspects of Space Flight, Gordon and Breach Science Publishers, New York, 1964, (UNCLASSIFIED)
- (15) Effects of Flow Separation on Apollo Saturn V First Stage Aerodynamics (U), by T. J. Lowery, NASA MSFC Memo R-AERO-AD-68-35, June 10, 1968, (UNCLASSIFIED)
- (16) Static Aerodynamic Characteristics of the Apollo-Saturn V Vehicle (U), by Vehicle Aerodynamics Section, NASA TM X-53517, September 16, 1966, (UNCLASSIFIED)
- (17) Analysis of Flow Separation Effect on the Dynamics of a Large Space Booster (U), by Lars-Eric Ericsson and J. Peter Reding, Journal of Spacecraft and Rockets, July-August 1965, (UNCLASSIFIED)
- (18) Saturn V POGO and a Solution (U), by Roy L. Rich, Presented at the AIAA Structural Dynamics and Aeroelasticity Specialists Conference, April 16-17, 1969, (UNCLASSIFIED)



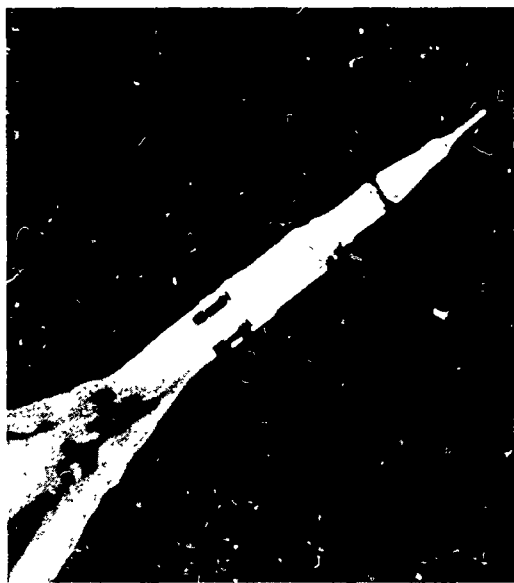
(U) FIG. 1. Exhaust Recirculation and Plume-Induced Flow Separation



(U) FIG. 2. Related Separation Phenomena



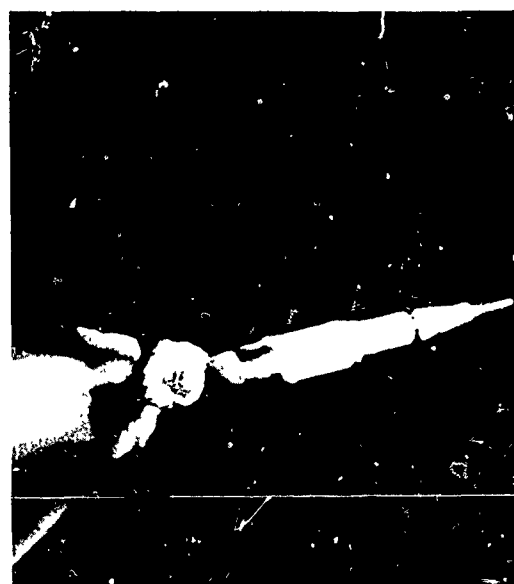
(U) FIG. 3. AS-502, 97,269 Ft.
 $M_\infty = 3.68$, $Ls/D=1.13$



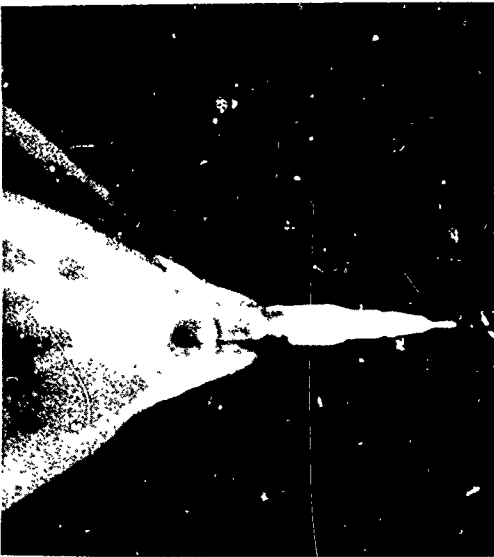
(U) FIG. 4. AS-502, 119,110 Ft.
 $M_\infty=4.42$, $Ls/D=2.69$



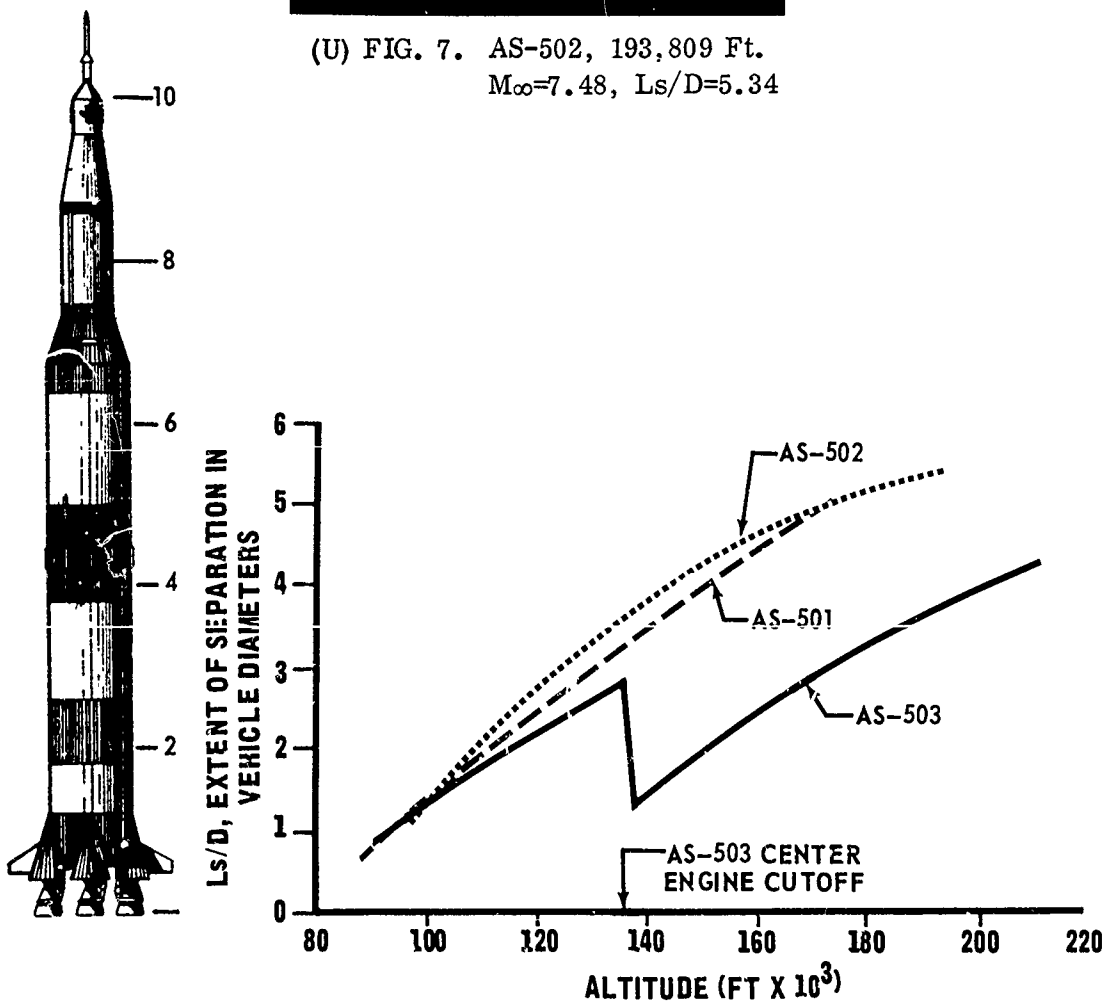
(U) FIG. 5. AS-502, 143,396 Ft.
 $M_\infty=5.18$, $Ls/D=3.96$



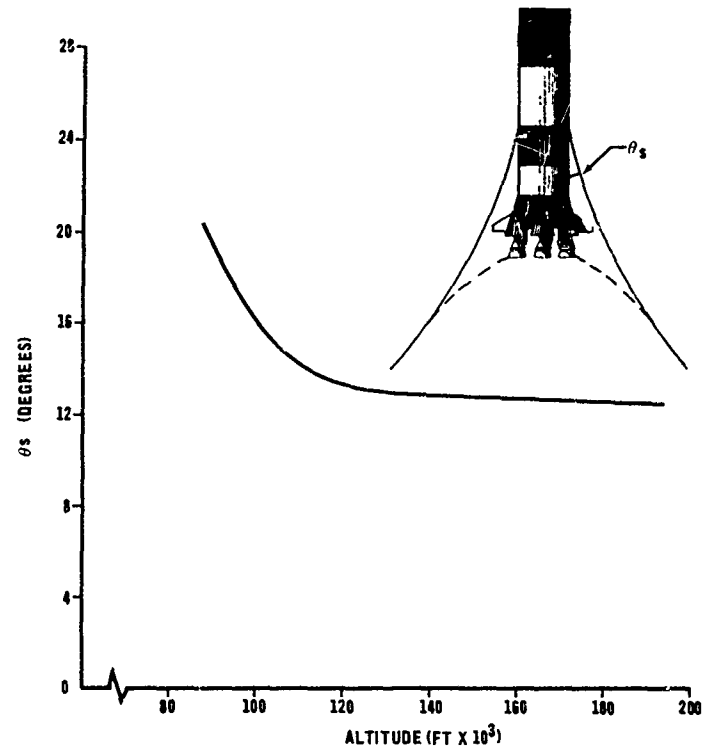
(U) FIG. 6. AS-502, 170,278 Ft.
 $M_\infty=6.28$, $Ls/D=4.90$



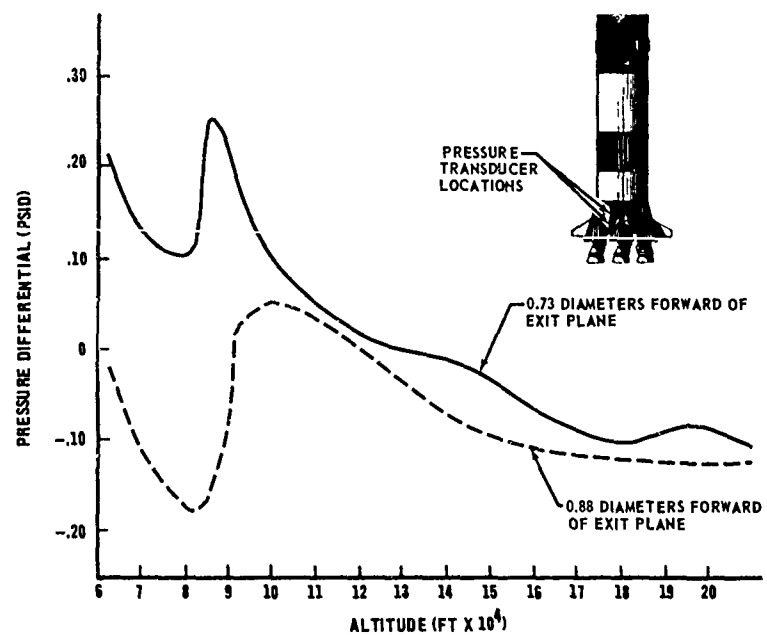
(U) FIG. 7. AS-502, 193,809 Ft.
 $M_\infty=7.48$, $L_s/D=5.34$



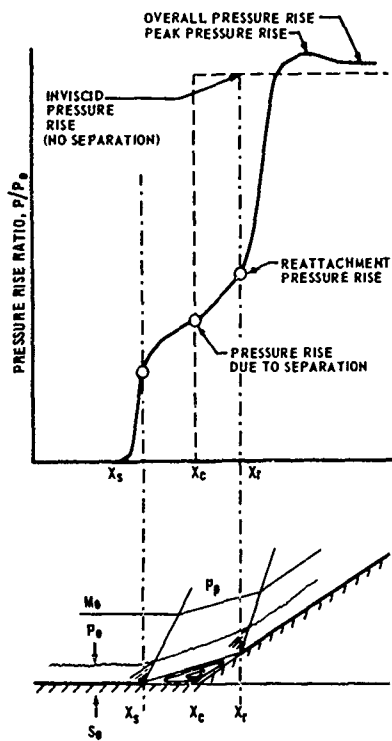
(U) FIG. 8. Saturn V Separation Point Progression with Altitude



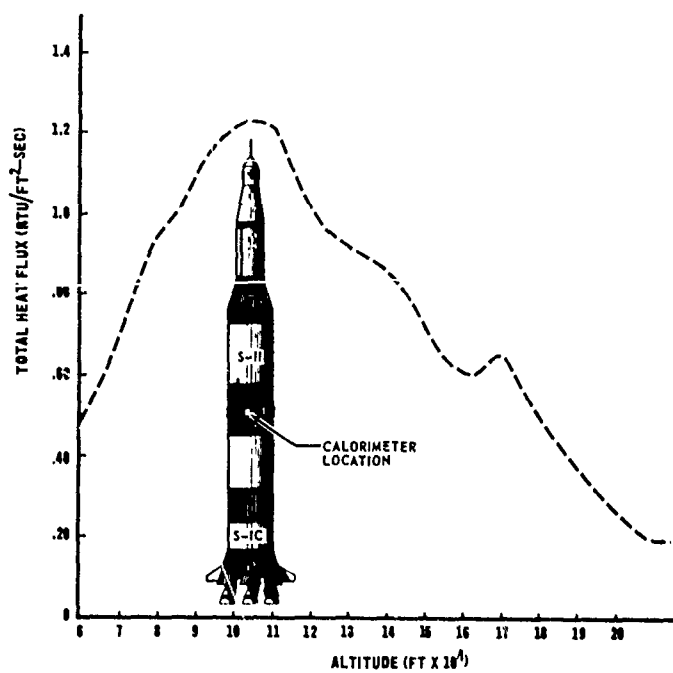
(U) FIG. 9. Angle of Separated Flow Boundary as a Function of Altitude



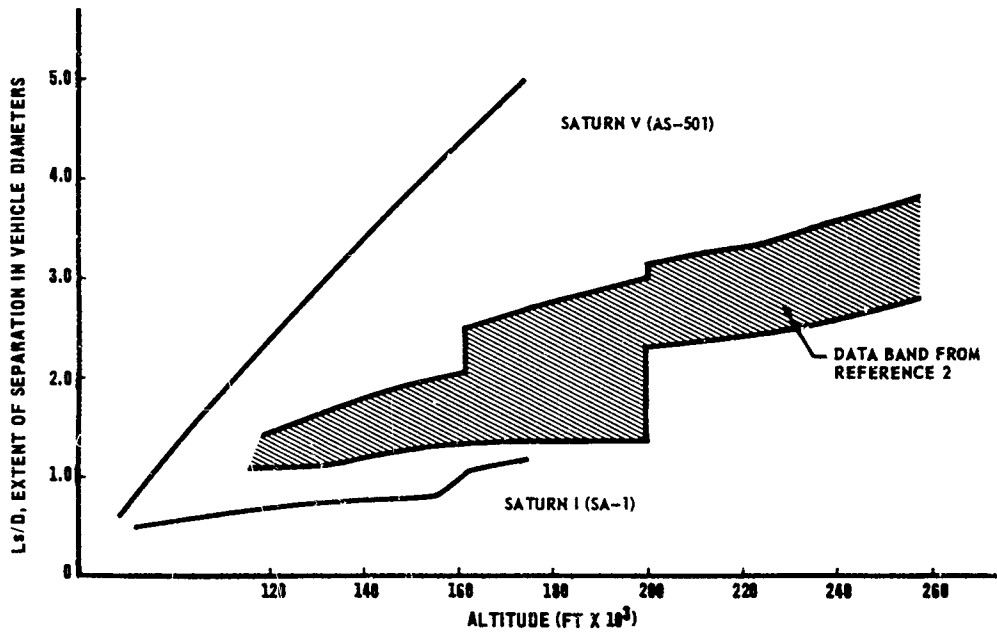
(U) FIG. 10. Differential Between Surface and Free Stream Pressures



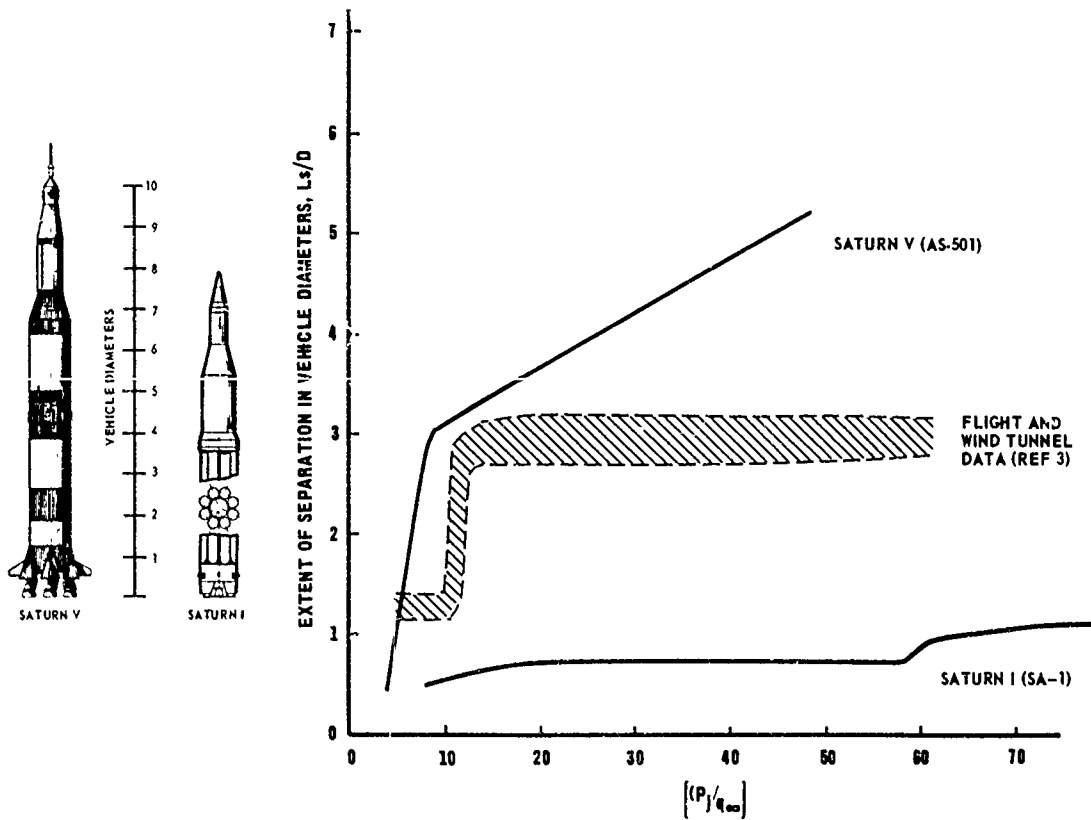
(U) FIG. 11. Wall Pressure Distribution in the Vicinity of Separation, Turbulent Flow



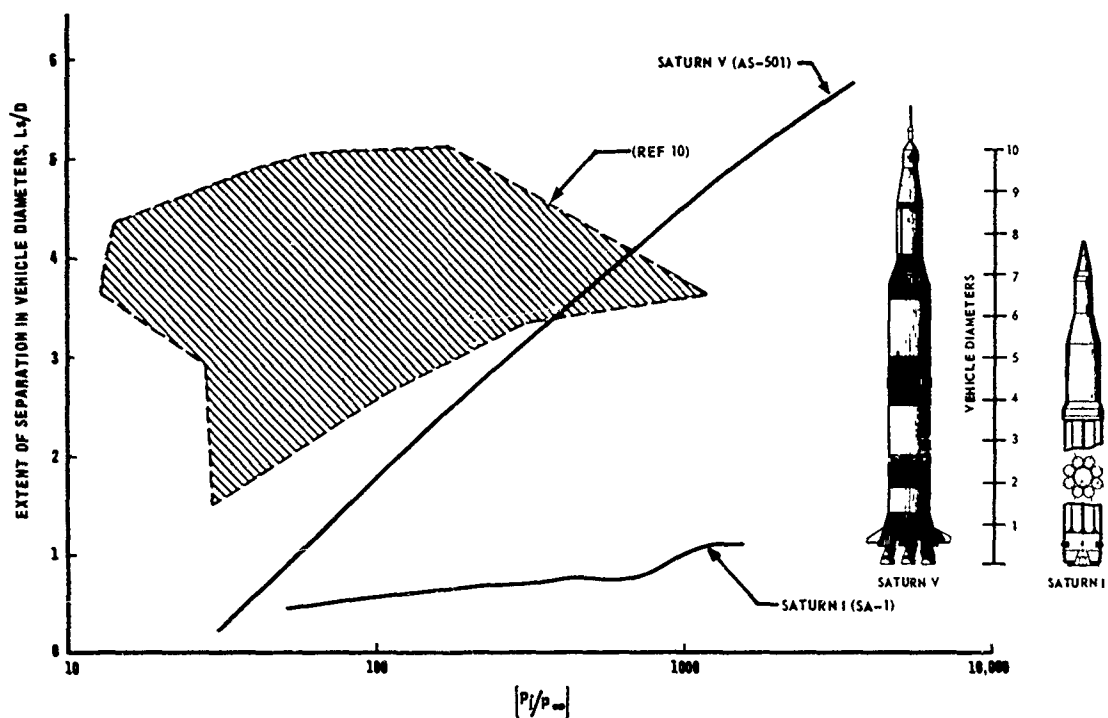
(U) FIG. 12. Typical Total Calorimeter Data



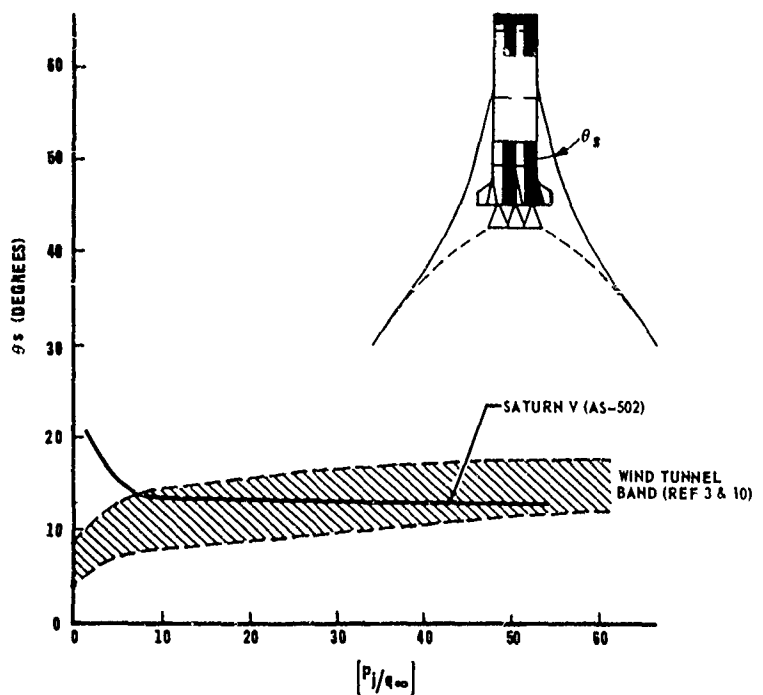
(U) FIG. 13. Separation Point Progression Comparison with Altitude



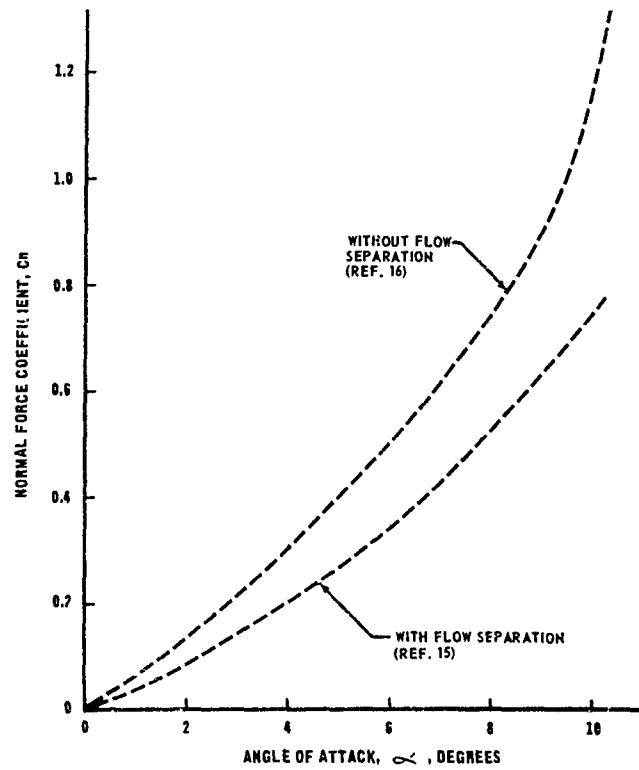
(U) FIG. 14. Separation Point Progression Comparison with P_j/q_∞



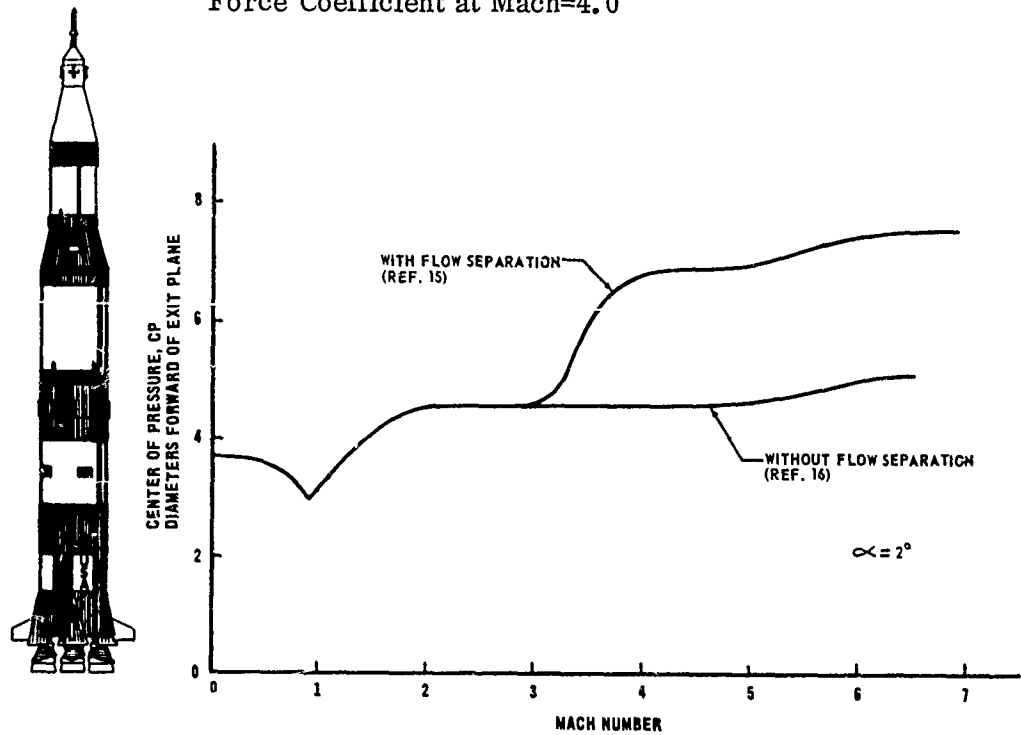
(U) FIG. 15. Separation Point Progression Comparison with P_j/q_∞



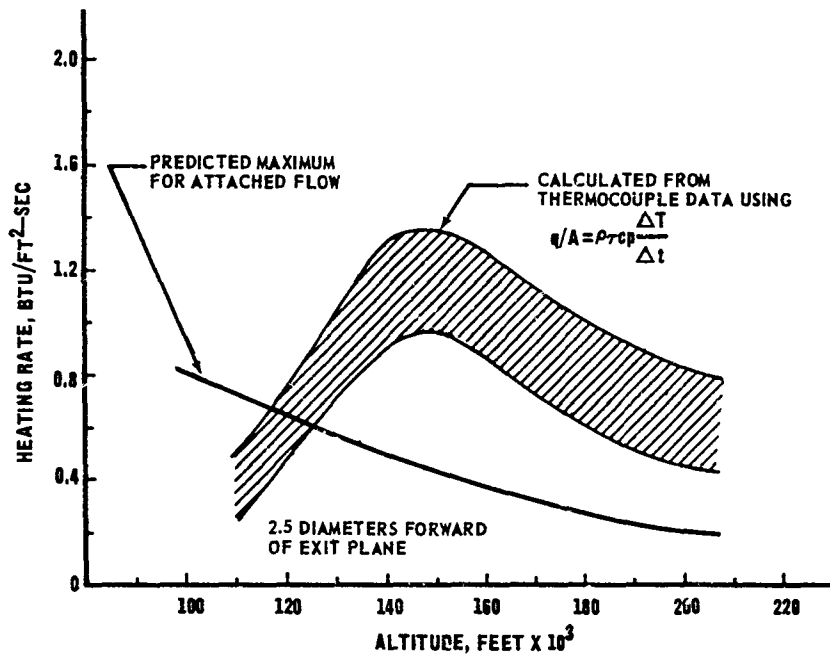
(U) FIG. 16. Angle of the Separated Flow Boundary as a Function of P_j/q



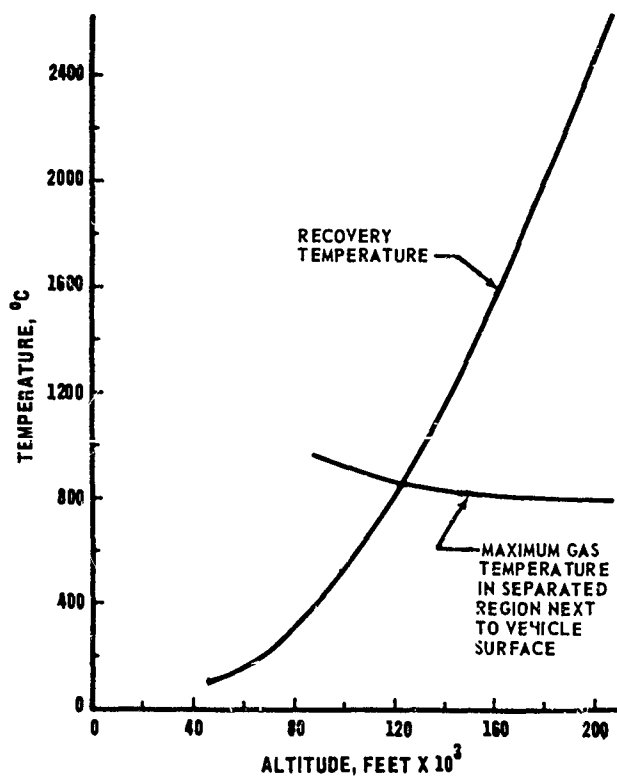
(U) FIG. 17. Effect of Plume-Induced Flow Separation on Saturn V Normal Force Coefficient at Mach=4.0



(U) FIG. 18. Effect of Plume-Induced Separation on Saturn V Center of Pressure



(U) FIG. 19. Heat Flux Comparison for Attached and Separated Flow Regions



(U) FIG. 20. Comparison of Recovery Temperature and Maximum Gas Temperature in Separated Region next to Vehicle Surface

UNCLASSIFIED

Security Classification

DOCUMENT CONTROL DATA - R & D

(Security classification of title, body of abstract and indexing annotation must be entered when the overall report is classified)

1. ORIGINATING ACTIVITY (Corporate author) Naval Weapons Center China Lake, California 93555		2a. REPORT SECURITY CLASSIFICATION UNCLASSIFIED
2b. GROUP		
3. REPORT TITLE PROCEEDINGS OF THE 8TH NAVY SYMPOSIUM ON AEROBALLISTICS. VOLUME 3		
4. DESCRIPTIVE NOTES (Type of report and inclusive dates)		
5. AUTHOR(S) (First name, middle initial, last name)		
6. REPORT DATE June 1969		7a. TOTAL NO. OF PAGES 396
8a. CONTRACT OR GRANT NO		7b. NO. OF REFS 115
b. PROJECT NO		9a. ORIGINATOR'S REPORT NUMBER(S) TS 69-199
c.		9b. OTHER REPORT NO(S) (Any other numbers that may be assigned this report)
d.		
10. DISTRIBUTION STATEMENT THIS DOCUMENT IS SUBJECT TO SPECIAL EXPORT CONTROLS AND EACH TRANSMITTAL TO FOREIGN GOVERNMENTS OR FOREIGN NATIONALS MAY BE MADE ONLY WITH PRIOR APPROVAL OF THE NAVAL WEAPONS CENTER.		
11. SUPPLEMENTARY NOTES		12. SPONSORING MILITARY ACTIVITY Naval Air Systems Command Naval Ordnance Systems Command Naval Material Command Washington, D.C. 20360
13. ABSTRACT		

DD FORM 1473 (PAGE 1)

1 NOV 65
S/N 0101-807-6801

UNCLASSIFIED

Security Classification

UNCLASSIFIED

Security Classification

14 KEY WORDS	LINK A		LINK B		LINK C	
	ROLE	WT	ROLE	WT	ROLE	WT
Aeroballistics Navy Aeroballistics Symposium Aerodynamics Missile Stability Jet Effects Heat Transfer						

DD FORM 1 NOV 1973 (BACK)
(PAGE 2)

UNCLASSIFIED

Security Classification